Science and Technology of Nuclear Installations

Multiphysics Multiscale Coupling Modeling for Nuclear Reactor and Its Uncertainty Quantification

Lead Guest Editor: Tomasz Kozlowski
Guest Editors: Han Zhang, Kostadin Ivanov, and Fu Li

Multiphysics Multiscale Coupling Modeling for Nuclear Reactor and Its Uncertainty Quantification

Science and Technology of Nuclear Installations

Multiphysics Multiscale Coupling Modeling for Nuclear Reactor and Its Uncertainty Quantification

Lead Guest Editor: Tomasz Kozlowski
Guest Editors: Han Zhang, Kostadin Ivanov, and Fu Li

Contents

New Strategies in the Code of Uncertainty and Sensitivity Analysis (CUSA) and Its Application in the Nuclear Reactor Calculation
Jiayu Du, Chen Hao, Ji Ma, Peijun Li, Xiaoyu Zhou, and Lixun Liu
Research Article (16 pages), Article ID 6786394, Volume 2020 (2020)

Perturbation Theory-Based Whole-Core Eigenvalue Sensitivity and Uncertainty (SU) Analysis via a 2D/1D Transport Code
Ji Ma, Chen Hao, Lixun Liu, and Yuekai Zhou
Research Article (13 pages), Article ID 9428580, Volume 2020 (2020)

Hindawi
Science and Technology of Nuclear Installations
Volume 2020, Article ID 8265146, 15 pages
https://doi.org/10.1155/2020/8265146

Research Article

A New Precursor Integral Method for Solving Space-Dependent Kinetic Equations in Neutronic and Thermal-Hydraulic Coupling System

Yingjie Wu, Baokun Liu, Han Zhang, Jiong Guo, Fu Li, Jinlin Niu, Yizhen Wang, and Menglei Cui

Institute of Nuclear and New Energy Technology, Collaborative Innovation Center of Advance Nuclear Energy Technology, Key Laboratory of Advanced Reactor Engineering and Safety of Ministry of Education, Tsinghua University, Beijing 100084, China

Correspondence should be addressed to Han Zhang; han-zhang@tsinghua.edu.cn

Received 14 November 2019; Revised 4 September 2020; Accepted 16 October 2020; Published 3 November 2020

Academic Editor: Iztok Tiselj

The accurate prediction of the neutronic and thermal-hydraulic coupling system transient behavior is important in nuclear reactor safety analysis, where a large-scale nonlinear coupling system with strong stiffness should be solved efficiently. In order to reduce the stiffness and huge computational cost in the coupling system, the high-performance numerical techniques for solving delayed neutron precursor equation are a key issue. In this work, a new precursor integral method with an exponential approximation is proposed and compared with widely used Taylor approximation-based precursor integral methods. The truncation errors of exponential approximation and Taylor approximation are analyzed and compared. Moreover, a time control technique is put forward which is based on flux exponential approximation. The procedure is tested in a 2D neutron kinetic benchmark and a simplified high-temperature gas-cooled reactor-pebble bed module (HTR-PM) multiphysics problem utilizing the efficient Jacobian-free Newton–Krylov method. Results show that selecting appropriate flux approximation in the precursor integral method can improve the efficiency and precision compared with the traditional method. The computation time is reduced to one-ninth in the HTR-PM model under the same accuracy when applying the exponential integral method with the time adaptive technique.

1. Introduction

The reactor is a system involving many physical phenomena, such as neutron kinetics and thermal-hydraulics. Specifically, the neutron flux distribution directly influences the heat release and affects the thermal-hydraulics in the reactor [1]. Hence, the accurate and efficient solution of the neutron field is the first but crucial step for the successful simulation of the whole coupling system and has attracted persistent attention in the field of nuclear reactor safety analysis [2]. The variation of neutron flux and delayed neutron precursor always has a smaller time scale than thermal-hydraulic variables but may lead to a significant change of heat release in the core. For the delayed neutron precursor, six additional equations are usually required to describe its transient behavior, leading to the significantly enhanced scale of the whole neutronic/thermal-hydraulic coupled equation system. Since the delayed neutron precursor equations are only simple ordinary differential equations without the space operator, it could be analytically solved the delayed neutron precursor concentration by integrating their equations over time. As a result, the amounts of precursor concentration variables are eliminated, and the number of unknowns is significantly reduced. The analytical precursor concentrations consist of the integral of neutron flux over time and then eliminate precursor variables in the neutron flux equation. Therefore, the integral of neutron flux overtime should be accurately calculated.

The linear flux hypothesis based on Taylor expansion approximation is widely used to calculate the integral of neutron flux over time [3–6]. A new exponential form flux is

proposed in this work to calculate the integral of neutron flux over time, inspired by the ideas of the stiffness confinement method (SCM) [7] and frequency transform method [8]. The truncation errors of the proposed exponential approximation and Taylor approximation are analyzed and compared. Moreover, since the coefficient of the exponential function reflects the time scale of neutron kinetics, a time step control method is also derived to reduce calculation cost and ensure precision. In order to pursue the high computational performance, an advanced Jacobian-free Newton–Krylov (JFNK) method [9] is employed to solve space-dependent neutron kinetic diffusion equations and the neutronic/thermal-hydraulic coupled system.

The remaining content is organized as follows. In Section 2, the outline of the numerical method for the space-dependent kinetic equations and precursor integral method is introduced. Exponential flux approximation as well as Taylor approximation methods are also derived in this section. Numerical results and discussions with regard to the precursor integral method are given in Section 3, and the simulation results of the exponential flux approximation method with time control are appended. Finally, conclusion remarks are provided in Section 4.

2. Mathematical Background

The mathematical background is presented in this section. In detail, the space-dependent neutron kinetic equations, including a neutron diffusion equation and delayed neutron equations, are described in Section 2.1. The precursor integral method with different approximated expansion methods is presented and discussed in Section 2.2. Expansion functions are employed in this section, including the Taylor series and a new exponential function. Error analysis of both expansion functions is discussed in Section 2.3. An adaptive time step method is proposed through the exponential function. In Section 2.4, an efficient fully implicit algorithm, JFNK, is introduced.

2.1. Space-Dependent Neutron Kinetic Equations. The time-dependent Boltzmann transport equations and time-dependent precursor equations are used to describe the neutron kinetic problems. The equations are as follows:

$$\begin{aligned}\frac{1}{v_g}\frac{\partial\phi_g(r,t)}{\partial t} &= \nabla\cdot D_g(r,t)\nabla\phi_g(r,t) - \Sigma_{t,g}(r,t)\phi_g(r,t)\\ &\quad + \sum_{g'=1}^{G}\Sigma_{s,g'}\longrightarrow{}_g\Phi_g(r,t) + \chi_{p,g}\left(1-\beta_{\text{total}}\right)\\ &\quad\cdot\sum_{g'=1}^{G}\nu\Sigma_{f,g'}(r,t)\phi_g,(r,t) + \sum_{m=1}^{M}\lambda_m\chi_{d,m,g}C_m(r,t),\end{aligned} \tag{1}$$

$$\frac{\partial C_m(r,t)}{\partial t} = \beta_m\sum_{g'=1}^{G}\nu\Sigma_{f,g'}(r,t)\phi_{g'}(r,t) - \lambda_m C_m(r,t). \tag{2}$$

Equation (1) is discretized in space by using the conventional finite difference method. Compared with other truncation errors, the spatial discretization error is treated as high-order term and can be ignored.

To discretize the time derivatives in equations (1) and (2), we invoke the simple first-order approximation as follows:

$$\begin{aligned}\frac{1}{v_g}\frac{\partial}{\partial t}\phi(t) &\approx \frac{\phi(t+\Delta t)-\phi(t)}{v\Delta t} =: \frac{\phi^{(n+1)}-\phi^{(n)}}{v_g\Delta t_n},\\ \frac{\partial}{\partial t}C_m(t) &\approx \frac{C_m(t+\Delta t)-C_m(t)}{\Delta t} =: \frac{C_m^{(n+1)}-C_m^{(n)}}{\Delta t_n}.\end{aligned} \tag{3}$$

In the numerical simulation, the time intervals $t\in[0,T]$ are divided into several intervals from $t_0=0$, and the Δt_n is the time step length for step n. The selection of time step length depends on the accuracy of the time discretization scheme and the dynamic time scale of physical quantities. A suitable time step should be chosen to make a balance between accuracy and efficiency. For the explicit scheme, the time step always suffers from stability limitation. As a result, the time step is usually quite small to satisfy the stability requirement, leading to a relatively large computational cost. Therefore, the fully implicit scheme is used in this work due to its advantage of the unconditional stability [10].

The number of delayed neutron variables is slightly more than the number of multigroup neutron fluxes, and occupies a large part in the solution of the whole system. As shown in equation (2), the precursor concentration is only related to the local neutron fission rate. Therefore, the solution system contains a large number of simple ordinary differential equations. Numerous research studies discussed the numerical solution of equations (1) and (2). The other main problem of these analysis consists in the so-called stiffness of the system [11]. According to Chao's work [7], there is an abrupt turn in neutron flux, reflecting the stiffness characteristic due to the orders of magnitude difference between the time coefficients in equation (4). Stiff differential equations frequently arise in physical situation characterized by the existence of greatly differing time constants [12].

2.2. Precursor Integral Method. As mentioned above, the stiffness and delayed neutron variables make the neutron kinetic problem difficult to solve. The precursor integral method was born to solve the problem. Precursor concentrations are not sensitive to the stiffness of the problem [10]. This phenomenon indicates the possibility of proposing a method to avoid the difficulty of stiffness in evaluation of $C_m^{(n+1)}$ and confine it to that of $\phi^{(n+1)}(\vec{r},g)$. Integrating equation (2) and eliminating variables $C_m^{(n+1)}$ in time-space neutron kinetic equations can effectively reduce stiffness in equations. The precursor concentrations for current time $(n+1)$ are easily derived from the integral:

$$\lambda_m C_m^{(n+1)} = \lambda_m C_m^{(n)} + \beta_m \sum_{g'=1}^{G} \int_{t^n}^{t^{(n+1)}} \nu\Sigma_{fg'}(\vec{r})\phi_{g'}(\vec{r},t). \tag{4}$$

An analytical neutron flux distribution $\phi(\vec{r},g,t)$ is applied to solve the integral, and $C_m^{(n+1)}$ can be solved analytically by integral equation (4). Since precursor concentrations are not sensitive to the stiffness [13], $C_m^{(n+1)}$ is acceptable during simulation. It is noted that $\lambda_m C_m$ is actually a nonlinear term according to equation (4). The key to this method is precisely calculating integral in equation (4). In general, the numerical approximation of the integral term can be realized by using expansion functions.

The precursor integral method has two benefits. One is that the discretized time step can be enlarged because of the decoupling of stiffness due to the elimination of precursor variables. Although the stiffness is still present, the precursor concentration variables are eliminated which is beneficial for efficient solving. Moreover, the solving equations become nonlinear equations because of the existence of nonlinear terms in equation (4).

2.2.1. Taylor Approximation of Neutron Flux. The unknown functions are commonly approximated by Taylor series. Applying expansion to neutron flux at initial of time step t^n,

$$\phi_g(\vec{r},t) = \phi_g(\vec{r},t^n) + \dot{\phi}_g(\vec{r},t^n)(t-t^n) + o(t^2). \tag{5}$$

Considering the zero-order and first-order expansions of neutron flux, equation (4) can be rewritten as

$$\lambda_m C_m^{(n+1)}(\vec{r}) = e^{-\lambda_m(t^{n+1}-t^n)}\left\{\lambda_m C_m^n(\vec{r}) + \beta_m \int_{t^n}^{t^{n+1}} \mathrm{d}t' \sum_{g'=1}^{G} \nu\Sigma_{f,g'}\left[\phi_g(\vec{r},t^n) + \dot{\phi}_g(\vec{r},t^n)(t'-t^n)\right]\lambda_m e^{\lambda_m(t'-t^n)}\right\}. \tag{6}$$

Solving the integral is difficult because of the time derivate term. When applying implicit scheme, the term can be approximated by forward difference:

$$\dot{\phi}_g(\vec{r},t^n) = \frac{\phi_g\left(r,t^{(n+1)}\right) - \phi_g(r,t^n)}{t^{(n+1)} - t^n}. \tag{7}$$

Integrate equation (6) in time $t^n \le t \le t^{(n+1)}$:

$$\begin{aligned}\lambda_m C_m^{(n+1)} = {} & \beta_m \sum_{g'=1}^{G} \nu\Sigma_{f,g'}\phi_{g'}\left(t^{n+1}\right) + \left(\lambda_m C_m^n - \beta_m \sum_{g'=1}^{G} \nu\Sigma_{f,g'}\phi_{g'}(t^n)\right)e^{-\lambda_m(t^{n+1}-t^n)} \\ & - \beta_m \sum_{g'=1}^{G} \nu\Sigma_{f,g'} \frac{\phi_{g'}\left(t^{n+1}\right) - \phi_{g'}(t^n)}{\lambda_m\left(t^{n+1}-t^n\right)}\left(1 - e^{-\lambda_m(t^{n+1}-t^n)}\right).\end{aligned} \tag{8}$$

Precursor concentrations can be analytically acquired through neutron flux expansion. If zero-order neutron flux Taylor expansion is used in equation (5), we can obtain

$$\lambda_m C_m^{(n+1)} = e^{-\lambda_m\left(t^{(n+1)}-t^n\right)}\left\{\lambda_m C_m^n + \beta_m \sum_{g'=1}^{G} \nu\Sigma_{f,g'}\phi_{g'}(t^n)\left[e^{\lambda_m\left(t^{(n+1)}-t^n\right)} - 1\right]\right\}. \tag{9}$$

2.2.2. Exponential Approximation of Neutron Flux. As mentioned above, flux approximation technique is a key to the precursor integral method. The same as the precursor integral method, precursor concentration is analytical acquired utilizing trial functions. Inspired by the idea of the SCM method, the neutron kinetic frequency is defined:

$$w_g(\vec{r},t) \equiv \frac{\partial}{\partial t}\ln\left(\phi_g(\vec{r},t)\right). \tag{10}$$

Without considering the feedback effect, equations (1) and (2) are first-order linear differential equation with constant coefficients. The time characteristics of neutron flux are usually in exponential form. Since the neutron flux changes from the beginning of the time step ϕ^n, it is assumed that its solution at current time step is

$$\tilde{\phi}_g(\vec{r},t) = \hat{\phi}_g(r,t)\exp\left(w_g(\vec{r},t-t^n)(t-t^n)\right). \tag{11}$$

The coefficient preceding the exponential functions is the weak time-dependent part of neutron flux. Supposing this part is flat flux distribution in the time step, we have

$$\hat{\phi}_g(\vec{r},t) = \hat{\phi}_g(\vec{r},t^n) = \phi_g(\vec{r},t^n). \tag{12}$$

The frequency $w_g(\vec{r},t-t^n)$ used in equation (11) still has time dependence, which can be difficult to handle in the implicit method. Therefore, an approximation is used, which is the average value in time step:

$$\overline{w}_g(\vec{r}) = \frac{\ln\left(\phi_g\left(r,t^{n+1}\right)/\phi_g\left(r,t^n\right)\right)}{t^{n+1}-t^n}. \tag{13}$$

Substitute equation (11) into equation (4), and integral on time $t^n \le t \le t^{(n+1)}$:

$$\lambda_m C_m = e^{-\lambda_m\left(t^{n+1}-t^n\right)}\left\{\lambda_m C_m^n + \sum_{g'=1}^{G} \nu\Sigma_{f,g'}\lambda_m\beta_m\phi_{g'}(\vec{r},t^n)\frac{1}{\overline{w}_g(\vec{r})+\lambda_m}\left[e^{\left[\overline{w}_g(\vec{r})+\lambda_m\right](t'-t^n)}-1\right]\right\}. \tag{14}$$

By substituting the formula into the transient neutron diffusion equation, the neutron space-time kinetic problem can be completely solved. Because the average frequency $\overline{w}_g(\vec{r})$ contains variables at the current time $\phi^{(n+1)}$, it should be emphasized that each iteration average frequency $\overline{w}_g(\vec{r})$ must be updated.

2.3. Truncation Error Analysis. In this section, the precision of flux approximation and time discretization are analyzed within the context of a neutron kinetic problem. The partial differential equations (PDEs) are defined in the above section, and here, we discuss the origin of truncation error.

Equation (1) can be rewritten as

$$\frac{\mathrm{d}\vec{\phi}(t)}{\mathrm{d}t} = A(t)\vec{\phi}(t). \tag{15}$$

Two types of time discretization are discussed in this work:

A first-order accurate method (backward Euler):

$$\frac{\vec{\phi}^{n+1}-\vec{\phi}^{n}}{\Delta t} = \mathbf{A}^{n+1}\vec{\phi}^{n+1}. \tag{16}$$

A second-order accurate method (Crank–Nicolson):

$$\frac{\vec{\phi}^{n+1}-\vec{\phi}^{n}}{\Delta t} = \frac{1}{2}\left(\mathrm{A}^{n+1}\vec{\phi}^{n+1}+\mathrm{A}^{n}\vec{\phi}^{n}\right). \tag{17}$$

A truncated Taylor series will help to reveal the appearance of time discretization errors, for example,

$$\phi^n = \phi^{n+1} - \Delta t\dot{\phi}^{n+1} + \frac{\Delta t^2}{2}\ddot{\phi}^{n+1} - \frac{\Delta t^3}{6}\dddot{\phi}^{n+1} + O\left(\Delta t^4\right). \tag{18}$$

We use the simplified notation $\dot{\phi} \equiv (\mathrm{d}\phi/\mathrm{d}t)$.It is understood that any time integration method can fail to maintain its designed or asymptotic, convergence rate if the time step is too large. The truncation error in the expansion would become dominant and could not be omitted when time is roughly discretized.

The truncation errors for different time discretization schemes are derived.

Backward Euler:

$$\left[\frac{\mathrm{d}\vec{\phi}(t)}{\mathrm{d}t} - \mathbf{A}(t)\vec{\phi}(t)\right]^{n+1} = \frac{\Delta t}{2}\frac{\mathrm{d}^2\phi}{\mathrm{d}t^2} + O\left(\Delta t^2\right). \tag{19}$$

Crank–Nicolson:

$$\left[\frac{\mathrm{d}\vec{\phi}(t)}{\mathrm{d}t} - \mathbf{A}(t)\vec{\phi}(t)\right]^{n+1} = \frac{\Delta t^2}{12}\frac{\mathrm{d}^3\phi}{\mathrm{d}t^3} + o\left(\Delta t^3\right). \tag{20}$$

There is a nonlinear term in integral precursor equation:

$$C_m^{(n+1)} = \frac{1}{\Delta t_n}C_m^{(n)} + \beta_m\sum_{g'=1}^{G}\nu\Sigma_f(\vec{r},g')\phi_g^{(n+1)}. \tag{21}$$

As mentioned earlier, the nonlinear terms are linearized by different neutron flux approximation methods. Hence, the truncation error occurs and depends on the level of linearization. When adopting the backward Euler method, the truncation error is

$$\left[\frac{\mathrm{d}\vec{\phi}(t)}{\mathrm{d}t} - \mathbf{A}(t)\vec{\phi}(t)\right]^{n+1} = \frac{\Delta t}{2}\frac{\mathrm{d}^2\phi}{\mathrm{d}t^2} + \lambda_m \in (C_m) + o\left(\Delta t^2\right). \tag{22}$$

It can be seen from equation (22) when applying flux approximation that an additional truncation error is involved. The higher-order flux approximations permit accurate precursor concentration as well as smaller truncation error. As demonstrated above, the error is introduced by the deviation between neutron flux approximation $\phi(\vec{r},t')$ and actual value $\phi(\vec{r},t')$ in the integrals. The truncation error of C_m is

$$\in (C_m) = e^{-\lambda_m\left(t^{n+1}-t^n\right)}\beta_m\int_{t^n}^{t}\mathrm{d}t'\sum_{g'=1}^{G}\nu\Sigma_{f,g'}\left[\phi(\vec{r},t') - \phi(\widetilde{\vec{r},t'})\right]\lambda_m e^{\lambda_m(t'-t^n)}, \tag{23}$$

and when using zero-order Taylor approximation, the truncation error is

$$\in_{\text{zero-order Taylor}}(C_m) = e^{-\lambda_m(\Delta t)}\beta_m \int_0^{\Delta t} \mathrm{d}\Delta t' \sum_{g'=1}^{G} \nu \sum_{f,g'} \lambda_m e^{\lambda_m \Delta t'} \left[\dot{\phi}(t^n)\Delta t' + \frac{1}{2}\ddot{\phi}(t^n)\Delta t'^2 + o\left(\Delta t'^3\right)\right]. \tag{24}$$

Here, $\Delta t, t^n$ stands for length of time step and last time point, respectively. Utilizing the integral characteristics of exponential function, the truncation error introduced by zero-order Taylor neutron flux approximation is

$$\in_{\text{zero-order Taylor}}(C_m) = \beta_m \sum_{g'=1}^{G} \nu \sum_{f,g'} \dot{\phi}(t^n)\Delta t + o\left(\Delta t^2\right). \tag{25}$$

After similar derivation, the truncation error of the first-order Taylor approximation can be obtained:

$$\in_{\text{first-order Taylor}}(C_m) = \frac{1}{2}\beta_m \sum_{g'=1}^{G} \nu \sum_{f,g'} \ddot{\phi}(t^n)\Delta t^2 + o\left(\Delta t^3\right). \tag{26}$$

Replaced by exponential expansion, the actual neutron flux is expanded by Taylor series:

$$\in_{\text{exponential}}(C_m) = e^{-\lambda_m(\Delta t)}\beta_m \int_0^{\Delta t} \mathrm{d}\Delta t' \sum_{g'=1}^{G} \nu\Sigma_{f,g'}\lambda_m e^{\lambda_m \Delta t'} \left[\left(\dot{\phi}(t^n) - \phi(t^n)\omega\right)\Delta t' + \frac{1}{2}\left(\ddot{\phi}(t^n) - \phi(t^n)\omega^2\right)\Delta t'^2 + o\left(\Delta t'^3\right)\right]. \tag{27}$$

Substituting ω by equation (13) gives

$$\phi(t^n)\omega = \frac{\phi(t^n)\ln\left(\phi^{(n+1)}/\phi^n\right)}{\Delta t} = \frac{\phi^{(n+1)} - \phi^n}{\Delta t} = \phi(\dot{t}^n), \tag{28}$$

$$\phi(\ddot{t}^n) - \phi(t^n)\omega^2 \approx \frac{\dot{\phi}^{(n+1)}\phi^{(n-1)} - \dot{\phi}^n\phi^n}{\Delta t\phi^n}. \tag{29}$$

Bring equations (28) and (29) into equation (31) and the truncation error can be analyzed according to above results:

$$\in_{\text{zero-order Taylor}}(C_m) \gg \in_{\text{first-order Taylor}}(C_m) \,\&\, \in_{\text{exponential}}(C_m). \tag{30}$$

Two kinds of truncation errors are discussed in this section, time discretization error and flux approximation error, receptively. Each truncation error is a function of time step Δt, which means that the selection of time step will affect errors in varying degrees. For the flux approximation method, exponential and first-order Taylor expansion will provide high-order precision. Therefore, the focus of our work is to analyze and compare the accuracy and efficiency of two approximation methods.

2.4. Time Step Control Method in Exponential Approximation. Time step control method is widely used in neutron program as described in SPANDEX [14]. It is almost impossible to predict the truncation error accurately in neutron kinetic calculations, especially for the implicitly discretized diffusion equation. Within the tolerance of introduced truncation error, we proposed an adaptive time step method to reduce computational cost as much as possible.

The adaptive time step method assumes an exponential time dependence in neutron flux, which is identical with exponential approximation in the precursor integral method. Applying backward Euler time discretization and fully implicit formulation in neutron kinetic equations,

$$\frac{\partial\phi}{\partial t} = \omega\phi \longrightarrow \frac{\phi^{(n+1)} - \phi^{(n)}}{\Delta t_n} = \omega\phi^{(n+1)}, \tag{31}$$

Equation assumes an exponential time dependence $e^{\omega t}$ in neutron flux. This is feasible since the neutron flux can be expressed as a series of exponential functions in the point reactor neutron dynamic method. After a sufficient time, the solution will be dominated by asymptotic period $T \equiv s_0^{-1}$ (s_0 is the least negative root). At that time, ω is equal to s_0^{-1}. Two forms of neutron flux expression can be obtained by exponential expansion and variable derivation:

$$\phi(t + \Delta t) = \phi(t)\exp(\omega\Delta t) \approx \phi(t)\left(1 + \omega\Delta t + \frac{1}{2!}\omega^2\Delta t^2 + O\left(\Delta t^3\right)\right),$$
$$\phi^{(n+1)} = \phi^{(n)}\frac{1}{1 - \omega\Delta t_n} \approx \phi^{(n)}\left(1 + \omega\Delta t_n + \omega^2\Delta t_n^2 + O\left(\Delta t_n^3\right)\right). \tag{32}$$

The truncation error $\in$ of neutron flux is

$$\in = \phi(t)\frac{1}{2}\omega^2\Delta t^2 + O\left(\Delta t^3\right). \tag{33}$$

The value of relative power is important in validation of transient neutron kinetic cases. The estimated time step is derived in which relative power error $\in_{\text{power}}$ is taken into account:

$$\epsilon_{\text{power}} = \frac{\sum_g \sum_V \phi(\vec{r}, g)\nu\Sigma_f (1/2)\omega(\vec{r}, g)^2 \Delta t^2}{\sum_g \sum_V \phi(\vec{r}, t)\nu\Sigma_f}, \quad (34)$$

$$\Delta t = \left(\frac{\sum_g \sum_V \phi(\vec{r}, g)\nu\Sigma_f \epsilon_{\text{power}}}{\sum_g \sum_V \phi(\vec{r}, t)\nu\Sigma_f (1/2)\omega(\vec{r}, g)^2} \right)^{1/2}. \quad (35)$$

For the selection of $\omega(\vec{r}, g)$, the average frequency in Section 2.2.2 is a good estimation which describes the dynamic changes in neutron flux. In order to make the estimation more conservative, it is often helpful to multiply an empirical coefficient η_{em} in equation (35).

Equation (34) analytically constructs a roughly estimation of truncation error. Even though the truncation error is obtained through numerous approximations and based on several assumptions, it can reflect the order of magnitude about relative power error. Equation (35) gives the length of time steps given an expected truncation error. Different from traditional time control strategy which utilizes dynamic time scale and empirical functions, this new adaptive time step method could select time step on the basis of expectant precision. Meanwhile, this method could work with exponential expansion in the precursor integral method.

2.5. JFNK Method. Implicit formulations are well-suited to maintain the asymptotic balance in complex multiple time-scale problems, because all relevant terms in the partial differential equation (PDE) system can be approximated at the same time level [8]. However, implicit algorithms usually are related to nonlinear PDEs and require nonlinear solver. The residual equations $\vec{F}(\vec{x}) = 0$ obtained from discretization of the nonlinear system are used in the Jacobian-free Newton–Krylov method. The nonlinear terms are solved using a Newton–Modified equation, which requires inverting the Jacobian system $J_m \delta\vec{x_m} = -\vec{F}(\vec{x_m})$, where $J_m = (\partial\vec{F}/\partial\vec{x_m})$ is so-called Jacobian matrix. The updated scheme is $\vec{x_{m+1}} = \vec{x_m} + \delta\vec{x_m}$, and the iteration proceeds until $|\vec{F}(\vec{x_{m+1}})| < \varepsilon_a + \varepsilon_r |\vec{F}(\vec{x_0})|$. Here, ϵ_a and ϵ_r are an absolute and a relative tolerance, respectively. The inversion is performed iteratively using Krylov methods [15] (typically, GMRES), which could be facilitated by a Jacobian-free implementation and preconditioner. The Jacobian-free scheme uses the finite difference approach to approximate the matrix-vector production without building the Jacobian matrix explicitly. The preconditioner is based on reformulating the Jacobian system as $\mathrm{J}P^{-1}P\delta\vec{x} = \vec{F}$ (right preconditioning), where P^{-1} approximates the inversed Jacobian matrix, and it should be computational inexpensive.

3. Analysis and Computational Results

3.1. Implementation. In order to verify the efficient of the precursor integral method and compare the different flux approximation methods in integral, especially the exponential form, we have developed the space-dependent neutron kinetic solver based on diffusion theory and the multigroup approximation. In the kinetic solver, the finite volume method is used for spatial discretization. Note that implicit scheme is applied in our work and can achieve stability with the expense of increased computational cost. The main sources of two truncation errors, i.e., truncation error in time discretization and delayed neutron integral technique, are analyzed in space-dependent neutronic kinetic calculation. In the previous section, we demonstrated that flux approximations may have a significant impact on the accuracy of a numerical scheme. The precursor integral method is tested with the above flux approximation method and the results are compared with those obtained from other methods. At the same time, the importance of two kinds of truncation errors is compared. A time control method is implemented in HTR-PM transient, and the result of CPU time is shown compared with the fixed time step method. The problems include step reactivity insertion and ramp input. In the following section, the examples are described separately.

For solving partial differential equations with nonlinear term, the preconditioned JFNK method is the core of the algorithm. An efficient physic-based preconditioning method is implemented in this solver, and we use incomplete LU factorization to obtain the inverse of preconditioning matrix.

3.2. TWIGL Benchmark. TWIGL seed-blanket reactor kinetic benchmark is implemented as a verification calculation to confirm the performance of the precursor integral method for the space-dependent kinetic equations. Two reactivity insertion cases are included in the TWIGL benchmark problem [16]. The original TWIGL bench problem consists of a two-dimensional core, as shown in Figure 1, and material properties are shown in Table 1.

In addition, the spatial mesh widths for x and y directions are $\Delta x = 1\,\text{cm}$ and $\Delta y = 1\,\text{cm}$ in the configurations. The performance of each method is evaluated by relative power.

3.2.1. Reactivity Insert Cases. Accurate calculate neutron relative power is essential in neutron kinetic problems, which needs to properly simulate the changes in neutron flux and precursor concentration. The relative power is given by

$$P_{\text{RelativePower}} = \frac{P_{\text{CurrentPower}}}{P_{\text{InitialPower}}}. \quad (36)$$

Reactivity introduction is one of the most classical neutron dynamic problems. The TWIGL benchmark provides two ways of reactivity introduction. The first case simulates a step reactivity insertion in a thermal reactor without extern neutron source. In this case, $\sum_{a,2}(t) = \sum_{a,2}(0) - 0.0035\,(t = 0.0s)$. The other reactivity input model which has linear reactivity function of time (the ramp input) is considered. This ramp reactivity takes the form $\sum_{a,2}(t) = \sum_{a,2}(0) \times (1 - 0.11667t)\,(t \le 0.2s)$. Numerical simulations

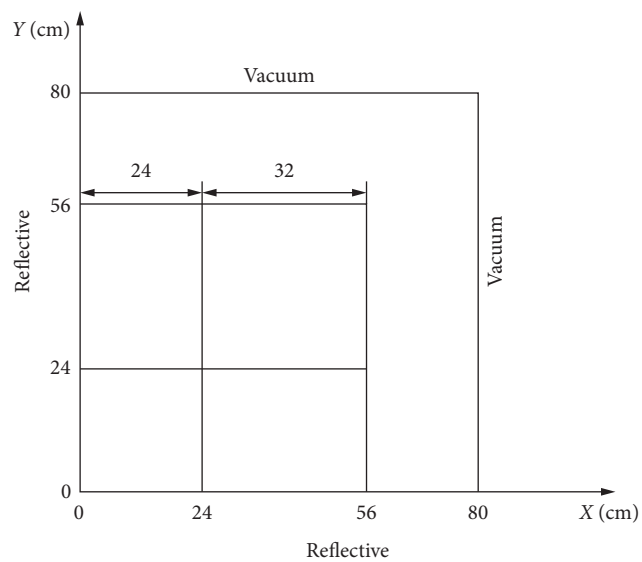

Figure 1: TWIGL benchmark.

Table 1: Material parameters in TWIGL benchmark problem.

Material	Group	D (cm)	$\sum_a$ (cm)	$\nu\sum_f$ (cm)	χ	$\Sigma_{s,g\to1}$	$\Sigma_{s,g\to2}$
1	1	1.4	0.010	0.007	1.0	0.0	0.01
	2	0.4	0.150	0.200	0.0	0.0	0.00
2	1	1.4	0.010	0.007	1.0	0.0	0.01
	2	0.4	0.150	0.200	0.0	0.0	0.00
3	1	1.3	0.008	0.003	1.0	0.0	0.01
	2	0.5	0.050	0.060	0.0	0.0	0.00

were performed for three precursor treatments: independent variable, Taylor expansion approximation, and exponential expansion approximation. Backward Euler time discretization is applied in these case and time steps are selected as 10 ms and 20 ms. Five reference points are selected in the following tables.

From Tables 2 and 3, the results indicate the following:

(1) Compared with the method which treats precursor concentrations as independent variables, the neutron precursor integral method is superior in terms of the accuracy, but an appropriate neutron flux approximation should be employed in analytical precursor concentration expression.

(2) The results of ramp reactivity are not as accurate as those of step reactivity with the same time step length. This suggests that the length of time step should be changed for considering different ways of reactivity insertion.

(3) Different flux approximations in the precursor integral method introduce truncation errors of different sizes. Higher-order flux approximations decrease the error of the results by a magnitude.

(4) The exponential approximation gives the most accurate result among precursor integral methods in step reactivity insertion. As mentioned above, first-order Taylor and exponential approximations generate second-order time precision, and the result of these methods shows good accuracy.

The above simulations of reactivity introduction problems test relative power changes in a period with the same time step. This suggests that a shorter time step size is necessary for accurate simulation. The influence of time step selection on simulation accuracy is also a problem that needs to be paid attention. Considering different time step selections among simulations, a time period of 0 ~ 50 ms in these two reactivity input cases is chosen. Because of the lack of reference solution, the result of the independent precursor variable method of minimum time step is chosen as base solution. The numerical results are shown in Tables 4 and 5.

It can be seen that all methods produce larger truncation errors as time step increases from Tables 4 and 5, which is due to the fact that the expression with truncation error contains the time step term Δt. A time step length greater than 10 ms simulates relative power error close to 10%. Considering the efficiency and accuracy of the calculation, the time step used for subsequent calculation is 10ms.

Previous simulations have compared several different precursor integral methods using different flux approximate methods and different length of time steps. This part focuses on the influence of time discretization on the calculation accuracy, and thus, the Crank–Nicolson method and backward Euler method are applied in simulations. The

Table 2: Comparison of relative power (percentage error) between independent precursor methods and precursor integral methods for step reactivity insertion.

t (s)	Δt (ms)	Reference	Independent variables	Zero-order Taylor expansion	First-order Taylor expansion	Exponential expansion
0.0	—	1.00000	1.00000	1.00000	1.00000	1.00000
0.1	10.0	2.06156	2.06046 ($-5.3e-2$)	2.05874 ($-1.4e-1$)	2.05960 ($-9.5e-2$)	2.05963 ($-9.3e-2$)
	20.0	—	2.05693 ($-2.2e-1$)	2.05355 ($-3.9e-1$)	2.05524 ($-3.1e-1$)	2.05526 ($-3.0e-1$)
0.2	10.0	2.07887	2.07888 ($-4.8e-4$)	2.07712 ($-8.4e-2$)	2.07800 ($-4.1e-2$)	2.07803 ($-4.0e-1$)
	20.0	—	2.07888 ($-4.8e-4$)	2.07535 ($-1.7e-1$)	2.07712 ($-8.4e-2$)	2.07714 ($-8.3e-2$)
0.3	10.0	2.09625	2.09627 ($+9.5e-4$)	2.09447 ($-8.5e-2$)	2.09538 ($-4.2e-2$)	2.09541 ($-4.0e-2$)
	20.0	—	2.09630 ($+2.4e-3$)	2.09270 ($-1.7e-1$)	2.09451 ($-8.3e-2$)	2.09453 ($-8.2e-2$)
0.4	10.0	2.11378	2.11381 ($+1.4e-3$)	2.11197 ($-8.6e-2$)	2.11290 ($-4.1e-2$)	2.11293 ($-4.0e-2$)
	20.0	—	2.11384 ($+2.8e-3$)	2.11017 ($-1.7e-1$)	2.11203 ($-8.2e-2$)	2.11205 ($-8.1e-2$)
0.5	10.0	2.13146	2.13150 ($+1.8e-3$)	2.12962 ($-8.6e-2$)	2.13057 ($-4.1e-2$)	2.13060 ($-4.0e-2$)
	20.0	—	2.13153 ($+3.3e-3$)	2.12779 ($-1.7e-2$)	2.12969 ($-8.3e-2$)	2.12971 ($-8.2e-2$)

Table 3: Comparison of relative power (percentage error) between independent precursor methods and precursor elimination methods for ramp reactivity insertion.

t (s)	Δt (ms)	Reference	Independent variables	Zero-order Taylor expansion	First-order Taylor expansion	Exponential expansion
0.0	—	1.00000	1.00000	1.00000	1.00000	1.00000
0.1	10.0	1.30832	1.30935 ($-7.9e-2$)	1.30906 ($-5.6e-2$)	1.30921 ($-6.7e-2$)	1.30922 ($-6.8e-2$)
	20.0	—	1.31036 ($-1.5e-1$)	1.30977 ($-1.1e-1$)	1.31007 ($-1.3e-1$)	1.31009 ($-1.3e-1$)
0.2	10.0	1.95908	1.96410 ($+2.6e-1$)	1.96273 ($+1.8e-1$)	1.96342 ($+2.3e-1$)	1.96346 ($+2.2e-1$)
	20.0	—	1.96842 ($+4.7e-1$)	1.96564 ($+3.3e-1$)	1.96704 ($+4.1e-1$)	1.96712 ($+4.1e-1$)
0.3	10.0	2.07503	2.07578 ($+3.6e-2$)	2.07403 ($-4.8e-2$)	2.07491 ($-5.6e-3$)	2.07496 ($-3.1e-3$)
	20.0	—	2.07636 ($-6.4e-1$)	2.07286 ($-1.0e-1$)	2.07462 ($-1.9e-2$)	2.07472 ($-1.5e-2$)
0.4	10.0	2.09239	2.09326 ($+4.1e-2$)	2.09147 ($-4.4e-2$)	2.09237 ($-8.1e-4$)	2.09242 ($+1.6e-3$)
	20.0	—	2.09416 ($+8.4e-2$)	2.09058 ($-8.6e-2$)	2.09238 ($-1.9e-4$)	2.09248 ($+4.3e-3$)
0.5	10.0	2.10988	2.11077 ($+4.1e-2$)	2.10894 ($-4.4e-2$)	2.10987 ($-8.0e-4$)	2.10992 ($+1.7e-3$)
	20.0	—	2.11169 ($+8.5e-2$)	2.10803 ($-8.7e-2$)	2.10988 ($-9.7e-5$)	2.10998 ($+4.4e-3$)

Table 4: TWIGL relative power transient reference problem step reactivity insertion at 50 ms.

t (ms)	Independent variables	Zero-order Taylor expansion	First-order Taylor expansion	Exponential expansion
0.1	2.044782	2.044766 ($-7.82e-4$)	2.044775 ($-3.42e-4$)	2.044777 ($-2.44e-4$)
1	2.042971	2.042809 ($-9.64e-4$)	2.042890 ($-9.25e-2$)	2.042896 ($-9.22e-2$)
10	2.018193	2.016678 ($-1.37e0$)	2.017436 ($-1.34e0$)	2.017459 ($-1.33e0$)
50	1.875968	1.870072 ($-8.54e0$)	1.872973 ($-8.41e0$)	1.873018 ($-8.40e0$)

Table 5: TWIGL relative power transient reference problem ramp reactivity insertion at 50 ms.

t (ms)	Independent variables	Zero-order Taylor expansion	First-order Taylor expansion	Exponential expansion
0.1	1.124625	1.124624 ($-8.89e-5$)	1.124624 ($-8.89e-5$)	1.124624 ($-8.89e-5$)
1	1.124676	1.124571 ($-4.80e-3$)	1.124583 ($-3.73e-3$)	1.124683 ($-3.73e-3$)
10	1.125223	1.124158 ($-4.15e-2$)	1.124174 ($-4.01e-2$)	1.124179 ($-3.96e-2$)
50	1.128223	1.121703 ($-2.59e-1$)	1.121963 ($-2.36e-2$)	1.121985 ($-2.34e-2$)

relative power errors of two reactivity insertion cases are investigated with $\Delta t = 10$ ms.

The numerical results of the simulations are shown in Figure 2. It can be observed that the numerical result from the low-order method (backward Euler) provides large truncation error compared with the high-order method (Crank–Nicolson). Also from Figure 2, it can be observed that the error of the low-order time discretization method is relatively large in the time of reactivity introduction, due to the fact that backward Euler scheme cannot accurately represent the violent change of neutron flux. However, when neutron reaction rate is stable, the relative error of the method will be less. It is also important to point out that the higher-order time discretization scheme has the most significant effect on the reduction of relative error.

A computational efficiency study was also performed in these two reactivity insertion cases. The computation time which treats the precursor as independent variables is much larger than the precursor integral method. This is due to an overlarge solution vector dimension used in the independent variable method causes high computation cost, and this will result in too much inner iterations. Figure 3 shows that the decrease in time step causes exponential CPU time rise. Crank–Nicolson scheme does not bring too much

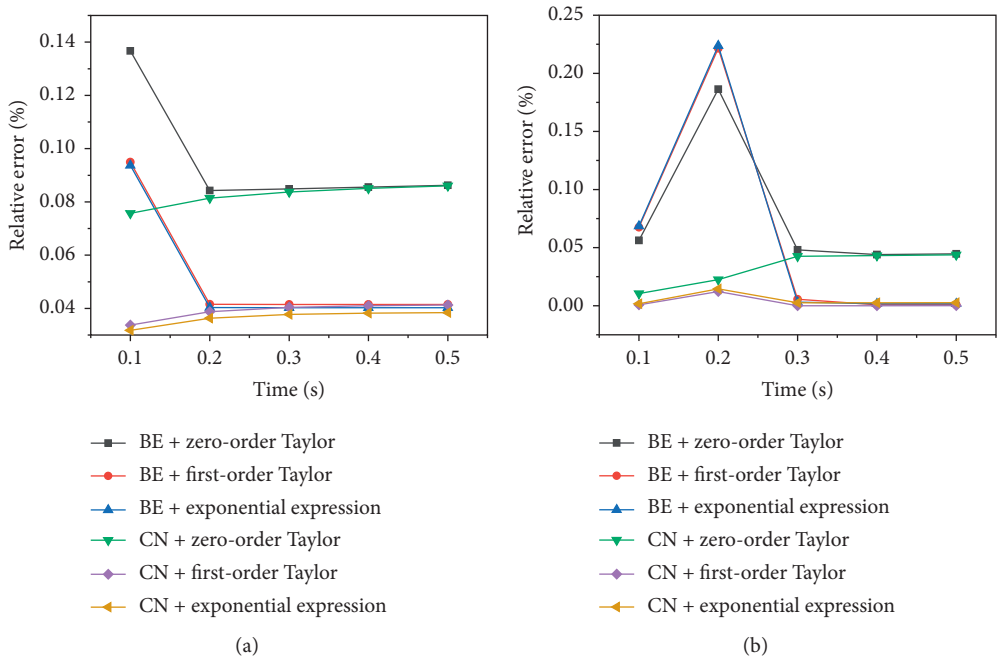

Figure 2: Relative power error of TWIGL reactivity insertion problem in $\Delta t = 10$ ms.

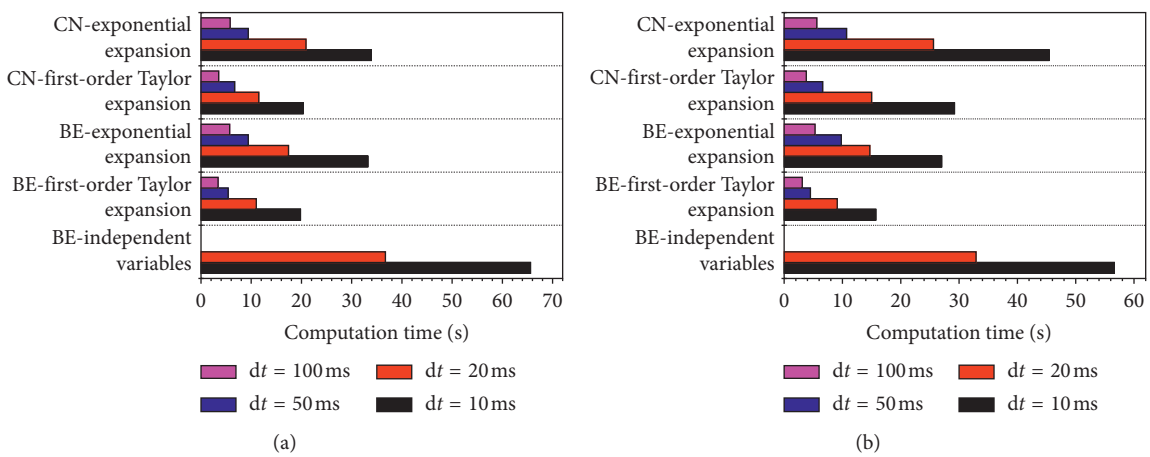

Figure 3: Relative power error of TWIGL reactivity insertion problem in $\Delta t = 10$ ms.

computational burden compared with backward Euler scheme, and this is mainly because the difference of two methods is only whether they inherit the previous time step's information. The precursor integral method with exponential flux approximation shows robustness and a relatively high computational efficiency for the numerical simulations of TWIGL neutron kinetic problems.

3.3. HTR-PM Model. In the previous section, the precursor integral method is proved to be of higher accuracy, less computing time, and memory storage than any other methods. In addition, the first-order Taylor approximation and exponential approximation methods could still maintain a high accuracy even at a larger time step. The selection of time step depends on the dynamical time scale and characteristic of the nonlinear system. Some special numerical characteristics could occur when coupling neutron with thermal-hydraulic [1].

The high-temperature gas-cooled reactor-pebble bed module (HTR-PM), which is under construction in Shidao Bay, Shandong Province, consists of two nuclear modules, and one shared steam turbine [17]. Each module contains its own reactor core, helical coiled one-through steam generator, helium turbine, and vertical pipes. The flowing helium is heated from 250°C to 750°C in the reactor region, where many complex phenomena related to the neutron physics and thermal-hydraulics exist [18]. Therefore, the present modeling mainly focuses on these issues, especially the solution of neutron and physical quantities affecting the precursors significantly. In terms of the algorithm, the JFNK method is employed to solve this multiphysics nonlinear problem.

Table 6: Six sets of delayed neutron precursor parameters.

Group	1	2	3	4	5	6
β	$4.9588e-4$	$3.0678e-3$	$2.6332e-3$	$5.4992e-2$	$1.8051e-3$	$3.5614e-4$
$\lambda\,(s^{-1})$	$1.2729e-2$	$3.1470e-2$	$1.1841e-1$	$3.1652e-1$	$1.4092e0$	$3.7677e0$

3.3.1. Reactor Physics Model. There are many elements including pebble bed, reflector, carbon bricks, and helium flow region in the HTM reactor model. The artificial homogenization sections generated by the dedicated nuclear physics software V.S.O.P [19] are used to characterize different material composition. The neutron energy is divided into four energy groups. The reactor core is modeled as a two-dimensional region in r-z coordinate, in which the left boundary is treated as a symmetric boundary, while the remained boundaries are considered as vacuum boundaries. In the solution, the cross-sections are updated according to the temperature field from thermal-hydraulic calculation [20]:

$$\begin{aligned}\Sigma_g &= B_1 + B_2 \cdot \sqrt{T_s + 50} + B_3 \cdot (T_s + 50) \\ &\quad + B_4 \cdot T_s + B_5 \cdot (T_s)^2,\end{aligned} \tag{37}$$

where T_s is solid (pebble bed area and reflector) temperature, B_1, B_2, B_3, B_4, and B_5 are constant coefficients.

Four-group diffusion equations are used to solve neutron flux. Six sets of delayed neutron precursor are considered in neutron kinetic simulation. Decay constant and delayed neutron portion are shown in Table 6.

3.3.2. Thermal-Hydraulic Model. In the thermal-hydraulic model, the HTR-PM core is divided into 7 regions, such as pebble bed, gas plenums in the top, and bottom reflectors. These regions are characterized by different materials. The properties of these materials and some other constitutive relations for thermal-hydraulic calculation are obtained from KTA safety standards [21] and the simplified version of empirical correlations in TINTE [22]. As to the numerical technique, the finite difference method is employed to discretize the governing equations with regard to the thermal-hydraulic quantities and neutron physics quantities on the same grid.

Solid temperature equation:

$$\begin{aligned}&\frac{\partial}{\partial t}(1-\varepsilon)\rho c T_s - \left(\frac{1}{r}\frac{\partial}{\partial r} r\left(\lambda_{s,\mathrm{eff}}\frac{\partial}{\partial r}\right) + \frac{\partial}{\partial z}\left(\lambda_{s,\mathrm{eff}}\frac{\partial}{\partial z}\right)\right)T_s \\ &\quad - q + \alpha\left(T_s - T_f\right) = 0.\end{aligned} \tag{38}$$

Fluid temperature equation:

$$\begin{aligned}&\frac{\partial}{\partial t}\varepsilon\rho_f c_p T_f - \left(\frac{1}{r}\frac{\partial}{\partial r} r\left(\lambda_{f,\mathrm{eff}}\frac{\partial}{\partial r}\right) + \frac{\partial}{\partial z}\left(\lambda_{f,\mathrm{eff}}\frac{\partial}{\partial z}\right)\right)T_f \\ &\quad + \left(\frac{1}{r}\frac{\partial}{\partial r} r\mu_r + \frac{\partial}{\partial z}\mu_z\right)c_p T_f + \alpha\left(T_f - T_s\right) = 0.\end{aligned} \tag{39}$$

Mass flux equation:

$$\begin{aligned}\mu_r &= -\frac{1}{W}\frac{\partial}{\partial r}p, \\ \mu_z &= -\frac{1}{W}\left(\frac{\partial}{\partial z}p - \rho g\right),\end{aligned} \tag{40}$$

where T_s, T_f, and p are solid temperature, fluid temperature, and pressure, respectively, μ_r and μ_z are mass fluxes, λ_s, λ_f, α, C_p, and ε are solid effective thermal conductivity coefficient, fluid effective thermal conductivity coefficient, convective heat transfer coefficient, fluid heat capacity, and porosity, and W, ρ, and g are resistance factor, density, and acceleration of gravity, respectively.

The coolant channel model in HTR-PM is simplified into one dimension because the diameter of the tube is rather small. General design parameters are shown in Table 7.

Table 7: Design parameters of the HTR-PM.

Parameters	Design value
Reactor power (MWt)	250×2
Inlet helium temperature (°C)	250
Outlet helium temperature (°C)	750
Helium mass flow rate (kg/s)	96
Helium pressure of primary loop (MPa)	7.0

3.3.3. Numerical Result. As stated previously, the solution of thermal-hydraulic field and neutron physics field in the HTR-PM reactor model is performed on the same spatial mesh shown in Figure 4. This nonuniform mesh is constructed following the high-temperature gas-cooled reactor safety analysis program TINTE, which is verified in the design and analysis of HTR-PM.

A transient case is investigated in this paper. By amplifying the fission cross-section at the steady state, a positive reactivity $\rho = 0.31595$ is introduced into the HTR-PM reactor core model. The time duration of this transient is 0.8 s. Compared with the simulation results at the steady state shown in Figure 5, it is observed that this transient leads to a significant change to the solid temperature, fluid temperature field, outlet temperature of the core, and power in the core, as shown in the figure. Figure 6.

In this transient, the total power of the reactor has increased to 1.6 times within 0.8 s. The power approaches an almost steady value at the end of this transient, indicating the reactor does not reach the prompt criticality.

Three methods, namely, zero-order Taylor expansion, first-order Taylor expansion, and exponential expansion are employed to approximate the flux in the precursor integral method, where two time steps, i.e., $\Delta t = 100$ ms and 10 ms, under a backward Euler time discretization scheme are adopted to solve this transient problem. The comparisons of

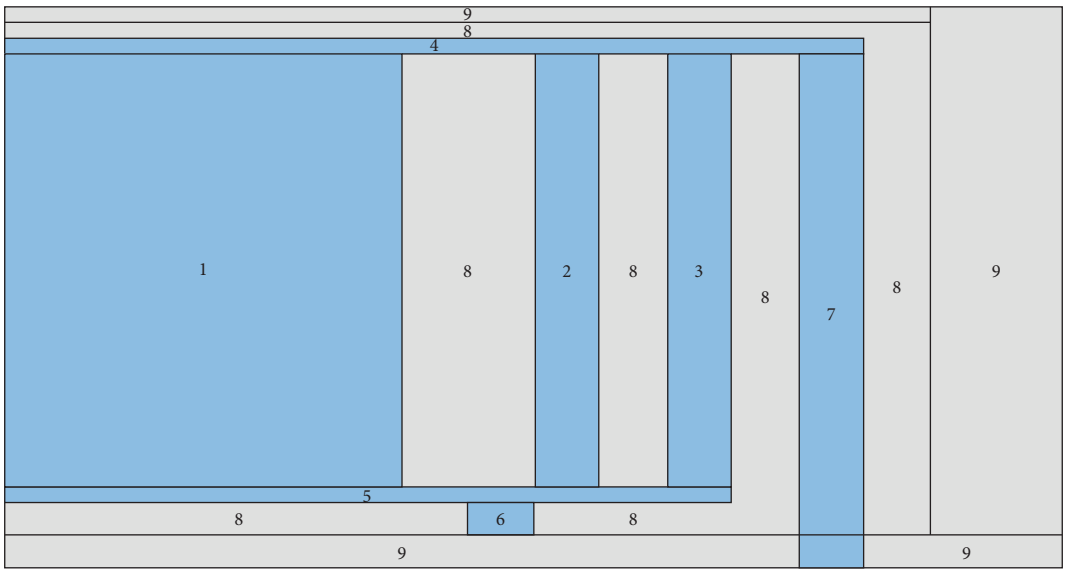

Figure 4: Simplified computation model for the HTR-PM. Blue area represents the flow region, and the gray area represents the solid region. (1) Pebble-bed core; (2) control rod channel; (3) simulated leakage flow; (4) cold helium plenum; (5) hot helium plenum; (6) core outlet; (7) helium gap; (8) side reflector; (9) carbon brick.

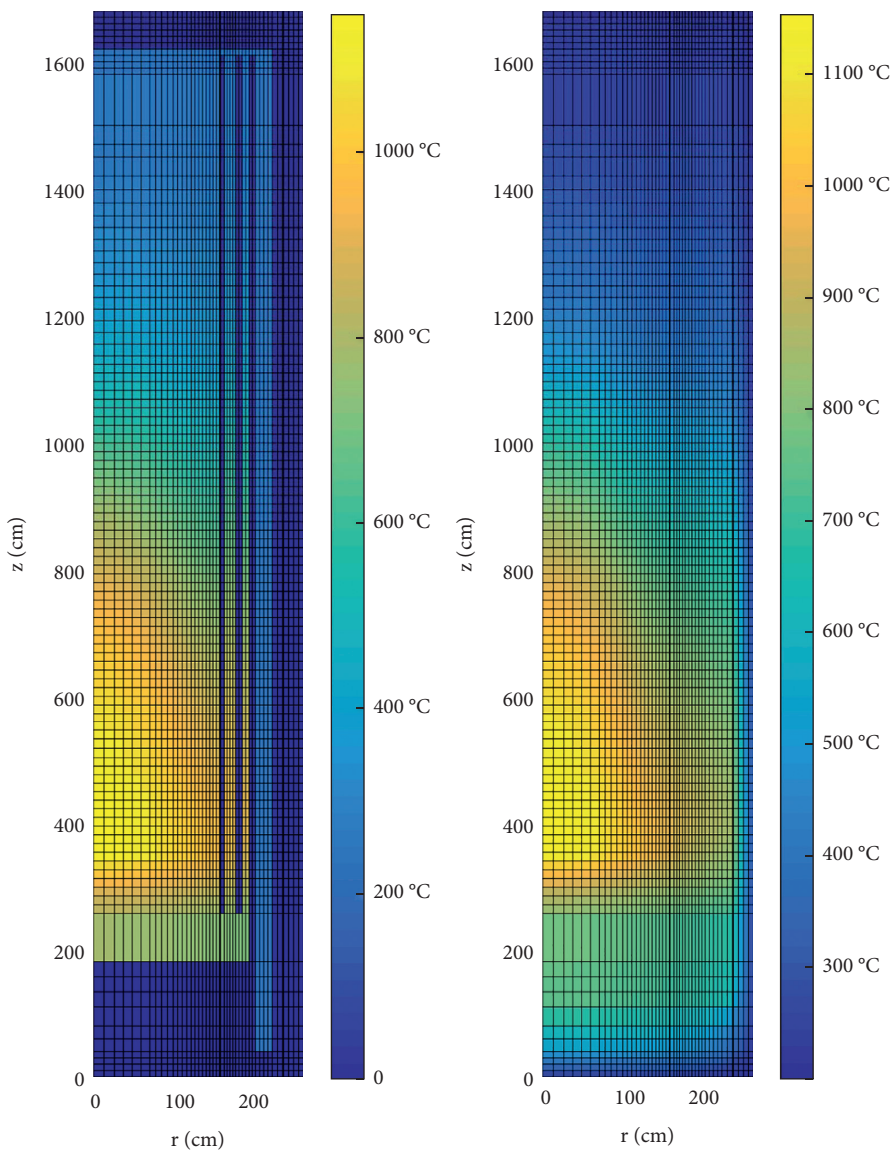

Figure 5: Simplified HTR-PM model fluid temperature and solid temperature in steady state.

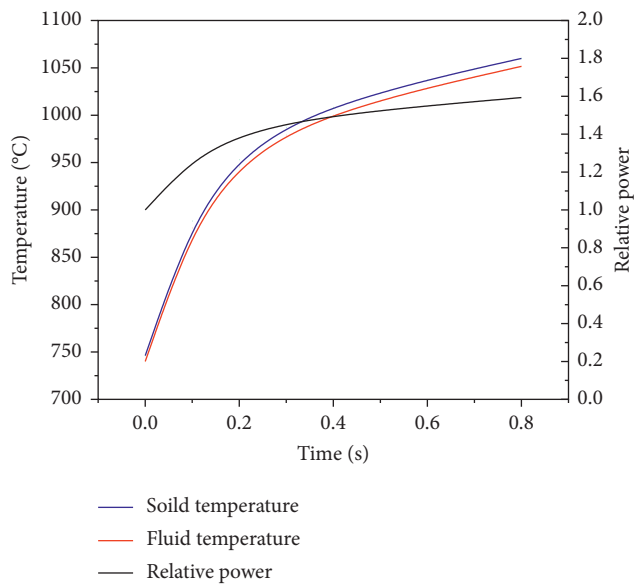

Figure 6: HTR-PM transient relative power and outlet temperature change in 0.8 s.

Table 8: Comparison among flux approximations in the precursor integral method for HTR-PM reactivity insertion in $\Delta t = 100$ ms.

t (s)	Δt (s)	Independent variables $\Delta t = 0.1$ ms	Zero-order Taylor expansion	First-order Taylor expansion	Exponential expansion
0.0	—	1.00000	1.00000	1.00000	1.00000
0.1	100.0	1.26681	1.21258 (−4.28e0)	1.21549 (−4.05e0)	1.21559 (−4.04e0)
—	10.0	—	1.25987 (−5.47e − 1)	1.26017 (−5.24e − 1)	1.26134 (−4.32e − 1)
0.2	100.0	1.38952	1.33279 (−4.08e0)	1.33866 (−3.66e0)	1.33883 (−3.64e0)
—	10.0	—	1.38296 (−4.72e − 1)	1.38363 (−4.23e−1)	1.38424 (−3.79e − 1)
0.3	100.0	1.45391	1.40613 (−3.28e0)	1.41429 (−2.72e0)	1.41449 (−2.71e0)
—	10.0	—	1.44884 (−3.48e − 1)	1.44977 (−2.85e − 1)	1.44978 (−2.84e − 1)
0.4	100.0	1.49410	1.45511 (−2.60e0)	1.46484 (−1.95e0)	1.46507 (−1.94e0)
—	10.0	—	1.49020 (−2.61e − 1)	1.49129 (−1.88e − 1)	1.49129 (−1.88e − 1)
0.5	100.0	1.52388	1.49118 (−2.14e0)	1.50196 (−1.43e0)	1.50220 (−1.42e0)
-	10.0	—	1.52071 (−2.08e−1)	1.52188 (−1.31e − 1)	1.52189 (1.30e − 1)
0.6	100.0	1.54891	1.52024 (−1.85e0)	1.53172 (−1.10e0)	1.53195 (−1.08e0)
—	10.0	—	1.54615 (−1.78e − 1)	1.54738 (−9.87e − 2)	1.54738 (−9.87e − 2)
0.7	100.0	1.57157	1.54533 (−1.66e0)	1.55731 (−9.07e − 1)	1.55754 (−8.92e − 1)
—	10.0	—	1.56903 (−1.61e − 1)	1.57029 (−8.14e − 2)	1.57029 (−8.14e − 2)
0.8	100.0	1.59289	1.56809 (−1.55e0)	1.57029 (−8.14e − 2)	1.58066 (−7.67e − 1)
—	10.0	—	1.59046 (−1.52e − 1)	1.59175 (−7.15e − 2)	1.59175 (−7.15e − 2)

the results are shown in Table 8. In these two tables, the reference result is derived from a case which treats precursors as independent variables and uses a rather small time step $\Delta t = 0.1$ ms. From Table 8, it is observed that all methods lead to a well-agreed result to the reference solution, which is due to these three approximations of $\lambda_m C_m$ are all accurate. However, for a larger time step, the result derived from zero-order Taylor expansion deviates a lot from the reference solution because of excessive truncation error, which is shown in Table 8. In addition, it is also found that the results from two higher-order approximations of neutron flux, viz, first-order Taylor expansion and exponential expansion are almost identical. Therefore, it is concluded that these two methods are more stable and qualitatively correct than the zero-order Taylor approximation.

To evaluate the effect of time discretization on the solution, another scheme, i.e., Crank–Nicolson, is also employed. The relative power error of exponential expansion and first-order Taylor expansion using different time steps ($\Delta t = 0.001$ s, 0.01 s, 0.05 s, and 0.1 s) under both time discretization schemes is shown in Figure 7. In the figure, it is indicated that backward Euler (BE) and Crank–Nicolson (CN) schemes are both accurate at a small time step, but CN is more accurate than BE at a larger time step due to a second-order truncation error in time discretization. Even in the largest time step ($\Delta t = 0.1$ s), relative power error is restricted within 1% using the CN scheme. Moreover, it is also shown that the BE scheme introduces a large error at the beginning of the transient, but decreases rapidly with time proceeding due to the stable asymptotic period of reactor. Compared to the BE scheme, the CN scheme leads to a rather smaller relative power error at any time due to a higher precision in time discretization. In addition, no obvious difference is observed between exponential approximation and first-order Taylor approximation using the

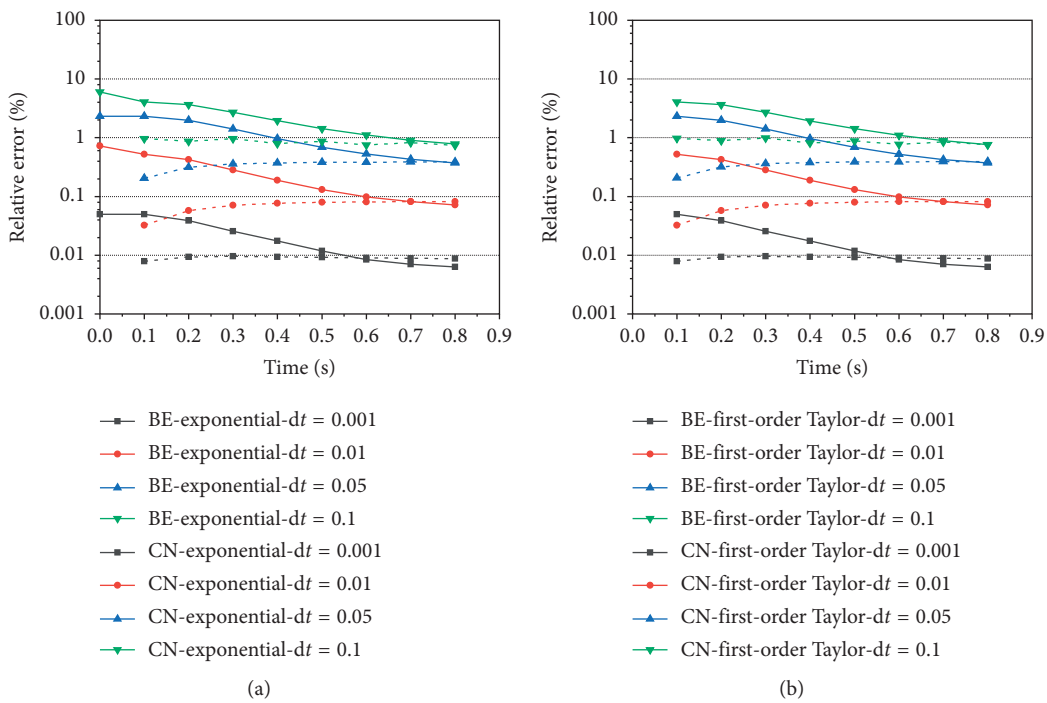

Figure 7: The relative power error of exponential expansion and first-order Taylor expansion in different time discretization and time steps.

same second-order time discretization, which means that time discretization dominates the truncation error.

3.3.4. Time Step Control Method. The time step control technique stated in Section 2.4 is verified in this section. A reactivity insertion model identical to that in HTR-PM is used. In this transient, the time step is determined by the criterion shown as equation (35). Figure 8 shows the variation of estimated time step with time of different time step. It is of interest that the exponential approximation of flux is adopted here since the time adapt method is derived from this approximation.

In Figure 8, it is noted that the estimated time step increases continuously as time proceeds, which means that the neutron fluxes change dramatically at the beginning of the transient and tend to be stable gradually. To maintain the accuracy of the results, a small time step is required initially, while a large time step is also feasible after almost 0.6 s because of a relatively stable exponential variation of neutron flux. In addition, it is also observed that the estimated time step corresponding to $\Delta t = 50$ ms is the smallest compared to $\Delta t = 1$ ms and 10 ms, which is due to a ω increase of truncation error under large time step. Therefore, the smaller the Δt_{adapt}, the smaller the estimated time step.

Figure 9 shows the comparison of relative power error of the time adapt method and fixed time steps, i.e., $\Delta t = 1$ ms, 10 ms, 50 ms, and 100 ms. Both CPU time and number of time step are included in this figure. For the time adapt method, the initial time step is 1ms to resolve fast change of neutron flux and other time steps are determined by equation (5). Figure 9 indicates that the time adapt method can realize a relatively low and stable error. In addition, it is found a continuous drop of error at fixed time step, which means that the fixed time step does not respond to the change of neutron flux well. After almost 0.6 s, the time step is larger because the neutron flux changes slowly then and small time step is no longer required to reduce calculation time. The results indicate that the time adapt method is a powerful tool to balance the computational cost and precision in neutron kinetic calculation.

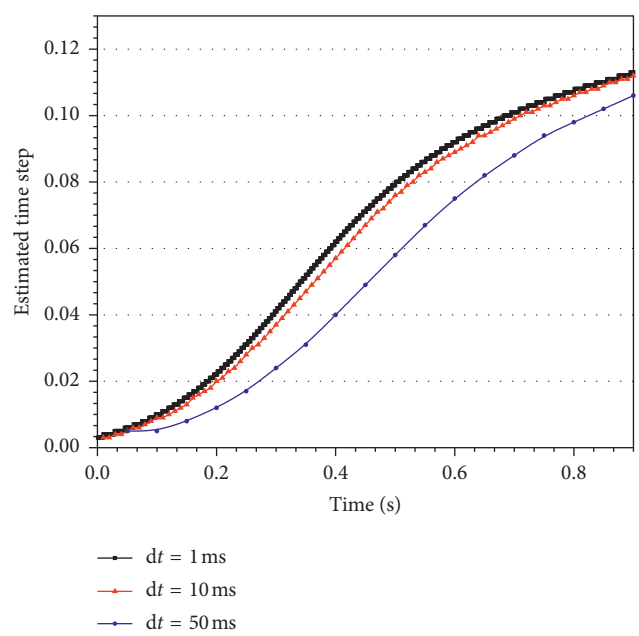

Figure 8: Estimated time step during transient.

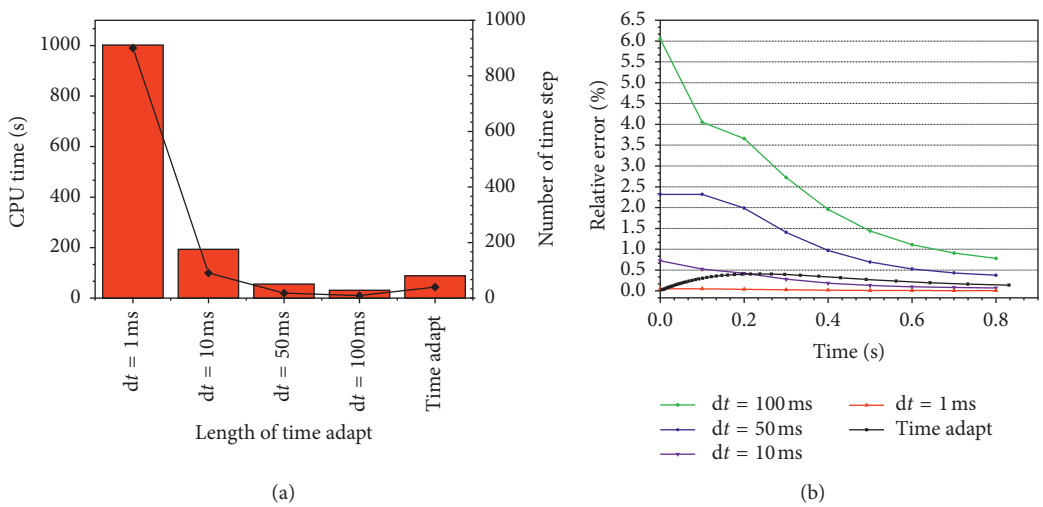

Figure 9: Computational cost and relative power error for the fixed time step method and time adapt method.

The relative errors of power compared with the fixed time step $\Delta t = 1$ ms, 10 ms, 50 ms, and 100 ms and the time adapt method are shown in Figure 9. CPU times and number of time step in each method are also provided in the figure. The initial time step of the time adapt method is 1 ms, and equation (35) is used to determine the next time step. Figure 9 indicates that the time adapt method can maintain errors at a relatively stable value. Fixed time step methods result in a continuous error drop which reflects in this figure. This also means that the fixed time step method has not responded to the change of neutron flux. The result is that the time adapt method initially takes smaller time steps in order to resolve fast change in neutron flux. After approximately 0.6 second into the transient, the time adapt method takes longer time steps because the neutron flux is now changing more slowly and the very small time step is no longer required in order to reduce calculation time. The time adapt method used here can balance computational cost and precision in neutron kinetic calculation.

4. Conclusion

The work presents an exponential flux approximation technique in the precursor integral method, which is shown to be advantageous for solving space-dependent neutron kinetic equations. Because the neutron flux is approximated by exponential function, the coefficients in the function reflect the reactor asymptotic period. This means that the time step control algorithm can be based on the coefficients, and an adaptive time step method is proposed which is instructed by an predicted error. Truncation error analysis among different flux approximations used in the precursor integral method is performed in this work. The method of treating the precursor as independent variables is appended as a contrast. Nonlinear term appeared, and efficient nonlinear solution method, JFNK, is utilized. There are two sources leading to numerical errors in transient calculation, viz, time discretization and delayed neutron integral technique. Analytical insight on the effects of the time discretization and neutron flux approximation method is obtained. The numerical verification of the method above is carried out in TWIGL neutronic benchmark. Besides, more realistic applications are extended. HTR-PM multiphysics problem is presented with a thermal-hydraulic and a four-group neutron kinetic model in 2D cylindrical coordinate. The main remarks can be drawn as follows:

(i) The traditional method of treating the delayed neutron precursor as independent variables causes expansive calculation cost compared with the precursor integral method. The CPU time can be reduced by more than half in using precursor integral methods.

(ii) First-order Taylor approximation and exponential approximation for neutron flux can provide sufficient accuracy of calculation and the stability of numerical results in neutron kinetic problems. The comprehensive performance of exponential approximation is better.

(iii) Time discretization dominates the truncation error of transient calculation. The time discretization of second-order accuracy is suggested in the calculation of neutron dynamics.

(iv) The time adapt method proposed in this work is proven to be efficient in HTR-PM transient calculation. This method is based on exponential flux approximation and has the features of small error and low computational cost for solving neutron kinetic equations.

In the future work, more cases will be tested in neutronic and thermal-hydraulic coupling problem, in which precursor integral method with exponential approximation is used for solving neutron kinetic problem.

Notations

β: Groupwise fraction
χ: Fission spectra
λ: Decay constants of delayed neutron groups
ϵ: Truncation error
F: Residual function
J: Jacobian matrix
v: Neutron velocity
w: Frequency coefficient
ν: Prompt neutron yield
ϕ: Scalar neutron flux
Σ_s: Fission cross-section
Σ_f: Fission cross-section
τ: Dynamical time scale
C: Delayed neutron precursor concentration
D: Diffusion coefficient
m: Number of delayed neutron groups
g: Number of neutron energy groups.

Data Availability

The data used to support the findings of this study are available from the corresponding author upon request.

Conflicts of Interest

The authors declare that they have no conflicts of interest.

Acknowledgments

This work was supported by the Chinese National Natural Science Foundation Project (11505102 and 11375099), Chinese National S&T Major Project (2018ZX06 902013), and IAEA CRP (I31020).

References

[1] O. Zerkak, T. Kozlowski, and I. Gajev, "Review of multi-physics temporal coupling methods for analysis of nuclear reactors," *Annals of Nuclear Energy*, vol. 84, pp. 225–233, 2015.

[2] M. N. Avramova and K. N. Ivanov, "Verification, validation and uncertainty quantification in multi-physics modeling for nuclear reactor design and safety analysis," *Progress in Nuclear Energy*, vol. 52, no. 7, pp. 601–614, 2010.

[3] M. Tamitani, T. Iwamoto, and B. R. Moore, "Development of kinetics model for BWR core simulator AETNA," *Journal of Nuclear Science and Technology*, vol. 40, no. 4, pp. 201–212, 2003.

[4] Y. A. Chao and P. Huang, "Theory and performance of the fast-running multidimensional pressurized water reactor kinetics code, SPNOVA-K," *Nuclear Science and Engineering*, vol. 103, no. 4, pp. 415–419, 1989.

[5] H. Zhang, J. Guo, Li Fu, Y. Xu, and T. J. Downar, "An assessment of coupling algorithms in HTR simulator TINTE," *Nuclear Science and Engineering*, vol. 190, no. 3, pp. 287–309, 2003.

[6] T. Downar, "PARCS V3.0 U.S. NRC Core Neutronics Simulator User Manual," UM-ERS-tnqh_x2010;0001, University of Michigan, Ann Arbor, MI, USA, 2013.

[7] Y.-An Chao and A. Attard, "Resolution of the stiffness problem of reactor kinetics," *Nuclear Science and Engineering*, vol. 90, pp. 40–46, 1985.

[8] D. A. Knoll, L. Chacon, L. G. Margolin, and V. A. Mousseau, "On balanced approximations for time integration of multiple time scale systems," *Journal of Computational Physics*, vol. 185, no. 2, pp. 583–611, 2003.

[9] D. A. Knoll and D. E. Keyes, "Jacobian-free Newton–krylov methods: a survey of approaches and applications," *Journal of Computational Physics*, vol. 193, pp. 357–397, 2004.

[10] A. Pautz and A. Birkhofer, "Dort-td: a transient neutron transport code with fully implicit time integration," *Nuclear Science and Engineering*, vol. 145, no. 3, pp. 299–319, 2003.

[11] A. E. Aboanber, "Generalized and stability rational functions for dynamic systems of reactor kinetics," *International Journal of Nuclear Energy*, vol. 2013, Article ID 903904, 12 pages, 2013.

[12] T. M. Sutton and B. N. Aviles, "Diffusion theory methods for spatial kinetics calculations," *Progress in Nuclear Energy*, vol. 30, no. 2, pp. 119–182, 1996.

[13] D. L. Hetrick, *Dynamics of Nuclear Reactors*, The University of Chicago Press, Chicago, IL, USA, 1971.

[14] B. N. Aviles, "Development of a variable time-step transient nem code: Spandex," *Transactions of the American Nuclear Society Journal*, vol. 68, pp. 425–427, 1993.

[15] P. N. Brown and Y. Saad, "Hybrid krylov methods for nonlinear systems of equations," *SIAM Journal on Scientific and Statistical Computing*, vol. 11, no. 3, pp. 450–481, 1990.

[16] L. A. Hageman and J. B. Yasinsky, "Comparison of alternating direction time-differencing methods with other implicit methods for the solution of the neutron group-diffusion equations," *Nuclear Science and Engineering*, vol. 38, pp. 8–32, 1969.

[17] Z. Zhang and Z. Wu, "Current status and technical description of Chinese 2 x 250 MW htr-pm demonstration plant," *Nuclear Engineering and Design*, vol. 239, no. 7, pp. 1212–1219, 2009.

[18] H. Zhang, J. Guo, L. Jianan, N. Jinlin, L. Fu, and X. Yunlin, "The comparison between nonlinear and linear preconditioning JFNK method for transient neutronics/thermal-hydraulics coupling problem," *Annals of Nuclear Energy*, vol. 132, pp. 357–368, 2019.

[19] H. J. Rütten, K. A. Haas, H. Brockmann, and W. Scherer, "VSOP (99/05) Computer Code System for Reactor Physics and Fuel Cycle Simulation," Forschungszentrum Jüllich, Germany, vol. 4189, 2005.

[20] X. F. Zhou, *JFNK based on nodal expansion method for simultaneous solution of coupled systems*, Ph.D. thesis, Tsinghua University, Beijing, China, 2016.

[21] KTA Rule, "Reactor Core Design of High-emperature Gas-ooled Reactors Part 2: Heat Transfer in Spherical Fuel Elements", Geschäftsstelle des Kerntechnischen Ausschusses beim Bundesamt für Strahlenschutz, Salzgitter, Germany, 1983.

[22] H. Gerwin, W. Scherer, and A. Lauer, "Tinte-a two-dimensional code for reactor dynamics," *Berichte des Forschungszentrums Jülich Jül-4294*, 2009.

Hindawi
Science and Technology of Nuclear Installations
Volume 2020, Article ID 8014521, 21 pages
https://doi.org/10.1155/2020/8014521

Research Article

Lognormal-Based Sampling for Fission Product Yields Uncertainty Propagation in Pebble-Bed HTGR

Yizhen Wang, Menglei Cui, Jiong Guo, Jinlin Niu, Yingjie Wu, Baokun Liu, and Fu Li

Institute of Nuclear and New Energy Technology, Collaborative Innovation Center of Advance Nuclear Energy Technology, Key Laboratory of Advanced Reactor Engineering and Safety of Ministry of Education, Tsinghua University, Beijing 100084, China

Correspondence should be addressed to Jiong Guo; guojiong12@tsinghua.edu.cn

Received 14 November 2019; Revised 29 July 2020; Accepted 12 August 2020; Published 25 September 2020

Academic Editor: Alejandro Clausse

Uncertainty analyses of fission product yields are indispensable in evaluating reactor burnup and decay heat calculation credibility. Compared with neutron cross section, there are fewer uncertainty analyses conducted and it has been a controversial topic by lack of properly estimated covariance matrix as well as adequate sampling method. Specifically, the conventional normal-based sampling method in sampling large uncertainty independent fission yields could inevitably generate nonphysical negative samples. Cutting off these samples would introduce bias into uncertainty results. Here, we evaluate thermal neutron-induced U-235 independent fission yields covariance matrix by the Bayesian updating method, and then we use lognormal-based sampling method to overcome the negative fission yields samples issue. Fission yields uncertainty contribution to effective multiplication factor and several fission products' atomic densities at equilibrium core of pebble-bed HTGR are quantified and investigated. The results show that the lognormal-based sampling method could prevent generating negative yields samples and maintain the skewness of fission yields distribution. Compared with the zero cut-off normal-based sampling method, the lognormal-based sampling method evaluates the uncertainty of effective multiplication factor and atomic densities are larger. This implies that zero cut-off effect in the normal-based sampling method would underestimate the fission yields uncertainty contribution. Therefore, adopting the lognormal-based sampling method is crucial for providing reliable uncertainty analysis results in fission product yields uncertainty analysis.

1. Introduction

Reactor design and safety analysis rely on accurate calculations of system responses with properly evaluated uncertainties. There has been an increasing need for evaluating the credibility of reactor safety. Pebble-bed high temperature gas-cooled reactor (pebble-bed HTGR) is a multiphysics nonlinear coupled system, including neutron transport and complex heat transfer hydraulics behaviour [1]. In order to systematically and thoroughly investigate the uncertainties propagation in pebble-bed HTGR, an IAEA Coordinated Research Plan (CRP) [2, 3] has been initiated after the start of OECD/NEA UAM-LWR [4]. Recent advances regarding uncertainty propagation analysis in pebble-bed HTGR mainly concern the nuclear cross section uncertainties propagation in reactor neutronic calculations [5–9]. As pebble-bed HTGR allows fuels recirculation during fuel cycles and adopts higher fuel enrichment (8.5 wt.%), fuels usually could achieve larger burnup values, and then fission product yields could be nonnegligible uncertainty sources in reactor burnup and decay heat calculations. Their uncertainties contributions to important reactor burnup responses need to be considered properly for evaluating the credibility of rector safety-related quantities of interest (QoI), e.g., maximum fuel pebble temperature.

Fission product yield describes the fraction of a certain fission product produced per fission. During the measurements of fission product yields, correlated errors or covariances may exist when using the same equipment or methods [10]. However, they are ignored in evaluated

nuclear data library. Also, self-consistent fission yields data set should follow several physical constraints such as binary fission, mass conservation, and charge conservation [11]. These constraints could introduce covariances between fission yields data. As the fission yields' covariances in current releases of evaluated nuclear data libraries are still absent, e.g., ENDF/B-VII.1, many methods are developed to estimate these covariances information based on the imposed physical constraints. The Bayesian updating method is widely used in data assimilation, data adjustment, and model fitting problems. It refines parameters by taking both the prior information about those parameters and the likelihood which refers to new data into consideration [10, 12]. It allows estimating the covariance matrix of fission yields by sequentially introducing the above physical constraints. In the domain of fission yields adjustment, it is introduced by Kawano and Chadwick [13] to update Pu-239 fission yields with chain yields to reduce the independent fission yields discrepancy in ENDF/B-VII.1. Pigni et al. [14] expand it to involve cumulative fission yields into covariances estimation. The difference between chain yields-based updating and cumulative fission yields-based updating is further investigated by Fiorito et al. [15, 16]. Based on the provided independent and cumulative fission yields uncertainties information in ENDF/B-VII.1, this work adopts the Bayesian updating method to estimate the independent fission yields covariances.

Sampling-based methods for uncertainty analysis or stochastic UQ methods [17] require properly perturbed samples to provide reliable uncertainty analysis results of QoI. As it is observed from the evaluated nuclear data library, independent fission yields generally have larger uncertainties. Random sampling on these yields under normal distribution could generate nonphysical negative samples. Cutting off these negative yield samples by setting them to zero could artificially omit some information from the original fission yields distribution, resulting in biased uncertainty analysis results. This zero cut-off effect on quantified uncertainty has not been well studied. This raises question whether normal distribution is sufficient for describing inherently positive random variables with large uncertainties only given their mean values and covariance matrix. Smith et al. [18] propose to replace normal distribution with lognormal distribution by the principle of maximum entropy [10], and Žerovnik et al. [19, 20] investigate this method in the sampling resonance parameters where negative samples problem was encountered as in fission yields. This work proposes an implementation of the lognormal-based sampling method in fission product yields sampling.

The present work is organized as follows: Section 2 describes the nomenclature of fission product yields and the burnup calculation of pebble-bed HTGR. An implemented stochastic UQ method for fission yields uncertainty propagation is described in Section 2.3. The Bayesian updating method and the lognormal-based sampling method are detailed in Section 3. Finally, results of fission yields uncertainty contributions to effective multiplication factor and several important fission products atomic densities are provided and discussed in Section 4.

2. Model Description and Uncertainty Propagation

2.1. ENDF/B-VII.1 Fission Product Yields Sublibrary. Fission product yield characterizes the fraction of a particular fission product nuclide produced per fission. A compound nucleus is formed when a fissile nucleus is bombarded by an incident neutron. As its energy overcomes the fission barrier, this compound nucleus could undergo fission. A brief description of the fission process is illustrated (see Figure 1). After the scission of compound nucleus, primary fission fragments are produced and they would undergo deexcitation by releasing prompt neutrons due to their high neutron to proton ratios. After the emission of prompt neutrons, the remaining fission fragments referred to as fission products would undergo β decay, isomeric transition, or particle emission along their corresponding decay chain and finally reach stable nuclides. Each fission product is identified by its mass number A, charge number Z, and isomeric state I and is denoted as the triplet (A, Z, I)

A detailed description about the nomenclature of fission product yields could be found in [11] and they are briefly summarized as follows. IFYs and CFYs determine the fraction of a fission product at different stages in the fission process. IFYs denoted as $y(A, Z, I)$ are the fraction of a fission product produced directly from one fission after the emission of prompt neutrons but prior to any radioactive decays. Because IFYs are produced before any radioactive decay in the fission system, they should be subject to the physical constraints of fission system, e.g., binary fission, conservation of mass, and charge number. CFYs denoted as $c(A, Z, I)$ determine the total fraction of a fission product produced over all time after one fission. It involves not only the direct production from fission but also the contributions from the decay of other products.

The current releases of ENDF/B-VII.1 fission yield sublibrary provide fission yields data for 31 fission actinides from Th-227 to Fm-255. Though energy-dependence issues within fission spectrum are highlighted in current releases of evaluated nuclear data library and neutron induced Pu-239 fission yields at 2.0 MeV are supplemented to allow users to linearly interpolate yields between 0.5 MeV and 2.0 MeV for high accuracy purpose [22], other fission actinide fission yields data are taken directly from ENDF/B-VI evaluated by England and Rider [23] in 1993. Three fission systems for U-235 are evaluated with respect to incident neutron energy, namely, 0.0253 eV thermal energy, 0.5 MeV fission spectrum energy, and 14.0 MeV high energy. IFYs and CFYs are evaluated for 1,247 fission products in thermal neutron induced U-235 fission yield (see Figure 2). The relationship between IFYs and CFYs [11] is referred to as (1), where $b(A', Z', I' \longrightarrow A, Z, I)$ is the branching ratio:

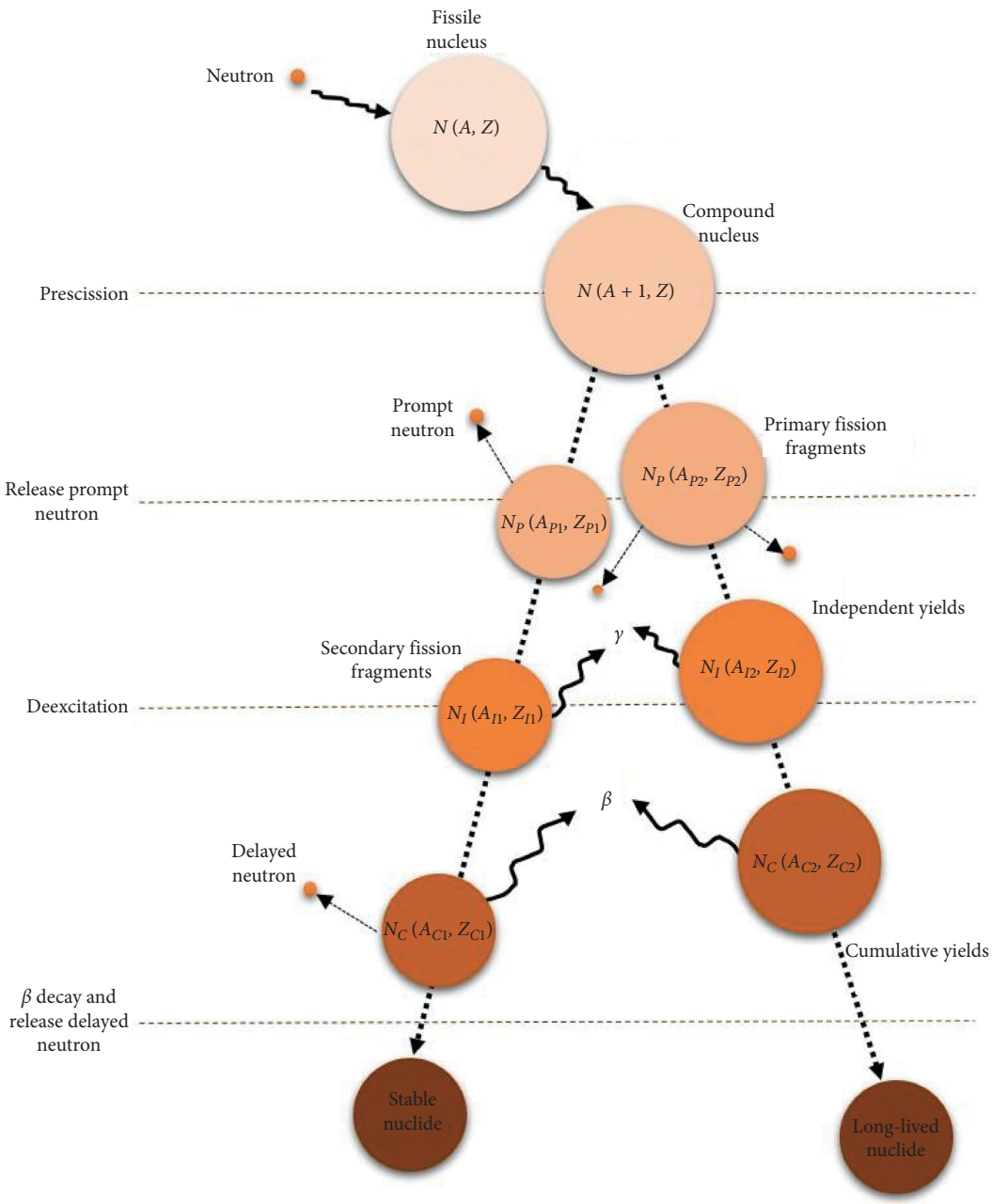

Figure 1: Neutron induced fission process [21]. The fission products refer to the fission fragments after the emission of prompt neutrons. Independent fission yields (IFYs) characterize the fraction of a fission product produced before any radioactive decay, whereas cumulative fission yields (CFYs) describe the fraction of that produced product over all time after a fission.

$$c(A,Z,I) = y(A,Z,I) + \sum_{(A',Z',I')} b(A',Z',I' \longrightarrow A,Z,I)c(A',Z',I'). \quad (1)$$

It could be found that most IFYs appear in the upper region of β-stability line and they are most likely to undergo β^- decay to reach a stable state. As CFYs involve the production of a certain fission product from the decay of other fission products as shown in (1), the peaks of CFYs distribution in neutron-charge number figure tend to be closer to the β-stability line (see Figure 2).

The evaluation of fission yields data requires a combined work of experimental measurements and theoretical model predictions. It is natural for the evaluated fission yields possessing uncertainties originated from measurement errors and theoretical model parameters uncertainties. Although England and Rider provide the uncertainties (standard deviation) of each fission product yield in their original work, covariances information between fission yields has not been provided since then. Those covariances information is crucial for representing the physical constraints imposed on IFYs, and they should be estimated properly in order to generate self-consistent IFYs

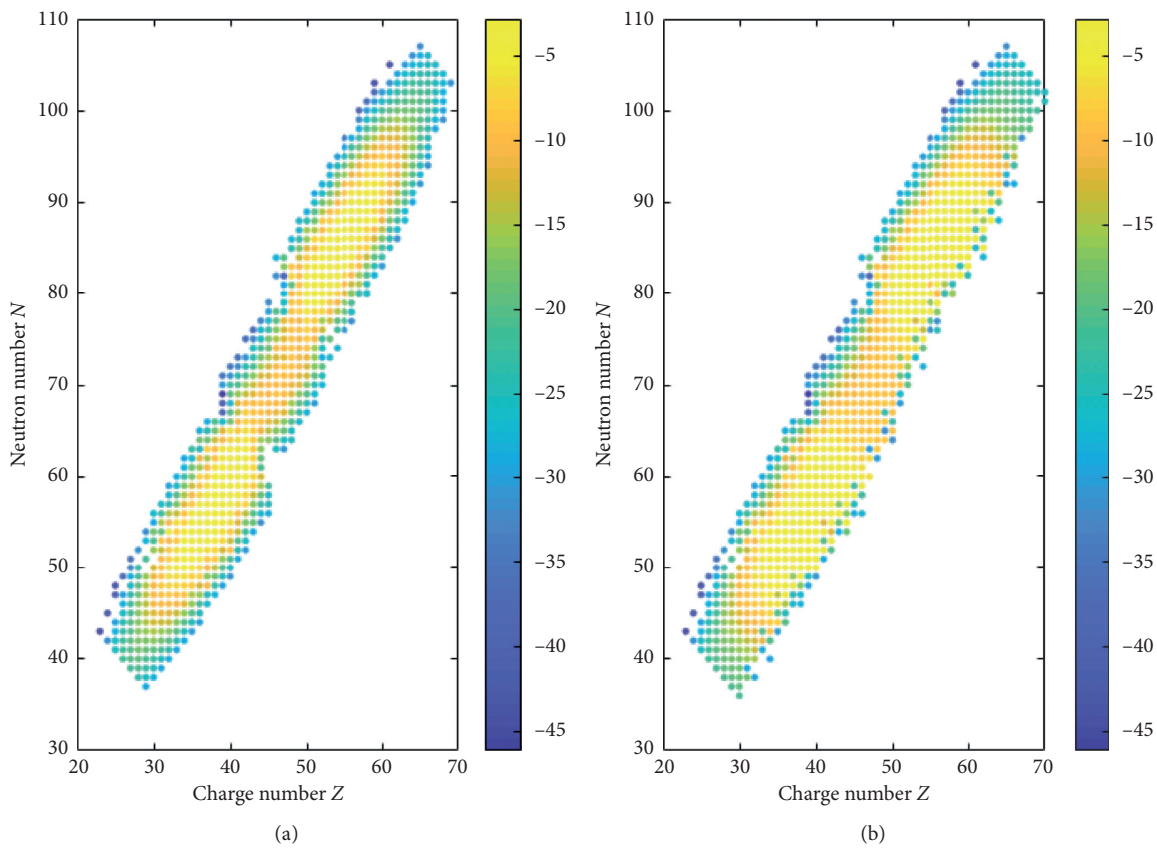

Figure 2: Thermal neutron induced U-235 fission yield data in ENDF/B-VII.1. The natural logarithm values of fission yields are plotted. (a) Independent yields. (b) Cumulative yields.

perturbations. This work focuses on the propagation of thermal neutron induced U-235 fission yields uncertainties to burnup simulation of pebble-bed HTGR based on ENDF/B-VII.1. The estimation of covariances information will be detailed in Section 3.1.

2.2. Pebble-Bed HTGR Burnup Model and Built-In Fission Yields Analysis. Pebble-bed HTGR core (see Figure 3(a)) consists of spherical fuel elements or fuel pebbles. Each of these pebbles is composed of a spherical graphite matrix in the centre where thousands of small coated particles (known as TRISO particles) are embedded. These particles contain UO2 kernel in the centre with four structural coating layers surrounding it (see Figure 3(b)). During reactor operation, these fuel pebbles are consistently flowing downward from the top of the core to the bottom and are irradiated at different core spectrum regions randomly. Fuel recirculation is a characterized fuel cycling procedure adopted in pebble-bed HTGR which is different with that applied in Light Water Reactor (LWR). Such recirculation allows fresh fuel pebbles being loaded into the core and spent fuel pebbles being discharged online without shutting reactor down. More importantly, this recirculation permits fuel pebbles running through core multiple times before they are finally being discharged. Because of the fuels recirculation, there exist running-in phase and equilibrium core states. The equilibrium core state refers to the nuclei compositions inside the core kept unchanged with time and therefore effective multiplication factor being stable at a certain value. This could give a more flattened power distribution across the core and higher average discharge burnup value. The V.S.O.P. computer code system [26] is developed to perform burnup calculation of pebble-bed HTGR by simulating the fuels recirculation process stepwise and conduct spectrum calculation online at each spectrum region inside the core. A detailed description of this simulation process could be found in these articles [27].

The built-in fission product chain in V.S.O.P. code involves 44 fission products and among these 44 fission products' data, 14 are taken as IFYs, while 30 are taken as CFYs. These data are taken from ENDF/B-IV and ENDF/B-V. An additional "nonsaturating" fission product is evaluated to account for the sum of many lumped fission yields which are not explicitly included in the chain [26]. The comparison between these built-in fission yields and replacing them with the current releases in ENDF/B-VII.1 is conducted to examine the availability of V.S.O.P. code for fission yields uncertainty propagation. This investigation is conducted on HTR-PM [28] with 8.7% fuel enrichment (while 8.5% enrichment is applied in actual design).

The impact of each built-in fission yield on k_{eff} at equilibrium core state is investigated individually by replacing them with ENDF/B-VII.1. It should be noted that

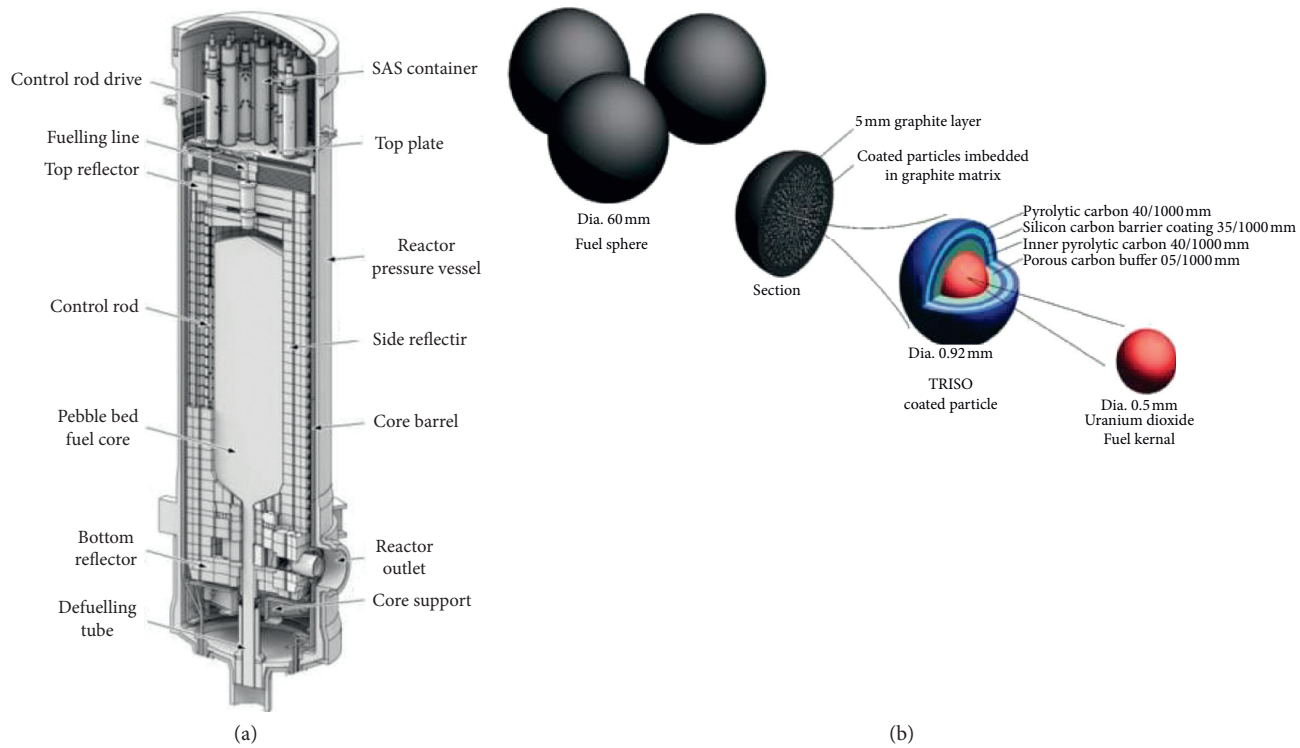

Figure 3: Pebble-bed HTGR core. (a) Core geometrical of PBR250 design [24]. (b) Fuel pebbles [25].

built-in fission yields library in V.S.O.P. includes a combination of IFYs and CFYs, and they are presented separately (see Tables 1 and 2).

IFYs are evaluated by subtracting the total contributions of its precursors from experimental measured CFYs. With the improvement of CFYs measurements, the evaluated IFYs become more precise. It could be seen from the table that IFYs in ENDF/B-VII.1 are lower than the built-in fission yields used in V.S.O.P. Except the large discrepancy in the fission yield of Mo-95, all the impacts from replacing fission yields are lower than 20 pcm. The overall impact is 67 pcm (see Table 3) when all the yields are replaced without FP-44. The difference is acceptable in effective multiplication factor calculations when substituting built-in V.S.O.P. fission yields with ENDF/B-VII.1 fission yields. The V.S.O.P. burnup model is further used to conduct fission product yields uncertainty propagation as described in Section 2.3.

2.3. Uncertainty Quantification Scheme. The HTR-PM [28] reactor core is modelled in V.S.O.P. computer code system to analyse the uncertainty propagation of fission yields in this work. 15 times recirculation of fuel is adopted and the average discharge burnup value is around 90, 210 MW · d/tU with fresh fuel having 8.5 wt.% enrichment. As fuel recirculation tightly couples the neutronics and burnup calculation spatially inside the core, it is difficult to separate the uncertainty propagation step by step. Stochastic UQ method is used to investigate the uncertainty propagation in equilibrium core state. An uncertainty propagation scheme is proposed in this work (see Figure 4).

Two sampling methods are implemented in this work, namely, normal-based sampling and lognormal-based sampling. Different from normal-based sampling, lognormal-based sampling requires a lognormal transformation of the original mean vector and covariance matrix. When the IFYs samples are generated, their corresponding CFYs are calculated and combine them to form self-consistent fission yield samples. These combined IFYs and CFYs samples are propagated to V.S.O.P. HTR-PM model for further uncertainty analysis. Detailed Bayesian updating method description and lognormal-based sampling procedures will be introduced in Section 3.

3. Fission Product Yield Perturbation

3.1. U-235 Thermal Neutron-Induced IFYs Covariances Estimation. Bayesian updating method or the generalized least square method (GLSM) is a data adjustment method, which allows the prior data being updated with combination of new knowledge about these data. Such knowledge could be measured data or physical constraints imposed on these prior data. The present work applies Bayesian updating method to estimate the covariance matrix of IFYs based on ENDF/B-VII.1 thermal neutron induced U-235 fission yields sublibrary. The specification of this method is briefly recalled as follows.

Consider a multivariate linear regression model shown in

$$c = Xy + \varepsilon, \tag{2}$$

where c and $y \in \mathbb{R}^{n\times 1}$ are observables and parameters to be updated or estimated, respectively. $X \in \mathbb{R}^{n\times n}$ is the design

Table 1: Comparison between V.S.O.P. built-in yields and ENDF/B-VII.1 in k_{eff} prediction (IFYs).

Index	Fission product	Fission yields			k_{eff}		
		V.S.O.P.	ENDF/B-VII.1	Relative difference to ENDF/B-VII.1 (%)	V.S.O.P.	ENDF/B-VII.1	Difference to ENDF/B-VII.1 (pcm)
1	Rh-103	$1.8580E-11$	$6.3796E-13$	96.57	1.01027	1.01027	0
2	Pd-105	$9.8300E-13$	$0.0000E+00$	100.00	1.01027	1.01027	0
3	Xe-131	$1.5400E-08$	$1.4199E-09$	90.78	1.01027	1.01027	0
4	Cs-133	$5.0800E-07$	$7.9194E-09$	98.44	1.01027	1.01027	0
5	Cs-134	$3.5700E-07$	$3.8547E-08$	89.20	1.01027	1.01027	0
6	Nd-143	$9.5000E-13$	$4.7997E-14$	94.95	1.01027	1.01027	0
7	Pm-148m	$7.4900E-09$	$8.0994E-11$	98.92	1.01027	1.01027	0
8	Pm-148g	$5.7300E-08$	$4.4497E-11$	99.92	1.01027	1.01027	0
9	Sm-147	$0.0000E+00$	$0.0000E+00$	0.00	1.01027	1.01027	0
10	Sm-148	$6.9500E-13$	$1.6399E-14$	97.64	1.01027	1.01027	0
11	Sm-149	$0.0000E+00$	$1.7099E-12$	—	1.01027	1.01027	0
12	Sm-151	$0.0000E+00$	$4.7497E-09$	—	1.01027	1.01027	0
13	Eu-154	$1.6300E-08$	$9.6993E-10$	94.05	1.01027	1.01027	0
14	Gd-155	$4.4100E-11$	$4.0797E-12$	90.75	1.01027	1.01027	0

Table 2: Comparison between V.S.O.P. built-in yields and ENDF/B-VII.1 in k_{eff} prediction (CFYs).

Index	Fission product	Fission yields			k_{eff}		
		V.S.O.P.	ENDF/B-VII.1	Relative difference to ENDF/B-VII.1 (%)	V.S.O.P.	ENDF/B-VII.1	Difference to ENDF/B-VII.1 (pcm)
1	Xe-135	$6.6023E-02$	$6.5385E-02$	0.97	1.01027	1.01044	−17
2	FP-44	$9.4760E-01$	$9.4760E-01$	0.00	1.01027	1.01027	0
3	Xe-136	$6.2701E-02$	$6.3127E-02$	−0.68	1.01027	1.01027	0
4	Kr-83	$5.3076E-03$	$5.3620E-03$	−1.02	1.01027	1.01027	0
5	Zr-95	$6.4678E-02$	$6.5027E-02$	−0.54	1.01027	1.01027	0
6	Mo-95	$1.6410E-06$	$6.5029E-02$	-3.96×10^{10}	1.01027	1.00911	116
7	Mo-97	$5.9600E-02$	$5.9968E-02$	−0.62	1.01027	1.01027	0
8	Tc-99	$6.1284E-02$	$6.1087E-02$	0.32	1.01027	1.01028	−1
9	Ru-101	$5.0501E-02$	$5.1725E-02$	−2.42	1.01027	1.01026	1
10	Ru-103	$3.1411E-02$	$3.0309E-02$	3.51	1.01027	1.01042	−15
11	Rh-105	$1.0199E-02$	$9.6416E-03$	5.47	1.01027	1.01030	−3
12	Pd-108	$7.1032E-04$	$5.4125E-04$	23.80	1.01027	1.01028	−1
13	Ag-109	$2.9903E-04$	$3.1221E-04$	−4.41	1.01027	1.01027	0
14	Cd-113	$1.2425E-04$	$1.4038E-04$	−12.98	1.01027	1.01027	0
15	I-131	$2.8325E-02$	$2.8907E-02$	−2.05	1.01027	1.01022	5
16	Xe-133	$6.7859E-02$	$6.6991E-02$	1.28	1.01027	1.01032	−5
17	Pr-141	$5.8929E-02$	$5.8470E-02$	0.78	1.01027	1.01028	−1
18	Pr-143	$5.9710E-02$	$5.9558E-02$	0.25	1.01027	1.01029	−2
19	Nd-144	$5.4523E-02$	$5.4996E-02$	−0.87	1.01027	1.01027	0
20	Nd-145	$3.9339E-02$	$3.9334E-02$	0.01	1.01027	1.01027	0
21	Nd-146	$2.9912E-02$	$2.9969E-02$	−0.19	1.01027	1.01027	0
22	Pm-147	$2.2701E-02$	$2.2467E-02$	1.03	1.01027	1.01035	−8
23	Pm-149	$1.0888E-02$	$1.0816E-02$	0.59	1.01027	1.01031	−4
24	Sm-150	$5.4130E-06$	$2.9998E-07$	94.46	1.01027	1.01027	0
25	Pm-151	$4.2044E-03$	$4.1877E-03$	0.40	1.01027	1.01028	−1
26	Sm-152	$2.7057E-03$	$2.6691E-03$	1.35	1.01027	1.01029	−2
27	Eu-153	$1.6264E-03$	$1.5828E-03$	2.68	1.01027	1.01029	−2
28	Eu-155	$3.3025E-04$	$3.2136E-04$	2.69	1.01027	1.01028	−1
29	Gd-156	$1.3517E-04$	$1.4853E-04$	−9.88	1.01027	1.01027	0
30	Gd-157	$6.4651E-05$	$6.1506E-05$	4.86	1.01027	1.01027	0

matrix that represents linear mapping between estimating parameters and observables. $\varepsilon \in \mathbb{R}^{n\times1}$ are the measurement errors of observables with expectation $E[\varepsilon] = 0 \in \mathbb{R}^{n\times1}$ and variance $\text{Var}[\varepsilon] = V \in \mathbb{R}^{n\times n}$. By the principle of maximum information entropy, it is objective and plausible to assign Gaussian distribution on this error. Similarly, estimating parameters y could also be assigned Gaussian distribution given their expectation $E[y] = y_0$ and variance $\text{Var}[y] = Z_0$. The generalized least square problem [29] is formulated by the following minimization in the domain of estimating

Table 3: Reference calculation between built-in fission yields of V.S.O.P. and ENDF/B-VII.1 (all substitution without FP-44).

Built-in V.S.O.P. fission yields	k_{eff} ENDF/B-VII.1 fission product yields (without update)	Difference to ENDF/B-VII.1 (pcm)
1.01027	1.00960	67

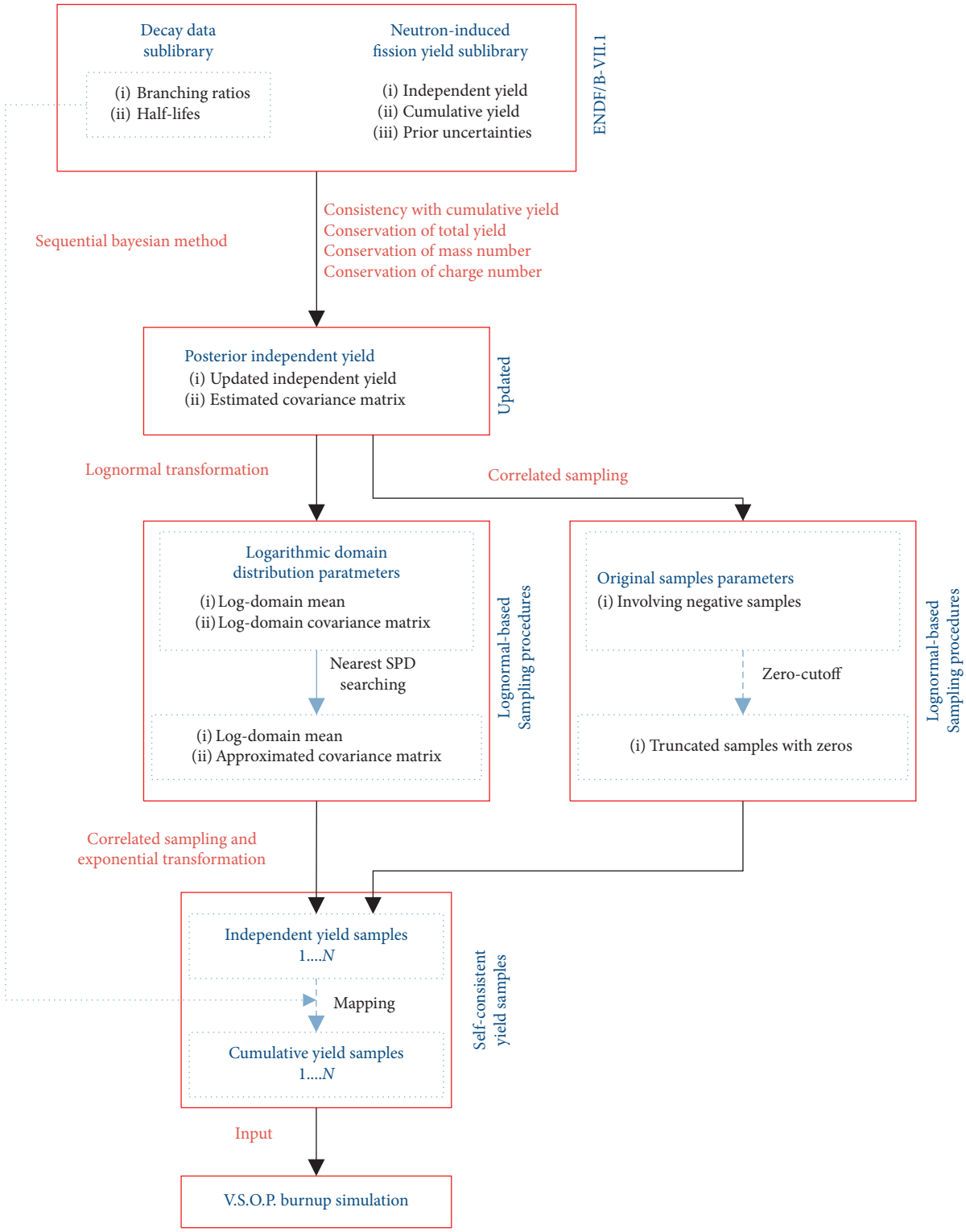

Figure 4: Flow chart of fission product yields uncertainty propagation.

parameters to find the best least square estimated parameters as

$$\min_y \chi^2 = \left[(Xy - c)^T V^{-1} (Xy - c) + (y - y_0)^T Z_0^{-1} (y - y_0) \right]. \tag{3}$$

The above minimization process could also be interpreted in the perspective of Bayesian updating. Consider the estimated parameters have a prior of Gaussian distribution with density $p(y)$ in

$$p(y) = \left(\frac{1}{(2\pi)^{(n/2)} |Z_0|^{(1/2)}} \right) \exp\left\{ -\left(\frac{1}{2}\right) (y - y_0)^T Z_0^{-1} (y - y_0) \right\}. \tag{4}$$

And likelihood function determines the probability of any candidate estimated parameters appearing in the observables distribution. Then, likelihood function $p(c \mid y \mid)$ is given as

$$p(c \mid y) = \left(\frac{1}{(2\pi)^{(n/2)} |V|^{(1/2)}} \right) \exp\left\{ -\frac{1}{2} (Xy - c)^T V^{-1} (Xy - c) \right\}. \tag{5}$$

The posterior distribution of estimated parameters $\mathbf{y}$ is therefore calculated by Bayesian theorem and it gives

$$p(y \mid c) = \frac{p(c \mid y)}{p(c)} p(y) \propto p(c \mid y) p(y). \tag{6}$$

Considering the conjugacy between Gaussian prior and likelihood, the posterior estimated parameters follows Gaussian distribution as well. Under quadratic loss, the optimal estimates of true values and their uncertainty are the mean vector and covariance matrix of the posterior distribution. It is worthwhile to mention that the estimated mean vector could maximize the exponential term in (3) and this could also lead to the solution of GLSM in (3).

The posterior estimated parameters are obtained as

$$y_{\text{post}} = y + Z_1 X^T V^{-1} [c - X y_0], \tag{7}$$

where Z_1 is the posterior covariance matrix of estimated parameters and it is shown in (8), and after applying Woodbury matrix identity, it is reformed as (9):

$$Z_1 = \left(Z_0^{-1} + X^T V^{-1} X \right)^{-1}, \tag{8}$$

$$Z_1 = Z_0 - Z_0 X^T \left(V + X Z_0 X^T \right)^{-1} X Z_0. \tag{9}$$

Here, regarding IFYs as estimated parameters y with prior covariance matrix Z_0 (diagonal matrix with only consideration of each fission yields uncertainty in ENDF/B-VII.1), observables c represent the evaluated CFYs in ENDF/B-VII.1, total independent yields, fission system total mass number, and charge number, respectively. The corresponding design matrix could be formulated as follows:

(1) Consistency with CFYs: $c = My$, where M is the Q-matrix proposed in [11]. It could be formulated from the linear mapping in (1) with the provided branching ratios data in ENDF/B-VII.1 decay sublibrary. This updating process follows Luca Fiorito's updating procedures [15] on CFYs consistency in JEFF-3.1.2. Different than in previous work [14], this work explicitly constructs this design matrix with branching ratios rather than obtaining each element via direct perturbations using a burnup code. Such procedures allow direct examination of consistency between IFYs and CFYs in the current releases of ENDF/B-VII.1. Total IFYs, total mass number, and total charge number conservations are implemented following the procedures proposed in Pigni et al.'s work [14]. The updating results of IFYs' covariance matrix are in

$$Z_1 = Z_0 - Z_0 M^T \left(V + M Z_0 M^T \right)^{-1} M Z_0. \tag{10}$$

(2) Conservation of binary fission: $T_y = U^T y$, where $\mathbf{U} \in \mathbb{R}^{n \times 1}$ is a unity vector. The sum of total yield T_y is 2.0 with summation precision of $\sigma^2_{\text{sum}} = 1.0 \times 10^{-5}$. The updated covariance matrix subsequent to (10) is listed in (11). It should be noticed that ternary fissions may occur; however they are not considered in ENDF/B-VII.1 and these ternary fissions are not included in this updating process:

$$Z_2 = Z_1 - Z_1 U \left(\sigma^2_{\text{sum}} + U^T Z_1 U \right)^{-1} U^T Z_1. \tag{11}$$

(3) Conservation of fission system mass number: $T_M = N^T Y$, where $N \in \mathbb{R}^{n \times 1}$ whose element corresponds to the mass number of each fission product. The total mass number of fission system is conserved to 233.57915 (considering the average prompt neutrons released at 0.0253 eV is 2.42085 recorded in ENDF/B-VII.1 and mass defect of U-235 is not considered). The assumed variance of total mass number is 1.0×10^{-5}. The updated covariance matrix subsequent to (11) is shown in

$$Z_3 = Z_2 - Z_2 N \left(\sigma^2_{\text{sum}} + N^T Z_2 N \right)^{-1} N^T Z_2. \tag{12}$$

(4) Conservation of fission system charge number: $T_C = W^T y$, where $W \in \mathbb{R}^{n \times 1}$ with each element being the charge number of each fission product considered. The total charge number of fission system is conserved as 92.05318. This total charge number is calculated from the charge numbers of each fission product weighted by their corresponding IFYs provided in ENDF/B-VII.1. It is observed in

this work that if we take the total charge number as exactly 92.0, the calculated CFYs calculated from updated IFYs will have large discrepancy with CFYs provided in the library. And this discrepancy will be narrowed when we take the decimal digits into consideration. The updated covariance subsequent to (12) is shown in

$$Z_4 = Z_3 - Z_3 W\left(\sigma_{\text{sum}}^2 + W^T Z_3 W\right)^{-1} W^T Z_3. \quad (13)$$

Correlation matrix of updated IFYs is plotted (see Figure 5). These correlations are introduced sequentially to cooperate the consistency with CFYs, conservation of binary fission, mass number, and charge number of fission system. Figure 5(a) shows that there is a significantly two-humped tendency in the correlation distribution. This tendency is similar with the two-humped distribution of IFYs, where many correlations are introduced from the conservation constraints in fission system, while fewer correlations are introduced between humped part and valley part. And Figure 5(b) presents a close look of the correlations among fission product index range from 65 to 245. It could be noticed that the diagonal of this correlation matrix is divided into several small groups regarding different decay chains. IFYs within each decay chain have negative correlation with each other introduced from the consistency of CFYs.

The updated IFYs are compared with the prior fission yields recorded in ENDF/B-VII.1 (see Figure 6). It could be seen that small adjustment is introduced to fission product yields in the two-humped part, while larger adjustment is introduced in the valley and two tail parts. This is mainly because IFYs in those parts have smaller prior fission yields and they are not as accurately evaluated as those larger ones in the two-humped part. Therefore, more adjustments are expected in those regions. The updated and prior standard deviations are presented and compared (see Figure 7). It could be seen that the adopted updating procedures could reduce the uncertainty of updated IFYs. This is mainly due to the introduced constraints that further constrain the uncertainty of these fission yields and introduce covariances among them.

The final updated covariance matrix of IFYs Z_4 and the posterior IFYs mean vector y_4 are applied to generate the perturbation samples of IFYs. The detailed sampling procedures are further discussed in the following section.

3.2. Lognormal-Based Sampling Procedures. Considering IFYs are inherently positive, random sampling under normal distribution could draw unphysical negative samples. These negative samples would appear significantly when the sampled parameters have large uncertainty (e.g., relative difference $\sigma/\mu > 30\%$). Smith et al. concluded that when the relative uncertainty of a random variable exceeds 30%, the probability distribution of this parameter chosen to represent its physical uncertain information tends to be skewed noticeably [18] and the drawn negative samples fraction tends to grow. It could therefore be concluded that normal distribution is not adequate to describe inherently positive random variables whose uncertainties are large, because it could not capture the skewness of random variable distribution. By the principle of maximum information entropy, lognormal distribution is suggested to be the optimal choice for inherently positive parameter when only expectation and variance are known about this parameter [10, 29]. Larger relative uncertainty would result in a more skewed distribution (shown in Figure 8). Lognormal distribution is shifting to a normal-like distribution as its relative uncertainty becomes lower than 30%, where skewness of the distribution is not significant.

The updated posterior IFYs relative uncertainties are compared with prior relative uncertainties (see Figure 9) in our previous work [30]. Except for a few fission products which have their relative uncertainties increased, most fission products have their corresponding relative uncertainties decreased to around 42%. The increased relative uncertainty fission products are Ag130m0, Cd129m0, Sn127m1, Cd126m0, In126m0, Sb124m1, Zn123m1, Ag115m0, Y93m1, Y93m0, Se85m1, and Ge77m0. Their relative uncertainties increased due to their updated smaller posterior mean values. From Figure 10, it could be seen that most fission yields standard deviations have been reduced because of the updating process. However, the above fission products have their mean value updated even smaller and that makes their relative uncertainties increased. Compared with the listed monitor fission products for fission of U-235 in Fiorito et al.'s work [15], they are not included and we may think they are less relevant to the reactor burnup and critical calculation. When applying simple random sampling procedures under normal distribution, drawing samples in $\mathbb{R}^{n\times S}$ from the $N(y_4, Z_4)$, where n is the number of fission yields and S is the sample size, it is almost impossible to draw a sample set with all positive yields as the yields domain is too large (e.g., $n > 900$).

In this work, lognormal random sampling procedures are applied to generate IFYs perturbation samples. The sampling follows the development of Žerovnik et al. [19] and applies it into the generation of IFYs samples. Multivariate lognormal distribution is defined as

$$L = \ln(y) \sim N(\mu_l, Z_l), \quad (14)$$

where y is the posterior IFYs with expectation y_4 and covariance matrix Z_4 estimated by Bayesian updating method discussed in Section 3.2 and $L \in \mathbb{R}^{n\times 1}$ is the natural logarithmic value of independent yields. μ_l and Z_l are the corresponding mean and covariance matrix of IFYs in the natural logarithmic domain. The detailed derivation of their relation with parameters in original domain (y_4 and Z_4) could be found in [20]. The basic idea is recapped in the following.

Consider the preservation of probability; the relation between random variables in original domain and logarithmic domain is formulated in

$$p_L(l)\mathrm{d}l = p_Y(y)\mathrm{d}y. \quad (15)$$

The lognormal distribution density is therefore derived as in

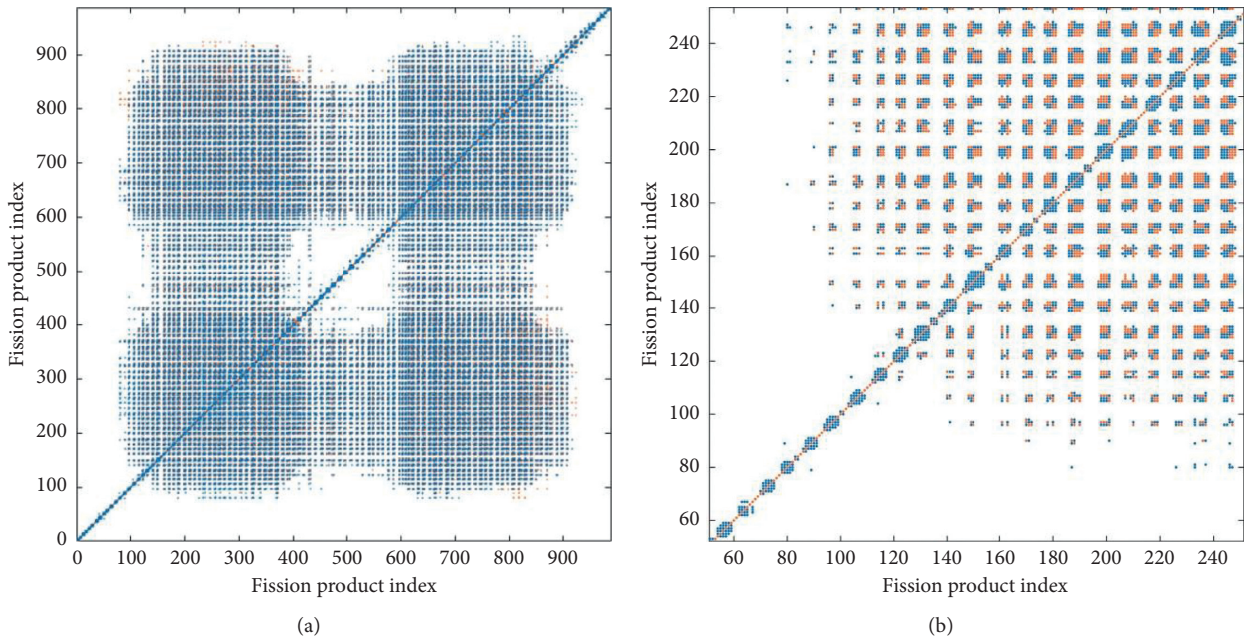

Figure 5: Estimated IFYs correlation matrix. (a) All the estimated correlation information. (b) Section of the estimated correlation information. Red dot indicates the positive correlation and blue dot indicates the negative correlation. The fission product index refers to each fission product identified by its charge number Z, mass number A, and isomeric state I ($ZZAAAI$). These indices are grouped by the mass number and arranged in a descending manner. For each mass group, charge number is ordered in an ascending manner to cooperate the β^- decay.

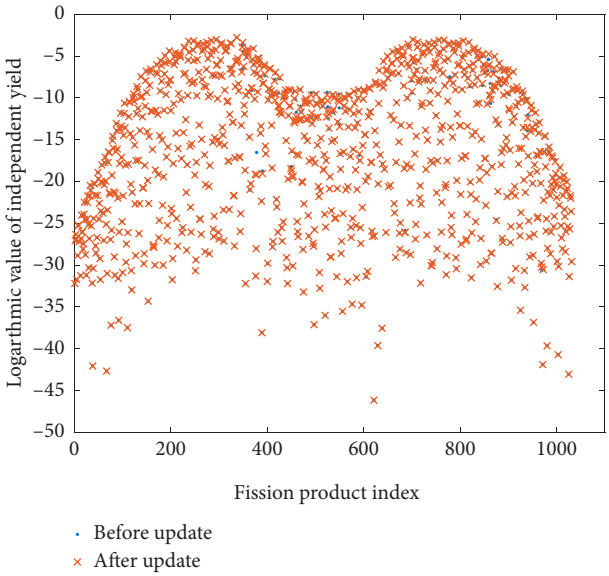

Figure 6: IFYs distribution before and after sequential Bayesian updating. Natural logarithm is presented on the y-scale. The fission product index refers to each fission product identified by its charge number Z, mass number A, and isomeric state I ($ZZAAAI$). These indices are grouped by the mass number and arranged in a descending manner.

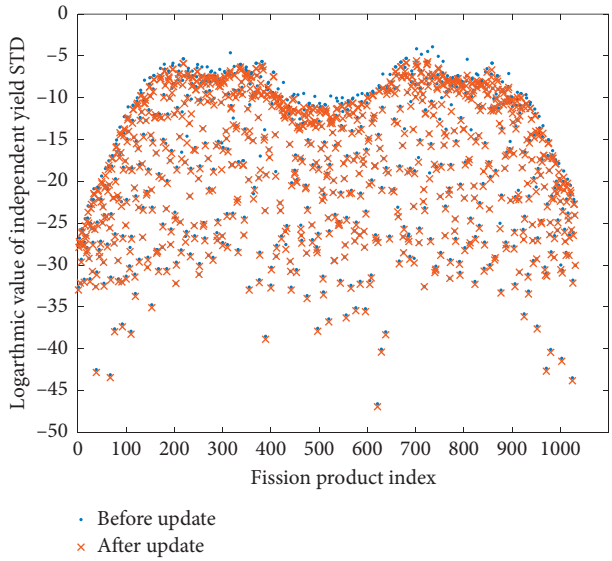

Figure 7: IFYs standard deviation (STD) distribution before and after sequential Bayesian updating. Natural logarithm is presented on the y-scale. The fission product index refers to each fission product identified by its charge number Z, mass number A, and isomeric state I ($ZZAAAI$). These indices are grouped by the mass number and arranged in a descending manner.

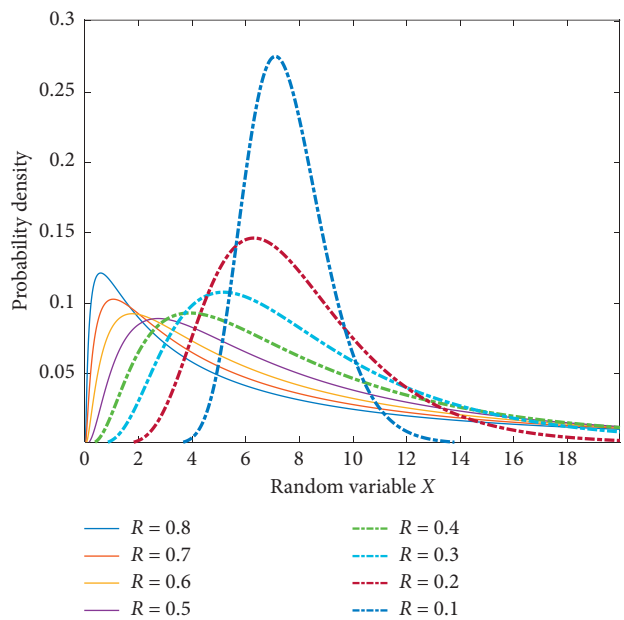

Figure 8: Lognormal distribution of random variable X in terms of its relative uncertainty. Relative uncertainty $R = (\sigma_X/\mu_X)$ is ranged from 10% to 80% and $\mu_X = 2.0$. Dashed line shows the distribution with relative uncertainty lower than or equal to 40%, whereas solid line indicates the distribution with relative uncertainty larger than 40%.

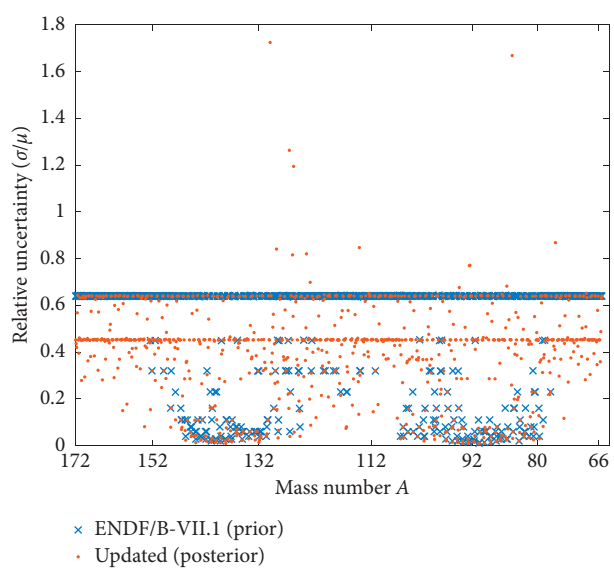

Figure 9: Relative uncertainties of prior and posterior independent yields in ENDF/B-VII.1 of fission products. These fission products are grouped with their corresponding mass number and the first mass numbers are labelled in this figure [30]. The increased relative uncertainty fission products are Ag130m0, Cd129m0, Sn127m1, Cd126m0, In126m0, Sb124m1, Zn123m1, Ag115m0, Y93m1, Y93m0, Se85m1, and Ge77m0.

$$p_Y(y) = \frac{1}{(2\pi)^{(n/2)}\left|Z_l\right|^{(1/2)}\prod_{i=1}^{n} y_i}\exp\left\{-\frac{1}{2}\left[\ln(y)-\mu_l\right]^T Z_l^{-1}\left[\ln(y)-\mu_l\right]\right\}. \quad (16)$$

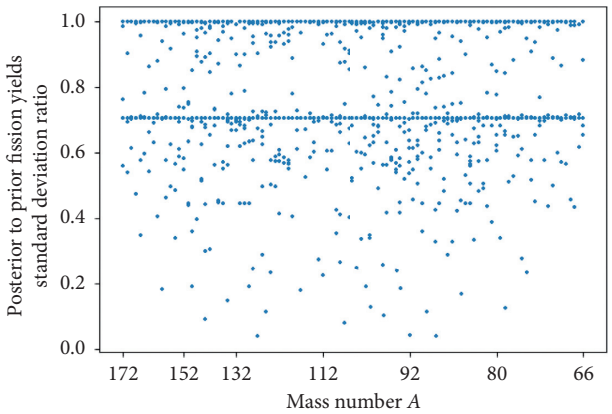

Figure 10: Posterior to prior fission yields standard deviation ratios. These fission products are grouped with their corresponding mass number and the first mass numbers are labelled in this figure.

With the logarithmic density function, each element in μ_l and Z_l is derived as

$$\mu[\ln(y_i)] = \ln(y_i) - \left(\frac{\mathrm{Var}[\ln(y_i)]}{2.0}\right), \tag{17}$$

$$\mathrm{cov}\left[\ln(x_i),\ \ln(x_j)\right] = \ln\left[\frac{\mathrm{cov}(y_i, y_j)}{\mu[y_i]\mu[y_j]} + 1\right], \tag{18}$$

where $\mathrm{cov}(y_i, y_j)$ and $\mu[y_i]$ are retrieved from the posterior updated IFYs covariance matrix Z_4 and updated IFYs mean vector y_4. With the calculated distribution parameters μ_l and Z_l, the lognormal-based IFYs sampling procedures could be conducted as follows:

(1) Obtain prior IFYs information including IFYs value y_0 as well as its covariance matrix Z_0 from ENDF/B-VII.1 fission yield sublibrary. Implement Bayesian updating procedures detailed in Section 3.2 on the prior information and obtaining the updated IFYs mean vector y_4 and the estimated covariance matrix Z_4.

(2) Consider IFYs follow lognormal distribution, and transform y_4 and Z_4 into natural logarithmic domain with (17) and (18). The normal distribution parameters of natural logarithmic yields are obtained as mean vector μ_l and covariance Z_l.

(3) The transformed logarithmic domain covariance could not remain symmetric positive definite (SPD) due to the numerical error in the transformation procedure. A nearest-SPD searching algorithm [31] is therefore applied to search for the nearest SPD approximation of the calculated covariance matrix in the sense of least Frobenius norm difference. The approximated SPD logarithmic domain covariance matrix is thus obtained as Z_l'.

(4) Implement the simple random sampling procedures in the logarithmic yield domain with distribution parameters mean μ_l and approximated SPD covariance matrix Z_l'. And the generated logarithmic fission yields sample matrix $P_{n\times S}$ is obtained where n denoted the number of fission products considered and S is sample size.

(5) Take the exponential transformation of each element in sample matrix $P_{n\times s}$ and the sampled negative-free samples are generated and denoted as $Y_{n\times S}$.

The nearest-SPD searching algorithm approximates non-SPD covariance matrix Z_l by an approximated matrix Z_l' with relative difference in Frobenius norm $(\|Z_l - Z_l'\|_F/\|Z_l\|) = 9.74\%$ and their corresponding eigenvalues distributions are presented in Figure 11. The nearest-SPD searching algorithm could approximate a non-SPD covariance matrix while most of its eigenvalue unchanged.

The approximation that resides in the above sampling procedures is the SPD approximation of calculated covariance matrix. This approximation could affect consistency of each drawn IFYs sample with the physical constraints imposed on it. There are 1,000 IFYs samples drawn with the lognormal sampling procedures. And the sample mean and standard deviation (STD) for each fission product yield and Pearson's correlation coefficient between these fission yields are calculated and justified by comparison with its corresponding population values in updated y_4 and Z_4 (see Table 4).

Table 4 indicates that the proposed lognormal sampling procedures could obtain an overall representation of IFYs population distribution considering the lower RMSE. However, there still exist a few fission products listed in Figure 12 having large biases compared with their corresponding population values considering the maximum of absolute relative difference. After comparing these fission products with the monitor fission products for thermal neutron induced U-235 fission listed in Fiorito et al.'s work [15], they are not included and could be considered less relevant to reactor burnup and criticality calculations. These outliers' appearance could result from the nearest-SPD procedures and a further investigation regarding this will be conducted in future work. Figure 13 presents the sampled Pearson's correlation coefficients relative difference to their corresponding population values. It could be seen that simple random sampling procedure is not an efficient sampler for sampling low correlation fission yields $(|\rho| < 0.1)$ as shown in the neighbour around 0.00 in this figure. However, these low correlations could have little impact on the uncertainty quantification of fission yields compared with large correlations. As for the larger correlations $(|\rho| > 0.25)$, 1,000 samples are sufficient for maintaining the Bayesian updated correlations and this discrepancy could be further reduced when increasing the sample size. A more efficient sampler, like Latin Hypercubic Sampler (LHS), could be adopted to guarantee more precise results when using 1,000 samples and this will be adopted in future work.

The consistency of IFYs samples with these imposed physical constraints is justified in Table 5. The conservation parameters (e.g., total fission yields, total mass number, and total charge number) are calculated for each yield samples and the mean and standard deviation are summarized to compare with the target conservation value. It is found that although the consistency is not strictly restored as the

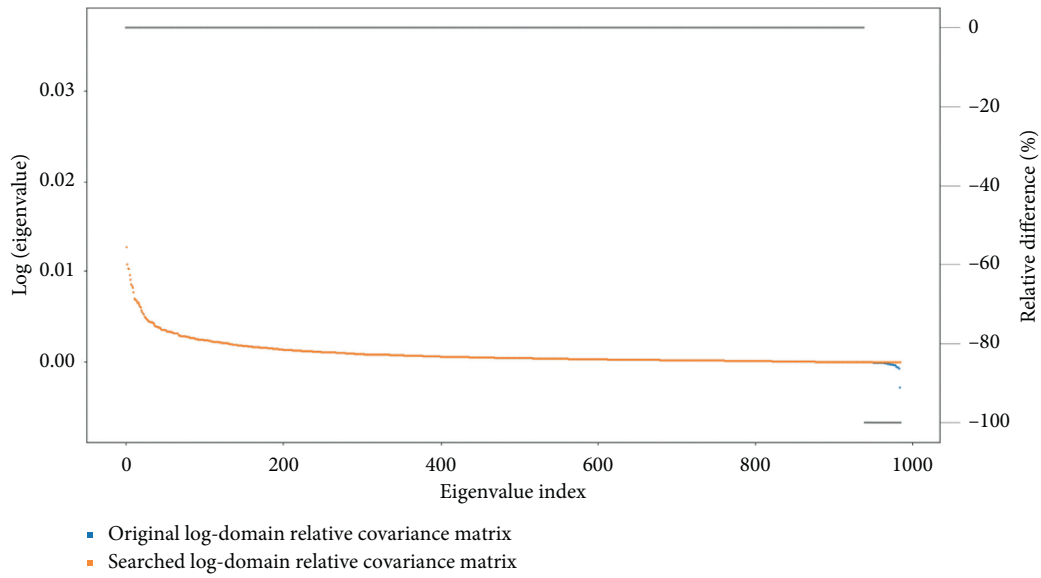

Figure 11: Eigenvalue distribution of relative covariance matrix. Blue dots show the eigenvalue distribution of transformed logarithmic relative covariance. Red dots show the eigenvalue distribution of approximated relative covariance matrix searched by nearest-SPD algorithm. Grey lines show the relative difference of these eigenvalues.

Table 4: Independent yield samples justification.

Relative difference	Mean	RMSE	Max of absolute
Sample mean	8.244×10^{-4}	1.604×10^{-2}	1.456×10^{-1}
Sample STD	6.492×10^{-3}	6.016×10^{-2}	8.926×10^{-1}
Sample ρ	-9.494×10^{-4}	1.212×10^{-4}	7.933×10^{0}
Comment	STD: sample standard deviation; ρ: Pearson's correlation coefficient RMSE: root mean square error Max of absolute: the maximum absolute value of relative difference		

standard deviation of the total yield is larger than the imposed 10^{-5}, their mean values are close enough to the target value indicating the constraints are maintained. The large standard deviation is originated from the approximation mentioned above.

In order to examine the difference between normal-based sampling and lognormal-based sampling, 1,000 samples are drawn from the IFYs distribution of Zr95m0, Mo95m0, and Cs134m0. Notation m0 indicates these fission products are at ground state. The IFYs of these three fission products are explicitly involved in V.S.O.P. burnup calculation and are important for reactor decay heat release calculations. Especially for Cs134m0, it is one of the main decay heat contributors of UOX fuels in long-term after reactor shutdown [32]. The updated relative uncertainty of Zr95m0 IFY is 16.1% while Cs134m0 and Mo95m0 have their relative uncertainties of 38.4% and 65.7%, respectively. From the sampled histogram of these fission products IFYs samples (see Figures 14–16), lognormal-based sampling procedures (blue bars) could effectively capture the skewness of these fission yields and permit "negative-free" samples. It is also observed that the skewness of these fission products would become larger as their relative uncertainties become larger (e.g., Mo95m0 and Cs134m0).

4. Results and Discussion

4.1. Uncertainty Analysis of the Effective Multiplication Factor at Equilibrium Core. The unperturbed burnup calculation is conducted with V.S.O.P. built-in fission yields library and ENDF/B-VII.1 posterior fission yields. Figure 17 shows that reactor achieved the equilibrium state after operating longer than 2500 days. Effective multiplication factor calculated from ENDF/B-VII.1 posterior fission yields is compared with that calculated from V.S.O.P. built-in fission yields and the total discrepancy at equilibrium core state (which is at the end point of fuel cycle time in Figure 17) is lower than 50 pcm which is small enough for the following fission product yields uncertainty propagation analysis. The comparison between ENDF/B-VII.1 posterior fission yields predicated k_{eff} (black dashed line) and built-in yields predicted k_{eff} (orange dashed line) are shown in Figure 18(b). This discrepancy is within the sampling distribution of k_{eff}.

1,000 fission yields samples are generated with normal-based sampling procedures and lognormal-based sampling procedures and they are propagated to V.S.O.P. burnup calculation to obtain k_{eff} samples under equilibrium core state (3049 days). The sample distributions from these two sampling procedures are drawn and compared (see Figure 18). It is obvious from the comparison that normal-based samples contain fewer distribution information compared with lognormal samples as its distribution range is smaller than that in lognormal samples. This is due to the zero cut-off procedure of the uncontrolled negative samples. Such procedure artificially omits certain information in the original fission yields distributions and could not provide a

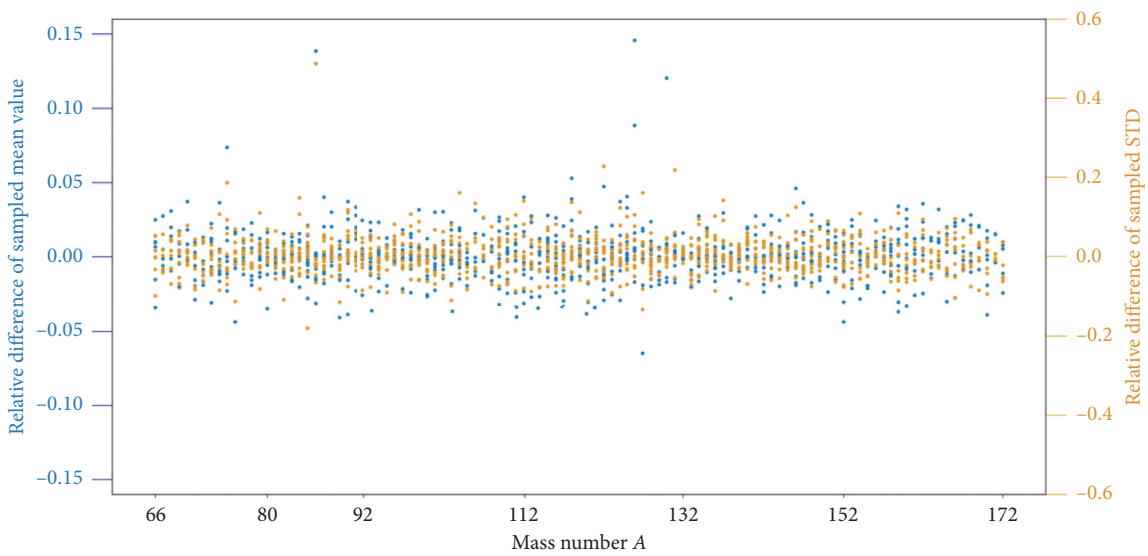

Figure 12: Relative difference of lognormal-based sampled independent fission yields mean values (blue dots) and STD (orange dots) to Bayesian updated values. The outlier fission products are (mean values) Ag130m0, Sn127m1, Cd126m0, In126m0, In118m1, Br86m1, and Ge75m0 and (STD values) Sb131m0, Ag130m0, Cd126m0, Sn122m0, and Br86m1.

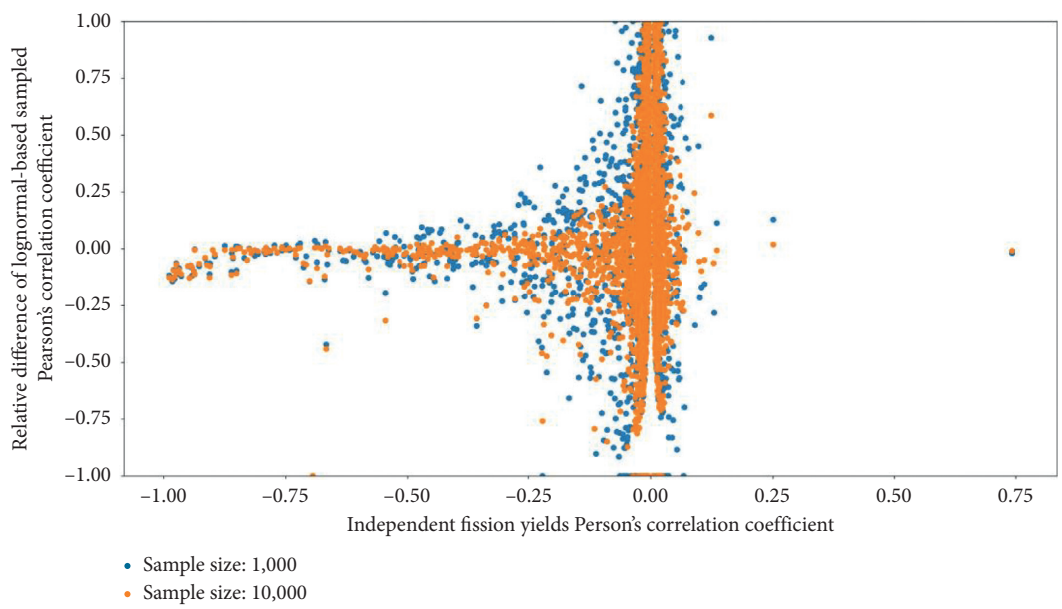

Figure 13: Relative difference of lognormal-based sampled independent fission yields Pearson's correlation coefficients to Bayesian updated values against Bayesian updated correlation coefficients. Blue dots represent the values obtained from 1,000 samples and orange dots represent the values obtained from 10,000 samples.

Table 5: Independent yield physical constraints consistency.

Constraint	Target	Mean	STD
Binary fission	2.00000	2.00062	4.1960×10^{-3}
Mass number	233.57915	233.64866	4.6685×10^{-1}
Charge number	92.05318	92.07647	1.8432×10^{-1}

correspondingly reasonable and satisfied sampling distribution of k_{eff}. In this sense, lognormal sampling procedures overcome this problem by imposing a more plausible distribution on fission yields and allow the generation of smaller perturbed samples. Therefore, it leads to a negative skewness (long tail in left) of effective multiplication factor distribution and permits a more rational and persuasive sampling distribution.

The uncertainty analysis results are presented (see Table 6). The propagated sampled distribution of k_{eff} from normal-based sampling method passes the normality test with p value 0.3737 and the quantified relative uncertainty is around 1.09×10^{-4}. Lognormal samples provide a skewed k_{eff} distribution and fails the normality test with p value smaller than 0.05. The quantified relative uncertainty from

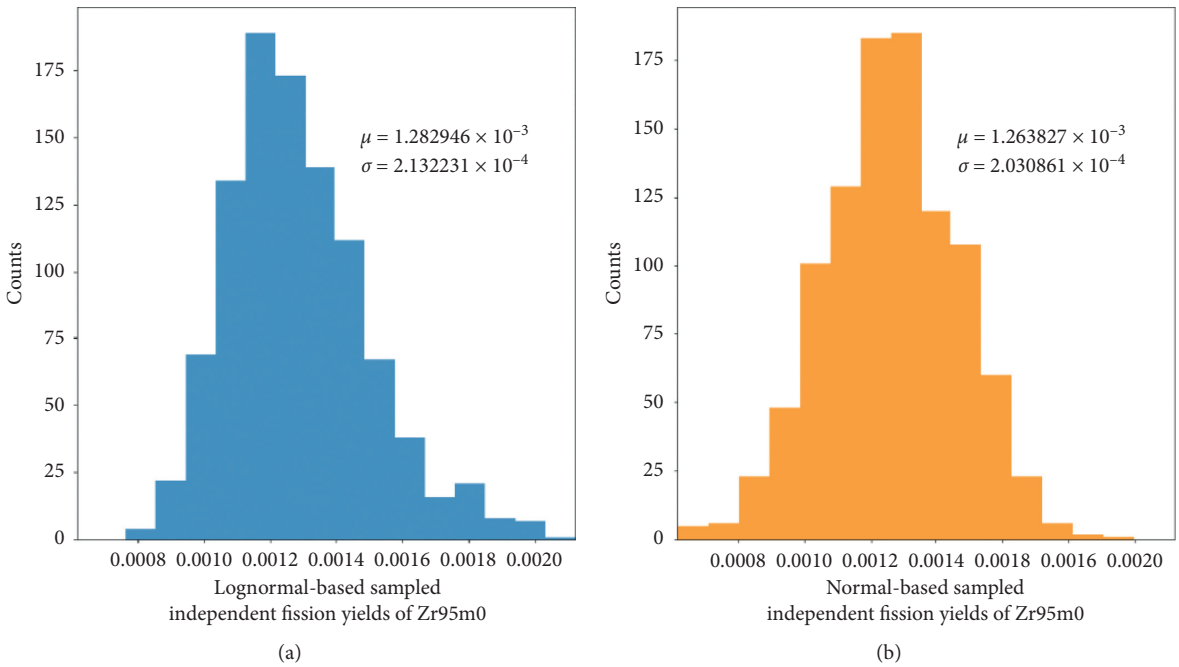

Figure 14: Histogram comparison of lognormal sampled (a) and normal sampled (b) independent fission yields of Zr95m0. This fission product has relative uncertainty of 16.1%. The text presents the sampled mean value and STD and the population mean and STD for Zr95m0 are 1.271856×10^{-3} and 2.029263×10^{-4}.

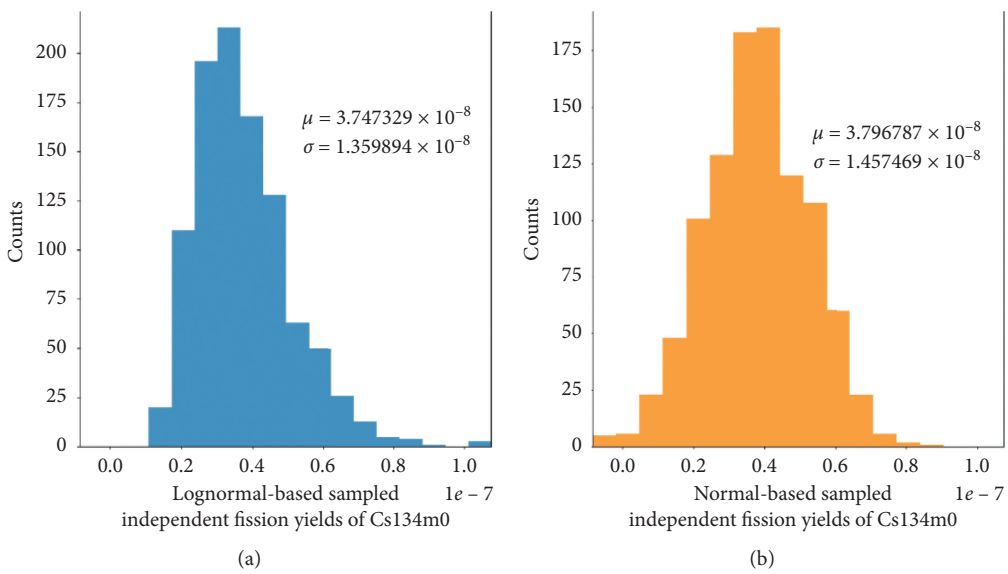

Figure 15: Histogram comparison of lognormal sampled (a) and normal sampled (b) independent fission yields of Cs134m0. This fission product has relative uncertainty of 38.4%. The text presents the sampled mean value and STD and the population mean and STD for Cs134m0 are 3.8544056×10^{-8} and 1.456322×10^{-8}.

this distribution is 2.58×10^{-4}. The k_{eff} quantified from lognormal-based sampling method is larger than that from normal-based sampling method, and this shows that the zero cut-off effect in normal-based sampling method could cause underestimation of fission product yields uncertainty contribution to QoIs.

4.2. Uncertainty Analysis of Certain Fission Products Atomic Densities. In this section, fission products Zr95m0, Mo95mo, and Cs134m0 atomic densities uncertainties contributed from fission products yields are quantified. Specifically, their uncertainties differences from different sampling methods are compared and discussed. From the

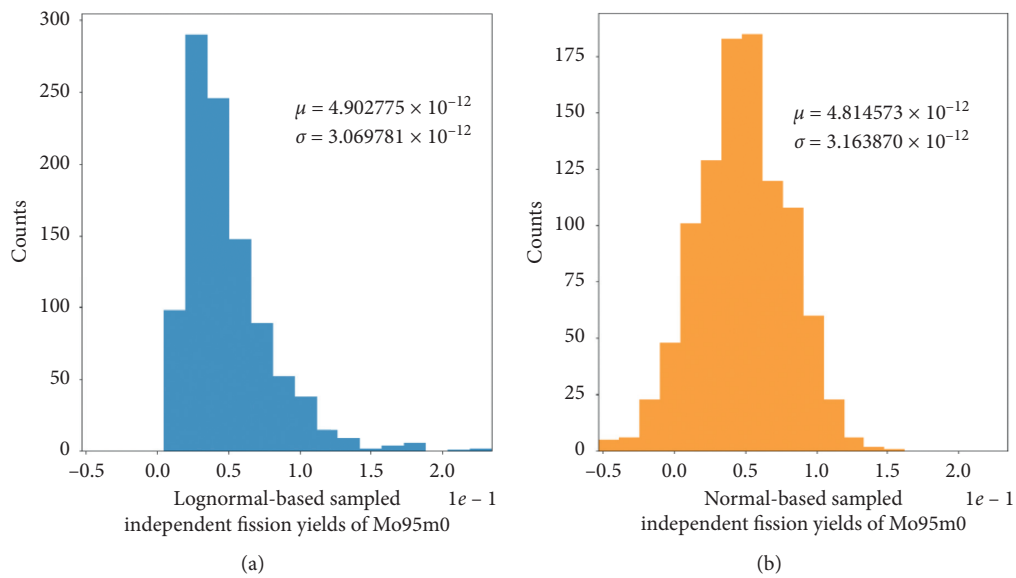

Figure 16: Histogram comparison of lognormal sampled (a) and normal sampled (b) independent fission yields samples of Mo95m0. This fission product has relative uncertainty of 65.7%. The text presents the sampled mean value and STD and the population mean and STD for Mo95m0 are 4.939650×10^{-12} and 3.161380×10^{-12}.

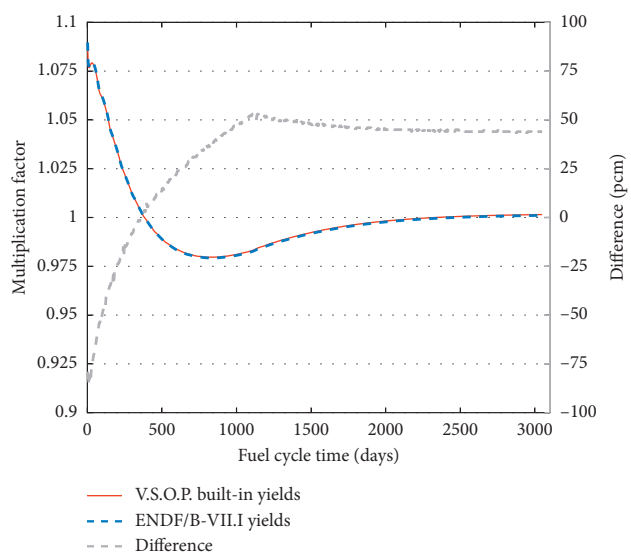

Figure 17: Multiplication factor predictions with operation time. Operation time involves a running-phase (0–2500 days) and equilibrium core state (3049 days). The multiplication factor prediction differences of V.S.O.P. built-in yields and ENDF/B-VII.1 posterior yields are plotted.

discussions in Section 3.2, Zr95m0, Cs134m0, and Mo95m0 have their IFYs relative uncertainties of 16.1%, 38.4%, and 65.7%, respectively. And their IFYs sampling results shown in Figures 14–16 (blue bars) indicate that the skewness of the sampled distribution becomes significant with their fission yields relative uncertainties increasing. When we adopt normal-based sampling procedures to a skewed distribution, there will be more negative samples values and the zero cut-off would deliver more underestimation into the uncertainty analysis results.

Figures 19–21 track the atomic density of Zr95m0, Mo95m0, and Cs134m0 in the loaded 9.8 kg fresh fuel (with enrichment 8.5 wt.%) in HTR-PM along with their irradiation. The horizontal axis indicates the average burnup values of these fuels. As HTR-PM allows recirculation of fuels, 15 times recirculation is adopted in this analysis, which indicates these fresh fuels will be reloaded into the core 15 times before they are finally discharged. The discharged burnup value or the end point of the horizontal axis is 90210.44 MW·d/tU. Throughout the burnup process, the thermal power of reactor core is kept at 250 MW.

The atomic densities of Zr-95m0 fluctuate along with the increases of fuels burnup value. This fluctuation is due to the fuel recirculation procedures adopted in V.S.O.P. burnup

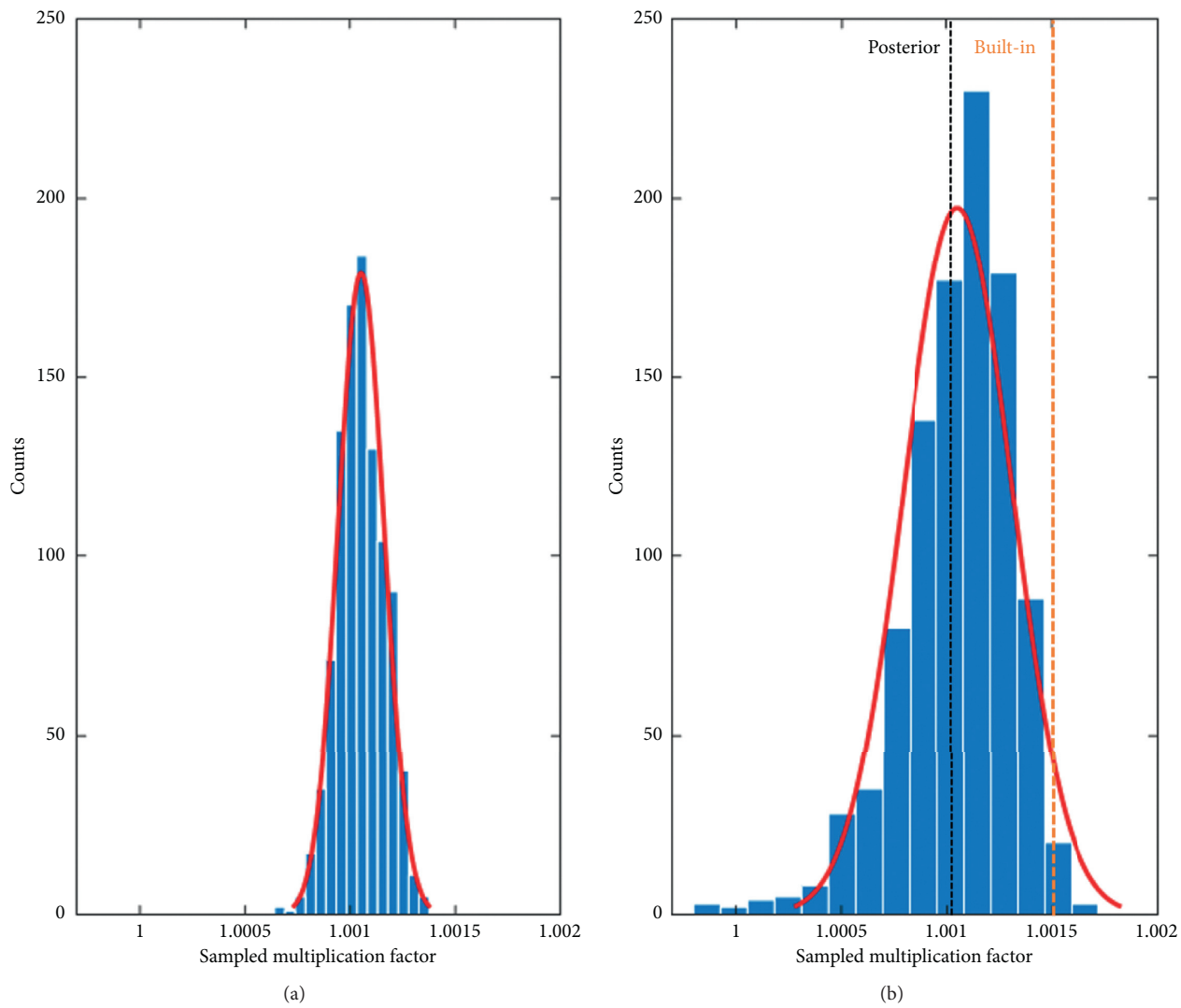

Figure 18: Histogram of 1,000 multiplication factor samples obtained at equilibrium core state. (a) Samples obtained by normal-based sampling procedures. (b) Samples obtained by lognormal-based samples procedures. Red line indicates the superimposed fitted normal density from the sampled data.

Table 6: Uncertainty analysis results and comparison of multiplication factor at equilibrium core state.

Sampling procedures	Nominal prediction V.S.O.P with ENDF/B-VII.1 posterior fission yields	Fission yield uncertainty analysis results			
		Samples mean	Relative uncertainty	95% CI	Normality test[(2)]
Normal	1.00106	1.00105	$1.09E-04$	$[1.05E-04, 1.14E-04]$	Passed: $p = 3.737E-01$
Lognormal	1.00106	1.00105	$2.44E-04$	$[2.44E-04, 2.76E-04]$[(1)]	Failed: $p = 1.103E-04$
Comment	(1) 95% confidence interval is estimated by bootstrapping method with 100,000 bootstrap samples (2) Normality test is conducted on the z-scores of multiplication factor samples with the K-S test				

calculations. There are total 14 lower valleys that appeared in dashed line of Figure 19 which corresponds to the 14 times reloading of the fuels from the bottom of the core to the top. For each reloading, the fuels will be irradiated again during their passes through the core. As it could be seen from Figures 19–21, except for the atomic densities' decrease of Zr95m0 along with the increase of average burnup values, Mo95m0 and Cs134m0 have their atomic densities accumulated throughout the whole burnup process. During the burnup process, their atomic densities relative uncertainties

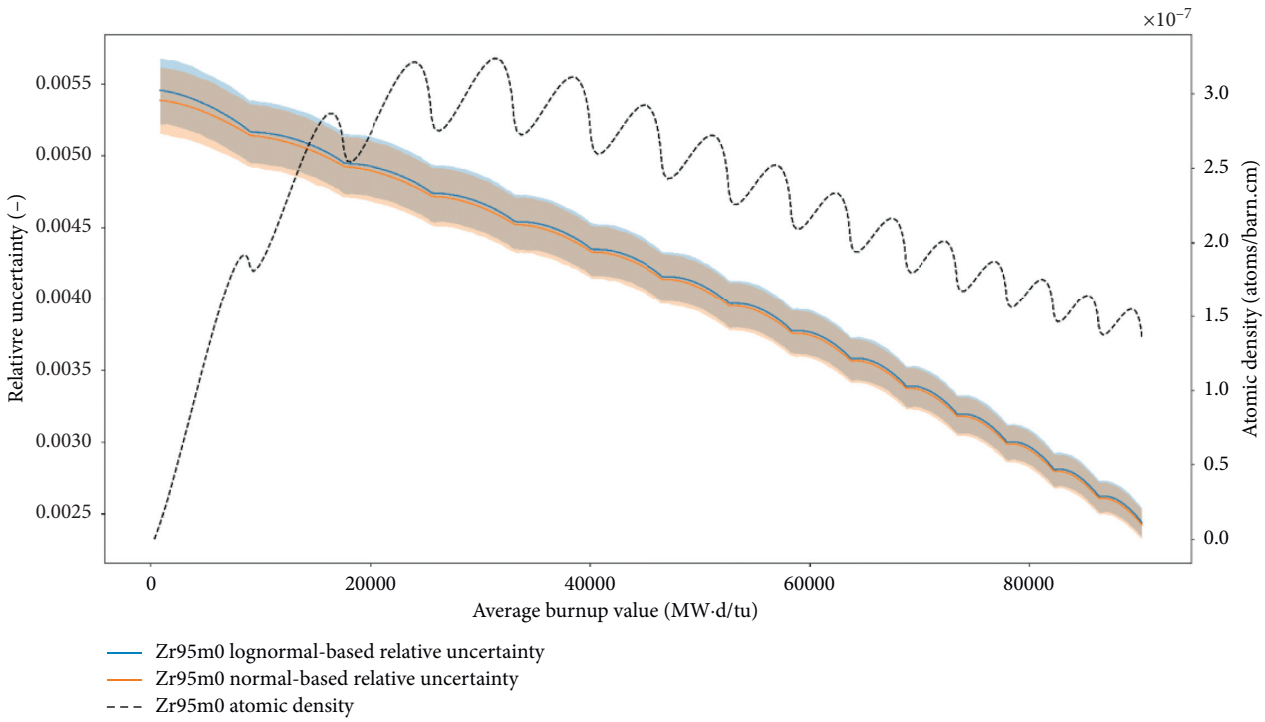

Figure 19: Relative uncertainties of Zr95m0 against fuels average burnup values. Lognormal-based sampling results (blue line) and normal-based sampling results (orange line) are plotted. The shades in this figure are the 95% confidence interval of relative uncertainties.

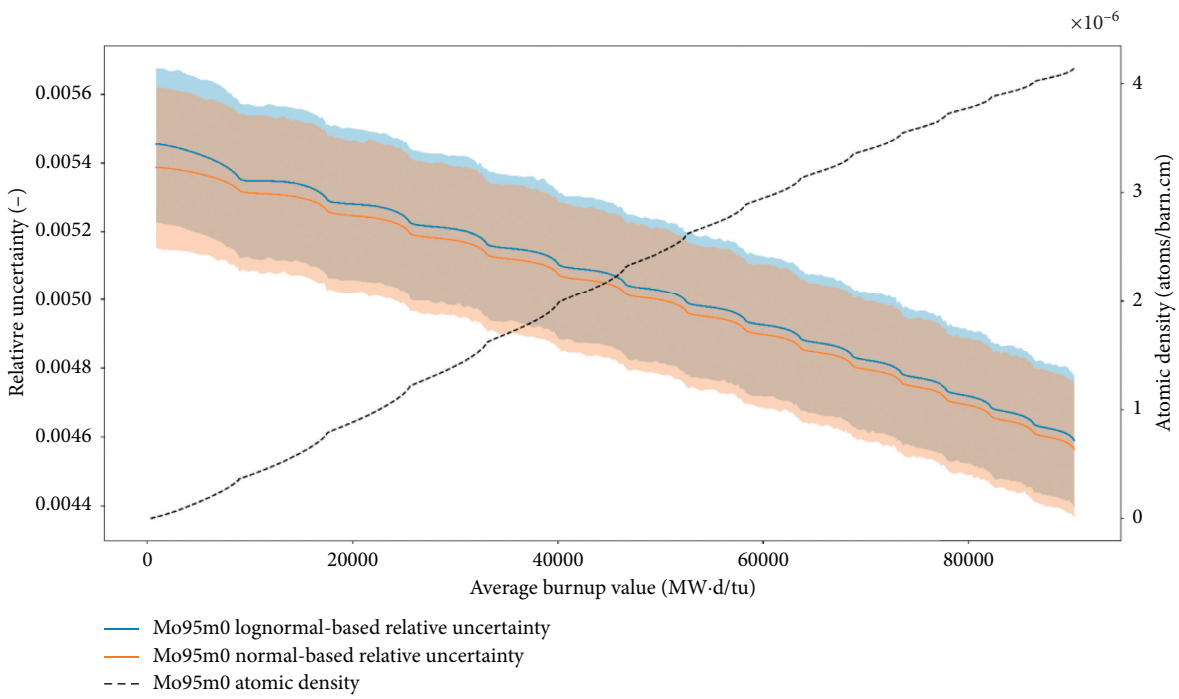

Figure 20: Relative uncertainties of Mo95m0 against fuels average burnup values. Lognormal-based sampling results (blue line) and normal-based sampling results (orange line) are plotted. The shades in this figure are the 95% confidence interval of relative uncertainties.

contributed from thermal neutron induced U-235 fission products yields are investigated.

The atomic density relative uncertainties of the above three fission products varying with the average burnup values of fuels are plotted in Figures 19–21 (blue and orange

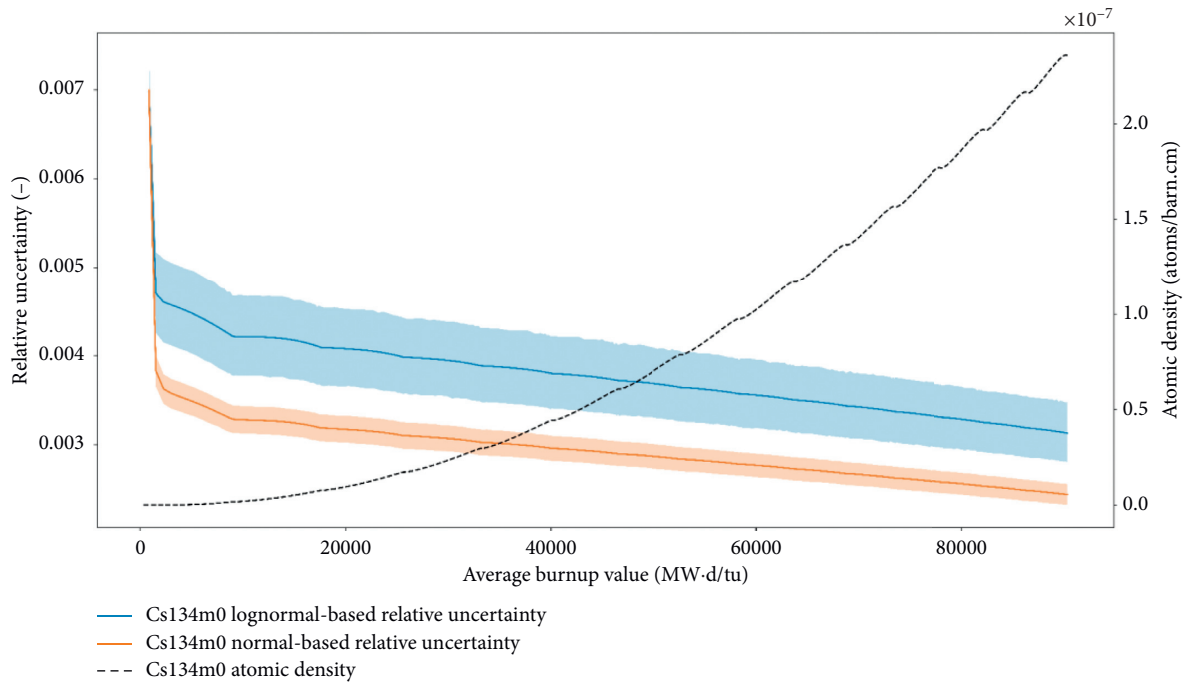

Figure 21: Relative uncertainties of Cs134m0 against fuels average burnup values. Lognormal-based sampling results (blue line) and normal-based sampling results (orange line) are plotted. The shades in this figure are the 95% confidence interval of relative uncertainties.

Table 7: Uncertainty analysis results of Zr95m0, Mo95m0, and Cs134m0.

Fission products	Atomic density (atoms/barn·cm)	Fission yield uncertainty analysis results		
		Normal-based relative uncertainty (%)	Lognormal-based relative uncertainty (%)	Relative difference to lognormal-based relative uncertainty (%)
Zr95m0	1.3532×10^{-7}	0.242	0.244	−0.8
Mo95m0	4.1478×10^{-6}	0.456	0.458	−0.4
Cs134m0	2.3575×10^{-7}	0.244	0.313	−22.0
Comment	These results show atomic densities in 9.8 kg heavy metal irradiated up to 90210.44 MW (d/tU)			

solid line). The blue and orange shadings in these figures are the 95% confidence interval of relative uncertainty computed by bootstrap method. From these figures, it is worth to mention that lognormal-based sampling quantified atomic density relative uncertainties are larger than that quantified from normal-based sampling for all of these three fission products. This is reasonable as zero cut-off adopted in normal-based sampling method would artificially omit some information provided by fission yields distributions, and this would result in an underestimated atomic density relative uncertainty quantification result. After closely comparing the atomic density relative uncertainties underestimation for Zr95m0 and Cs34m0, it could be seen that this underestimation effect will be enlarged when the fission products IFYs have larger relative uncertainties (Zr95m0: 16.1% and Cs134m0: 38.4%). This is because lognormal distribution would resemble normal distribution when the random variate has smaller relative uncertainty, as discussed in Section 3.2. And in this case, lognormal-based sampling results would be in agreement with those calculated from normal-based sampling. Therefore, this underestimation would be narrowed.

Besides, another interesting phenomenon is observed here. This underestimation seems not positively correlated with the relative uncertainty of random variates, as it is seen from comparison between Mo95m0 and Cs134m0. Although Mo95m0 has its relative uncertainty (65.7%) larger than Cs134m0 (38.4%), the underestimation effect observed from Figures 20 and 21 shows that the underestimation effect of Mo95m0 is smaller than that of Cs134m0. One possible reason could be the decay of these fission products. As Mo95m0 is the direct descendant of Zr95m0 whose half-life is around 64 days, its atomic density relative uncertainty is contributed both from its own fission yields uncertainty and the atomic density uncertainty of Zr95m0. As Zr95m0 atomic density uncertainty is less underestimated, the atomic density relative uncertainty underestimation in Mo95m0 is therefore counterbalanced. While Cs134m0 is treated as stable fission products in V.S.O.P. burnup fission product chains, its atomic density relative uncertainty is directly related to its fission yields uncertainty and large

atomic density relative uncertainty underestimation could be seen. The atomic density relative uncertainties of all these three fission products quantified at 90210.44 MW·d/tU are summarized in Table 7.

5. Conclusions

The present work proposed a stochastic UQ method for propagation fission products yields uncertainties. V.S.O.P. code [26] is used to conduct the burnup calculation of HTR-PM reactor core with allowing 15 times recirculation of fuel pebbles [30]. Uncertainties of thermal neutron induced U-235 IFYs are investigated in this work based on ENDF/B-VII.1. Bayesian updating method is applied to estimate the covariance matrix of IFYs. Lognormal-based sampling method is implemented to generate perturbations of yields samples. The differences of quantified uncertainties between conventional normal-based sampling method and lognormal-based method are addressed and investigated. Specifically, the effect of zero cut-off procedures used in normal-based sampling method is studied and discussed. From the above investigation, conclusions are summarized as follows:

(1) Lognormal-based sampling method could effectively overcome the negative samples generation caused by the large relative uncertainties in fission yields data. Compared with normal-based sampling method, it could provide reasonable and negative-free fission yields samples to permit a more plausible and reasonable QoI sampling distribution for further uncertainty analysis.

(2) The contribution of thermal neutron induced U-235 fission yields uncertainties in ENDF/B-VII.1 to k_{eff} of pebble-bed HTGR at equilibrium core is 0.0258%. This contribution is smaller than that from neutron cross section 0.48% at equilibrium core [33].

(3) The zero cut-off procedures used in conventional normal-based sampling method to overcome the negative fission yields samples appearance would underestimate the uncertainty analysis results. For relative uncertainty of effective multiplication factor, it would underestimate the results by 0.0149% which is around 42% of results obtained from lognormal-based sampling method. For atomic density relative uncertainty, the underestimations are also observed, and especially for Cs134m0, this zero cut-off effect would underestimate the atomic density relative uncertainty by 22% compared with lognormal-based quantified results.

It is worth to mention that there are several approximations and simplifications made during the Bayesian updating process and implementing of lognormal-based sampling methods in this work. The considered constraints for Bayesian updating independent yields covariance matrix are preliminary in this work and a more complete and comprehensive study regarding this will be conducted in future work. Also, the effect of using nearest SPD algorithm in implementing lognormal-based sampling method will be investigated in the future. For the following work, additional fission systems will be investigated with the proposed uncertainty propagation scheme. And a sensitivity analysis of effective multiplication factor to fission yields should be conducted to determine the reason behind the formation of effective multiplication factor skewed distribution.

Nomenclature

IFYs or $y(A, Z, I)$:	Independent fission yields
CFYs or $c(A, Z, I)$:	Cumulative fission yields
A:	Nuclide mass number
Z:	Nuclide charge number
I:	Nuclide isomeric state
$b(A', Z', I' \longrightarrow A, Z, I)$:	Branching ratio
k_{eff}:	Effective multiplication factor
y_4:	Bayesian updated IFYs mean vector
Z_4:	Bayesian updated IFYs covariance matrix
μ_l:	Natural logarithmic value of IFYs mean vector
Z_l:	Natural logarithmic value of IFYs covariance matrix
Z_l':	Nearest-SPD approximated Z_l
SPD:	Symmetric positive definite
μ:	Mean
σ:	Standard deviation
ρ:	Pearson's correlation coefficient
$\mathbb{R}^{n\times 1}$:	n-dimension real vector
$\mathbb{R}^{n\times n}$:	n-dimension real matrix.

Data Availability

The data used to support the findings of this study are available from the corresponding author upon request.

Conflicts of Interest

The authors declare that there are no conflicts of interest regarding the publication of this paper.

Acknowledgments

This work was supported by the Chinese National Natural Science Foundation Project nos. 11505102 and 11375099, Chinese National S&T Major Project 2018ZX06902013, and IAEA CRP I31020.

References

[1] H. Zhang, J. Guo, J. Lu, J. Niu, F. Li, and Y. Xu, "The comparison between nonlinear and linear preconditioning JFNK method for transient neutronics/thermal-hydraulics coupling problem," *Annals of Nuclear Energy*, vol. 132, pp. 357–368, 2019.

[2] International Atomic Energy Agency (IAEA), *HTGR Reactor Physics, Thermal-Hydraulics and Depletion Uncertainty Analysis*, International Atomic Energy Agency (IAEA), Vienna, Austria, 2020, https://www.iaea.org/projects/crp/i31020.

[3] B. Tyobeka, F. Resitsma, and K. Ivanov, "HTGR reactor physics, thermal-hydraulics and depletion uncertanty analysis: a proposed IAEA coordinated research project," in *Proceedings of the International Conference on Mathematics and Computational Methods Applied to Nuclear Science and Engineering (M&C 2011)*, Rio de Janeiro, Brazil, 2011.

[4] K. Ivanov, C. Parisi, and O. Cabellos, "Uncertainty analysis in reactor physics modeling," *Science and Technology of Nuclear Installations*, vol. 2013, Article ID 697057, 2 pages, 2013.

[5] L. Wang, J. Guo, and Li Fu, "Difference of graphite capture cross sections in ENDF/B libraries," in *Proceedings of the International Conference on Nuclear Engineering (ICONE23)*, Chiba, Japan, 2015.

[6] F. Bostelmann, G. Strydom, F. Reitsma, and K. Ivanov, "The IAEA coordinated research programme on HTGR uncertainty analysis: phase I status and Ex. I-1 prismatic reference results," *Nuclear Engineering and Design*, vol. 306, pp. 77–88, 2016.

[7] F. Bostelmann and G. Strydom, "Nuclear data uncertainty and sensitivity analysis of the VHTRC benchmark using SCALE," *Annals of Nuclear Energy*, vol. 110, pp. 317–329, 2017.

[8] P. Rouxelin, G. Strydom, A. Alfonsi, and K. Ivanov, "The IAEA CRP on HTGR uncertainties: sensitivity study of PHISICS/RELAP5-3D MHTGR-350 core calculations using various SCALE/NEWT cross-section sets for Ex. II-1a," *Nuclear Engineering and Design*, vol. 329, pp. 156–166, 2018.

[9] C. Hao, Y. Cheng, and Q. Teng, "Quantification and mechanism analysis of the kinf uncertainty propagated from nuclear data for the TRISO particle fuel pebble," *Annals of Nuclear Energy*, vol. 127, pp. 248–256, 2019.

[10] F. H. Fröhner, "Assigning uncertainties to scientific data," *Nuclear Science and Engineering*, vol. 126, no. 1, pp. 1–18, 1997.

[11] M. F. James, R. W. Mills, and D. R. Weaver, "A new evaluation of fission product yields and the production of a new library (UKFY2) of independent and cumulative yields," *Progress in Nuclear Energy*, vol. 26, no. 1, pp. 1–29, 1991.

[12] X. Wu, T. Kozlowski, H. Meidani, and K. Shirvan, "Inverse uncertainty quantification using the modular Bayesian approach based on Gaussian process, part 1: theory," *Nuclear Engineering and Design*, vol. 335, no. 15, pp. 339–355, 2018.

[13] T. Kawano and M. B. Chadwick, "Estimation of ^{239}Pu independent and cumulative fission product yields from the chain yield data using a Bayesian technique," *Journal of Nuclear Science and Technology*, vol. 50, no. 10, pp. 1034–1042, 2013.

[14] M. T. Pigni, M. W. Francis, and I. C. Gauld, "Investigation of inconsistent ENDF/B-VII.1 independent and cumulative fission product yields with proposed revisions," *Nuclear Data Sheets*, vol. 123, pp. 231–236, 2015.

[15] L. Fiorito, C. J. Diez, O. Cabellos, A. Stankovskiy, G. Van den Eynde, and P. E. Labeau, "Fission yield covariance generation and uncertainty propagation through fission pulse decay heat calculation," *Annals of Nuclear Energy*, vol. 69, pp. 331–343, 2014.

[16] L. Fiorito, A. Stankovskiy, G. Van den Eynde, C. J. Diez, O. Cabellos, and P. E. Labeau, "Generation of fission yield covariances to correct discrepancies in the nuclear data libraries," *Annals of Nuclear Energy*, vol. 88, pp. 12–23, 2016.

[17] J. C. Helton, J. D. Johnson, C. J. Sallaberry, and C. B. Storlie, "Survey of sampling-based methods for uncertainty and sensitivity analysis," *Reliability Engineering & System Safety*, vol. 91, no. 10-11, pp. 1175–1209, 2006.

[18] D. L. Smith, D. G. Naberejnev, and L. A. Van Wormer, "Large errors and sever conditions," *Nuclear Instruments and Methods in Physics Research A*, vol. 488, no. 1-2, pp. 342–361, 2002.

[19] G. Žerovnik, A. Trkov, and I. A. Kodeli, "Correlated random sampling for multivariate normal and log-normal distributions," *Nuclear Instruments and Methods in Physics Research Section A: Accelerators, Spectrometers, Detectors and Associated Equipment*, vol. 690, pp. 75–78, 2012.

[20] G. Žerovnik, A. Trkov, D. L. Smith, and R. Capote, "Transformation of correlation coefficients between normal and lognormal distribution and implications for nuclear applications," *Nuclear Instruments and Methods in Physics Research Section A: Accelerators, Spectrometers, Detectors and Associated Equipment*, vol. 727, pp. 33–39, 2013.

[21] T. K. Shin Okumura, P. Jaffke, P. Talou, T. Yoshida, and S. Chiba, "Fission product yield calculations by the Hauser-Feshbach statistical decay and beta decay," 2019, https://indico.cern.ch/event/675816/contributions/2905172/attachments/1675473/2689797/Okumura.pdf.

[22] M. B. Chadwick, M. Herman, P. Obložinský et al., "ENDF/B-VII.1 nuclear data for science and technology: cross sections, covariances, fission product yields and decay data," *Nuclear Data Sheets*, vol. 112, no. 12, pp. 2887–2996, 2011.

[23] T. R. England and B. F. Rider, *Evaluation and Compilation of Fission Product Yields*, Los Alamos National Laboratory, Los Alamos, NM, USA, 1994.

[24] F. Resitsma, Gerhard Strydom, B. Tyobeka, and K. Ivanov, "The IAEA coordinated research program on HTGR reactor physics, thermal-hydraulics and depletion uncertainty analysis: description of the benchmark test cases and phases," in *Proceedings of the HTR 2012*, pp. 1–16, Tokyo, Japan, 2012.

[25] G. Brähler, M. Hartung, J. Fachinger, K.-H. Grosse, and R. Seemann, "Improvements in the fabrication of HTR fuel elements," *Nuclear Engineering and Design*, vol. 251, pp. 239–243, 2012.

[26] H. J. Rütten, K. A. Haas, H. Brockmann, and W. Scherer, "VSOP (99/05) computer code system for reactor physics and fuel cycle simulation," *Forschungszentrum Jülich GmbH, ISR*, vol. 4189, 2005.

[27] Q. Wang, D. She, B. Xia, and L. Shi, "Evaluation of pebble-bed homogenized cross sections in HTGR fuel cycle simulations," *Progress in Nuclear Energy*, vol. 117, Article ID 103041, 2019.

[28] Z. Zhang, Y. Dong, F. Li et al., "The Shandong shidao bay 200 MW e high-temperature gas-cooled reactor pebble-bed module (HTR-PM) demonstration power plant: an engineering and technological innovation," *Engineering*, vol. 2, no. 1, pp. 112–118, 2016.

[29] L. Donald, "Smith, probability, statistics, and data uncertainties in nuclear science and technology," 1991.

[30] Y. Wang, M. Cui, J. Guo, and Li Fu, "Fission yield uncertainty propagation in multi-pass refueling pebble-bed HTGR," in *Proceedings of the PHYSOR 2020: Transition to a Scalable Nuclear Future*, Cambridge, UK, March 2020.

[31] N. J. Higham, "Computing a nearest symmetric positive semidefinite matrix," *Linear Algebra and its Applications*, vol. 103, pp. 103–118, 1988.

[32] Y. Bilodid, E. Fridman, D. Kotlyar, and E. Shwageraus, "Explicit decay heat calculation in the nodal diffusion code DYN3D," *Annals of Nuclear Energy*, vol. 121, pp. 374–381, 2018.

[33] L. Wang, "Nuclear data uncertainty and sensitivity analysis in pebble-bed HTR," Institute of Nuclear and New Energy Technology, Tsinghua University, Beijing, China, Doctor of philosophy, 2016.

Hindawi
Science and Technology of Nuclear Installations
Volume 2020, Article ID 4765046, 11 pages
https://doi.org/10.1155/2020/4765046

Research Article

Studies on Key Effect Factors of Natural Circulation Characteristics for Advanced PWR Reactor Cavity Flooding System

Dekui Zhan,[1] **Xinhai Zhao**,[1] **Shaoxiong Xia**,[1] **Peng Chen**,[1] **and Huandong Chen**[2]

[1]*China Nuclear Power Technology Research Institute, Shenzhen 518000, China*
[2]*Sino-French Institute of Nuclear Engineering and Technology, Sun Yat-sen University, Zhuhai 519000, China*

Correspondence should be addressed to Dekui Zhan; zhandekui@cgnpc.com.cn

Received 24 December 2019; Revised 26 March 2020; Accepted 29 June 2020; Published 1 September 2020

Academic Editor: Han Zhang

In order to enhance the ability of severe accident mitigation for Pressurised Water Reactor (PWR), different kinds of severe accident mitigation strategies have been proposed. In-Vessel Retention (IVR) is one of the important severe accident management means by External Reactor Vessel Cooling. Reactor cavity would be submerged to cool the molten corium when a severe accident happens. The success criterion of IVR strategy is that the heat flux which transfers from the corium pool must be lower than the local critical heat flux (CHF) of the reactor pressure vessel (RPV) outside wall and the residual thickness of the RPV wall can maintain the integrity. The residual thickness of RPV is determined by the heat flux transfer from the corium pool and the cooling capability of outer wall of the RPV. There are various factors which would influence the CHF and the cooling capability of outer wall of the RPV. In order to verify the optimized design which is beneficial to the heat transfer and the natural circulation outside the actual reactor vessel, a large-scale Reactor Vessel External Cooling Test (REVECT) facility has been built. A large number of sensitivity tests were carried out, to study how these sensitivity factors affect CHF value and natural circulation. Based on the test results, the structure of the test section flow channel has an obvious effect on the CHF distribution. The flow channel optimized can effectively enhance the CHF value, especially to enhance the CHF value near the "heat focus" region of the molten pool. The water level in the reactor pit has also a great impact on the natural circulation flow. Although natural circulation can be maintained with a low water level, it will lead to a decrease of the cooling capacity. Meanwhile, some noteworthy test phenomena have been found, which are also essential for the design of the reactor pit flooding system.

1. Introduction

The probability of severe accidents in nuclear power plants is much low, but once a severe accident occurs, it will cause the nuclear reactor core to melt. The core corium relocates to the lower head, forming a molten pool and transferring heat to the RPV wall. If the molten pool cannot be effectively cooled down, the pressure vessel may be melted through due to excessive thermal load, which greatly increases the possibility of radioactive material release to the environment. Then, how to maintain the integrity of RPV and limit the corium in the lower head become the focus of research on mitigation measures for severe accidents worldwide.

External Reactor Vessel Cooling (ERVC) to achieve In-Vessel Retention (IVR) is an important mitigation measure for severe accidents. Due to its advantage of low construction difficulty and good economy, IVR-ERVC is widely used in the 3rd generation million-kilowatt nuclear power plants. Chinese advanced pressurized water reactor mainly adopts this strategy to mitigate severe accidents.

In the design of IVR-ERVC, the reactor pit flooding system is one of the most important dedicated safety systems. In order to verify the effectiveness of IVR-ERVC, it is necessary to carry out related research to evaluate the factors that affect the cooling capability of the reactor pit flooding system. The factors include the design of RPV flow channel, the water level in the reactor pit, and so forth. In this paper,

the description of a new reactor pit flooding system and the REVECT (Reactor Vessel External Cooling Test) facility are introduced and the influence factors of cooling capability are studied. Based on the REVECT tests, a series of problems which have confused the designers in long-time are solved. The research results have been applied to the engineering design of reactor pit flooding system and the establishment of management guidelines for severe accidents in new nuclear power plants.

2. Research Status

After the occurrence of a postulated severe accident, corium will collapse into lower head of RPV. The disposal mode of corium becomes a common concern. Currently, there are mainly two treatment ways for corium cooling: (1) Ex-Vessel Retention (EVR): this method is mainly used in EPR. The specific method is setting a core catcher at the bottom of containment, which has functions of isolating molten debris and concrete as well as providing long-term cooling. EVR strategy is also adopted in Tianwan nuclear power plant (NPP) in China. (2) In-Vessel Retention (IVR): IVR strategy is implemented to remove decay heat from the RPV and to keep the corium in the RPV [1]. This strategy has also been used in VVER440, AP1000, HPR1000, and APR1400 [2].

In order to verify the effectiveness of the IVR strategy, some different test facilities which are used to simulate the flow and heat transfer characteristics have been built, such as ULPL test facility and HERMES-HALF test facility. The conclusions of the tests are as follows. (1) An aged copper surface exhibits a similar coolability performance as the external surface of the RPV wall, which is verified by ULPU and BETA-NC test [3–5]. (2) Optimized flow channel can enhance the CHF of the external surface of lower head. (3) The chemical properties of some coolants can affect the CHF. For instance, the coolant with boric acid can decrease the CHF to some extent.

In China, different types of CHF tests and related analyses have been performed in recent years. Based on a large-scale test facility, Yang [6] investigated the CHF characteristics of chemical solution boiling on a downward facing curved surface. It was found that the CHF of mixed solution of H_3BO_5 and Na_3PO_4 increases firstly and then decreases with the increase of Na_3PO_4 concentration. Through a two-dimensional full-scale facility FIRM, Wei [7] discovered that the aging effect could enhance the CHF of SA508 owing to the generation of Fe_3O_4 oxide. To study the CHF margin of External Reactor Vessel Cooling (ERVC) for Chinese AP1400, the FIRM subcooled flow boiling facility conducted by State Nuclear Power Technology Research & Development Center (SNPTRD) was built [8]. It was also shown that the concentration of Na_3PO_4 has an important effect on the CHF behavior. Based on the experimental data, a CHF correlation for IVR-ERVC was developed by Mei et al. [9] with considering the effects of surface orientation, thermal effusively and corrosion. Besides, Tan and Kuang [10] preliminarily determined nominal values of reactor vessel insulation design parameters according to ERVC related functional reliability criteria and related statistical analysis. Guo et al. [11] proposed a new method to study the transient feasibility of IVR-ERVC in which a theoretical CHF model was developed for the outer surface of the lower head. Jin et al. [12] performed the study on in-vessel and ex-vessel coupled analysis of IVR-ERVC phenomena for large-scale PWR by using MELCOR. Cheng et al. [13] used a CDF code Fluent coupled with a boiling model by UDF (User-Defined Function) to investigate the CHF of ERVC which was validated by experimental CHF values obtained by SNPTRD.

Even though a large number of tests and analyses have conducted, there are little test results about the effect of the key factors on the CHF distribution, such as the geometry of flow channel and the water level in the reactor cavity. The above key factors are also essential for the reactor flooding system design.

3. Design and Management of Reactor Flooding System for Advanced PWR

3.1. Reactor Pit Flooding System. The reactor pit flooding system is a dedicated severe accident mitigation system to achieve the IVR-ERVC. Generally, the reactor pit flooding system is composed of a reactor pit injection system and a natural circulation system. When a severe accident happens, cooling water can be injected into the reactor cavity to submerge the RPV via passive injection mode or active injection mode. The decay heat is finally removed through the natural circulation in the reactor cavity to maintain the integrity of RPV.

The passive reactor pit injection subsystem mainly consists of the reactor pit flooding tank located on a place higher than the main coolant pipes of Reactor Coolant System (RCP) in the containment, pipelines, and valves. During a severe accident after entering the severe accident management guideline (SAMG), the valves on the passive injection pipes are opened by the operator, and the water in the reactor pit flooding tank flows to the reactor pit by gravity with a large flow rate. When the water level in the pit flooding tank drops to a certain threshold, the injection is switched to small flow rate to compensate for the water loss due to evaporation, ensuring the reactor cavity to be kept flooded.

The active reactor pit injection is provided by active water injection pipelines which connect to the in-containment refuelling water storage tank (IRWST). When the reactor pit flooding tank is depleted, the cooling water is taken by pump from the IRWST and is injected into the reactor pit after cooled by Component Cooling Water System or Extra Cooling System. The schematic diagram of passive reactor pit injection subsystem and active reactor pit injection subsystem is illustrated in Figure 1.

Since the core outlet temperature reaches 650°C, which is a significant temperature alarm for the NPP to carry out the severe accident management guideline (SAMG), the operator opens the valves on the passive injection pipelines to submerge the reactor pit with a large flow rate. Then, the water injection flow is switched to small flow rate phase to make up the evaporated water. Before the IVR tank is empty, the operator starts up the pump to inject water from the in-containment refuelling water storage tank (IRWST).

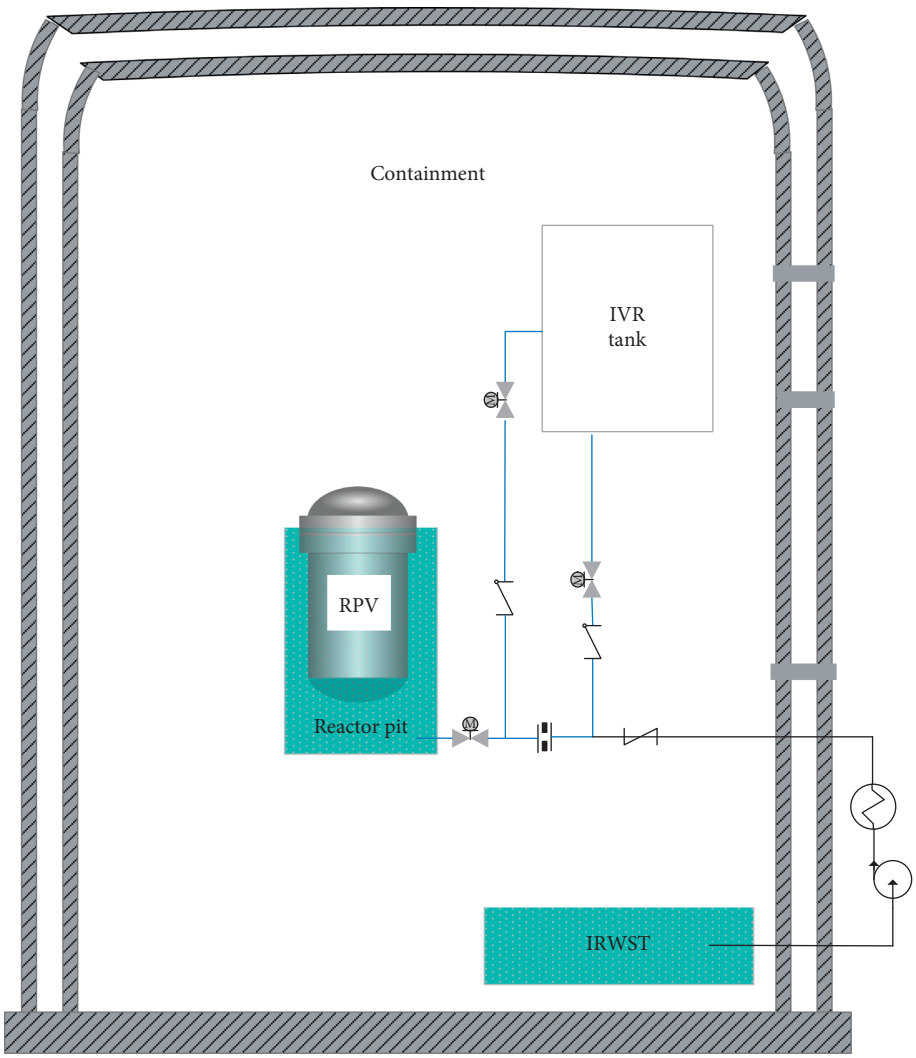

Figure 1: Design scheme of reactor pit flooding system.

3.2. Key Phenomena of Natural Circulation in the Reactor Cavity. The main phenomena and the cooling process related to the implementation of the reactor pit flooding system after severe accidents are as follows.

When the cooling water is injected into the reactor pit under severe accident conditions, the water inlets and steam outlets can be automatically opened. And the cooling water can enter the flow channel around the RPV to cool it directly.

During a severe accident, the molten corium will drop down and fall into the water pool in the lower plenum. The corium pool will heat up the internal wall of the lower plenum. And many bubbles on the external surface of RPV will produce under the heating of the lower head. Natural circulation will form due to the density difference in the circulation loop. The water-steam two-phase flow will flow upward to the steam vent ports. The water-steam separation will occur at the top of the cylinder space around the support ring. Finally, the water will flow back into the reactor pit by the recirculation pipes. The structural drawing of reactor pit is shown in Figure 2.

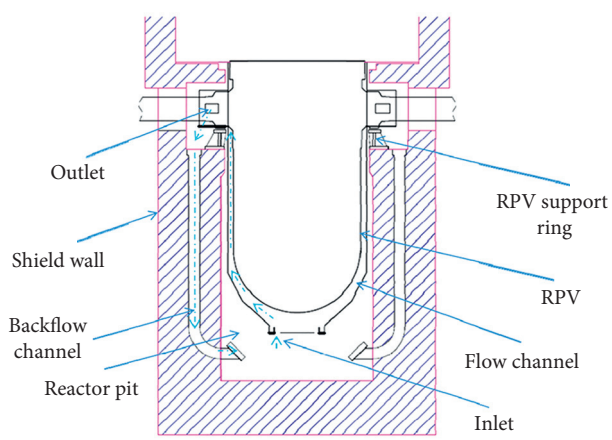

Figure 2: The natural circulation in the reactor pit.

Natural circulation forms in the flow channel after the reactor cavity being flooded. The specific cooling process after the severe accidents in the reactor pit is as follows.

(1) The cooling water is heated by RPV outside wall and many bubbles produce
(2) The water-steam flows upward along the gap between RPV outside wall and insulation and then vents out through the steam vent port of insulation
(3) The water flows back into the reactor cavity by backflow channel after steam-water separation

3.3. REVECT Test Facility

3.3.1. Presentation of IVR Test Facility. To study the influencing factors which determine the CHF distribution along the outer surface of the RPV and natural circulation flow, the REVECT (Reactor Vessel External Cooling Test) facility test facility for the advanced generation PWR has been built. The flowchart and the overview diagram of the REVECT test facility are shown in Figures 3 and 4. The test facility consists of electrical system, cooling system, power control system, primary loop and instrumentation and control (I&C) system, and so forth. The REVECT facility is a two-dimensional facility with a full-height circulation loop and a 1 : 1 radial scaled slice-type test section. The test section is the key component of the facility composed of a copper heating section and stainless steel flow channel, as the simulator of the RPV lower head and the flow path between the RPV and its insulation, respectively. Hundreds of cartridge heaters are inserted into the copper heating section to simulate the decay heat. The heating section is divided into more than 20 heating zones to realize independent heating power control of different zones. The stainless steel flow channel is bounded by several baffles which are used to simulate the insulation structure of the RPV lower head. The schematic diagram of the test section is shown in Figure 4. An integrated water tank is located under the test section in connection with the stainless steel flow channel, to simulate the reactor pit space under the RPV insulation. The upper water tank is located at the top of the facility, to simulate the annular region around the RPV support ring in the prototype. The main parameters of the REVECT facility are listed in Table 1.

The heating section is used to simulate the lower head of RPV after a large amount of molten corium relocated in it. The material of the heating block is copper. The width of heating block is constant in the test section. The slice-type heating section is divided into more than 20 independent power control zones to realize the simulation of the decay power distribution of the prototype along the lower head. Three baffles are installed in the flow channel to simulate the structure and the gap size of the RPV lower head insulation flow channel. In each heating zone, there are pairs of thermocouples installed in two concentric circles within the heating block to obtain the temperature data, so that the heat flux could be calculated according to the measured temperature under the Fourier heat conduction equation. The structure of the test section is shown in Figure 5. The main parameters of the test section are listed in Table 2.

3.3.2. Key Phenomena in the REVECT Facility Loop. The REVECT test facility can simulate the structure of circulation loops in the prototype. For example, the geometry of the test section is the same as that of the flow channel outside the RPV. It can simulate the flow and the heat transfer characteristic which is similar to the actual phenomena in the flow channel outside the lower head of the RPV. The height of the upward flow pipe is the same as that in the prototype and the resistance characteristic of the upward pipe and the steam exhaust ports are considered. The upward pipe and the steam exhaust ports can simulate the two-phase flow in the flow channel outside the RPV cylinder part and the steam vent ports. The integrated tank can simulate the cylinder space around the support ring of the RPV. The phenomenon of water-steam separation takes place in the integrated tank which also happens above the cylinder space around the support ring of the RPV. The resistance characteristic of the downward pipe is also modelled. It can simulate the recirculation pipes in the reactor pit shield wall.

3.4. Test Research on the Key Techniques for Reactor Pit Flooding System. In the design of the reactor pit flooding system for new type nuclear power plants, the research focuses on the natural circulation flow rate and CHF distribution. The reasons are the following.

(1) CHF distribution: the design of the flow channel has a great relation with the CHF value on the outer wall of the lower head of RPV. The specific influencing factors are as follows: the flow channel structure of RPV metal insulation, the area and the inlet position of RPV metal insulation, and the area of the outlet of RPV metal insulation for steam venting.
(2) Natural circulation: natural circulation flow rate is also closely related to the CHF value on the outer wall of the lower head. The larger the natural circulation flow rate is, the higher the value of CHF is. The factors which affect the natural circulation flow include the design of the backwater channel, water level, the makeup amount of water. The vibration frequency and amplitude of the two-phase flow which is important for the design of RPV metal insulation are also necessary to be considered.

3.4.1. Input Power. The power control strategy used in this experiment was proposed by Professor Theofanous et al. [1] at the University of California, USA. The similarity criterion that makes the flow of test section is similar to that of the prototype. The similarity criterion is successfully applied to IVR of AP600, AP1000, and APR1400. In the test, it mainly includes the following two aspects:

(1) The superficial vapor velocities of downstream position match up with the prototype for all $\theta > \theta_m$;
(2) The vapor flow rates build up gradually, so as to smoothly approach the value required at $\theta \leq \theta_m$, while allowing a "natural" development of boundary layer in all of the upstream region.

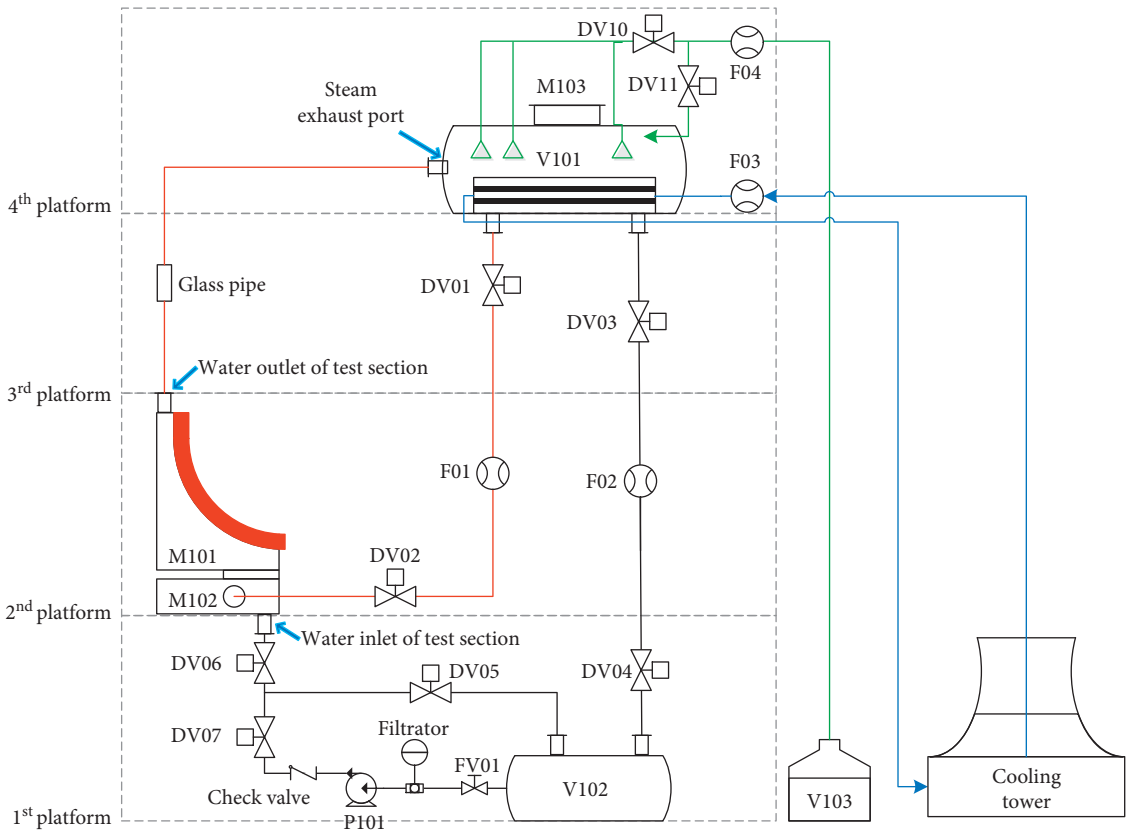

Figure 3: The flowchart of REVECT test facility.

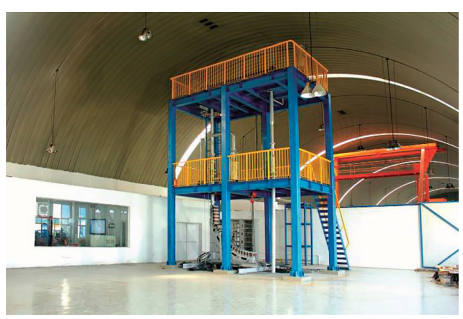

Figure 4: Overview of REVECT test facility.

The upstream θ power distribution calculation formula is

$$q_e(\theta) = q_p(\theta)\frac{\sin\theta}{\sin\theta_m}, \quad \text{for } \theta \le \theta_m. \tag{1}$$

For downstream locations of the test area, the power distribution calculation formula is the following:

$$\begin{aligned}\int_{\theta_m}^{\theta} q_e(\theta')\mathrm{d}\theta' &= J_p(\theta_m) + \frac{1}{\sin\theta}\int_{\theta_m}^{\theta} q_p(\theta')\sin(\theta')\mathrm{d}\theta' - J_e(\theta_m) \\ &= \overline{\overline{q_p}}(1-\cos\theta_m)\left(\frac{1}{\sin\theta} - \frac{1}{\sin\theta_m}\right) + \frac{1}{\sin\theta}\int_{\theta_m}^{\theta} q_p(\theta')\sin(\theta')\mathrm{d}\theta', \quad \text{for } \theta > \theta_m,\end{aligned} \tag{2}$$

Table 1: Key parameters of REVECT facility.

Parameters	Value/definition	Remarks
Test pressure	Atmosphere	Pressure in upper water tank
Water temperature at inlet of test section	~100°C	The saturation temperature corresponds to the pressure of the upper water tank
Target water level of the upper water tank	7300 mm	The elevation of the bottom of the heating section is selected as the 0 m level, the same as the prototype
Elevation of steam exhaust port	8000 mm	Relative to the bottom of the heating section
Circulation type	Natural circulation	The same as the prototype
Working fluid	Deionized water	
Steam/water outlet area of the upflow pipe	~0.01 m^2	About 1/100 of the prototype RPV insulation steam invent port area
Cooling water inlet area of the test section	~0.01 m^2	About 1/100 of the prototype RPV insulation cooling water inlet port area
Structure of baffles	3-part multilateral structure	With the same structure and "gap size" distribution as the prototype
Circulation resistance	Scaling as the prototype to ensure the consistence of the comprehensive resistance of facility and the prototype	Based on the geometry and resistance distribution analysis of the prototype flow path

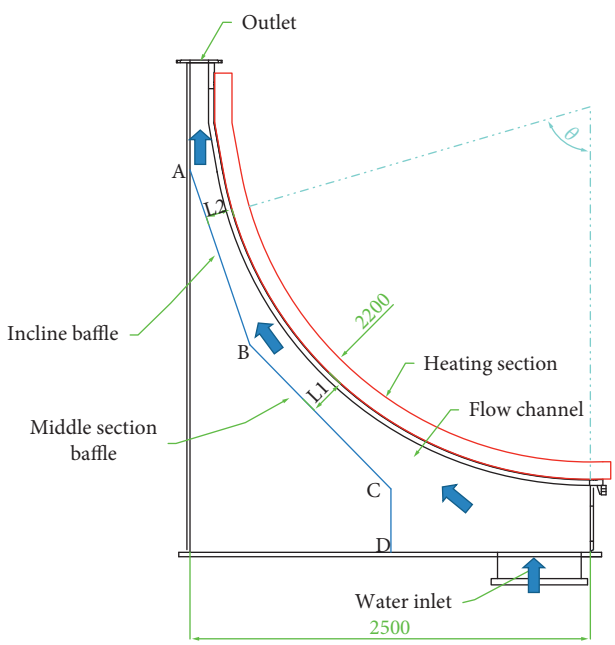

Figure 5: Schematic of the test section.

where $\overline{\overline{q_p}}$ is an average flux over $0 < \theta \leq \theta_m$ defined by

$$\overline{\overline{q_p}} = \frac{\sin\theta_m}{1-\cos\theta_m}\int_0^{\theta_m} q_p(\theta')\sin(\theta')\mathrm{d}\theta'. \quad (3)$$

The theoretical and actual input heat flux density distribution in the test heating zone 23 is shown in Figure 6.

4. Sensitivity Study on the Different Structure of the Flow Channel

4.1. Test Conditions. Nine test conditions (FC01-FC09) with different flow channel distances and different baffle structures were performed. The specific test conditions are shown in Table 3. The flow channel consists of three straight baffles and heating surfaces of the test section. The baffles mainly include a vertical section (CD), a middle section baffle (BC), and an inclined baffle (AB). The sensitivity tests were divided into three stages. In the first stage, the minimum distance from the middle section baffle (BC) to the heating surface is 250 mm, then, adjusting the incline baffle (AB) to different three positions. So three different flow channel structures are formed (FC01-FC03). Similarly, in the second and third stages, the minimum distances from the middle baffle to the heat section surface are set as 200 mm and 150 mm, respectively, then adjusting the incline baffle to different positions to perform the sensibility analysis.

4.2. Test Results of Sensitivity Study on the Different Flow Channels. Figure 7 shows the CHF distribution under three different test conditions (FC01-FC03).

The CHF value of FC01 changes in a "wave shape" with the increase of the azimuth angle, and the CHF value is relatively small. The CHF values of FC02 and FC03 show a "W-shape" change with the azimuth angle change from 35° to 85°.

Figure 8 gives the CHF test data in the second stage (FC04-FC06). The CHF values are similar to the test results of FC01-FC03. The CHF value of FC04-FC06 also changes in a "W-shape" from 35° to 90°.

Figure 9 shows the CHF test data in the third stage (FC07-FC09). The CHF values of these three tests (FC07-FC09) are higher than those in the former two stages, and the CHF values of most areas are greater than 1.4 MW/m^2. With the increase of the azimuth angle from 35° to 90°, the CHF value in the third stage increases firstly and then decreases until the position of 68° and then increases. The CHF values of the FC07 and FC08 change relatively smoothly, and the value is relatively large. The CHF values of most areas are larger than 1.5 MW/m^2. Besides, the baffle with a minimum distance of 100 mm (FC09) can increase

Table 2: Key parameters of REVECT test section.

Parameters	Value/ definition	Remarks
Circumferential scale of the test section to prototype	1 : 100	
Radial scale of the heating section to the prototype RPV	1 : 1	With the same outer diameter as the as the prototype RPV lower head
Height scale of the natural circulation loop to the prototype RPF system	1 : 1	
Number of independent heating zones	23	Cover the angular range of 0°–90°
Designed maximum surface heat flux	~2.5 MW/m^2	The actual heat flux is lower than 1.4 MW/m^2
Width of flow channel	150–250 mm	Effective width
Outer diameter of the heating section	4800 mm	The same as the prototype RPV lower head

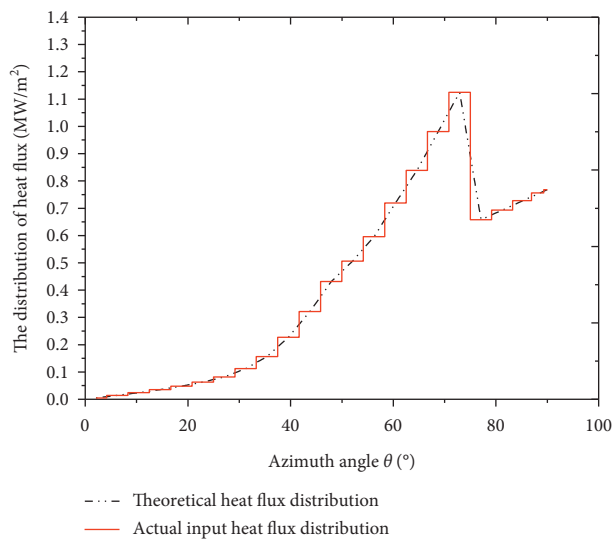

Figure 6: Theoretical and actual input heat flux distribution in zone 23.

Table 3: Test conditions for the flow channel optimization.

No.	Test types	Minimum distance of flow channel L1/L2	Temperature of the inlet	Pressure
1	Flow channel optimization test FC01	250/250 mm	~100°C	1 bar
2	Flow channel optimization test FC02	250/210 mm	~100°C	1 bar
3	Flow channel optimization test FC03	250/140 mm	~100°C	1 bar
4	Flow channel optimization test FC04	200/200 mm	~100°C	1 bar
5	Flow channel optimization test FC05	200/180 mm	~100°C	1 bar
6	Flow channel optimization test FC06	200/130 mm	~100°C	1 bar
7	Flow channel optimization test FC07	150/150 mm	~100°C	1 bar
8	Flow channel optimization test FC08	150/145 mm	~100°C	1 bar
9	Flow channel optimization test FC09	150/100 mm	~100°C	1 bar

the CHF value at the position between 52° and 64° and inhibit the CHF value in the upstream at the position between 68° and 72°.

The nine test results show that when the flow channel distance ranges from 250 mm to 200 mm and then further decreases to 150 mm, CHF value tends to increase; while the distance of flow channel continued to decrease to 100 mm (FC09), the CHF value begins to decrease at the upstream heating zone. It can be considered that the CHF value tends to increase with the space of flow channel decreases, but the value of CHF will be inhibited when the distance of flow channel decreases to a certain level.

4.3. Optimization of the Flow Channel Structure Outside the RPV. The above results show that different flow channel configurations lead to different CHF distributions. According to the test results, the optimal design of the structure for the

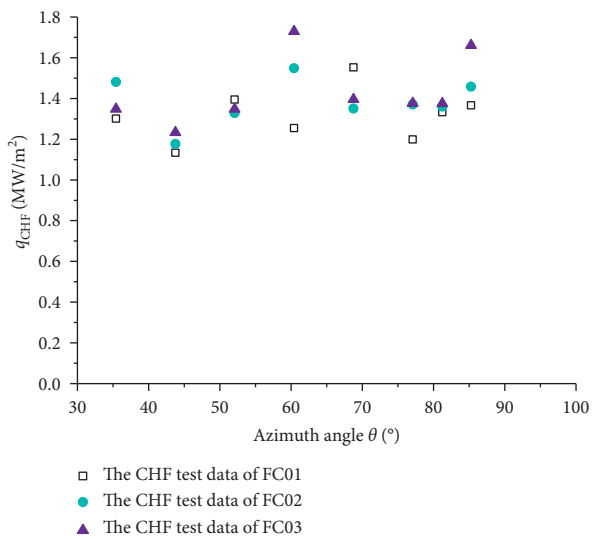

Figure 7: CHF distribution of the FC01-FC03 test conditions.

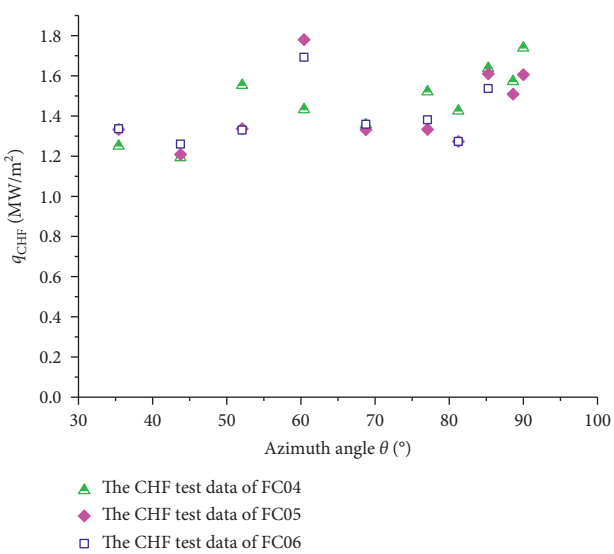

Figure 8: CHF distribution of the FC04-FC06 test conditions.

insulation is obtained and the verification test under the optimized structure is carried out. The test results show that even though the CHF date at the position of 52° is lower than that before being optimized, the CHF data with the optimized flow channel at higher angles (67°–90°) are obviously larger than the experimental data in the case that the flow channel is not optimized. The average increase amplitude is about 20%. The schematic of optimized flow channel is shown in Figure 10. That means that there is larger margin for the heat focus effect owing to the optimized flow channel. The comparison of CHF values between optimized and non-optimized flow channels (FC08) is shown in Figure 11.

The mechanism could be that when the distance changes from 250 mm to 140 mm, the velocity of the two-phase flow changes to higher, the film boiling is more unlikely to happen. While the distance further decreases to 100 mm, the

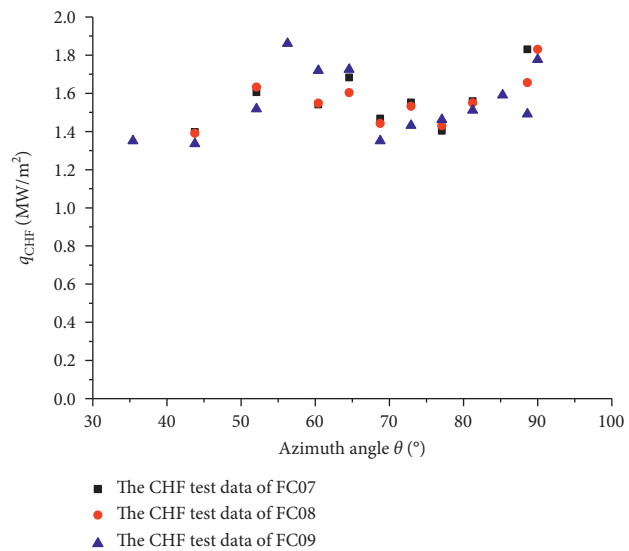

Figure 9: CHF distribution of the FC07-FC09 test conditions.

two-phase flow with many large bubbles is likely to block the flow channel, so the film boiling at the position of the minimum distance is more likely to happen.

5. Natural Circulation Flow and Evaporated Water

5.1. Test Condition. Tests of different water levels in the reactor cavity are also conducted to study the effect on the natural circulation characteristic. The details of test condition are shown in Table 4.

5.2. Test Results

5.2.1. The Flow Rate of the Nature Circulation and the Evaporation. The natural circulation flow exceeds 40 m^3/h. Due to 1 : 100 circumferential scale of the test section to prototype, the natural circulation flow rate is about 4000 m^3/h for the actual nuclear power plants. The test result shows that the natural circulation flow is very large once the steady natural circulation forms, so the backflow channel is essential. Besides, the test results also show that there is about 0.5 m^3 water evaporated per hour, so small flow rate (>50 m^3/h) is needed to inject into reactor cavity to make up the water and keep the level of water in the reactor cavity at the higher height.

5.2.2. Water Level Effect. According to the test results, the natural circulation can be maintained if the water level is between 8 m and 5 m, but the circulation flow rate is obviously decreased with lower water level. When the water level drops to 6.5 m, especially, the intermittent discharge occurs, causing the pressure in the flow channel to fluctuate correspondingly. The results are shown in Figures 12 and 13. Due to the phenomenon of intermittent discharge in the flow channel and the adverse cooling condition, the temperature on the outer surface of the lower head of RPV may rise at the same

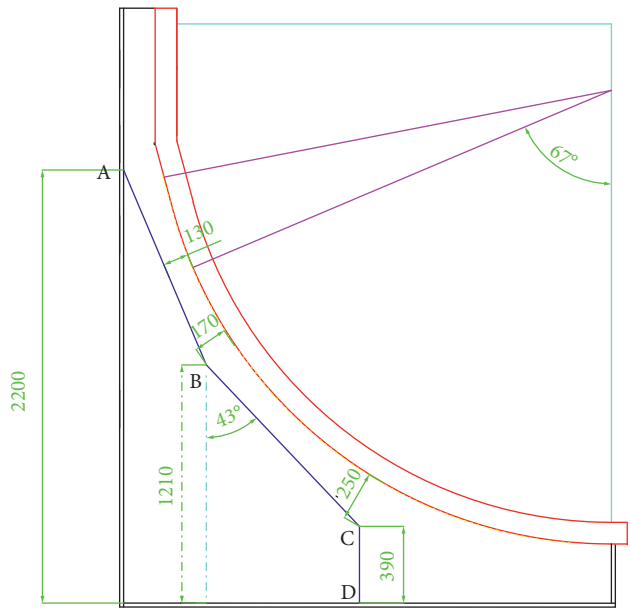

Figure 10: The schematic diagram with the optimized flow channel of the test section.

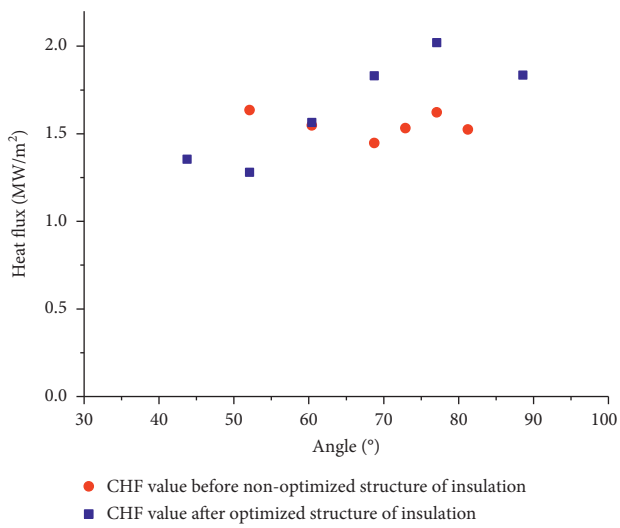

Figure 11: Comparison of CHF values between optimized and nonoptimized flow channels.

Table 4: Test conditions for the natural circulation characteristics.

No.	Test types	Water level	Temperature of the inlet	Pressure
1	Natural circulation characteristics tests NC01	8 m-5 m	~100°C	1 bar

time, which is not conducive to the cooling of the lower head. Therefore, in the design of reactor cavity flooding system, a clear request is made for the lowest water level of the reactor cavity after water injection. The water level of the reactor cavity must be kept as high as possible to ensure that the natural circulation can be maintained with larger flow rate and take away more decay heat from the corium pool.

5.2.3. Vibration Frequency and Amplitude. To obtain the variation of the vibration frequency of the two-phase flow in the flow channel with different water levels in the reactor cavity, the fluctuation pressure and frequency of the two-phase flow in the flow channel are considered.

When the liquid level decreases from 8 m to 7 m, the fluctuation pressure is within ±10 kPa. When the water level is

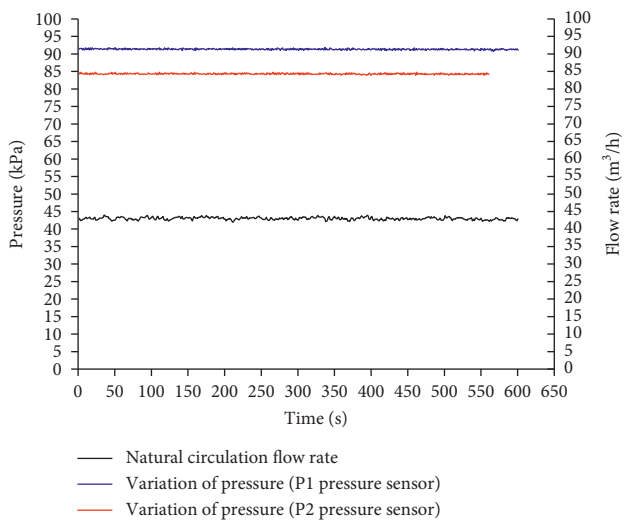

Figure 12: Fluctuation pressure is stable with water level of 8 m.

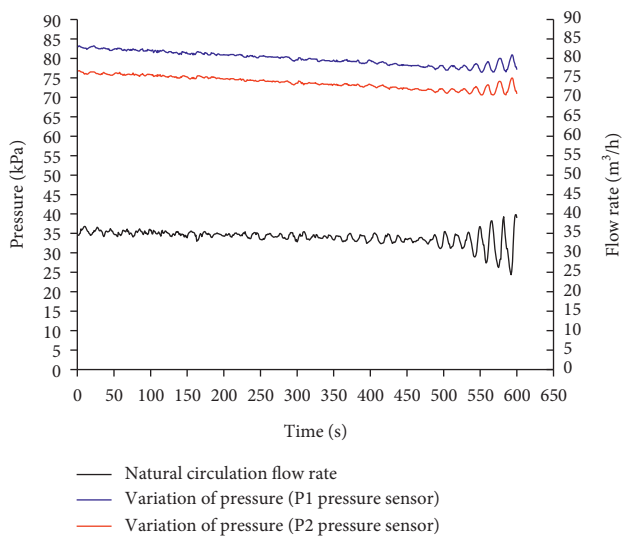

Figure 13: Fluctuation pressure is changing unstably with water level decreases.

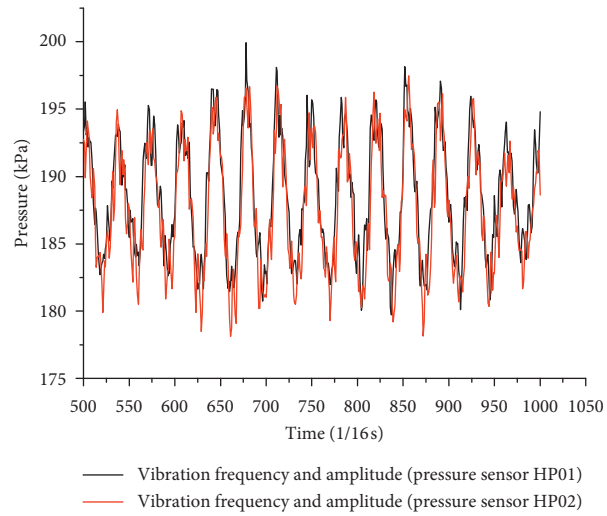

Figure 14: Vibration frequency and amplitude with water level of 8 m.

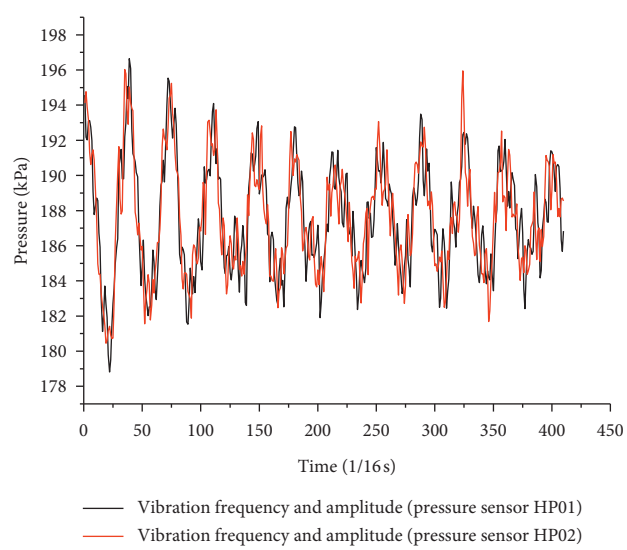

Figure 15: Change of vibration frequency and amplitude with water level decreases.

high, the pressure fluctuation is regular and the frequency is about 1.4 Hz. With the decrease of water level, the pressure fluctuation begins to appear irregular, but the fluctuation pressure is still in the range of ±10 kPa. So it can be found that the pressure fluctuation range shows a decreasing trend with the decrease of water level and the fluctuation frequency is about 1.1 Hz at a relatively regular fluctuation, as shown in Figures 14 and 15.

Based on test results, in order to prevent the occurrence of resonance phenomenon after reactor pit injection system is implemented, which may lead to the destruction of the insulation, the inherent frequency of the insulation is required to avoid 1.1 Hz–1.4 Hz and the antivibration pressure of insulation needs to be more than ±10 kPa at the same time.

6. Conclusions

Based on the above experimental results, the natural circulation characteristics of two-phase flow are investigated in detail when implementing the reactor pit flooding system after severe accidents and the following design requirements are proposed for the reactor pit flooding system for new type nuclear power plants. The specific requirements are as follows:

(1) The flow channel structure outside the RPV has a significant effect on the CHF value. The flow channel optimized can effectively enhance the CHF value, especially to enhance the CHF value near the "heat focus" region of the molten pool. Therefore, the

effectiveness of the IVR-ERVC strategy can also be further enhanced.

(2) Natural circulation flow can exceed 4000 m^3/h after reactor pit flooding system is implemented. Therefore, multiple backwater flow channels must be set to ensure that the water discharged from the outlet of insulation can flow back into the reactor pit again.

(3) The water level in the reactor pit has a great impact on the natural circulation flow. Although natural circulation can be maintained with low water levels, it will lead to a decrease in the cooling capacity. Therefore, the water level must be maintained as much as possible at higher position.

(4) The inherent frequency of RPV insulation is required to avoid 1.1 Hz–1.4 Hz and the antivibration pressure of insulation needs to be more than ±10 kPa at the same time.

Data Availability

The data used in the study have been included in the article.

Conflicts of Interest

The authors declare that there are no conflicts of interest regarding the publication of this article.

Acknowledgments

This work was supported by National Key R&D Program of China (Grant no. 2018YFB1900100).

References

[1] T. G. Theofanous, C. Liu, S. Addition, S. Angelini, O. Kymaelaeinen, and T. Salmassi, "In-vessel coolability and retention of a core melt," vol. 1, Office of Scientific and Technical Information, Oak Ridge, TN, USA, 1996.

[2] T. G. Theofanous, S. J. Oh, and J. H. Scobel, "In-vessel retention technology develoopment and use for advanced PWR designs in the USA and Korea," vol. 14, Office of Scientific and Technical Information, Oak Ridge, TN, USA, 2004.

[3] T. N. Dinh, J. P. Tu, and T. G. Theofanous, "Two phase natural circulation flow in AP-1000 in-vessel retention-related ULPU-V facility experiments," in *Proceedings of the ICAPP'04*, Pittsburge, PA, USA, June 2004.

[4] Y. H. Jeong, W. P. Baek, and S. H. Chang, "CHF experiments for IVR-RVC using 2-D slice test section," in *Proceedings of the Korean Nuclear Society Spring Meeting*, Kwangju, South Korea, May 2002.

[5] T. G. Theofanous, J. P. Tu, A. T. Dinh, and T. N. Dinh, "The boiling crisis phenomenon, part I: nucleation and nucleate boiling heat transfer," *Experimental Thermal and Fluid Science*, vol. 26, no. 6-7, pp. 775–792, 2002.

[6] S. Yang, "Experimental study on critical heat flux of chemical water boiling on a downward facing curved surface for IVR-ERVC strategy," *Nuclear Power Engineering*, vol. 6, pp. 23–27, 2016.

[7] W. Tao, "Experimental research on influence of real surface material and aging effect on ERVC-CHF of RPV," *Atomic Energy Science and Technology*, vol. 50, p. 1786, 2016.

[8] H. Chang, T. Hu, W. Lu, S. Yang, and X. Zhang, "Experimental study on CHF using a full scale 2-D curved test section with additives and SA508 heater for IVR-ERVC strategy," *Experimental Thermal & Fluid Science*, vol. 84, pp. 1–9, 2017.

[9] Y. Mei, Y. Shao, S. Gong, Y. Zhu, and H. Gu, "Effects of surface orientation and heater material on heat transfer coefficient and critical heat flux of nucleate boiling," *International Journal of Heat & Mass Transfer*, vol. 121, pp. 632–640, 2018.

[10] G. Tan and B. Kuang, "Geometric optimization and reliability assessment of reactor vessel insulation for IVR-ERVC based on passive system functional reliability concept," *Atomic Energy Science and Technology*, vol. 3, pp. 54–60, 2011.

[11] R. Guo, W. Xu, Z. Cao, X. Liu, and X. Cheng, "A new method to study the transient feasibility of IVR-ERVC strategy," *Progress in Nuclear Energy*, vol. 87, pp. 47–53, 2016.

[12] Y. Jin, W. Xu, and X. Liu, "In- and ex-vessel coupled analysis of IVR-ERVC phenomenon for large scale PWR," *Annals of Nuclear Energy*, vol. 8, pp. 322–337, 2015.

[13] X. Cheng, T. Hu, D. Chen, Y. Zhong, and H. Gao, "CFD simulation on critical heat flux of flow boiling in IVR-ERVC of a nuclear reactor," *Nuclear Engineering & Design*, vol. 304, pp. 70–79, 2016.

Hindawi
Science and Technology of Nuclear Installations
Volume 2020, Article ID 2562747, 12 pages
https://doi.org/10.1155/2020/2562747

Research Article

Thermal Hydraulic and Neutronics Coupling Analysis for Plate Type Fuel in Nuclear Reactor Core

Linrong Ye,[1] Mingjun Wang,[1] Xin'an Wang,[1] Jian Deng,[2] Yan Xiang,[3] Wenxi Tian,[1] Suizheng Qiu,[1] and G. H. Su[1]

[1]*State Key Laboratory of Multiphase Flow in Power Engineering, Department of Nuclear Science and Technology, Xi'an Jiaotong University, Xi'an 710049, China*
[2]*Science and Technology on Reactor System Design Technology Laboratory, Nuclear Power Institute of China, Chengdu, China*
[3]*Royal Institute of Technology (KTH), Stockholm 11428, Sweden*

Correspondence should be addressed to Mingjun Wang; wangmingjun@mail.xjtu.edu.cn and Jian Deng; dengjian_npic@163.com

Received 12 December 2019; Revised 10 June 2020; Accepted 29 June 2020; Published 28 August 2020

Academic Editor: Fu Li

The thermal hydraulic and neutronics coupling analysis is an important part of the high-fidelity simulation for nuclear reactor core. In this paper, a thermal hydraulic and neutronics coupling method was proposed for the plate type fuel reactor core based on the Fluent and Monte Carlo code. The coupling interface module was developed using the User Defined Function (UDF) in Fluent. The three-dimensional thermal hydraulic model and reactor core physics model were established using Fluent and Monte Carlo code for a typical plate type fuel assembly, respectively. Then, the thermal hydraulic and neutronics coupling analysis was performed using the developed coupling code. The simulation results with coupling and noncoupling analysis methods were compared to demonstrate the feasibility of coupling code, and it shows that the accuracy of the proposed coupling method is higher than that of the traditional method. Finally, the fuel assembly blockage accident was studied based on the coupling code. Under the inlet 30% blocked conditions, the maximum coolant temperature would increase around 20°C, while the maximum fuel temperature rises about 30°C. The developed coupling method provides an effective way for the plate type fuel reactor core high-fidelity analysis.

1. Introduction

The high-fidelity simulation for reactor core requires more physics field coupling due to the strong feedback existing in the nuclear reactor, such as the reactivity interaction between core neutronics transport and thermal hydraulics. The neutron flux distribution determines the core power distribution and further determines the temperature distributions of fuel and coolant, which would affect the neutron fission cross sections, leading to the variation of core power distribution. Due to the strong feedback effects, the thermal hydraulics and neutronics research should be coupled together to achieve the accurate performances of coolant and fuel assembly in nuclear reactor core, especially in some unexpected accident conditions due to the large temperature variation. In the early years, neutron transport was often calculated with simplified point reactor neutron kinetics model due to the limited computing capability, and the results were usually conservative. With the development of computational capability, it has been feasible to realize the multiphysics coupling analysis for nuclear reactor high-fidelity simulations.

Actually, several thermal hydraulic and neutronics coupling analyses have been performed in the past several decades. Ji et al. coupled Monte Carlo code MCNP5 and system code RELAP5 to explore the feasibility of the pseudomaterial method for Doppler feedback in the VHTGR. In this study, the cross section libraries were interpolated to obtain the neutron cross sections at arbitrary temperature [1]. Hu and Uddin developed a new explicit coupling scheme using User Defined Function (UDF) to couple MCNP5 and Fluent, and some promising results were achieved [2]. Cardoni realized MCNP5 and STAR-CCM+ coupling to calculate 3D PWR fuel pin cell model and

3×3 model and obtained high-fidelity results of coolant temperature and density, fuel temperature, and power distribution, successfully demonstrating the coupling effects [3]. Yan et al. coupled STAR-CCM+ and deterministic code DeCART to calculate PWR 3×3 model with new mesh mapping methods [4]. Hoogenboom et al. built a flexible thermal hydraulic and neutronics coupling scheme with Python [5]. Sjenitzer et al. proposed a new method to perform transient coupling with Monte Carlo code [6]. Ward et al. used coupled system code RELAP5 and 3D spatial kinetics code PARCS to simulate safety performance of the I^2S-LWR plant during accident conditions [7]. The thermal hydraulic and neutronics coupling algorithm in transient problems for the high-temperature gas-cooled reactor simulator TINTE was evaluated and developed [8]. Results indicated that the proposed coupling algorithms Picard and JFNK were better compared with the original semi-implicit coupling algorithm in TINTE.

In terms of plate type fuel reactor core analysis, Tian et al. developed a thermal hydraulic analysis code for China Advanced Research Reactor (CARR). The heat transfer and flow distribution characteristics in the reactor core were studied [9]. Gong et al. found that all fuel and cladding temperatures were below the design limits and remained safe with the inlet velocity ranging from 4.5 m/s to 7.5 m/s for the hottest assembly in 20 MW plate type fuel reactor [10]. Lu et al. analyzed the blockage accident of one assembly channel in 10 MW plate type fuel reactor, and the results showed that the obstructed channel causes temperature rise in adjacent channels. In addition, it was found that there was no boiling in obstructed channel except for the hot channel because of lateral heat conduction of adjacent channels [11]. Bousbia-Salah et al. calculated the neutron flux and power distribution of 10 MW MTR using MCNP5 code, and it showed that the MCNP5 was reliable for the plate type fuel core simulation and the calculation results were in good agreement with previous study [12]. Xoubi et al. investigated the impact of enrichment on neutron flux in the in-core facility of 10 MW MTR with OpenMC and found the importance of flux trap calculation while considering the conversion of reactor core from HEU to LEU [13]. It also demonstrated the feasibility of the Monte Carlo method in analyzing plate type fuel reactor.

It can be seen that most of the thermal hydraulic and neutronics coupling studies are performed for PWR rod bundle type fuel in the literatures, while the coupling analysis on plate type fuel reactor core is rare. Therefore, an innovative thermal hydraulic and neutronics coupling method was proposed based on the Fluent and Monte Carlo code through the UDF module for the plate type fuel reactor core in this paper. A typical plate type fuel assembly was analyzed with the coupling code, and the thermal hydraulic and neutronics features were studied and analyzed in detail.

2. Mathematic Model

The CFD method is widely utilized in the nuclear reactor thermal hydraulic analysis currently, especially for the local detailed three-dimensional flow and heat transfer process, such as the coolant mixing in the reactor core [14]. The basic of CFD method is the fundamental governing equations of fluid dynamics, including the mass, momentum, and energy conservation equations. For single-phase flow, the mass and momentum equations are given as follows:

$$\frac{1}{p}\frac{\partial \rho}{\partial t} + \nabla \cdot u = 0, \qquad \rho \frac{Du}{Dt} = \rho F + \nabla \cdot \sigma, \tag{1}$$

where the u is the velocity, ρ is the density, F is the body force per unit of fluid mass, and σ is the stress tensor.

For incompressible Newtonian fluid, the Navier–Stokes equations are given as follows:

$$\nabla \cdot u = 0, \tag{2}$$

$$\rho\left(\frac{\partial \rho}{\partial t} + u \cdot \nabla u\right) = \rho F - \nabla \cdot p + \nabla^2 u, \tag{3}$$

$$\rho c_P\left(\frac{\partial T}{\partial t} + u \cdot \nabla u\right) = \nabla \cdot (\lambda \nabla T) + q^{\prime\prime\prime} + \overline{\phi}, \tag{4}$$

where the T is temperature, p is pressure, c_p is the specific hear capacity at constant pressure, λ is thermal conductivity, $q^{\prime\prime\prime}$ is volumetric heat source, and $\overline{\phi}$ is the dissipation function. For the steady calculation in the paper, the time derivative term is eliminated.

For solid domains like fuel and cladding, heat conduction equation can be simplified from equation (4) as follows:

$$\rho c_P \frac{\partial T}{\partial t} = \nabla \cdot (\lambda \nabla T) + q^{\prime\prime\prime}. \tag{5}$$

For fuel, the volumetric heat source is fission heat or the heat generated by γ-rays in cladding. In this paper, the heat in cladding is ignored and $q^{\prime\prime\prime}$ is zero in cladding domain.

The direct numerical solution (DNS) method directly solves Navier–Stokes equations, and huge computing cost is required to simulate turbulence effect, which is unfavorable in reactor scale simulation. The computing cost could be decreased by applying turbulence models. For steady-state simulation, the Reynolds-averaged Navier–Stokes-based (RANS-based) models, which describe time-averaged motion of fluid flow, are widely used in the engineering fields. The typical RANS-based models include the Reynolds stress model (RSM) and the models that introduce eddy viscosity hypothesis such as the k-ε model and k-ω model. The standard k-ε model is the most common turbulence model used in CFD, and its equation is described below as an example of RANS-based model [15]:

$$\rho \frac{Dk}{Dt} = \frac{\partial}{\partial x_i}\left[\left(u + \frac{u_t}{\sigma_k}\right)\frac{\partial k}{\partial x_i}\right] + G_k + G_b - \rho\varepsilon,$$
$$\rho \frac{D\varepsilon}{Dt} = \frac{\partial}{\partial x_i}\left[\left(u + \frac{u_t}{\sigma_\varepsilon}\right)\frac{\partial \varepsilon}{\partial x_i}\right] + C_{1\varepsilon}\frac{\varepsilon}{k}\left(G_k + C_{2\varepsilon}G_b\right) - C_{2\varepsilon}\rho\frac{\varepsilon^2}{k}, \tag{6}$$

where μ_t is turbulent viscosity and it is modelled as $u_t = \rho C_\mu (\varepsilon^2/k)$, G_k is turbulent kinetic energy produced by laminar velocity gradient, G_b is turbulent kinetic energy produced by buoyancy, and $C_{1\varepsilon}$, $C_{2\varepsilon}$, C_μ, σ_k, and σ_ε are model constants.

The Monte Carlo method is a stochastic algorithm based on probability statistics. The neutron transport in nuclear reactor is random with certain statistical properties, which fits the scope of application of the Monte Carlo method well. For the application of the Monte Carlo method in neutron transport, it simulates several histories of neutron from generating to disappearing continuously, instead of solving neutron transport equations directly.

With large numbers of neutron samples, many average parameters such as neutron flux distribution, k_{eff}, energy in the reactor, and the confidence interval are obtained according to central limit theory. For critical problem in Monte Carlo code, the fission source begins with a typical history and is converged after enough neutron generations.

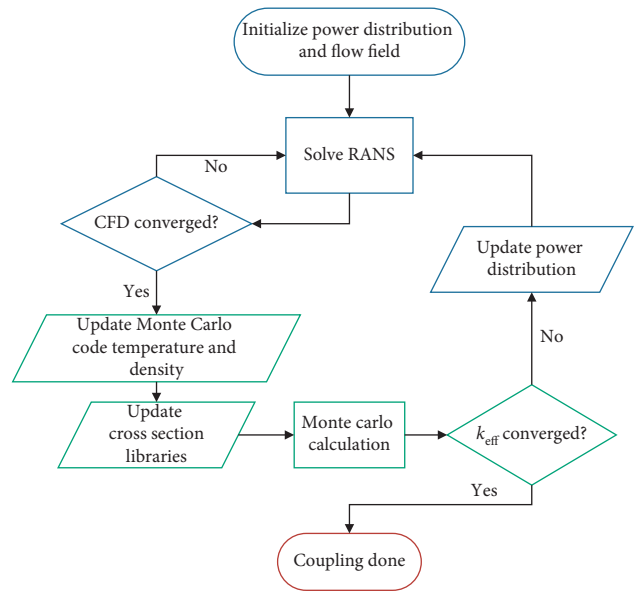

Figure 1: The thermal hydraulic and neutronics coupling scheme.

3. Coupling Method

The coupling method between thermal hydraulic code and neutronics code is mainly divided into external coupling and internal coupling. The internal coupling integrates the two codes together and the data transfer process is achieved inside the integrated code. Although this method has relatively high accuracy and performs well in parallelism, it requires massive modification on the codes. The external coupling is achieved through user interface module to transfer data between two codes without modification on the codes. Therefore, the two codes are able to remain independent during external coupling process. In this paper, the UDF, which is a powerful user interface of Fluent for secondary development [16], is compiled to couple Fluent and neutronics codes and realize the transfer data between the two codes. The Fluent meshes are mapped with Monte Carlo code cells through UDF module. The Monte Carlo code provides heat source term to the Fluent meshes, while the Fluent results renew the temperature and density for Monte Carlo code, leading to the update of cross sections in the input file. The detailed coupling scheme is presented in Figure 1. The fuel domain in Fluent is provided with power distribution and the flow field is initialized, and then the CFD calculation begins. When the residual of continuity in Fluent is under 10^{-4}, the calculated temperature and density are extracted. The Monte Carlo code input file is updated with the data and the cross section libraries are renewed. Then, the Monte Carlo code calculation begins. After Monte Carlo calculation, the fission energy deposition in the output file is extracted and transformed into power density, in which case the Fluent source term would be updated. The coupling code finally determines whether the iteration converges by monitoring k_{eff}.

In this paper, the geometry of plate type fuel assembly is simple and the one-to-one node mapping method optimized for plate type fuel model is adopted during the code coupling scheme. The mapping scheme is achieved through UDF traversing the coordinates of models in Fluent and Monte Carlo code and matching the cell ID, which makes it available for mapping considerable number of meshes, providing high accuracy at the cost of a little longer time. The mapping strategy also makes it convenient to modify the code to fit new plate type fuel model. The heat source term in Fluent is calculated by Monte Carlo code, and thus Monte Carlo code would not provide the power distribution directly. The tally module in Monte Carlo code is necessary for the fission energy deposition, and it is transformed into power density according to the following equation:

$$q_{v,i} = \frac{PD_i}{\sum_{i=1}^{n} D_i \cdot V_i}, \tag{7}$$

where $q_{v,i}$ is the power density of mesh i, P is the total fuel power, D_i is the average fission energy deposition in cell i, and V_i is the volume of cell i.

The initial heat source is provided by Monte Carlo code, and the new temperature and density are updated in the Monte Carlo code input file at each time step of Fluent calculation convergence. Then, the cross section and thermal $S(\alpha, \beta)$ libraries are updated according to new temperatures. There are mainly three methods to update the libraries: (a) update the libraries corresponding to the exact temperatures; (b) generate libraries with temperature interval of 2~5 K with NJOY in advance and perform grouping approximation based on the calculated temperature; and (c) generate libraries with larger temperature interval and perform interpolation based on the calculated temperatures. The calculation cost of method (a) is too high. Method (b) costs less but still requires high memory. Compared to method (a), the computing cost of method (c) is less and the

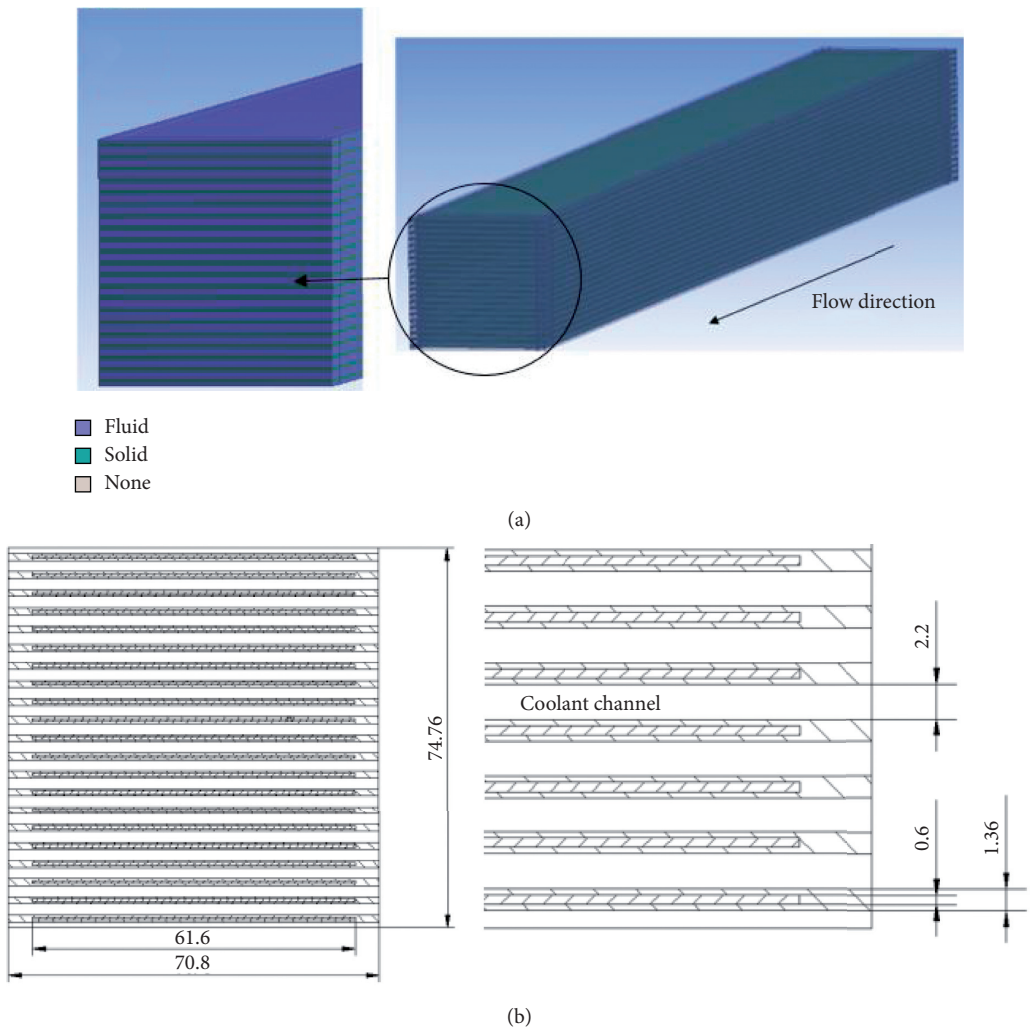

Figure 2: The model of a typical plate type fuel assembly.

deviation of k_{eff} is just about 30 pcm, and finally method (c) is selected. The cross section libraries with 25°K temperature interval and thermal $S(\alpha, \beta)$ libraries with 50°K temperature interval are generated using NJOY. The cross section at any temperature for each cell is obtained by interpolating the libraries of adjacent temperature points. The details of the interpolation method are shown as follows:

$$f_L = \frac{\sqrt{T_H} - \sqrt{T}}{\sqrt{T_H} - \sqrt{T_L}},$$
$$\Sigma(T) = f_L \Sigma(T_L) + (1 - f_L)\Sigma(T_H), \quad (8)$$

where T_H is the highest temperature of selected interval, T_L is the lowest one, Σ is the macrosection, and f_L is the portion of lower temperature library.

4. Thermal Hydraulic and Neutronics Coupling Analysis

An active zone model of U_3Si_2-Al plate type fuel assembly in a typical reactor core is built in the paper. The model structure and cross sections are presented in Figure 2. The detailed parameters are presented in Table 1, and properties of fuel pellet and cladding are presented in Table 2 [17]. The variations of density, heat conduction coefficient, and coolant dynamic viscosity with temperatures are presented as follows:

Table 1: The fuel structure parameters.

Parameters	Values
Volume (mm × mm × mm)	76.2 × 76.2 × 1375
Number of plates	21
Fuel thickness (mm)	0.6
Fuel width (mm)	850
Fuel length (mm)	61.6
Plate thickness (mm)	1.36
Plate length (mm)	890
Plate width (mm)	70.8
Gap between plates (mm)	2.2
Cladding thickness (mm)	0.38
Roughness of surface	3.2×10^{-6}

Table 2: The material properties.

Position	Material	Density ($kg \cdot m^{-3}$)	Heat conduction coefficient ($W \cdot m^{-1} K^{-1}$)	Specific heat capacity ($J \cdot g^{-1} K^{-1}$)
Fuel	U_3Si_2-Al	6030	50.7	$0.892 + 0.00046T - 0.71 \times (0.749 + 0.00038\,T)$
Cladding	6061-O aluminum alloy	2700	$131.25 + 8.33 \times 10^{-2}\,T$	0.897

$$\rho(T) = 1000.68 - 0.00351 \times T - 0.00461 \times T^2 + 7.5898 \times 10^{-6} \times T^3, \quad (9)$$

$$\lambda(T) = 0.5509 + 0.002606 \times T - 1.318 \times 10^{-5} \times T^2, \quad (10)$$

$$\mu(T) = 0.00177 - 4.91 \times T + 6.46 \times 10^{-7} \times T^2 - 3.13 \times 10^{-9} \times T^3. \quad (11)$$

The unit in equations (9) to (11) and Table 2 is K. All the temperature-dependent parameters are hooked by UDF.

Some reasonable assumptions are taken for simplifications: (a) symmetrical boundary conditions are set except the inlet and outlet; (b) the inlet and outlet planes are constant pressure surface; (c) no gap exists between fuel pellet and cladding; and (d) the impact of oxidation film on the fuel plate is ignored. The operation pressure is 0.683 MPa, and the inlet temperature is 308 K. Prior to the coupling analysis, grid and turbulence model independent sensitivities are performed and the core neutronics model is validated.

Totally five grid schemes are generated to perform the constant power steady-state calculation. The variations of pressure drop and temperature at outlet with grid numbers are presented in Figure 3. It can be seen that the scheme with 95256 meshes could be regarded as the grid-independent solution.

Three turbulence models, realizable k-ε, standard k-ω, and RSM are selected for sensitivity analysis to determine the most suitable turbulence model. The calculated coolant temperature and pressure are presented in Figure 4. It can be seen that the turbulence model selection has very limited influence on the calculation results, and finally the realizable k-ε model is selected in the paper.

The enrichment of ^{235}U is 19.75% ± 0.20%, and uranium density in the fuel pellet is 4.3 gU/cm^3. Nuclei component and design value of atomic density are presented in Table 3.

The meshing model in Monte Carlo code and Fluent is similar. The inlet and outlet planes are set as the vacuum boundary, and other boundaries are set as reflection. Totally 120 batches are run at one iteration, and each batch has 10000 neutron histories. Before counting, 20 neutron batches are skipped for convergence of fission source to reduce the final deviation. The libraries of neutron fission cross sections in fuel and neutron scattering cross sections in coolant are shown in Tables 4 and 5.

The reactivity coefficient calculation is performed to validate the feasibility of built neutronics model. The eight groups of calculations are carried out to determine the coolant temperature coefficient and fuel temperature coefficient. Group details are presented in Table 6, and the results with 95% confidence interval are presented in Table 7. The liner fitting is done after transforming k_{eff} to reactivity coefficient, as shown in Figures 5 and 6. The average fuel temperature coefficient is -2.086×10^{-5} (K), and average coolant temperature coefficient is -5.33×10^{-5} (K). The two coefficients documented in the literature are -2.2745×10^{-5} (K) and -8.0734×10^{-5} (K), and it can be seen that they are close to the calculated value in this paper. It demonstrates that the neutronics model and cross section settings are reliable.

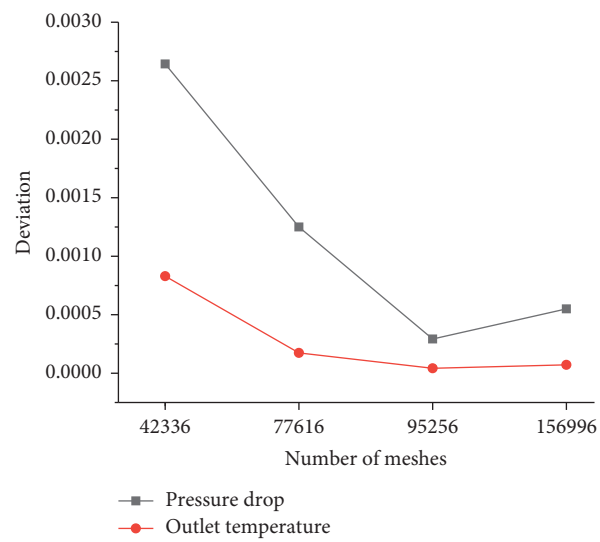

Figure 3: Variations of coolant temperature and pressure drop with different grid numbers.

4.1. Normal Operation Condition. The coupling and noncoupling simulations were performed, respectively, and the results are compared. For noncoupling simulation, cosine power distribution is applied as the heat source. In this case, the inlet velocity is set to 7.0 m/s, and the total assembly power is set to 7.85 MW. k_{eff}, outlet temperature, and pressure of each iteration are shown in Figure 7. It can be seen that after 5 iterations, the calculation is generally converged.

Figure 8 shows the coupled power density distribution in the whole assembly. The power distribution in a single plate along the thickness is treated as uniform distribution since its dimension is much smaller compared to that in the height and width direction. Figure 9 shows the comparison of power distribution in the middle plate between coupling analysis and noncoupling analysis. The calculated power

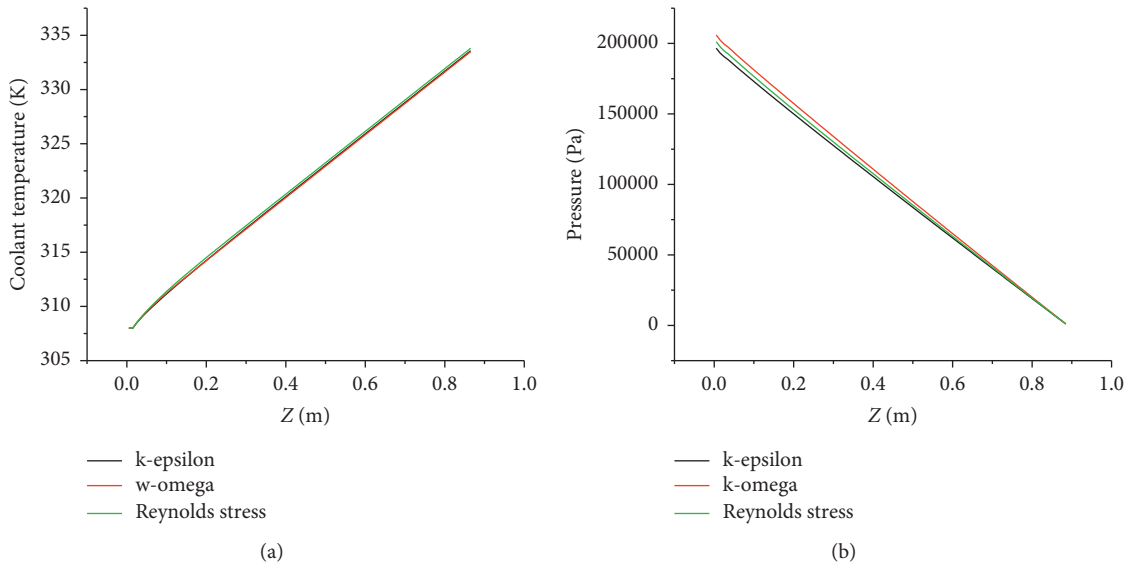

Figure 4: Results of coolant temperature and pressure drop with different turbulence models.

Table 3: Nuclide information for the fuel pellet.

Nuclide	Density (barn-cm)
Al	$3.1633e-2$
Si	$7.2719e-3$
^{235}U	$2.1763e-3$
^{238}U	$8.7315e-3$

Table 4: The variations of neutron fission cross-sections with temperature in fuel.

Temperature (K)	ID extension
300	0.10c
325	0.11c
350	0.12c
375	0.13c
400	0.14c
425	0.15c
450	0.16c
475	0.17c
500	0.18c
525	0.19c
550	0.20c
575	0.21c
600	0.22c
625	0.23c
650	0.24c
675	0.25c

Table 5: The variations of neutron scattering cross-sections with temperature in coolant.

Temperature (K)	ID extension
293	00.32t
323	01.32t
373	02.32t
423	03.32t

Table 6: Group information.

Number	T_{fuel} (K)	T_{water} (K)	ρ_{water} (g•cm^{-3})
1	300	308	0.99430
2	350	308	0.99430
3	400	308	0.99430
4	450	308	0.99430
5	500	308	0.99430
6	400	338	0.98081
7	400	368	0.96217
8	400	398	0.93926

Table 7: The k_{eff} results of each group.

Number	$k_{eff} \pm 95\%$ CI
1	1.59693 ± 0.00126
2	1.59539 ± 0.00112
3	1.59164 ± 0.00119
4	1.58958 ± 0.00131
5	1.58662 ± 0.00134
6	1.59010 ± 0.00105
7	1.58651 ± 0.00117
8	1.58463 ± 0.00116

with coupling analysis code is larger near the edge in the width direction compared to that with noncoupling analysis method due to the space self-shielding effect, which enlarges the fission rate near the edge. Figure 10 shows the variation of power distribution with the iterations, from the initial shape to the 5th iteration. The powers increase at the both ends, and power peak is lowered with the coupling analysis. It can be seen that the power is a little higher in the inlet side, while it is lower in the outlet side, and the power peak moves to the inlet side after coupling. It is because the coolant temperature is lower and the density is higher in the inlet side, where the moderation effect is stronger than that in the

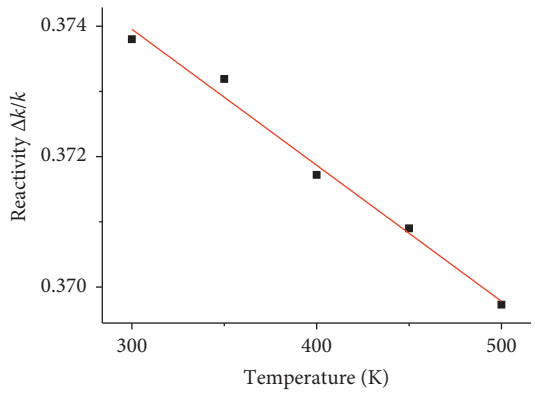

Figure 5: Reactivity-fuel temperature.

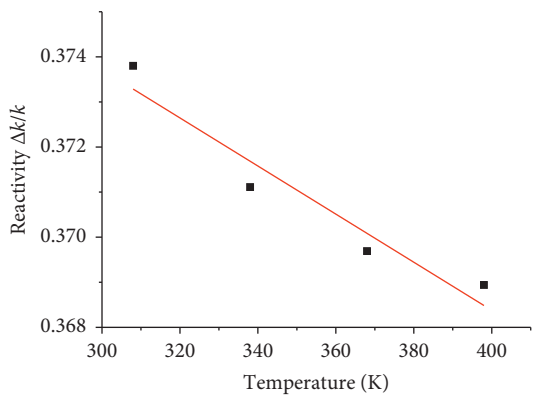

Figure 6: Reactivity-coolant temperature.

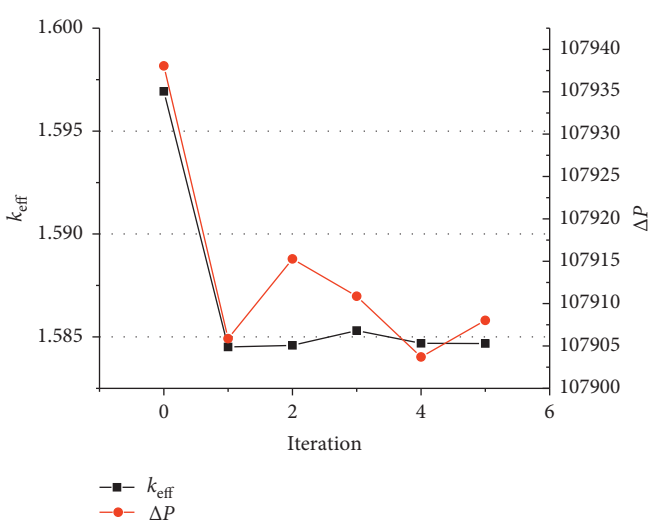

Figure 7: The variations of k_{eff} and pressure drop with iterations.

outlet side, making the thermal neutron flux higher and fission rate greater. The variation of power distributions before and after coupling shows that the coupling code introduces the feedback effect between thermal hydraulic and neutronics and the feasibility of coupling code is proved.

Figure 11 shows the comparison of coolant temperature distributions in the assembly before and after coupling analysis. Figure 12 provides the quantitative comparison of

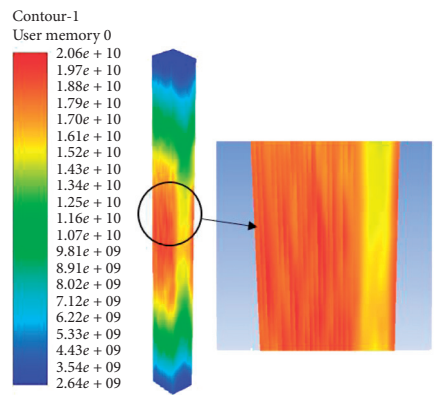

Figure 8: The power distribution in the whole assembly.

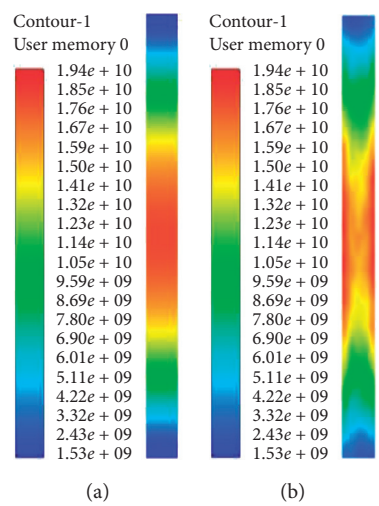

Figure 9: The power density contours in the middle plate. (a) Noncoupled. (b) Coupled.

temperatures of coolant, cladding, and fuel pellet between the noncoupled and coupled analysis. The temperature peak with coupled analysis is lower than that with noncoupled analysis, indicating that cosine power distribution assumption is conservative. Figure 13 shows the variation of average heat transfer coefficient in the height direction. It increases at the beginning rapidly and descends along the flow direction gradually.

4.2. Blockage Condition Analysis. For the plate type fuel reactor, under certain accident conditions such as debris flowing into reactor and fuel blistering, the flow channel blockage will happen, causing temperature to increase sharply inside the fuel plate and leading to large temperature gradient along the plate, which may induce structure rupture of plates and cause severe consequences [18]. The fuel assembly operation features under the blockage conditions are analyzed with the coupling code in this section.

Totally three positions at the inlet of assembly are modelled as the solid partly to realize the fuel assembly blockage conditions. The cross sections of inlet blockage model are presented in Figure 14, and the 30% blockage of

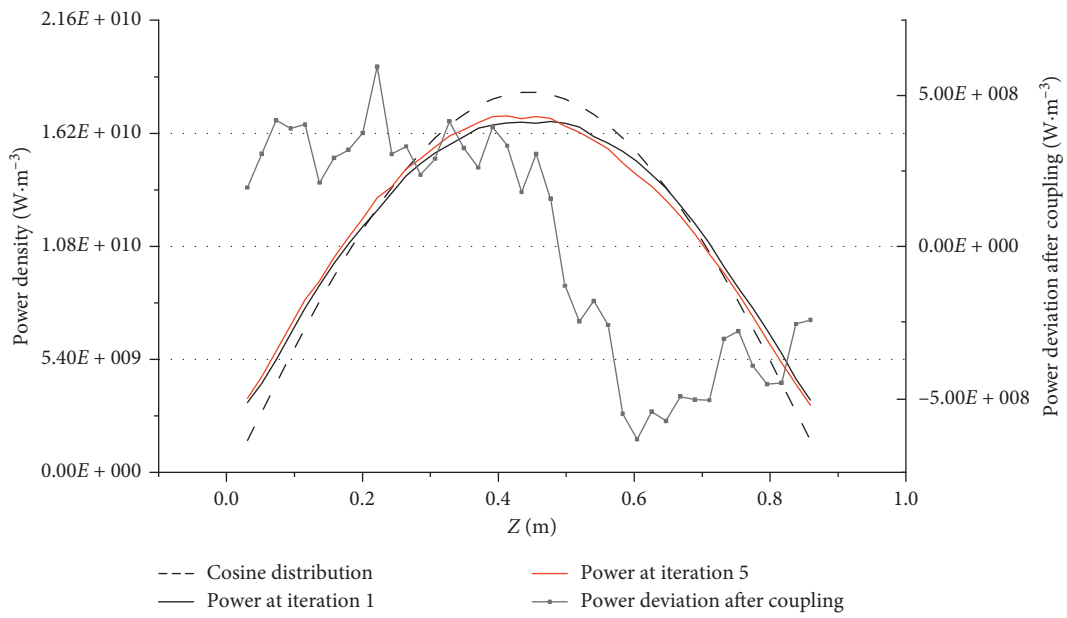

Figure 10: The average axial power profiles before and after coupling.

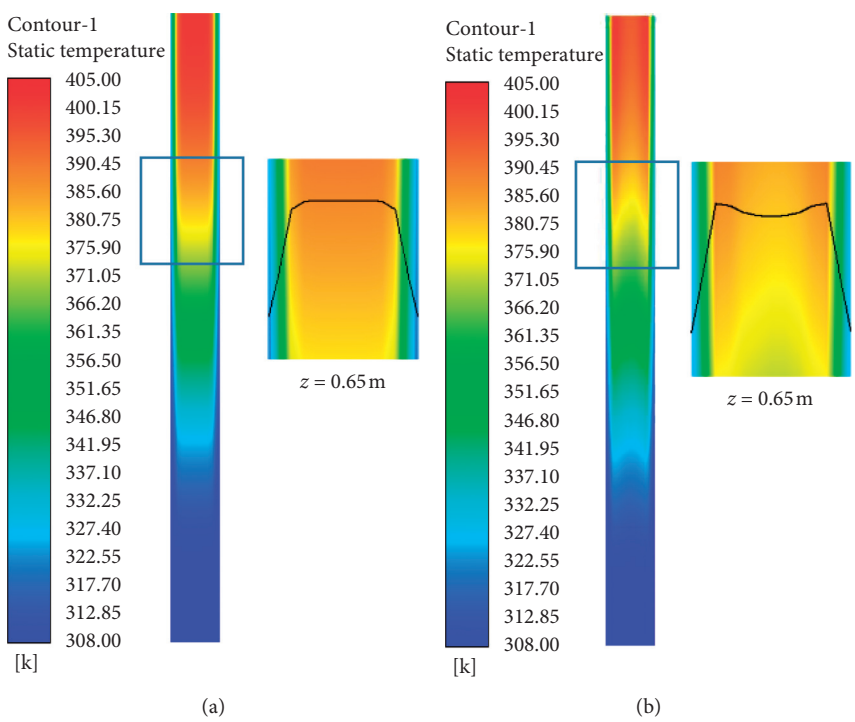

Figure 11: The coolant temperature contours. (a) Noncoupled. (b) Coupled.

channel is set. The material is set as steel, and the corresponding Monte Carlo code coolant cells are changed into steel cells.

Figure 15 presents the coolant temperature in the whole assembly, and Figure 16 shows the temperature contours at $z = 0.285$, just behind the obstructed location. It can be seen that blockage causes temperature rise in both coolant and fuel plates. The temperatures of fuel plates along $x = -0.025$ are presented in Figure 17. The third blockage condition causes higher temperature rise due to the reflective boundary set in the Monte Carlo code. Figure 18 shows the x-direction temperature of fuel plates pointed with the black arrow in Figure 16. The large temperature gradient could be observed in all three conditions, which would threaten the fuel mechanical behaviors.

As thermal hydraulic and neutronics coupling effect is introduced in the calculation, the effect of blockage on local heat transfer can be more accurately obtained. The thermal

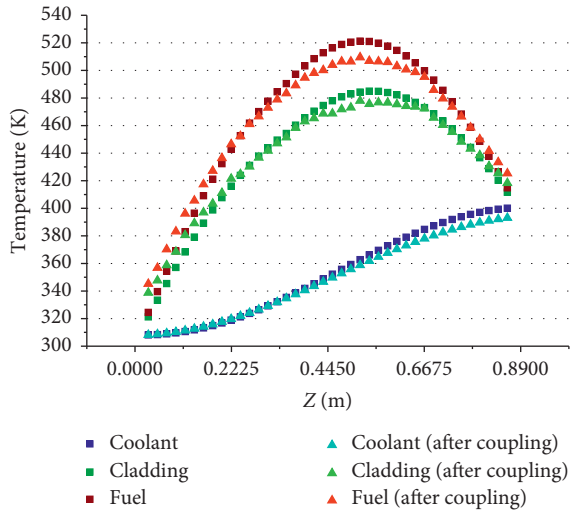

Figure 12: The variations of temperature along Z direction before and after coupling.

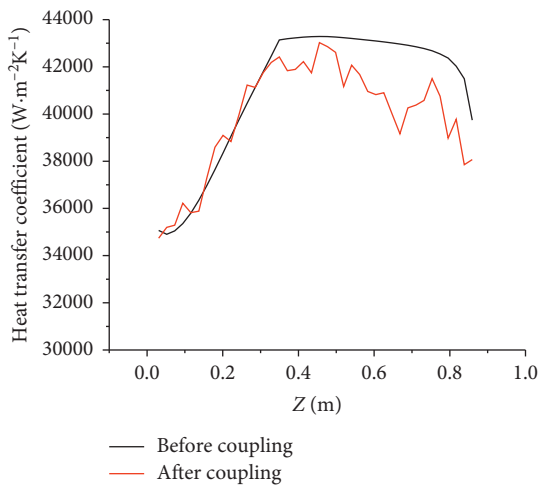

Figure 13: The variations of heat transfer coefficients along flow channels before and after coupling.

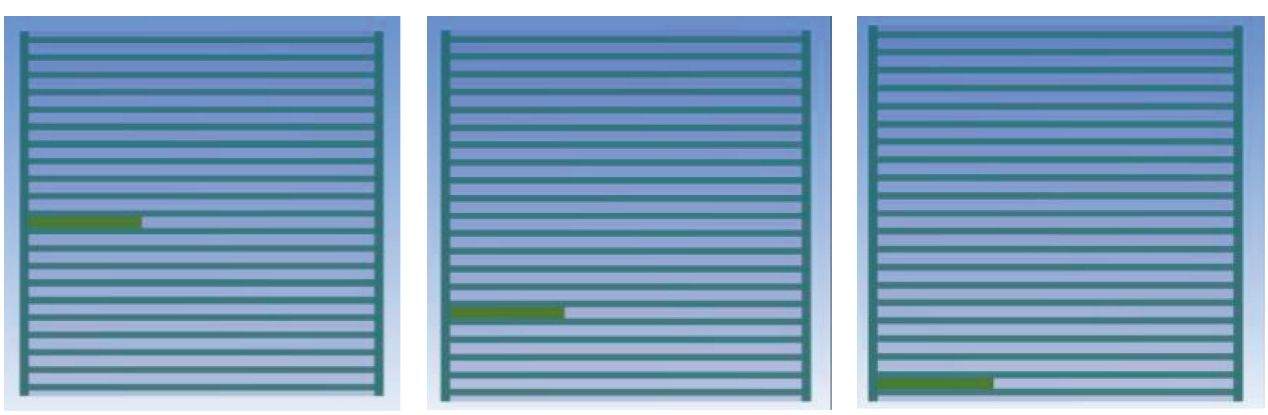

(a) (b) (c)

Figure 14: The blockage condition setting at inlet. (a) Blockage 1. (b) Blockage 2. (c) Blockage 3.

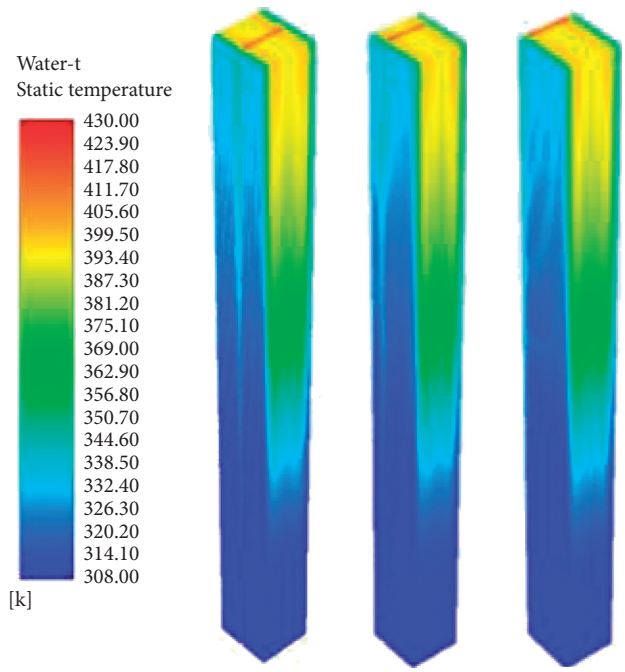

Figure 15: The assembly coolant temperatures under three inlet blockage conditions.

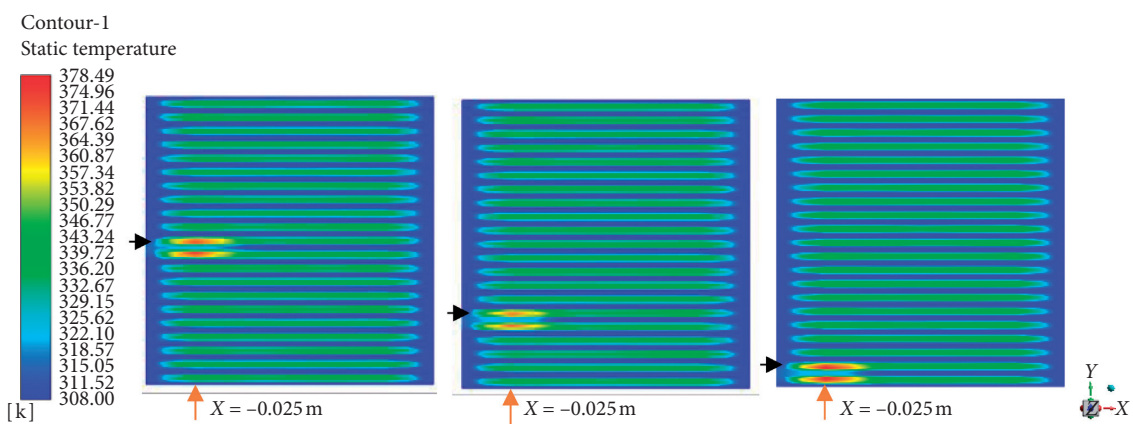

Figure 16: The temperature contours at $z = 0.0285$ m.

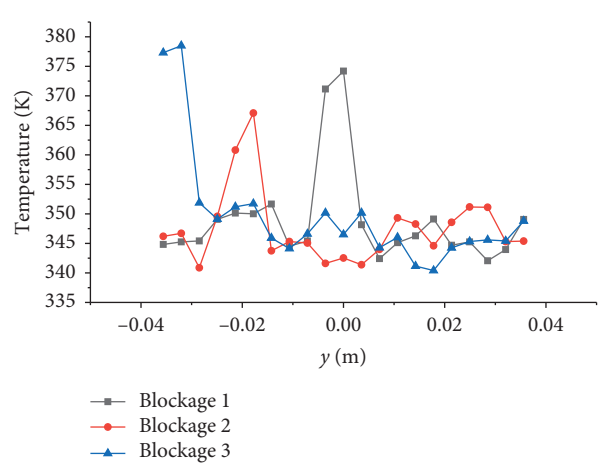

Figure 17: The fuel plate temperatures at $z = 0.0285$ m and $x = -0.025$ m.

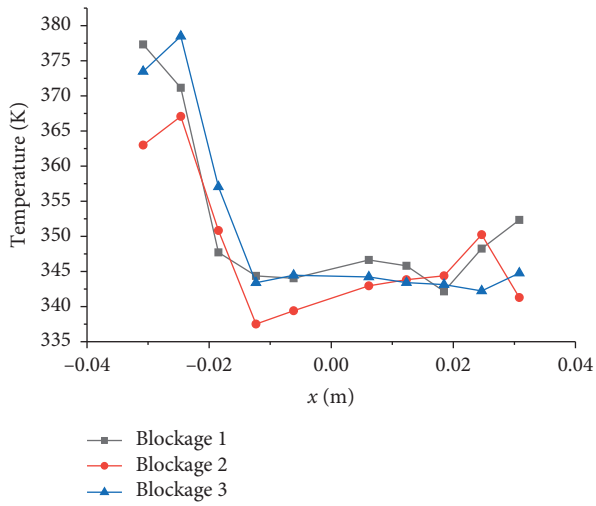

Figure 18: The variations of fuel plate temperatures along x-direction.

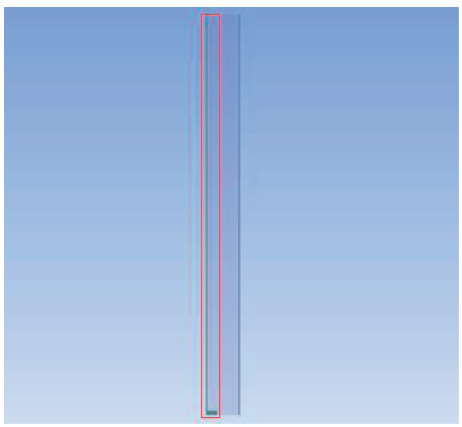

Figure 19: The highlighted position.

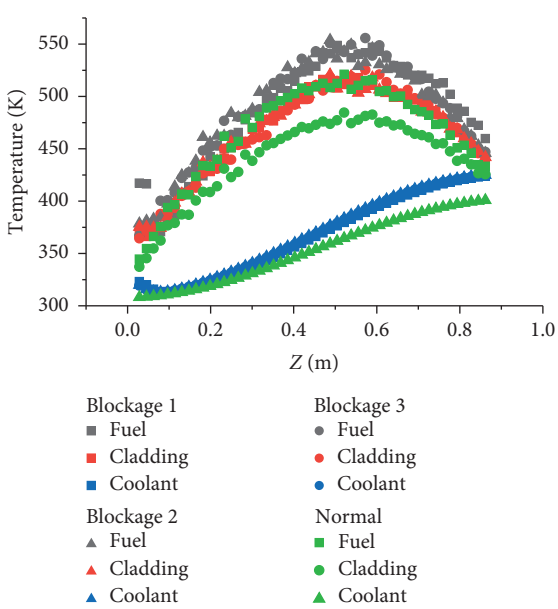

Figure 20: The variations of local temperatures in the height direction.

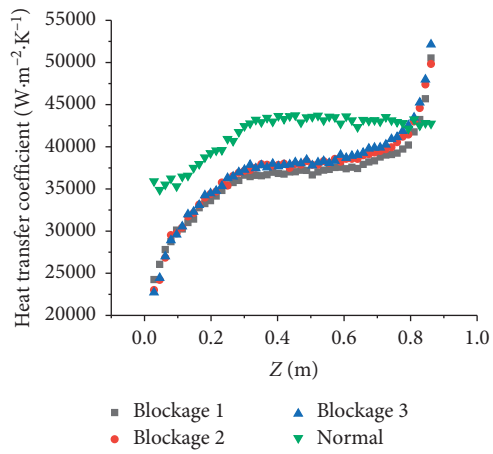

Figure 21: The variations of local heat transfer coefficients in the height direction.

hydraulic parameters in highlighted position (as shown in Figure 19) are studied. The local temperatures of fuel pellet, cladding, and coolant under three blockage conditions and normal conditions are presented in Figure 20. For the 30% blockage in one channel, the coolant velocity decreases, causing local heat transfer coefficient to decrease greatly. As shown in Figure 21, the heat transfer coefficient generally decreases by 5×10^3 W/(m^2·K), and the maximum decrease is over 10^4 W/(m^2·K), leading to coolant temperature increase around 20°C at the outlet and fuel maximum temperature increase about 30°C.

5. Conclusion

In this paper, a thermal hydraulic and neutronics coupling scheme was proposed for plate type fuel reactor core. The coupling platform is based on the Fluent and Monte Carlo code through the UDF module. Then, the thermal hydraulic and neutronics coupling analysis for the plate type fuel assembly was performed in detail. The mesh-independent analysis and turbulence model sensitivity analysis were carried out to determine the number of meshes and turbulence model firstly. Results show that the accuracy of power distribution is well improved and temperature distributions of fuel pellet, cladding, and coolant are refined due to the feedback effect introduction. The power density distribution in the width direction is not uniform, and the power near the edge is higher than that at inner position. Following the normal operating condition study, the blockage condition analysis with the coupling code was performed. Under the conditions of 30% blockage in one channel, the heat transfer coefficient decreases obviously. The maximum coolant temperature would increase around 20°C, and the maximum fuel temperature rises about 30°C. This work provides a promising analysis tool for the plate type nuclear reactor core high-fidelity simulation.

Data Availability

The access to data is restricted due to the commercial confidentiality.

Conflicts of Interest

The authors declare that there are no conflicts of interest.

Acknowledgments

This research was supported by the National Natural Science Foundation of China (no. 11705139).

References

[1] J. Conlin, W. Ji, J. C. Lee, and W. R. Martin, "Pseudo material construct for coupled neutronic-thermal-hydraulic analysis of VHTGR," *Thermal Hydraulics of Next-Generation Nuclear Reactors*, vol. 92, pp. 225–227, 2005.

[2] J. Hu and R. Uddin, "Coupled neutronics and thermal-hydraulics simulations using MCNP and FLUENT," *Transactions of the American Nuclear Society*, vol. 98, pp. 606–608, 2008.

[3] J. N. Cardoni, *Nuclear Reactor Multi-Physics Simulations with Coupled MCNP5 and STAR-CCM+*, University of Illinois, Champaign, IL, USA, 2011.

[4] J. Yan, B. Kochunas, M. Hursin, T. Downar, Z. Karoutas, and E. Baglietto, "Coupled computational fluid dynamics and MOC neutronic simulations of Westinghouse PWR fuel assemblies with grid spacers," in *Proceedings of the 14th International Topical Meeting on Nuclear Reactor Thermalhydraulics (NURETH-14)*, Toronto, Canada, September 2011.

[5] J. E. Hoogenboom, A. Ivanov, V. Sanchez, and C. Diop, "A flexible coupling scheme for Monte Carlo and thermal-hydraulics codes," in *Proceedings of the International Conference on Mathematics and Computational Methods Applied to Nuclear Science And Engineering*, Rio de Janeiro, Brazil, May 2011.

[6] B. L. Sjenitzer, J. E. Hoogenboom, J. Jiménez Escalante, and V. Sanchez Espinoza, "Coupling of dynamic Monte Carlo with thermal-hydraulic feedback," *Annals of Nuclear Energy*, vol. 76, pp. 27–39, 2015.

[7] A. M. Ward, M. J. Wang, M. D. Neumann, M. Memmott, A. Manera, and T. J. Downar, "A simulation of I2S-LWR selected transients," *Annals of Nuclear Energy*, vol. 145, 2020.

[8] H. Zhang, J. Guo, J. Lu, F. Li, Y. Xu, and T. J. Downar, "An assessment of coupling algorithms in HTR simulator TINTE," *Nuclear Science and Engineering*, vol. 190, no. 3, pp. 287–309, 2018.

[9] W. X. Tian, S. Z. Qiu, Y. Guo, G. H. Su, and D. N. Jia, "Development of a thermal-hydraulic analysis code for CARR," *Annals of Nuclear Energy*, vol. 32, no. 3, pp. 261–279, 2005.

[10] D. X. Gong, S. F. Huang, G. B. Wang, and K. Wang, "Heat transfer calculation on plate-type fuel assembly of high flux research reactor," *Science and Technology of Nuclear Installations*, vol. 2015, Article ID 198654, 13 pages, 2015.

[11] Q. Lu, S. Qiu, and G. H. Su, "Development of a thermal-hydraulic analysis code for research reactors with plate fuels," *Annals of Nuclear Energy*, vol. 36, no. 4, pp. 433–447, 2009.

[12] A. Bousbia-Salah, H. Benkharfia, N. Kriangchaiporn, A. Petruzzi, F. D'Auria, and N. Ghazi, "MTR benchmark static calculations with MCNP5 code," *Annals of Nuclear Energy*, vol. 35, no. 5, pp. 845–855, 2008.

[13] N. Xoubi, S. A. Darda, A. Y. Soliman, and T. Abulfaraj, "An investigative study of enrichment reduction impact on the neutron flux in the in-core flux-trap facility of MTR research reactors," *Nuclear Engineering and Technology*, vol. 52, 2020.

[14] H. Ju, M. Wang, C. Chen et al., "Numerical study on the turbulent mixing in channel with Large Eddy Simulation (LES) using spectral element method," *Nuclear Engineering and Design*, vol. 348, pp. 169–176, 2019.

[15] V. H. Kaarle and M. Weeratunge, *An Introduction to Computational Fluid Dynamics: The Finite Volume Method*, Pearson Education, London, UK, 2007.

[16] X. Zhao, M. Wang, C. Chen et al., "Three-dimensional study on the hydraulic characteristics under the steam generator (SG) tube plugging operations for AP1000," *Progress in Nuclear Energy*, vol. 112, pp. 63–74, 2019.

[17] A. M. Zhang and Y. L. Kang, "Design of U3Si2-Al plate-type fuel element for China advanced research reactor," in *Proceedings Of the 18th International Conference On Nuclear Engineering (ICONE18)*, Xi'an, China, May 2010.

[18] L. Li, D. Fang, D. Zhang et al., "Flow and heat transfer characteristics in plate-type fuel channels after formation of blisters on fuel elements," *Annals of Nuclear Energy*, vol. 134, pp. 284–298, 2019.

Hindawi
Science and Technology of Nuclear Installations
Volume 2020, Article ID 5090597, 14 pages
https://doi.org/10.1155/2020/5090597

Research Article

Transient Study on the HTR-PM with TINTE-vPower Coupling Code Package

Jun Sun, Ximing Sun, and Yanhua Zheng

Institute of Nuclear and New Energy Technology, Collaborative Innovation Center of Advanced Nuclear Energy Technology, Key Laboratory of Advanced Reactor Engineering and Safety of Ministry of Education, Tsinghua University, Beijing 100084, China

Correspondence should be addressed to Yanhua Zheng; zhengyh@mail.tsinghua.edu.cn

Received 11 November 2019; Accepted 25 February 2020; Published 25 August 2020

Guest Editor: Han Zhang

The high-temperature gas-cooled reactor pebble-bed module (HTR-PM) nuclear power plant consists of two nuclear steam supply system modules, each of which drives the steam turbine by the superheated steam flow and is fed by the heated-up water flow. The shared steam/water system induces mutual effects on normal operation conditions and transients of the nuclear power plant, which is worthy of safety concerns and intensive study. In this paper, a coupling code package was developed with the TINTE and vPower codes to understand how the HTR-PM operated. The TINTE code was used to analyze the reactor core and primary circuit, while the vPower code simulated the steam/water flow in the conventional island. Two TINTE models were built and coupled to one vPower model through the data exchange in the steam generator models. Using this code package, two typical transients were simulated by decreasing the primary flow rate or introducing the negative reactivity of one module. Important parameters, including the reactor power, the fuel temperature, and the reactor inlet and outlet helium temperatures of two modules, had been studied. The calculation results preliminarily proved that this code package can be further used to evaluate working performance of the HTR-PM.

1. Introduction

Modular high-temperature gas-cooled reactor (HTR) is well-known for the high safety, high efficiency, and processing heat applications capability. A commercial-scale 200 MWe pebble-bed modular high-temperature gas-cooled reactor (HTR-PM) has been designed and is now under construction in Shandong Province, China [1]. Most of the construction and installation work have been finished, and the connection to the electric grid will be expected in the end of 2020.

The HTR-PM nuclear power plant (NPP) consists of two nuclear steam supply system (NSSS) modules, each of which contains independent reactor core, steam generator (SG), and passive reactor cavity cooling system (RCCS). The steam generated in two NSSS modules is supplied to one steam turbine [2]. After following through the condenser and deaerator, the water is pumped by two pumps, respectively, and fed back to two SGs again. Furthermore, the 600 MWe commercial NPP with six similar NSSS modules and only one steam turbine is in the standard design phase. With this typical multimodule design, the transient or perturbation in one module will inevitably influence the operating features of other modules. Study on this coupling or interaction characteristics is important for further understanding and safe operation of the plant.

Engineering simulators have been developed to study the operating features of multimodule HTRs, especially for the intermodule influences during power load regulations or accidents [3, 4]. Benefited from the full-scope models and real-time simulations, engineering simulators can present coupled dynamic behaviors of the whole NPP by well-balanced computational cost and accuracy. In the integral supporting system of vPower code, reactor core models are simplified, while appropriate models of helium blowers, SGs, RCCSs, secondary systems, control systems, and electric

system are coupled and managed in data transfer [5]. Without adequate detailed reactor core model, the vPower code of engineering simulator can only match the main parameters of the NPP and loses accuracies of distribution parameters.

To further improve the simulation accuracy, a coupling code package was developed with the TINTE and vPower codes. TINTE code is used to carry out the analysis of reactor core and primary circuit, while vPower code performs the secondary circuit calculation, including the primary side of the SGs. These two codes are connected through components of SGs. In this paper, two cases, including the primary flow rate decrease and the reactivity introduction of one module, were simulated with this code package. The phenomena in two modules, including some important parameters such as the reactor power, the fuel temperature, and the helium temperatures, were studied.

HTR-PM is shortly described in Section 2. Sections 3 and 4 provide description of the TINTE code and vPower code, and the coupling method between different circuits with these two codes is shortly discussed in Section 5. The calculation results are presented in Section 6. Finally, Section 7 presents the summary and conclusion.

2. HTR-PM

As mentioned above, there are two pebble-bed modular reactors in the HTR-PM NPP coupling with one steam turbine generators, whose total power is 500 MWt and its electrical efficiency is about 42%. For each reactor module, it consists of a high-temperature pebble-bed reactor and a once-through steam generator, as well as its connecting horizontal coaxial tube. The helium goes through the reactor core and is heated up to 750°C, then transfers the heat to the secondary circuit water in the SG, and finally produces the high-pressure superheated steam. The helium at the SG outlet is cooled to about 250°C by the secondary circuit water. Then, this cold helium, driven by the helium blower, enters the reactor again through the outer annular channel of the coaxial duct [6, 7]. Each equilibrium state reactor core has an average in height of 11 m and a diameter of 3.0 m, which is a randomly packed pebble bed by roughly 420,000 spherical fuel elements.

The flow diagram of power conversion is shown in Figure 1, and the key parameters are provided in Table 1.

3. TINTE Code and Model

3.1. TINTE Code. The TINTE (TIme-dependent Neutronics and TEmperatures) is a special-designed and well-developed code by the Research Center Jülich to evaluate the nuclear and thermal transient behavior of pebble-bed high-temperature gas-cooled reactors. The performance of TINTE has been validated by the well-known open/blind benchmarks [8–11] and has been widely used in the pebble-bed high-temperature reactor design [12–14], such as the HTR-PM in China and PBMR in South Africa. VSOP99 (also developed for pebble-bed high-temperature gas-cooled reactor by the Research Center Jülich) is used to prepare state parameters, e.g., the cross sections, the power, and burnup histories, for TINTE calculation. There are several computational modules in TINTE to consider the complex multiphysics coupling effect in the pebble-bed high temperature reactor, such as the 2D neutronic diffusion module, 2D thermal-hydraulic module, the corrosion module, and the automatic control module. In this work, we focus on the thermal-hydraulic module, whose conservation equations and main correlations are as follows [15, 16].

(1) Pebble-bed heat conservation equation:

$$\frac{\partial}{\partial t}(1-\varepsilon)\rho_s c_s T_s = \nabla(1-\varepsilon)\lambda_f \nabla T_s + q_s + \alpha\left(T_g - T_s\right), \tag{1}$$

where the term q_s and $\alpha(T_g - T_s)$ represent the heat flux from the fuel element and the convective heat transfer term between the pebble bed and coolant helium, respectively. λ_f is the effective thermal conductivity, which considers the effects of radiation, gas and solid conduction, and contact conduction. The detail discussion about the correlations of effective thermal conductivity in the pebble-bed region could be found in [17–21].

(2) Helium continuity equation:

$$\nabla \vec{u} = 0. \tag{2}$$

(3) Helium momentum equation:

$$\nabla p - \rho_g \vec{g} + W\vec{u} = 0, \tag{3}$$

where the resistance coefficient W could be determined as follows [22]:

$$W = \Psi \cdot \frac{(1-\varepsilon)|\vec{u}|}{\varepsilon 2\, d}, \tag{4}$$

$$\Psi = \frac{320}{(Re/1-\varepsilon)} + \frac{6}{(Re/1-\varepsilon)^{0.1}}. \tag{5}$$

(4) Helium energy equation:

$$\frac{\partial}{\partial t}\rho_g c_g T_g + \nabla\left(\vec{u}\rho_g c_g T_g\right) = \nabla\lambda_g \nabla T_g + \alpha\left(T_s - T_g\right), \tag{6}$$

where the heat transfer coefficient of the surface of spherical fuel elements could be calculated, according to the German safety guide KTA3102.2 [23].

$$Nu = 1.27 \times \frac{Pr^{1/3}}{\varepsilon^{1.18}} Re^{0.36} + 0.033 \times \frac{Pr^{1/2}}{\varepsilon^{1.07}} Re^{0.86}. \tag{7}$$

3.2. TINTE Model of HTR-PM. The calculation models for the HTR-PM have been established based on some reasonable approximations and simplifications. The 2D heat conduction and gas convection model of HTR-PM reactor is

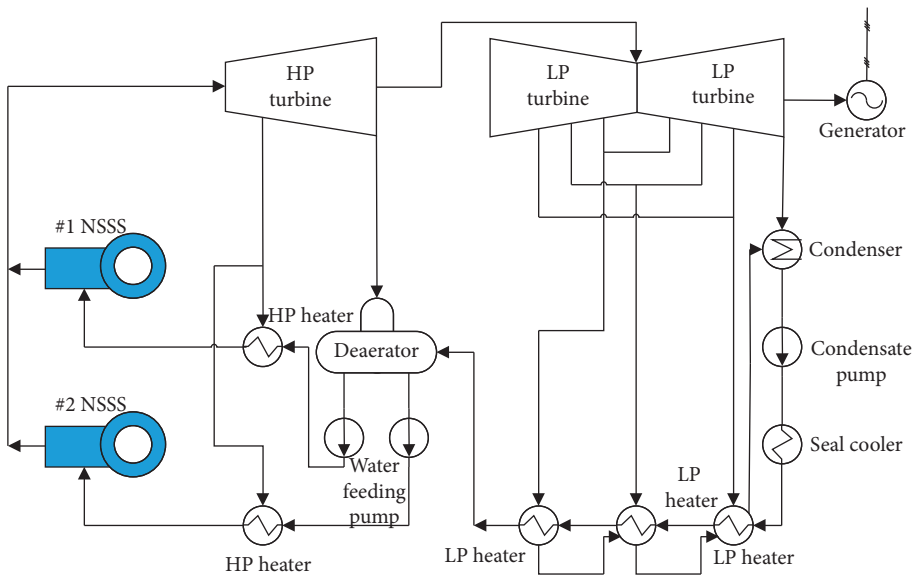

Figure 1: Flow diagram of power conversion [3].

Table 1: Main design parameters of the HTR-PM [2].

Parameter	Value
Reactor total thermal power (MWt)	2×250
Rated electrical power (MWe)	210
Average core power density (MW/m^3)	3.22
Net electrical efficiency (%)	42
Primary helium pressure (MPa)	7
He temperature at reactor inlet/outlet (°C)	250/ 750
Primary helium flow rate (kg/s)	96
Core main flow rate (kg/s)	≥86.4
Heavy metal loading per fuel element (g)	7
Enrichment of fresh fuel element (for the equilibrium core) (%)	8.5
Active core diameter (m)	3
Equivalent active core height (m)	11
Diameter of the RPV (m)	~6.0
Number of fuel elements in one module	420,000
Number of fuel passages through the core	15
Average burnup (GWd/tU)	90
Main steam pressure (MPa)	13.9
Main steam temperature (°C)	571
Main feedwater temperature (°C)	205

shown in Figure 2, including the pebble-bed core, reflectors, carbon bricks, core vessel, RPV, water cooling panel of RCCS, and reactor building. In this model, the pebble-bed core, a porous medium with the void fraction of 0.39, is divided into 6 nodes along the radius and 20 nodes along the height.

A 1D model for the primary circuit is also built and shown in Figure 3. In this model, rectangular figures represent the different components such as the hot-gas duct, the SG, and the blower, while circular figures are the nodal points used to connect the components. The 1D primary circuit model is through two nodal points ("core inlet" and "core outlet") connected to the 2D model via two corresponding components ("core inlet cavity" and "core outlet" shown in Figure 2).

In the below, one 2D model along with the connected 1D model is called as one TINTE model for a HTR-PM reactor module. To analyze the coupling behavior of the HTR-PM, two same models are built.

4. VPOWER Code and Model

4.1. vPower Code. The vPower code is an integrated simulation software developed by Beijing Neoswise Science and Technology Limited Company in China. The vPower code has user friendly interfaces (see Figure 4) based on Windows operation system and has many integrated, object-oriented graphical modeling tools, which can solve the built-in thermal fluid networks and electrical power flow networks. Powerful toolboxes are capable of simulating typical components of power plants, such as pipes, valves, steam turbines, deaerators, pumps, condensers, separators, and a variety of heat exchangers. Control systems and electrical supply of those components also have respective toolboxes. Moreover, the vPower code also supplies graphical tools to draw digital operating interfaces. Well-organized code architecture creates levels of data management and time schedule [5] and makes the vPower code widely serve for many simulators of coal-fired plants in China.

Moreover, the vPower code has unique functions of embedding a series of user-developed models, which extends the application of the vPower code into NPP simulators. Since 2009, Tsinghua University employed the vPower code to establish the HTR-PM engineering simulator by developing typical models of reactor core neutronics, helium flow, fuel pebbles, graphite blocks, helium circulators, once-through helical coil SGs, and control rods. Besides the newly developed models of the nuclear island, the conventional island components, as well as necessary human machine interfaces (HMIs), were also developed to form the full-

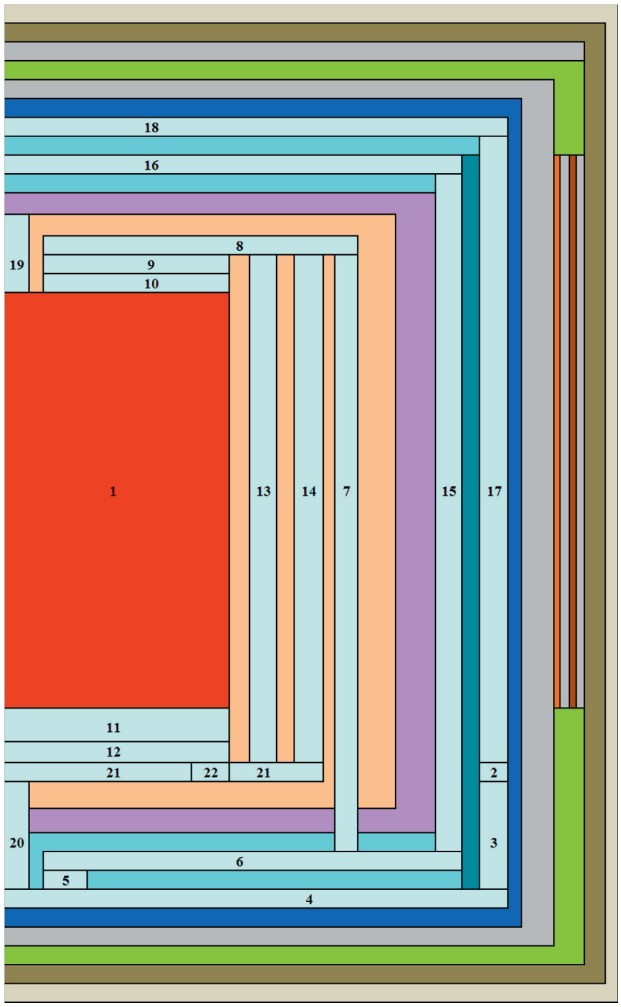

Fluid area
1: core;
2: core inlet cavity;
3: core inlet channel;
4: RPV bottom cavity;
5: RPV bottom flow passage;
6: core bottom cavity;
7: coolant channel;
8: cold helium plenum;
9: top reflector flow passage;
10: core top cavity;
11 and 12: bottom reflector flow passage;
13: control rod channel;
14: bypass flow;
15-18: helium gap;
19: charging tube;
20: discharging tube;
21: hot helium plenum;
22: core outlet.

Solid area
Graphite reflector;
Carbon brick;
Metal internals;
Core barrel;
RPV;
Air gap;
Water cooling panel;
Metallic plate;
Thermal insulation;
Concrete wall;
Air boundary.

Figure 2: 2D TINTE model of the HTR-PM reactor in *r-z* coordinates.

scope simulation capability. Great efforts have been made to balance the computational cost and model accuracy in two aspects. As one challenge, the neutronic behavior is described by the improved quasistatic method to solve the three-dimensional space-time dynamic equations. The efficient solver also contributes to get the solutions of each step fast enough [24]. The other challenge is from the complicated three-dimensional gas flow and heat transfer inside the reactor core. Since the built-in thermal fluid network assumes it as the combinations of many one-dimensional flow paths and heat transfer paths, flow network and heat transfer network models can represent the reactor core flow and heat transfer and save computational time significantly [25]. After 3 years of effort, the engineering simulator of HTR-PM was able to perform the normal operation conditions well and basic abnormal scenarios in real time [5]. Following that, the engineering simulator was used to simulate the start-up and shut-down processes of the HTR-PM NSSS modules step by step and supported the confirmation of commissioning programs and detailed procedures [26, 27].

4.2. vPower Model of HTR-PM. The HTR-PM engineering simulator models by the vPower code mainly consist of reactor core section, SG, secondary loop section, control system, and electric system. The reactor core section has been described in many previous papers [5, 24, 25, 27]. In the current paper, the SG model and the secondary loop section are introduced to be coupled with the TINTE model of reactor core.

Each NSSS module of the HTR-PM has independent SG using helical coil heat transfer tube bundles. The engineering simulator developed a new component model of the helical coil heat transfer tube bundle to calculate the pressure drops and heat transfers in both the helium flow side and the steam/water side, as well as the heat transfer from helium to steam/water through the tube walls [26], shown in Figure 5(a). The matrix of SG model shows the configuration of 19 bundles, each one of which is divided into 16 subsections in height. In Figure 5(b), 19×16 components are connected by flow nodes and flow links to simulate helium flows in the primary side, while in Figure 5(c), the same components are again connected in the secondary side to simulate water/steam flows. The reuse of the SG component model can couple the calculations of flow and heat transfer of primary and secondary sides. Correlations of pressure drop and convection in both the primary and secondary sides were also described in [28]. Since the function of SG is significant to transfer reactor core heat into water/steam flow, the SG model is key to couple nuclear and conventional islands. In the engineering simulator of the HTR-PM, the vPower code is carefully tested and agrees well with design data [27, 28].

Seen from Figure 1, the water/steam side of SG serves as part of secondary side of the HTR-PM NPP. The engineering simulator of the HTR-PM also establishes models for components of the high-pressure and low-pressure cylinders of the steam turbine, the condenser, the condensate pumps, the low-pressure and high-pressure heaters, the deaerator, feedwater pumps, and many valves. These components are connected by one-dimensional pipes to form the complete water/steam flow network, which is solved by built-in thermal fluid solver. Several HMIs indicate more details of the secondary side models in Figures 6 and 7. Models and operation data of the secondary side of HTR-PM engineering simulator were also carefully tested to match the

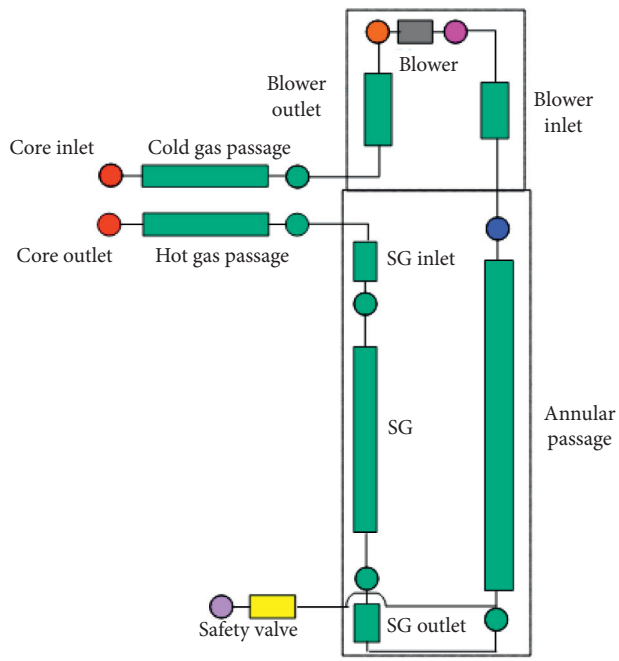

Figure 3: 1D TINTE model of the HTR-PM primary circuit.

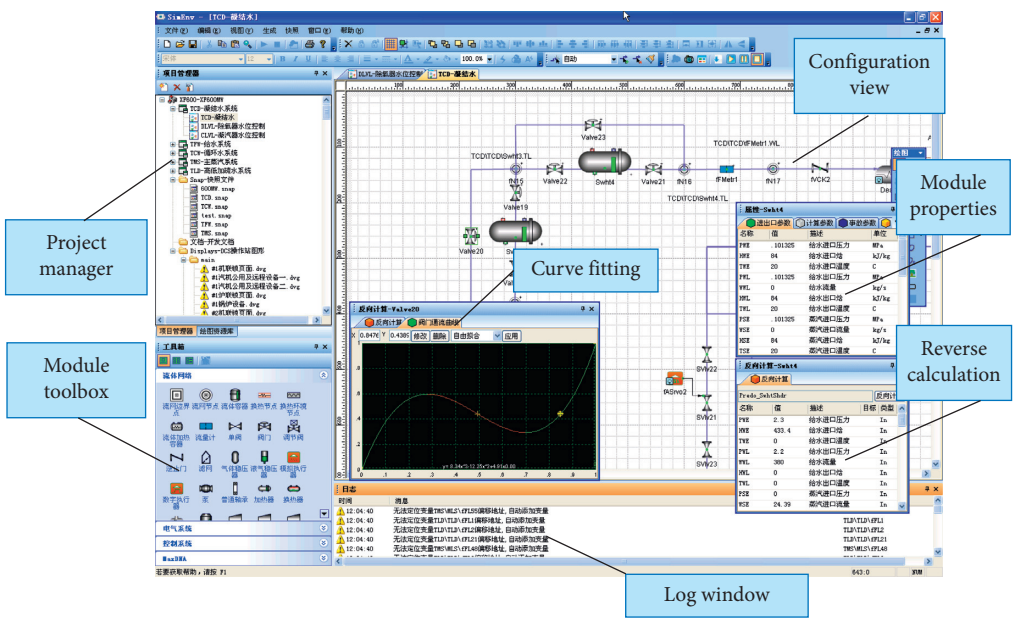

Figure 4: Interface of vPower code.

design parameters, which can continue to support the coupling with the TINTE code.

5. Coupling between Different Circuits

A coupling code package based on TINTE code and vPower code has been developed to study the coupling characteristics of the HTGR plants with more than one reactor module, and the data communication between these two codes can be controlled by an independent platform. In HTR-PM analysis, two TINTE models are connected to one vPower model.

Coupling method between different circuits with these two codes can be explained as follows:

(1) Two TINTE models are, respectively, connected to one vPower model through the SG components, as shown in Figure 8.

(2) In the TINTE model, only the behavior of reactor core and primary circuit is analyzed, which means the heat load Q (the heat transferred from the helium

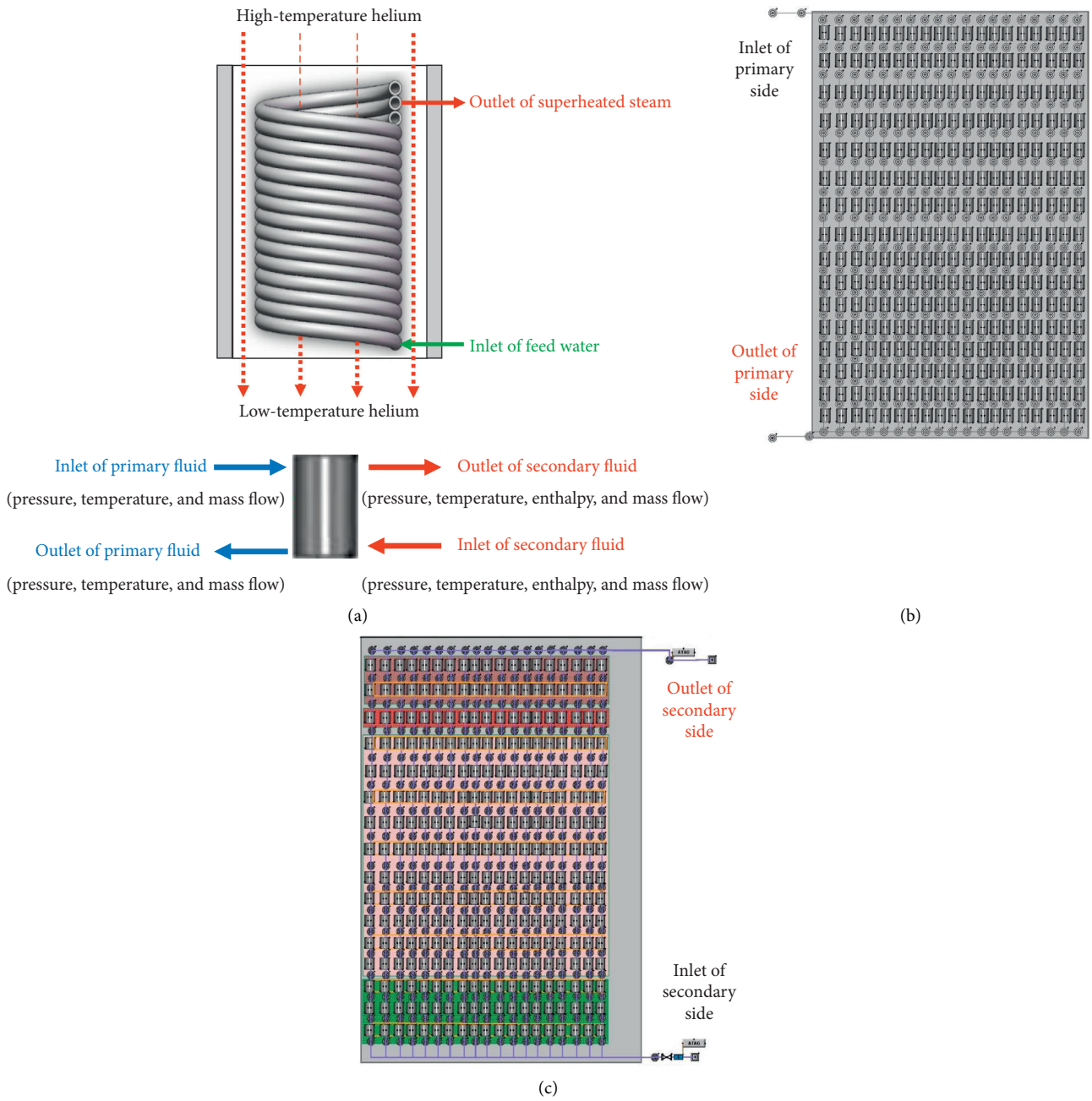

Figure 5: The matrix model of SG in vPower code: (a) the typical bundle and its model of vPower code; (b) SG model of the primary side; (c) SG model of the secondary side.

side to the water/steam side in the SG) needs to be set as a boundary condition.

(3) In the vPower model, the behavior of the secondary circuit, but also including the helium side of the SG, will be analyzed. With the given value of the inlet temperature (T_{in}), inlet pressure (P_{in}), and mass flow rate (F) in the helium side, the heat transfer between the primary circuit and the secondary circuit can be calculated.

(4) A steady state needs to be achieved firstly.

To perform a steady-state calculation, for example, for the HTR-PM in normal operation of 100% rated power, some input parameters should be set according to the design, including the heat reactor nuclear power, the SG heat load (Q), the helium mass flow rate (F), and core inlet helium temperature (T_{out}) for two TINTE models, as well as the SG inlet helium temperature (T_{in}), SG inlet feedwater temperature, helium mass flow rate (F), and feedwater mass flow rate for one vPower model. The resistance coefficients in the above models also need to be

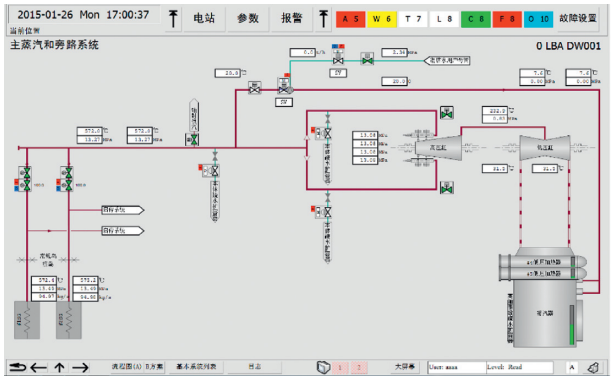

Figure 6: HMI for the main steam system in vPower code.

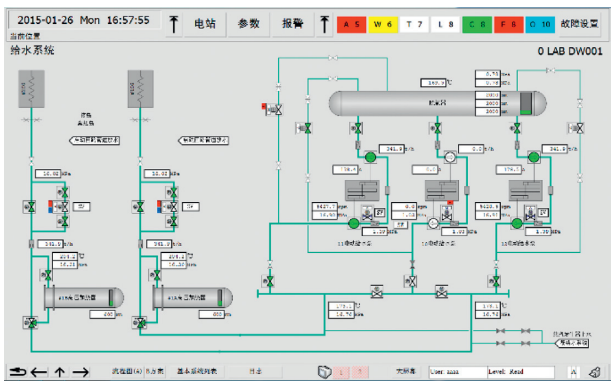

Figure 7: HMI for the feedwater system in vPower code.

adjusted according to the design so as to get the correct pressure drops.

Thus, an initial steady state for TINTE models and vPower model can be reached, and the values of Q, F, T_{in}, and T_{out} in different models are consistent.

(5) During the transient calculation, for example, in the time point t_0, calculation will firstly be performed in two independent TINTE codes. Then, the calculation results of each module, including the SG inlet helium temperature (T_{in}), inlet pressure (P_{in}), and helium mass flow rate (F), will be transmitted to act as the input data of the corresponding SG component, and the calculation will be performed by the vPower code. Finally, the calculation results of the vPower code, including the SG heat load (Q) and the SG outlet temperature (T_{out}), will be transmitted back to the TINTE model and act as the input data for calculation of next time point.

(6) After calculation in a certain time point has finished, TINTE code can self-adjust the next time step, Δt, according to the calculation error. In this code package, after calculation in the time point t_0 has finished, two time steps, Δt_1 and Δt_2, will be given by two independent TINTE codes. The platform then will compare these two time steps and select the smaller one to determine the time point for next TINTE and vPower calculation.

6. Calculation Results

It is assumed that both NSSS modules of HTR-PM are initially operated in 100% rated power when an unexpected transient or perturbation occurs in the #2 module. Two cases are simulated in this paper:

Case 1: the primary flow rate decreases linearly from 100% to 80% rated flow rate in 15 minutes

Case 2: a negative reactivity of 0.1% $\Delta k/k$ is introduced in 2 minutes linearly

These cases aim to test the ability of this coupling code package to analyze the interaction behavior between two modules. The possible operator action, as well as the automatic response of the reactor protection system, is not considered.

6.1. Primary Flow Rate Decrease in Module One. Figures 9–14 show some calculation results of case 1. The decrease in the primary flow rate will result in the decrease of the heat quantity transferred from the primary helium side to the secondary water/steam side in the SG, as shown in Figure 9 (dashed line). The heat transfer between the reactor core and primary coolant is also impaired, resulting in the increase in the fuel temperature, as shown in Figure 10. It also can be seen that the increase in the average fuel temperature during the first several minutes is very small, which is due to the

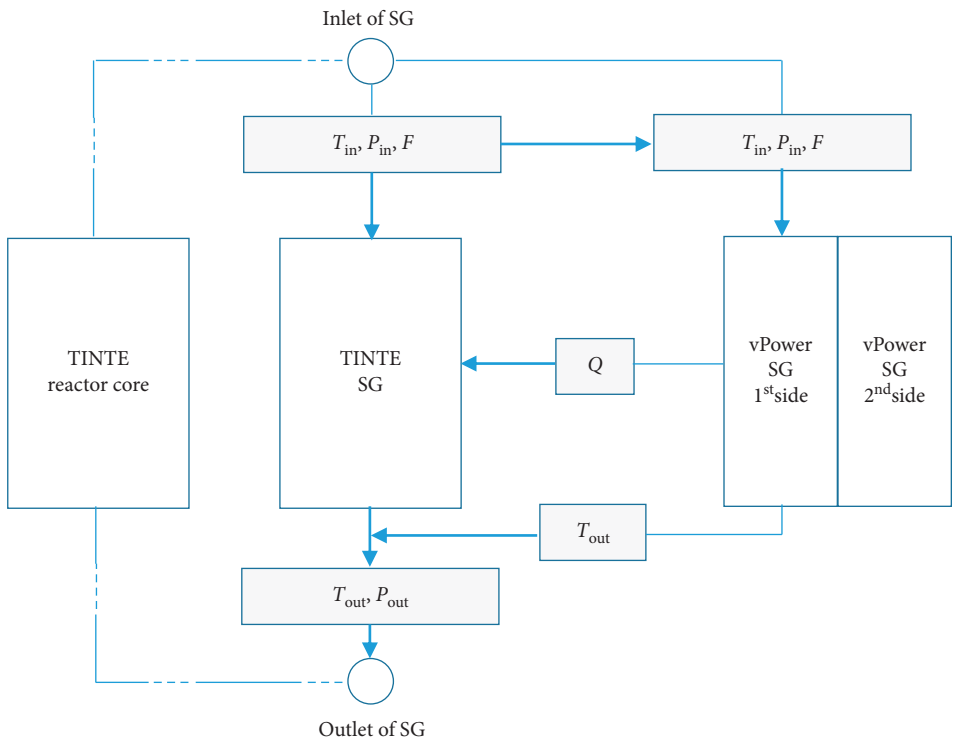

Figure 8: Coupling and data communication between TINTE and vPower.

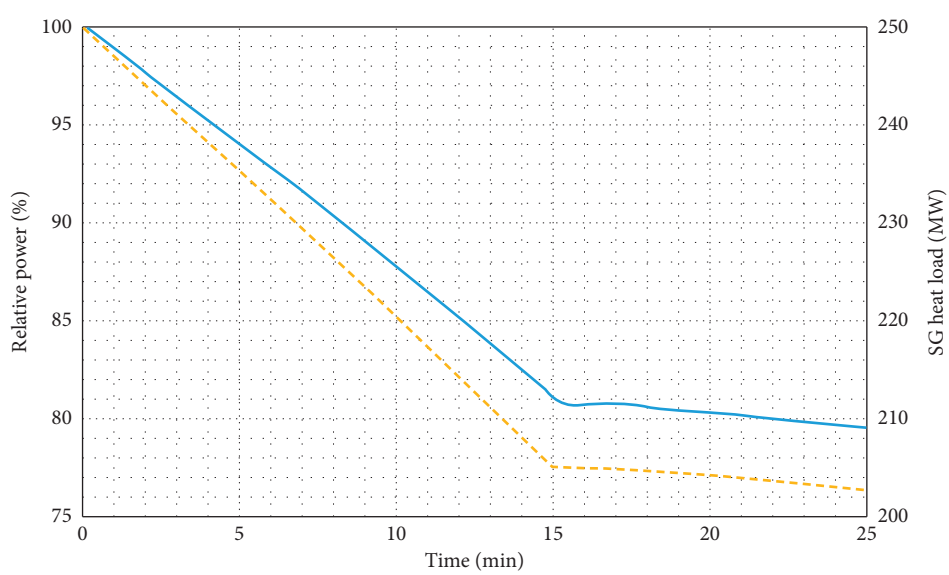

Figure 9: Relative power and SG heat load of #2 module in case 1 (solid line: relative power; dashed line: SG heat load).

large heat capacity of the HTR-PM core (totally about 80 t fuel elements and 250 t reflector graphite in one reactor module). With the increase in the fuel temperature, the reactor power will decrease by negative temperature feedback, as the solid line in Figure 9 shows, which will result in the subsequent decrease in the average fuel temperature.

In the HTR-PM, primary coolant flows from the top to the bottom in the pebble-bed core and the maximum fuel temperature appears at the bottom of the core. With the decrease in the primary helium flow rate, the maximum fuel temperature and the resulting core outlet (namely, the SG inlet) helium temperature will increase continuously, but very slowly, as the dashed lines in Figures 10 and 11 show. These two curves begin to decline in about 15 minutes affected by the power decrease. It also can be seen from Figure 11 that, because of the larger mass flow rate of the secondary side compared to that of the primary side, the SG outlet helium temperature will decrease continuously.

As in the HTR-PM, the steam from two SGs will converge and then flow into one turbine, and the power decrease

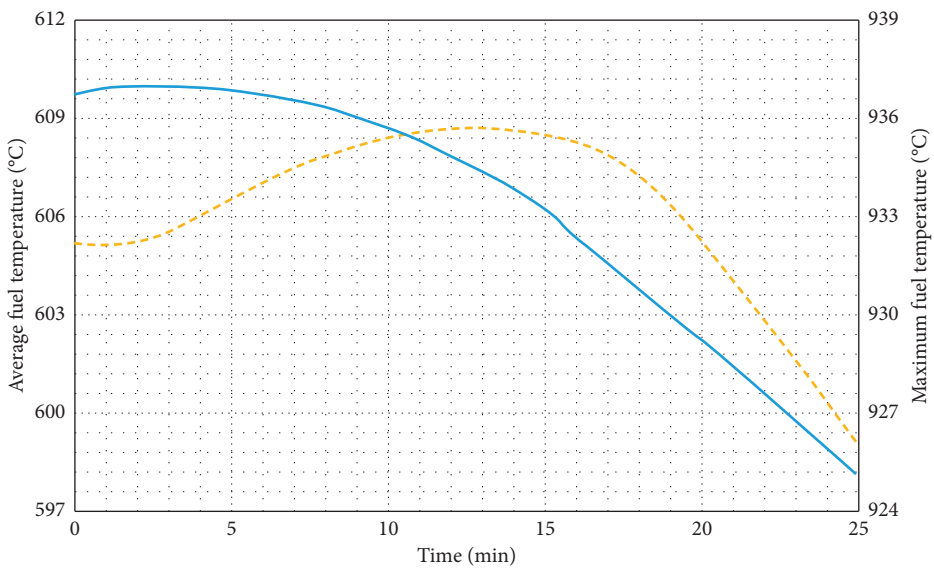

Figure 10: Average and maximum fuel temperature of #2 module in case 1 (solid line: average; dashed line: maximum).

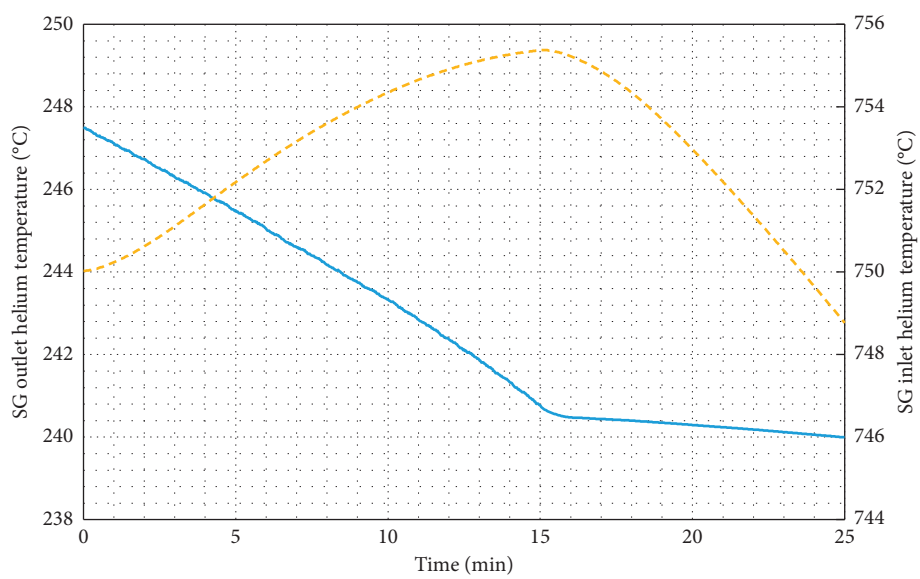

Figure 11: SG outlet and inlet helium temperature of #2 module in case 1 (solid line: outlet; dashed line: inlet).

in #2 module will also result in the small decrease in the feedwater temperature back to the SGs (as shown in Figure 12), so as to result in the small decrease in the SG outlet helium temperature in #1 module (Figure 13). The helium flows back to the reactor core with a little lower temperature and will then cause a little increase in the reactor power in #1 module due to the negative temperature feedback (Figure 14).

6.2. Reactivity Introduction of Module One. In this case, a negative reactivity of about 0.1% is introduced into #2 module in 2 minutes, resulting in decrease in power (solid line in Figure 15) and the consequent decrease in fuel temperature (Figure 16) and core outlet helium temperature (dashed line in Figure 17, the SG inlet helium temperature). The decrease in the SG inlet helium temperature will also cause the decrease in outlet helium temperature after it transfers the heat to the water/steam in the secondary circuit and flows back to the reactor (solid line in Figure 17).

It can be seen from Figure 17 that the core outlet helium temperature will decrease from about 750°C to less than 720°C in 20 minutes due to the decrease in the reactor power, while the decrease in the SG outlet helium temperature is only about several degrees. This can be explained by the coinstantaneous decrease in the heat transfer capacity between two sides of the SG, as the dashed line in Figure 15 shows.

As shown in Figure 15, the reactor power will rise over again due to the fuel temperature decrease and the resulting negative temperature feedback. After a little fluctuation, the

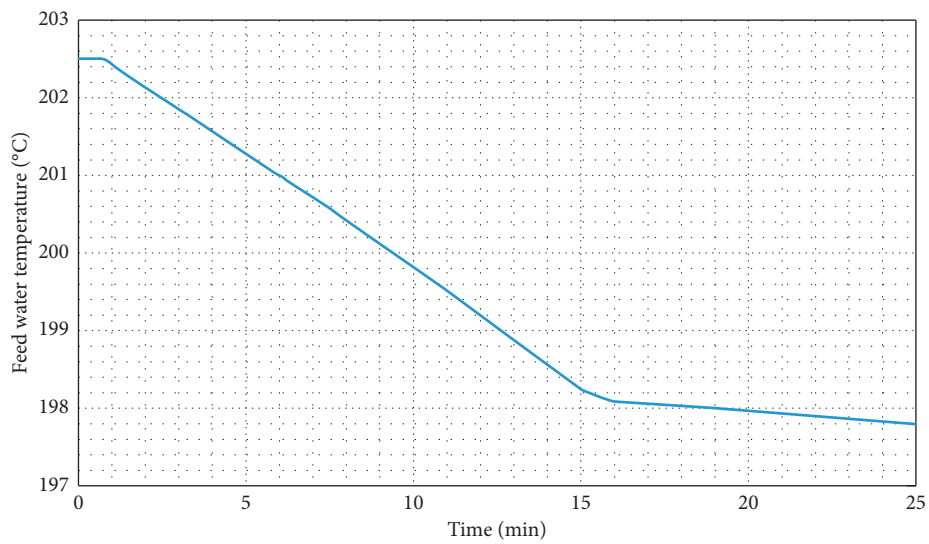

Figure 12: Feedwater temperature in case 1.

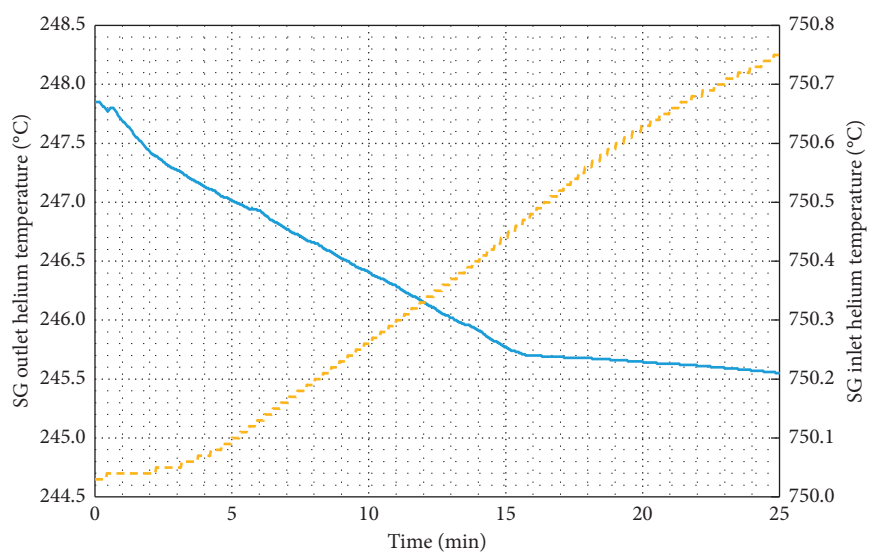

Figure 13: SG outlet and inlet helium temperature of #1 module in case 1 (solid line: outlet; dashed line: inlet).

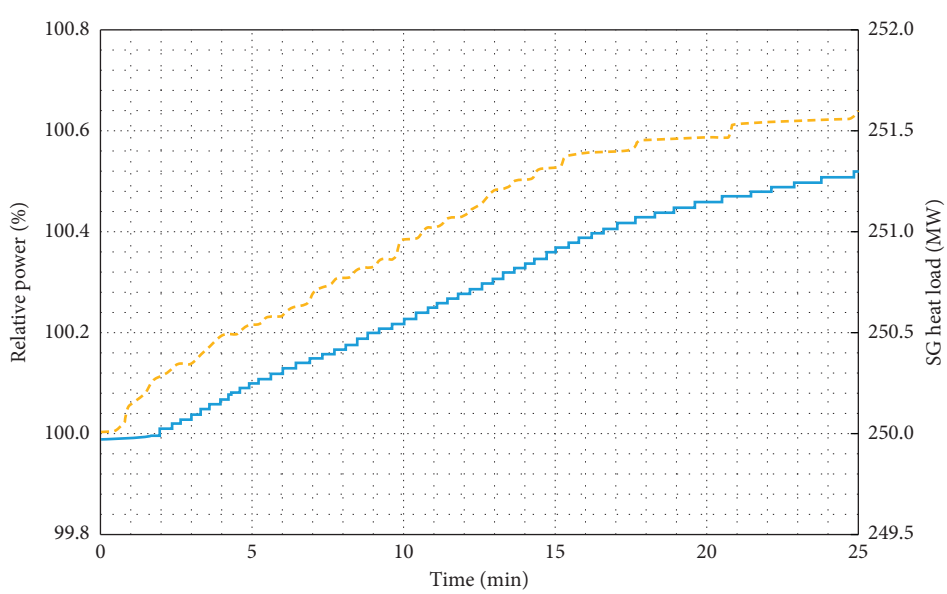

Figure 14: Relative power and SG heat load of #1 module in case 1 (solid line: relative power; dashed line: SG heat load).

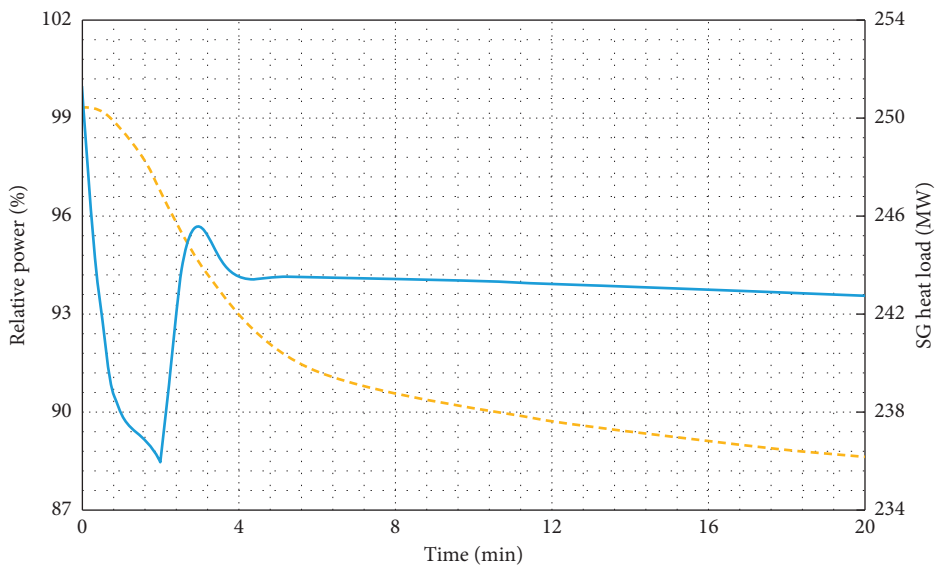

Figure 15: Relative power and SG heat load of #2 module in case 2 (solid line: relative power; dashed line: SG heat load).

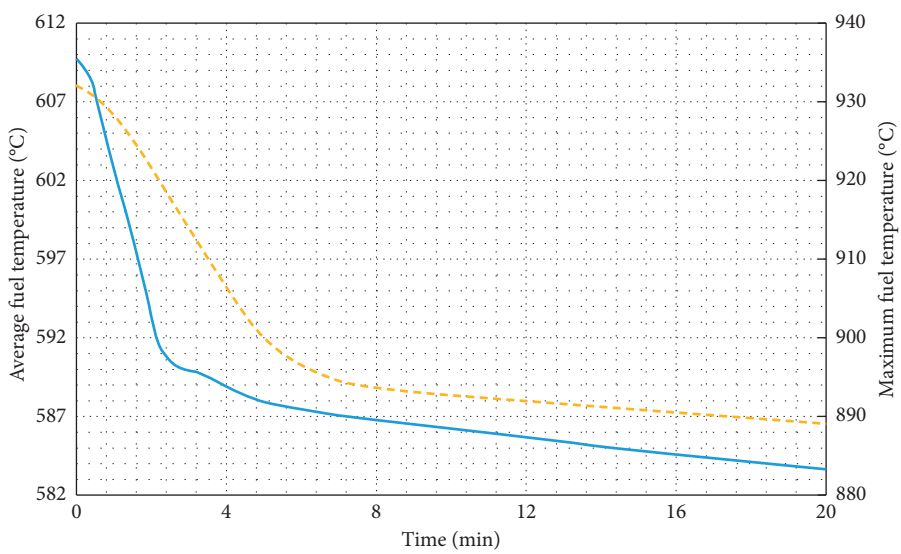

Figure 16: Average and maximum fuel temperature of #2 module in case 2 (solid line: average; dashed line: maximum).

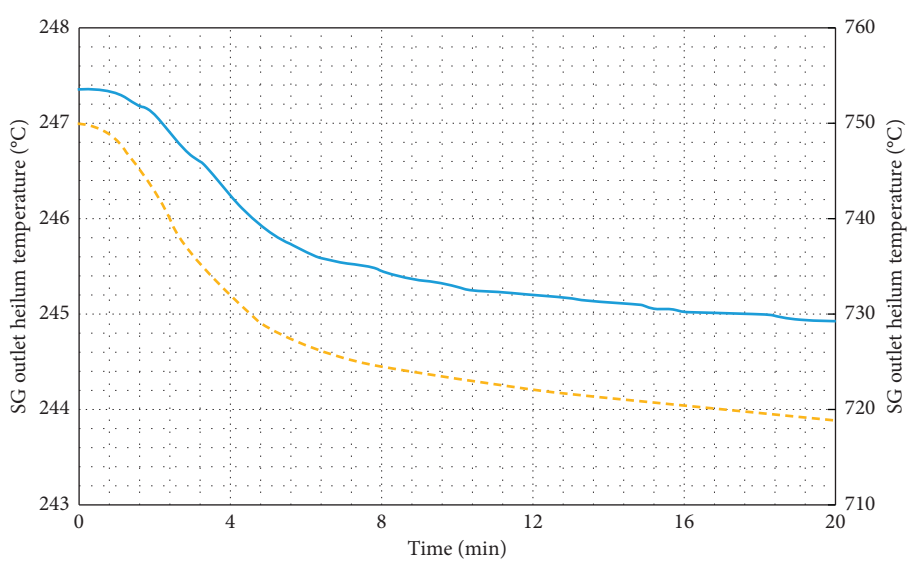

Figure 17: SG outlet and inlet helium temperature of #2 module in case 2 (solid line: outlet; dashed line: inlet).

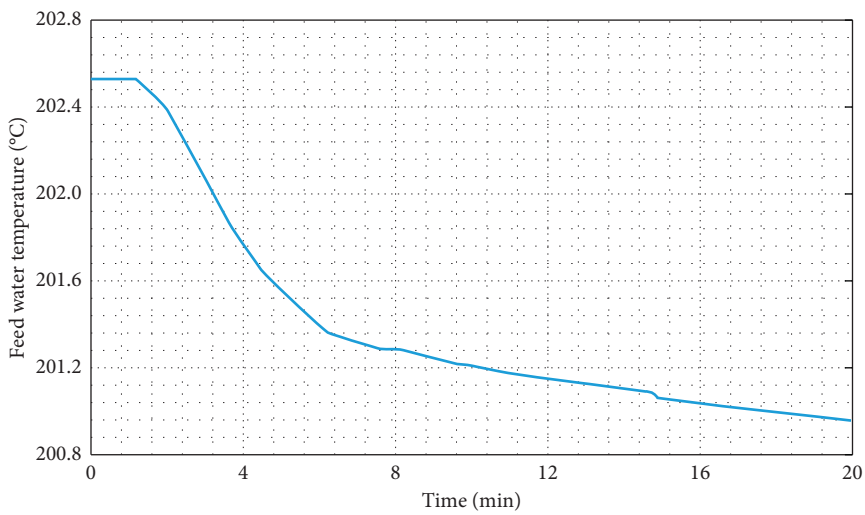

Figure 18: Feedwater temperature in case 2.

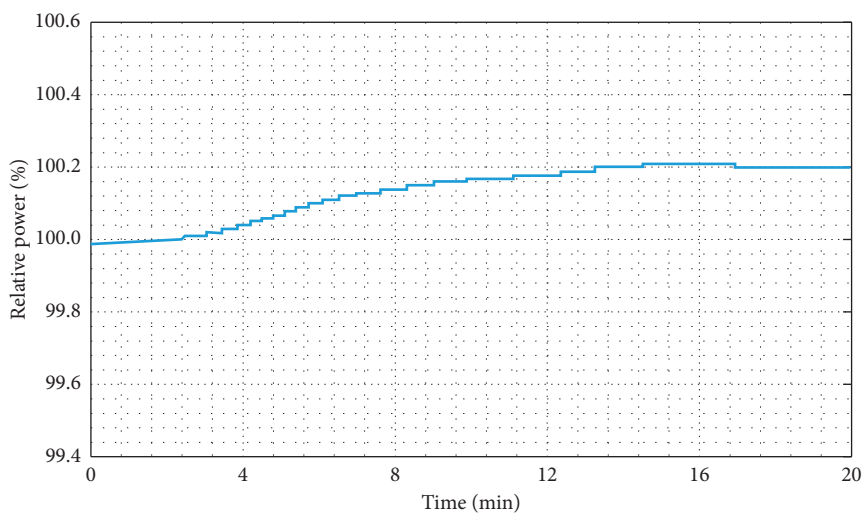

Figure 19: Relative power of #1 module in case 2.

power maintains a stable value lower than the initial rated power.

Again, the power decrease in #2 module will result in the small decrease in the feedwater temperature back to the SGs (Figure 18), so as to result in the small decrease in the SG outlet helium temperature in #1 module. The helium flowing back to the reactor core with a little lower temperature will then cause a little increase in the reactor power in #1 module due to the negative temperature feedback (Figure 19).

7. Summary and Conclusion

The modular HTGR is recognized as a candidate for the generation IV nuclear energy system technology and has well-known inherent safety features. The commercial-scale 200 MW HTR-PM consists of two NSSS modules and one turbine. Furthermore, the design with more NSSS modules connected to one turbine will be considered in the future. It would be very important and necessary to understand the coupling characteristics between these modules, especially when some transients occur at part of the modules.

A coupling code package has been developed based on the TINTE code and vPower code. These two codes are connected through components of SG. TINTE code is used to carry out the analysis of reactor core and primary circuit, while vPower code performs the secondary circuit calculation, including the primary side of the SGs. A platform is used to transfer data between these two codes, including time steps.

Two cases, including the primary flow rate decrease and the negative reactivity introduction of one module, had been simulated with this code package, and the calculation results were introduced in this paper. The preliminary calculation results can explain the phenomena during the transients. It shows that the coupling code package has the ability to analyze the coupling and interaction behavior between two modules.

Besides, the code package needs to be further improved and optimized, and more simulation should be performed. Further analysis on the coupling behavior between different modules would provide important support for the future development of the modular HTGRs.

Nomenclature

c_g: Helium heat capacity
T_g: Helium temperature
c_s: Pebble-bed heat capacity
T_s: Pebble-bed temperature
d: Diameter of fuel element
$\vec{u}$: Helium velocity
$\vec{g}$: Gravity acceleration
α: Convective heat transfer coefficient
Nu: Nusselt number
ε: Porosity of the pebble bed
p: Helium pressure
ρ_g: Helium density
Pr: Prandtl number
ρ_s: Pebble-bed density
q_s: Heat flux from the fuel element
λ_f: Pebble-bed effective thermal conductivity
Re: Reynolds number
λ_g: Helium thermal conductivity.

Data Availability

The data used to support the finding of this study, for example, the data used to build the model of HTR-PM, have not been made available because these belong to engineering design parameters and could not be available at present.

Conflicts of Interest

The authors declare that they have no conflicts of interest.

Acknowledgments

This paper was supported by the National S&T Major Project (Grant no. ZX06902013) and Tsinghua University Initiative Scientific Research Program (20197050014).

References

[1] Z. Zhang and Y. Sun, "Economic potential of modular reactor nuclear power plants based on the Chinese HTR-PM project," *Nuclear Engineering and Design*, vol. 237, no. 23, pp. 2265–2274, 2007.

[2] Z. Zhang, Z. Wu, D. Wang et al., "Current status and technical description of Chinese 2×250MWth HTR-PM demonstration plant," *Nuclear Engineering and Design*, vol. 239, no. 7, pp. 1212–1219, 2009.

[3] D. Liu, J. Sun, Y. L. Sun, X. L. Xu, Z. Sui, and Y. L. Ma, "A preliminary Research for the operating characteristics of the multi-module nuclear reactor system," 2015.

[4] D. Liu, J. Sun, Z. Sui, X. L. Xu, Y. L. Ma, and Y. L. Sun, "Modeling and simulation of the multi-module high temperature gas-cooled reactor," *Proceedings of the HTR*, vol. 239, 2014.

[5] Z. Sui, J. Sun, C. Wei, and Y. Ma, "The engineering simulation system for HTR-PM," *Nuclear Engineering and Design*, vol. 271, pp. 479–486, 2014.

[6] Y. Zheng, L. Shi, and Y. Dong, "Thermohydraulic transient studies of the Chinese 200MWe HTR-PM for loss of forced cooling accidents," *Annals of Nuclear Energy*, vol. 36, no. 6, pp. 742–751, 2009.

[7] Y. Zheng, J. Lapins, L. Shi, and Z. Zhang, "Thermal hydraulic analysis of a pebble-bed modular high temperature gas-cooled reactor with ATTICA3D and THERMIX codes," *Nuclear Engineering and Design*, vol. 246, pp. 286–297, 2012.

[8] H. Laurien, W. Scherer, and E. Teuchert, "The TINTE modular code system for computational simulation of transient processes in the primary circuit of a pebble-bed high-temperature gas-cooled reactor," *Nuclear Science and Engineering*, vol. 103, no. 3, pp. 302–312, 1989.

[9] W. Scherer, H. Gerwin, T. Kindt et al., "Analysis of reactivity and temperature transient experiments at the AVR high-temperature reactor," *Nuclear Science and Engineering*, vol. 97, no. 58, 1987.

[10] Y. Sun and H. Genrvln, "On the validation of the reactor-dynamics code system TINTE post calculation of the experiment SANA-I with a central heating element," *KFA-IB-93-13*, vol. 97, 1987.

[11] Y. Sun, "Voruntersuchungen zum experiment NACOK mit dem reaktordynamik-programm TINTE," *KFA-ISR-IB-14/93*, vol. 97, 1993.

[12] Y. Zheng, L. Shi, and Y. Wang, "Water-ingress analysis for the 200MWe pebble-bed modular high temperature gas-cooled reactor," *Nuclear Engineering and Design*, vol. 240, no. 10, pp. 3095–3107, 2010.

[13] P. Liu, Z. Chen, Y. Zheng et al., "Study on air ingress of the 200 MWe pebble-bed modular high temperature gas-cooled reactor," *Annals of Nuclear Energy*, vol. 98, pp. 120–131, 2016.

[14] Z. Chen, X. Chen, Y. Zheng et al., "Air ingress analysis of chimney effect in the 200 MWe pebble-bed modular high temperature gas-cooled reactor," *Annals of Nuclear Energy*, vol. 106, pp. 143–153, 2017.

[15] H. Gerwin, *Das zweidimensionale reaktordynamikprogramm TINTE, Teil: Grundlagen und Lösungsverfahren. Jül-2167*, Kernforschungsanlage JülichGmbH, New York, NY, USA, 1987.

[16] H. Zhang and J. Guo, "The improvement of coupling method in TINTE by fully implicit scheme," *Nuclear Science and Engineering*, vol. 98, 2018.

[17] K. Robold, *Wärmetransport im inneren und in der randzone von kugelschüttungen*, Jül-1796-RW, New York, NY, USA, 1982.

[18] P. Zehner and E. U. Schlünder, "Einfluss der wärmestrahlung und des druckes auf den wärmetransport in nicht-durchströmten schüttungen," *Nuclear Science and Engineering*, vol. 4, 1982.

[19] M. Schürenkrämer and H. Barthels, *Experimentelle untersuchungen zur thermohydraulik in kugelschüttungen im vergleich mit dem rechenprogramm Thermix-2D. Die untersuchung des dispersiven wärmetransportes am beispiel einer kaltgassträhne*, Jül-1839-RW, New York, NY, USA, 1983.

[20] H. Barthels and M. Schürenkrämer, *Die effective wärmeleitfähigkeit in kugelschüttungen unter besonderer berücksichtigung des hochtemperatur-reaktors*, Jül-1893-RW, New York, NY, USA, 1984.

[21] Y. Zheng, M. M. Stempniewicz, Z. Chen, and L. Shi, "Study on the DLOFC and PLOFC accidents of the 200 MWe pebble-bed modular high temperature gas-cooled reactor with TINTE

and SPECTRA codes," *Annals of Nuclear Energy*, vol. 120, pp. 763–777, 2018.

[22] Y. Zheng, "Reactor core design of high-temperature gas-cooled reactors, Part 3: loss of pressure through friction in pebble bed cores," *KTA3102*, vol. 3, 1981.

[23] Y. Zheng, "Reactor core design of high-temperature gas-cooled reactors, Part 2: heat transfer in spherical fuel elements," *KTA*, vol. 2, 1983.

[24] C. Wei, Z. Sui, Y. Ma, X. Jing, and W. Shan, "Application of improved quasi-static method to high temperature gas cooled reactor simulator," *Nuclear Engineering and Design*, vol. 271, pp. 337–340, 2014.

[25] J. Sun, Z. Sui, C. L. Wei, Y. L. Ma, W. Z. Shan, and L. Shi, "Thermal hydraulic models of the HTR simulator," 2012.

[26] D. Liu, J. Sun, X. Xu, and Y. Sun, "Simulation and analysis of start-up process of high temperature gas-cooled reactor," *Atomic Energy Science and Technology*, vol. 48, pp. 594–598, 2014, (in Chinese).

[27] D. Liu, *Research on the Operating Characteristics of Multi-Module High Temperature Gas-cooled Nuclear Power Plants*, Tsinghua University, London, UK, (in Chinese), 2015.

[28] D. Liu, J. Sun, and Y. Sun, "Modeling and analysis of once-through steam generator in HTR-PM," *Atomic Energy Science and Technology*, vol. 50, no. 6, pp. 995–1001, 2016, (in Chinese).

Hindawi
Science and Technology of Nuclear Installations
Volume 2020, Article ID 3961095, 14 pages
https://doi.org/10.1155/2020/3961095

Research Article

Nuclear Data Uncertainty Quantification and Propagation for Safety Analysis of Lead-Cooled Fast Reactors

Ishita Trivedi,[1] **Jason Hou**,[1] **Giacomo Grasso**,[2] **Kostadin Ivanov**,[1] **and Fausto Franceschini**[3]

[1]*Department of Nuclear Engineering, North Carolina State University, 2500 Stinson Drive, Burlington Engineering Lab, Raleigh, NC 27695, USA*
[2]*ENEA-FSN-SICNUC-PSSN, v. Martiri di Monte Sole 4, Bologna 40129, Italy*
[3]*Westinghouse Mangiarotti SPA, v. Timavo 59, Monfalcone 34074, Italy*

Correspondence should be addressed to Ishita Trivedi; itrived@ncsu.edu

Received 27 December 2019; Accepted 6 June 2020; Published 12 August 2020

Academic Editor: Arkady Serikov

In this study, the Best Estimate Plus Uncertainty (BEPU) approach is developed for the systematic quantification and propagation of uncertainties in the modelling and simulation of lead-cooled fast reactors (LFRs) and applied to the demonstration LFR (DLFR) initially investigated by Westinghouse. The impact of nuclear data uncertainties based on ENDF/B-VII.0 covariances is quantified on lattice level using the generalized perturbation theory implemented with the Monte Carlo code Serpent and the deterministic code PERSENT of the Argonne Reactor Computational (ARC) suite. The quantities of interest are the main eigenvalue and selected reactivity coefficients such as Doppler, radial expansion, and fuel/clad/coolant density coefficients. These uncertainties are then propagated through safety analysis, carried out using the MiniSAS code, following the stochastic sampling approach in DAKOTA. An unprotected transient overpower (UTOP) scenario is considered to assess the effect of input uncertainties on safety parameters such as peak fuel and clad temperatures. It is found that in steady state, the multiplication factor shows the most sensitivity to perturbations in ^{235}U fission, ^{235}U ν, and ^{238}U capture cross sections. The uncertainties of ^{239}Pu and ^{238}U capture cross sections become more significant as the fuel is irradiated. The covariance of various reactivity feedback coefficients is constructed by tracing back to common uncertainty contributors (i.e., nuclide-reaction pairs), including ^{238}U inelastic, ^{238}U capture, and ^{239}Pu capture cross sections. It is also observed that nuclear data uncertainty propagates to uncertainty on peak clad and fuel temperatures of 28.5 K and 70.0 K, respectively. Such uncertainties do not impose per se threat to the integrity of the fuel rod; however, they sum to other sources of uncertainties in verifying the compliance of the assumed safety margins, suggesting the developed BEPU method necessary to provide one of the required insights on the impact of uncertainties on core safety characteristics.

1. Introduction

In the past two decades, a renewed interest has surfaced in Generation IV lead/lead-bismuth cooled fast reactors (LFRs). Enhanced safety characteristics of lead/lead-bismuth—including relative chemical inertness, retention of hazardous radionuclides such as iodine and caesium, and high boiling point [1]—promote the choice of the LFR as an economically competitive Generation IV reactor with enhanced safety and sustainability. However, LFRs lack of plant operational history, compared to conventional Light Water Reactor (LWR) designs. Insufficient experimental data challenges the trustworthiness of numerical results and therefore accentuates the need for input uncertainty analysis in modelling. Evaluation of these uncertainties provides a better understanding of their impact on the reactor core design and identification of design safety limits.

In this work, the Best Estimate Plus Uncertainty (BEPU) method [2] is used to quantify the impact of nuclear data uncertainties on the performance and safety parameters of LFR systems. In the previous studies, the Total Monte Carlo (TMC) approach assessed the effect of uncertainties originating from lead and plutonium isotopes cross sections on core parameters including criticality and coolant void worth. A comparison of

uncertainties originating from different nuclear data libraries was also provided [3–5]. However, the objective here is to develop a systematic approach for the quantification of nuclear data input uncertainties in LFR systems. Nuclear data uncertainties from ENDF/B-VII.0 cross section libraries are propagated through multiple scales of reactor modelling including lattice, full core, and system level. Sensitivity and uncertainty analysis is performed using generalized perturbation theory (GPT) [6] with variance covariance library COMMARA-2.0 [7]. The analysis also ranks the most contributing nuclide-reaction pairs to total uncertainty of output parameters. The targeted output uncertainties include eigenvalue and reactivity feedback coefficients such as Doppler, core radial expansion, and fuel/coolant/structure density worth coefficients. Nuclear data uncertainties are then propagated through the system model as standard deviations associated with respective feedback coefficients, which are perturbed using stochastic sampling approach to assess core safety capabilities.

2. Reactor Design and Simulation

2.1. Core Description. The demonstration lead-cooled fast reactor (DLFR) core was conceptualized by the Westinghouse Electric Company (WEC) in collaboration with Italian National Agency for New Technologies, Energy and Sustainable Economic Development (ENEA) and Argonne National Lab (ANL). A generic version of the DLFR design is developed and applied to the current study.

The DLFR is a pool-type LFR with the thermal output of 500 MW fuelled with uranium oxide (UO_2). Figures 1 and 2 show one-third of the DLFR core map and the assembly radial layout of the DFLR core, respectively [8]. The core comprises 163 hexagonal assemblies arranged in a triangular lattice with a pitch of 30.4 cm. This includes 82 fuel assemblies divided into two enrichment zones (inner and outer cores) and three safety assemblies, surrounded by 78 reflector/shield assemblies [8].

Finger absorber rods (FARs), as shown in Figure 2, represent unitary elements of regulation, control, and safety banks. Control safety banks are primarily for reactor control whereas regulation rods are utilized for the fine-tuning of reactivity [8]. They are designed to enter the hollow space of a central beam tube in subassemblies (Figure 2(a)) from the top or bottom of the core. Bottom-inserted FARs encapsulate a reflector column atop an absorber column. After a bottom-inserted FAR is withdrawn, the reflector part of the FAR sits beside the active core and the absorber part is located below the core. The top-inserted FARs only have an absorber column. After a top-inserted FAR is withdrawn, the absorber sits above the core, as shown in Figure 2(b) [8].

Three safety assemblies (S2) located in the inner core ring three (Figure 1) are envisioned for SCRAM. Figure 2(b) shows the withdrawn position of S2 assemblies aside a fuel assembly for understanding purposes only.

2.2. Computational Tools and Methodologies. The DLFR core is modelled using the Argonne Reactor Computation (ARC) Code suite, developed, and maintained by ANL [9]. Within ARC, MCC-3.1 [10] coupled with the two-dimensional (2D)

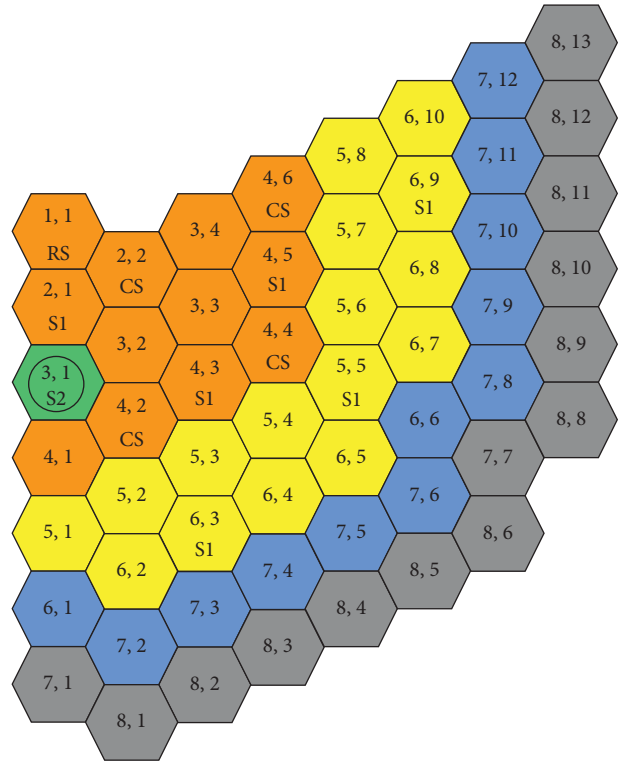

Figure 1: Radial core map with regulation (RS), control (CS), and safety (S1, S2) systems. There are inner and outer core (rings 1–6), reflector (ring 7), and shield (ring 8) subassemblies.

S_N transport solver TWODANT [11] is used to generate the condensed multigroup cross sections. In the conventional method shown in Figure 3, MCC-3.1 first calculates condensed regionwise self-shielded cross sections in 230 ultrafine group (UFG) starting from a 2082-groups ENDF/B-VII.0 master library and provides them to TWODANT [10, 11]. TWODANT performs transport calculations on an equivalent *R-Z* model of the core to derive regionwise flux solutions [11]. In the final step, MCC-3.1 generates regionwise 33 Broad-Group (BG) cross sections using the flux solutions from TWODANT. The DIF3D code receives the cross sections for flux calculations on the whole core using the variational nodal transport solver (VARIANT) [12]. The angular flux solution and scattering approximation are expanded to the 3rd order.

The two-dimensional (2D) assembly and core models are also developed in Serpent 2 [13] for lattice calculations and model verification. Periodic boundary conditions are set on the lattice level. The simulations are performed in the all-rods-out condition with the safety rods (S2) withdrawn below core. Neutron population is set to be 100,000 with 2000 active and 300 inactive neutron generations.

The three-dimensional (3D) model setup maintains an axial temperature gradient for all core components above, below, and at the active core level [8]. Consequently, the neutronics model accounts for temperature dilatation effects on all structural components and material densities. All dimensions and densities are adjusted by factors governed by their respective coefficients of linear thermal expansion:

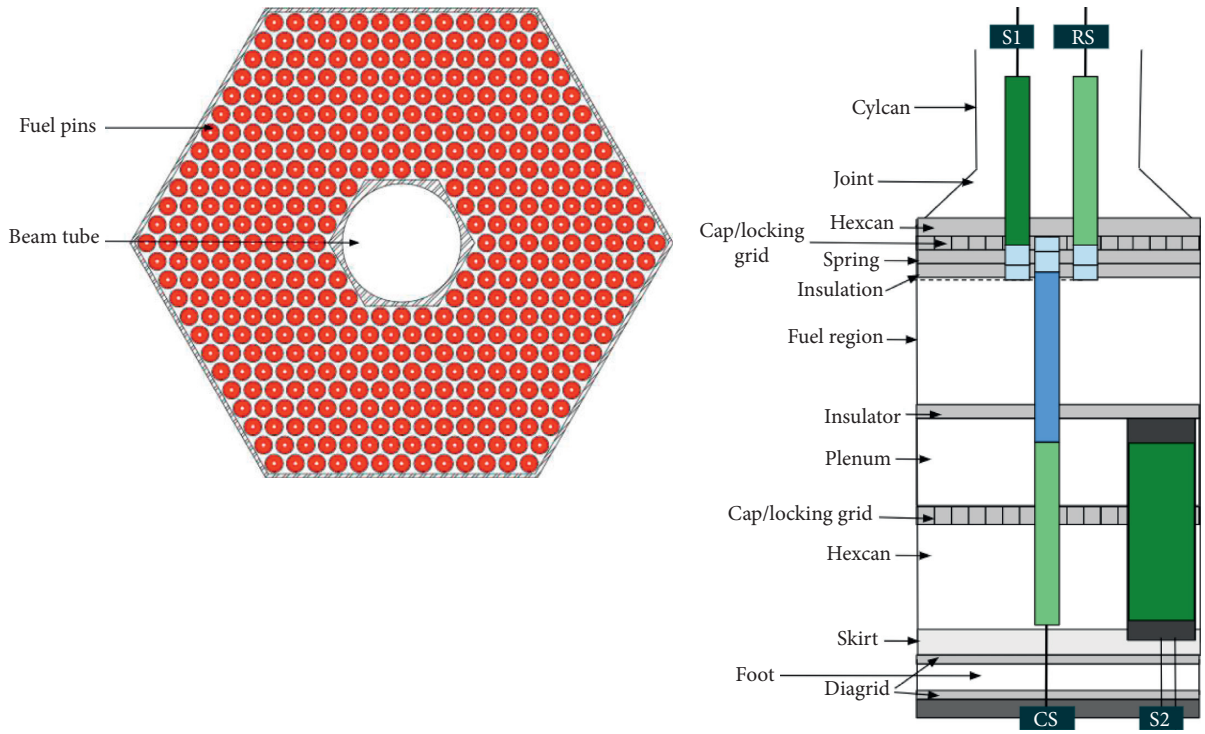

(a) (b)

Figure 2: Radial fuel assembly map (a) with axial positioning of regulation (RS), control (CS), and safety (S1, S2) systems in withdrawn position (b).

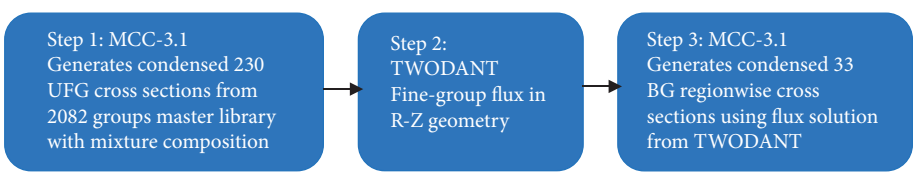

Figure 3: Conventional cross section generation method in ARC.

$$\alpha_T = \frac{1}{L}\left(\frac{\mathrm{d}L}{\mathrm{d}T}\right), \tag{1}$$

where L and T represent nominal length and expansion temperature, respectively. The thermal expansion data of fuel, coolant, and structural materials are provided in [14, 15].

2.3. Improved Cross Section Generation Method. As detailed previously, the unique design of the DLFR involves partially inserted FARs in the withdrawn position (Figure 2(b)), where the absorber/reflector material sits in the centre of the fuel assemblies. The axial heterogeneity must be preserved for a proper treatment of the self-shielding effects during the cross section generation. Therefore, intermediate steps were developed for improving the accuracy of the self-shielded cross sections in addition to the conventional method shown in Figure 3 where assemblies are homogenized using a zero-dimensional (0D) mixture geometry. The workflow of the improved cross section generation method is given below.

(i) Using the conventional method (Figure 3), DLFR fuel subassembly is represented with various 0D homogenized axial regions, shown in Figure 2(b), in 0D mixture geometry with an equivalent *R-Z* model in TWODANT. This provides 230-groups region-wise flux solutions in the axial direction for fuel assemblies. MCC-3.1 then computes condensed cross sections in 33 BG for one fuel subassembly type. Such cross sections are generated with the conventional method for each fuel subassembly type individually. Six fuel subassembly types constitute the DLFR—inner core assembly without FAR, inner core assemblies with RS, S1, and CS type FARs, outer core assembly without FAR, and outer core assemblies with S1 type FARs [8].

(ii) Cross sections for nonmultiplying assemblies (shield, reflectors, and S2 safety system) are generated using the conventional process outlined in Figure 3. The core is built with homogenized mixture geometry for different subassemblies

represented with an RZ model (Figure 4) in TWODANT for leakage calculations. Regionwise flux solutions from TWODANT are stored in an *rzmflx* file [11].

(iii) Radial leakage is incorporated in the fuel cross sections from step I. MCC-3.1 performs a separate set of calculations for the active core region utilizing 1D heterogeneous cell treatment capabilities [16]. The 1D cylindrical geometry option of MCC-3.1 is adapted by superimposing *rzmflx* flux spectrum from step II to the 1D cell transport solutions. This approach simultaneously accounts for the heterogeneity effects in the fuel region and interregion leakage effect within the core. Figure 4 shows the 1D fuel assembly model where the beam tube and fuel rings in Figure 2(a) correspond to equivalent cylindrical rings 1, 2, in Figure 5. Each cylinder is now subdivided into 1D subcylinders separating the materials contained within the original cylinder, more details on this methodology are provided in [16].

(iv) Different region cross sections from all subassemblies are merged into one ISOTXS format file for all other calculations.

2.4. Reactor System Model. The reactor system is modelled with the limited, noncommercial version of SAS4A/SASSYS-1, called MiniSAS [17]. MiniSAS excludes some capabilities such as severe accident modelling from SAS4A/SASSYS-1 [18]. The overall system design for DLFR is adapted from the ABR1000 system [19] for preliminary safety analysis due to the unavailability of the actual system model when this work was carried out. The system includes a primary heat transfer system and emergency heat removal system (DRACS) driven by natural circulation. Coolant flows from the hot pool to heat exchangers and returns back into the cold pool. Primary pumps ensure the forced convection of the coolant to extract heat from the reactor. A once-through steam generator is modelled in the secondary circuit. LFR specific parameters are obtained from the existing DLFR data, including a core flow rate of 28,560 kg/s, coolant inlet temperature at 663.3 K, and rated core thermal power of 500 MW [8]. Additional relevant specifications are provided in Table 1.

The reactor core is modelled by two vertical parallel thermal-hydraulic channels, representing the inner core and outer core region, respectively. A single fuel pin structure surrounded by coolant is used for representing each channel. Assembly average power, average coolant flow rate, Doppler feedback coefficient, and axial power profiles are specified individually per channel. The fuel pin is discretized into 10 radial temperature nodes and 20 axial segments [18]. A simple radial expansion model [18] from MiniSAS is incorporated to account for core flowering effect.

2.5. Uncertainty Quantification and Propagation Methods. The Uncertainty Quantification and Propagation (UQ&P) quantifies the influence of input uncertainties on the outputs for a given model. In this section, uncertainties originating from nuclear data are evaluated and propagated through the reactor system to assess their impact on core safety during transients. Deterministic and stochastic sampling methods are considered for UQ&P at different stages of core modelling.

In a large or complex model, with a system of multiple perturbed equations for each input variation, uncertainty analysis via sampling-based methods is not feasible. Nuclear data uncertainty propagation using stochastic sampling is computationally very expensive during cross section generation. An alternative approach is to apply perturbation-based methods for quantifying output uncertainties in the neutronic model. These output parameters are input in the system model where they are stochastically sampled within respective standard deviations. This method will greatly reduce computation time and resources.

As such, generalized perturbation theory (GPT) based on truncating the Taylor expansion of a response parameter [6] is applied to the DLFR core to quantify uncertainties on steady state parameters, namely, the main eigenvalue and reactivity feedback coefficients. Five different feedback coefficients are considered, including the Doppler coefficient, radial expansion coefficient, and fuel/coolant/structure density worth. For Doppler feedback coefficient, fuel temperature is increased by 500 K from the operating temperature (1200 K). The radial expansion is realized by increasing the assembly pitch by 2.5% while preserving the mass of fuel and structure. Fuel, coolant, and structure density worth are computed by introducing a 5% decrease in nominal density in active core region only. These perturbations are chosen based on literature review [20].

Feedback uncertainties are propagated deterministically through the reactor system, while the stochastic sampling method is used to sample input uncertainties and statistically analyse output responses during transients. Both methods and their applications are explained in further sections.

2.6. Generalized Perturbation Theory. GPT uses deterministic sensitivity and uncertainty (S&U) methods to compute sensitivity coefficients. Sensitivity coefficients reflect the relative change of an integral core parameter (such as eigenvalue) with respect to the relative changes in multigroup nuclear data. After obtaining the sensitivities (S_i) associated with each integral parameter, the total contribution of uncertainties attributed to these coefficients can be determined using Pearson correlation coefficients and covariance matrices [6].

For a given core parameter R_i, the sensitivity coefficient matrix $\overrightarrow{S_R}$ is defined as

$$S_R = \begin{bmatrix} S_1 \\ \vdots \\ S_i \\ \vdots \\ S_N \end{bmatrix}, \quad \text{for } 1 \le i \le N, \tag{2}$$

where N is equal to the nuclide-reaction number × energy groups. For example, for ^{235}U fission reaction for 33 energy groups, $N = 1 \times 33$. A sensitivity coefficient relative to an isotope j, a reaction x in an energy group g, is

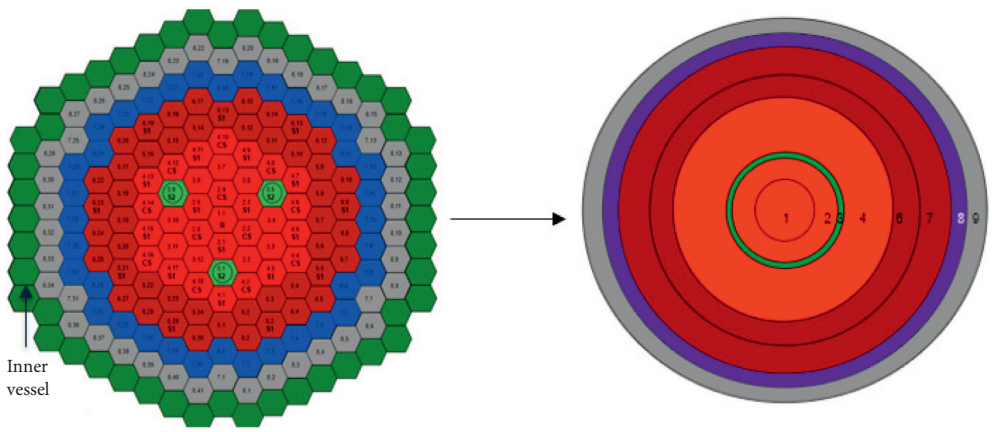

Figure 4: Full core RZ representation in TWODANT.

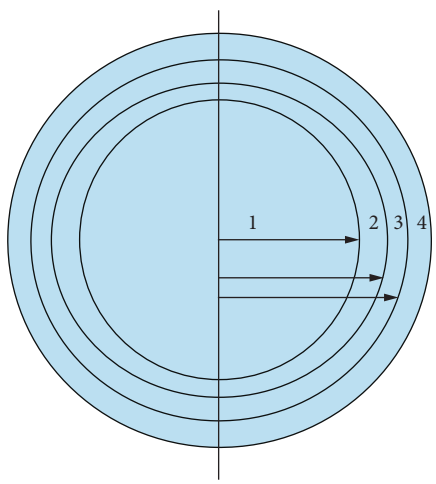

Figure 5: 1D cylindrical representation of the active region in MCC-3.1.

Table 1: System model specifications for the current DLFR system in MiniSAS.

System Components	Description
Coolant flow rate	28,560 kg/s
Coolant inlet	663.3 K
Fuel/coolant type	Oxide/lead
Core channels	2 channels: IC and OC
Heat exchanger (HX)	4 identical HX—1 is modelled in SAS
Steam generator	Once-through SG
Pump	Normalized pump head vs. time provided for the intermediate and primary pumps
Direct reactor auxiliary cooling system (DRACS)	Emergency cooling system

$$S_{j,x,g} = \frac{\partial R/R}{\partial \sigma_{j,x,g}/\sigma_{j,x,g}} = \frac{\partial R}{\partial \sigma_{j,x,g}} \frac{\sigma_{j,x,g}}{R}, \tag{3}$$

with a first-order perturbation, the Sandwich rule derives the uncertainty I_i^2 for the ith core parameter R_i [6, 21] by folding the respective sensitivities with the variance covariance matrix (VCM) of input parameter:

$$I_i^2 = S_i^T D S_i, \tag{4}$$

where D is the variance covariance matrix structured as

$$D = \left(D_{x,j}\right) = \begin{bmatrix} D_{11} & D_{12} & \cdots & \cdots & D_{1N} \\ D_{21} & \cdots & & & \\ \vdots & & D_{jj} & & \\ \vdots & & & \cdots & \\ D_{N1} & & & & D_{NN} \end{bmatrix}. \tag{5}$$

In this work, ENDF/B-VII.0 nuclear data uncertainties provided in 33 energy macrogroups are considered with VCM COMMARA-2.0 [7, 21]. Working versions of COMMARA-2.0 were released and tested by ANL and Idaho National Lab (INL).

Sensitivity ($S_{\alpha,\sigma}$) of a feedback coefficient (α) equation (6) points to changes induced in reactivity from perturbation in nuclear data (σ) as

$$S^{j}_{\rho,\sigma} = \frac{\partial \rho_j}{\partial \sigma_{i,x,g}} \frac{\partial \sigma_{i,x,g}}{\rho_j}, \tag{6}$$

where $j = (1, 2)$ corresponds to a base case and perturbed case, respectively.

The feedback coefficient α is obtained from PERSENT [22]. It represents a change in reactivity between the base and perturbed core states caused by a change in core parameters (temperature/density/pitch). For the Doppler coefficient, a base case sensitivity of reactivity ($S^{1}_{\rho,\sigma}$) to nuclear data perturbations is obtained at nominal temperature. Similarly, a perturbed case provides sensitivities ($S^{2}_{\rho,\sigma}$) at Doppler temperature to perturbations to σ. Then, (7) [13] provides the sensitivity of the feedback coefficient $S_{\alpha,\sigma}$ by combining $S^{1}_{\rho,\sigma}$ and $S^{2}_{\rho,\sigma}$ using the reactivity change ($\Delta\rho = 1/k^1 - 1/k^2$) from the base to the perturbed case [23]:

$$S_{\alpha,\sigma} = \frac{S^{2}_{\rho_2,\sigma}/k^2 - S^{1}_{\rho_1,\sigma}/k^1}{\Delta\rho}. \tag{7}$$

The total uncertainty I^2 of α can be described using (6) as $I^2 = S^{T}_{\alpha,\sigma}\, D\, S_{\alpha,\sigma}$.

PERSENT employs an adjoint-based sensitivity analysis method. Sensitivity functions are evaluated from adjoint variables without solving the system of perturbed equations for each input parameter change. The solution of the corresponding adjoint transport equation includes the change in eigenvalue based on perturbations in cross sections [22]. In Serpent, a collision-history approach computes the GPT calculations, which determines the sensitivity coefficient calculations based on classical perturbation theory [24].

2.7. Stochastic Sampling. The Uncertainty Quantification (UQ) and optimization code DAKOTA [25] extend the uncertainty propagation through transient scenarios using stochastic sampling. DAKOTA is a multilevel parallel object-oriented framework for S&U analysis along with other capabilities [25]. Two types of stochastic sampling-based approaches are available in the DAKOTA—Monte Carlo (MC) and Latin Hypercube Sampling (LHS) method. The LHS approach stratifies each uncertain parameter domain into N bins (N being the number of samples). So, each bin can only contain one sample at a time. Consequently, this method requires fewer samples for convergence than an MC approach, where the samples are randomly selected from the parameter domain [25].

For transient simulations, a Python interface couples DAKOTA to the external code (SAS4A/SASSYS-1) [19]. The coupling was developed at ANL for UQ in Sodium Fast Reactors (SFRs) [19]. DAKOTA drives the interface through a system call, reads the perturbed parameters in the SAS4A/SASSYS-1 input file, and executes the external code to run simulations. A Python script parses the output files to gather responses of interest in "results" file [19]. DAKOTA then reads the "results" file to perform the statistical analysis. The mean and 5%/95% intervals of response functions (peak fuel/clad/coolant temperatures) to 1% perturbation of DLFR feedback coefficients have been studied in this work. Figure 6 provides a schematic understanding of the DAKOTA/SAS4A/SASSYS-1 coupling scheme.

3. Results and Discussion

3.1. Model Verification. Lattice level results from ARC and Serpent are compared to quantify the difference between the models using nominal cases developed at equilibrium core composition. Table 2 provides eigenvalues obtained from an outer core fuel assembly and 2D core at Beginning/End of Cycle (BOC/EOC, resp.). Observed differences in eigenvalues from heterogeneous Monte Carlo and homogenized MCC-3.1/DIF3D calculations are attributed to differences in cross section generation and modelling capabilities of the two codes [10, 13]. A comparison of BOC core power distribution and assembly flux is shown in Figures 7 and 8, which show the relative error is less than 10% for most assemblies. The Monte Carlo relative statistical error from Serpent for all flux and power values is in the order of 10^{-3}. The assemblies showing larger differences of 11.6%, 13.4%, 14.8%, and 16.1% are located in the outer core near reflectors which cause flux distortions in that region.

To quantify the differences from the improved cross section generation methodology, two sets of cross sections are generated using methods outlined in Figures 3 and 9, respectively, for the same core model in DIF3D. A difference of 950 pcm is found at BOC between respective eigenvalues. The new cross section generation method gives k_{eff} of 1.0332 at BOC. The conventional method provides a lower eigenvalue of 1.0231 due to homogenization of fuel and absorber within the assembly. Considering the importance of the self-shielding process, the improved cross section generation approach is adapted for assessing all core performance parameters. Further work is underway to verify these results using code-to-code comparison with Serpent (Monte Carlo). Homogeneous and heterogeneous 2D assembly and core models developed in ARC using the conventional two-step (Figure 3) and improved cross section Figure 9 methods will be compared with the same models developed in Serpent. It is anticipated that the largest difference is from homogenization of absorber regions within the assembly.

3.2. Uncertainty Analysis. This section provides nuclear data UQ results at multiple scales of reactor modelling using a systematic approach. Uncertainties are obtained for steady state parameters including eigenvalue and feedback coefficients using statistical correlations from COMMARA-2.0. Top nuclide-reaction pair uncertainty contributors to respective parameters are also identified. Uncertainties are further propagated to the system model for computing standard deviations of fuel/clad/coolant temperatures

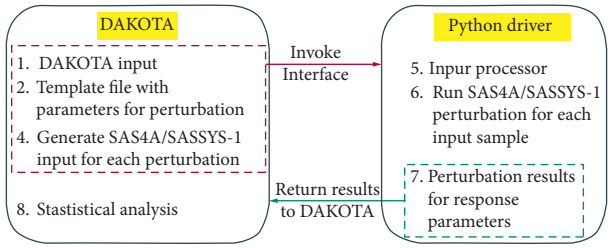

Figure 6: Schematic of the Python interface between DAKOTA and SAS4A/SASSYS-1.

Table 2: Eigenvalue comparison between serpent-2.0 and MCC-3.1/DIF3D.

	Serpent	MC^2-3.1	Δ pcm	% $\delta k/k$
Outer core	k_∞			
BOC	1.28194 ± 0.00014	1.28121	44.4	−0.05
EOC	1.25681 ± 0.00015	1.25813	−83.5	0.10
	Serpent	DIF3D		
2D core	k_∞			
BOC	1.17683 ± 0.00018	1.1688	583.8	0.66
EOC	1.15126 ± 0.00017	1.1437	574.2	0.91

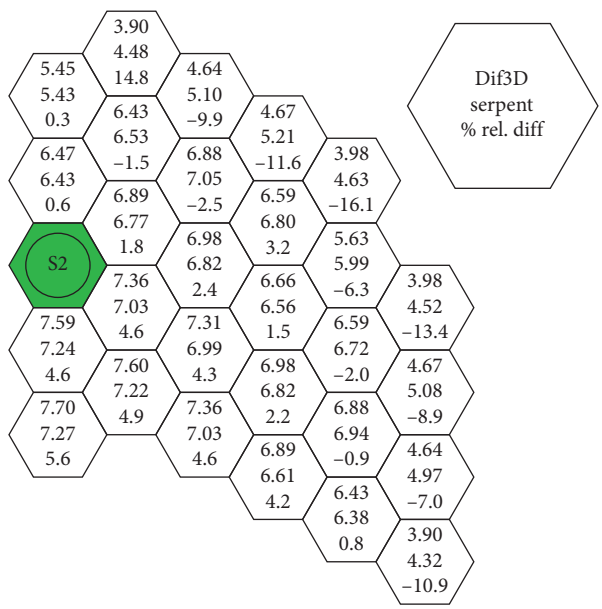

Figure 7: Power (MW) and relative difference (%) between serpent and Dif3D.

during UTOP transient. This provides an insight on the effect of uncertainties on core safety capabilities.

3.3. S&U Analysis of Lattice Level. Assemblywise S&U analysis is performed in Serpent as shown in Figures 10 and 11. The S&U profiles are generated for inner and outer core assemblies at BOC and EOC, respectively. Based on the sensitivity results, uncertainties relative to nuclide-reaction pairs are computed using the "Sandwich rule" described previously. The top five contributors to the uncertainty in k_{inf} at BOC and EOC for an inner core assembly are shown in Table 3.

The largest contribution to uncertainty in k_{inf} comes from heavy metals ^{235}U and ^{238}U. From Figures 10 and 11, the multiplication factor is noticeably sensitive to perturbations in the ^{235}U fission, ^{235}U ν, and ^{235}U capture cross section pairs. However, by considering reaction pair correlation coefficients from COMMARA-2.0 [7], the largest uncertainty contribution to the eigenvalue is from ^{235}U capture and ^{238}U inelastic reaction pairs.

On the 2D core level, Figure 12 shows large positive sensitivity of the eigenvalue to perturbations in ^{235}U ν cross section. At BOC, a positive perturbation in ^{235}U ν cross section leads to a positive response on reactivity. Similarly, negative sensitivity profile of ^{238}U-capture cross section is

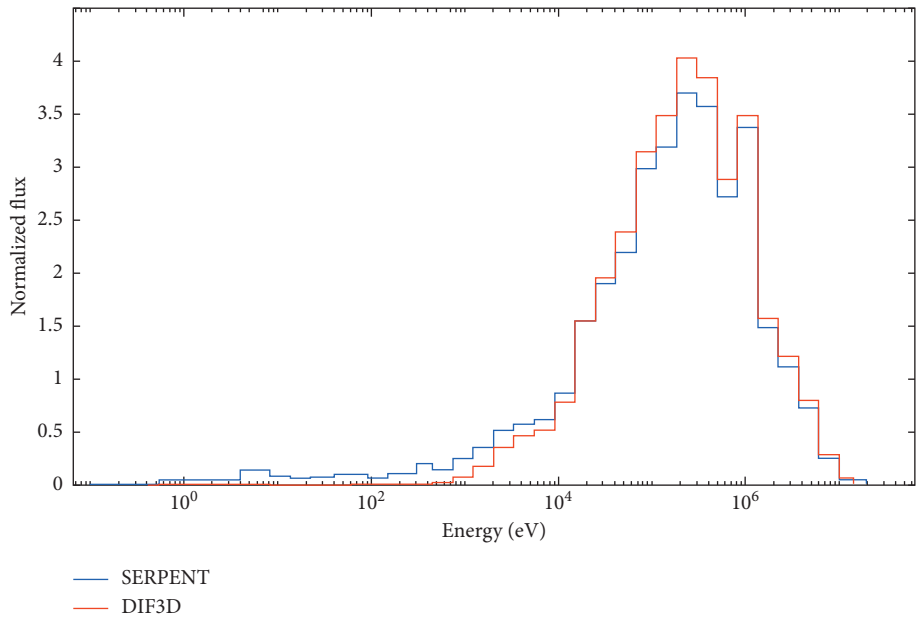

Figure 8: Normalized flux spectrum comparison for the central assembly (1, 1) between Dif3D and serpent.

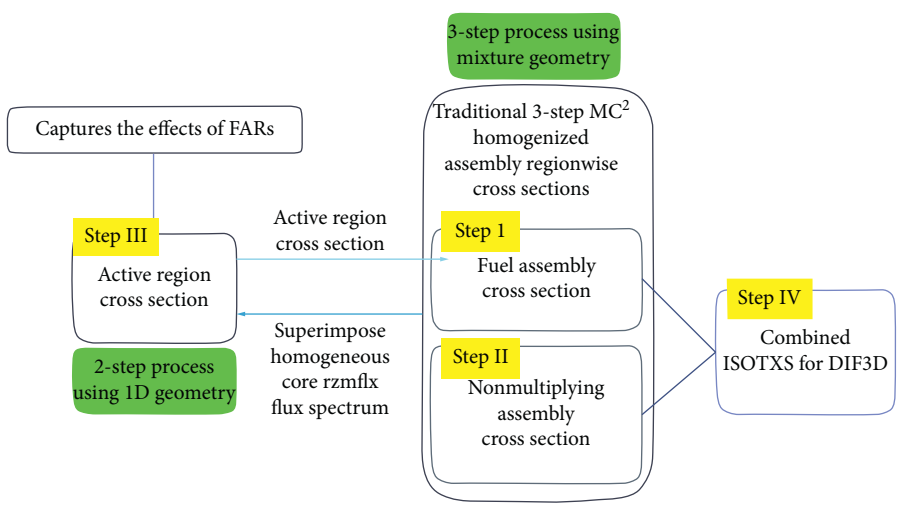

Figure 9: Improved cross section generation methodology for DLFR core.

evident since an increase of this reaction cross section type will lead to absorption of fast neutrons and decrease of the neutron population, introducing negative reactivity.

In addition, a substantial amount of uncertainty contribution from ^{235}U capture-^{235}U capture reaction pair is shown in Figure 13. This is not a surprising result considering the high enrichment in the core at BOC. The ^{238}U inelastic-^{238}U inelastic reaction pair provides the next largest contribution. Contribution from the top two nuclide-reaction pairs accounts for 85% of the uncertainty in k_{eff}. Furthermore, there is good comparison between the uncertainty profiles from Serpent and PERSENT based on the trends observed in Figure 13, although the values are not distinguishable in the lower energy range. This is likely due to the low flux in that region as shown in Figure 8. Comparisons between the remaining three nuclide-reaction pairs show a consistent trend between the two codes even with minor differences due to variations in the data points being obtained from two different codes.

3.4. S&U Analysis of Core Reactivity Feedback. Reactivity feedback coefficients are summarized in Table 4 to provide an understanding of the reactivity response to changes in temperature during reactor operation. The total uncertainty of each feedback coefficient from perturbations in nuclear data is also given in Table 4. Total uncertainty describes the total variance in the reactivity feedback parameter from perturbations in nuclear data.

The breakdown of the total uncertainty of neutronic feedback coefficients from Table 4 is provided in Figures 14 and 15 to show contributions from various reaction

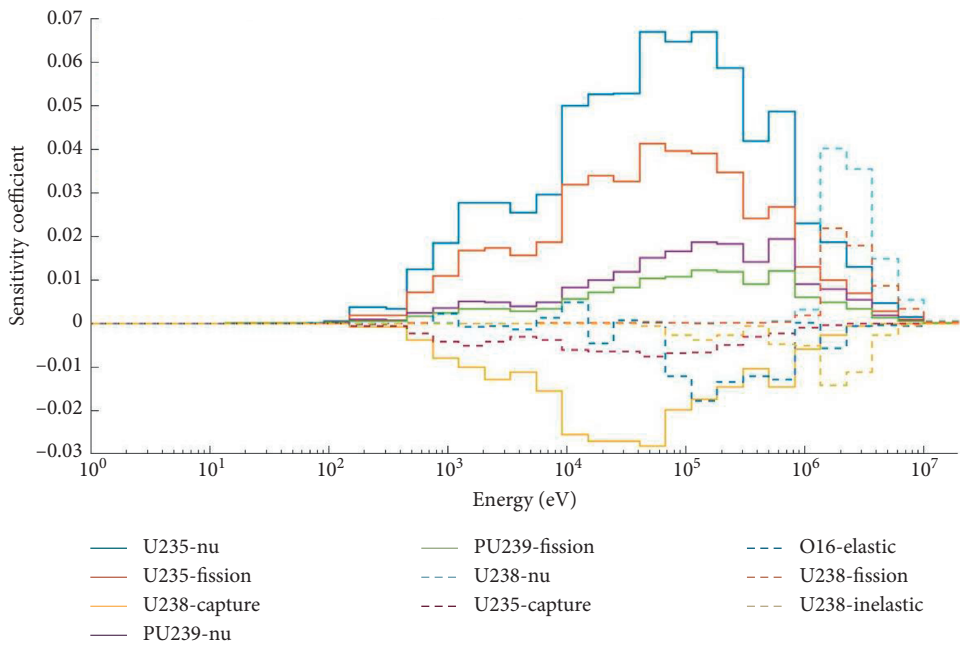

Figure 10: Sensitivity profile of k_{inf} for inner core assembly with BOC composition.

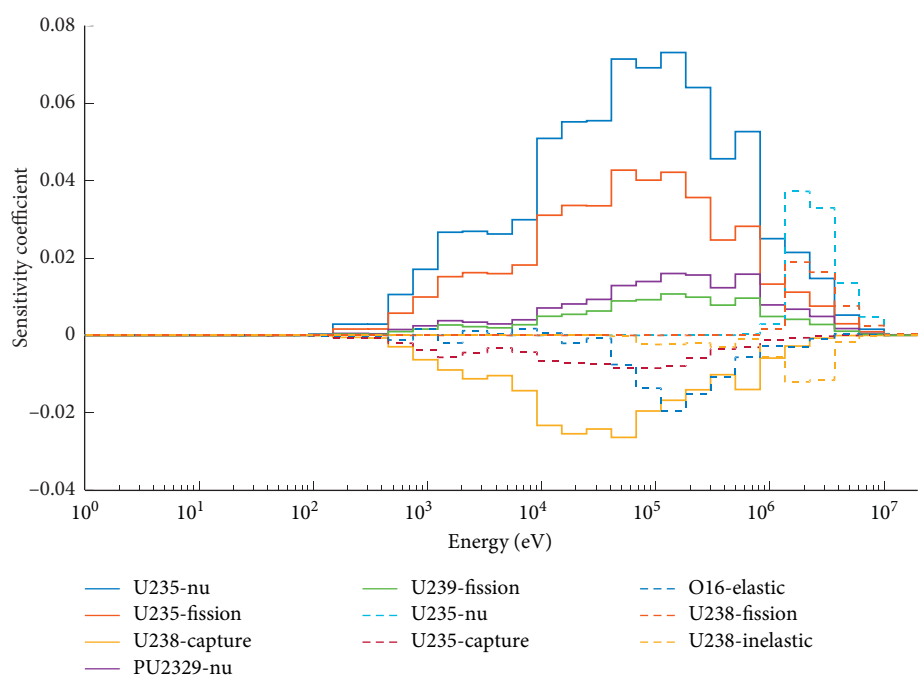

Figure 11: Sensitivity profile for outer core assembly with EOC composition.

channels. A large contribution is observed for Doppler reactivity and fuel density feedback coefficient (Figures 14(a) and 15(a), resp.) with BOC composition, where the majority of the uncertainty is seen to originate from ^{238}U inelastic scattering (Figure 14(a)) in high-energy range above 1 MeV. This can be associated with the significant sensitivity of the feedback coefficients to the perturbations in ^{238}U inelastic reaction cross section and strong reaction channel correlation in this energy range. For core radial expansion and structure feedback (Figures 14(b) and 15(b), resp.), ^{235}U fission and capture cross sections become significant in the epithermal range. Decreased structural density leads to reduced moderation, increased fission, and addition of uncertainty contribution from ^{235}U. Similarly, expansion of core pitch increases the coolant volume inside the reactor and adds negative reactivity.

Table 3: Relative contribution to uncertainty of k_{inf} for an inner assembly from serpent at BOC and EOC.

Rank	Uncertainty Contribution (%)			
	Nuclide/nuclide-reaction	BOC	Nuclide/nuclide-reaction	EOC
1	^{235}U (n, γ)/^{235} U (n, γ)	65.8	^{235}U (n, γ)/^{235}U (n, γ)	54.7
2	^{238}U (n, n')/^{238}U (n, n')	19.1	^{238}U (n, n')/^{238}U (n, n')	27.9
3	^{238}U (n, γ)/^{238}U (n, γ)	5.11	^{238}U (n, γ)/^{238}U (n, γ)	5.86
4	^{235}U fission/^{235}U fission	1.74	^{235}U fission/^{235}U fission	1.81
5	^{56}Fe elastic/^{56}Fe elastic	1.73	^{16}O (n, n)/^{16}O (n, n)	1.52

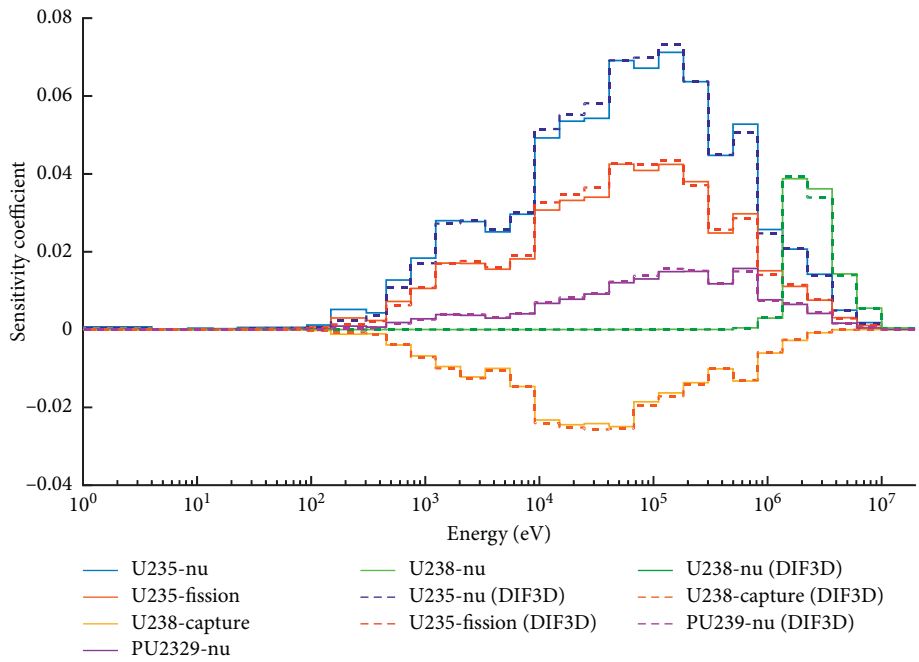

Figure 12: Sensitivity profiles for the top five cross sections to which k_{inf} is most sensitive at BOC (solid lines for serpent results, dashed lines for DIF3D results).

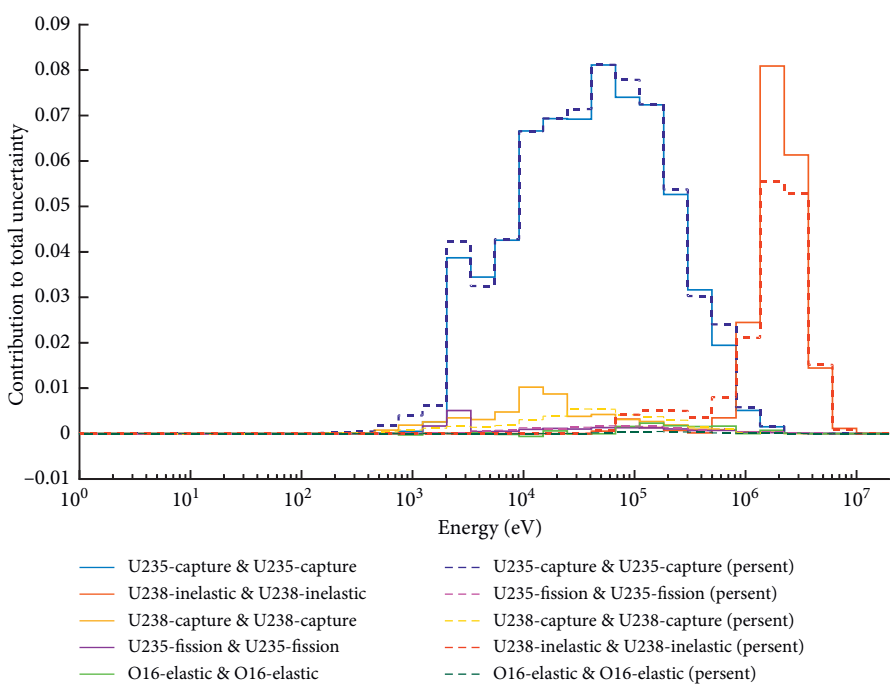

Figure 13: Uncertainty contribution from the main five isotopes at BOC (solid lines for serpent results, dashed lines for DIF3D results).

Table 4: Steady state neutronic reactivity feedback coefficients.

	$\Delta\rho$ doppler	$\Delta\rho$ fuel	$\Delta\rho$ coolant	$\Delta\rho$ structure	$\Delta\rho$ radial expansion
Coefficient (pcm/K)	−0.9240	−2.1450	−0.1720	+0.155	−0.8314
$\Delta\rho$ (pcm)	−713.51	−1423.98	−70.51	116.53	−851.31
Total uncertainty (%)	0.0102	0.1488	0.8398	0.0404	0.0637

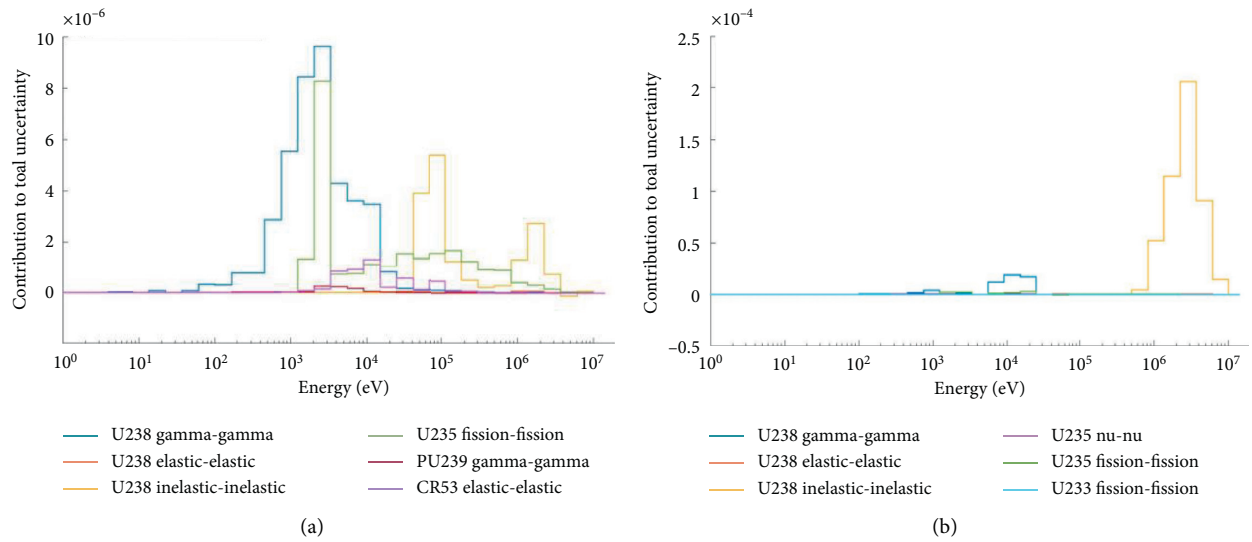

Figure 14: Contribution of major nuclide-reactions to uncertainties of (a) Doppler and (b) radial feedback coefficients.

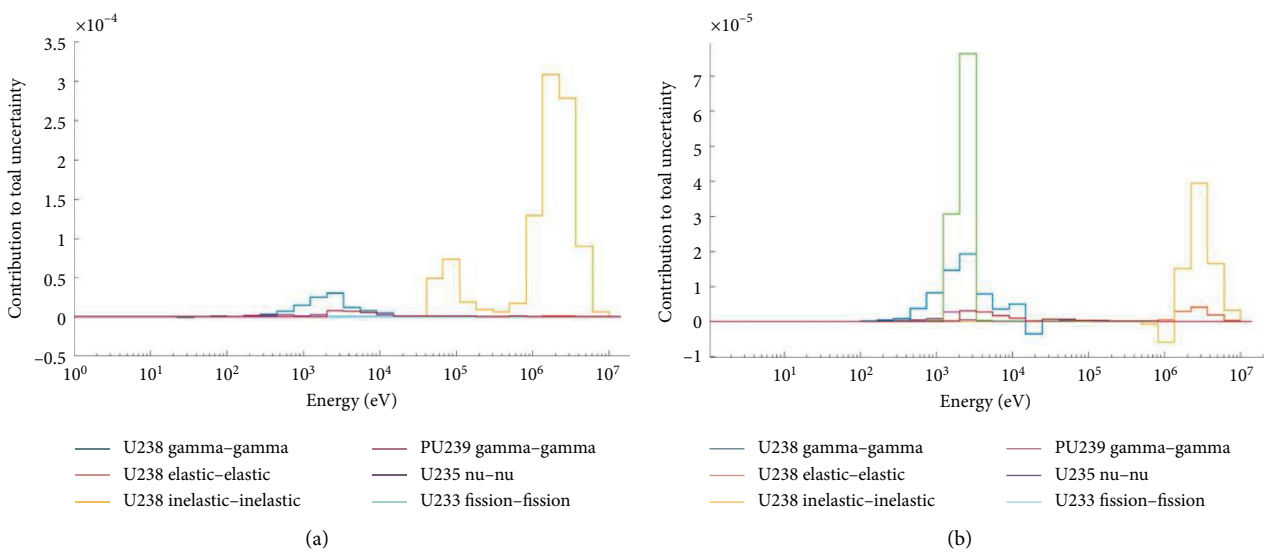

Figure 15: Contribution of major nuclide-reactions to uncertainties of (a) fuel and (b) structure feedback coefficients.

3.5. S&U Analysis of System Transient Simulations. After establishing steady state conditions, MiniSAS evaluates the temperature increase and associated reactivity feedback during an unprotected transient overpower (UTOP) accident. The transient is simulated with reactivity insertion of \$0.5 over 15 seconds to represent inadvertent rod withdrawal accident with reactivity ramp. No safety or control rods enter the core during this event. The pumps operate at full speed with heat transfer occurring via primary loop and emergency heat removal through DRACS. The remaining parameters conserve the nominal state conditions. Figure 16 shows the peak fuel, clad, and coolant temperatures as a function of transient time.

The reactivity ramp during transient increases the fuel temperature (Figure 16(a)) due to the increasing power, which in turn triggers a large negative Doppler reactivity countering the positive reactivity excursion (Figure 16(b)). Additional

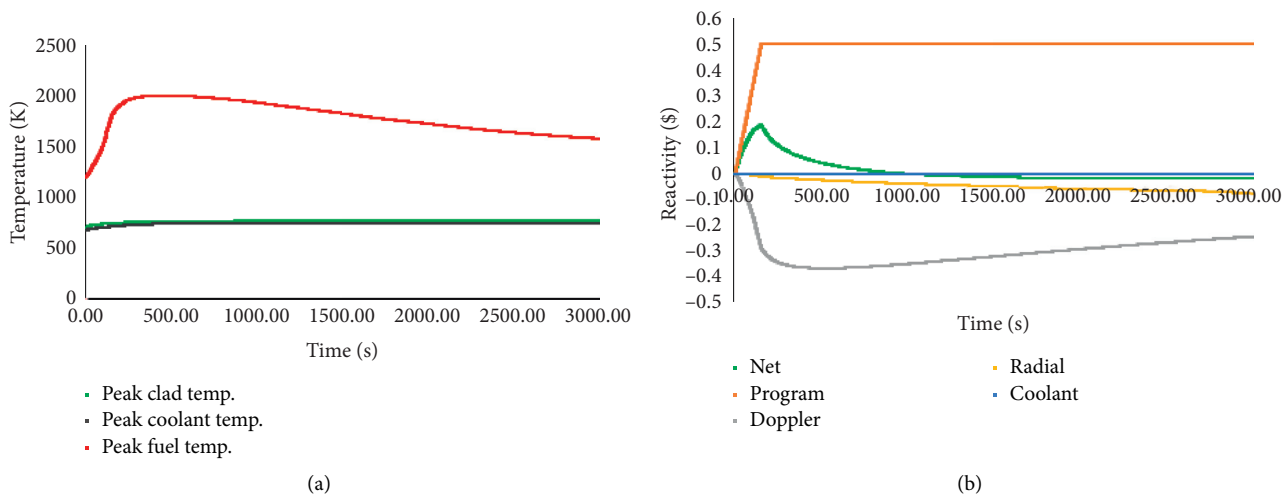

Figure 16: UTOP peak temperatures (a) and breakdown of the reactivity feedback by contribution (b).

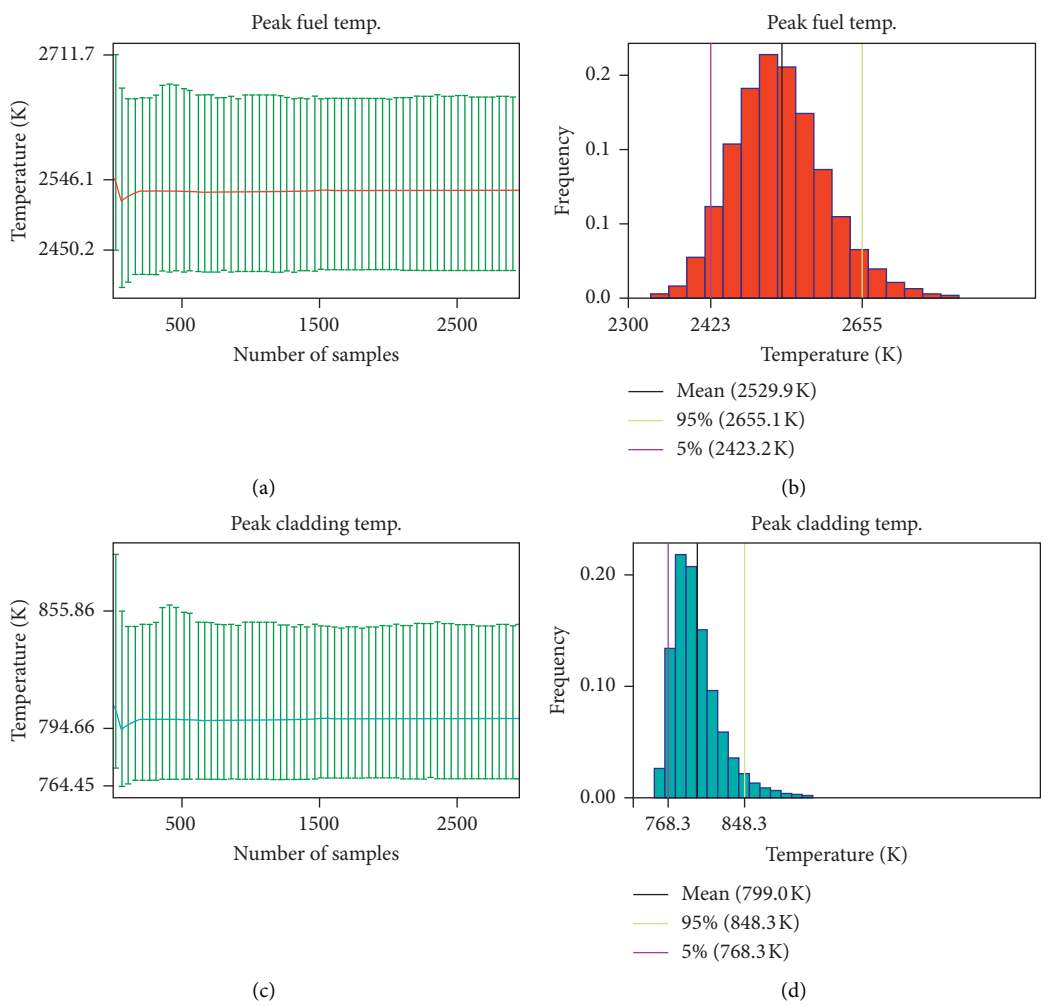

Figure 17: Sample convergence and spread of data for peak fuel and cladding temperatures during UTOP.

negative reactivity feedback from core flowering effect compensates for the remaining positive reactivity inserted during the transient. The fuel peak temperature remains well below the melting point of 3200 K for UO_2 fuel [15].

User-defined input uncertainties are propagated independently by perturbing input feedback coefficients on a normal distribution using LHS. Considering the preliminary nature of the SAS model, feedback parameters are currently

perturbed by 1% to set up a framework for UQ&P. This will be updated in future work.

An initial analysis is performed to obtain peak mean temperatures during transient. Due to the lack of substantial references for the DLFR, results are compared with a more mature LFR design, ALFRED, and its safety limits [26]. Figure 17 shows the peak fuel and cladding temperatures distribution for 3,000 samples analysed in DAKOTA with the 5%/95% interval bounds. The mean value for the DLFR peak fuel temperature is 2529.9 K, which is lower than the 3093.1 K observed for the ALFRED core during UTOP [26]. This is suspected due to different fuel types used in ALFRED (MOX) and the different reactivity insertion assumed in the safety analysis (0.7$ in 10 s) [26]. The mean peak clad temperature for the DLFR at 799.0 K is below the safety margin of 650°C (923.1 K) established in ALFRED [26] considering the creep rupture of stainless steel (used in both core designs). Lastly, both DLFR temperature values display large uncertainties of 70.0 K and 28.5 K for the peak fuel and clad temperatures, respectively, compared to similar analysis done on ABR1000 which shows 1.01°C and 0.84°C uncertainty in the two temperatures, respectively [19]. These large uncertainties for DLFR peak temperatures could be from the associated uncertainty of feedback coefficients (Table 4) which are being propagated independently without consideration of correlations between uncertainties. Therefore, further analysis is needed to investigate the magnitude of these uncertainties including correlated propagation of uncertainties. Sensitivity analysis of the peak fuel and clad temperatures to perturbation of these system model parameters will also be conducted to identify contributors of these uncertainties.

4. Conclusions and Future Work

In this paper, nuclear data input uncertainties in the DLFR core are studied using the Best Estimate Plus Uncertainty Methods. Primary modelling and UQ tools include the ANL fast reactor code suite ARC and Serpent-2.0. The core model is developed in Dif3D with cross sections generated by MCC-3.1 coupled with TWODANT. Serpent-2.0 is used to perform the lattice calculations and to verify ARC core parameters (eigenvalues, flux, and power profiles). On full core level, a modified cross section generation methodology is implemented in MCC-3.1 to improve the representation of the radial and axial heterogeneity in fuel assemblies. Preliminary results show a difference of 950 pcm in eigenvalues between conventional and improved methods. Further verification of the improved cross section method will be performed with Serpent and NEAMS Workbench/PyARC [27] in the future work.

In steady state, the uncertainties of the eigenvalue and feedback coefficients are quantified using perturbation theory by the PERSENT code with covariance matrix COMMARA-2.0. The multiplication factor shows the most sensitivity to perturbations in ^{235}U-fission cross section and ^{235}U ν and ^{238}U-capture cross section. This is followed by ^{239}Pu and ^{238}U-capture cross sections as the fuel experiences burnup. A statistical correlation coefficients matrix from COMMARA-2.0 determines the contribution of uncertainties from various nuclide-reaction pairs to identify the top contributing parameters. The ^{235}U capture-^{235}U capture and ^{238}U inelastic-^{238}U inelastic reaction pairs contribute the most to uncertainty at BOC. Propagation of these uncertainties through the reactor system will provide an insight on core safety capabilities.

The propagation of uncertainties requires standard deviations of reactivity feedback coefficients for five reactivity feedbacks, including the Doppler coefficient, radial expansion coefficient, and fuel/coolant/structure density worth. Significant uncertainty contributors of these coefficients are traced back to common nuclide-reaction pairs including ^{238}U inelastic and ^{238}U capture and ^{239}Pu capture cross sections. These uncertainties are propagated through an UTOP transient to evaluate their contribution on core safety performance. The system modelled in MiniSAS is adapted from the AB1000 model with necessary modifications. Latin Hypercube Sampling technique implemented within DAKOTA propagates uncorrelated uncertainties through the system. Large uncertainties in peak clad and fuel temperatures of 28.5 K and 70.0 K, respectively, are observed for the simulated UTOP. The sources of uncertainties in transient temperatures have not yet been identified. It is suspected that large contributions are originating from uncertainties of various feedback coefficients which are propagated independently without considering correlations between the uncertainties themselves. Furthermore, these uncertainties can be magnified from approximations in coolant properties and fuel description in MiniSAS.

In the future work, sensitivity analysis will be performed to determine the magnitude of sensitivity of peak fuel/clad temperatures to perturbations in various feedback coefficients. The overall UQ&P methodology will be expanded to include other sources of uncertainties (e.g., manufacturing and fuel performance uncertainties) through multiple transient scenarios such as unprotected loss of flow (ULOF). Additionally, the UQ&P method will be improved to account for correlations between uncertainties of various feedback coefficients. Lastly, for all future LFR safety analysis, the currently approximated LFR system model will be updated with a DLFR specific SAS model, recently obtained from WEC.

Data Availability

Specifications of the DLFR and ALFRED core design and performance can be found in [8, 26]. Cross section libraries were made available with the codes and COMMARA-2.0 library can be found through the OECD/NEA website. The authors are the end user of the reactor design and covariance data but do not have permissions to distribute it. The calculation results have been shown in the paper that the readers already have access to.

Disclosure

The research was performed as part of the author's doctoral research appointment at North Carolina State University.

Conflicts of Interest

The authors declare that there are no conflicts of interest regarding the publication of this paper.

References

[1] OECD Nuclear Energy Agency, *Handbook on Lead-bismuth Eutectic Alloy and Lead Properties, Materials Compatibility, Thermal-hydraulics and Technologies*, OECD Nuclear Energy Agency, Paris, France, 2015.

[2] F. D'Auria, C. Camargo, and O. Mazzantini, "The best estimate plus uncertainty (BEPU) approach in licensing of current nuclear reactors," *Nuclear Engineering and Design*, vol. 248, pp. 317–328, 2012.

[3] E. Alhassan, H. Sjöstrand, J. Duan et al., "Uncertainty analysis of lead cross sections on reactor safety for electra," in *Proceedings of the Joint International Conference on Supercomputing in Nuclear Applications*, Monte Carlo, France, June 2014.

[4] E. Alhassan, H. Sjöstrand, P. Helgesson et al., "Uncertainty and correlation analysis of lead nuclear data on reactor parameters for the European lead cooled training reactor," *Annals of Nuclear Energy*, vol. 75, pp. 26–37, 2015.

[5] M. Milosevic, "Effects of uncertainties in lead cross section data in Monte Carlo analysis of lead cooled and reflected reactors," in *Proceedings of the Conference on Mathematics & Computational Sciences (M&C)*, Monterey, CA, USA, 2007.

[6] R. C. Smith, *Uncertainty Quantification Theory Implementaion and Application*, Society of Indian Automobile Manufacturers, Raleigh, NC, USA, 2014.

[7] M. Herman, *AFCI-2.0 Neutron Cross Section Covariance Library*, Brookhaven National Laboratory, Upton, NY, USA, 2011.

[8] G. Grasso, *Demonstration Lead-cooled Fast Reactor*, Westinghouse Electric Company, Pittsburgh, PA, USA, 2016.

[9] B. J. Toppel, *Argonne Reactor Computation (ARC) System*, Argonne National Laboratory, Lemont, IL, USA, 1967.

[10] M. A. Smith, *MCC-3: Multigroup Cross-Section Generation Code for Fast Reactor Analysis*, Argonne National Laboratory, Lemont, IL, USA, 2013.

[11] R. Alcouffe, *User Guide for TWODANT: A Code Package for Two-Dimensional Diffusion Accelerated Neutral Particle Transport*, Los Alamos National Laboratory, Los Alamos, NM, USA, 1984.

[12] K. L. Derstine, *Dif3D: A Code Package to Solve One, Two, and Three Dimensional Finite Difference Dissuion Theory Problems*, Argonne National Laboratory, Lemont, IL, USA, 1984.

[13] J. Leppanen, M. Pusa, T. Viitanen, V. Valtavirta, and T. Kaltiaisenaho, "The serpent Monte Carlo code: status, development and applications," in *Proceedings of the Supercomputing In Nuclear Applications + Monte Carlo*, Monte Carlo, France, June 2014.

[14] A. Del Nevo, "Modelling and analysis of nuclear fuel pin behavior for innovative lead cooled FBR," 2014.

[15] S. G. Popov, *Thermophysical Properties of MOX and UO2 Fuels Including the Effects of Irradiation*, Oak Ridge National Laboratory, Knoxville, TN, USA, 2000.

[16] C. Lee, "Improved reactivity worth estimation of MCC-3/DIF3D in fast reactor analysis," in *Proceedings of the ANS Summer Meeting*, San Antonio, TX, USA, 2015.

[17] T. H. Fanning, *Status of the SAS4A/SASSYS-1 Safety Analysis Code*, Argonne National Laboratory, Lemont, IL, USA, 2017.

[18] T. H. Fanning, *SAS4A/SASSYS-1 Code Improvements for FY 2016*, Argonne National Laboratory, Lemont, IL, USA, 2016.

[19] N. Stauff, "Uncertainty quantification of ABR transient safety analysis," in *Proceedings of the Best Estimate Plus Uncertainty (BEPU)*, Lucca, Italy, 2018.

[20] G. Dan, "LFR design: safety, neutronics, thermal hydraulics, structural mehcanics, fuel, core and plant design," in *Handbook of Nuclear Engineering*, pp. 2821–2824, Springer, Berlin, Germany, 2010.

[21] N. Stauff, "Uncertainty quantification of ABR transient safety analysis-nuclear data uncertainties," in *Proceedigs of the Best Estimate Plus Uncertainty (BEPU)*, Lucca, Italy, 2018.

[22] M. A. Smith, *VARI3D & PERSENT: Perturbation and Sensitivity Analysis*, Argonne National Laboratory, Lemont, IL, USA, 2013.

[23] N. Stauff, *Private Communication*, Argonne National Laboratory, Lemont, IL, USA, 2019.

[24] M. Aufiero, A. Bidaud, M. Hursin et al., "A collision history-based approach to sensitivity/perturbation calculations in the continuous energy Monte Carlo code serpent," *Annals of Nuclear Energy*, vol. 85, pp. 245–258, 2015.

[25] B. M. Adams, "Dakota, a multilevel parallel object-oriented framework for design optimization, parameter estimation, uncertainty quantification, and sensitivity analysis: version 6.9 manual," 2018.

[26] G. Grasso, C. Petrovich, D. Mattioli et al., "The core design of alfred, a demonstrator for the European lead-cooled reactors," *Nuclear Engineering and Design*, vol. 278, pp. 287–301, 2014.

[27] N. Stauff, *Status of the NEAMS and ARC Neutronic Fast Reactortools Integration to the NEAMS Workbench*, Argonne National Laboratory, Lemont, IL, USA, 2019.

Hindawi
Science and Technology of Nuclear Installations
Volume 2020, Article ID 6798738, 12 pages
https://doi.org/10.1155/2020/6798738

Research Article

Numerical Simulation and Validation for Early Core Degradation Phase under Severe Accidents

Dekui Zhan,[1] Xinhai Zhao,[1] Shaoxiong Xia,[1] Peng Chen,[1] and Huandong Chen[2]

[1]*China Nuclear Power Technology Research Institute, Shenzhen 518000, China*
[2]*Sino-French Institute of Nuclear Engineering and Technology, Sun Yat-sen University, Zhuhai 519000, China*

Correspondence should be addressed to Xinhai Zhao; zhaoxinhai2@cgnpc.com.cn

Received 20 December 2019; Revised 26 March 2020; Accepted 24 June 2020; Published 3 August 2020

Academic Editor: Kostadin Ivanov

Early core degradation determines the amount of hydrogen generated by cladding oxidation as well as the temperature, the mass, and the composition of corium that further relocates into the lower head of reactor pressure vessel (RPV), which is essential for the effectiveness analysis of in-vessel retention (IVR) and hydrogen recombiners. In this paper, the mechanisms of controlling phenomena in the early phase of core degradation are analysed at first. Then, numerical models adopted to calculate (1) core heating up, (2) cladding oxidation, (3) dissolution between molten zirconium and fuel pellets, and (4) formation of a molten pool in the core active section are presented. Compared with integral codes for severe accident analysis (such as MAAP and MELCOR), the models in this paper are established at the fuel pin level and the calculation is performed in 3D, which can capture the detail local phenomena during the core degradation and eliminate the average effect due to equivalent rings used in integral codes. In addition, most of the control equations in this paper are calculated by implicit schemes, which can improve the accuracy and stability of the calculation. In the simulation, the calculation oxidation is calculated by using the oxygen diffusion model, while the dissolution is calculated with Kim, Hayward, Hofmann, and IBRAE models to perform uncertainty analysis. For the validation, the cladding oxidation model is verified by Olander theoretical cases in the conditions of both steam-rich and steam-starved. The dissolution models are validated by the RIAR experiment. The code is overall verified by Phebus FPT0 on the integral phase of core early degradation. According to the simulation results, it can be inferred that the dissolution reaction between the molten zirconium and fuel pellets is the main reason for the melting of UO_2 at low temperature. In the case of starved steam, part of the fuel pellets can melt down even at 2248 K and relocate to the bottom of the core, which is much lower than the melting point of UO_2 (3113 K).

1. Introduction

In the Chernobyl and Fukushima accidents, the melted reactor cores caused a large amount of radioactive material to be released into the environment. It is essential to study the severe accident phenomena for the design of dedicated mitigation measures to cease the accident process and reduce its consequences.

Accidents that can cause the core to melt down mainly include (1) the station blackout accident (SBO), (2) the large break loss of coolant accident (LBLOCA) superimposed with the failure of safety injection pumps, and (3) the anticipated transient without scram (ATWS) [1]. Although the initial events are different, the phenomena in the core early degradation are approximately identical. The controlling phenomena include core uncovery, core heating up, failure of control rods, dissolution of UO_2 and ZrO_2 by molten zirconium, failure of the cladding oxide layer, corium relocation and solidification, and formation of a molten pool in core active section.

For the cladding oxidation, under the condition that the solid zirconium alloy is thick enough and the steam is sufficient, the oxidation of zirconium alloy is dominated by the oxygen diffusion, in which the chemical reaction rate follows the parabolic law [2]. Correlations of Urbanic and Heidrick [3], Prater and Courtright [4], and Leistikow-Schanz [5] are widely used in the calculation of cladding oxidation.

De Luze et al. [6] summarized the failure temperatures of Ag-In-Cd control rods in different experiments, including CORA-9, QUENCH-13, and Phebus FPT1. The failure temperatures of control rods in most experiments are between 1400 and 1700 K. It can be concluded that the eutectic reaction between the solid stainless steel and the zirconium alloy is the reason for the partial melting of the cladding and guide tube at about 1400 K, while the dissolution of zirconium by the molten stainless steel and Ag-In-Cd absorber causes the guide tube to be broken in a wide range at around 1700 K.

Crucible experiments found that the dissolution process of UO_2 can be divided into two phases, including the saturation phase and the precipitation phase. Hofmann [7], Hayward and George [8], and Kim and Olander [9] established separately dissolution models based on their experiments, respectively. However, significantly different results were discovered during the precipitation period. The dissolution of UO_2 reaches saturation in Kim and Hayward experiments while Hofmann found the dissolved UO_2 mass continues to increase and follows the parabolic law. The ZrO_2 dissolution process is also separated into two stages, including the erosion stage and the corrosion stage [10], in which the correlation of Hofmann is widely used.

Based on the experimental data and mechanism research studies, many integral codes for severe accident analysis were developed, including MELCOR, SCDAP/RELAP5, and ASTEC. The temperature criteria and the oxide thickness criteria are widely used in most codes to predict the failure moment of the cladding oxide layer. For the relocation process of melt after the failure of the cladding oxide layer, candling model is established in MELCOR by analogy with the flow of molten droplets of the candle along the wall [11]. LIQSOL model is developed in SCDAP/RELAP5 based on the experimental results of CORA, PBF-SFD, and FLHT [12]. Decanting model and porous media model are adopted in ASTEC, which can simulate the radial and axial relocation of corium simultaneously [13].

Due to the consideration of computing efficiency, equivalent rings are widely used in integral codes. However, radial power factors of assemblies in the same ring are different, especially between assemblies with black rods and without black rods. When equivalent rings are adopted in the modelling, the power factors of high-power assemblies are actually averaged, causing the delay of the calculated degradation process. It means that integral codes may underestimate the time of some important events in the reactor, such as the start time of cladding oxidation, the failure of the zirconium cladding (namely, the fission product begins to be released in large quantities), and the downward relocation of the molten materials, which are important for accident analysis. In this paper, the models are established at the fuel pin level and the calculation is performed in 3D which can capture more detailed local phenomena during the core degradation phase and eliminate the average effect due to equivalent rings used in integral codes to achieve more accurate simulation for the early phase of core degradation.

2. Mechanism of Early Core Degradation

In this section, the mechanisms of controlling phenomena in the early core degradation phase are presented based on the literature review.

2.1. Oxidation of Zirconium Cladding. The reaction of zirconium cladding with steam is the most important phenomenon in the core degradation, which generates not only a large amount of heat but also a great quantity of hydrogen. With neglecting considering the hydrogen absorption in the cladding, the zirconium oxidation can be divided into the following stages [7]: (1) diffusion of steam to the outer surface of cladding; (2) chemical absorption of steam; (3) dissociation of steam molecules into oxygen and hydrogen; (4) diffusion of oxygen from the outer surface of cladding to the inside, forming ZrO_2, α-Zr(O), and β-Zr three layers in sequence; (5) recombination of hydrogen; and (6) diffusion of hydrogen molecules into the bulk of the flow channel, causing the hydrogen content in the flow channel to increase.

2.2. Dissolution of UO_2 and ZrO_2. Based on the analysis of the experimental results of Hayward, Kim, and Hofmann, Olander [14] proposed that during the saturation period, the UO_2 dissolution is dominated by natural convection mass transfer. Liquid U with a density of $1.7 \times 10^4\,\mathrm{kg/m^3}$ is produced by a chemical reaction at the interface between the molten zirconium alloy and the solid UO_2. However, the density of the liquid Zr is only $6 \times 10^3\,\mathrm{kg/m^3}$. The difference in density between liquids U and Zr causes significant convection in the melt. During this period, the U content in the melt increases continuously and gradually reaches the saturation. Dissolved U and O are quickly transferred to the central region of the melt and mixed well with the molten Zr. Therefore, it is found in the experiments that the ratios of U, Zr, and O are uniformly distributed in the molten zone. In the precipitation stage, Olander does not suppose that UO_2 will continue to be dissolved. At the end of the saturation period, the dissolution reaction of UO_2 is ceased, and the mass ratio of U and Zr in the melting zone is kept unchanged. During this period, O in the UO_2 crucible continues to diffuse into the molten zone, causing the previously saturated (U, Zr, O) melt to be supersaturated to precipitate the $(U, Zr)O_{2-x}$ ceramic phase.

The dissolution of ZrO_2 is similar to that of UO_2. Based on the ZrO_2 crucible experiments, Hayward and George [10] speculated that in the erosion period, the dissolution of ZrO_2 is caused by a significant convective effect. The newly dissolved ZrO_2 is quickly brought into the melt central zone. Therefore, no transition layer was created in the experiment in this period. Thereafter, the oxygen concentration gradient at the interface gradually decreases causing the convective effect to be weakened. Once the mass flux of oxygen entering the melt by diffusion is greater than that by dissolution, the erosion period is ceased. In the following period, oxygen in the ZrO_2 crucible continues to diffuse into the melt driven by the difference of oxygen potential. Near the interface region,

ZrO_2 in the crucible is reduced to ZrO_{2-x} and the metallic zirconium in the melt is oxidized to ZrO_{2-x}. Therefore, it was shown in the experiment that the thickness of the ZrO_{2-x} transition layer increased not only towards the crucible region but also towards the melt central region.

2.3. Cladding Oxide Layer Failure. The cladding of fuel rods is oxidized by steam at high temperature. Then, a ZrO_2 oxide layer is formed on the outside of the cladding. The oxide layer with a high melting point (2963 K) will hold up the molten (U, Zr, O) in the cladding, preventing the downward relocation of the melt. However, the ZrO_2 oxide layer is dissolved by the metallic Zr in the molten (U, Zr, O), causing the oxide layer to become thinner. In addition, the creep effect at high temperatures reduces the ability of the oxide layer to hold up the melt and its yield limit decreases with increasing temperatures. Therefore, when the thickness of the oxide layer is reduced to a certain threshold, the oxide layer can no longer hold up the (U, Zr, O) melt. Then, the (U, Zr, O) melt is released to relocate downwards.

2.4. Corium Relocation. According to CORA W1 and W2 experimental results, Veshchunov and Palagin [15] infer that in the first period, the molten cladding materials flow down rapidly in the form of droplets or rivulets at about 0.5 m/s. Owing to a large temperature gradient below the front, the molten materials refreeze in the interrod space forming local blockages (debris) and accumulating the melt in the form of molten pool. The melt mass in the molten pool gradually increases. Once the solidified crust at the bottom cannot support the weight of the melt, the molten pool will relocate downwards. During the relocation process, the molten zirconium alloy in the molten pool will dissolve adjacent fuel pellets and be oxidized by steam. The dissolution reaction and the oxidation reaction cause U in the melt to reach a supersaturated state to produce the (U, Zr)O_{2-x} ceramic phase precipitate. The presence of the (U, Zr)O_{2-x} ceramic phase precipitate increases the viscosity of the melt, thereby preventing the molten pool from rapidly relocating towards the bottom of the bundle. At the same time, the oxidation reaction generates a large amount of heat raising the temperature of the melt. Therefore, the solubility of U in the melt is increased, resulting in the reduction of the (U, Zr)O_{2-x} ceramic phase and the viscosity of the melt. Consequently, the molten pool moves downwards with a slow characteristic velocity $1\sim2 \times 10^{-3}$ m/s. As the molten pool relocates downwards, fresh melt continues to accumulate in the molten pool, causing the molten pool to expand in the radial and axial directions to form a massive slug flow.

3. Numerical Simulation Method

In this section, the physical models adopted in the simulation are presented for the phenomena mentioned above.

3.1. Bundle Heat Transfer. The core heating up is accompanied by heat conduction, convection heat transfer, and radiation heat transfer. For the convective heat transfer, the Dittus–Boelter forced convection correlation is adopted when there are drive pumps and the coolant flow rate is large, while the natural convection correlations are used in the case that the flow of coolant is driven by the buoyancy. The models introduced in the following sections are used to calculate the transient heat conduction in the fuel rods and the radiation heat transfer between rods.

3.2. Transient Heat Conduction. The two-dimensional axisymmetric unsteady heat conduction equation is used to solve the transient temperature distribution in the fuel rods and control rods. The governing equation is given by

$$\rho c_P \frac{\partial T}{\partial t} = \frac{1}{r}\frac{\partial}{\partial r}\left(\lambda r \frac{\partial T}{\partial r}\right) + \frac{\partial}{\partial z}\left(\lambda \frac{\partial T}{\partial z}\right) + \dot{S}, \quad (1)$$

in which $\dot{S}$ is the volumetric heat generation rate. For the absorbers in control rods, $\dot{S} = 0$, while for the fuel pellets,

$$\dot{S} = \frac{H_{\text{tot}}}{N_{\text{f}} V_{\text{f}}} P_{\text{z}} P_{\text{r}}, \quad (2)$$

in which H_{tot} is the total power of core decay heat. P_{z} is the axial power factor. P_{r} is the radial power factor of fuel assemblies. N_{f} is the number of fuel rods in an assembly. V_{f} is the volume of a fuel rod in one axial node. The following equation is obtained by integrating equation (1):

$$a_P T_P^{n+1} = a_E T_E^{n+1} + a_W T_W^{n+1} + a_N T_N^{n+1} + a_S T_S^{n+1} + b. \quad (3)$$

The coefficients in equation (3) are shown in (4)~(6), where the geometric parameters are defined in Figure 1.

$$\begin{aligned} a_E &= \frac{r_P \Delta r}{(\delta z)_E/\lambda_E}, \\ a_W &= \frac{r_P \Delta r}{(\delta z)_W/\lambda_W}, \\ a_N &= \frac{r_N \Delta z}{(\delta r)_N/\lambda_N}, \\ a_S &= \frac{r_S \Delta z}{(\delta r)_S/\lambda_S}, \end{aligned} \quad (4)$$

$$a_P = a_E + a_W + a_N + a_S + a_P^0, \quad (5)$$

$$\begin{aligned} a_P^0 &= \frac{(\rho c)_P \Delta V}{\Delta t}, \\ b &= \dot{S}\Delta V + a_P^0 T_P^n, \\ \Delta V &= 0.5\left(r_N + r_S\right)\Delta r \Delta z. \end{aligned} \quad (6)$$

3.3. Radiation Heat Transfer. The radiative heat transfer is calculated at the fuel pin level. Due to the shielding effect, central rod P only radiates heat directly to the surrounding 16 rods as shown in Figure 2. According to the geometric position, the surrounding rods can be divided into three types: 1, 2, and 3. The radiative view factors are X_1, X_2, and

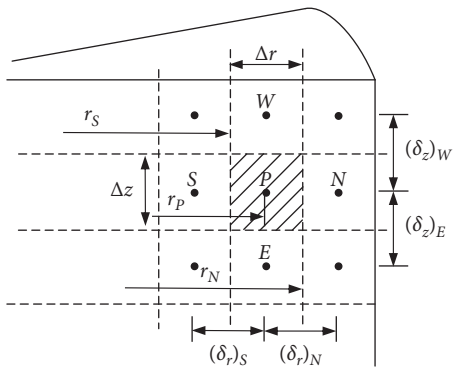

Figure 1: Schematic of mesh generation for fuel pellets or absorbers.

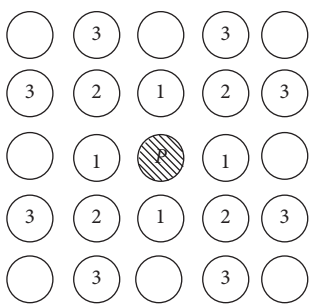

Figure 2: Schematic of the radiation model between rods.

X_3, respectively. Then, the effective radiation for central rod P is calculated as follows:

$$J_P^{n+1} = \varepsilon\sigma T_P^4 + (1-\varepsilon)\sum_{k=1,4} J_{1,k}^{n+1} X_1 + (1-\varepsilon)\sum_{k=1,4} J_{2,k}^{n+1} X_2 + (1-\varepsilon)\sum_{k=1,8} J_{3,k}^{n+1} X_3, \tag{7}$$

where J_1, J_2, and J_3 are the effective radiation at the outer surface of rods 1, 2, and 3, respectively. The radiative heat flux at the outer surface of rod P is given by

$$q_P = \frac{\varepsilon}{1-\varepsilon}\left(\sigma T_P^4 - J_P^{n+1}\right). \tag{8}$$

3.4. Cladding Oxidation. The oxygen diffusion model proposed by Olander [16] is adopted to calculate the oxidation of cladding, in which the cladding is divided into the oxide layer (ZrO_2) and the metal layer (including a-Zr(O) and β-Zr). The oxidation rate depends on the amount of steam available, the thickness of the metal layer as well as the diffusion rate of oxygen in the cladding (namely temperature). According to the amount of available steam, the steam state in the flow channel can be divided into two cases: steam-rich and steam-starved. The amount of steam available is calculated by the molar steam balance:

$$V_{\mathrm{ch}} M_{\mathrm{g}} \frac{dy_i}{dt} = F_{\mathrm{g}}\left(y_{i-1} - y_i\right) - A_{\mathrm{cl}}\dot{w}, \tag{9}$$

in which $M_{\mathrm{g}} = p_{\mathrm{tot}}/RT$ is the molar density of gas. y_i is the steam mole fraction in the bulk gas in node i. The total gas molar flow rate is denoted by F_{g} and A_{cl} is the external surface area of the cladding. The steam absorption rate is given by

$$\dot{w}_{\mathrm{a}} = k_{\mathrm{g}} M_{\mathrm{g}}\left(y_i - y_{\mathrm{cl}}\right), \tag{10}$$

where y_{cl} is the steam molar fraction at the cladding outer surface. The oxygen diffusion rate in the cladding is given by

$$\dot{w}_{\mathrm{d}} = \frac{\rho_{\mathrm{Zr}} D_{\mathrm{o}}\left(C_{\mathrm{s}} - C_{\mathrm{a}}\right)}{\delta}, \tag{11}$$

in which the molar density of Zr in ZrO_2 is denoted as ρ_{Zr} and D_{o} is the diffusion coefficient of oxygen in the oxide layer. C_{s}, C_{a}, and C_{b} are the O/Zr ratio at the outer surface of the oxide layer, at the interface in the oxide layer side, and at the interface in the metal layer side, respectively, which are determined by Zr-O phase diagram. The oxidation rate $\dot{w}$ is calculated as the minimum of $\dot{w}_{\mathrm{a}}$ and $\dot{w}_{\mathrm{d}}$. In the case of oxidation when both oxide and metal phases are present, the thickness of the oxide layer δ is calculated as follows:

$$\delta^{n+1} = \delta^n + \frac{\Delta t}{G\left(C_{\mathrm{a}} - C_{\mathrm{b}}\right)}\left[-\frac{D_{\mathrm{M}} C_{\mathrm{b}}}{4E^2\xi^n}\left(\frac{\bar{c}^{\,n}}{C_{\mathrm{b}}}\right) + \frac{G D_{\mathrm{o}}}{\delta^n}\left(C_{\mathrm{s}} - C_{\mathrm{a}}\right)\right], \tag{12}$$

where D_{M} is the diffusion coefficient of oxygen in α-Zr(O). The average oxygen content in the metal layer $\bar{c}$ is determined by the following equation:

$$\bar{c}^{\,n+1} = \bar{c}^{\,n} + C_{\mathrm{b}}\Delta t\left[\frac{D_{\mathrm{M}}}{\left(2E\xi^n\right)^2}\left(\frac{\bar{c}}{C_{\mathrm{b}}}\right) - \frac{G}{\xi^n}\left(1 - \frac{\bar{c}^{\,n}}{C_{\mathrm{b}}}\right)\left(\frac{\mathrm{d}\delta}{\mathrm{d}t}\right)^{n+1}\right]. \tag{13}$$

For the case of oxidation in all-metal cladding or in all-oxide cladding, other controlling equations are used to calculate the oxide thickness and the average oxygen content in the metal layer.

3.5. Dissolution of UO_2 and ZrO_2. Hofmann [7], Hayward and George [8], and Kim and Olander [9] established dissolution models based on their experiments, respectively. However, the results of each experiment in the precipitate period are significantly different. In the calculation, all the three models as well as the IBRAE model are used to simulate the dissolution of UO_2 and ZrO_2 and will be verified by the RIAR test in the next section.

3.5.1. Kim UO_2 Dissolution Model. When the Ra number in the (U, Zr, O) melt is greater than 1000, the natural convection model is adopted [9]:

$$C_{\mathrm{U}}^{n+1} = C_{\mathrm{U}}^{S} - \left[\left(C_{\mathrm{U}}^{S} - C_{\mathrm{U}}^{n}\right)^{-(1/4)} + \frac{0.54S}{4V}\left(\frac{gD_{\mathrm{U}}^{3}}{\nu d}\right)^{(1/4)}\Delta t\right]^{-4}. \tag{14}$$

Otherwise, the diffusion model is used [9]:

$$C_{\mathrm{U}}^{n+1} = \left[C_{\mathrm{U}}^{n2} + \frac{4D_{\mathrm{U}}}{\pi e^{2}}C_{\mathrm{U}}^{S2}\Delta t\right]^{0.5}, \tag{15}$$

in which C_{U} is the mass fraction of U in the bulk melt. S, V, and ν are the UO_2, (U, Zr, O) contact surface, the volume, and viscosity of (U, Zr, O), respectively. d is the diameter corresponding to S and e is the (U, Zr, O) mixture thickness.

3.5.2. Hayward UO_2 Dissolution Model. Based on crucible experiments, Hayward found that the mass fraction of U in the melt can be calculated as follows [8, 17]:

$$C_{\mathrm{U}}^{n+1} = C_{\mathrm{U}}^{S} - \left(C_{\mathrm{U}}^{S} - C_{\mathrm{U}}^{n}\right)\cdot \exp\left[-k_{\mathrm{U}}\Delta t\right], \tag{16}$$

in which k_{U} is a constant related to the contact area and the initial oxygen content.

3.5.3. Hofmann UO_2 and ZrO_2 Dissolution Model. The crucible experiments of Hofmann show that UO_2 is rapidly dissolved in the initial period, and the mass fraction of UO_2 in the melt rapidly increases to 35.8%. Subsequently, UO_2 is continuously dissolved, and the UO_2 mass fraction in the melt follows the parabolic law [7]:

$$C_{\mathrm{UO_2}}^{n+1} = 0.358 + \left[\left(C_{\mathrm{UO_2}}^{n} - 0.358\right)^{2} + Kp_{1}\Delta t\right]^{0.5}, \tag{17}$$

$$Kp_{1} = 1.02\times 10^{11}\exp\left(\frac{-6.77\times 10^{5}}{\mathrm{RT}}\right). \tag{18}$$

The ZrO_2 dissolution model is calculated in a similar form of equation (7):

$$C_{\mathrm{ZrO_2}}^{n+1} = 0.233 + \left[\left(C_{\mathrm{ZrO_2}}^{n} - 0.233\right)^{2} + Kp_{2}\Delta t\right]^{0.5}, \tag{19}$$

$$Kp_{2} = 1.47\times 10^{10}\exp\left(\frac{-6.66\times 10^{5}}{\mathrm{RT}}\right). \tag{20}$$

3.5.4. Simultaneous Dissolution of UO_2 and ZrO_2. For the calculation of the simultaneous dissolution of UO_2 and ZrO_2, the first method is to assume it as two separate processes. Within one time step, the dissolution of UO_2 is calculated firstly according to the models mentioned above, and then the dissolution of ZrO_2 with Hofmann correlation is calculated until the mixture composition reaches the liquidus in the (U, Zr, O) ternary phase diagram. The second method is to adopt the IBRAE model proposed by Veshchunov et al. [18, 19], which can be used to calculate the simultaneous dissolution of UO_2 and ZrO_2 as well as the oxidation of (U, Zr, O) mixture. In the IBRAE model, both intact fuel rods and the molten pool can be considered as UO_2, (U, Zr, O) mixture, and ZrO_2 three-layer structure. The interface movement rate can be derived from the flux match. For the interface of UO_2 and (U, Zr, O),

$$\frac{\mathrm{d}r_{1}}{\mathrm{d}t} = \frac{-D_{\mathrm{O}}^{\mathrm{UO_2}}\left(\partial\rho_{\mathrm{O}}/\partial r\right)\big|_{I_1} - k_{\mathrm{O}}\left(I_{1}\right)\left[c_{\mathrm{O}}^{\max} - c_{\mathrm{O}}\left(B\right)\right]}{\rho_{\mathrm{O}} - \left(g_{1} + g_{2}c_{\mathrm{M}}\right)\left(\rho_{\mathrm{U}}/c_{\mathrm{M}}\right)}. \tag{21}$$

For the interface of (U, Zr, O) and ZrO_2,

$$r_{3}\frac{\mathrm{d}r_{3}}{\mathrm{d}t} - r_{2}\frac{\mathrm{d}r_{2}}{\mathrm{d}t} = r_{2}\frac{D_{\mathrm{O}}^{\mathrm{ZrO_2}}\left(\partial\varphi_{\mathrm{O}}/\partial r\right)\big|_{I_2} - k_{\mathrm{O}}\left(I_{2}\right)\left(c_{\mathrm{O}}^{\max} - c_{\mathrm{O}}\left(B\right)\right)}{\varphi_{\mathrm{O}} - g_{1}\left(\rho_{\mathrm{U}}/c_{\mathrm{M}}\right)}, \tag{22}$$

where r_1, r_2, and r_3 are positions of boundaries of the solid UO_2 and ZrO_2 layers. ρ_i, c_i, and φ_i are the molar densities of different components (i = O, U, and Zr) in UO_2, (U, Zr, O) mixture, and ZrO_2, respectively. The molar density of the melt is denoted by c_{M}. g_1 and g_2 are temperature-dependent parameters which determine the position of liquidus line in the ternary phase diagram.

The oxygen concentration in the melt in (21) and (22) can be calculated by the mass conservation equations, while the oxygen concentration gradient at interface I_1 is calculated by the diffusion equation of oxygen in solid UO_2 with moving boundary conditions. For the oxygen concentration gradient at the interface I_2,

$$\begin{aligned}
&\text{if steam} - \text{rich}, \quad D_{\mathrm{O}}^{\mathrm{ZrO_2}}\frac{\partial\varphi_{0}}{\partial r}\Big|_{I_2} \approx D_{\mathrm{O}}^{\mathrm{ZrO_2}}\frac{\varphi_{0}\left(B\right) - \varphi_{0}\left(I_{1}\right)}{r_{3} - r_{2}},\\
&\text{if steam} - \text{starved}, \quad D_{\mathrm{O}}^{\mathrm{ZrO_2}}\frac{\partial\varphi_{0}}{\partial r}\Big|_{I_2} \approx k_{\mathrm{g}}M_{\mathrm{g}}y_{i}.
\end{aligned} \tag{23}$$

3.6. Criteria of Cladding Oxidation Layer Failure. In the steam-rich case, the oxidation reaction in the cladding dominates. Oxidation of cladding continues until it is completely oxidized. In the calculation, it is assumed that the fuel pellets and cladding will melt together once the temperature reaches the eutectic point (2673 K).

In the steam-starved condition, the dissolution reaction in the cladding dominates. In the calculation, it is assumed that the cladding oxide layer will fail once the (U, Zr, O) mixture temperature exceeds the α-Zr(O) melting point (2248 K) and the oxide layer thickness is less than 300 μm.

3.7. Corium Relocation. Based on the explanation of Veshchunov and Palagin on CORA W1 and W2 experimental results [15], the corium relocation downward in the bundle is considered as the slug flow with fixed velocity 1×10^{-3} m/s. During the relocation, convective heat exchange with the steam, radiant heat exchange with the surrounding nonadjacent rods, and the heat generated by corium oxidation are considered. The energy equation during relocation is given by

$$\rho c_{p}\frac{\mathrm{d}\left(T_{\mathrm{mp}}V_{\mathrm{mp}}\right)}{\mathrm{d}t} = Q_{\mathrm{ox}} - A_{\mathrm{mp}}h\left(T_{\mathrm{mp}} - T_{\mathrm{g}}\right) - Q_{\mathrm{rad}}. \tag{24}$$

4. Separate Effect Validation

In this section, the physical models for both the oxidation reaction and dissolution reaction which are the two of the most important phenomena in the early phase of core degradation will be verified.

4.1. Oxidation of Zirconium Cladding. The oxidation model is validated with theoretical cases of a single fuel rod oxidation proposed by Olander [16]. Both steam-rich and steam-starved conditions are simulated. In order to simplify the model and constrain other variables, the effect of heat generation due to oxidation is not considered. Instead, the fuel rod temperature of each node is determined by the following equations:

$$T = T_0 + (RR)_L t, \quad T < T_{trans}, \tag{25}$$

$$T = T_{trans} + (RR)_H (t - t_{trans}), \quad T \geq T_{trans}, \tag{26}$$

in which T_0 is the initial temperature. The temperature at which the microstructure of the oxide layer begins to change from tetragonal to cubic is denoted by T_{trans} with a value of 1773 K. $(RR)_L$ and $(RR)_H$ are the temperature ramp rates below and above the transition temperature.

In the steam-starved case, the inlet steam flow rate is 2×10^{-2} m/s. The temperature ramp rates $(RR)_L$ and $(RR)_H$ are 1.0 K/s and 2.5 K/s, respectively. The steam mole fraction in the flow channel at different positions is illustrated in Figure 3. The cladding oxygen absorption rate $\dot{w}$ increases as the temperature of the fuel rod rises. Therefore, the steam mole fraction in the flow channel gradually decreases. When the steam-starved condition occurs, the oxygen absorption from the flow channel is limited by the amount of steam available. Once the oxygen absorption rate of the cladding from the flow channel is less than the diffusion rate of oxygen from the oxide layer to the metal layer, the oxide layer will become thinner, as shown in Figure 4.

In the steam-rich case, the inlet steam flow rate is 1 m/s. The temperature ramp rates $(RR)_L$ and $(RR)_H$ are 0.7 K/s and 1.0 K/s, respectively. The steam mole fraction in the flow channel at different positions is presented in Figure 5. It can be seen that the steam mole fraction in the flow channel decreases steeply at around 600 s. It is explained by the fact that the temperature of the rod increases to around 1773 K at which the microstructure of the oxide layer changes from tetragonal to cubic, causing the diffusion of oxygen in the oxide layer increasing rapidly and large amount of steam consumed. After 750 s, the steam mole fraction in the 210 cm and 390 cm flow channels increase since the cladding below 210 cm has been sufficiently oxidized. Then, the consumption of steam is reduced so that the steam mole fraction arriving above 210 cm increases. After 880 s, the steam mole fraction in the flow channel drops again due to the increase in the temperature of the fuel rod causing the increase of the oxygen diffusion rate in the oxide layer and the metal layer. The variation of fractional oxide layer thickness in cladding is shown in Figure 6.

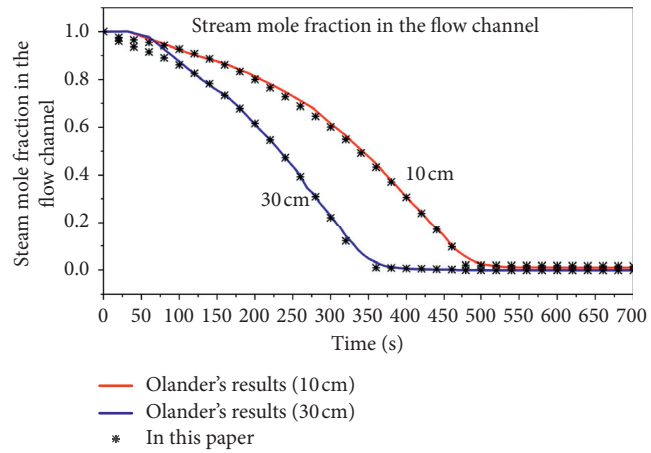

Figure 3: Comparison of steam mole fractions in the flow channel.

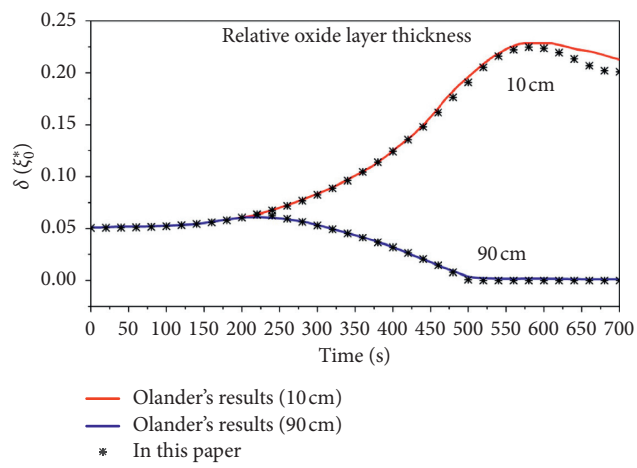

Figure 4: Comparison of fractional oxide layer thickness in cladding.

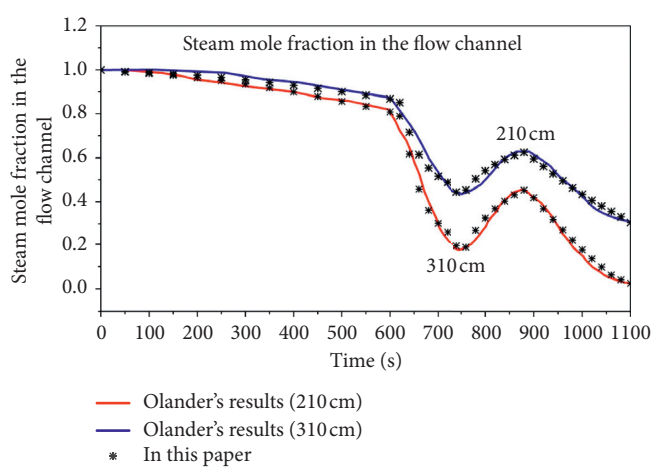

Figure 5: Comparison of steam mole fractions in the flow channel.

It can be seen from Figures 3–6 that the calculation results in this paper are consistent with the results of Olander, whether it is steam-rich or steam-starved. Then the

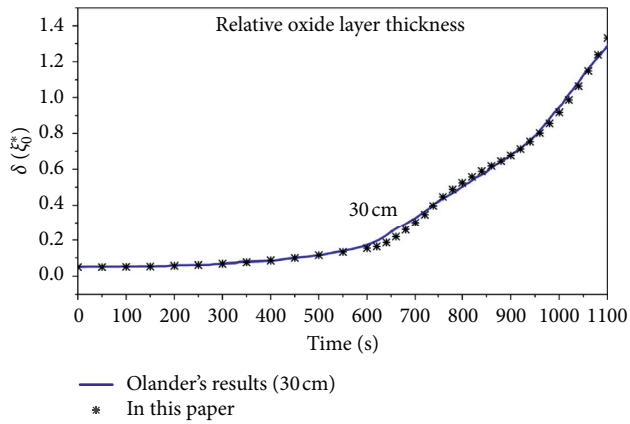

Figure 6: Comparison of fractional oxide layer thickness in cladding.

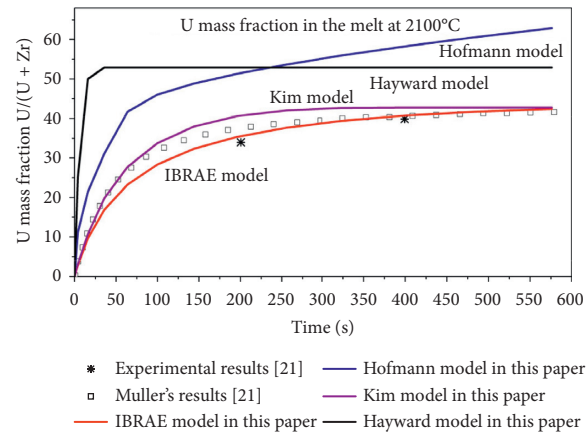

Figure 7: U mass fraction in the melt changes with time at 2100°C.

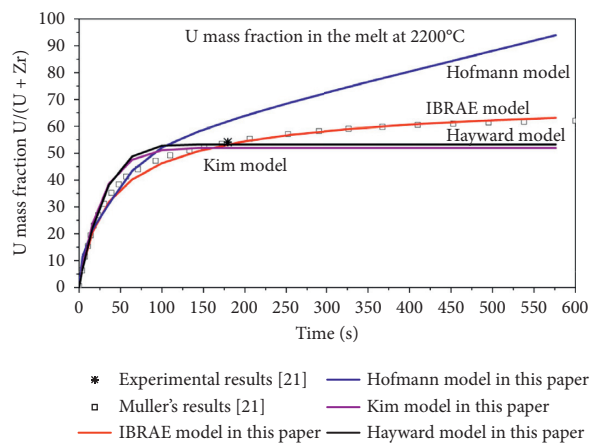

Figure 8: U mass fraction in the melt changes with time at 2200°C.

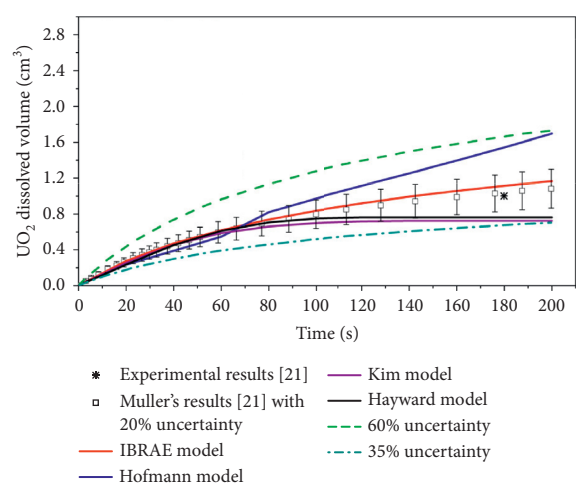

Figure 9: Comparison of dissolved UO_2 volume for different models at 2200°C.

rationality of the oxidation model in this paper can be verified.

4.2. Dissolution of UO_2 and ZrO_2. RIAR test [20] is used to verify physical models for the simultaneous dissolution of UO_2 and ZrO_2 and perform the uncertainty analysis.

Figures 7 and 8 show the U mass fraction in the (U, Zr, O) mixture calculated by different models compared with experimental values and Muller's simulation results [20]. Since there is no limit on the solubility, the solid UO_2 is continuously dissolved by the molten mixture, which causes the U mass fraction in the melt to increase approximately linearly with time in the Hofmann model. But in Kim and Hayward models, the dissolution of UO_2 is limited by its solubility in the (U, Zr, O) mixture. It can be inferred from the ternary phase diagram that there is a competition between UO_2 dissolution and ZrO_2 dissolution. It means that the solubility of UO_2 is reduced due to the dissolution of ZrO_2. In the simulation with Kim and Hayward models at 2200°C, the dissolution rate of ZrO_2 calculated by Hofmann parabolic correlation is overpredicted. Excessive and rapid dissolution of ZrO_2 makes the U in the mixture quickly reach saturation, thereby reducing the volume of solid UO_2 dissolved. In the IBRAE model, the simultaneous dissolution of ZrO_2 and UO_2 is characterized by a complete mathematical model instead of the experimental correlations. The results calculated by the IBRAE model in this paper are in agreement with Muller's results and experimental values.

Muller's results are considered as a reference to perform uncertainty analysis. Dissolved volumes of UO_2 and ZrO_2 at 2200°C are presented in Figures 9 and 10, respectively. Within 100 s after the occurrence of UO_2 dissolution, dissolved volumes of UO_2 calculated by each model are approximately consistent, during which the maximum uncertainty range does not exceed 20%. Then, due to the premature saturation of U in the melt, the dissolution of UO_2 in Hayward and Kim models is ceased with 35% uncertainty at 200 s. However, because of no limit on solubility and high dissolution rate, the volume of UO_2 dissolved using the Hofmann model is maximum and with the uncertainty of 60% at 200 s. As shown in Figure 10, the uncertainty of ZrO_2 dissolved volume is close to 300%. The calculated volumes of ZrO_2 dissolved by Kim, Hayward, and Hofmann models are considerably different from

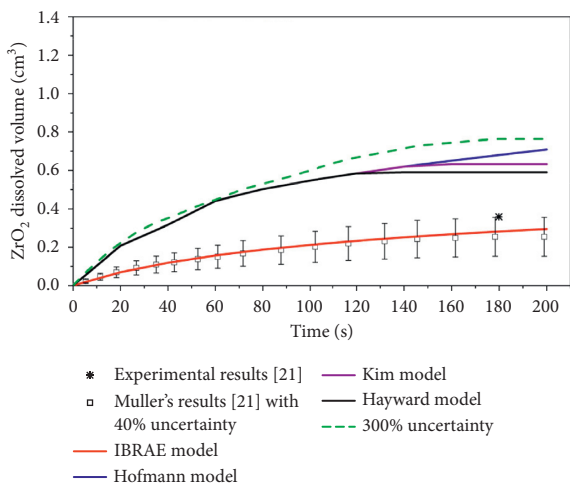

Figure 10: Comparison of dissolved ZrO_2 volume for different models at 2200°C.

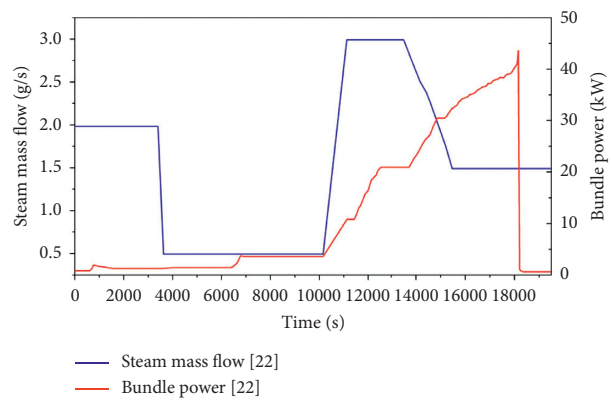

Figure 11: Bundle power and steam flow rate in Phebus FPT0.

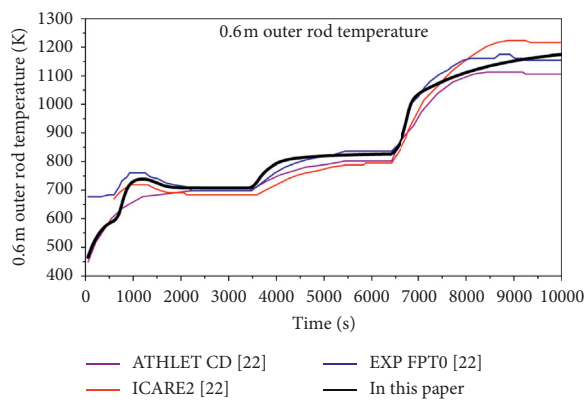

Figure 12: Variation of outer ring fuel rod temperature at 0.6 m.

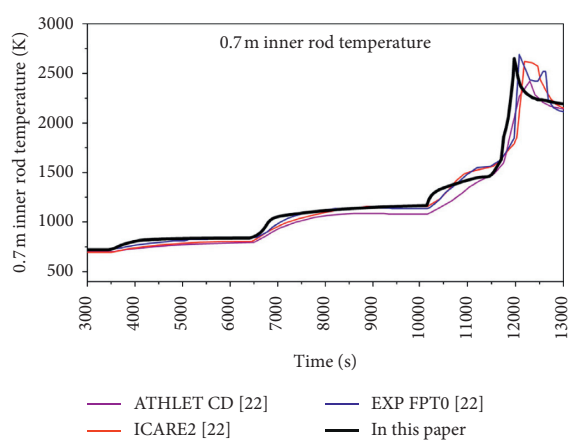

Figure 13: Variation of inner ring fuel rod temperature at 0.7 m.

Muller's results, which can be explained by the over-predicted dissolution rate of ZrO_2 caused by the Hofmann correlation. Therefore, it can be inferred that since the dissolution rate of ZrO_2 is high but the dissolution rate of UO_2 is low for Hayward and Kim models, it may cause the failure time of the cladding oxide layer to be advanced while the mass of UO_2 dissolved at this stage is under-estimated. On the contrary, it will overestimate the volume of UO_2 dissolved by using the Hofmann model, which is suitable for conservative calculations.

In severe accidents, the dissolution of UO_2 by molten zirconium is usually accompanied by cladding oxidation. In the steam-rich case, the zirconium cladding may be completely oxidized to ZrO_2. The increase of oxygen content in the (U, Zr, O) mixture will greatly reduce the solubility of U. Therefore, only when the temperatures of UO_2 and ZrO_2 exceed the melting point or reach the eutectic temperature, UO_2 and ZrO_2 can relocate to the bottom of the core as corium. But in the steam-starved condition, the zirconium water reaction occurs but is not intense, forming a thin ZrO_2 oxide layer on the outside of cladding. In this case, the molten zirconium dissolves UO_2 inward and dissolves ZrO_2 outward. As a result, some of the fuel pellets melt at the temperature far below its melting point. The dissolved UO_2 is relocated downward in the form of (U, Zr, O) mixture, while the undissolved UO_2 in the same pellet collapses in the form of debris. Therefore, the temperature corresponding to the meltdown of core is greatly reduced.

5. Integral Effect Validation

In-pile experiments Phebus FPT provide a reliable benchmark for numerical simulation of the core degradation process. In this paper, the integral effect of the core early degradation phase is verified by Phebus FPT0 experiment [21, 22]. The input bundle power and steam flow rate are shown in Figure 11. Considering the pressure tube is immersed in circulating cooling water with temperature 438 K, the temperature of the outer surface of the pressure tube is approximately supposed as 438 K.

Figure 12 shows the comparison of temperature at 0.6 m in the calibration phase (0~10000 s) between the simulation results of this paper, ATHLET CD, and ICARE2 as well as experimental values. In this period, due to the increase in power and the decrease in steam flow, the temperature variation of fuel rods can be divided into three rising stages

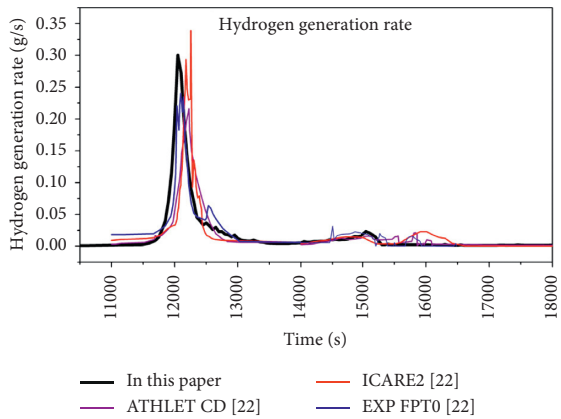

Figure 14: Hydrogen generation rate.

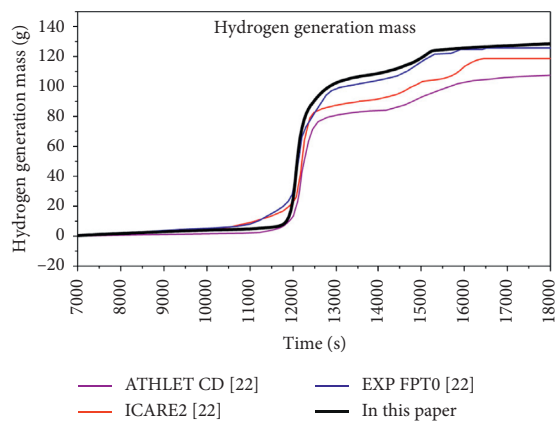

Figure 15: Cumulative hydrogen generation mass.

and three platform stages. It can be seen from Figure 13 that the temperature of the fuel rod at 0.7 m increases sharply at around 12000 s. This period is so-called oxidation escalation phase (10000~13000 s), during which the power of the bundle increases causing the temperature of the bundle rises again. After the cladding temperature exceeds 1500 K, cladding oxidation becomes significant, generating a large amount of heat and hydrogen. Figures 14 and 15 show the hydrogen generation rate and the cumulative hydrogen generation mass, respectively. The hydrogen generated mass calculated in this paper during this period is 90.83 g, which is close to the experimental value 85 g. Figure 16 presents the variation of temperature at 0.6 m in the corium relocation phase (13000 s~18000 s). The distribution of temperature along the height throughout the simulation is shown in Figure 17.

Figures 13 and 16 show that the maximum temperatures at 0.6 m and 0.7 m exceed 2500 K in the oxidation escalation phase, while the maximum temperature at 0.8 m is only 2250 K, as shown in Figure 18. It can be explained that in this phase, massive steam consumed in the middle and lower regions of the bundle causes a short period of steam starved in the upper region, as shown in Figure 19. In the steam-starved case, it is assumed in the calculation that

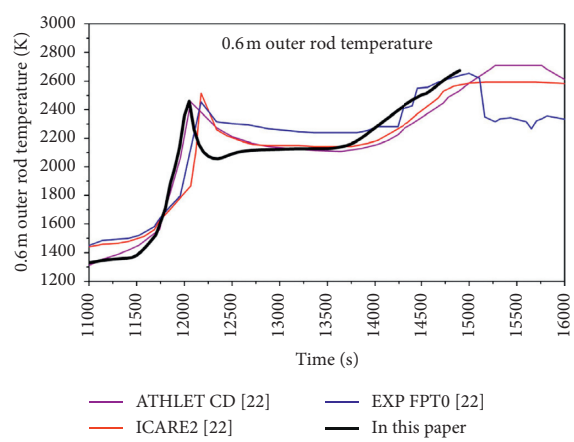

Figure 16: Variation of outer ring fuel rod temperature at 0.6 m.

once the temperature of fuel rods exceeds the α-Zr(O) melting point (2248 K) and oxide layer thickness is less than 300 μm, the cladding oxide layer will fail and the previous hold-up (U, Zr, O) melt will relocate downwards. As presented in Figure 17, some dissolved fuel pellets begin to relocate downward after 11970 s, which is quite in agreement with the experimental value 12050 s. Based on the simulation results, it can be inferred

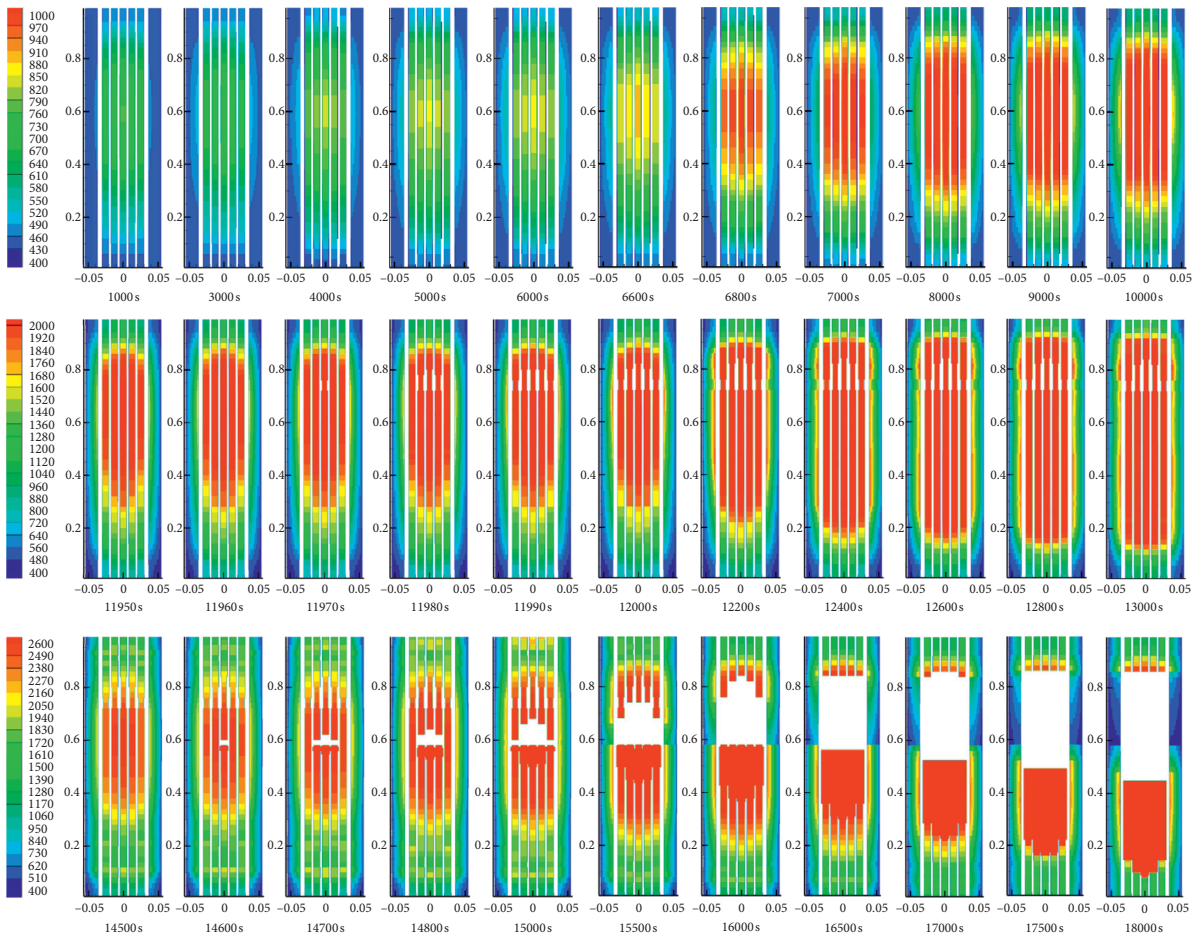

Figure 17: Temperature distribution along the height.

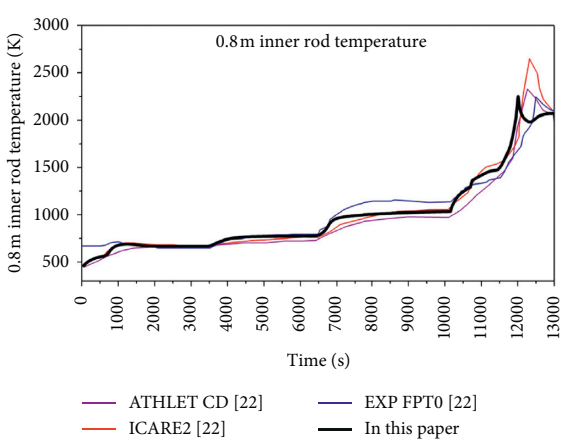

Figure 18: Variation of inner ring fuel rod temperature at 0.8 m.

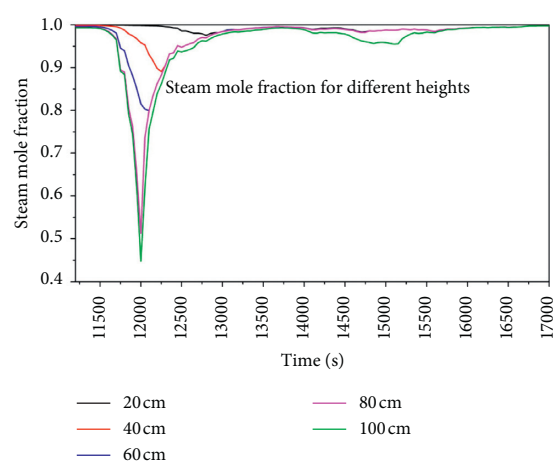

Figure 19: Variation of steam mole fraction at different heights.

that the reason for rapid accident process of LBLOCA may be not resulted from the fuel rapidly rising to its melting point due to lack of cooling, but a large scale of cladding melts, forming a molten metal pool in the flow channel, and dissolving the adjacent fuel pellets, causing the fuel to melt down at much lower temperatures compared with its melting point 3113 K.

6. Conclusions

In this paper, based on the detailed analysis of the mechanism of controlling phenomena in the early phase of core degradation, fine models at the fuel pin level are established in 3D and programed by Fortran to calculate (1)

core heating up, (2) zirconium cladding oxidation, (3) dissolution reaction between molten zirconium and fuel pellets, and (4) formation of molten pool in the core active section.

Analysis of dissolution models shows that there is a considerable uncertainty in the Hofmann ZrO_2 dissolution correlation, which may cause the failure time of the cladding oxide layer to be advanced while the mass of UO_2 dissolved is underestimated by using Kim or Hayward models. According to the simulation results of Phebus FPT0, it can be inferred that the dissolution reaction between the molten zirconium and fuel pellets is the main reason for the melting of UO_2 at low temperatures. In the steam-starved case, part of the fuel pellets can melt down even at 2248 K and relocate to the bottom of the core, which is much lower than the melting point of UO_2.

Nomenclature

A: Area
B: Bulk
$\bar{c}$: Average oxygen content in the metal layer
C: Mass fraction
c_p: Specific heat
D: Diffusion coefficient
E: Parameter to solve oxygen content
G^{-1}: Pilling–Bedworth ratio of ZrO_2
h: Convective heat transfer coefficient
I: Interface
J: Effective radiation
k: Mass transfer coefficient
p: Pressure
q: Heat flux density
Q: Heat generation rate
r: Radius
R: Universal gas constant
$\dot{S}$: Volumetric heat generation rate
t: Time
T: Temperature
V: Volume
y: Mole fraction of steam in mixed gas
z: Axial height
δ: Thickness of oxide layer
ε: Surface emissivity
λ: Thermal conductivity
ξ: Thickness of remaining metal
ρ: Density
σ: Stefan–Boltzmann constant.

Subscripts

ch: Flow channel
cl: Cladding
d: Diffusion
g: Gas
i: Node i
mp: Molten pool
o: Oxygen
ox: Oxidation
r: Radial direction
rad: Radiation
tot: Total
z: Axial direction.

Superscripts

n: Time step n
S: Saturation.

Data Availability

The data used to support the findings of this study are included within the article.

Conflicts of Interest

The authors declare that there are no conflicts of interest regarding the publication of this article.

Acknowledgments

This work was supported by the project National Key R&D Program of China (Grant no. 2018YFB1900100).

References

[1] L. U. O. Bang-Qi and J. Lin, "Severe accident mitigation measure and severe accident sequence of CPRl000 nuclear power plant," *Nuclear Power Engineering*, vol. 31, no. s1, pp. 1–3, 2010.

[2] G. Schanz, B. Adroguer, and A. Volchek, "Advanced treatment of zircaloy cladding high-temperature oxidation in severe accident code calculations," *Nuclear Engineering & Design*, vol. 232, no. 1, pp. 85–96, 2004.

[3] V. F. Urbanic and T. R. Heidrick, "High-temperature oxidation of zircaloy-2 and zircaloy-4 in steam," *Journal of Nuclear Materials*, vol. 75, no. 2, pp. 251–261, 1978.

[4] J. T. Prater and E. L. Courtright, *Properties of Reactor Fuel Rod Materials at High Temperatures, NUREG/CR-4891, PNL-6164*, Pacific Northwest Laboratory, Richland, WA, USA, 1987.

[5] S. Leistkow and G. Schanz, "Oxidation kinetics and related phenomena of Zircaloy-4 fuel cladding exposed to high temperature steam and hydrogen-steam mixtures under PWR accident conditions," *Nuclear Engineering and Design*, vol. 103, no. 1, pp. 65–84, 1987.

[6] O. De Luze, T. Haste, M. Barrachin, and G. Repetto, "Early phase fuel degradation in Phébus FP: initiating phenomena of degradation in fuel bundle tests," *Annals of Nuclear Energy*, vol. 61, pp. 23–35, 2013.

[7] P. Hofmann, G. Schanz, and A. Skokan, *Chemical Interactions of Reactor Core Materials up to Very High Temperatures (KfK-4485)*, Forschungszentrum Karlsruhe, Karlsruhe, Germany, 1989.

[8] P. J. Hayward and I. M. George, "Dissolution of UO_2 in molten zircaloy-4 part 3: solubility from 2000 to 2500°C," *Journal of Nuclear Materials*, vol. 232, no. 1, pp. 1–12, 1996.

[9] K. T. Kim and D. R. Olander, "Dissolution of uranium dioxide by molten zircaloy," *Journal of Nuclear Materials*, vol. 154, no. 1, pp. 102–115, 1988.

[10] P. J. Hayward and I. M. George, "Dissolution of ZrO_2 in molten zircaloy-4," *Journal of Nuclear Materials*, vol. 265, no. 1-2, pp. 69–77, 1999.

[11] R. O. Gauntt, R. K. Cole, C. M. Erickson et al., *MELCOR Code Manual-Version 1.8.6, USNRC NUREC/CR 6119 Rev. 3, SAND2005-5713*, Sandia National Laboratoires, Albuquerque, CA, USA, 2001.

[12] NRC, *RELAP5/RELAP5/MOD3 Code Manual, Volume V: Assessment of Modeling of Reactor Core Behavior during Severe Accidents (NUREG/CR-6150)*, Idaho National Engineering and Environment Laboratory, Idaho Falls, ID, USA, 2001.

[13] O. Coindreau, "ASTEC V2.1: physical modelling of the ICARE module," IRSN, Fontenay-aux-Roses, France, PSN-RES/SAG/2016-00422, 2017.

[14] D. R. Olander, "Interpretation of laboratory crucible experiments on UO_2 dissolution by liquid zirconium," *Journal of Nuclear Materials*, vol. 224, no. 3, pp. 254–265, 1995.

[15] M. S. Veshchunov and A. V. Palagin, "Modeling of chemical interactions of fuel rod materials at high temperatures II. Investigation of downward relocation of molten materials," *Journal of Nuclear Materials*, vol. 252, no. 1-2, pp. 110–120, 1998.

[16] D. R. Olander, "Materials chemistry and transport modeling for severe accident analyses in light-water reactors I: external cladding oxidation," *Nuclear Engineering and Design*, vol. 148, no. 2-3, pp. 253–271, 1994.

[17] P. J. Hayward and I. M. George, "Dissolution of UO_2 in molten zircaloy-4 part 1: solubility from 2000 to 2200°C," *Journal of Nuclear Materials*, vol. 208, no. 1-2, pp. 35–42, 1994.

[18] M. S. Veshchunov, A. V. Boldyrev, V. E. Shestak, and K. Mueller, "Analysis of molten pool physico-chemical interactions and interpretation of the Phebus FP tests observations," *Nuclear Engineering and Design*, vol. 238, no. 7, pp. 1728–1742, 2008.

[19] M. S. Veshchunov, K. Mueller, and A. V. Berdyshev, "Molten corium oxidation model," *Nuclear Engineering and Design*, vol. 235, no. 22, pp. 2431–2450, 2005.

[20] K. Müller, A. Goryachev, V. Smirnov et al., *Simultaneous Dissolution of UO_2 and ZrO_2 by Molten Zircaloy. New Experiments and Modelling (FZKA-6947)*, Forschungszentrum Karlsruhe, Karlsruhe, Germany, 2004.

[21] K. Müller, B. Toth, M. S. Veshunov et al., *Final Interpretation Report of the PHEBUS Test FPT0: Bundle Aspects*, European Commission 6th Euratom Framework Programme, JRC, Brussels, Belgium, 2007.

[22] B. Clément, N. Hanniet-Girault, G. Repetto et al., "LWR severe accident simulation: synthesis of the results and interpretation of the first Phebus FP experiment FPT0," *Nuclear Engineering and Design*, vol. 226, no. 1, pp. 5–82, 2003.

Hindawi
Science and Technology of Nuclear Installations
Volume 2020, Article ID 7526864, 18 pages
https://doi.org/10.1155/2020/7526864

Research Article

Best-Estimate Plus Uncertainty Framework for Multiscale, Multiphysics Light Water Reactor Core Analysis

Jason Hou, Maria Avramova, and Kostadin Ivanov

Department of Nuclear Engineering, North Carolina State University, Raleigh, NC 27695, USA

Correspondence should be addressed to Jason Hou; jason.hou@ncsu.edu

Received 27 December 2019; Accepted 25 February 2020; Published 31 July 2020

Academic Editor: Iztok Tiselj

Tremendous work has been done in the Light Water Reactor (LWR) Modelling and Simulation (M&S) uncertainty quantification (UQ) within the framework of the Organization for Economic Cooperation and Development (OECD)/Nuclear Energy Agency (NEA) LWR Uncertainty Analysis in Modelling (UAM) benchmark, which aims to investigate the uncertainty propagation in all M&S stages of the LWRs and to guide uncertainty and sensitivity analysis methodology development. The Best-Estimate Plus Uncertainty (BEPU) methodologies have been developed and implemented within the framework of the LWR UAM benchmark to provide a realistic predictive simulation capability without compromising the safety margins. This paper describes the current status of the methodological development, assessment, and integration of the BEPU methodology to facilitate the multiscale, multiphysics LWR core analysis. The comparative analysis of the results in the stand-alone multiscale neutronics phase (Phase I) is first reported for understanding the general trend of the uncertainty of core parameters due to the nuclear data uncertainty. It was found that the predicted uncertainty of the system eigenvalue is highly dependent on the choice of the covariance libraries used in the UQ process and is less sensitive to the solution method, nuclear data library, and UQ method. High-to-Low (Hi2Lo) model information approaches for multiscale M&S are introduced for the core single physics phase (Phase II). In this phase, the other physics (fuel and moderator), providing feedback to neutronics M&S in a LWR core, and time-dependent phenomena are considered. Phase II is focused on uncertainty propagation in single physics models which are components of the LWR core coupled multiphysics calculations. The paper discusses the link and interactions between Phase II to the multiphysics core and system phase (Phase III), that is, the link between uncertainty propagation in single physics on local scale and multiphysics uncertainty propagation on the core scale. Particularly, the consistency in uncertainty assessment between higher-fidelity models implemented in fuel performance codes and the rather simplified models implemented in thermal-hydraulics codes, to be used for coupling with neutronics in Phase III is presented. Similarly, the uncertainty quantification on thermal-hydraulic models is established on a relatively small scale, while these results will be used in Phase III at the core scale, sometimes with different codes or models. Lastly, the up-to-date UQ method for the coupled multiphysics core calculation in Phase III is presented, focusing on the core equilibrium cycle depletion calculation with associated uncertainties.

1. Introduction

The sensitivity analysis (SA) and uncertainty quantification (UQ) have been integrated into the nuclear reactor design and safety analysis to establish the accuracy and confidence bounds for best-estimate modelling and simulation codes. Traditional approach for nuclear reactor safety involved deliberately pessimistic hypotheses in computations to satisfy required safety margins; however, this approach usually tends to produce excessive conservatisms. In recent years, the accuracy of the computational codes has been improving with the use of more realistic models and hypotheses as well as increased computation resources. The best-estimate approach, typically accompanied with confidence bounds obtained from uncertainty analysis, is regarded in both nuclear industries and regulation as an acceptable alternative to the traditional conservative regulation approach. The Organization for Economic Cooperation and Development (OECD)/Nuclear Energy Agency (NEA) benchmark for Uncertainty Analysis in Modelling

(UAM) of Light Water Reactors (LWRs) (known as the LWR UAM benchmark) has been established for over a decade to facilitate the development, assessment, integration, and validation of available SA and UQ methods for best-estimate LWR design and safety calculations, which are currently used in the nuclear power generation industry and regulation. Three main domains of nuclear reactor engineering, corresponding to the three major physics phenomena in reactor systems, are considered in the benchmark, namely, the neutronics, thermal-hydraulics, and fuel thermal/mechanical behaviour.

The benchmark first defines several exercises by subdividing the complex LWR systems into smaller problems with varying scales (corresponding to a pin cell, assembly, and core geometry model), each of which will contribute to the total uncertainty of the final coupled system calculation with assumptions made at each geometric level well identified. The uncertainties of the resulting LWR system calculations are determined for each step and are then propagated through an integral LWR system Modelling and Simulation (M&S) for which high quality plant experimental data exist. The benchmark is being carried out in three phases, namely, the neutronics, core, and system phases [1–3]. Three major LWR types are selected based on previous benchmark experience and available data: Pressurized Water Reactor (PWR), Boiling Water Reactor (BWR), and Russian design of PWR (VVER). For each exercise, several test problems are considered in order to cover the different situation targets: reactor types, normal operation conditions, and accidental transients. Significant amount of research and development has been accomplished since the beginning of the LWR UAM benchmark. This paper summarizes the current status of the method development and implementation with a focus on the PWR test cases due to the page limit.

The rest of the paper is organized as the following: Section 2 provides an overview of the two classes of UQ methods that have been developed and applied to the benchmark exercises, as well as the specification of TMI-1 reactor related test cases. Section 3 summarizes one of the concluding activities of the stand-alone neutronics phase (Phase I), that is, the comparative analysis of the results submitted for PWR related cases for understanding the general trend of the uncertainty of core parameters due to the nuclear data uncertainty. The UQ methodologies developed for the core single physics phase (Phase II) are discussed in Section 4, primarily focusing on thermal-hydraulics and fuel M&S. Special attention is given to the link and interactions between Phase II and the multiphysics core and system phase (Phase III), that is, the link between uncertainty propagation in single physics on local scale and multiphysics uncertainty propagation on the core scale. Section 5 presents the current status of the uncertainty propagation and quantification method development for the multiphysics coupled PWR core simulation. Last, the general conclusion of the study and future work are provided in Section 6.

2. Uncertainty Quantification Methodologies

2.1. Sources of Uncertainties. In principle, the sources of input uncertainties in computer code simulations include data uncertainties (e.g., nuclear data, geometry, and materials (manufacturing or technological uncertainties)); uncertainties in physical models and numerical methods (e.g., approximations in the numerical solution, nodalization, homogenisation approaches); and uncertainties due to the imperfect knowledge of boundary and initial conditions. Input uncertainties are defined for each exercise as a combination of new uncertainties and the ones propagated from previous exercises.

2.2. Uncertainty Quantification Methodologies. In general, two sets of uncertainty quantification (UQ) methods were pursued by the participants in the LWR UAM benchmark, namely, the deterministic and stochastic methods.

The deterministic method calculates the sensitivity of the system response R with respect to uncertain input parameter σ using Perturbation Theory (PT) and computes an estimate for the covariance matrix $\mathrm{Cov}[R]$ by linearizing the response $R \approx S\sigma$. Here, S is the response vector sensitivity matrix. With the linearization, the covariance matrix can be calculated by folding sensitivities with the Variance and Covariance Matrix (VCM) of input parameters:

$$\mathrm{Cov}[R] \approx \mathrm{Cov}[S\sigma] = S\mathrm{Cov}[\sigma]S^T, \tag{1}$$

where $\mathrm{Cov}[\sigma]$ denotes the VCM of the input parameter σ. Equation (1) is known as the first-order uncertainty propagation formula or the so-called "Sandwich rule" [4]. The sensitivity matrix can be calculated using various codes and an example is given in [5].

The sampling method relies on the sampling of the uncertain input parameters provided in the VCM and statistically analyses the calculated output responses. The variance is computed using

$$\mathrm{Var}[R] = \frac{\sum_{i=1}^{N_s} (R_i - \overline{R})^2}{N_s - 1}, \tag{2}$$

where N_s is the number of samples and $\overline{R}$ is the sample mean of the response. Examples of the implementation of the statistical sampling can be found in [6, 7].

The potential difference between the calculated uncertainty using deterministic and sampling methods can often be justified by the relative confidence intervals, which is related to the sampling approach. For a given sample size, the confidence bounds of uncertainties of core output responses could be quantified if normality assumption is valid. If a simple random sample size N is obtained from a normally distributed population with true mean μ and true standard deviation σ_{true}, then the following constructed parameter χ^2 follows a chi-square distribution with $N-1$ degree of freedom:

$$\chi^2 = \frac{(N-1)\sigma_p^2}{\sigma_{\mathrm{true}}^2}, \tag{3}$$

where σ_p^2 is the sample variance. For a two-sided uncertain parameter, the criterion of 95% confidence level indicates that 95% of the χ^2 value is bounded inside the interval of $[\chi^2_{1-\alpha/2}, \chi^2_{\alpha/2}]$. The confidence interval of the standard deviation σ_{true} can be derived as

$$\frac{(N-1)\sigma_p^2}{\chi^2_{\alpha/2}} < \sigma^2_{\text{true}} < \frac{(N-1)\sigma_p^2}{\chi^2_{1-\alpha/2}}. \quad (4)$$

Figure 1 shows the upper and lower limit of the 95% and 99% confidence level are depicted as a function of the sample size. For a two-sided distribution, the 95% confidence interval of the χ^2 is evaluated as $[\chi^2_{2.5\%}, \chi^2_{97.5\%}]$, which covers the true variance of R with 95% confidence level. Therefore, the 95%/95% confidence interval of the true uncertainty can be mathematically determined as [90% $\sigma_{p.}$, 113% $\sigma_{p.}$].

2.3. TMI-1 Specification. This paper summarizes the recent advancement in the LWR UAM benchmark, focusing on the PWR exercises based on the Three Mile Island Unit 1 (TMI-1) reactor, which is used as an example to illustrate the developments and implementations performed with the LWR UAM benchmark framework.

The TMI-1 core consists of 177 fuel assemblies, each of which contains 208 fuel rods, 16 guide tubes, and 1 instrumentational tube. There are 11 types of fuel assemblies in the TMI-1 active core with various fuel enrichment (4.00%, 4.40%, 4.85%, 4.95%, and 5.00%) and configurations with regard to the configuration of the burnable poison (BP), gadolinium pins ($GdO_2 + UO_2$), and control rod banks. Figure 2 depicts one octant of the core radial layout, where assembly H8 is located in the core center. Detailed geometry setup, material composition, and enrichment can be obtained from LWR UAM benchmark specifications [1, 3].

3. Uncertainty Propagation in Reactor Physics Simulations

The first phase of the LWR UAM benchmark [1] is dedicated to the stand-alone multiscale neutronics M&S and carried out in three steps, each corresponding to one of the steps of the standard LWR simulation approach: cell physics (to produce multigroup microscopic cross section libraries), lattice physics (to derive multigroup homogenized macroscopic cross section sets), and core physics (to assess full-core performance parameters). The sources of the input uncertainties considered in Phase I exercises include the neutron cross section data, supplemented by the VCMs, and as-built manufacturing uncertainties in material composition and geometric dimensions.

Most participants of the Phase I exercises focused on the quantification and propagation of nuclear data induced uncertainty; thus the VCM is simply the nuclear data covariance information, available either by processing covariance data files provided by major nuclear data libraries (NDLs) or in the SCALE code package [8]. Two SCALE VCMs have been used: the 44-group library distributed with SCALE 6.0 and SCALE 6.1 and the updated library available in SCALE 6.2 which is based on 56-group and 252-group structures [8]. The former contains uncertainty data for 401 materials with important isotopes taken from high-fidelity nuclear data evaluations including ENDF/B-VII.0, ENDF/B-VI, and JENDL-3.3. The latter is based on the EDNF/B-VII.1

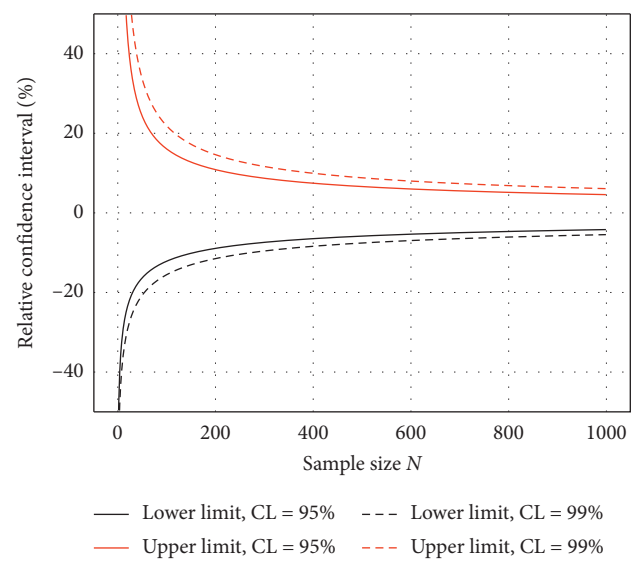

Figure 1: Relative confidence interval for the confidence level of 95% and 99%.

data for 187 nuclides, combined with information of ~215 nuclides from the SCALE 6.1 VCM. Note that in many cases, the SCALE VCMs were transformed into a user specified energy group structure to satisfy the requirement of the neutronics code used in the UQ and propagation process [9]. Table 1 provides a summary of numerical calculations carried out to obtain the results corresponding to the neutronics cases, including the NDL, transport code (solution method), VCM, and UQ method.

3.1. Cell Physics. For each test case in Exercise I-1, the following results are requested from the participants: calculated k-inf and its associated uncertainty, the top five neutron-nuclide reactions that contribute the most uncertainty to k-inf, and covariances of selected one-group cross sections generated in the pin cell calculation.

A two-dimensional (2D) model adopted from the TMI-1 reactor was chosen as the representative PWR test problem. It is fuelled with 4.85% enriched UO_2 fuel, and both Hot Zero Power (HZP) and Hot Full Power (HFP) conditions were specified. In total, 22 sets of results have been submitted for the HZP conditions, from which calculation related information was collected to facilitate the comparative analysis of the results in order to reveal the relation between the choice of calculation parameters (e.g., transport solution method, covariance library, and UQ method) and output uncertainties. Figure 3 shows the predicted k-inf and associated uncertainties. The nominal value of k-inf spans a range of ~1200 pcm, which is believed to be a result of the differences among neutron transport solvers and base nuclear data libraries involved in the calculation and/or potential modelling errors. Further investigation is required to quantify the contributions to this rather large deviation. The averaged nominal value and Relative Standard Deviation (RSD), or $\Delta k/k$, of all predicted k-inf are 1.43019 and 0.52%, respectively.

	8	9	10	11	12	13	14	15
H	4.00 CR(7)	4.95 4Gd + BP	5.00 4Gd CR(2)	4.95 4Gd + BP	4.40 CR(7)	5.00 4Gd + BP	4.85 4Gd CR(6)	4.85 4Gd
K		4.95 4GD CR(2)	4.95 4Gd + BP	4.85 4Gd CR(4)	4.95 4Gd + BP	5.00 4Gd CR(5)	5.00 8Gd	4.95 8Gd
L			4.95 4Gd CR(6)	4.95 4Gd + BP	4.95 4Gd APSR(8)	5.00 4Gd + BP	4.40 CR(1)	4.85 4Gd
M				4.40 CR(5)	4.95 BP	4.95 4Gd CR(3)	5.00 8Gd	
N					5.00 4Gd CR(7)	5.00	4.95 4Gd + BP	
O						5.00 4Gd		
P								
R								

A C –Control rod type and group number
B B –Gd and BP pin configuration
C A –Fuel enrichment, unit: wt.%

Figure 2: A quarter-core representation of TMI-1 reactor.

More detailed analyses were performed to determine the correlation between each of the calculation parameters. The uncertainty of k-inf and the results indicate that the choice of the covariance library strongly impacts the RSD of k-inf, as shown in Figure 4, while other parameters have limited influence. The average RSD of k-inf calculated using the SCALE 6.0/SCALE 6.1 covariance libraries is below 0.5% (0.47% and 0.48%, resp.), while the value corresponding to SCALE 6.2 is 0.54%. Only one dataset each was submitted using the SCALE 5.1 and JENDL-4.0 covariance libraries and the RSDs are ~0.5%. The ENDF/B-VII.1 covariance data yields the highest k-inf RSD of 0.61%, despite the fact that the one dataset with extreme low uncertainty is included. It is difficult to determine the reason of low uncertainties presented in the comparison (e.g., Cases 7 and 13) based on the submitted data, and hence further investigation will be performed.

The trend above can be explained by the difference of the covariance information in various sources. On one hand, the covariance data in the ENDF evaluations are generated as part of the cross section evaluation process and represent uncertainties and correlations in differential data. The use of this covariance to calculate uncertainties for integral quantities such as k-inf will usually result in an overestimation of the uncertainty. On the other hand, a range of different tests, such as the critical benchmark experiments, are performed to investigate and adjust the new covariance data from the NDL before being incorporated into the SCALE covariance libraries [9]. For example, two of the changes that have significant impacts on many experiments are the modifications made to the covariance data for nu-bar (average number of neutrons per fission reaction ν) of ^{235}U and ^{239}Pu, with the first one relevant to the case study shown in this paper. The uncertainty of ^{235}U nu-bar in the thermal range increases from 0.31% in SCALE 6.1 to 0.7% in ENDF/B-VII.1, which is responsible for differences exhibited in the covariance testing in the low-enriched, water moderated uranium oxide pin array (LCT) systems. Consequently, it was reduced to 0.39% in SCALE 6.2 library, which is consistent with the value in JENDL-3.3 [8]. This explains why the calculated RSD of k-inf using SCALE 6.2 data is slightly higher than that using SCALE 6.0/SCALE 6.1, while the value corresponding to ENDF/B-VII.1 is the largest.

It is convenient to use the PT method to compute the sensitivity coefficients of output variables with respect to nuclear data as compared with the sampling approach, thus making it possible to determine the most influential nuclide-reaction pair to the predicted k-inf uncertainties by sorting them from greatest to least variance fraction. For the TMI-1 HZP case, 13 sets of submitted results include such information and Figure 5 shows the occurrence of various nuclide-reaction pairs as the top 5 contributors. Although a certain degree of diversity can be found in the ranking as it includes up to 10 nuclide-reaction pairs, some reactions dominate the contribution to the uncertainty of k-inf, such as ^{238}U capture, ^{235}U nu-bar, and ^{235}U capture.

Table 1: Summary of submitted results of stand-alone neutronics cases.

Case	NDL	Transport code	VCM	UQ method	Contributed cases
1	ENDF/B-VI	SERPENT 2	SCALE 6.0	Deterministic	I-1
2	ENDF/B-VI	MULTICELL	SCALE 5.1	Deterministic	I-1, I-2
3	ENDF/B-VII.0	XSDRNPM	SCALE 6.1	Deterministic	I-1
4	ENDF/B-VI	CASMO-4	SCALE 6.0	Deterministic	I-1, I-2, I-3
5	ENDF/B-VII.0	CASMO-5MX	SCALE 6.0	Sampling	I-1
6	ENDF/B-VII.0	NEWT	SCALE 6.1	Deterministic	I-1, I-2
7	ENDF/B-VII	MCNP5	SCALE 6.0	Deterministic	I-1, I-2
8	ENDF/B-VII.1	Polaris	SCALE 6.2	Sampling	I-1
9	ENDF/B-VII.1	NEWT	SCALE 6.2	Sampling	I-1
10	ENDF/B-VII.0	NEWT	SCALE 6.2	Sampling	I-1
11	JENDL-4.0	CASMO5	JENDL-4.0	Sampling	I-1, I-2, I-3
12	ENDF/B-VII.0	NEWT	ENDF/B-VII.1	Deterministic	I-1
13	ENDF/B-VII.1	McCARD	ENDF/B-VII.1	Deterministic	I-1
14	ENDF/B-VII.1	MCS	ENDF/B-VII.1	Deterministic	I-1
15	ENDF/B-VII.1	MCS	SCALE 6.1	Deterministic	I-1
16	ENDF/B-VII.1	STREAM	SCALE 6.2	Deterministic	I-1
17	ENDF/B-VII.1	STREAM	ENDF/B-VII.1	Deterministic	I-1
18	ENDF/B-VII.1	STREAM	ENDF/B-VII.1	Sampling	I-1
19	ENDF/B-VII.0	NEWT	SCALE 6.1	Deterministic	I-1, I-2
20	ENDF/B-VII.1	NEWT	SCALE 6.2	Deterministic	I-1, I-2
21	ENDF/B-VII.1	HELIOS2	SCALE 6.1	Sampling	I-1, I-2
22	ENDF/B-VII.0	NEWT	SCALE 6.1	Sampling	I-1, I-2
23	ENDF/B-VII.1	NEWT	SCALE 6.2	Sampling	I-1, I-2
24	ENDF/B-VI	NEWT	SCALE 6.1	Deterministic	I-1, I-2
26	ENDF/B-VII.0	NEWT	SCALE 6.2	Sampling	I-2
27	JEFF-3.1.2	WIMS	Mixed[1]	Sampling	I-1
28	ENDF/B-VII.1	NEWT	SCALE 6.2	Sampling	I-2
29	ENDF/B-VII.1	COBAYA	SCALE 6.2	Sampling	I-3
30	ENDF/B-VII.1	NEWT	SCALE 6.2	Sampling	I-3
31	ENDF/B-VI	MGRAC	SCALE 6.1	Sampling	I-3
32	ENDF/B-VII.1	NEWT	SCALE 6.2	Sampling	I-3
33	ENDF/B-VII.2	NEWT	SCALE 6.2	Sampling	I-3
34	ENDF/B-VII.0	RMC	SCALE 6.0	Sampling	I-3
35	ENDF/B-VII.1	Polaris	SCALE 6.2	Sampling	I-3

[1]Covariance data were collected from various sources, including JEFF-3.2, ENDF/B-VII.1, JENDL-4.0, and TENDL-2011.

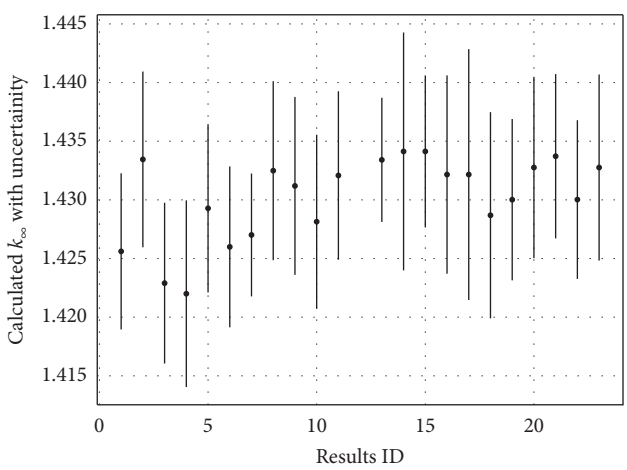

Figure 3: Mean value and uncertainty of calculated k-inf of TMI-1 HZP cell physics case.

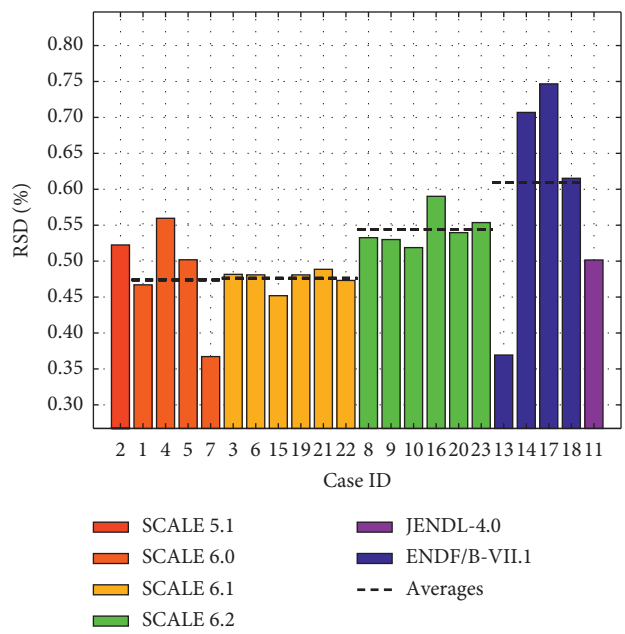

Figure 4: Relative k-inf uncertainty grouped by covariance libraries utilized for TMI-1 HZP cell physics case.

By definition, these main contributors to the uncertainty are identifiable due to (1) the highest sensitivities associated with such reactions, or (2) the highest value of the associated

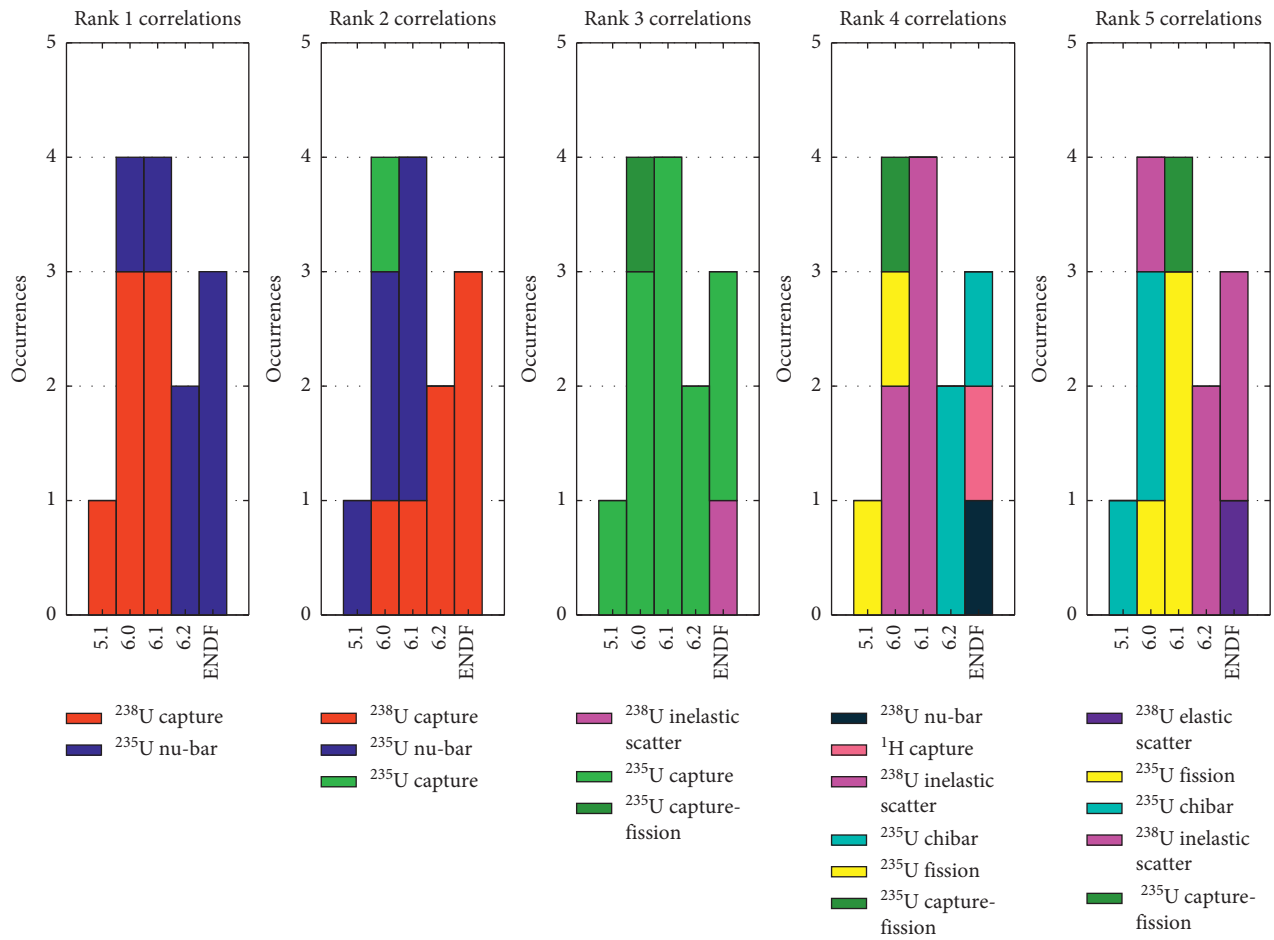

Figure 5: Ranking of the five nuclide-reaction pairs with the highest contribution to the k-inf uncertainty. SX = SCALE X covariance library and E7.1 = ENDF/B-VII.1 covariance library.

covariances, or (3) a combination of both. For example, the *k*-inf is quite sensitive to the ^{238}U capture cross section, especially in the unresolved resonance regions, while the evaluated cross sections exhibit large uncertainties [10]. This is why, on one hand, ^{238}U capture reaction is the predominant component to the total uncertainty when covariance libraries of SCALE 5.1/SCALE 6.0/SCALE 6.1 are utilized. On the other hand, ^{235}U nu-bar tops the ranking if the SCALE 6.2 or ENDF/B-VII.1 covariance libraries are used, which again confirms the evolution of the ^{235}U nu-bar uncertainty as described above. The ^{235}U capture is another important contributor as it almost always ranks the third regardless which covariance library is used. The sensitivity profile of the three most influential nuclide-reaction pairs is depicted in Figure 6. It is worth mentioning that some nuclide-reaction pairs only associate with the ENDF/B-VII.1 covariance library, including the ^{1}H capture, ^{238}U nu-bar, and ^{238}U elastic scattering, which can also be explained by the difference in covariance libraries. For example, the ^{1}H thermal capture in SCALE covariance library is adopted from JENDL 3.3 [11], which is lower than that in ENDF/B-VII.1 by a factor of five.

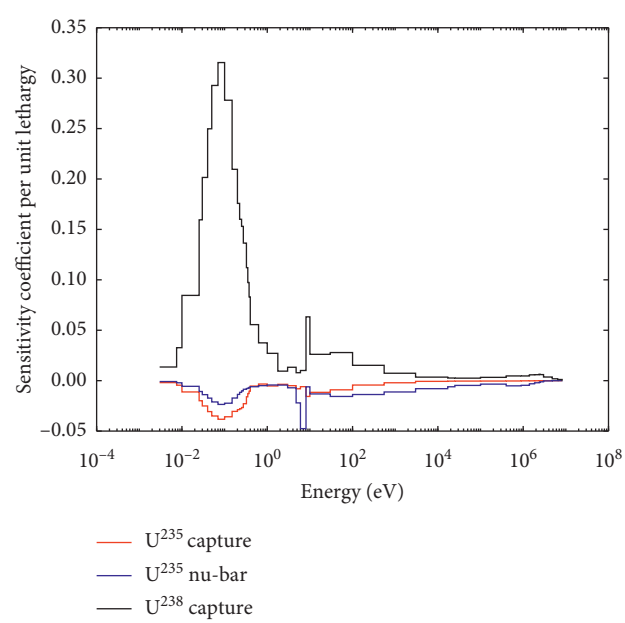

Figure 6: Sensitivity profiles of most important contributor to uncertainty of *k*-inf, PWR pincell case.

3.2. Lattice Physics. The main focus of this exercise is placed on the propagation of nuclear data uncertainties through lattice calculations to the uncertainty of target output variables, primarily the few-group constants (homogenized cross sections and other nodal parameters). The other sources of uncertainty to be considered in this exercise are the uncertainties associated with methods and modelling approximations embedded in the lattice codes.

The PWR lattice model is a 2D fuel assembly of 15×15 rods with 1 central instrumental tube, 16 guide tubes, and 4 corner Godlinia pins containing integral Gd burnable poisons. The case was modelled under both unrodded and rodded conditions at HZP and HFP. There are 12 and 11 sets of results submitted for the HZP unrodded and rodded case, respectively.

Figure 7 compares the predicted *k*-inf uncertainty of the unrodded and rodded lattice, from which it can be seen that the RSD in the unrodded case is slightly lower than that in the rodded case, regardless of the choice of the VCM, mainly due to the higher nominal value of k-inf when the absorber material is absent in the unrodded model. A similar trend of the VCM's influence is observed as in cell physics results; that is, the use of SCALE 6.2 leads to larger predicted uncertainties (after removing one obvious outlier from the results), which is primarily caused by the large uncertainty of the ^{235}U nu-bar.

The uncertainties of the homogenized two-group nu-fission cross sections are compared based on the VCM, as shown in Figure 8. Again, the higher nuclear data uncertainty of the nu-bar reaction in SCALE 6.2 is responsible for the large value of RSD calculated by Case 23. It can also be found that the uncertainty of homogenized nu-fission cross section is more profound in the fast group than the thermal group consistently. For example, the value is ~0.62% in the fast group versus ~0.49% in the thermal group in Case 23. It is known that the ^{235}U nu-bar covariance is lower in the fast and epithermal range than in the thermal energy range in the SCALE 6.2 VCM [8], so are the sensitivity coefficients of system *k*-inf with respect to the ^{235}U nu-bar and fission cross section [12]. The comparison reflects the fact that the nominal value of nu-fission in the thermal group ($0.19\,\mathrm{cm}^{-1}$) is more than 10 times larger than that in the fast ($9.1 \times 10^{-3}\,\mathrm{cm}^{-1}$) group.

The relationship between the *k*-inf, flux, and group constants (cross sections, diffusion coefficients, and assembly discontinuity factors) in the two-group representation can be determined by calculating the correlation coefficients between variables. Selected correlation coefficient matrices are depicted in Figure 9, in which red and blue colours represent positive and negative correlation, respectively, between two parameters, while correlation close to zero, in white, indicates that there is a low correlation.

On one hand, the matrices agree well with each other and similar trend is observed. For example, the fast flux is negatively correlated, and the thermal flux is positively correlated, with Group 1 absorption, scattering, and transport cross sections. A higher positive correlation is found between *k*-inf and Group 2 nu-fission cross section. On the other hand, some unique features are also observed only in one of the cases. Case 12 shows strong cross-correlations between the scattering and transport cross sections of both thermal and fast group. As a result, large correlation coefficients are shown for the total cross section in Groups 1 and 2. In Case 6, the values of *k*-inf related correlation coefficients are generally larger for cross sections and fluxes, as compared with the other three cases. Further investigations are necessary to identify the reason of those features, that is, whether it is associated with the VCM used in the calculation; however, it is expected that the difference will be propagated with the group constants to the core calculation and will affect the uncertainty of the core parameters.

3.3. Core Physics. The uncertainties of the few-group cross sections evaluated in Exercise I-2 are to be propagated through the stand-alone neutronics core calculation in Exercise I-3 to the parameters of interest such as the core *k*-eff and power distribution. Various uncertainty propagation methodologies can be used, as summarized in Table 2 [12]. In the full deterministic approach, the PT calculation is performed at both lattice and core level, and the VCM of the few-group homogenized constants generated in the lattice calculation is used to evaluate the uncertainty of core responses. The one-step approach relies on the stochastic sampling method on both lattice and core levels and is named as such because it involves a one-to-one connection between lattice calculations to generate the few-group cross section library and the core calculation that read this library as input [13]. The two-step approach combines the stochastic sampling and deterministic methods. Detailed explanation and a complete list of references can be found in [12].

It should be noted that all the aforementioned approaches follow the standard reactor simulation procedure, which involves the generation of homogenized constants, simplification of core geometry, and application of lower order solvers such as the nodal diffusion method. The major modelling difference occurs on whether the spatial homogenisation is performed over the assembly or pin cell. Either way, this procedure will inevitably introduce additional discrepancies to the calculated uncertainty of core responses.

The PWR model defined in the core physics is the TMI-1 fresh core at HZP state with all control rods fully inserted. In total, 9 sets of results have been collected. Most results were obtained using the one-step and two-step approaches mentioned above, such as in [14], except for Cases 11 and 35, where the direct full-core transport calculation was performed with explicit modelling of the geometry. The estimated relative uncertainties of the core eigenvalue are shown in Figure 10, and the average value over all 9 sets of results is 0.49%, which is close to the observed values in the pin cell and lattice calculations. Also similar to the previous cases is the dependency of the uncertainty on the VCM choice; that is, the calculation using the SCALE 6.2 VCM tends to yield higher uncertainties compared with other libraries, primarily due to the large uncertainty in the neutron production rate. It should be noted that the input uncertainty in the full-core calculation has a wider spectrum than in the previous steps because of more complicated material compositions (e.g., addition of neutron absorber) and increased approximation to the neutron transport solution.

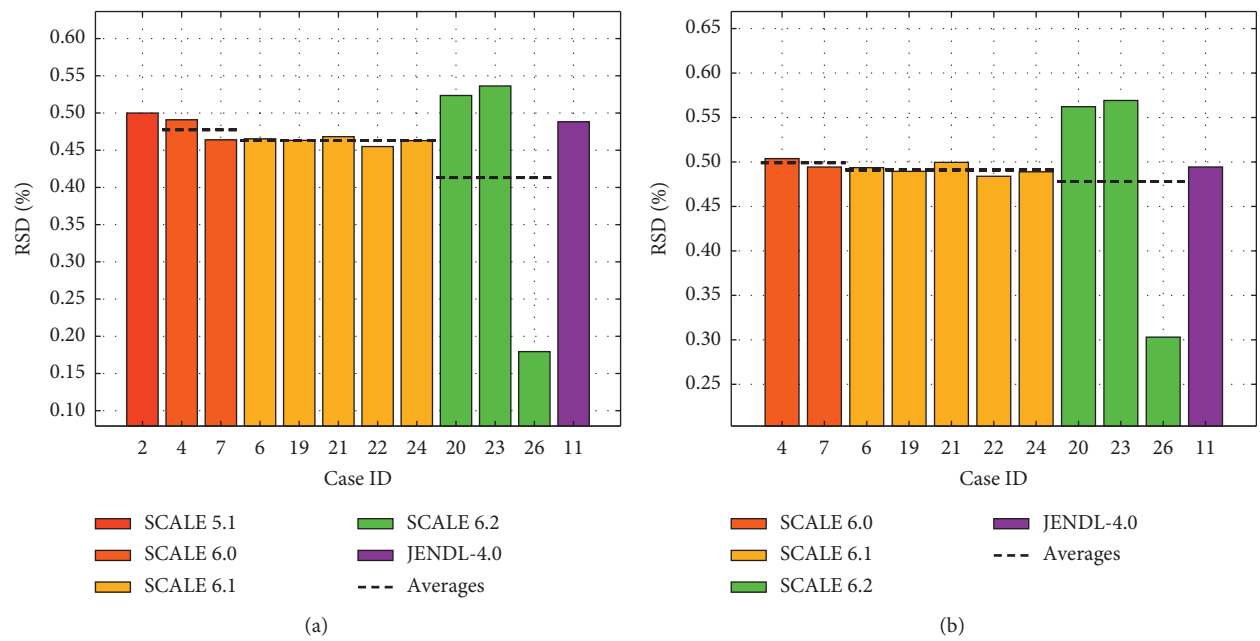

Figure 7: RSD of predicted k-inf at HZP under (a) unrodded and (b) rodded conditions.

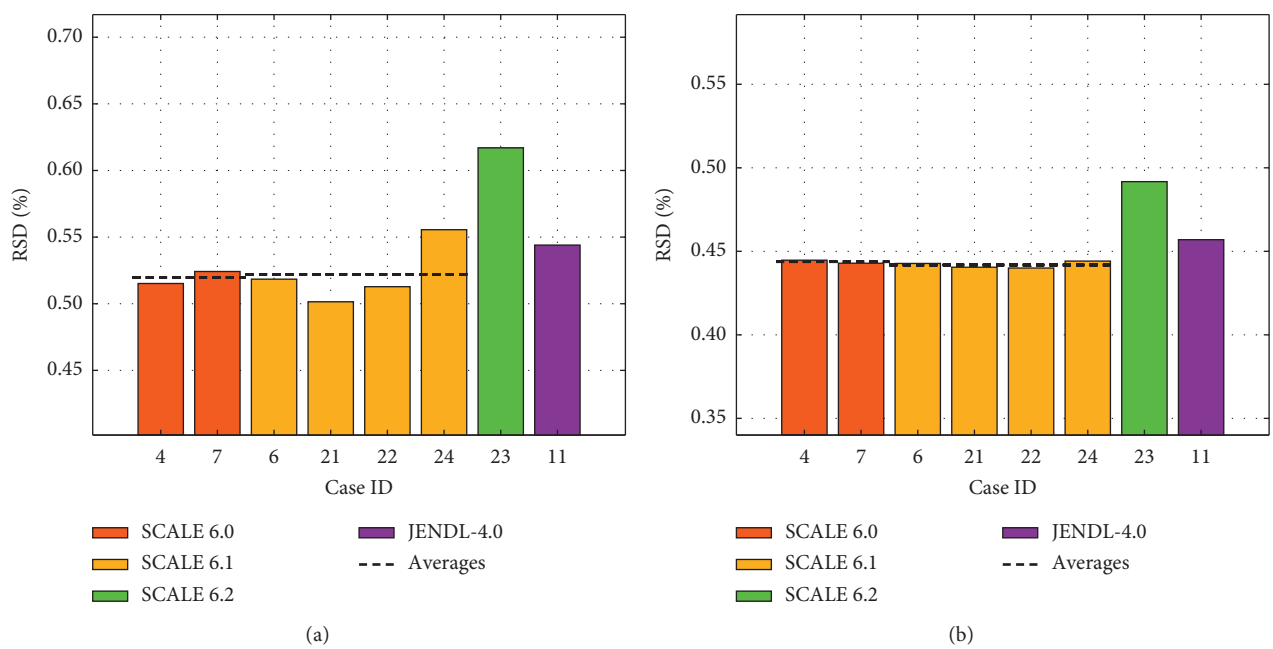

Figure 8: RSD of predicted $\nu\Sigma_f$ cross section for unrodded lattice case: (a) fast group and (b) thermal group.

4. Uncertainty Propagation in Fuel Behaviour and Thermal-Hydraulics Simulations

4.1. Interactions between Multiscale Single Physics and Multiphysics Modelling. In Phase II, the other physics (fuel and moderator), providing feedback in a LWR core, and time-dependent phenomena are considered. Phase II is focused on uncertainty propagation in single physics models which are components of the LWR core coupled multiphysics calculations. Phase III is focused on propagation of multiple uncertainties in coupled multiphysics steady state, cycle depletion, and transient calculations. The interactions between Phase II and Phase III are shown in Figure 11.

Exercise II-2 considers time-dependent neutronics phenomena–depletion (slow time phenomena) and kinetics (fast time phenomena). This exercise develops also methodologies for cross section modelling, that is, for generation of parameterized cross section, kinetics, and other nodal parameters' uncertainty libraries to be used in multiphysics calculations in

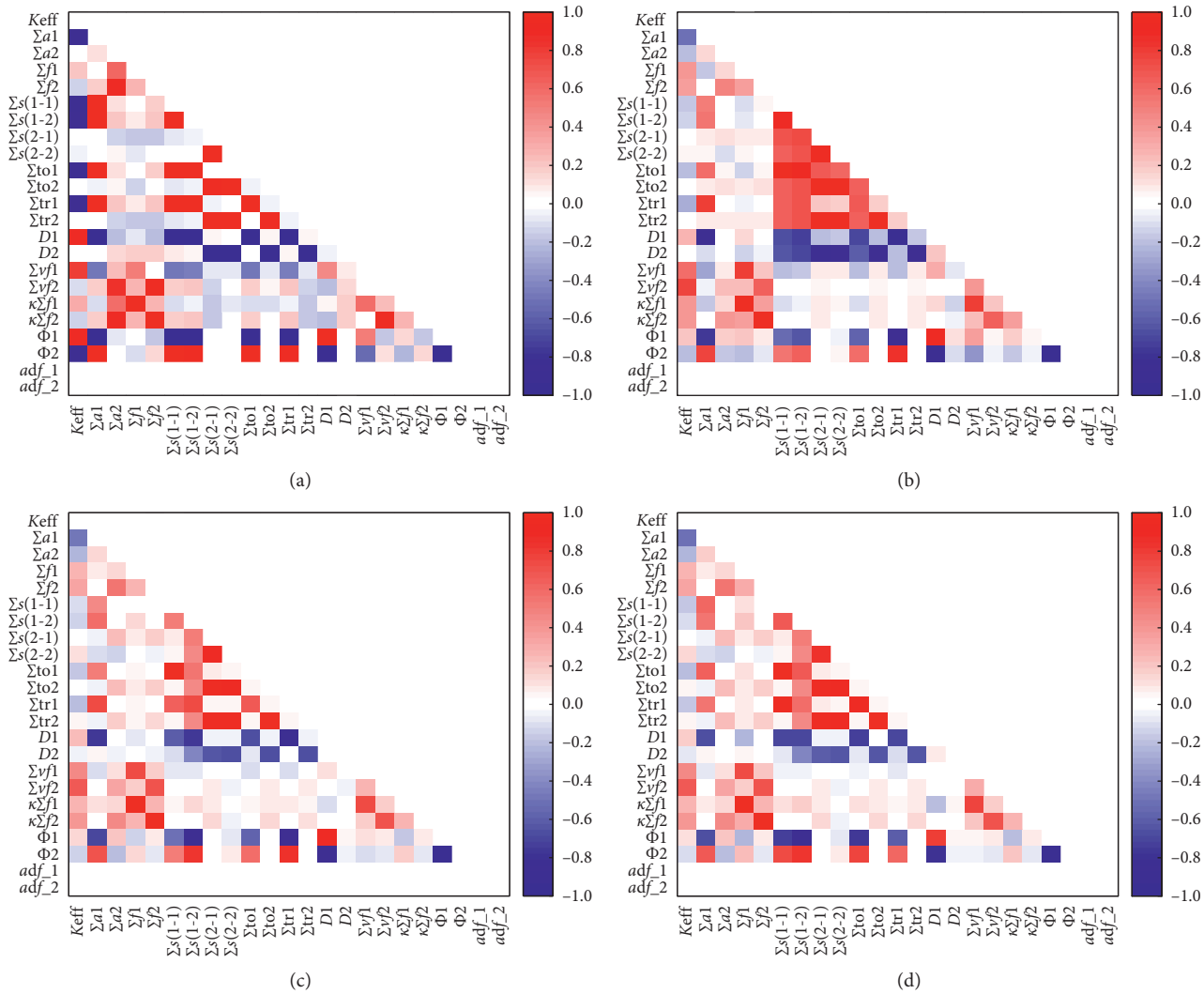

Figure 9: Correlation coefficient matrix of the two-group homogenized cross sections of the unrodded lattice from (a) Case 6, (b) Case 10, (c) Case 11, and (d) Case 12.

Table 2: Uncertainty propagation methodologies in reactor full-core simulations [12].

	Cell/lattice calculation	Intermediate data	Core simulation
Fully deterministic	Deterministic	VCM	Deterministic
One-step	Sampling	Random libraries	Sampling
Two-step	Deterministic	VCM and random libraries	Sampling
	Sampling	VCM	Deterministic

Phase III. Such methodology developed using the Sampler/Polaris sequence of SCALE 6.2.1 [8] is shown in Figure 12.

4.2. Fuel Modelling. Exercise II-1 is dedicated to fuel physics in steady state and transient conditions. The focus is on consistency in uncertainty assessment between fine models implemented in fuel performance codes and the rather simplified lumped models implemented in thermal-hydraulics codes, to be used for coupling with neutronics tools in Phase III [15].

High-fidelity fuel performance codes are used to model a single fuel rod, using detailed technological and operation data (geometry, enrichment, burnup, etc.) and high-fidelity models for fission gas release, cladding corrosion, swelling, and so forth. These codes are used in Exercise II-1, while low-fidelity models, embedded in thermal-hydraulics codes, are usually preferred for full-core computation in Phase III. In this way Exercise II-1 propagates uncertainties in fuel physics consistently using high-fidelity fuel performance codes. The focus is on manufacturing, boundary conditions, and subset of modelling (material properties) uncertainties.

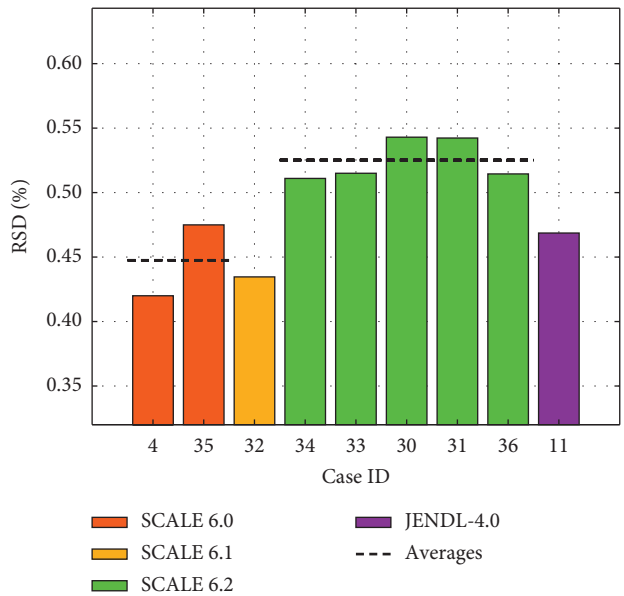

Figure 10: RSD of predicted k-eff of TMI-1 core simulation at HZP.

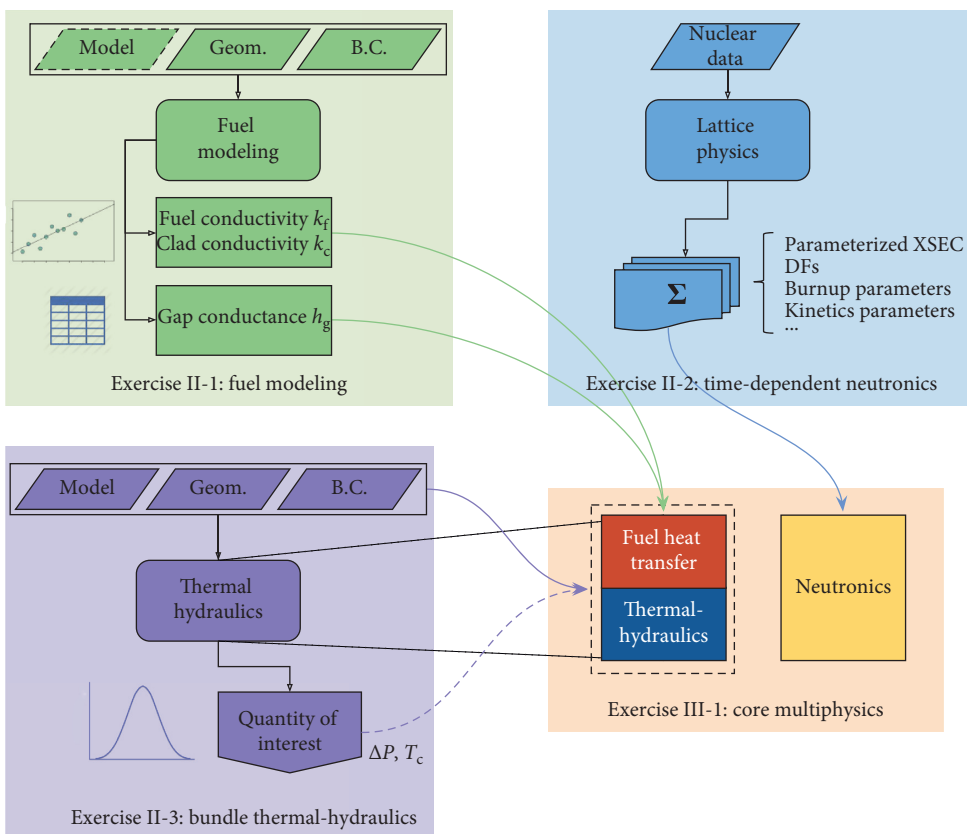

Figure 11: Interactions of Phase II and Phase III of the LWR UAM benchmark.

Figure 13 shows comparisons of benchmark participants' results using high-fidelity fuel performance codes for the PWR depletion test case based on TMI-1 fuel rod design. Exercise II-1 includes also a special test case (modelling of one axial node/rodlet of single pin) to evaluate the capability of simplified lumped fuel rod models of system and sub-channel thermal-hydraulics codes to predict fuel temperature as compared to fuel performance codes.

The so-called Doppler temperature is the main fuel physical feedback quantity used in full-core coupled

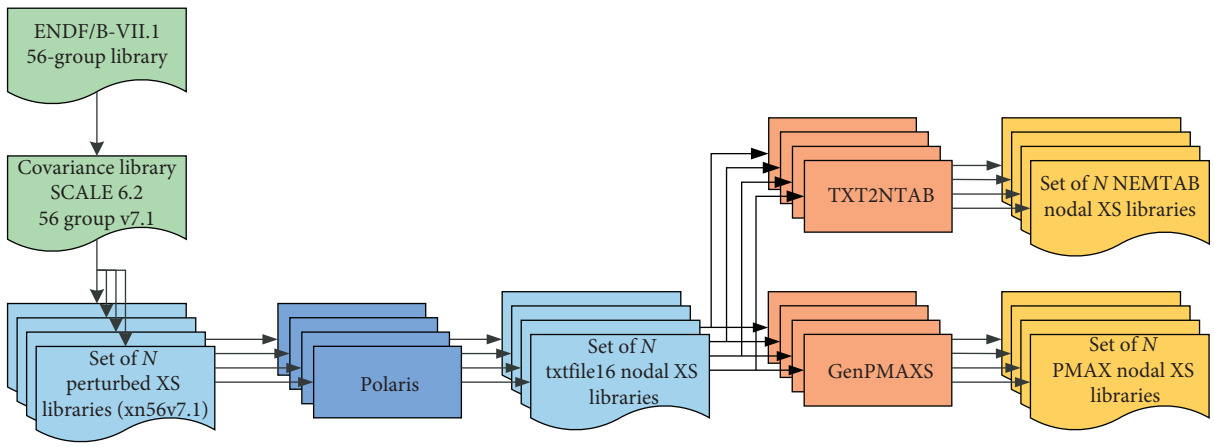

Figure 12: Process of generation of parameterized cross section libraries plus uncertainties.

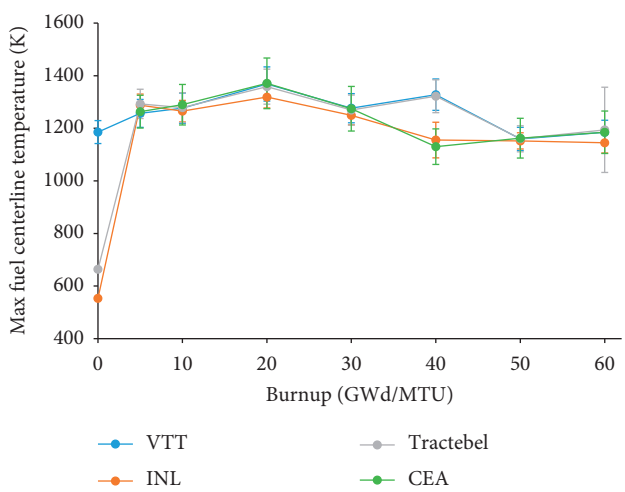

Figure 13: PWR depletion test case based on TMI-1 fuel rod design.

multiphysics calculations. The Doppler temperature is a kind of "fuel equivalent temperature" which is used to calculate the Doppler feedback. Several methods exist to calculate it from the fuel pellet temperature distribution. A common method is to apply a weighted average between the centreline temperature and the surface temperature.

Actually the fuel temperature is calculated either for an average lumped fuel rod at assembly (or nodal) level (in the simplified lumped models of thermal-hydraulics codes) or for an individual rod in a pin-by-pin (or cell-by-cell) calculation (in fuel performance codes). In both cases, the fuel temperature is a result of a one-dimension heat conduction problem solution. In Phase III in the coupled multiphysics calculations, the temperature is calculated for each node of the core (3D distribution radial and axial directions) using tabulated fuel properties, the nuclear/thermal power given by neutronics, and the local thermal-hydraulic conditions as solved by the core thermal-hydraulics model. The rod-to-coolant heat transfer coefficient is also given by thermal-hydraulics or defined by the user as input parameter. The heat conduction problem is actually solved in two different regions: the cladding (without heat source) and the fuel pellet. The gap is modelled by a thermal resistance (or conductance), directly provided as an input data by the user, or calculated by a dedicated correlation. The fuel and cladding specific thermal properties (density, heat capacity, and conductivity) are also provided, usually as functions of the temperature and of the local burnup.

Since in a high-fidelity fuel performance code a single rod is modelled, the fuel temperature is calculated at each axial and radial node of the meshing of the fuel rod, and the resolution of the thermal problem takes into account all the possible physical phenomena that affect the fuel geometry and thermal properties. In summary, in a fuel performance code, fuel temperature field, fuel rod geometry, and gap conductance can be assessed. Uncertainty propagation can be performed on the three most important modelling quantities: fuel thermal conductivity, cladding thermal conductivity, and gap conductance. To summarize, the calculations performed within the framework of Exercise II-1 with higher-fidelity fuel performance codes help to develop parameterized values and associated uncertainty bounds for these three parameters to be used in the coupled multiphysics calculations in Phase III. The following data for the gap conductance, fuel, and claddings thermal conductivities is generated using high-fidelity fuel performance codes—(i) the mean value and (ii) associated uncertainty—both as functions of the following parameters: for cladding conductivity $k_c(T)$, as function of temperature (T); for fuel conductivity $k_f(\mathrm{Bu}, T)$, as function of burnup (Bu) and temperature (T); and for gap conductance, $h_g(\mathrm{Bu}, P)$ as function of burnup (Bu) and power (P). These data are computed and parameterized for each type of fuel rod, that is, for each type of LWR fuel assembly of interest. We will refer the generation of this data as a preparation of Hi2Lo model information plus uncertainties using high-fidelity fuel models for lumped simplified lower-fidelity fuel models. The lookup table representation concept [2] is appropriate for steady state and cycle depletion calculations while for transient/accident simulations the high-to-low model calibration of selected coefficients in dynamic gap conductance correlations is preferred [16]. Please keep in mind that the uncertainty values could be extracted also from the experimental datasets and associated

uncertainties used to develop the corresponding correlations utilized in the fuel models. As an example, the uncertainty associated with the IAEA correlation for cladding conductivity is shown in Figure 14.

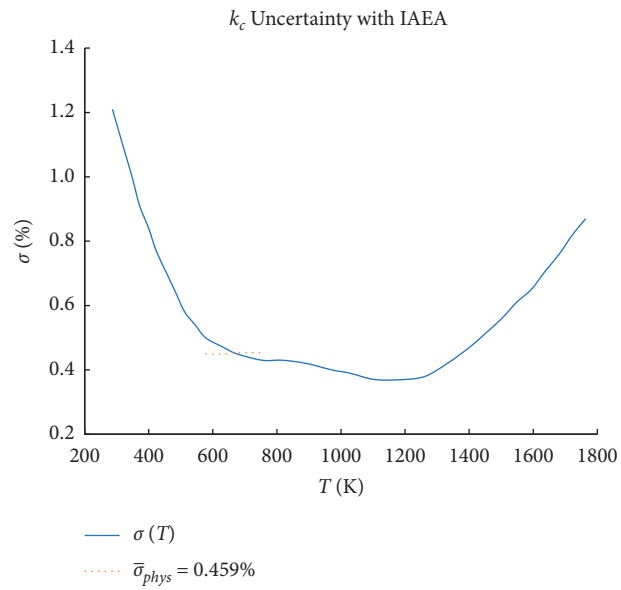

Figure 14: Cladding conductivity $k_c(T)$ uncertainty associated with the IAEA correlation.

4.3. Thermal-Hydraulics. As for fuel thermal and mechanical behaviour, there might be different thermal-hydraulic models used between Phases II and III. The uncertainty quantification on thermal-hydraulic models is established on a relatively small scale, that is, rod bundles, in Exercise II-3, while these results will be used in Phase III at the core scale. Detailed two-phase flow models, either at subchannel level or at Computational Fluid Dynamics (CFD) level, are used to model a single fuel bundle in Exercise II-3, while rather simplified models at fuel assembly level are utilized for full-core thermal-hydraulics in Phase III [15].

Considering that the feedback effect of thermal-hydraulics on core behaviour leads to identifying three main parameters of interest: the coolant temperature and/or void fraction and the cladding temperature (i.e., boundary condition for heat conduction problem in fuel rods) resulting from the heat transfer coefficient between the fuel rod and the coolant. These parameters highly depend on the flow: single-phase turbulent flow, nucleate boiling, or film boiling (post-CHF conditions).

Hence, Phase II should provide uncertainties on these parameters but also on the transition criteria between the three flow regimes. Due to the large range of available models for two-phase flow, the benchmark specification cannot address input uncertainties to be considered for each model and all closure laws. Nevertheless the consistency between Phases II and III should be verified by the participants when different codes or models are used (e.g., four-equation model versus two-fluid model). The methodology is the following: the modelling uncertainties have to be tuned in order to have the same effect on the coolant temperature, for example, at subchannel level (for which it is possible to compare the computations to the measurements).

As example, the obtained results of statistical uncertainty analysis performed with subchannel code CTF coupled with the statistical analysis tool, Design Analysis Kit for Optimization and Terascale Applications (DAKOTA) [17] for TMI-1 PWR assembly at normal operation conditions as part of Exercise II-3, are shown and discussed [18]. The statistical method repeatedly runs the code with inputs sampled from the specified input distributions of uncertainties in boundary conditions, geometry, and modelling. Through statistical analysis of the results, conclusions are drawn about the behaviour of the quantities of interest. For the uncertainty quantification, a Latin Hypercube Sampling (LHS) method with a sample size of 2000 was used. This number of samples was selected by utilizing the maximum proportion of reasonably available computational resources. The TMI-1 quarter assembly model at normal operation conditions is utilized. This case is unique because there is not significant void generation in the bundle; therefore, the fluid temperature is selected as a quantity of interest in place of the void fraction. The axial fluid temperature distribution in selected subchannel, axial cladding surface temperature distribution of selected rod, and exit fluid temperature distribution are all shown in Figure 15. An expected result of the single-phase nature of this case is that the standard deviations for all temperatures are approximately constant, especially within each individual axial distribution. The physical modelling of single-phase flow is simpler and better understood than two-phase modelling, which leads to smaller overall uncertainty in thermal-hydraulic simulations.

In has been shown previously that CFD codes could be used to generate Hi2Lo information with uncertainties for spacer grid and in-core structure modelling [19]. These CFD-informed models are developed using a physics-based approach which utilizes high-fidelity data to inform and calibrate a lower-fidelity simulation. It is important to consider only once input uncertainties. For example, the spacer grid effects (position and mixing) are investigated in Exercise II-3 for a given type of fuel bundle—in this case, TMI-1 PWR bundle. The resulting uncertainty will be considered later in Phase III in the overall uncertainty on investigated output parameters. The methodology utilizes CFD-based data for: grid-directed cross-flow model; grid-enhanced turbulent mixing model; grid-enhanced heat transfer model; and spacer grid pressure losses model. This data while utilized in lower-fidelity core thermal-hydraulics modelling as part of core multiphysics calculations in Phase III is supplemented with uncertainties propagated through the high-fidelity local CFD simulations. These uncertainties are part of input uncertainties propagated through global core multiphysics calculations.

5. Uncertainty Propagation in Multiphysics Reactor Core Simulations

5.1. Approach to Multiphysics Uncertainty Propagation. Phase III of the LWR UAM benchmark is focused on the prediction of key reactor parameters associated with LWR

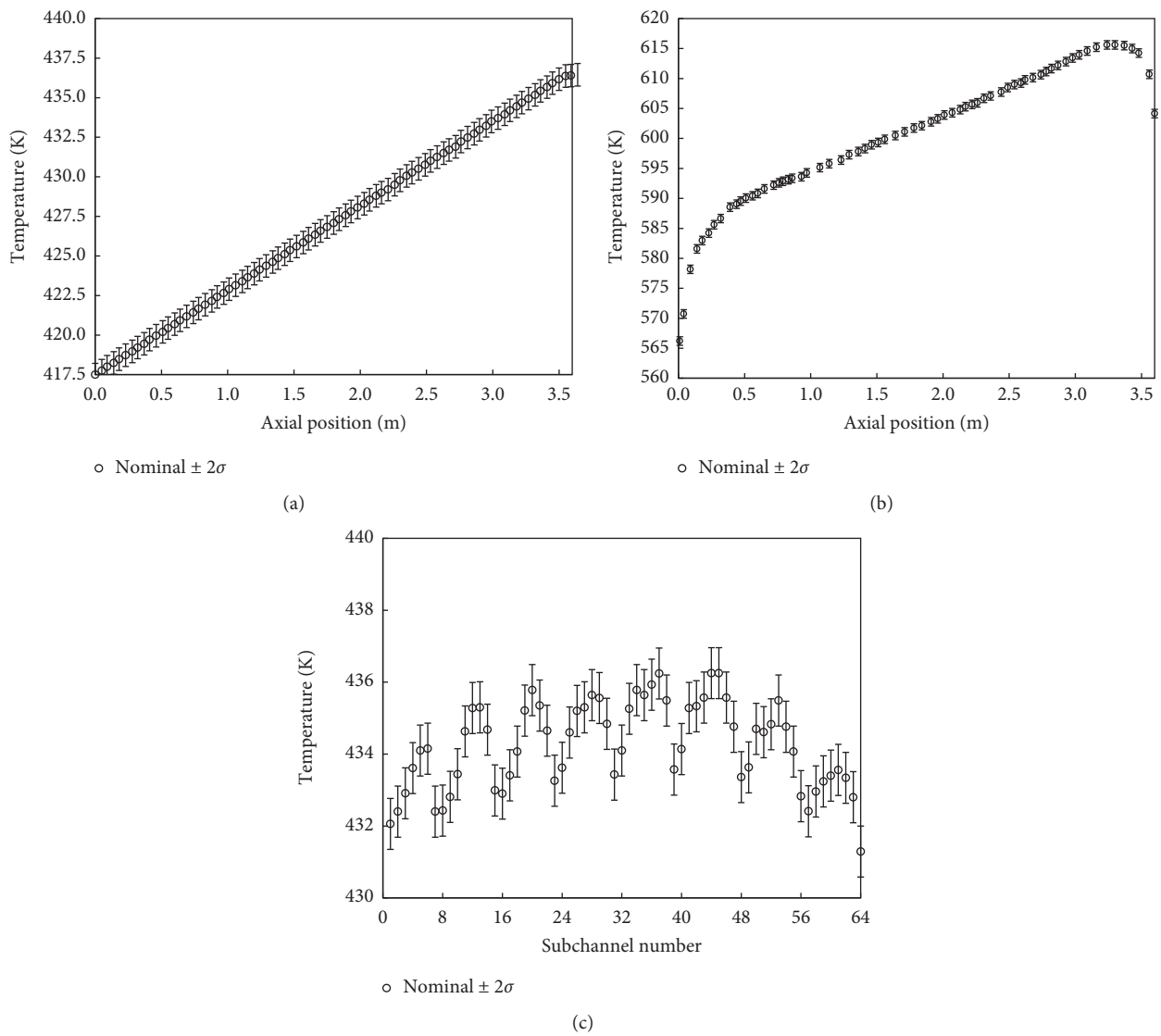

Figure 15: CTF/DAKOTA results for the TMI-1 PWR test case. (a) Axial fluid temperature distribution. (b) Axial surface cladding temperature distribution. (c) Exit fluid temperature distribution.

multiphysics simulations. Coupled fuel rod, thermal-hydraulics, and neutronics simulations are included by taking into account coupling/feedback effects between the three phenomena. Most of the progresses made so far are on Exercise III-1, which aims to identify and propagate input uncertainties through core multiphysics calculations.

Selected output uncertainties from various physics domains/phenomena have been evaluated in Phases I and II of exercises and will be used as input uncertainties in Exercise III-1. Those uncertainties can be given in the form of distributions, a single value, or multiple data files and will be combined with other sources of uncertainties in core multiphysics calculations. Following the multiscale, multiphysics modelling strategy defined in the current benchmark, one possible approach for propagating those uncertainties is proposed and demonstrated in Figure 16. The input uncertainty, as discussed below, stems from three physics domains of LWR modelling: neutronics, fuel modelling, and thermal-hydraulics.

The neutronics uncertainties are embedded in the two-group cross section libraries, which include parameterized cross sections, discontinuity factors (DFs), burnup, and kinetics parameters. The fuel modelling uncertainties are applied to the standard lumped fuel rod models of system and subchannel codes via three parameters related to the heat transfer from fuel to coolant: fuel thermal conductivity k_f, gap conductance h_g, and cladding thermal conductivity k_c. In general, the input uncertainties for the core thermal-hydraulic model include boundary conditions uncertainties, geometry uncertainties, and modelling uncertainties. At the first stage of implementing the method depicted in Figure 16, the uncertainties associated with different physics spaces are considered independent from each other and hence propagated separately towards the core simulation,

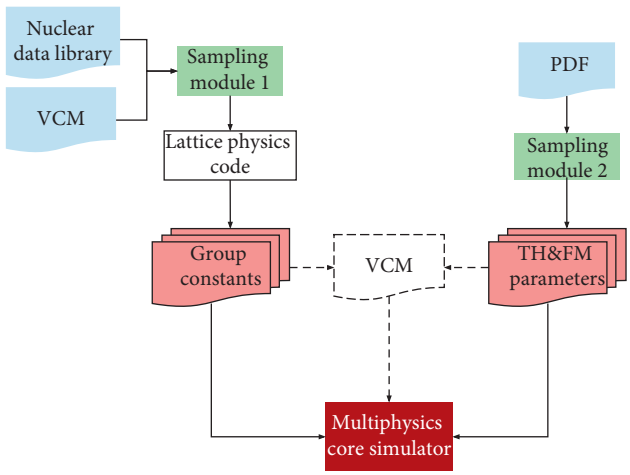

Figure 16: Uncertainty propagation methodology for coupled multiphysics M&S.

although the simulation itself is carried out using the coupled multiphysics code system.

5.2. Uncertainty Propagation for Cycle Depletion Calculations. The TMI-1 equilibrium cycle depletion case was specified in the LWR UAM benchmark, Exercise III-1, where the reactor core is depleted at HFP of 2771.9 MWth, with the average fuel temperature of 921 K. The mass flow rate through reactor core is assumed to be 16546.04 kg/s with the coolant inlet temperature of 562.67 K. Control rod Groups 1–6 are completed withdrawn, while Group 7 and the axial power shape rod (APSR) Group 8 are 90% and 30% withdrawn, respectively. The core is depleted for 664 EFPD before the critical boron concentration 5 ppm is reached.

The TMI-1 core was modelled using PARCS [20] with the fixed mesh size. The core is radially partitioned into 177 nodes based on the one-node-per-assembly configuration plus the radial reflector. Axially, the core is discretized into 24 equal nodes in the active core region and 1 node each for top and bottom reflector. The cross sections were generated as a function of fuel temperature, moderator density, boron concentration, control rod insertion, and depletion for 11 types of fuel assemblies. Cross sections for the 3 types of reflectors were assumed to be invariant as those generated under nominal state condition. The two-group homogenized cross sections were generated based on the ENDF/B-VII.1 library using Polaris, which is a 2D LWR lattice physics module in the SCALE 6.2.1 code system [8]. The fluid dynamics and heat transfer calculations were performed using the PATHS (PARCS Advanced Thermal-Hydraulics Solver) code [21] to provide thermal-hydraulics feedback for steady state and depletion calculation via the tight coupling with PARCS. The axial nodalization and spatial mapping (overlays) of thermal-hydraulics (TH), neutronics kinetics (NK), and heat structure (HTSTR) models in the coupled depletion simulation is shown in Figure 17.

The nominal depletion calculation was first performed using PARCS/PATHS and the results were compared against the reference solution provided in LWR UAM benchmark

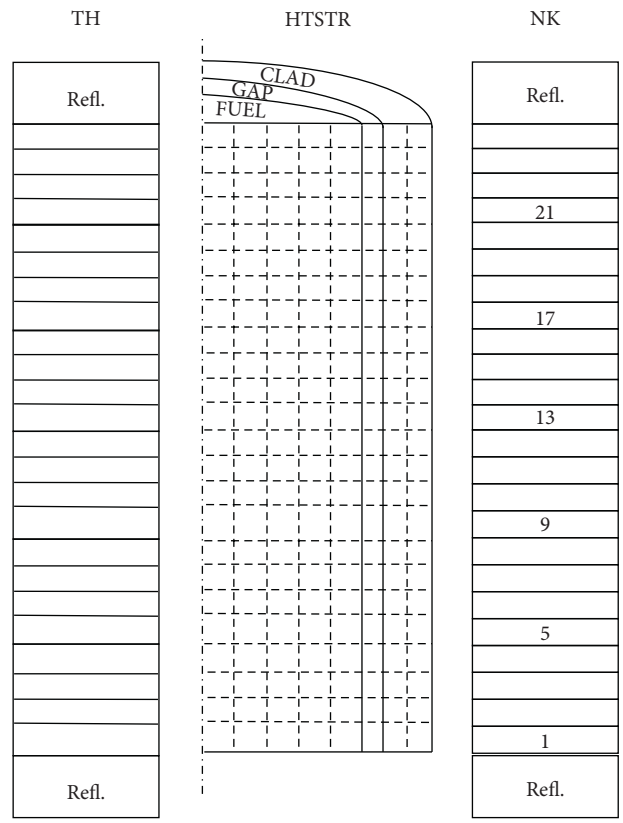

Figure 17: Nodalization and mapping of thermal-hydraulics (TH), neutronics kinetics (NK), and heat structure (HTSTR) models in the coupled depletion simulation.

specification. With a cycle length of 664 EFPD, critical boron concentration at EOC is 38 ppm, which compares favourably with the reference solution with an error of 33 ppm. Moreover, the maximum relative error of the assembly averaged burnup is −1.39%, as shown in Figure 18.

The uncertainty propagation and quantification were carried out following the approach described in Figure 16. On the neutronics side, this study utilized Sampler (represented by "sampling module 1") [8], a module for statistical uncertainty analysis in SCALE code package, to sample probability density functions (PDFs) defined in the SCALE 56-group covariance library and generate random samples of nuclear data for the subsequent lattice calculation. The few-group constants were then generated and converted by the lattice physics code Polaris [8]. On the thermal-hydraulics and fuel modelling side, DAKOTA (shown as "sampling module 2") [22] was employed to produce samples of selected parameters according to their PDFs (see Table 3), using the Latin Hypercube Sampling (LHS) method. The LHS is a stratified sampling technique for which the range of each uncertain variable is divided into segments of equal probability; as a result, it requires less numerous samples than the random sampling method to achieve the same accuracy in statistics. The perturbed input variables for the multiphysics simulator PARCS/PATHS were prepared by pairing one set of few-group constants with one sample of fuel modelling and thermal-hydraulics

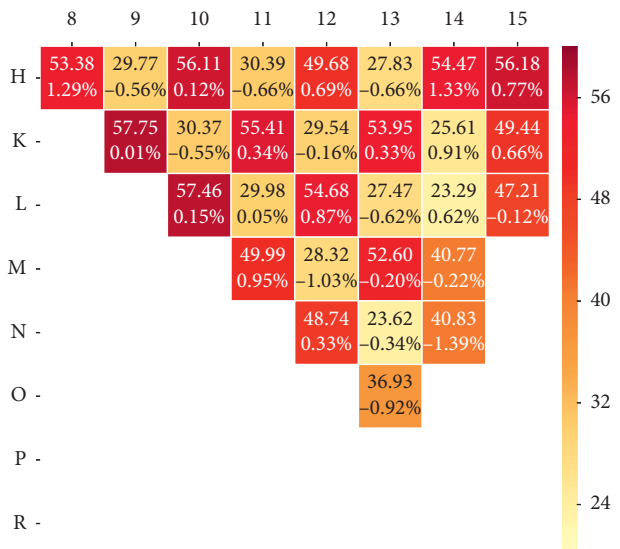

Figure 18: TMI-1 assembly power at EOC and relative errors against benchmark values.

Table 3: Input uncertainty of the couple multiphysics cycle depletion calculation.

Input parameters	Unit	Rel. std.	Distribution
Fuel thermal conductivity	W/m-K	0.55%	Normal
Clad thermal conductivity	W/m-K	0.45%	Normal
Gap conductance	$W/m^2/K$	[−20%, 22%]	Uniform
System pressure	MPa	1.00%	Normal
Flow rate	kg/s	1.50%	Normal
Power	kW	1.00%	Normal
Inlet fluid temperature	K	[−1.0, 1.0]	Uniform

parameters. For specific tolerance limits, the number of code runs (or the sample size) can be determined using Wilks' method [23]:

$$1 - \alpha^n - n(1-\alpha)\alpha^{n-1} \geq \beta, \tag{5}$$

where α is the uncertainty, β is the statistical confidence, and n represents the sample size. A total number of 146 sets of input variables were formulated in order to ensure that 95% of the results fall in a confidence level of 95%.

A python-based interface was developed to streamline the calculation and data processing, including feeding the input parameters, invoking core depletion calculation for 664 EFPD using PARCS/PATHS, and performing the statistical analysis of the collected output responses. The results are shown below.

Figure 19 shows the boron letdown curves of the unperturbed and perturbed depletion calculation as well as the associated statistical results. It can be seen that the peak boron concentration occurs at BOC for all sample runs with the values of 1786 ppm and 1809 ppm for the nominal case and sample mean, respectively. It also shows that the peak critical boron concentration will be bounded within the range of [1656, 1932 ppm] for the tolerance limit of 95% at a confidence level of 95%. Note that the critical boron

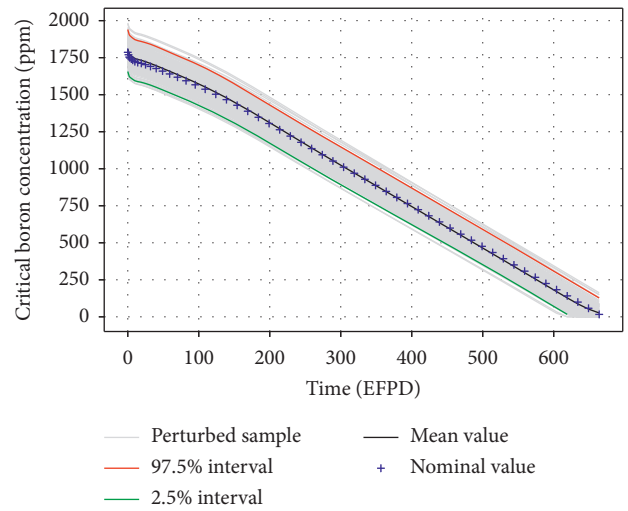

Figure 19: Critical boron concentration of unperturbed and perturbed cases.

concentration reduced to 5 ppm before reaching 664 EFPD in some perturbed cases, and the cycle lengths in those cases are thus shorter than others.

The radial and nodal power peaking factors are depicted in Figures 20 and 21, respectively, during the entire cycle depletion. In general, it can be found that the uncertainty of the peak relative power is larger at BOC than EOC. Among all perturbed cases, the 95th percentile of the distribution was calculated at each burnup step for the peak relative power to establish a tolerance limit with 95% confidence. The results are 1.395 and 1.777 for the peak radial and peak nodal power, respectively.

The assembly averaged burnup was also calculated with associated uncertainties, as shown in Figure 22. Since the assembly burnup is not considered as a safety parameter, the 95%/95% confidence interval was evaluated to quantify its uncertainty, as shown in (3), in addition to the sample mean and standard deviation. The maximum uncertainty of the assembly burnup is found to be 0.82% in assembly L13, which is equivalent to 0.84 GWD/MTU, and the 95%/95% confidence interval of the true uncertainty can be estimated as [0.73%, 0.93%].

The mean and upper bound (computed as mean value plus the deviation between the mean and the 95% intervals) of the cycle length were also calculated for all samples, which was determined when critical born concentration reaches 5 ppm, since it is shorter than 664 EFPD in some perturbed cases. By separately perturbing nuclear data and each of the fuel modelling and thermal-hydraulics parameters, the total uncertainties observed can be decomposed and the impacts of various uncertainty sources can be evaluated, as shown in Table 4. It is found that the total uncertainty of the cycle length is 36.2 days and mostly contributed by nuclear data uncertainty. Fuel modelling parameters are responsible for uncertainty of only 1.2 days, which is mostly dictated by the uncertainty of the gap conductance. Thermal-hydraulic parameters are responsible for uncertainty of 12.3 days, mostly stemming from the core power uncertainty.

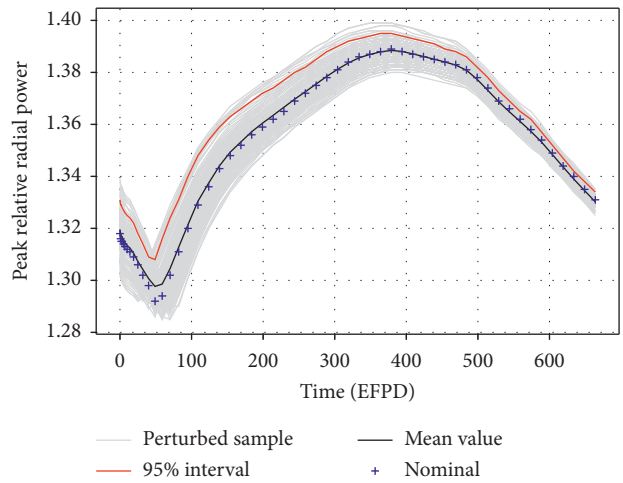

Figure 20: Peak relative assembly power of unperturbed and perturbed cases.

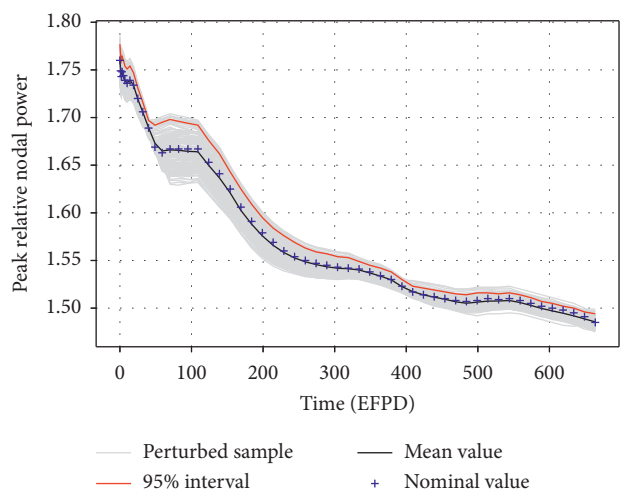

Figure 21: Peak relative nodal power of unperturbed and perturbed cases.

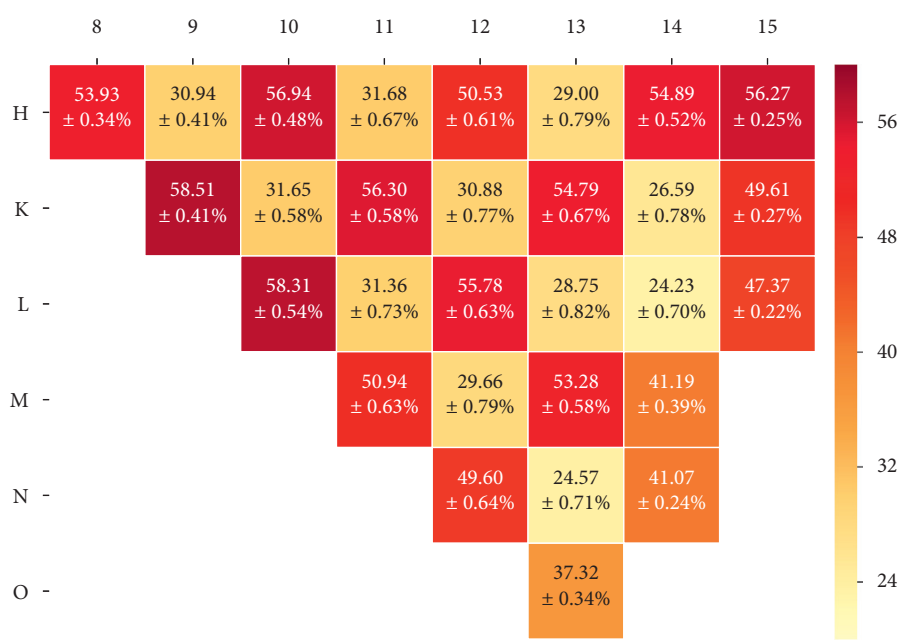

Figure 22: TMI-1 core burnup distribution with uncertainties.

Table 4: Impact of input uncertainties on cycle length, presented as mean + (95% interval–mean).

Perturbed input parameters	Cycle length (day)
Nuclear data only	656 + 33.4
FM parameters only	654 + 1.2
Fuel thermal conductivity	654 + 1.2
Clad thermal conductivity	654 + 0.5
Gap conductance	654 + 1.2
TH parameters only	655 + 12.3
System pressure	654 + 1.8
Flow rate	654 + 1.8
Power	654 + 13.1
Coolant inlet temperature	654 + 1.9
All	655 + 36.2

The results of the uncertainty breakdown indicate that the uncertainties of the core responses in the cycle depletion calculations are influenced by the input uncertainty of all three physics domains. This is consistent with the conclusion of previous studies, such as [14], that the uncertainty of power and reactivity is mostly dominated by the nuclear data uncertainty, while that of the temperature is strongly dictated by the uncertainty of fuel modelling and thermal-hydraulics variables. It is obvious that the evaluation of the input uncertainties is of paramount importance for determining the uncertainty of the responses.

6. Conclusions and Future Work

This paper summarizes the current status and outcome of the development of the Best-Estimate Plus Uncertainty (BEPU) framework for the multiscale, multiphysics LWR core analysis under the guidelines of the LWR UAM benchmark, primarily focusing on the PWR cases based on the TMI-1 reactor. The stand-alone neutronics exercises in Phase I are mainly concerned with the propagation of input uncertainties through the standard multistep LWR simulation procedure to key core parameters, such as the multiplication factor. It was observed that the uncertainty estimates for the system eigenvalue due to nuclear data in all scales (the pin cell, lattice, and core) are similar with the Relative Standard Deviation of approximately 0.5% $\Delta k/k$. Comparative analyses of all submitted results were then carried out to investigate the dependence of the predicted uncertainties of crucial core parameters on the choice of solution methods, nuclear data libraries, VCMs, etc. It was found that the k-inf (k-eff) uncertainty strongly depends on the VCM and the results generated using the VCM of ENDF/B-VII.1 and SCALE 6.2 lead to significantly larger values than those using other VCMs. The sensitivity analysis suggests that the large deviation of the ^{235}U nu-bar uncertainty in the thermal energy range is responsible for the disagreement. As a follow-up to the current work, similar analyses will be applied to benchmark cases belonging to other reactor types, including BWR, VVER, and Gen-III reactors. It was expected to help identify important nuclide/reaction types to the calculated uncertainty and make recommendations to the further improvement of the nuclear data evaluation for the nuclear reactor application. Other sources of input uncertainties, such as the manufacturing tolerances, will also be taken into consideration in the future comparative analysis.

Using the experience gained on Phase I, a consistent approach is defined in Exercise II-2 to parameterize the neutronics uncertainties in a form of few-group libraries to be propagated from Phase II to Phase III. Exercises II-1 and II-3 are used to characterize the uncertainties of high-fidelity fuel and thermal-hydraulics models regarding parameters of interest at core level, such as nodal Doppler temperature and coolant temperature. These uncertainties are defined as functions of local operating conditions at core level (pressure, burnup, etc.) in order to be propagated in Phase III with rather simplified models for fuel behaviour and core thermal-hydraulics. For the three selected fuel physics quantities, high-to-low-fidelity model information approach is applied, and the obtained uncertainties are propagated in the core multiphysics calculations. Phenomena Identification and Ranking Table (PIRT) analysis will be used for thermal-hydraulic quantities where common cross-cutting input has the strongest uncertainties impact for the envisioned initial steady state, cycle depletion, and transient applications. It is only in those quantities that the uncertainties will be propagated for full-core calculation. For such propagation, the experience accumulated in Exercise II-3 test problems is utilized. Finally, the multiphysics exercises of Phase III will result in safety and design quantities with the best-estimate value and the overall uncertainty.

In Phase III, the uncertainty quantification of the core equilibrium cycle depletion calculations was investigated. The core depletion calculation was performed using the PARCS/PATHS code, while Sampler and DAKOTA were employed to propagate input uncertainties through the calculation chain using the stochastic sampling method. Output responses including assembly burnup, critical boron concentration, peak power, and cycle length were evaluated. The maximum uncertainty in assembly burnup is found to be 0.82% and the uncertainty of cycle length is found to be 36.2 days, both of which are mostly contributed by the nuclear data uncertainty.

It was shown in the current and previous studies that the uncertainty of certain core responses is not equally contributed by the uncertainty of three physics domains under consideration. However, this does not mean that the impact of input uncertainty should be propagated and quantified in an independent way; that is, the correlations of input variables due to the common source of uncertainties must be accounted for consistently. Taking the nuclear data uncertainty for example, it obviously introduces uncertainties to the predicted fuel composition along the burnup cycle, which in turn has impact on the neutronics parameters (i.e., few-group cross sections), the boundary condition of the thermal-hydraulics calculation (i.e., heat flux), and the fuel modelling parameters (e.g., fuel thermal conductivity and gap conductance). All those variables are thus correlated and so are their uncertainties. Therefore, it is planned to develop a consistent uncertainty quantification method for the coupled core calculation by constructing the correlation

among selected input parameters, which is represented by the components and data flow in dashed line in Figure 16.

Data Availability

The data used to support the findings of this study are available from the corresponding author upon request.

Conflicts of Interest

The authors declare that they have no conflicts of interest.

Acknowledgments

The authors would like to acknowledge and recognise K. Zeng, N. Porter, and A. Toptan, current and former Ph.D. students, at the Reactor Dynamics and Fuel Modelling Group (RDFMG), Nuclear Engineering Department, North Carolina State University, who have contributed to the preparation of OECD/NEA LWR UAM benchmark specifications and development of methods as well as obtaining and analysing the results presented in this manuscript.

References

[1] K. Ivanov, M. Avramova, S. Kamerow et al., "Benchmark for uncertainty analysis in modelling (UAM) for the design, operation and safety analysis of LWRs," in *Specification and Support Data for Neutronics Cases (Phase I)*, vol. I, p. 7, NEA/NSC/DOC, Paris, France, 2013.

[2] M. Avramova, "Benchmark for uncertainty analysis in modelling (UAM) for the design, operation and safety analysis of LWRs," in *Specification and Support Data for Neutronics Cases (Phase II)*, Vol. II, NEA/NSC/DOC, Paris, France, 2017.

[3] J. Hou, "Benchmark for uncertainty analysis in modelling (UAM) for the design, operation and safety analysis of LWRs," in *Specification and Support Data for Neutronics Cases (Phase III)*, Vol. III, NEA/NSC/DOC, Paris, France, 2018.

[4] M. Pusa, "Perturbation-theory-based sensitivity and uncertainty analysis with CASMO-4," *Science and Technology of Nuclear Installations*, vol. 2012, Article ID 157029, 11 pages, 2012.

[5] B. Rearden, "TSUNAMI-: Control Module for One-imensional Cross-ection Sensitivity and Uncertainty," Oak Ridge National Laboratory, Oak Ridge, TN, USA, 2011.

[6] B. Krzykacz, E. Hofer, and M. Kloos, "A software system for probabilistic uncertainty and sensitivity analysis of results from computer models," in *Proceedings of the International Conference Probabilistic Safety Assessment and Management (PSAM-II)*, San Diego, CA, USA, January 1994.

[7] M. Williams, "A statistical sampling method for uncertainty analysis with SCALE and XUSA," *Nuclear Technology*, vol. 183, p. 515, 2012.

[8] B. Rearden and M. Jessee, "SCALE Code System, ORNL/TM-39, Version 6.2.1," UT Battelle, LLC, Oak Ridge Laboratory, Oak Ridge, TN, USA, 2016.

[9] W. Marshall, M. L. Williams, D. Wiarda et al., "Development and testing of neutron cross-section covariance data for SCALE 6.2," in *Proceedings of the International Conference on Nuclear Criticality Safety (ICNC 2015)*, Charlotte, NC, USA, September 2015.

[10] A. Trkov, G. L. Molnár, Z. Révay et al., "Revisiting the ^{238}U thermal capture cross section and gamma-ray emission probabilities from ^{239}Np decay," *Nuclear Science and Engineering*, vol. 150, no. 3, pp. 336–348, 2005.

[11] K. Shibata, T. Kawano, T. Nakagawa et al., "Japanese evaluated nuclear data library version 3 revision-3: JENDL-3.3," *Journal of Nuclear Science and Technology*, vol. 39, no. 11, pp. 1125–1136, 2002.

[12] E. Castro, S. Sánchez-Cervera, N. García-Herranz, and D. Cuervo, "Impact of the homogenization level, nodal or pin-by-pin, on the uncertainty quantification with core simulators," *Progress in Nuclear Energy*, vol. 104, pp. 218–228, 2018.

[13] I. Yankov, B. Collins, M. Klein et al., "A two-step approach to uncertainty quantification of core simulators," *Science and Technology of Nuclear Installations*, vol. 2012, Article ID 767096, 9 pages, 2012.

[14] K. Zeng, J. Hou, K. Ivanov, and M. A. Jessee, "Uncertainty quantification and propagation of multiphysics simulation of the pressurized water reactor core," *Nuclear Technology*, vol. 205, no. 12, pp. 1618–1637, 2019.

[15] K. Ivanov and M. Avramova, "Uncertainty analysis in modelling for Light water reactors consistent approach for multi-scale modelling," in *Proceedings of the ANS Best Estimate Plus Uncertainty International Conference (BEPU 2018)*, Real Collegio, Lucca, Italy, May 2018.

[16] G.-K. Delipei, J. Garnier, J.-C. Le Pallec, and B. Normand, "Uncertainty analysis methodology for multi-physics coupled rod ejection accident," in *Proceedings of the International Conference on Mathematics and Computational Methods Applied to Nuclear Science and Engineering (M&C)*, Portland, OR, USA, August 2019.

[17] K. Zeng, J. Hou, K. Ivanov, and J. Matthew, "Uncertainty analysis of Light water reactor core simulations using statistic sampling method," in *Proceedings of the International Conference on Mathematics & Computational 2017*, Jeju, Korea, April 2017.

[18] N. W. Porter, M. N. Avramova, and V. A. Mousseau, "Uncertainty quantification study of CTF for the OECD/NEA LWR uncertainty analysis in modeling benchmark," *Nuclear Science and Engineering*, vol. 190, no. 3, pp. 271–286, 2018.

[19] M. Avramova, "Developments in thermal-hydraulic subchannel modeling for whole core multi-physics simulations," *Nuclear Engineering and Design*, vol. 358, p. 110387, 2020.

[20] T. Downar, Y. Xu, and V. Seker, "PARCS–U.S. NRC core neutronics simulator, UM-NERS-09-0001," 2013.

[21] A. Wysocki, A. Ward, A. Manera et al., "The modeling of advanced BWR fuel designs with the NRC fuel depletion codes PARCS/PATHS," *Nuclear Technology*, vol. 190, no. 3, pp. 323–335, 2015.

[22] B. Adams, "Dakota, A Multilevel Parallel Object-riented Framework for Design Optimization, Parameter Estimation, Uncertainty Quantification, and Sensitivity Analysis: Version 6.5 User's Manual," Sandia National Laboratory, Albuquerque, NM, USA, 2016.

[23] S. S. Wilks, "Determination of sample sizes for setting tolerance limits," *The Annals of Mathematical Statistics*, vol. 12, no. 1, pp. 91–96, 1941.

Hindawi
Science and Technology of Nuclear Installations
Volume 2020, Article ID 2764634, 14 pages
https://doi.org/10.1155/2020/2764634

Research Article

Multiphysics Modeling and Validation of Spent Fuel Isotopics Using Coupled Neutronics/Thermal-Hydraulics Simulations

Dean Price, Majdi I. Radaideh, Travis Mui, Mihir Katare, and Tomasz Kozlowski

Department of Nuclear, Plasma, and Radiological Engineering, University of Illinois at Urbana-Champaign, Champaign, Illinois 61801, USA

Correspondence should be addressed to Tomasz Kozlowski; txk@illinois.edu

Received 27 December 2019; Revised 20 May 2020; Accepted 29 June 2020; Published 26 July 2020

Academic Editor: Manmohan Pandey

Multiphysics coupling of neutronics/thermal-hydraulics models is essential for accurate modeling of nuclear reactor systems with physics feedback. In this work, SCALE/TRACE coupling is used for neutronic analysis and spent fuel validation of BWR assemblies, which have strong coolant feedback. 3D axial power profiles with coolant feedback are captured in these advanced simulations. The methodology is applied to two BWR assemblies (2F2DN23/SF98 and 2F2D1/F6), discharged from the Fukushima Daini-2 unit. Coupling is performed externally, where the SCALE/T5-DEPL module transfers axial power data in all axial nodes to TRACE, which in turn calculates the coolant density and temperature for each of these nodes. Within a burnup step, the data exchange process is repeated until convergence of all coupling parameters (axial power, coolant density, and coolant temperature) is observed. Analysis of axial power, criticality, and coolant properties at the assembly level is used to verify the coupling process. The 2F2D1/F6 benchmark seems to have insignificant void feedback compared to 2F2DN23/SF98 case, which experiences large power changes during operation. Spent fuel isotopic data are used to validate the coupling methodology, which demonstrated good results for uranium isotopes and satisfactory results for other actinides. This work has a major challenge of lack of documented data to build the coupled models (boundary conditions, control rod history, spatial location in the core, etc.), which encourages more advanced methods to approximate such missing data to achieve better modeling and simulation results.

1. Introduction

The ability to accurately and efficiently predict end of life (EOL) fuel composition is essential in ensuring safe and economic management of spent nuclear fuel. In addition, verification, validation, and uncertainty quantification of neutronics/depletion codes with spent fuel data are important in order to evaluate the accuracy of such physics codes. Unfortunately, fuel depletion calculations are expensive to perform, making brute-force uncertainty analysis methods difficult to apply [1]. In single physics or decoupled simulations, it can often be difficult to directly simulate a particular experiment lacking detailed data. For example, time-dependent axial coolant density distributions are needed for light water reactor simulations, especially for boiling water reactors (BWRs) but data on this are rare. Approximations have been used in [2, 3] where an analytical form for axial coolant temperature distribution for a pressurized water reactor (PWR) is used. For BWRs, even with reported experimental data, major assumptions were needed to be made about the behavior of axial coolant density distributions in order to create verification models in [4]. However, such assumptions can introduce uncertainties in the calculations because void fraction feedback is not captured [5, 6]. The current study seeks to avoid this difficulty by coupling the thermal-hydraulics code TRACE to the T5-DEPL depletion sequence in SCALE for validation of spent fuel composition, thereby avoiding the need for detailed history of void distribution data.

Often, verification studies that use spent fuel compositions as a comparative metric rely on the concept of a ratio of computed to experimentally determined isotopic concentration or code bias (C/E) [2, 4, 7]. The results from these verification studies can be further used for uncertainty

quantification (UQ) [8]. Many methods of uncertainty quantification based on Monte Carlo parametric sampling [3, 9, 10] exist; data on C/E can be helpful in approximating uncertainty bounds of the isotopic concentrations in spent fuel analysis, similar to what has been done in [11]. An uncertainty analysis of a spent nuclear fuel storage system was performed in [5]. POLARIS was used to calculate the composition of commercial BWR spent fuel for 77 samples. This study [5] presented and compared BWR spent fuel isotopics for both actinides and fission products. Then, the study compared k_{eff} of a spent fuel cask based on code-predicted isotopic compositions with a cask based on experimentally reported isotopic compositions.

Neutronics and thermal-hydraulics coupling involves exchanging data on axial power distribution and coolant characteristics across physics codes [12]. This process can be done with external coupling [13], which is the method used in this study for validation of spent fuel isotopic composition (see Section 3). A variety of neutronics and thermal-hydraulics coupling studies have been conducted previously, which include coupling to subchannel codes (e.g., CTF), coupling to system codes (e.g., TRACE), and coupling to computational fluid dynamics codes (e.g., ANSYS/FLUENT). Internal coupling between Serpent 2-SUBCHANFLOW was carried out in [14], and the coupling scheme was benchmarked against TRIPOLI4-SUBCHANFLOW and MCNP5-SUBCHANFLOW. In addition, MCS neutronics was coupled to the CTF subchannel code to perform 3D pin-by-pin analysis of the BEAVRS benchmark [15]. Applications of coupling involving system codes have been used to simulate BWR accidents such as anticipated transient without scram using Simulate-3K/RELAP5 [16] and BWR instability accidents with TRACE/PARCS [17]. Lastly, nuclear applications that involve coupling to computational fluid dynamics codes were performed in [18, 19].

Overall, the present study seeks to develop advanced depletion models which include coupling to the thermal-hydraulics system code TRACE to aid in verification and validation of neutronic analysis. The spent fuel isotopic data will be used for validation. 3D neutronic models are developed using SCALE/T5-DEPL in order to capture axial effects in the lattice (e.g., axial power and nonuniform fuel composition). Also, TRACE is coupled to these neutronic models to provide a burnup-dependent axial void distribution. The coupling methodology is applied to two BWR benchmarks with reported isotopic measurements at end of cycle. The remaining sections of this paper are organized as follows. Section 2 presents brief descriptions of the BWR benchmarks used in the validation process. Section 3 presents the SCALE/TRACE coupling methodology. The results of this study and their discussion are presented in Section 4, while the conclusions drawn from this work are given in Section 5.

2. Description of Test Cases

2.1. Fukushima Daini-2 2F2D1 Assembly. The first benchmark used in analysis is the 2F2D1 BWR assembly from the Fukushima Daini-2 reactor. The design is 8×8-4 with 60 fuel rods and one water rod [20]. The top portion of Figure 1 presents the radial layout of the assembly. In this figure, the location of a special rod is marked, labeled "F6," where samples have been taken for isotopic analysis [21]. The F6 rod has an active height of 371 cm with 4.5 wt.% enrichment. Isotopics are measured at three different axial elevations shown in Figure 1(a). Within the dataset, an average void fraction and discharged burnup are reported for each sample. Sample power history is determined by scaling the reported total assembly power to enforce the given burnup to each sample.

2.2. Fukushima Daini-2 2F2DN23 Assembly. The second benchmark used in this study is taken from the same unit as the previous. This is the 2F2DN23 assembly from the Fukushima Daini-2 unit [22]. Similarly, this is an 8×8-2 design but with two smaller water rods. The bottom portion of Figure 1 presents the radial layout with pin-by-pin enrichment of this assembly. Again, the eight locations in which samples have been removed for analysis from a selected rod, the "SF98" rod, are labeled. For each of these samples, time-dependent power, constant and average void history, and discharged burnup are reported. The sample sections taken from this rod are all 0.5 mm in thickness. Sample 1 is taken from the naturally enriched (0.71 wt.%) region of the rod.

3. Methodology

TRACE [23] is a two-phase flow solver and best-estimate reactor system code developed by U.S. Nuclear Regulatory Commission (NRC) to analyze loss of coolant accident (LOCA), operational transients, and other accident scenarios within light water reactors (LWRs) such as PWR and BWR. TRACE is capable of simulating thermal-hydraulic phenomena in LWRs with high accuracy. It is a 1D (z-direction) code that solves the time-averaged and area-averaged two-phase two-fluid model equations. KENO-V.a is a 3D Monte Carlo neutronic solver in the SCALE code system developed by Oak Ridge National Laboratory [24, 25]. KENO-V.a performs 3D Monte Carlo criticality calculations for arbitrary geometries, and it operates in multigroup or continuous energy mode. KENO-V.a is able to determine k_{eff}, neutron lifetime, power and flux densities, and many other important reactor physics quantities.

3.1. Multiphysics Coupling. In this study, the nuclear fuel depletion sequence (T5-DEPL) is coupled to the thermal hydraulic code TRACE. By coupling a neutronics and thermal hydraulics code, there is no longer a need to rely on axial void fraction distributions—as these data can be missing or imprecise. A parametric description of the coupling scheme between these two simulated systems is shown in Figure 2. Internal to the T5-DEPL depletion sequence, KENO-V.a uses Monte Carlo neutron transport to calculate the axial power profile in all nodes, while ORIGEN is used to deplete the fuel in each node based on its respective power level. Externally, TRACE uses the nodal powers to

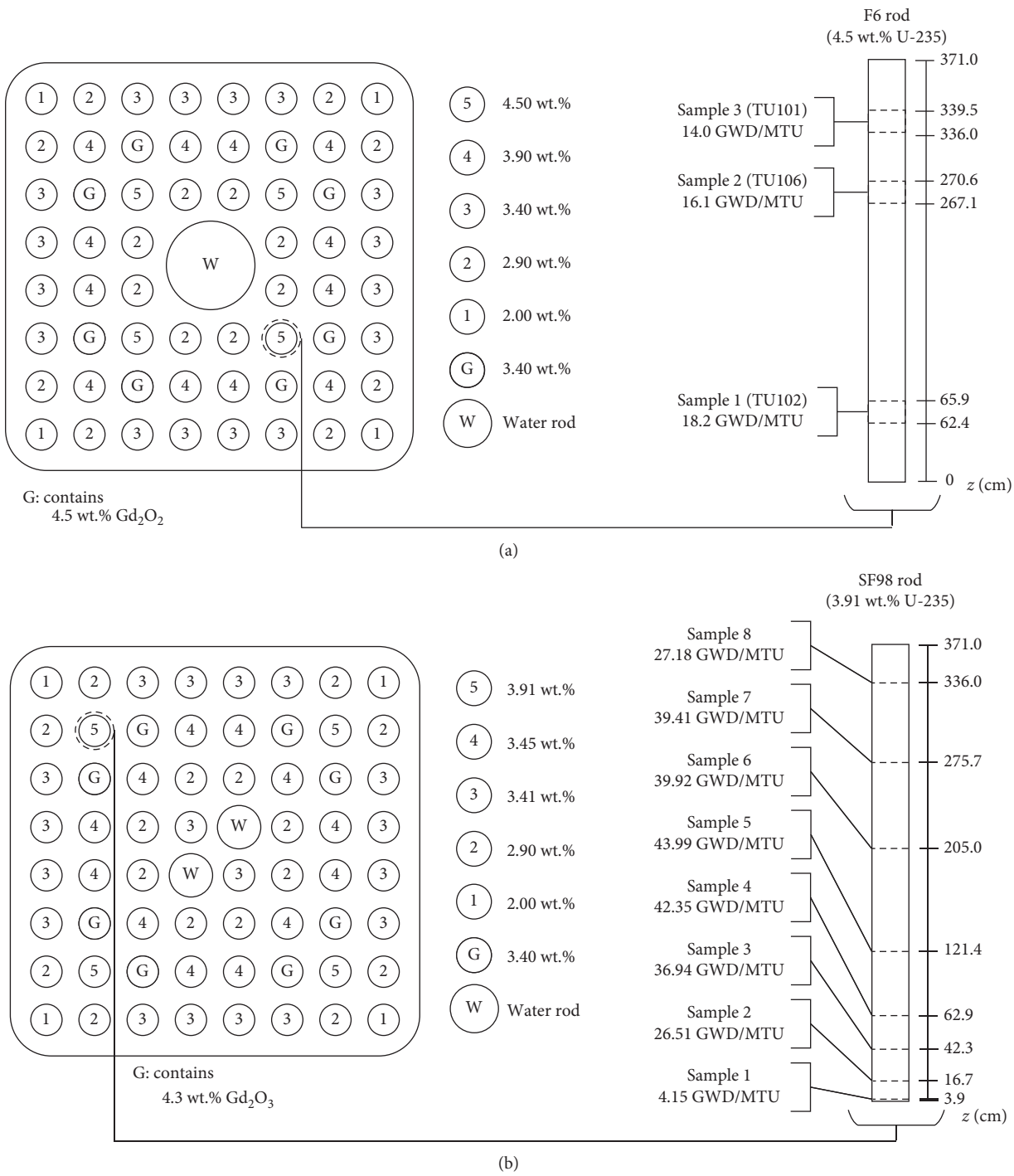

Figure 1: Pin layout and sample location for 2F2D1 assembly (a) and 2F2DN23 assembly (b) in the Fukushima Daini-2 unit. Sample thickness in SF98 rod is too thin for display (~ 0.5 mm).

calculate coolant density and temperature and return them to the T5-DEPL sequence for a new neutronics calculation. The coupling procedure is shown in Figure 3 and can be summarized as follows:

(1) The TRACE model is executed first with uniform power in all axial nodes. After completion, coolant density and temperature at each axial node are extracted from the TRACE output.

(2) The coolant density and temperature in all axial nodes are used to update the SCALE/T5-DEPL model. The updated neutronics input is executed and the axial power profile is extracted and normalized.

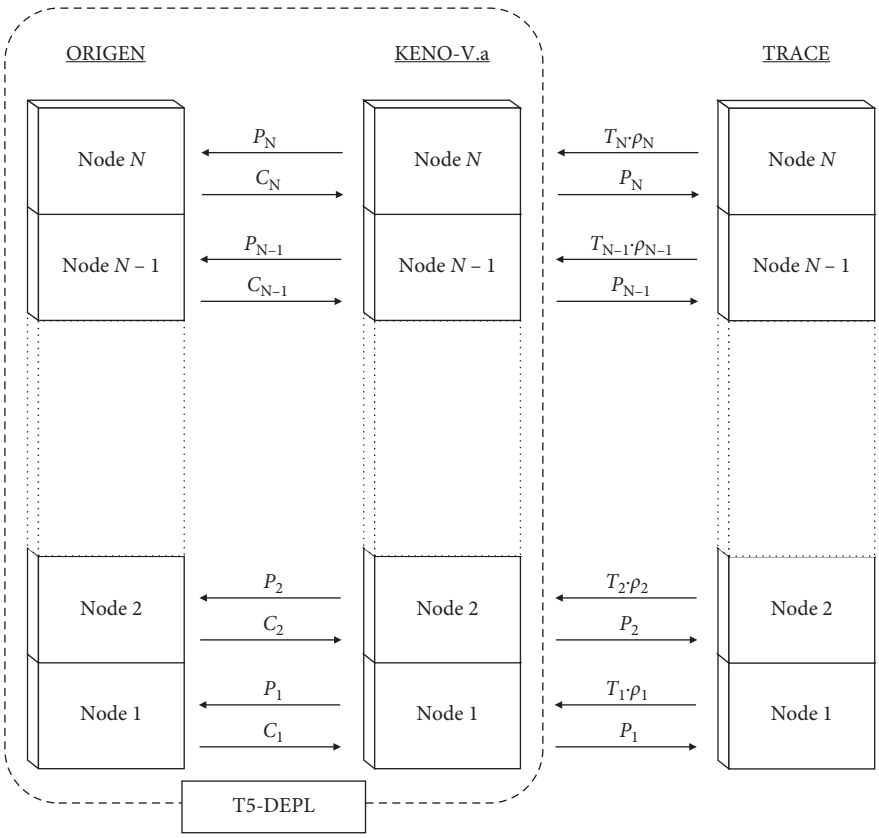

Figure 2: Two-way coupling of T5-DEPL and TRACE models.

(3) The updated axial power distribution is used in a new TRACE calculation, which yields updated coolant temperature and density.

(4) Steps 2-3 are repeated until the convergence criterion is met. The convergence criterion uses the average relative difference between two successive iterations in all axial nodes. When this quantity falls below a threshold value (e.g., 6%) for axial power, coolant density, and coolant temperature, the convergence criterion is satisfied and the loop is terminated.

(5) Steps 2–4 are repeated until all burnup steps are completed. The next burnup step is initiated upon completion of step 4.

3.2. Multiphysics Modeling. SCALE/T5-DEPL is used to model both the 2F2D1 and 2F2DN23 fuel assemblies in 3D with a reflective boundary condition radially and a vacuum boundary condition axially. The assembly is modeled in a square channel without rounded corners. The Monte Carlo parameters used are 1100 cycles with 20,000 neutrons per cycle, with an initial 100 cycles skipped. These parameters in KENO-V.a ensure about ~10 pcm uncertainty in k_{eff}.

For 2F2D1, twenty three nodes are used in the axial direction, which include three 3.5 cm thick axial slices to represent the samples (TU101, TU102, and TU106) in the F6 rod. For 2F2DN23, twenty one axial nodes are used, and they include eight 0.5 mm thick axial slices to represent the samples in the SF98 rod. For each sample tested, an irradiation/power history must be given to SCALE/T5-DEPL. Fortunately, there is an option in this code to ensure that the sample power can be specified. The option "power basis" in SCALE/T5-DEPL is used for each measured sample in the rods SF98/F6. To explain, the total power for all materials in the problem will be normalized such that the power in the sample material matches the sample power history specified. The burnup of each sample is measured during experiment and is reported in Figure 1. Matching this burnup value is essential in SCALE/T5-DEPL to achieve accurate validation of fuel isotopics. Fortunately, for the SF98 rod, the sample power is provided directly from the benchmark for each of the eight samples, and it is shown in Figures 4(b)–4(d).

However, only the total assembly power history is given for rod F6. Therefore, the assembly power provided by the benchmark is scaled such that the final burnup matches the sample burnup (i.e., 18.2, 16.1, and 14.0 GWD/MTU in Figure 1). Only the specific power values (kW/kg) are changed, while the total cycle time (418 days for 2F2D1) and time step length are maintained as in the benchmark. The adjusted sample power history is shown in Figure 4(a). The original power history and other neutronic parameters of this benchmark can be found in the SFCOMPO database [21].

TRACE is used to model the two assemblies as a BWR channel (CHAN) component with inlet boundary condition as a FILL component and outlet boundary condition as a BREAK component. The inlet flow rate is set to 17.56 kg/s,

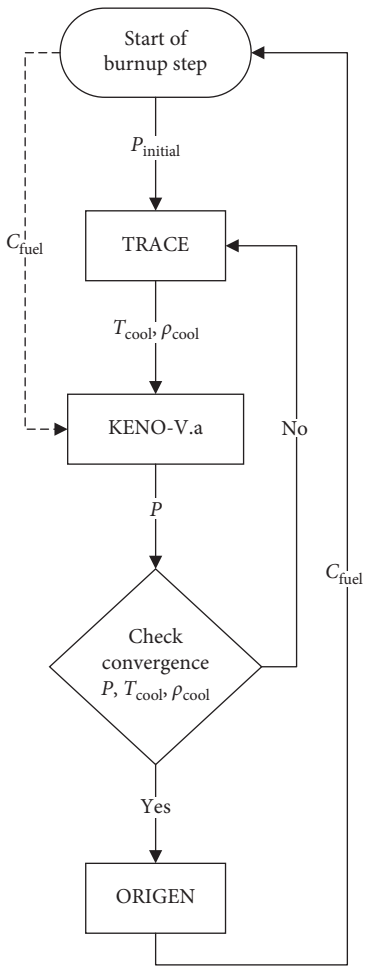

Figure 3: Process flow diagram for T5-DEPL, TRACE coupling. The notations are as follows: C_{fuel} gives the nodal fuel composition, P is the nodal power distribution, and T_{cool} and ρ_{cool} are temperature and density of the coolant, respectively. $P_{initial}$ is the converged power profile of the previous burnup step. For the first burnup step, $P_{initial}$ is a uniform power density to begin the iterative process.

while the inlet and outlet coolant temperatures are set to 550 K and 559 K, respectively. The total number and size of the axial nodes in TRACE match those in KENO-V.a. We ensured that mesh sizes in both KENO-V.a and TRACE are appropriate to avoid large numerical uncertainties in the calculations. The extraction of the coolant temperature and density from TRACE is done using the PyPost post-processor. Notice that since we model the assembly in TRACE as a single component, then the coolant properties calculated by TRACE are generalised for all rods including the SF98/F6 rods in the assembly. To have pin-by-pin resolution of the coolant distribution, subchannel codes (e.g., COBRA-TF) need to be used.

Since this problem involves depletion for multiple cycles, burnup-dependent simulation increases the complexity of the coupling process. Based on preliminary tests, we found that TRACE parameters tend to converge after 300–500 seconds following any power changes from KENO-V.a. Therefore, to reduce TRACE computational time, only a small time is simulated for coolant properties. Moving on, restart capabilities in SCALE are activated to keep track of isotopic composition. The converged values of material isotopic composition of the previous burnup step are used to initiate the calculations of the next time step. Then, on the last burnup step, the converged values of isotopic composition are used for validation. Lastly, it is worth acknowledging that the multiphysics feedback between the two physics is performed only when the power level changes. For 2F2D1, 8 power changes occur, while 2F2DN23 experiences 13 power changes; all are shown in Figure 4. Therefore, the convergence of all coupling parameters is ensured 8 times for 2F2D1 and 13 times for 2F2DN23, over the whole depletion time.

4. Results and Discussion

The results of this study are presented in two sections. First, verification of the coupling process is performed by analyzing the convergence and axial power behavior at the assembly level (i.e., the power basis option is deactivated and all assembly materials are depleted by specifying assembly power). In the second section, validation of the coupling process is performed by analyzing fuel isotopics at the sample level (i.e., the power basis option is activated by specifying sample power).

4.1. Neutronic Analysis (Assembly-Based). Convergence results at three burnup steps (beginning, middle, and end of irradiation time) are shown in Figure 5 for the 2F2DN23/SF98 benchmark and in Figure 6 for the 2F2D1/F6 benchmark. The convergence of the three coupling parameters: axial power, coolant density, and coolant temperature, is monitored. The convergence criterion is set to ensure that the *average relative difference* of all axial nodes falls below a threshold of 6% with at least *3 iterations* executed. The threshold value is expressed in relative form regardless of the coupling parameter unit and it balances between accuracy and computational costs. If the average relative difference of all axial nodes falls below 6% on the second iteration, another iteration will still be performed to reach 3 in total. The third iteration is used to identify the convergence, i.e., convergence cannot be ensured with two iterations only. However, if three iterations are not sufficient to converge, additional iterations are executed until all average relative differences fall below 6%.

For 2F2D1/F6, the results show fast convergence for all parameters as they all converge after 3 iterations (the minimum limit) at the three selected burnup steps. It is clear that the coupling parameters seem to vary little between iterations, implying that the feedback from coolant is not significant for this benchmark. This can be justified by the almost steady power level in Figure 4(a), which causes the void fraction to be almost constant with burnup. Therefore, for 2F2D1/F6, the evolution in the axial power profile captured by the SCALE/T5-DEPL 3D model is more significant than the evolution of the coolant properties in TRACE when considering reactor behavior over burnup. On

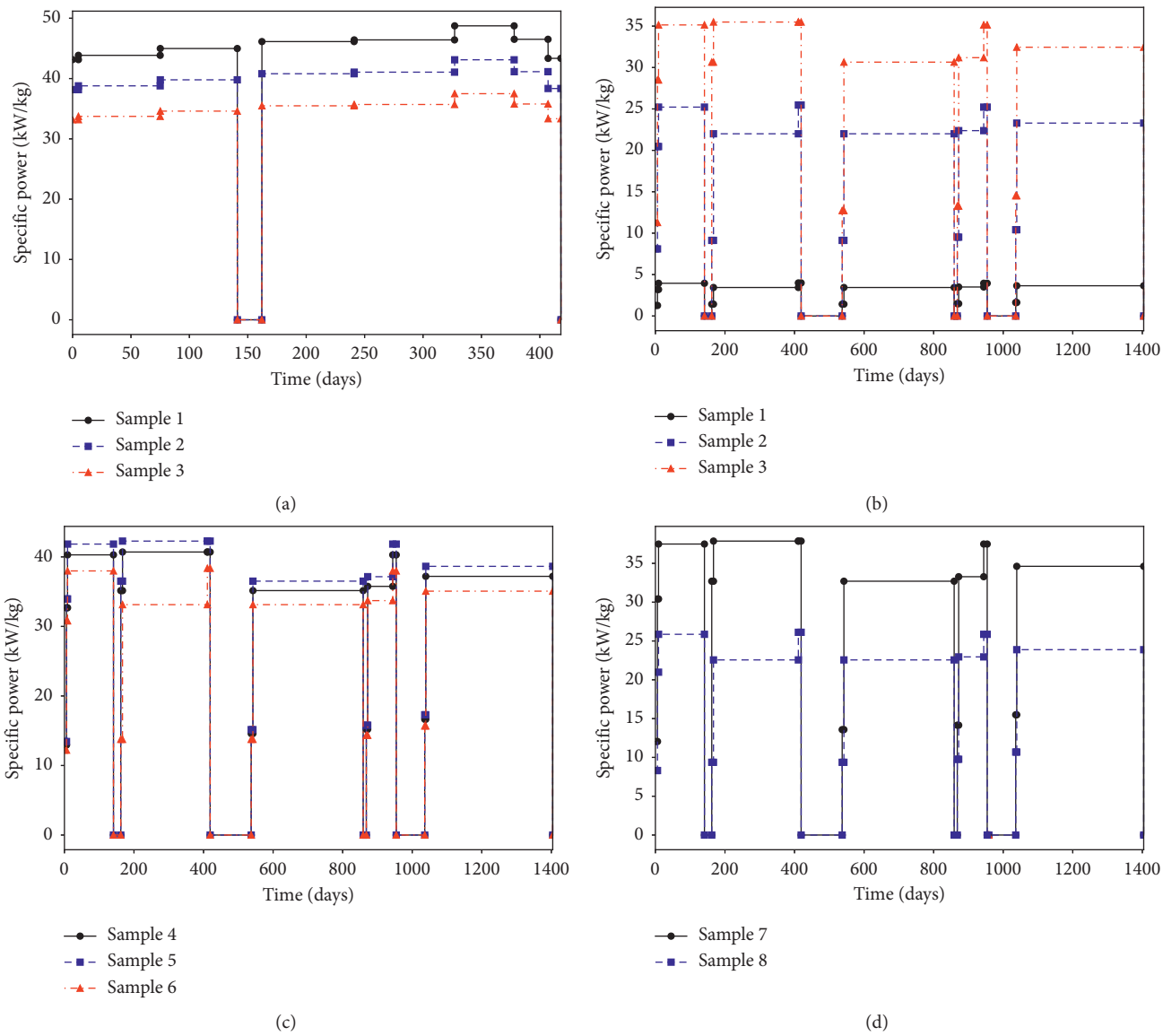

Figure 4: Sample power history for 2F2D1 assembly (a) and 2F2DN23 (b–d). (a) 2F2D1/F6. (b) 2F2DN23/SF98 (samples 1–3). (c) 2F2DN23/SF98 (samples 4–6). (d) 2F2DN23/SF98 (samples 7-8).

the other hand, for 2F2DN23/SF98, the results behave differently, as the system may converge within 3, 4, or 5 iterations, implying strong feedback from the coolant. This can be attributed to the higher variability in the power history associated with 2F2DN23/SF98, as can be observed in Figures 4(b)–4(d).

After confirming the convergence behavior of the coupling process, it is good to verify the change of some neutronic parameters with burnup. Figure 7 shows the variation of assembly k_∞ with burnup. For 2F2DN23, we can notice that k_∞ decreases significantly at beginning of cycle due to the xenon effect. Afterward, k_∞ starts to increase due to the depletion of gadolinium poison, until it reaches the reactivity peak, which is close to 10 GWD/MTU. Next, k_∞ continues to decrease toward the end of cycle due to the depletion of U-235. This is a typical behavior for BWR assemblies that are loaded with gadolinium rods. This behavior can be observed also for the 2F2D1 assembly, except that the simulated cycle length is shorter. We can see in Figure 7(b) that the reactivity peak is very close to 12 GWD/MTU, which is the end of cycle for 2F2D1. It is worth noticing that for some depletion steps in Figure 7(a), k_∞ seems not to converge (e.g., between 15 and 20 GWD/MTU), since we did not assign a constraint on converging k_∞ as a condition to exit the coupling loop, as described in Figure 2. Doing so will increase the computational costs significantly as k_∞ is a sensitive parameter. Nevertheless, the depletion trend is still clearly seen for this problem in spite of some incompletely converged k_∞ values.

The evolution of the axial power for the two sampled rods is plotted in Figure 8 for different burnup steps. For the SF98 rod, the samples span the axial direction. Therefore, the locations of the eight samples are used in Figure 8(a) for plotting. Since the irradiation time of the SF98 rod is long,

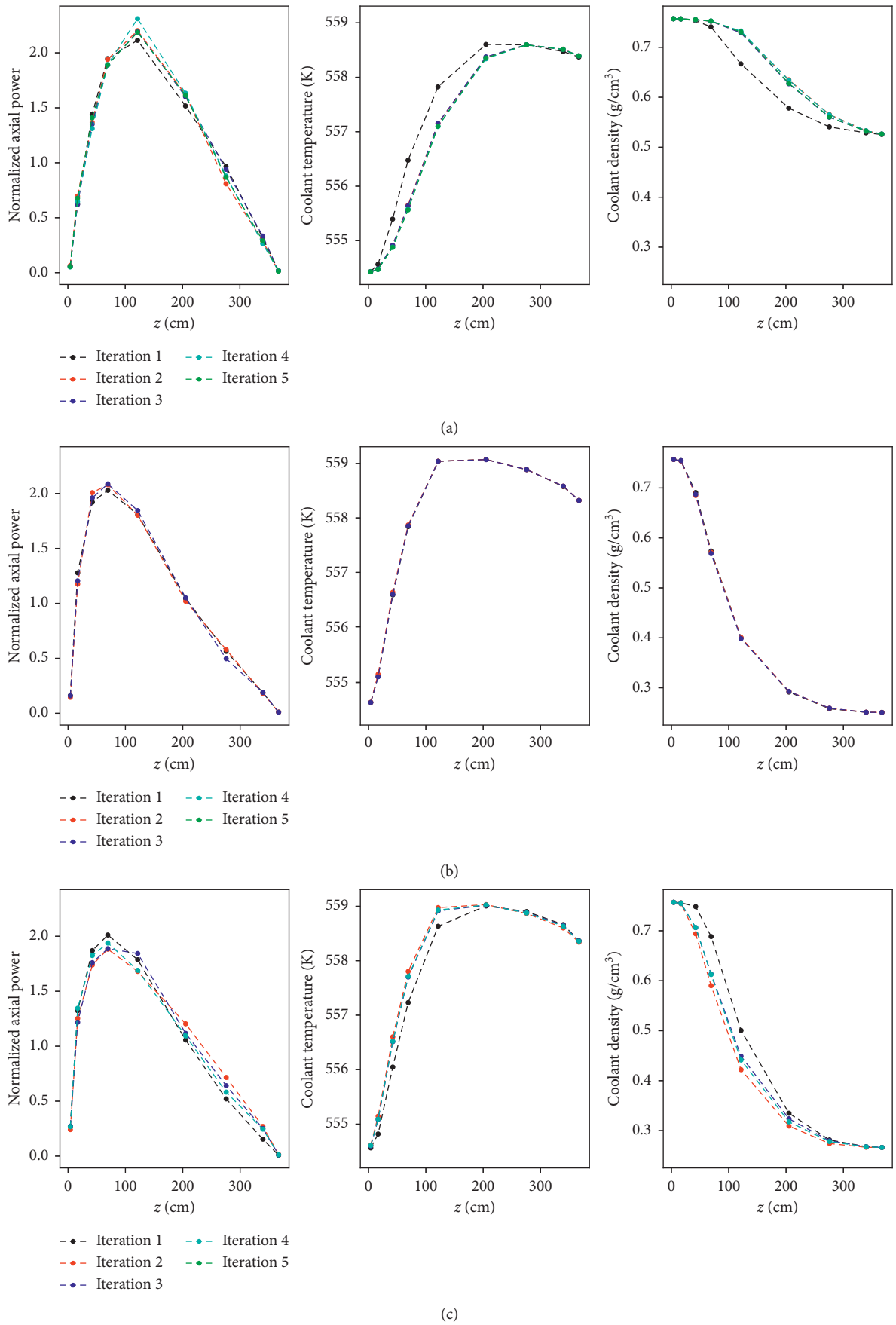

Figure 5: Convergence of neutronics and thermal-hydraulic coupling parameters based on the 2F2DN23/SF98 for three selected burnup steps. (a) BU step 1. (b) BU step 6. (c) BU step 13.

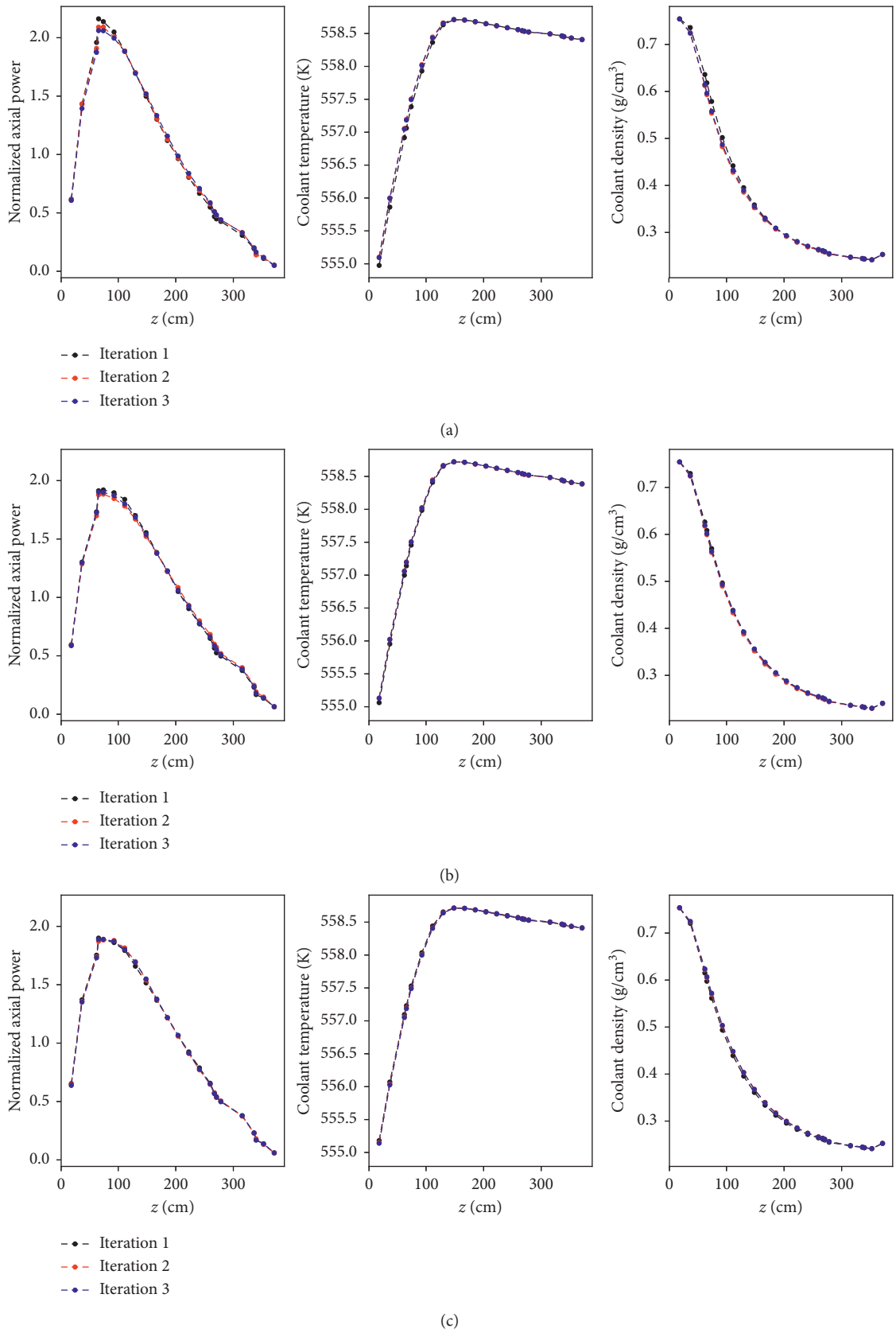

Figure 6: Convergence of neutronics and thermal-hydraulic coupling parameters based on the 2F2D1/F6 for three selected burnup steps. (a) BU step 1. (b) BU step 6. (c) BU step 13.

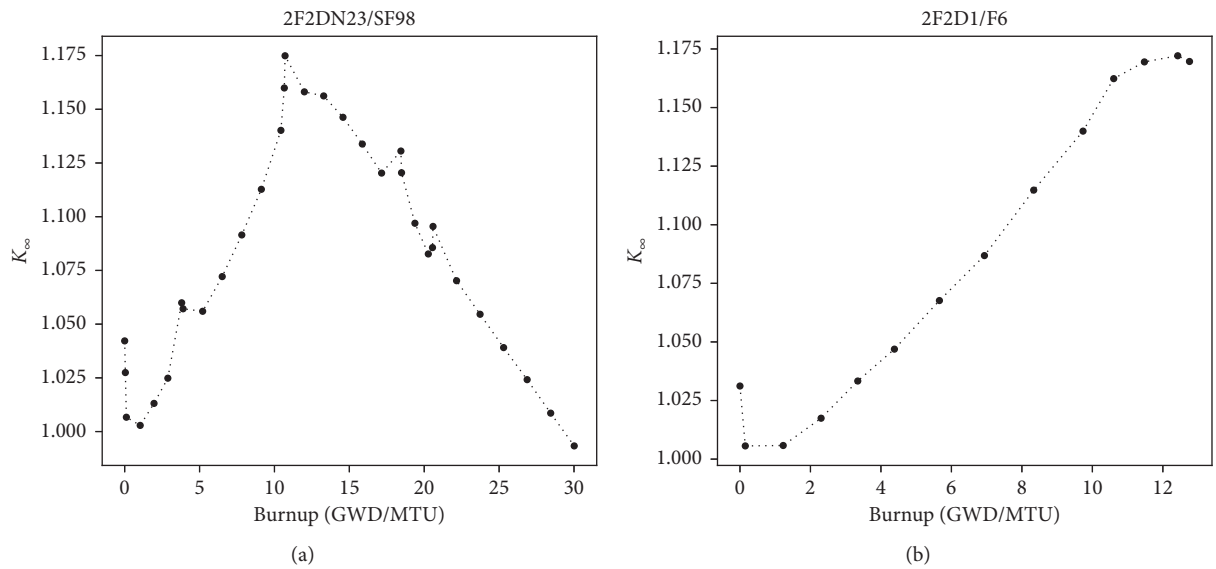

Figure 7: Variation of assembly k_∞ with burnup for 2F2DN23 (a) and 2F2D1 (b).

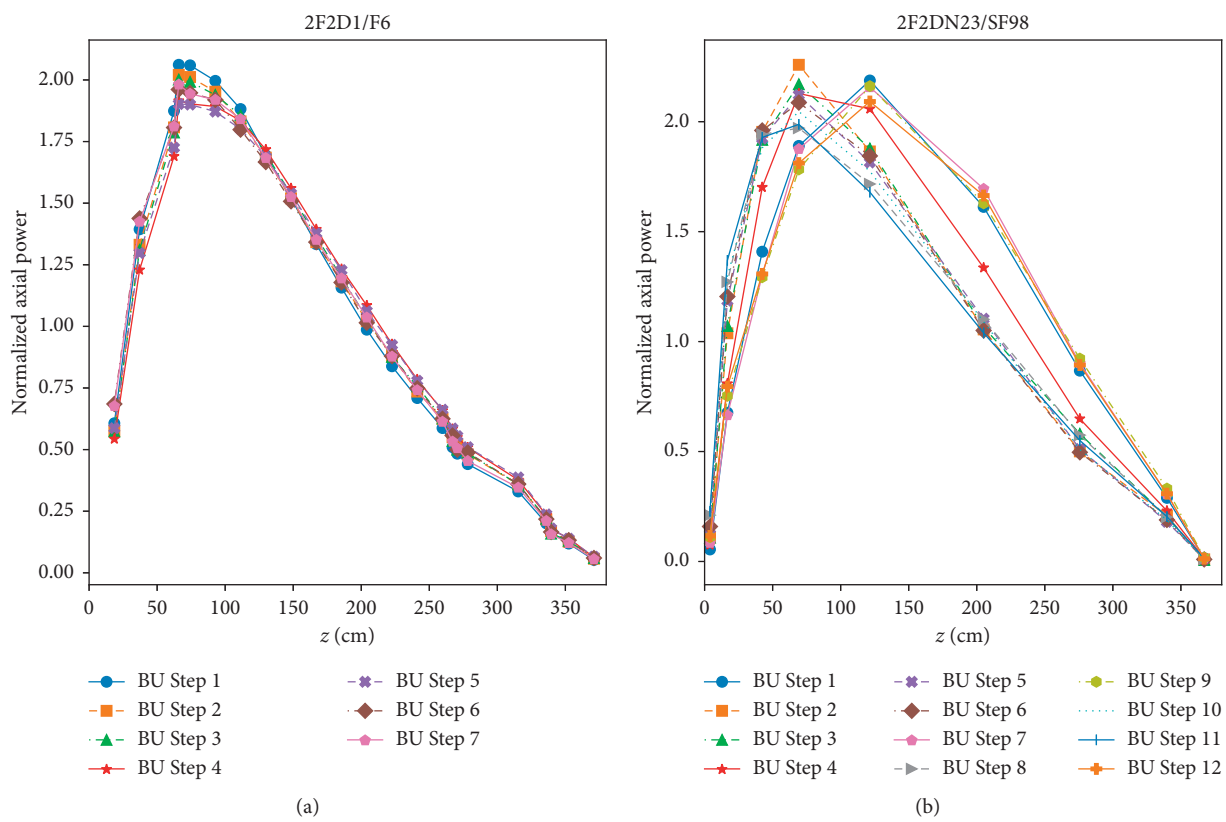

Figure 8: Variation of the axial power profile with burnup for the SF98 rod (a) and F6 rod (b).

the power profile experiences significant changes during the cycle time. On the other hand, for F6, all axial nodes are plotted due to the limited number of measured locations. The power profile for this benchmark did not experience a large change due to the short irradiation time. The bottom-peaked shape of the axial power is caused by the void distribution feedback of TRACE. Only small changes in the power peak at the channel bottom occur during burnup.

4.2. Isotopic Analysis (Sample-Based). To begin, all actinides and fission products are tracked, but six major actinides are plotted as a function of burnup at the sample level. The plots for these results are shown in Figure 9 for 2F2D1/F6 (three samples) and Figure 10 for 2F2DN23/SF98 (eight samples). As expected, the U-235 and U-238 concentrations decrease over burnup, while the remaining 4 actinides tend to build up as burnup increases. The differences in burnup for the last

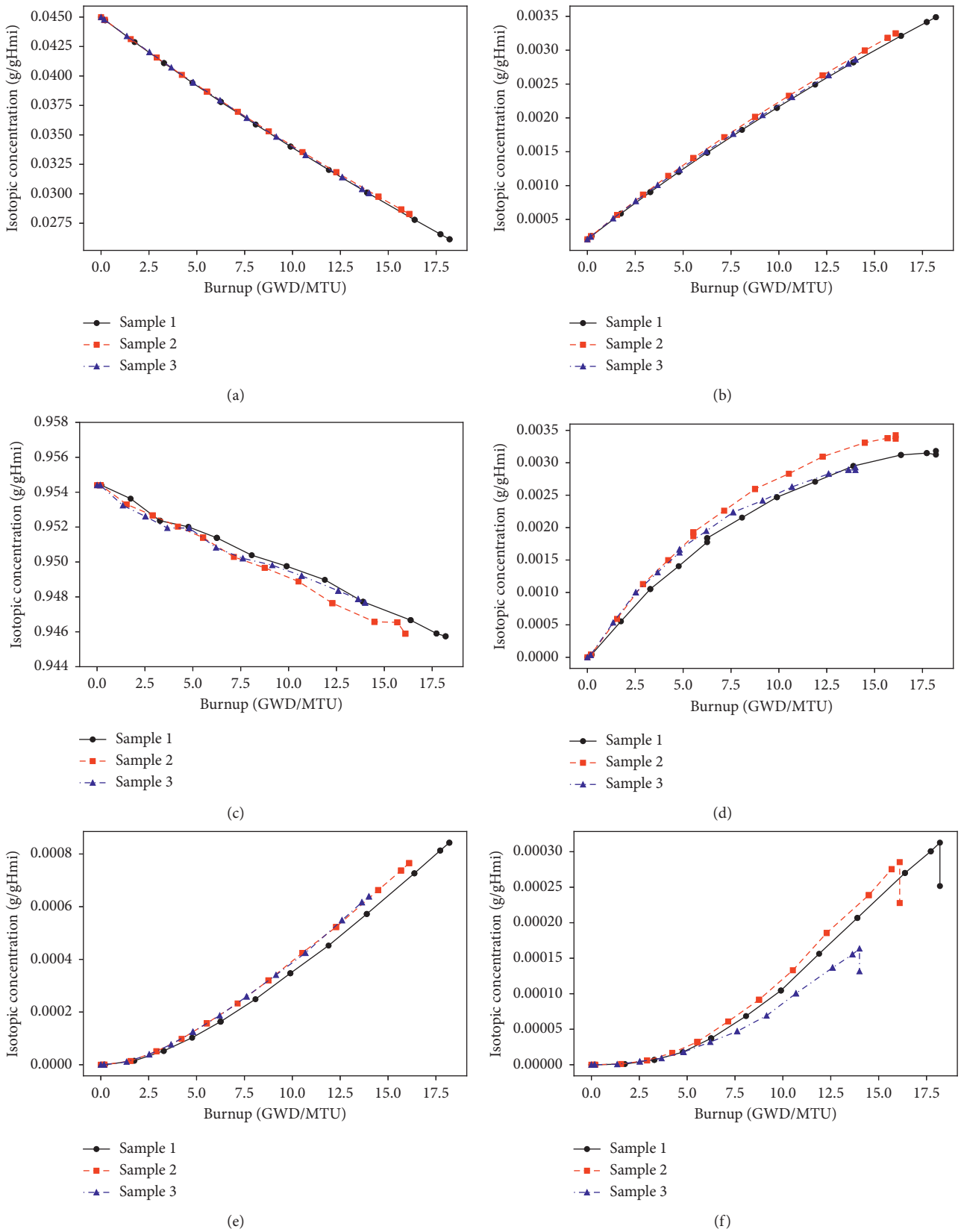

Figure 9: Variation of isotopic concentrations of six major actinides with burnup for the 2F2D1/F6 rod. Note: g/gHmi means that the isotope mass (g) is normalized to the grams of heavy metal observed initially in the region at the beginning of cycle. (a) U-235. (b) U-236. (c) U-238. (d) Pu-239. (e) Pu-240. (f) Pu-241.

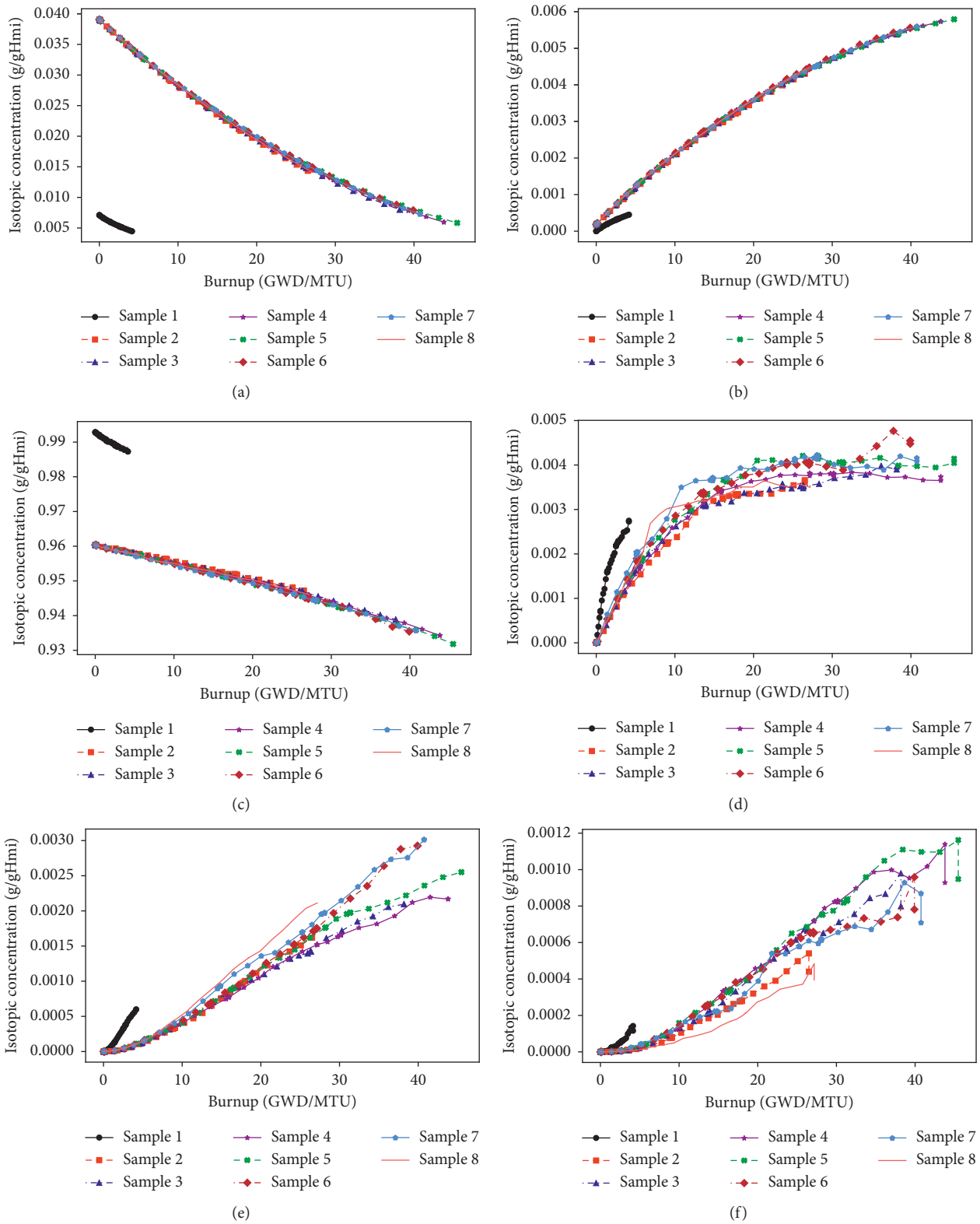

Figure 10: Variation of isotopic concentrations of six major actinides with burnup for the 2F2DN23/SF98 rod. Note: g/gHmi means that the isotope mass (g) is normalized to the grams of heavy metal observed initially at beginning of cycle. (a) U-235. (b) U-236. (c) U-238. (d) Pu-239. (e) Pu-240. (f) Pu-241.

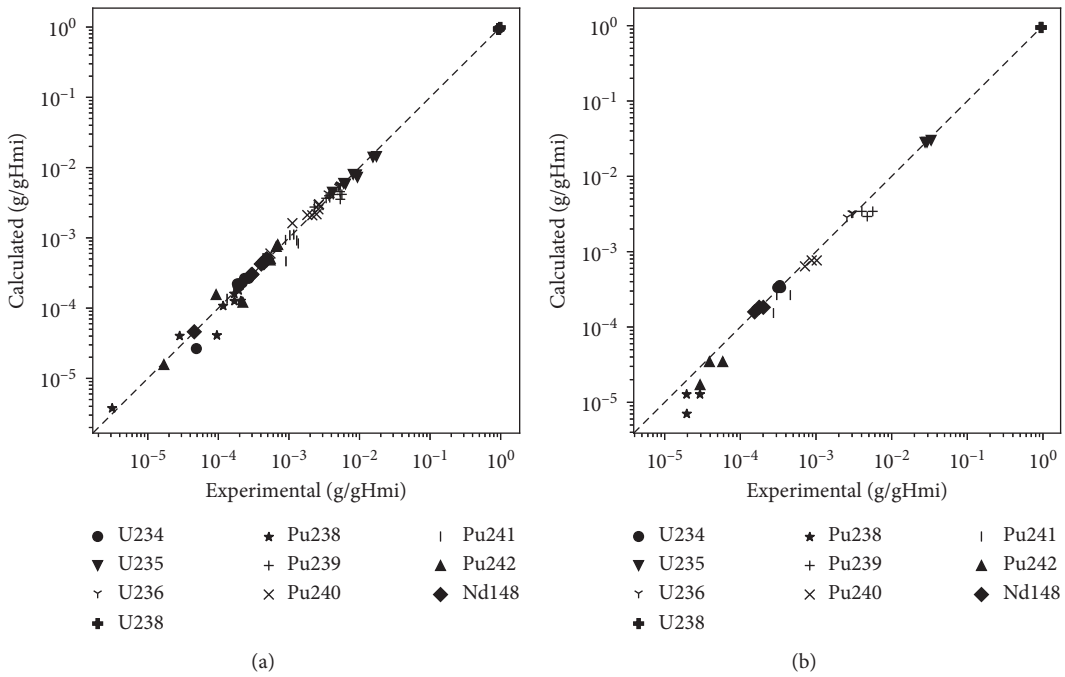

Figure 11: Validation of selected spent fuel isotopics in 2F2DN23/SF98 (a) and 2F2D1/F6 (b).

reported concentration in each sample are due to the differences in the sample burnup (see Figure 1). In general, uranium isotopes for all samples tend to change with the same slope. However, it is clear that plutonium isotopic concentrations are more sensitive to depletion conditions, as these isotopes build differently for each sample. The decay time before the rod measurement (~ 1500 days after rod discharge) causes a sharp decrease in Pu-241 concentration at end of life. This is also the case for the small increase in Pu-239 at end of cycle, due to the decay of other fission products into Pu-239. In addition, Figure 10 shows that sample 1 discharge burnup is much smaller than other samples, due to its location in the natural uranium region (0.71 wt.%).

The validation results of fuel isotopics are demonstrated in Figure 11 for selected isotopes in the two benchmarks. In addition, numerical values of the C/E ratio are listed in Table 1 for 2F2DN23/SF98 and in Table 2 for 2F2D1/F6. For completeness, the experimentally determined isotopic data are reported in Tables 3 and 4 of Appendix A, which can be used in conjunction with Tables 1 and 2 to obtain the calculated results. In the scatter plot of experimental versus calculated, the points that are closer to the diagonal line indicate better agreement with experiment. In this plot, the uranium isotopes as well as Nd-148 tend to have good agreement with data as can be inferred from their good C/E values. The good agreement for uranium isotopes can be attributed to their large content in the fuel and their low measurement error. Also, it was seen early that these isotopes are relatively insensitive to depletion conditions. The plutonium isotopes tend to have fair agreement with data, as their relative error can be as low as 2%, but as high as 64%.

In terms of uncertainty sources associated with this work, we believe uncertainty comes from three major sources: first, SCALE/T5-DEPL and the nuclear data libraries. Uncertainty in nuclear data, especially for minor actinides and fission products, can be a large factor particularly because the 56 multigroup energy library was used, which could be less accurate as compared to using continuous energy cross section library. The 56-group energy library was used because SCALE/T5-DEPL depletion calculations tend to be very slow with continuous energy cross sections. This coupling process requires multiple SCALE/T5-DEPL runs, so using continuous cross section libraries becomes impractical in terms of computational costs. The second uncertainty source is associated with the TRACE model, which is directly connected to the third source about lack of reported data. As this is a neutronics benchmark, very little information is provided to aid in building an accurate thermal-hydraulics model representing the fuel channel. Therefore, some assumptions about boundary conditions based on commercial BWRs (inlet flow rate, outlet temperature, friction coefficient, etc.) had to be made. These assumptions would affect the quality of coolant density and temperature predictions by TRACE. Additional missing pieces associated with neutronics include configuration of the assemblies that surround 2F2D1/2F2DN23 in the core, control blade history, SF98/F6 rod burnup, and fine-scale power history compared to the approximated profile provided by the benchmark. These factors are very important for realistic 3D modeling. Despite the previous challenges, satisfactory results are achieved at some axial elevations as indicated by the last row of Tables 1 and 2. The average relative difference for all isotopes can be less than 15% for some samples but can also be higher than that for other samples. It is worth mentioning that the current validation results are similar to previous efforts such as [4, 5, 8].

Table 1: Calculated/experimental (C/E) ratios for selected fuel isotopics in 2F2DN23/SF98.

Isotope	Sample 1	Sample 2	Sample 3	Sample 4	Sample 5	Sample 6	Sample 7	Sample 8
U-234	0.544	0.989	1.053	1.051	1.079	1.190	1.131	1.126
U-235	1.080	0.826	0.982	0.997	0.923	0.869	0.777	0.907
U-236	0.925	1.214	1.079	1.086	1.091	1.081	1.089	1.046
U-238	0.999	1.001	0.998	0.998	0.999	1.003	1.003	1.003
Pu-238	1.201	1.420	0.919	0.952	0.923	0.746	0.609	0.429
Pu-239	1.195	1.086	1.075	0.986	0.973	0.858	0.738	0.662
Pu-240	1.094	1.445	0.979	0.882	0.978	1.113	1.129	1.161
Pu-241	0.872	1.022	0.892	0.901	0.810	0.606	0.521	0.434
Pu-242	0.931	1.679	1.088	1.140	1.156	0.892	0.937	0.547
Nd-148	1.010	1.016	1.045	1.043	1.038	1.002	1.035	1.009
$\overline{\lvert C/E-1\rvert}$%	13.1	20.7	5.7	6.0	7.6	14.2	18.0	23.6

Last row includes the average relative difference in percent for each sample.

Table 2: Calculated/experimental (C/E) ratios for selected fuel isotopics in 2F2D1/F6.

Isotope	Sample 1	Sample 2	Sample 3
U-234	0.978	1.069	1.066
U-235	1.024	0.965	0.904
U-236	1.099	1.060	1.115
U-238	1.001	1.003	1.005
Pu-238	0.655	0.436	0.359
Pu-239	0.848	0.608	0.615
Pu-240	0.872	0.747	0.893
Pu-241	0.753	0.497	0.480
Pu-242	0.889	0.593	0.584
Nd-148	0.907	1.028	1.028
$\overline{\lvert C/E-1\rvert}$%	12.2	23.1	23.8

Last row includes the average relative difference in percent for each sample.

Table 3: Experimental data used for validation for the 2F2DN23/SF98 benchmark.

Isotope	Sample 1	Sample 2	Sample 3	Sample 4	Sample 5	Sample 6	Sample 7	Sample 8
U-234	$4.88E-05$	$2.68E-04$	$2.18E-04$	$1.98E-04$	$1.90E-04$	$1.86E-04$	$1.96E-04$	$2.35E-04$
U-235	$4.13E-03$	$1.74E-02$	$8.14E-03$	$5.97E-03$	$6.32E-03$	$9.06E-03$	$9.36E-03$	$1.55E-02$
U-236	$4.86E-04$	$3.55E-03$	$4.99E-03$	$5.28E-03$	$5.31E-03$	$5.14E-03$	$5.14E-03$	$4.29E-03$
U-238	$9.88E-01$	$9.46E-01$	$9.41E-01$	$9.36E-01$	$9.33E-01$	$9.33E-01$	$9.33E-01$	$9.43E-01$
Pu-238	$3.13E-06$	$2.83E-05$	$1.17E-04$	$1.68E-04$	$1.94E-04$	$1.69E-04$	$2.08E-04$	$9.54E-05$
Pu-239	$2.30E-03$	$3.37E-03$	$3.69E-03$	$3.79E-03$	$4.26E-03$	$5.30E-03$	$5.63E-03$	$5.34E-03$
Pu-240	$5.47E-04$	$1.12E-03$	$2.14E-03$	$2.46E-03$	$2.61E-03$	$2.63E-03$	$2.67E-03$	$1.82E-03$
Pu-241	$1.33E-04$	$4.31E-04$	$8.95E-04$	$1.03E-03$	$1.17E-03$	$1.29E-03$	$1.36E-03$	$9.08E-04$
Pu-242	$1.69E-05$	$9.29E-05$	$4.62E-04$	$6.62E-04$	$6.94E-04$	$5.43E-04$	$5.44E-04$	$2.22E-04$
Nd-148	$4.56E-05$	$2.91E-04$	$4.06E-04$	$4.66E-04$	$4.85E-04$	$4.41E-04$	$4.36E-04$	$3.00E-04$

Table 4: Experimental data used for validation for the 2F2D1/F6 benchmark.

Isotope	Sample 1	Sample 2	Sample 3
U-234	$3.41E-04$	$3.12E-04$	$3.33E-04$
U-235	$2.76E-02$	$2.93E-02$	$3.33E-02$
U-236	$2.96E-03$	$3.06E-03$	$2.57E-03$
U-238	$9.45E-01$	$9.43E-01$	$9.43E-01$
Pu-238	$1.95E-05$	$2.93E-05$	$1.96E-05$
Pu-239	$4.04E-03$	$5.63E-03$	$4.76E-03$
Pu-240	$8.78E-04$	$1.02E-03$	$7.15E-04$
Pu-241	$3.02E-04$	$4.59E-04$	$2.74E-04$
Pu-242	$3.90E-05$	$5.86E-05$	$2.94E-05$
Nd-148	$2.01E-04$	$1.77E-04$	$1.54E-04$

Finally, since lack of documentation was a major challenge for this work, future efforts will focus on incorporating machine learning and data science to aid in identifying the missing input parameters such that they can yield the desired output. Techniques such as Gaussian process optimization and deep reinforcement learning can be efficiently used for this purpose. These efforts can help in completing the current benchmarks to achieve accurate modeling and simulation.

5. Conclusions

Multiphysics coupling of SCALE/TRACE is used in this work for neutronic analysis and spent fuel validation of BWR spent

fuel isotopics. The coupling is performed externally where SCALE/T5-DEPL module sends axial power profile to TRACE, which returns coolant density and temperature. This process is repeated until convergence of all quantities at each time step. The methodology is applied to two BWR assemblies, discharged from the Fukushima Daini-2 unit. The neutronic analysis on assembly level shows that the coupling process is verified, where the 2F2D1/F6 benchmark seems to have insignificant void feedback. Validation of the coupling process is done through spent fuel isotopics data, which demonstrated good results for uranium isotopes and satisfactory results for other isotopes, given the significant lack of documented data faced in this work. Future work will include applying machine learning methods to help in identifying the missing data such that more accurate modeling and results can be achieved.

Appendix

A. Experimental Data

In this section, the experimentally determined isotopic data are reported in Tables 3 and 4 as reproduced from [21]. These data, in conjunction with Tables 1 and 2, can be used to calculate the simulated data.

Data Availability

The computer codes are from RSICC and U.S. NRC, and the data are from OECD/NEA; any person who is able to obtain codes from RSICC and U.S. NRC and data from OECD/NEA is able to do the same type of coupling and validation.

Conflicts of Interest

The authors declare that they have no conflicts of interest.

References

[1] M. I. Radaideh, D. Price, D. O'Grady, and T. Kozlowski, "Advanced BWR criticality safety part I: model development, model benchmarking, and depletion with uncertainty analysis," *Progress in Nuclear Energy*, vol. 113, pp. 230–246, 2019.

[2] G. Ilas, I. C. Gauld, and G. Radulescu, "Validation of new depletion capabilities and endf/b-vii data libraries in scale," *Annals of Nuclear Energy*, vol. 46, pp. 43–55, 2012.

[3] G. Radulescu, I. C. Gauld, and G. Ilas, "Scale 5.1 predictions of PWR spent nuclear fuel isotopic compositions," ORNL/TM-2010/44, Oak Ridge National Laboratory, Oak Ridge, TN, USA, 2010.

[4] U. Mertyurek, M. W. Francis, and I. C. Gauld, "SCALE 5 analysis of BWR spent nuclear fuel isotopic compositions for safety studies," Tech. Rep., ORNL/TM-2010/286, Oak Ridge National Laboratory, Oak Ridge, TN, USA, 2010.

[5] I. C. Gauld and U. Mertyurek, "Validation of bwr spent nuclear fuel isotopic predictions with applications to burnup credit," *Nuclear Engineering and Design*, vol. 345, pp. 110–124, 2019.

[6] Y. Ando and H. Takano, "Estimation of lwr spent fuel composition," Tech. Rep., Japan Atomic Energy Research Institute, Tokai, Japan, 1999.

[7] I. C. Gauld, J. M. Giaquinto, J. S. Delashmitt et al., "Re-evaluation of spent nuclear fuel assay data for the three mile island unit 1 reactor and application to code validation," *Annals of Nuclear Energy*, vol. 87, pp. 267–281, 2016.

[8] D. Price, M. I. Radaideh, D. O'Grady, and T. Kozlowski, "Advanced bwr criticality safety part ii: cask criticality, burnup credit, sensitivity, and uncertainty analyses," *Progress in Nuclear Energy*, vol. 115, pp. 126–139, 2019.

[9] N. García-Herranz, O. Cabellos, J. Sanz, J. Juan, and J. C. Kuijper, "Propagation of statistical and nuclear data uncertainties in Monte Carlo burn-up calculations," *Annals of Nuclear Energy*, vol. 35, no. 4, pp. 714–730, 2008.

[10] W. Zwermann, A. Aures, L. Gallner et al., "Nuclear data uncertainty and sensitivity analysis with xsusa for fuel assembly depletion calculations," *Nuclear Engineering and Technology*, vol. 46, no. 3, pp. 343–352, 2014.

[11] M. I. Radaideh, D. Price, and T. Kozlowski, "On using computational versus data-driven methods for uncertainty propagation of isotopic uncertainties," *Nuclear Engineering and Technology*, vol. 52, no. 6, pp. 1148–1155, 2020.

[12] J. C. Ragusa and V. S. Mahadevan, "Consistent and accurate schemes for coupled neutronics thermal-hydraulics reactor analysis," *Nuclear Engineering and Design*, vol. 239, no. 3, pp. 566–579, 2009.

[13] K. Ivanov and M. Avramova, "Challenges in coupled thermal-hydraulics and neutronics simulations for LWR safety analysis," *Annals of Nuclear Energy*, vol. 34, no. 6, pp. 501–513, 2007.

[14] M. Daeubler, A. Ivanov, B. L. Sjenitzer, V. Sanchez, R. Stieglitz, and R. Macian-Juan, "High-fidelity coupled Monte Carlo neutron transport and thermal-hydraulic simulations using Serpent 2/SUBCHANFLOW," *Annals of Nuclear Energy*, vol. 83, pp. 352–375, 2015.

[15] J. Yu, H. Lee, M. Lemaire, H. Kim, P. Zhang, and D. Lee, "Mcs based neutronics/thermal-hydraulics/fuel-performance coupling with ctf and frapcon," *Computer Physics Communications*, vol. 238, pp. 1–18, 2019.

[16] K. Nikitin, P. Mueller, A. Bruder, S. Walser, J. Judd, and D. Hiltbrand, "Bwr-4 atws modeling with relap5-s3k," *Nuclear Engineering and Design*, vol. 344, pp. 38–45, 2019.

[17] T. Kozlowski, A. Wysocki, I. Gajev et al., "Analysis of the OECD/NRC oskarshamn-2 BWR stability benchmark," *Annals of Nuclear Energy*, vol. 67, pp. 4–12, 2014.

[18] A. Grahn, S. Kliem, and U. Rohde, "Coupling of the 3d neutron kinetic core model dyn3d with the cfd software ansys-cfx," *Annals of Nuclear Energy*, vol. 84, pp. 197–203, 2015.

[19] R. Henry, I. Tiselj, and L. Snoj, "CFD/Monte-Carlo neutron transport coupling scheme, application to TRIGA reactor," *Annals of Nuclear Energy*, vol. 110, pp. 36–47, 2017.

[20] T. Yamamoto and M. Yamamoto, "Nuclear analysis of PIE data of irradiated BWR 8×8-2 and 8×8-4 UO2Fuel assemblies," *Journal of Nuclear Science and Technology*, vol. 45, no. 11, pp. 1193–1214, 2008.

[21] F. Michel-Sendis, I. Gauld, J. S. Martinez et al., "SFCOMPO-2.0: an OECD NEA database of spent nuclear fuel isotopic assays, reactor design specifications, and operating data," *Annals of Nuclear Energy*, vol. 110, pp. 779–788, 2017.

[22] Y. Nakahara, K. Suyama, J. Inagawa et al., "Nuclide composition benchmark data set for verifying burnup codes on spent light water reactor fuels," *Nuclear Technology*, vol. 137, no. 2, pp. 111–126, 2002.

[23] U.S.NRC, "TRACE V5.840 theory manual: fields equations, solution methods, and physical models," Tech. rep., US Nuclear Regulatory Commission, Washington, DC, USA, 2013.

[24] S. M. Bowman, "Scale 6: comprehensive nuclear safety analysis code system," *Nuclear Technology*, vol. 174, no. 2, pp. 126–148, 2011.

[25] B. T. Rearden and M. A. Jessee, "SCALE code system," Tech. rep., ORNL/TM–2005/39-V-6.2, Oak Ridge National Laboratory, Oak Ridge, TN, USA, 2018.

Hindawi
Science and Technology of Nuclear Installations
Volume 2020, Article ID 9235783, 21 pages
https://doi.org/10.1155/2020/9235783

Research Article

Sensitivity and Uncertainty Analysis of the Maximum Fuel Temperature under Accident Condition of HTR-PM

Chen Hao,[1] **Peijun Li**,[1] **Ding She**,[2] **Xiaoyu Zhou**,[1] **and Rongrui Yang**[1]

[1]*Fundamental Science on Nuclear Safety and Simulation Technology Laboratory, Harbin Engineering University, Harbin 150001, China*
[2]*Institute of Nuclear and New Energy Technology (INET), Tsinghua University, Beijing 100084, China*

Correspondence should be addressed to Ding She; sheding@tsinghua.edu.cn

Received 4 November 2019; Accepted 16 January 2020; Published 22 February 2020

Academic Editor: Tomasz Kozlowski

The maximum fuel temperature under accident condition is the most important parameter of inherently safe characteristics of HTR-PM, and the DLOFC accident may lead to a peak accident fuel temperature. And there are a variety of uncertainty sources in the maximum fuel temperature calculations, and thus the contributions of these uncertainty sources to the final calculated maximum fuel temperature should be quantified to check whether the peak value exceed the technological limit of 1620°C or not. Eight uncertainty input parameters are selected for inclusion in this uncertainty study, and their associated 2 standard deviation uncertainties and probability density functions are specified. Then, the DLOFC thermal analyses and uncertainty analysis are performed with the home-developed ATHENA and CUSA. The numerical results indicate that the pebble-bed effective conductivity and the decay heat contribute the most of the uncertainty in the DLOFC maximum fuel temperature while this peak fuel temperature is most sensitive to the initial reactor power and the decay heat. In short, uncertainties in these selected eight parameters lead to the two standard deviation (2σ) uncertainty of ±77.6°C (or 5.2%) around the mean value of 1493°C for the maximum fuel temperature under DLOFC accident of HTR-PM. At the same time, the LHS-SVDC method of CUSA is recommended to propagate uncertainties in inputs and 100–200 model simulations seem to be sufficient to get an uncertainty prediction with full confidence.

1. Introduction

The modular high-temperature gas-cooled reactor (MHTGR) such as the Chinese demonstration plant, named as high-temperature gas-cooled reactor-pebble bed module (HTR-PM) [1], is designed to retain its fission products inside the fuel coatings even if all active components for decay heat removal and reactivity control fail. One way to reach this goal is to make sure that the maximum fuel temperature during accident condition should not exceed the technological limit of 1620°C. The maximum fuel temperature under accident condition is the most important parameter of inherently safe characteristics of HTR-PM, which is about 900°C under normal operating conditions, far from the normal operation condition limit of 1200°C and the accident limit value of 1620°C. But during the depressurized loss of forced cooling (DLOFC) accident, the decay heat will be removed from the HTR-PM core only by physical ways such as heat conduction and radiation. Accounting for this, it may lead to a maximum accident fuel temperature. For other accidents, the fuel temperature is much lower than the fuel temperature during DLOFC because of the presence of helium with a certain pressure, which can enhance the ability of heat transfer in the HTR-PM core and flatten the temperature distribution depending on the helium natural circulation and heat conduction even if there is no forced flow [2].

The accurate prediction of maximum fuel temperature under accident condition is therefore most important to the nuclear reactor safety analysis and design. Considering that the HTR-PM is a complex nonlinear multiphysics, multiscale coupling system, the best-estimate (BE) methods with full consideration of the coupling among neutronics,

thermal hydraulics, fuel performance, and structural characteristics have now become the standard for the modern simulation of HTR-PM. Moreover, there are a variety of uncertainty sources in the maximum fuel temperature calculations, and thus the prediction should involve the propagation and quantification of uncertainty in the coupling HTR-PM. More importantly, the uncertainty analysis of the maximum fuel temperature can be used to improve the reliability of the calculated maximum fuel temperature, identify the importance of uncertainty sources, and ensure appropriate design margins. Then, it can be decided where additional efforts should be undertaken to reduce uncertainties in modeling and to improve the design itself. So as the researches progressed and best-estimate methods matured, a move toward the best-estimation plus uncertainty (BEPU) analysis occurs, which becomes a powerful numerical tool for the detailed analysis of the maximum fuel temperature under accident conditions.

As for the uncertainty analysis of the maximum fuel temperature under accident condition, there are a variety of uncertainty sources, such as the most unfavorable initial state, calculation methods, and uncertain input data. At the same time, the probability distribution types and variation range of each uncertainty source should be determined based on the experimental data or material characteristics or numerical simulation results. In this work, eight important uncertainty sources are selected based on some related papers [3, 4], preliminary sensitivity analysis via a home-developed thermal-hydraulic code ATHENA for HTGR, and our previous studies [5, 6]. Then, the accident thermal analyses are performed with the home-developed ATHENA, and another home-developed code CUSA is applied to perform the uncertainty quantification of the maximum fuel temperature propagated from the selected uncertainty sources.

The rest of the paper is organized as follows. The details of methodologies, model, and the analyzed designed basis event are described in Section 2, and then in Section 3, the selection of uncertainty sources, determination of uncertainties of these selected parameters, and sample generation are discussed. Sections 4 and 5 show a detailed analysis of the origin sensitivity and uncertainty information and uncertainty quantification of the maximum fuel temperature under accident condition. At last, conclusions drawn from this work are given in Section 6.

2. Methodologies and the Model Used in the Analysis

2.1. Description of HTR-PM and the Analyzed Designed Basis Event. The Chinese demonstration plant HTR-PM is selected as the reference model in this work, and the axial layout of the HTR-PM design is shown in Figure 1, and the general design parameters can be found in the cited paper [7]. The HTR-PM is designed to comply with the inherently safe characteristic principles of the MHTGR, which must be able to remove the decay heat passively from the core under any designed accident conditions. And the maximum fuel temperature should not exceed the 1620°C in all cases so as to contain all fission products inside the SiC layer of the TRISO-coated fuel. At the same time, HTR-PM has a large negative temperature coefficient. Therefore, it eliminates the possibility of large releases of radioactive materials into the environment for all possible accidents by far in the hypothetical regime [1].

In all design-basis accidents, only the DLOFC may lead to the highest fuel temperatures. In this design-basis accident, the core heats up following fast depressurization of the pressure vessel by the break of a tube with diameter of 65 mm (a kind of limiting accident) connected to it. Within a few minutes, the reactor losses nearly all of its coolant, helium gas, and the density of the coolant is at about 1 bar atmosphere. Hence, the natural convection in the core can be neglected and heat can then be removed from the core mainly by radiation and heat conduction. In the first hours of the accident, the radiation and heat conduction are not efficient enough to remove the decay heat so that the reactor starts to heat up. Then, the maximum fuel temperature continuously increases. With the decay heat production decreasing steadily and the radial temperature gradients in the core and structures increasing, it provides better conditions for heat transfer. After about 20–30 hours, the maximum fuel temperature is predicted to a peak value around 1500°C. More details of the DLOFC accidents of HTR-PM can be found in the cited paper [8].

2.2. Description of CUSA. The CUSA (the Code for Uncertainty and Sensitivity Analysis) was originally developed for uncertainty and sensitivity analysis of filling fraction of pebble bed and uranium loading of fuel pebble in pebble bed HTR [9]. The initial version only has some simple sampling and statistical functions based on the simple random sampling (SRS) method, Latin hypercube sampling (LHS) method, K-S test, and basic statistical theory. As the research progresses, a new version of CUSA has been developed based on some new proposed methods, such as the efficient sampling method to generate reasonable sample space for variables with different multivariate probability density function (PDF) and systematic theory analysis for uncertainty quantification to quantify the uncertainty of output and its associated error bar or confidence interval under a specific size of sample space. And some new functions, such as the user-friendly human-computer interaction platform, standardized input, code coupling, and plot, have also been developed by using QT language and C language on Windows operating system. An overview of basic functions and coupling relationship between different modules is illustrated in Figure 2. More details of the methodologies used in CUSA and some verification of the code can be found in the cited paper [10].

In this work, CUSA is used to generate sample space of input parameters according to their distribution and covariance information. Then, these sets of samples will be sent into the home-developed thermal hydraulics code ATHENA to produce a set of output maximum fuel temperature. At last, the statistical function in CUSA is applied to quantify the uncertainty of outputs propagated from inputs.

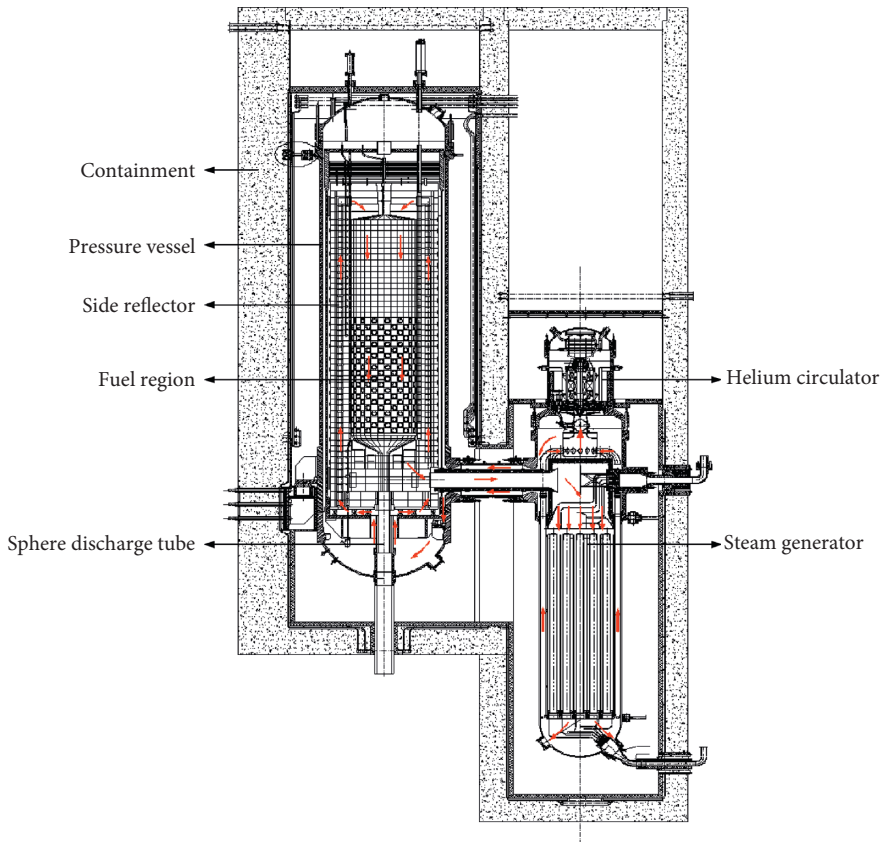

Figure 1: Cross section of the HTR-PM.

2.3. Description of ATHENA. ATHENA code is developed for high-temperature reactor thermal design by INET (Institute of Nuclear and New Energy Technology), Tsinghua University. It is based on rewriting the well-known German HTR thermal design code THERMIX [11], using modern programming style and user-friendly XML input format for better readability and maintainability. The main functionalities of ATHENA are identical to that of THERMIX, which have been well validated in HTGR steady and transient analyses. Sufficient numerical tests done in house have suggested that ATHENA code can reproduce THERMIX results very well. Besides, ATHENA has implemented several new calculation methods and functions, such as the fuel particle temperature calculation, which can extend the code's capability. ATHENA code can also be coupled with the PANGU code [12] to perform HTGR neutronics and thermal-hydraulic coupling analyses.

2.4. Uncertainty and Sensitivity Analysis Method. Maximum fuel temperature under accident condition is the most important and interesting parameter, which represents the level of inherently safe characteristics of modular HTGR. Therefore, the uncertainty in the calculated maximum fuel temperature is also one of the most important and interesting parameters. In this work, the statistical sampling-based uncertainty and sensitivity analysis method is selected to quantify the uncertainty of the maximum fuel temperature under accident condition. Using the statistical sampling method to perform uncertainty and sensitivity analysis, four challenges need to be handled reasonably.

The first challenge is a building of model for uncertainty propagation and quantification. In fact, we have not and could not have an analytical model for uncertainty propagation in a nuclear system. But any physical phenomena or process in a nuclear system can be described by using mathematical models, i.e., integral-differential/algebraic equations, and numerical tools can be used to solve these equations and then codes are developed. Indeed, we already have developed the ATHENA code, which can be used to assess the transient behavior of pebble-bed high-temperature gas-cooled reactor.

Second, the important uncertainty sources with their uncertainty information, i.e., mean, variance/covariance, and PDF, should be determined based on the experiment data or material characteristics or numerical simulation results. The problem is that the PDF is usually unknown and being replaced by approximations of normal or uniform distribution.

The next important issue is the efficient sampling methods should be used to generate a reasonable input sample space based on the basic uncertainty information. Especially the correlation information between different input parameters should be represented accurately and reasonably by the sample space, while it always fails when the

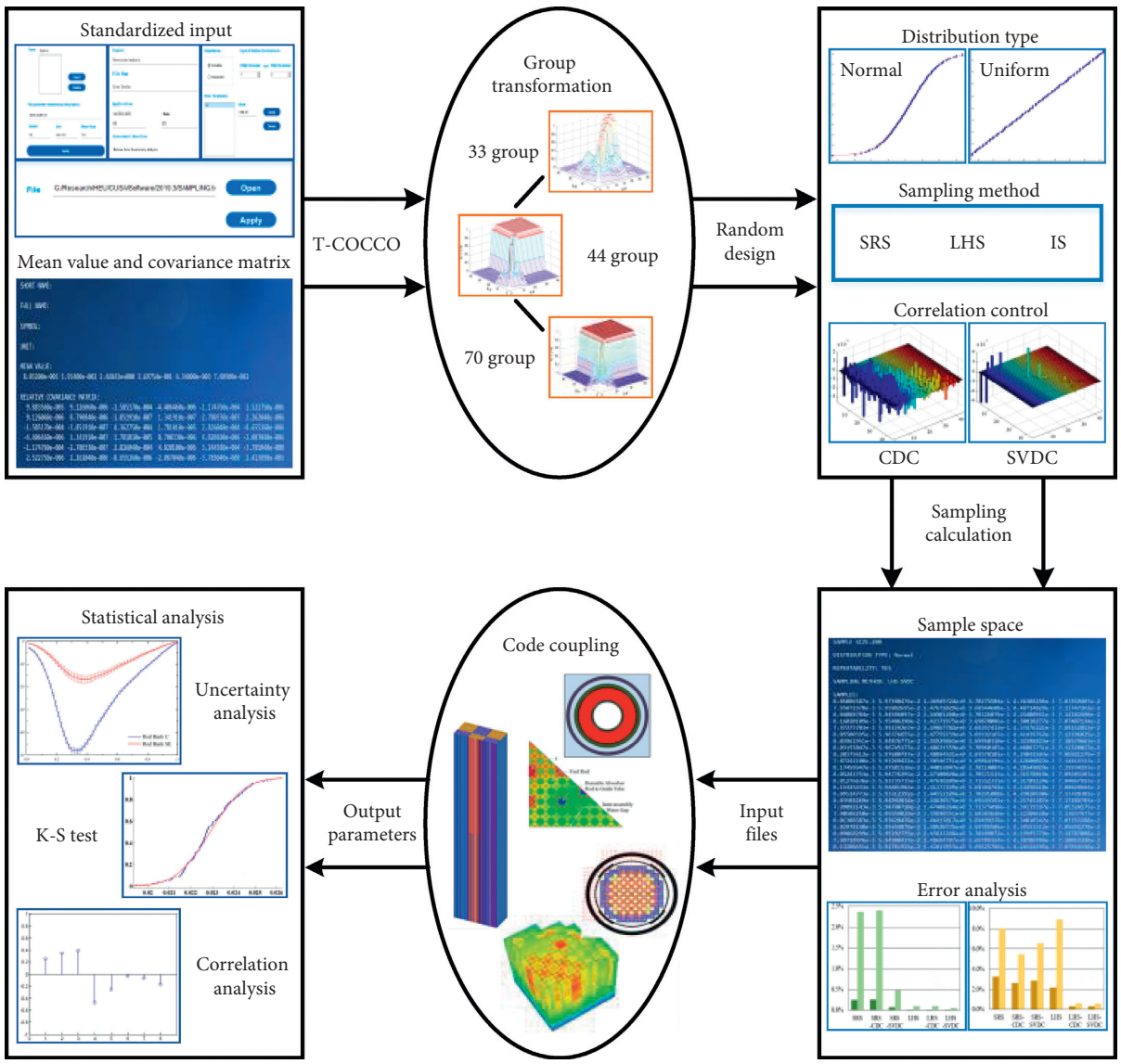

Figure 2: The function diagram of CUSA.

sample size is small if the traditional SRS or LHS method is used. In this work, an innovative LHS-SVDC method [13] built in CUSA is used to generate a reasonable sample space with a relatively small sample size.

The final problem corresponding to statistics is that a systematic theory analysis for uncertainty quantification should be conducted, which can be used to quantify the uncertainty of output and its associated error bar or confidence interval under a specific size of sample space.

Here, the implementation details of the sensitivity and uncertainty analysis of the maximum fuel temperature under DLOFC accident condition by using statistical sampling method based on CUSA and ATHENA are summarized:

(1) An in-depth analysis into the most unfavorable initial state, the process of decay heat production and removal of HTR-PM, is carried out firstly to determine all the uncertainty sources. Then, some important input parameters are selected from these uncertainty sources based on the direct perturbation sensitivity analysis method and conclusions drawn from some published papers. For the direct perturbation sensitivity analysis, the maximum fuel temperature under DLOFC accident is computed by using the ATHENA code with the nominal values of the input quantities, then with a selected input value increased by a certain percentage, and then with the value decreased by the same percentage. Then, the sensitivity coefficient of the maximum fuel temperature to some input value can be computed by using CUSA, and the uncertainty sources with a relatively small sensitivity coefficient will be excluded in this work.

(2) Determine the uncertainty information, such as the mean, covariance, and PDF of the selected uncertainty parameters, and correlation information

between different parameters based on experiment data, numerical simulations and the statistical analysis, material characteristics, the accuracy of the instrument and control (I&C) system, and so on. Then, a global relative covariance matrix is built, which represents the uncertainty and correlation information of uncertainty inputs. It is worth noting that all the selected uncertainty parameters are assumed obeying normal distributions and uniform distributions, respectively, in this work to further study the effect of PDF on the uncertainty of the maximum fuel temperature.

(3) The efficient sampling function built in the CUSA is applied to generate a good sample space for all the selected inputs. If the number of uncertainty inputs is M and the sample size is N, a $N \times M$ matrix of input samples will be generated by CUSA. In this work, different sampling methods built in CUSA are used to generate different sample spaces for further comparison of these sampling methods and analysis of the effect of sampling methods on the uncertainty analysis of the maximum fuel temperature.

(4) Each row of the $N \times M$ matrix is a random set of the selected uncertainty inputs, and the ATHENA code will be run N times by using each row of the input sample matrix to generate N sets of transient behaviors of HTR-PM under DLOFC accident, including the maximum fuel temperature.

(5) Finally, the statistical analysis functions built in CUSA are used to quantify the distribution type and the uncertainty of the maximum fuel temperature due to these selected uncertainty sources based on the N sets of ATHENA calculations. At the same time, the associated error bar or confidence interval under a specific sample size is also quantified. Further, the correlation analysis function can be also used to perform the sensitivity analysis.

3. Determination of the Uncertainties of Input Data and Sample Generation

3.1. Determination of the Uncertainties of Input. The maximum fuel temperature is mainly determined by the process of the decay heat production and removal under DLOFC accident condition of HTR-PM. To achieve a conservative value of the maximum fuel temperature, it is necessary to consider the most unfavorable initial state, including the initial core power, appearance of a higher peak power density when the operational power transients, and the inadvertently full insertion of the absorber rod. Furthermore, the basic nuclear data, the "multipass" fuel refueling scheme, spatial distribution of decay heat of the zone where the fuel temperature reaches to the maximum value, decay heat production rate, effective conductivity coefficient of the pebble bed, conductivity of graphitic matrix material, specific heat capacity of the fuel elements, effective conductivity and specific heat capacity of the reflector graphite, measurement of the initial temperature, the thermal property parameters of the core structures and outer components, and the heat transfer between pressure vessel and surface cooler all have an influence on the maximum fuel temperature, and these influences are different. In the cited paper [3], the preliminary uncertainty analysis of the maximum fuel temperature under DLOFC accident condition of the HTR-module reactor [14] due to most of the uncertainty sources mentioned above was performed and the numerical results indicate that the appearance of a higher peak power density when the operational power transients, the inadvertently full insertion of the absorber rod, the measurement of initial temperature, the thermal property parameters of the core structures and outer components, and the heat transfer between pressure vessel and surface cooler have a relatively small or only a marginal influence on the maximum fuel temperature under DLOFC accident condition. Therefore, these uncertainty parameters are not considered in our work and the basic uncertainty information of some parameters is requantified based on our previous studies. The details are summarized as follows.

Based on the design of HTR-PM, the thermal power of each pebble bed reactor is 250 MW. In the normal operation, the reactor core power is monitored by using the reactor real-time monitoring system. If the operating power deviates the designed value, the reactor control system will start and then the reactor can be still run on the nominal power level imposed by the reactor control system. In fact, the monitoring system and the control system for the reactor operation and adjustment have a measurement error of 1%, respectively, based on the practical experience of HTR-PM project. This leads to a conservative 2% uncertainty of the operation power, i.e., the 2 standard deviation value of the operation power is 2%. It is different with the value used in the cited paper [3], in which 5% is too conservative, and same as the value for the PBMR analysis [4].

Another important uncertainty source is the spatial distribution of decay heat of the zone where the fuel temperature reaches to the maximum value. The uncertainty of the initial operating power of the HTR-PM, the power, and burnup history together result in a certain uncertainty of the spatial distribution of the decay heat. Uncertainties inevitably exist in the nuclear data, pebble flow, filling fraction of the pebble bed, uranium loading, and so on, which will be propagated to the power and burnup history and operating power distribution. Furthermore, these uncertainties' sources result in a certain uncertainty of the amount of fission products, actinides, which are the main components of the total decay heat production rate. At the same time, a "multipass" fuel refueling scheme is used in HTR-PM, and the movement of pebbles itself has uncertainties and also has a large influence on the burnup and power history. In our previous studies [5], the in-depth uncertainty analysis of the peak value of the power distribution due to the parameters mentioned above was performed, and the uncertainty contributions of these parameters are summarized in Table 1.

The maximum fuel temperature under accident conditions always occurs in the zone where the power

Table 1: Summary of peak power uncertainty due to different uncertainty sources.

Uncertainty sources	Uncertainty of k_{eff} (%)	Uncertainty of peak power (%)
Mixed flow	—	±0.002
Filling fraction	±0.0161	±0.7
Uranium loading	±0.0005	±0.05
Cross section	±0.6621	±0.7

distribution reaches to the peak value. The conservative assumption is made that the uncertainty of the power distribution is the same as the uncertainty of the peak power, which further results in the same uncertainty of the spatial distribution of the decay heat. In this work, it is assumed very conservatively that a relative uncertainty of 5% in the operating power distribution causes the same uncertainty in the decay heat spatial distribution of the zone where the fuel temperature reaches to the maximum value, which covers the uncertainty contributions due to the calculation methods, nuclear data, filling fraction of pebble bed, uranium loading, multipass refueling scheme, and other parameters.

The decay heat production is calculated based on the HTR-specific German standard DIN 25485E [15], and this rule also sets rules for calculating the standard deviation of the decay of fission products. Then, a relative uncertainty of 2.85% in the decay heat production for HTR-PM is selected based on the established industry standards.

The effective conductivity coefficient of the pebble bed should fully account for the conduction and radiation in the irregular pebble bed of fuel spheres. In the cited paper [16], the standard deviations of this parameter for different temperatures were quantified, and from these results, an average uncertainty of 5% was derived for the relevant temperature range of HTR-Module. In our work, the same value of 5% for HTR-PM is selected.

The relative uncertainty of the conductivity of graphitic matrix material is 7%, and the associated value for the specific heat capacity of the fuel elements is 2.9% based on Kohtz's research [3]. According to Strydom's paper, the relative uncertainty is 5% for both the relative uncertainty of effective conductivity and specific heat capacity of the reflector graphite [4]. The same values are applied for the selected parameters in our research.

The uncertainty information of these parameters, such as the mean, two standard deviations, and PDF, are obtained from different sources and quantified based on the different mechanism analysis. For example, the uncertainty of the most unfavorable initial operating power is obtained from the accuracy of the reactor monitoring and control systems and also based on the expert engineering judgement. The material manufacturers determine the uncertainty of the specific heat and conductivity data. However, the relative uncertainty of the decay heat production rate is quantified by the established industry standards. As a result, there are no correlations between these uncertainty parameters and these inputs are independent. The details of the uncertainty of the selected 8 inputs are summarized in Table 2.

3.2. Generation and Verification of the Sample of Uncertainty Inputs. The uncertainty analysis based on the statistical sampling method costs time and efforts. And the size of the sample space is crucial for the uncertainty propagation and quantification by using this method. In this work, the home-developed CUSA is used to generate a reasonable sample space of the selected eight parameters. There are different sampling methods built in CUSA, such as the SRS, LHS, LHS-CDC, LHS-SVDC, and so on.

First, a global relative covariance matrix of the selected eight parameters is built, as shown in Figure 3, the diagonal elements of which represent the square of the relative standard deviation of each input, and the off-diagonal elements are equal to zero in this work due to the independence between different inputs. Based on this relative covariance matrix, three different sampling methods, SRS, LHS, and LHS-SVDC, are used to generate different sample spaces with some specific sample sizes of 100, 200, 500, and 1000, respectively, in this work.

Then, the K-S test function of CUSA is performed to identify the probability distribution type of the samples of each input. The process is to compare the cumulative probability density function (CDF) of the population samples of each input with a specific distribution, e.g., normal, uniform, exponent distribution, and so on. And the K-S level of the significance (about 0.5 to 1) confirms that the specific distribution type is the closest match to the samples. The results of the level of the significance of different distribution types for samples of the different input parameters with the sample size of 100 are shown in Tables 3 and 4.

The SRS and LHS are widely used for generating samples for propagating input uncertainties, and LHS-SVDC is an innovative efficient sampling method of CUSA. As shown in Tables 3 and 4, the samples obtained by all these three methods match good to the original distribution of each input, which means that the accuracy of the original distribution information is not lost by the samples. It is noteworthy that the level of the significance for the LHS method is equal to 1, which indicates that the samples completely obey the original distribution. It is due to the fact that samples are directly generated from the CDF of the input parameters. Only in this point of view, all these three methods can be used to generate a random sample space which obeys the original distribution types with a relatively small sample size.

Furthermore, for the LHS based method, one of the main advantages is that only a relatively small sample size is enough to represent the uncertainty information of one input due to its efficient stratified sampling technique based

Table 2: Uncertainty information of the eight selected input parameters.

Uncertainty inputs	Mean value	2 standard deviation values	PDF type
Reactor power (RP)/MW	250	±5 (2%)	Normal and uniform
Spatial distribution of decay heat adjustment factor (SDDH)	1	±0.05 (5%)	Normal and uniform
Decay heat adjustment factor (DH)	1	±0.0285 (2.85%)	Normal and uniform
Pebble bed effective conductivity adjustment factor (PBEC)	1	±0.05 (5%)	Normal and uniform
Graphitic matrix material conductivity adjustment factor (GMC)	1	±0.07 (7%)	Normal and uniform
Fuel element specific heat capacity adjustment factor (FEHC)	1	±0.029 (2.9%)	Normal and uniform
Reflector effective conductivity adjustment factor (REC)	1	±0.05 (5%)	Normal and uniform
Reflector specific heat capacity adjustment factor (RHC)	1	±0.05 (5%)	Normal and uniform

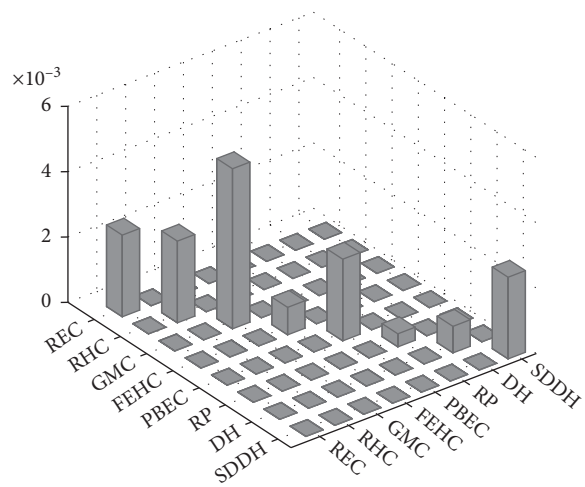

Figure 3: The global relative covariance matrix for the selected eight parameters.

Table 3: K-S test for the samples of the selected 8 inputs with normal distribution.

Input samples	The level of the significance for different distribution type								
	SRS method			LHS method			LHS-SVDC method		
	Normal	Uniform	Exponential	Normal	Uniform	Exponential	Normal	Uniform	Exponential
RP	0.655	$1.0e-5$	$6e-33$	1	$1.7e-2$	$4e-33$	0.985	$4.5e-3$	$5e-33$
SDDH	0.648	$1.2e-3$	$2e-29$	1	$1.8e-5$	$2e-29$	0.887	$1.5e-1$	$8e-31$
DH	0.831	$1.8e-3$	$2e-32$	1	$6.9e-5$	$1e-31$	0.515	$9.4e-4$	$4e-32$
PBEC	0.450	$2.0e-6$	$9e-30$	1	$5.6e-4$	$1e-29$	0.816	$6.7e-4$	$1e-30$
GMC	0.716	$4.9e-2$	$2e-28$	1	$2.3e-2$	$5e-28$	0.949	$4.5e-2$	$7e-29$
FEHC	0.943	$1.1e-7$	$3e-31$	1	$3.0e-5$	$2e-31$	0.517	$3.7e-4$	$1e-32$
REC	0.845	$9.8e-2$	$1e-30$	1	$7.1e-3$	$7e-30$	0.994	$7.7e-8$	$1e-30$
RHC	0.894	$3.9e-6$	$2e-29$	1	$1.0e-4$	$2e-29$	0.998	$2.2e-4$	$4e-30$

Table 4: K-S test for the samples of the selected 8 inputs with uniform distribution.

Input samples	The level of the significance for different distribution type								
	SRS method			LHS method			LHS-SVDC method		
	Normal	Uniform	Exponential	Normal	Uniform	Exponential	Normal	Uniform	Exponential
RP	0.268	0.450	$1e-33$	0.789	1	$1e-33$	0.419	0.815	$1e-33$
SDDH	0.238	0.944	$1e-31$	0.780	1	$1e-31$	0.218	0.412	$1e-31$
DH	0.348	0.651	$3e-33$	0.827	1	$4e-33$	0.339	0.984	$4e-33$
PBEC	0.584	0.582	$1e-31$	0.778	1	$1e-31$	0.503	0.972	$1e-31$
GMC	0.221	0.805	$3e-30$	0.779	1	$3e-30$	0.866	0.891	$4e-30$
FEHC	0.272	0.929	$4e-33$	0.789	1	$4e-33$	0.452	0.867	$4e-33$
REC	0.513	0.957	$1e-31$	0.820	1	$1e-31$	0.131	0.416	$1e-31$
RHC	0.469	0.980	$1e-31$	0.780	1	$1e-31$	0.319	0.774	$1e-31$

on the CDF. For the multivariate problem, samples of different inputs are randomly combined to form a random sample space in the process of generating random samples by using LHS-based methods, a more realistic random process. However, an extra statistical correlation between samples of different input parameters is inevitably introduced by using the SRS or LHS method, especially when the sample size is relatively small. Of course, increasing the sample size will decrease this introduced correlations, while the number of calculations increased drastically. To solve this problem, an innovative LHS-based method, LHS-SVDC, is proposed in our previous study and is used to generate a reasonable sample space with a relatively small sample size by using the correlation control techniques. The relative covariance matrix of the input samples generated by SRS, LHS, and LHS-SVDC with the sample sizes of 100, 200, 500, and 1000 is shown in Figures 4–7.

As illustrated in Figures 4–7, 100 samples are enough to represent a reasonable correlation information between different input parameters for the LHS-SVDC method, while more than 500 samples are needed by using the LHS method and even more for the SRS method. So, the LHS-SVDC method is recommended to perform the uncertainty propagation with a relatively small sample size and then to reduce the number of calculations dramatically. An example of the final outcome of this input preparation phase is shown in Table 5, where the random sample combination of the selected eight inputs with normal distribution is presented for the first 10 of the 100 sample population generated by using the LHS-SVDC method. And one example scatter plot for the 100 samples of the reactor power is shown in Figure 8 to be verified for conformance to the user's specifications.

4. Uncertainty Analysis of the Maximum Fuel Temperature under DLOFC

4.1. K-S Test to Determine the Distribution Type. For the uncertainty analysis of the maximum fuel temperature of HTR-PM under the DLOFC accident condition, statistical fitness tests on the calculated maximum fuel temperature are firstly performed to determine the properties of unknown distributions by using the K-S test function of CUSA. The K-S test is used to compare the cumulative probability density function of a population sample for conformance with a specific distribution, such as Normal, Uniform, Poisson, or Exponent distribution. In the K-S test, the terms "the level of significance" refer to the likelihood that the selected distribution type (for example, normal distribution) is representative of the sample population. The maximum number of the significant is equal to 1. And the lower the significance level, the more confident you can reject this fitness test.

The K-S test on the 100 maximum fuel temperature under DLOFC accident condition calculated by using ATHENA is performed, and the results of the level of significance for different distribution types are shown in Table 6. The K-S test results confirm that a normal distribution is much better matched to the maximum fuel temperature under DLOFC accident condition and it is not affected by the distribution type of inputs and the sampling methods.

The quality of the fit can be also visually assessed by the fitted curve, as shown in Figures 9 and 10, which also illustrate that a normal distribution is much better match to the maximum fuel temperature under DLOFC accident condition of HTR-PM.

As discussed above, the distribution type of the maximum fuel temperature is not affected by the distribution type of the inputs. However, this conclusion is established under certain conditions that are simultaneous perturbation of multiple input parameters, and in this work, the eight selected input parameters are sampled simultaneously. If only one input parameter is perturbed, then the distribution type of output is completely same as the input. Here, only the initial reactor power is sampled and 100 samples are generated. Then, 100 ATHENA runs generate 100 maximum fuel temperatures, and the K-S test is performed on these results; the fitted curve is shown in Figure 11, which further indicates that the distribution type of the maximum fuel temperature is same as the type of the initial reactor power. The same conclusion can also be drawn from the test of other input parameters.

4.2. Uncertainty Quantification of the Maximum Fuel Temperature. The time behavior of the maximum fuel temperature under the DLOFC accident condition is illustrated in Figures 12 and 13, where 200 sets of the selected eight inputs with uniform and normal distributions are randomly generated, respectively, by using the LHS-SVDC method and then 2 groups of 200 ATHENA simulations using these input samples generate 2 sets of the maximum fuel temperatures. As shown in Figures 12 and 13, the maximum fuel temperature of HTR-PM reaches a peak value after 20–30 hours during the DLOFC transient condition. The shapes of the curves are similar but the gradients are not identical due to the difference between the rate of energy deposition and the energy removal. For example, an increase in the initial reactor power will increase the fuel temperature, while an increase in the pebble bed effective conductivity will remove heat faster from the core and therefore lead to a lower fuel temperature. In each random set of samples of these eight inputs, low, average, and high values are randomly generated, and then results in different curves of the fuel temperature and the shift in time when the peak fuel temperature values are reached. Even more importantly, the spread in the maximum fuel temperature, i.e., the uncertainty of the maximum fuel temperature, is not constant with time; it increases in the first 30 hours and then tends to be stable. For example, it starts off with less than 5°C in the first hours and increases to 151°C for the cases with normal distributed inputs and increases to 165°C for the cases with uniform distributed inputs. And the highest fuel temperatures and the largest uncertainty variations do not occur at the same time point.

However, this study only compares the bounding value fuel temperature uncertainty for the DLOFC accident, regardless of when this point is reached, since the DLOFC peak fuel temperature is of major interest in reactor design safety studies. Before the uncertainty analysis of the maximum fuel

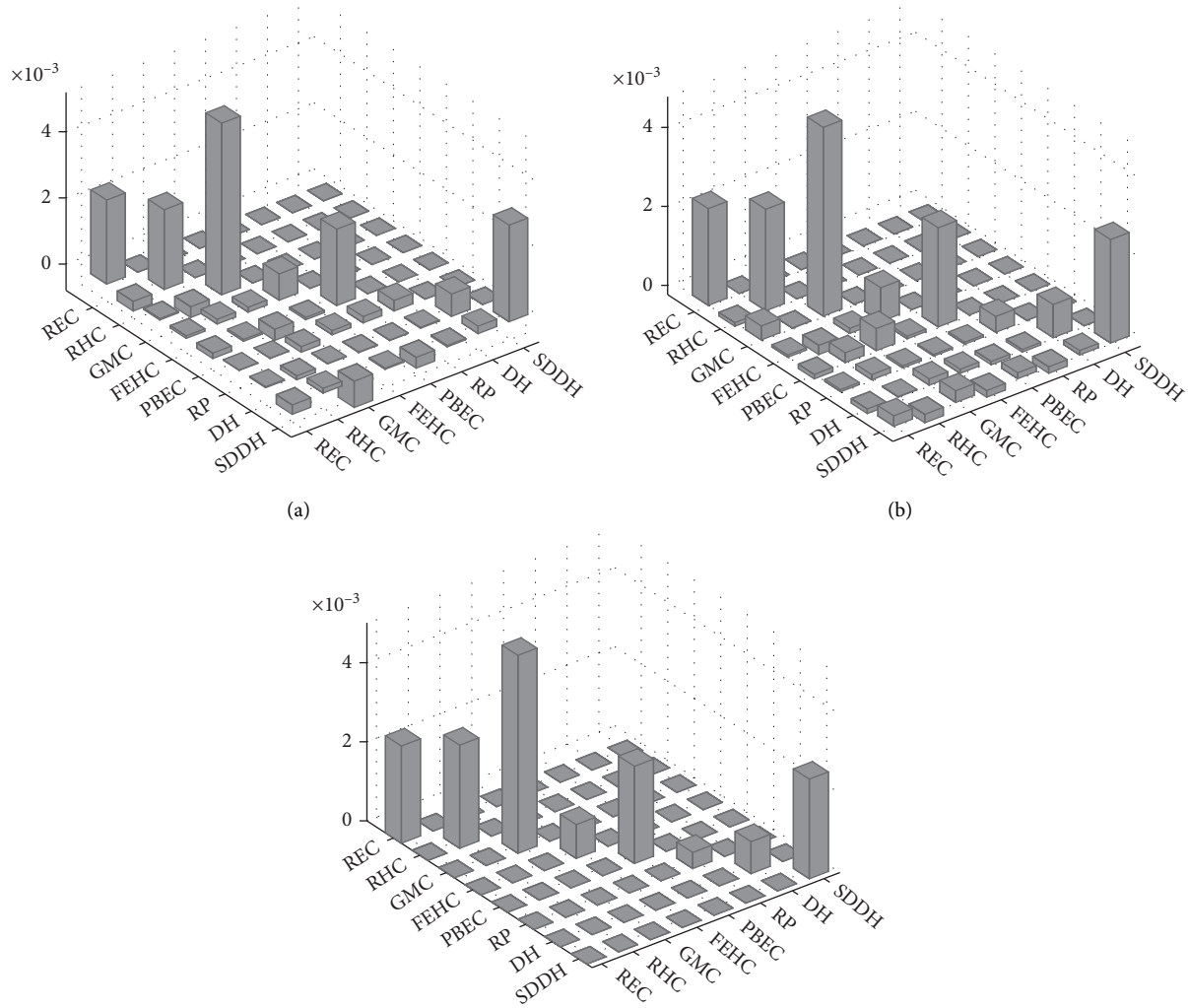

Figure 4: The relative covariance matrix generated by CUSA with the sample size of 100. (a) Generated by SRS. (b) Generated by LHS. (c) Generated by LHS-SVDC.

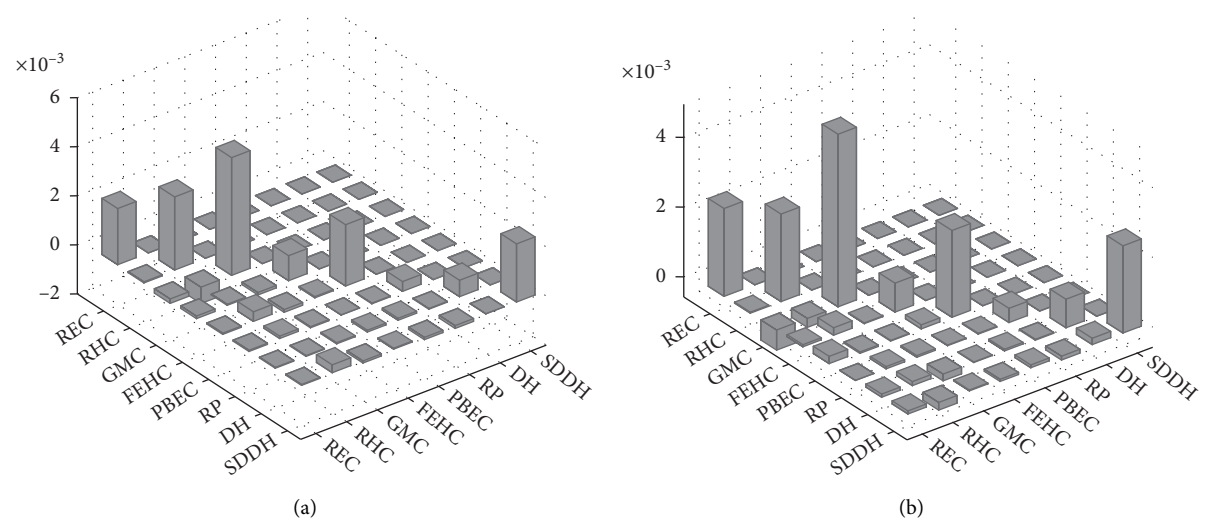

Figure 5: Continued.

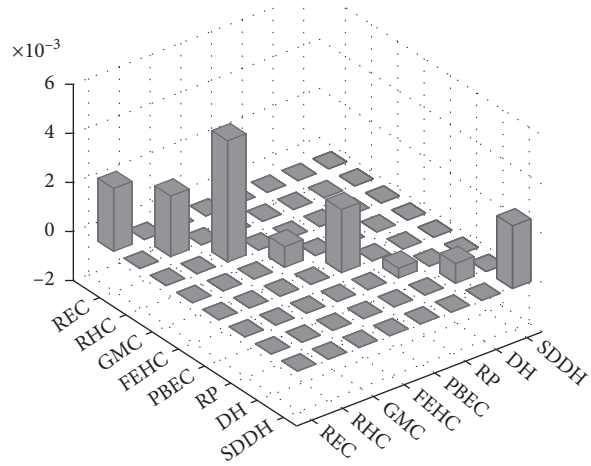

(c)

Figure 5: The relative covariance matrix generated by CUSA with the sample size of 200. (a) Generated by SRS. (b) Generated by LHS. (c) Generated by LHS-SVDC.

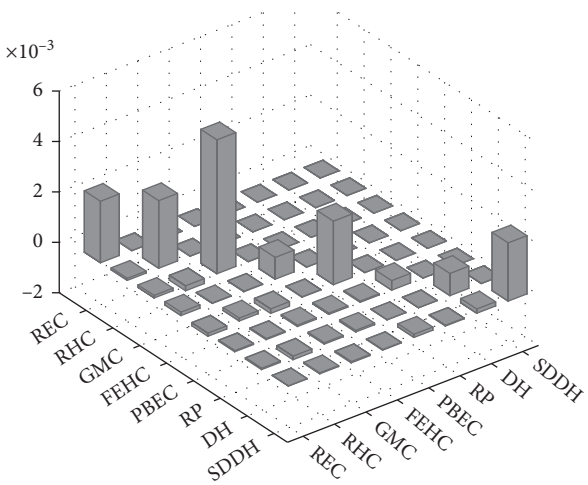

(a)

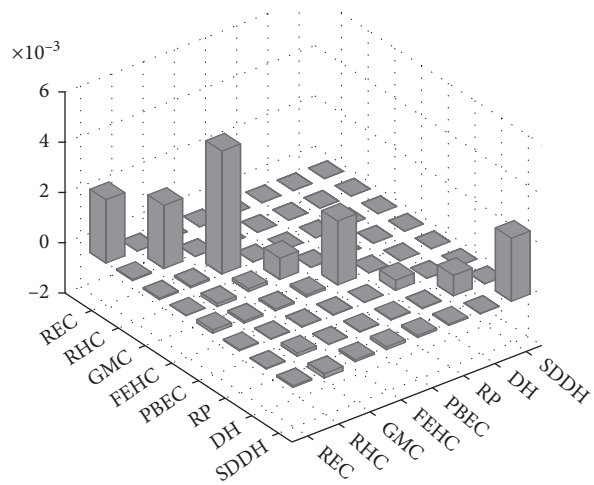

(b)

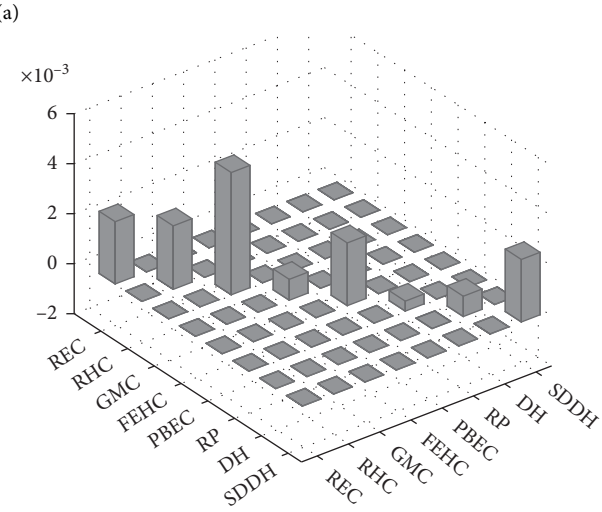

(c)

Figure 6: The relative covariance matrix generated by CUSA with the sample size of 500. (a) Generated by SRS. (b) Generated by LHS. (c) Generated by LHS-SVDC.

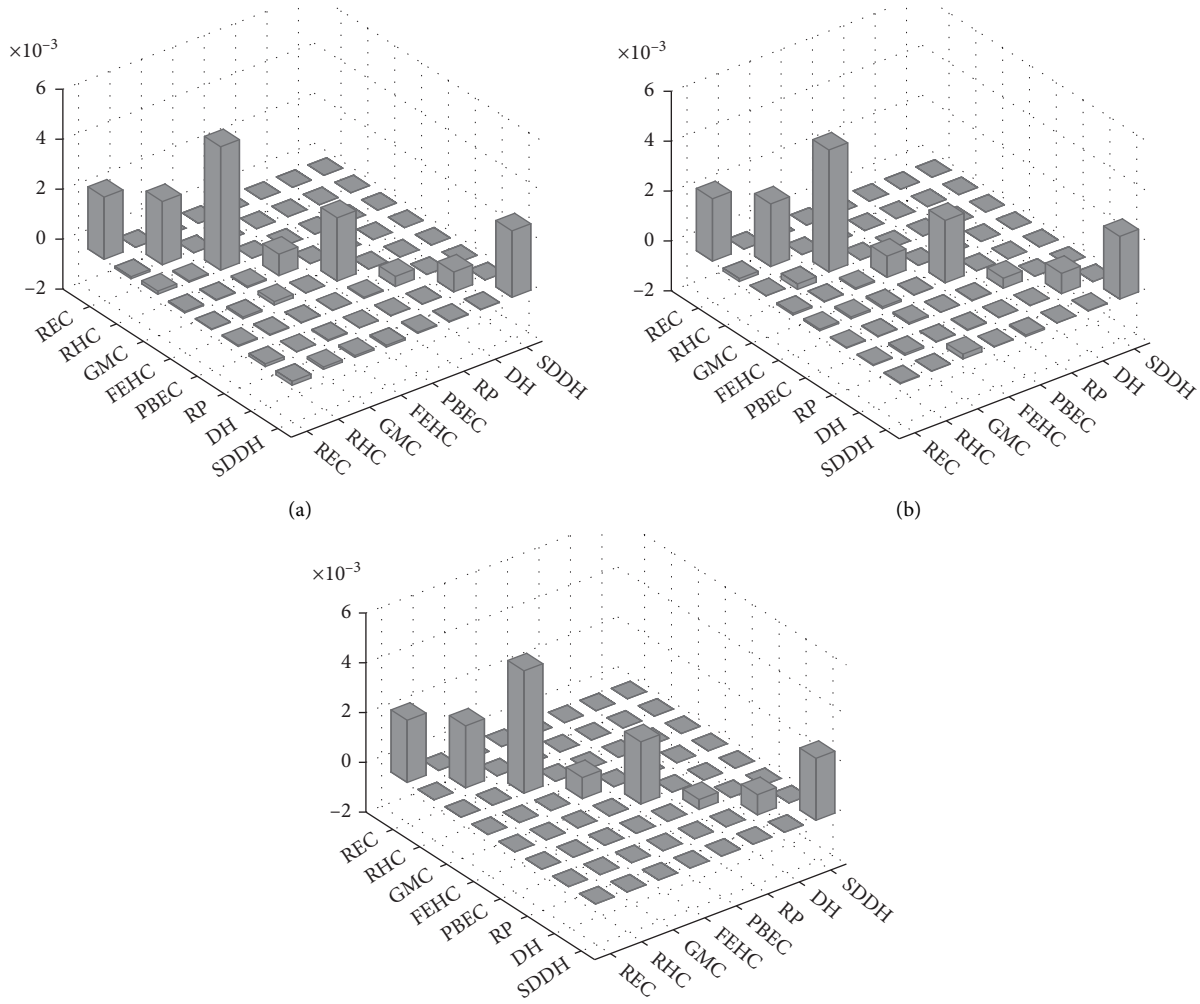

Figure 7: The relative covariance matrix generated by CUSA with sample size of 1000. (a) Generated by SRS. (b) Generated by LHS. (c) Generated by LHS-SVDC.

Table 5: The first 10 of 100 sample population generated by CUSA for ATHENA runs.

REC	RHC	GMC	FEHC	PBEC	RP	DH	SDDH
1.05849	1.05989	0.95205	0.98371	1.08143	270.35774	0.99952	1.01421
1.06185	1.04306	0.95419	1.03010	0.94797	236.99254	1.02898	0.98530
0.93493	0.95798	0.93444	1.03667	0.96050	240.12450	0.98993	0.94390
1.02865	1.03680	1.07565	1.01924	1.03976	259.93877	0.96448	1.00872
0.96513	0.97262	1.10942	1.03643	0.95577	238.94290	0.97945	0.94200
0.96957	0.92456	1.05200	1.04648	0.92850	232.12505	0.99408	1.04083
0.96754	1.03209	1.00583	0.98509	1.00321	250.80317	0.97693	0.96391
1.02825	1.03855	0.89534	0.95894	1.06039	265.09804	0.96592	0.93933
1.07443	0.98510	1.10846	0.97701	0.98598	246.49452	1.04387	1.03167
0.96391	1.05282	0.91569	1.04447	1.03938	259.84612	0.98099	0.95963

temperature under accident condition, the superiority of the LHS-SVDC technique for the statistical sampling-based uncertainty analysis method can be further verified by the uncertainties of the maximum fuel temperature due to the uncertainty samples generated by using different sampling methods, as shown in Figure 14. At the same time, the "sandwich" rule is also used to quantify the uncertainty of the maximum fuel temperature based on the calculated sensitivity coefficients for comparison, and the sensitivity analysis will be performed in the following section.

It is obviously found that the uncertainty of the maximum fuel temperature due to the selected eight input parameters tends to be stable or be very close to the results quantified by the sandwich rule when the sample size is

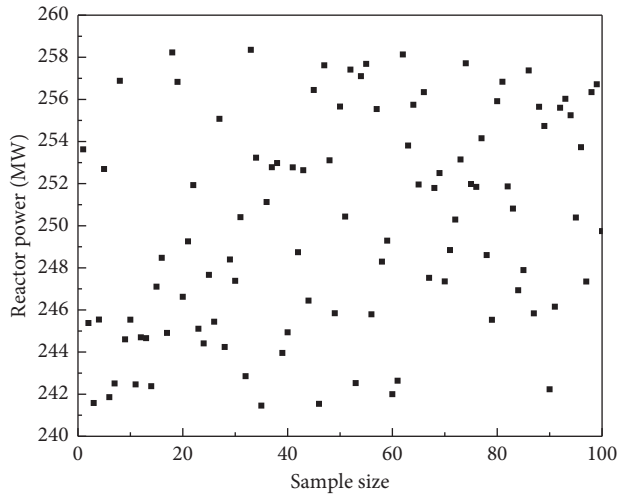

Figure 8: Sampled values of the reactor power (MW) for the 100 LHS-SVDC normal set.

Table 6: K-S test results for the 100 calculated maximum fuel temperatures.

Sampling method	The distribution type of input parameters	The level of significance for goodness of fit		
		Normal	Uniform	Exponential
LHS	Normal	0.676	$1.40e-2$	$2.1e-33$
	Uniform	0.753	$1.03e-4$	$4.5e-29$
SRS	Normal	0.725	$1.12e-3$	$7.2e-31$
	Uniform	0.813	$3.25e-4$	$5.6e-30$
LHS-SVDC	Normal	0.949	$7.09e-3$	$5.1e-29$
	Uniform	0.799	$4.28e-6$	$6.9e-30$

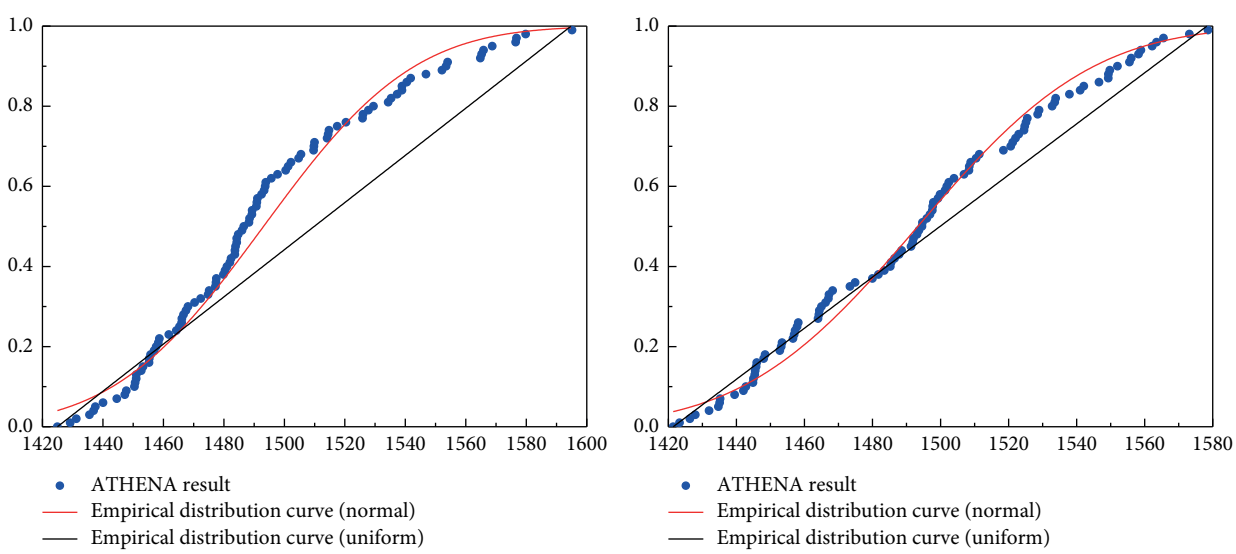

Figure 9: Continued.

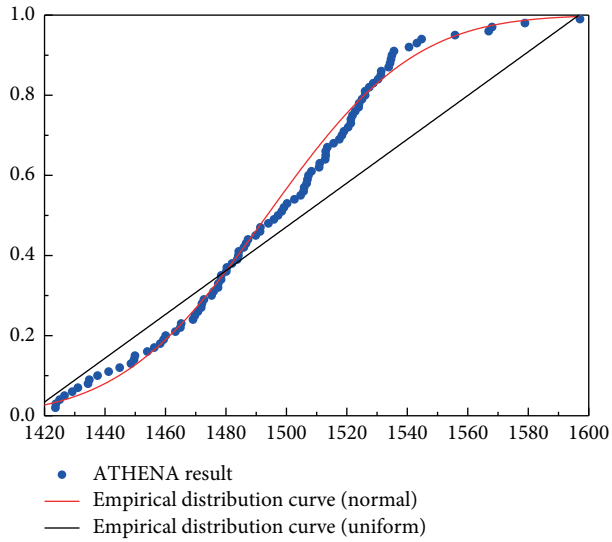

(c)

Figure 9: CDFs and fitted normal distribution results with inputs of uniform distribution. (a) SRS. (b) LHS. (c) LHS-SVDC.

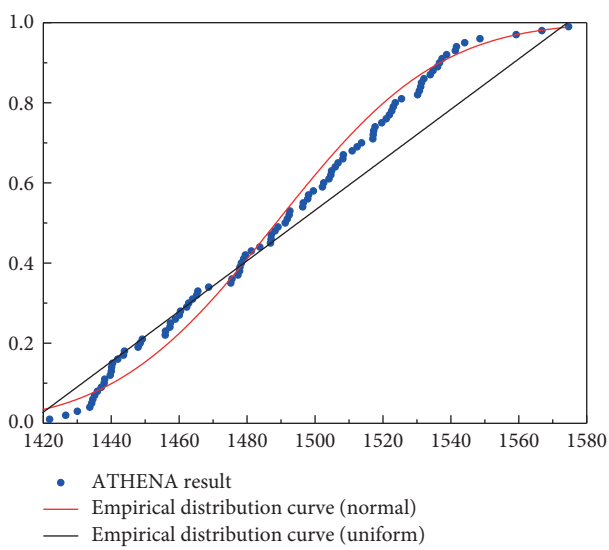

(a)

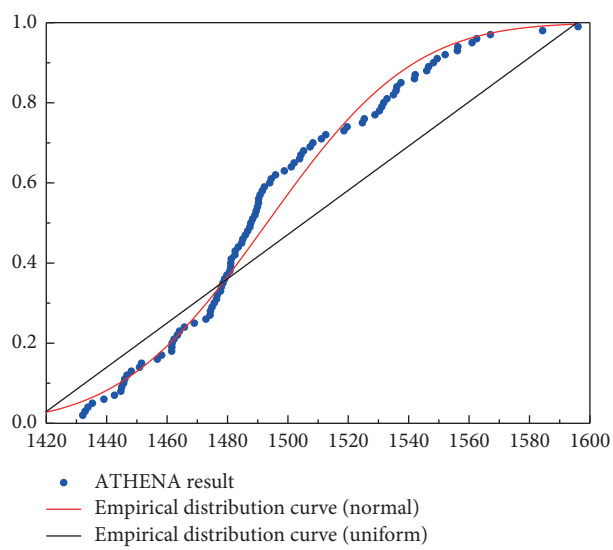

(b)

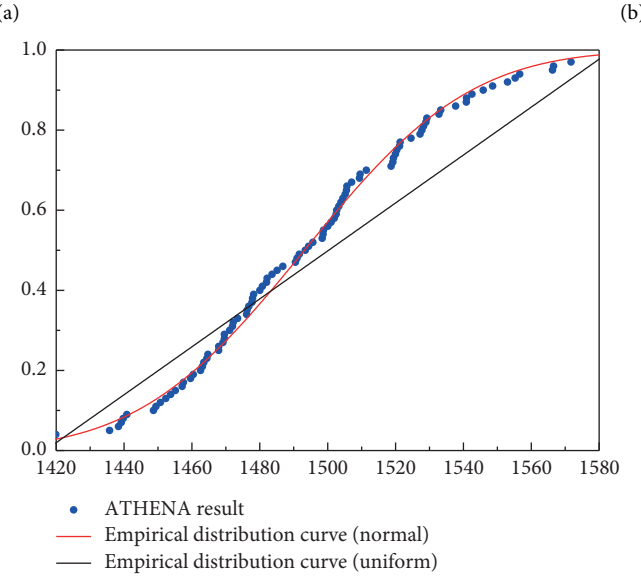

(c)

Figure 10: CDFs and fitted normal distribution results with inputs of normal distribution. (a) SRS. (b) LHS. (c) LHS-SVDC.

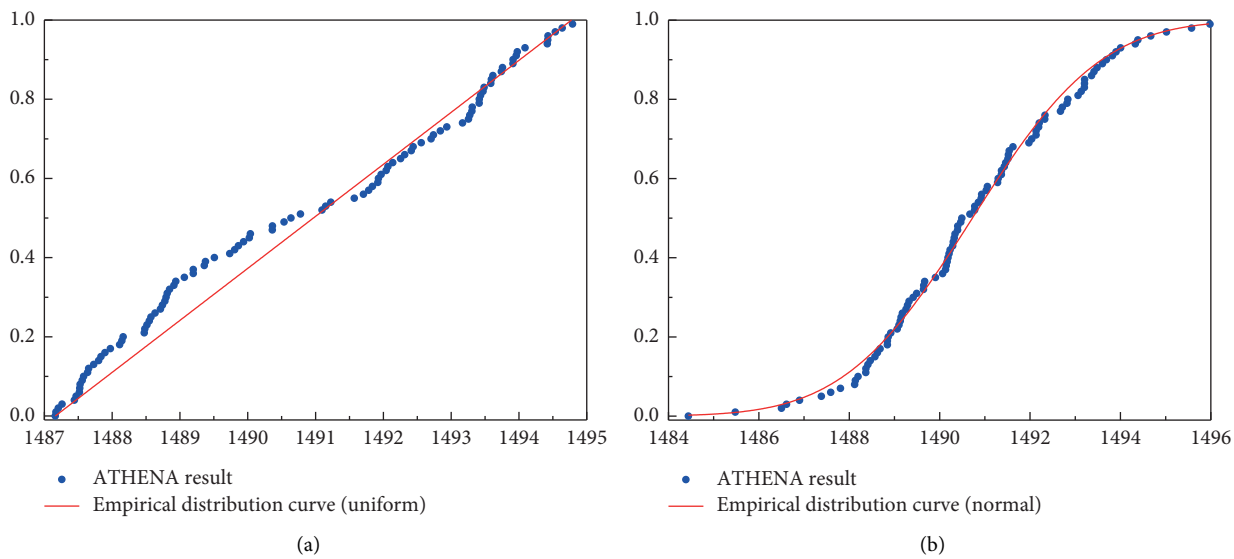

Figure 11: CDFs and fitted distribution results with input of different distributions. (a) RP with uniform distribution. (b) RP with normal distribution.

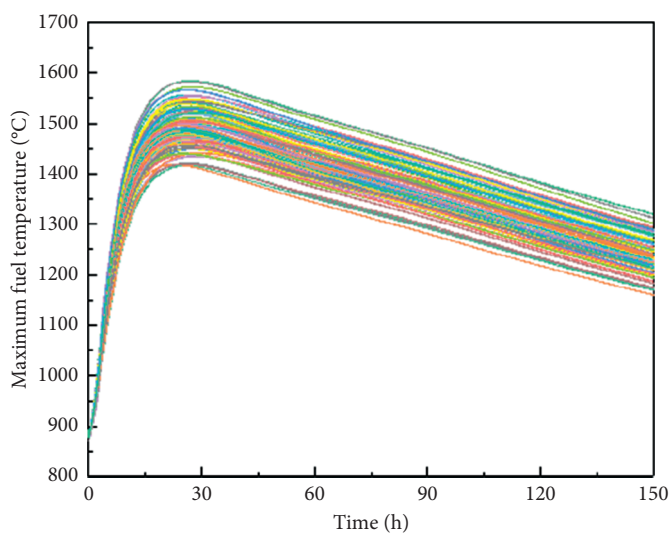

Figure 12: The time behavior of the maximum fuel temperature for the cases with normal distributed input parameters.

greater than 100 for LHS-SVDC methods. When the number of samples needs to be greater than 800 or even larger, then a relatively stable uncertainty can be obtained if the LHS or SRS method is used. At the same time, the size of the sample space is crucial for the uncertainty propagation by using the statistical sampling-based uncertainty analysis method, and a relative small size for less computation burden and stable uncertainty contribution is necessary. So, the sample size of LHS-SVDC is set to 100 in this work for uncertainty propagation and quantification as discussed above.

Once the sample size and the type of distribution of the maximum fuel temperature are identified, the mean, the standard deviation, and other uncertainty information, especially the error bar, can be further determined from the empirical distribution. It is worth noting that uncertainties inevitably exist in the calculated mean value, standard deviation, and relative uncertainty of the maximum fuel temperature by using the statistical sampling-based uncertainty analysis method due to the random sampling and statistical analysis. Figures 15–17 illustrate the 10 sets of the calculated mean value, standard deviation, and the relative uncertainty of the maximum fuel temperature due to random samples of the selected eight parameters generated by using SRS, LHS, and LHS-SVDC methods. Here, 10 sets of sample space are randomly generated, respectively, by using different sampling methods, and then ATHENA is used to perform the DLOFC simulations to generate 10 sets of maximum fuel temperature population, and each set has 100 values. As shown in Figures 15–17, the mean value, standard deviation, and the relative uncertainty indeed have uncertainties due to the random process, and these uncertainties will gradually decrease with the increment of the sample size.

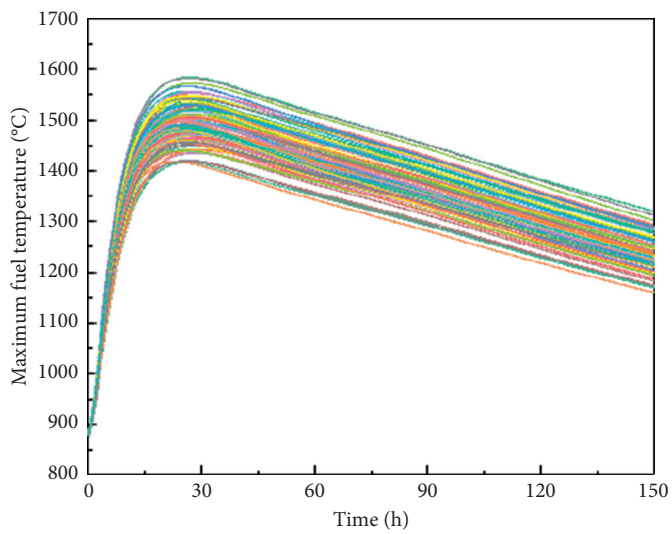

Figure 13: The time behavior of the maximum fuel temperature for the cases with uniform distributed input parameters.

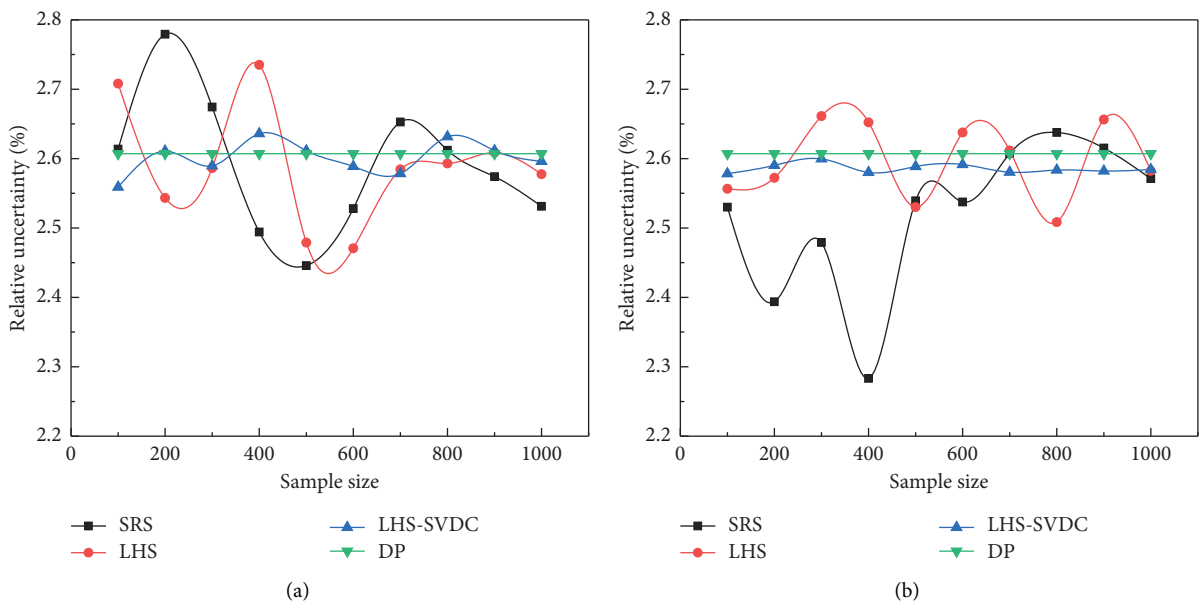

Figure 14: The relative uncertainty of the maximum fuel temperature propagated from the uncertainty samples generated by different sampling methods. (a) Inputs with uniform distribution. (b) Inputs with normal distribution.

These uncertainties under a specific size of sample space should be also quantified if the statistical sampling-based uncertainty analysis method is used and quantified by using the error bar function built in CUSA in this work.

A summary of the uncertainty information, such as the mean with its associated error bar, the standard deviation with its associated error bar, and the relative uncertainty of the maximum fuel temperature under DLOFC accident condition of HTR-PM due to the selected eight input uncertainty parameters with normal and uniform distribution quantified by using SRS, LHS, and LHS-SVDC sampling methods when the sample size is 100, is shown in Table 7. The following observations can be made based on the numerical results:

(1) The mean values of the maximum fuel temperature for all cases are almost identical, i.e., regardless of the sampling method, distribution types of inputs, or sample size, all these designed cases predict the same mean value, 1493°C, of the maximum fuel temperature under DLOFC accident condition of HTR-PM. However, the error bar, i.e., the uncertainty band of the mean value, is quite different and the uncertainty band of the mean value due to the random sampling for SRS method is quite larger, compared to the LHS and LHS-SVDC cases, which is also visually illustrated in Figure 15. In this case, the mean value of the DLOFC maximum fuel temperature can rise up to 1505°C if the SRS method with the sample size of 100

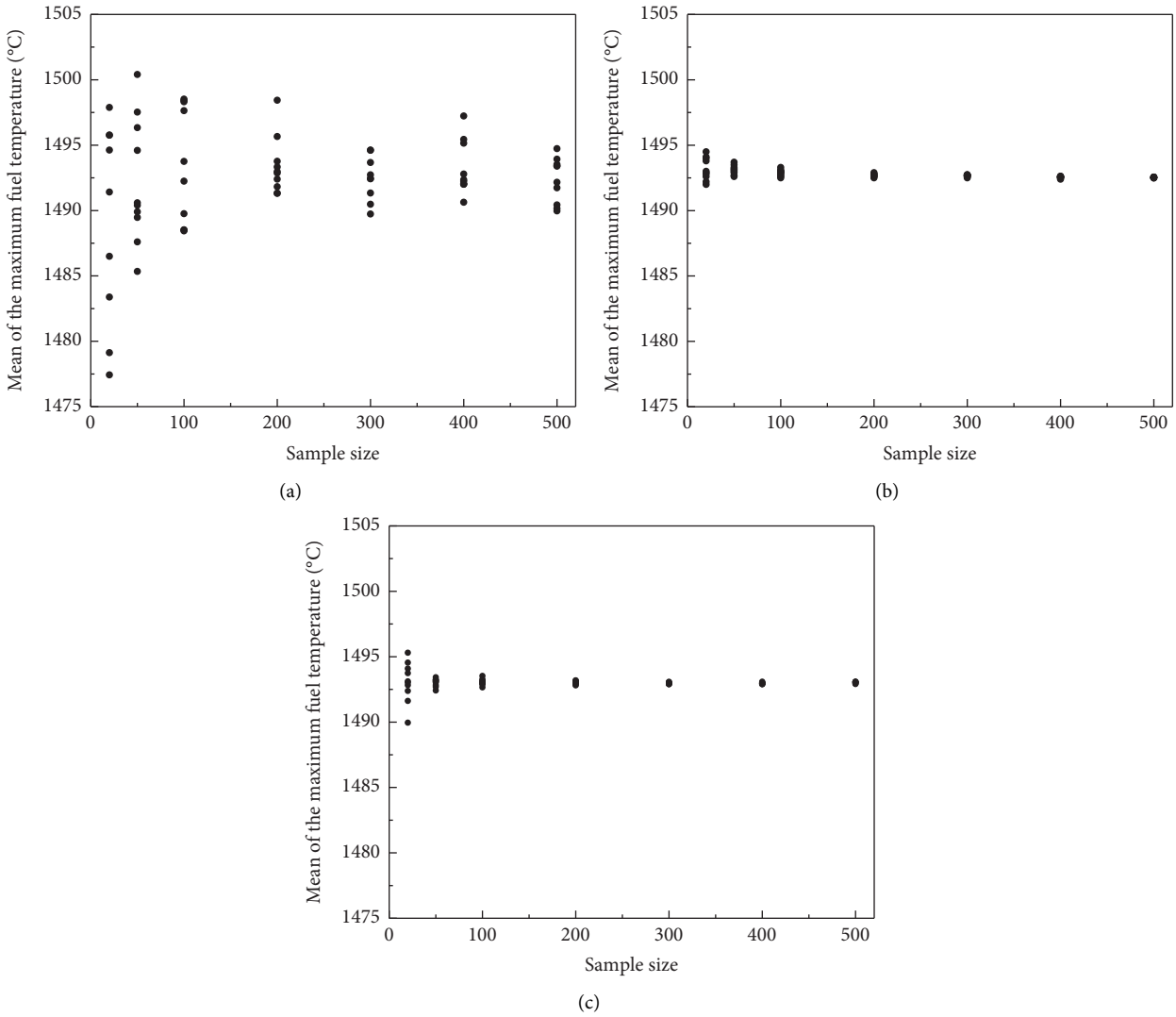

Figure 15: The 10 sets of the mean of the maximum fuel temperature due to the random samples generated by (a) SRS, (b) LHS, and (c) LHS-SVDC.

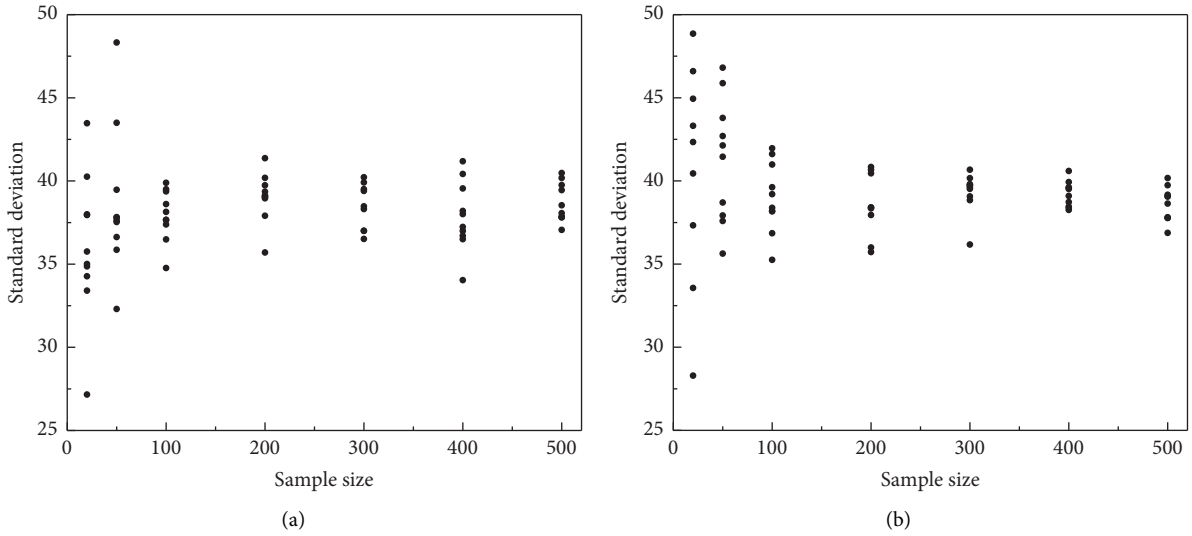

Figure 16: Continued.

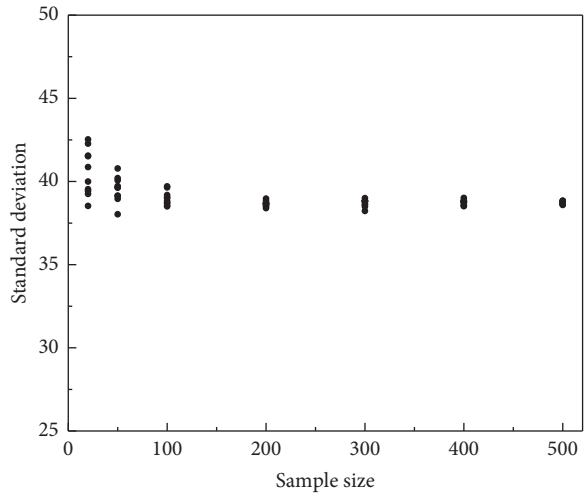

(c)

Figure 16: The 10 sets of the standard deviation of the maximum fuel temperature due to the random samples generated by (a) SRS, (b) LHS, and (c) LHS-SVDC.

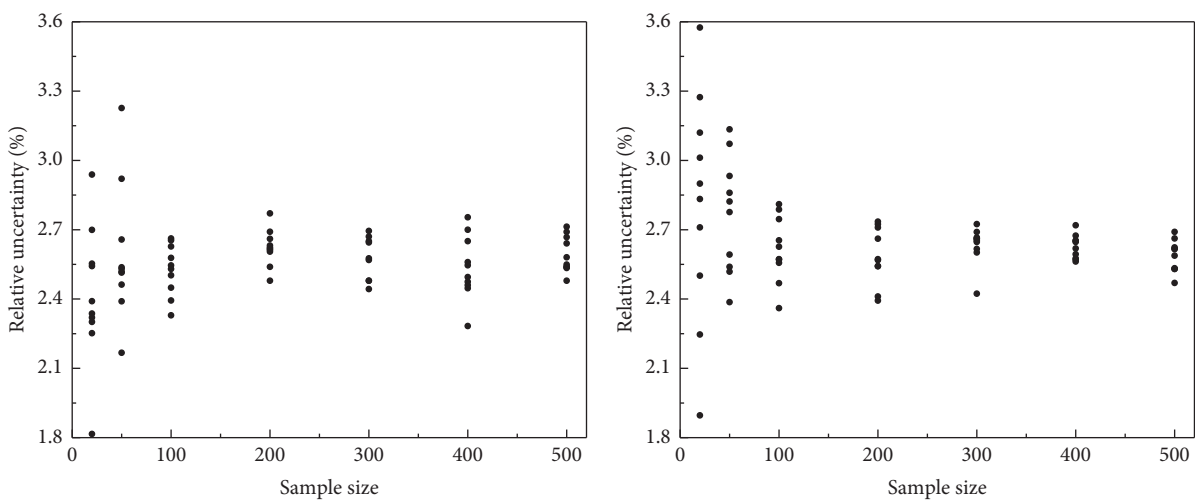

(a)

(b)

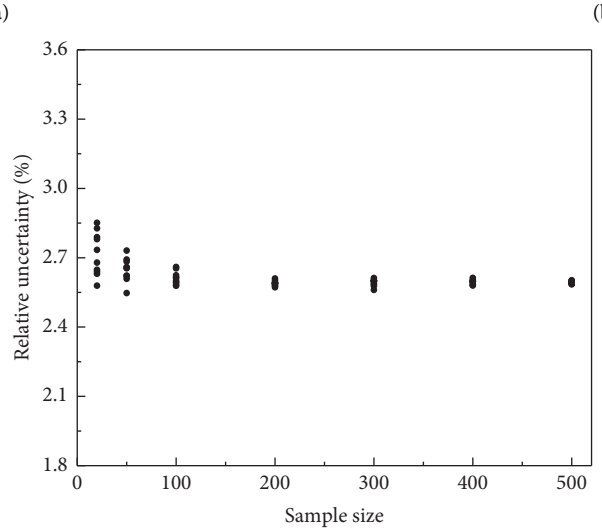

(c)

Figure 17: The 10 sets of the relative uncertainty of the maximum fuel temperature due to the random samples generated by (a) SRS, (b) LHS, and (c) LHS-SVDC.

is used, while the uncertainty band of the mean value for LHS and LHS-SVDC methods is nearly same and is also very small. Based on this point, this study recommends using LHS or LHS-SVDC to propagate the uncertainties of input parameters.

(2) The standard deviations of the maximum fuel temperature populations are also nearly same, 1°C variation on 39°C for example. Same as mean value, the uncertainty band of the standard deviation varies largely, which is directly related to the sampling method and sample size. Although this uncertainty band decreases with the increment of the sample size for all sampling methods, a nonnegligible uncertainty band still exists and a more reliable uncertainty prediction needs more simulations for LHS and SRS. So, the LHS-SVDC method is recommended to propagate uncertainties in inputs in this study.

(3) For distribution types of input parameters, using the uniform distribution could be expected to result in the sampling of high and low values more frequently for the SRS method, compared to the normal distribution. Since the probability of sampling a high, mean, or low value is same for the uniform distribution, there is relatively lower probability to sample from the low and high tails of the normal distribution if the SRS method is used. However, the probability is identical for both LHS and LHS-SVDC methods. This effect is mainly responsible for the slightly larger uncertainty band for 200 SRS uniform case, compared to the LHS and LHS-SVDC cases. However, this rule is not always successful and the uncertainty band mainly depends on the quality of samples generated by different sampling methods.

(4) Sample size, i.e., the number of model calculations, is crucial time-consuming factor for the statistical sampling-based uncertainty analysis method. 1000 is typically recommended in the typical statistical analysis [4]; indeed, the LHS and SRS methods need a relative large sample size to generate a reasonable sample space to propagate uncertainties, and then a more reliable uncertainty prediction with a small uncertainty band due to random process can be obtained. However, the numerical results indicate that 100–200 model simulations seem to be sufficient to get an uncertainty prediction with full confidence by using the LHS-SVDC method.

Overall, uncertainties in these selected eight parameters lead to a two standard deviation (2σ) uncertainty of ±77.6°C (or 5.2%) around the mean value of 1493°C for the maximum fuel temperature under DLOFC accident of HTR-PM, and the scatter plot for the maximum fuel temperature is shown in Figure 18 with the normal and uniform distributed inputs. This value mostly depends on the uncertainties of the selected input parameters, and taking into account of all known input parameters could possibly lead to a larger uncertainty bandwidth. It is worthy to note that the sampling methods and the sample size also have a nonnegligible effect on the mean value and uncertainty bandwidth, about 18°C difference for SRS 100 case.

Before a direct sensitivity study is performed to determine which of these selected eight input parameters are responsible for most of the uncertainty in the maximum fuel temperature under DLOFC accident, the individual uncertainty contribution of each parameter to the final uncertainty in the DLOFC peak fuel temperature is also quantified here by using the LHS-SVDC method with the sample size of 200, as shown in Table 8. The observation for distribution types of input is in agreement with the conclusion reached for the total uncertainty analysis, where the distribution types have little influence on the individual uncertainty contribution. The numerical results indicate that the pebble bed effective conductivity coefficient with a 2σ uncertainty of 5% contributes most to the uncertainty in the maximum fuel temperature, up to ±21.4 (1.4%), which is followed by the decay heat with an uncertainty of 2.85%, about ±20.5 (1.4%).

5. Sensitivity Analysis of the Maximum Fuel Temperature to Different Inputs

In order to investigate the impact of the selected eight parameters on the maximum fuel temperature, the central difference direct perturbation sensitivity technique in CUSA is applied. The peak fuel temperature is computed first with the nominal values of the selected eight parameters, then with a selected nominal input value increased by 1%, and then with this nominal value decreased by the same percentage. The direct perturbation sensitivity coefficient of the maximum fuel temperature to these inputs can be calculated as

$$S_{T_m,\alpha_i} = \frac{\delta T_m / T_m}{\delta \alpha_i / \alpha_i}. \quad (1)$$

Figure 19 illustrates the sensitivity coefficients of these eight input parameters to the maximum fuel temperature, and it can be found that changes in these inputs have opposite effects on the maximum fuel temperature. Here, the magnitude of these coefficients provides insight into the degree which a specific input parameter influences the maximum fuel temperature and the sign indicates a positive or negative effect on the peak fuel temperature. The initial reactor power, decay heat, and spatial distribution of decay heat have a positive effect on the maximum fuel temperature, i.e., an increase in these three parameters will lead to an increase in fuel temperature, while the other five parameters have a negative effect on the peak value. Although the pebble bed effective conductivity contributes the most to the uncertainty of the maximum fuel temperature, it is most sensitive to the initial reactor power and decay heat, followed by the pebble bed effective conductivity. According to the uncertainty analysis, the two primary drivers of uncertainty in the maximum fuel temperature are the decay heat and the pebble bed effective conductivity, and this finding is in agreement with the

Table 7: The uncertainty results of the maximum fuel temperature of HTR-PM.

Input information			Uncertainty information		
Distribution type	Sampling method	Sample size	Mean (°C)	Standard deviation	The relative uncertainty ($2\sigma/\mu$%)
	SRS		1492.8 ± 0.9	38.1 ± 2.0	5.10 ± 0.28
Uniform	LHS	100	1492.9 ± 0.3	37.1 ± 2.3	4.97 ± 0.30
	LHS-SVDC		1493.2 ± 0.8	38.4 ± 0.9	5.14 ± 0.12
	SRS		1493.4 ± 8.9	37.9 ± 3.0	5.08 ± 0.20
Normal	LHS	100	1493.1 ± 0.6	39.1 ± 4.0	5.22 ± 0.28
	LHS-SVDC		1493.1 ± 0.4	38.9 ± 0.8	5.22 ± 0.05
	SRS		1493.1 ± 0.9	38.3 ± 3.4	5.13 ± 0.23
Uniform	LHS	200	1492.9 ± 0.2	37.8 ± 3.5	5.06 ± 0.23
	LHS-SVDC		1492.9 ± 0.9	38.9 ± 0.9	5.21 ± 0.06
	SRS		1493.4 ± 4.4	39.1 ± 2.9	5.22 ± 0.20
Normal	LHS	200	1492.9 ± 0.2	38.5 ± 3.5	5.16 ± 0.22
	LHS-SVDC		1493.0 ± 0.2	38.6 ± 0.3	5.16 ± 0.02
	SRS		1492.3 ± 3.4	38.7 ± 2.3	5.18 ± 0.15
Normal	LHS	500	1492.9 ± 0.2	38.6 ± 2.1	5.16 ± 0.13
	LHS-SVDC		1493.0 ± 0.1	38.7 ± 0.2	5.18 ± 0.01

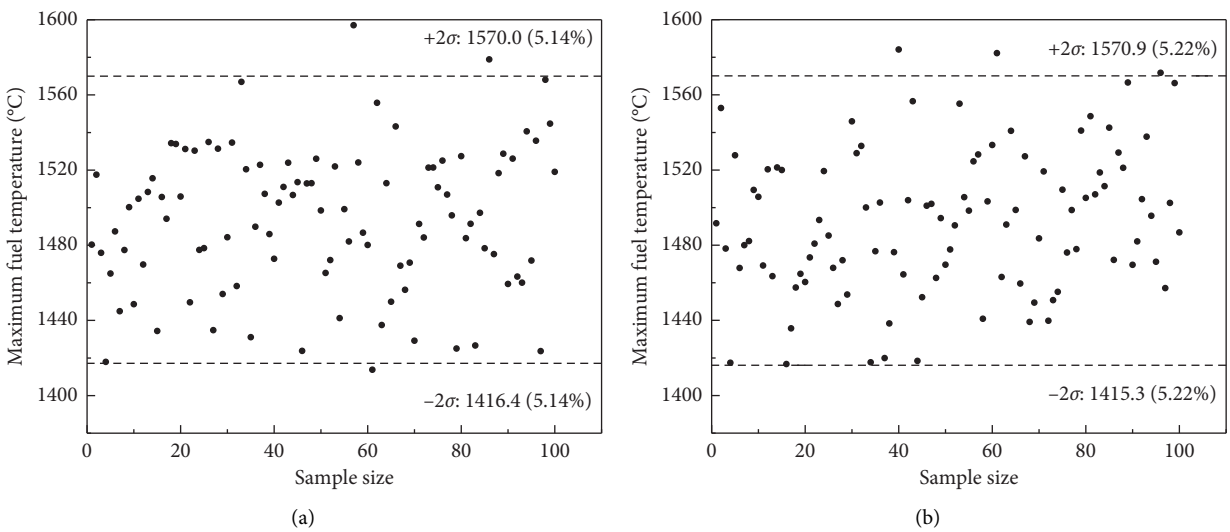

Figure 18: The maximum fuel temperature due to the inputs with uniform and normal distribution. (a) Inputs with uniform distribution. (b) Inputs with normal distribution.

Table 8: Contributions of each input to uncertainty of the maximum fuel temperature.

Uncertainty inputs	2 standard deviation values	Uncertainty contributions ($2\sigma/\mu$%)	
		Normal	Uniform
RP	±5 (2%)	1.96522	1.98074
SDDH	±0.05 (5%)	1.46286	1.55996
DH	±0.0285 (2.85%)	2.76174	2.72694
PBEC	±0.05 (5%)	2.86064	2.85728
GMC	±0.07 (7%)	1.99929	1.93838
FEHC	±0.029 (2.9%)	0.82778	0.82465
REC	±0.05 (5%)	0.29954	0.32348
RHC	±0.05 (5%)	0.17551	0.17794

sensitivity study results, where these two factors are also identified as being responsible for the largest changes in the fuel temperature. And the sensitivity coefficient of the maximum fuel temperature to the graphitic matrix material conductivity is relatively small, but its uncertainty contribution is larger due to its big uncertainty.

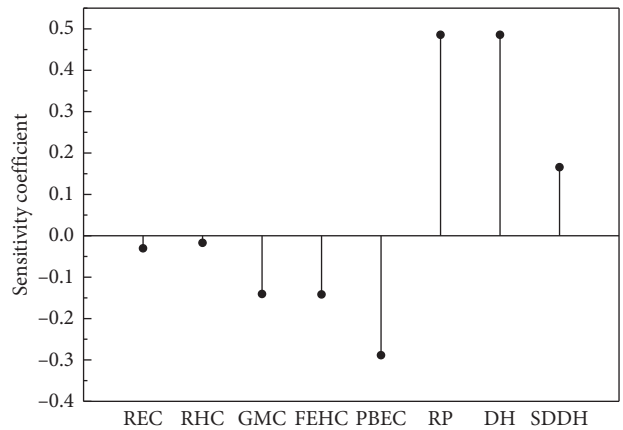

Figure 19: The sensitivity coefficient of the selected 8 inputs to the peak fuel temperature.

6. Conclusion

The maximum fuel temperature under accident condition is the most important parameter of inherently safe characteristics of HTR-PM, and the DLOFC accident may lead to a peak accident fuel temperature. Therefore, the accurate prediction of the maximum fuel temperature under accident condition is most important to the HTR-PM safety analysis and design. At the same time, there are a variety of uncertainty sources in the maximum fuel temperature calculations, and thus the contributions of these uncertainty sources to the final calculated maximum fuel temperature should be quantified to check whether the peak value exceed the technological limit of 1620°C or not.

In this work, eight uncertainty input parameters are selected for inclusion in this uncertainty study, the initial reactor power, the spatial distribution of decay heat, the decay heat, pebble bed effective conductivity, graphitic matrix material conductivity, fuel elements specific heat capacity, reflector effective conductivity, and its specific heat capacity. Even more importantly, the 2 standard deviation uncertainties and probability density functions of these inputs are specified based on the experimental data, material characteristics, expert judgements, operating experiences, some published numerical simulation results, and our previous studies. Then, the accident thermal analyses are performed with a home-developed ATHENA code, and the home-developed code CUSA is applied to perform the uncertainty quantification of the maximum fuel temperature propagated from the selected uncertainty sources. Simultaneously, a direct perturbation analysis by using CUSA is performed to obtain the sensitivity coefficients and to identify the primary contributors to the uncertainty of the maximum fuel temperature under DLOFC accident condition of HTR-PM.

It is found that the pebble bed effective conductivity and the decay heat contribute the most of the uncertainty in the DLOFC maximum fuel temperature while this peak fuel temperature is most sensitive to the initial reactor power and the decay heat. Overall, uncertainties in these selected eight parameters lead to a two standard deviation (2σ) uncertainty of ±77.6°C (or 5.2%) around the mean value of 1493°C for the maximum fuel temperature under DLOFC accident of HTR-PM, which make sure that the maximum fuel temperature during DLOFC accident condition does not exceed the technological limit of 1620°C of HTR-PM design. However, this value mostly depends on the uncertainties of the selected input parameters and taking into account of all known input parameters could possibly lead to a larger uncertainty bandwidth.

It is worthy to note that the sampling methods and the sample size also have a nonnegligible effect on the mean value and uncertainty bandwidth. And the LHS-SVDC method is recommended to propagate uncertainties in inputs, and then a more reliable uncertainty prediction with a small uncertainty band due to random process can be obtained. The numerical results indicate that 100–200 model simulations seem to be sufficient to get an uncertainty prediction with full confidence for applying the LHS-SVDC method.

Data Availability

The data used to support the findings of the study are available from the corresponding author upon request.

Conflicts of Interest

The authors declare that they have no conflicts of interest.

Acknowledgments

This work was supported by the National Key R&D Program of China (2018YFE0180900).

References

[1] Z. Zhang, Z. Wu, Y. Sun, and F. Li, "Design aspects of the Chinese modular high-temperature gas-cooled reactor HTR-PM," *Nuclear Engineering and Design*, vol. 236, no. 5-6, pp. 485–490, 2006.

[2] L. Shi and Y. Zheng, "Characteristic behavior of pebble-bed modular high-temperature gas-cooled reactor during loss of forced cooling accidents," *Atomic Energy Science and Technology*, vol. 43, no. z2, pp. 236–239, 2009.

[3] N. Kohtz and H. Haque, "Meeting fuel temperature limits in an HTR-module reactor during depressurized core heat-up," *Nuclear Engineering and Design*, vol. 137, no. 1, pp. 115–124, 1992.

[4] G. Strydom, *PEBBED Uncertainty and Sensitivity Analysis of the CRP-5 PBMR DLOFC Transient Benchmark with the SUSA Code*, Idaho National Laboratory (INL), Idaho Falls, ID, USA, 2011.

[5] C. Hao, "Uncertainty analysis in modelling of pebble bed HTR," Doctoral thesis, Tsinghua University, Beijing, China, 2014.

[6] C. Hao, F. Li, and Y. Zheng, "Comparative study on the method of uncertainty analysis in the maximum fuel temperature of HTR-PM," in *Proceedings of HTR 2014, Paper HTR2014-8-1282*, Weihai, China, October 2014.

[7] Z. Chen, X. Chen, Y. Zheng et al., "Air ingress analysis of chimney effect in the 200 MWe pebble-bed modular high temperature gas-cooled reactor," *Annals of Nuclear Energy*, vol. 106, pp. 143–153, 2017.

[8] Y. Zheng, M. M. Stempniewicz, Z. Chen, and L. Shi, "Study on the DLOFC and PLOFC accidents of the 200 MWe pebble-bed modular high temperature gas-cooled reactor with TINTE and SPECTRA codes," *Annals of Nuclear Energy*, vol. 120, pp. 763–777, 2018.

[9] H. Chen, L. Fu, G. Jiong, and W. Lidong, "Uncertainty and sensitivity analysis of filling fraction of pebble bed in pebble bed HTR," *Nuclear Engineering and Design*, vol. 292, pp. 123–132, 2015.

[10] J. Du, C. Hao, J. Ma, P. Li, X. Zhou, and L. Liu, "New strategies in the code of uncertainty and sensitivity analysis (CUSA) and its application in the nuclear reactor calculation," *Science and Technology of Nuclear Installations*, vol. 2020, Article ID 6786394, 16 pages, 2020.

[11] M. Schürenkrämer and H. Barthels, Experimentelle untersuchungen zur thermohydraulik in kugelschüttungen im vergleich mit dem rechenprogramm Thermix-2D. Die untersuchung des dispersiven wärmetransportes am beispiel einer kaltgassträhne, Jül-1839-RW, 1983.

[12] D. She, J. Guo, Z. Liu, and L. Shi, "PANGU code for pebble-bed HTGR reactor physics and fuel cycle simulations," *Annals of Nuclear Energy*, vol. 126, pp. 48–58, 2019.

[13] C. Hao, J. Ma, N. Xu, Q. Zhao, J. Du, and K. Zhu, "Uncertainty propagation analysis for control rod worth of PWR based on the statistical sampling method," *Annals of Nuclear Energy*, vol. 137, pp. 1–11, 2020.

[14] G. H. Lohnert, "Technical design features and essential safety-related properties of the HTR-module," *Nuclear Engineering and Design*, vol. 121, no. 2, pp. 259–275, 1990.

[15] German National Standard Institute, *Decay Heat Power in Nuclear Fuels of High-Temperature Reactors with Spherical Fuel Elements, Documentation and Illustration, DIN 25485*, German Nuclear Society, Berlin, Germany, 1990.

[16] K. Robold, "Wirmetransport im innern und in der randzone von kugelschiittungen," KFA Jiilich, Jülich, Germany, Dissertation, 1982.

Hindawi
Science and Technology of Nuclear Installations
Volume 2020, Article ID 6786394, 16 pages
https://doi.org/10.1155/2020/6786394

Research Article

New Strategies in the Code of Uncertainty and Sensitivity Analysis (CUSA) and Its Application in the Nuclear Reactor Calculation

Jiayu Du, Chen Hao, Ji Ma, Peijun Li, Xiaoyu Zhou, and Lixun Liu

Fundamental Science on Nuclear Safety and Simulation Technology Laboratory, Harbin Engineering University, Harbin 150001, China

Correspondence should be addressed to Chen Hao; haochen.heu@163.com

Received 4 November 2019; Accepted 14 January 2020; Published 11 February 2020

Academic Editor: Tomasz Kozlowski

Best-Estimation Plus Uncertainty (BEPU) analysis method can provide more information to improve the reliability of calculation results than the safety analysis with conservative assumption. And the statistical sampling-based uncertainty and sensitivity analysis methods are widely used in practical applications of the multiphysics, multiscale coupling nuclear reactor system. In this paper, a novel and efficient sampling method for inputs with normal and uniform distributions is introduced and a systematic theory for uncertainty and sensitivity analysis is established based on the classical statistical theory. Then the Code of Uncertainty and Sensitivity Analysis (CUSA) is updated based on these new strategies. For applications, the explicit and implicit effects for resonance and nonresonance isotopes are studied in depth, and a simple UO_2 pin cell is considered to examine the performance of CUSA and the total uncertainty and sensitivity analysis abilities. The numerical results indicate that the implicit sensitivity analysis model and the uncertainty quantification functions developed in CUSA are correct and can be used for sensitivity and uncertainty analysis in nuclear reactor calculations. Even more important, the LHS-SVDC is recommended to propagate the uncertainties in multigroup cross sections.

1. Introduction

Accurate estimation of key parameters of nuclear reactor is essential for both reactor simulation and safety analysis. Due to the fact that the nuclear reactor is a complex nonlinear multiphysics, multiscale coupling system, the high-fidelity simulations and modelling with full consideration of the coupling among neutronics, thermal hydraulics, fuel performance, and so on have now become the standard for modern evaluation of nuclear reactor system [1]. However, uncertainties inevitably propagate in the progress of nuclear reactor simulations [2, 3]. The uncertainties of input parameters, manufacturing tolerance, approximation in calculation models, and so on naturally exist [4]. As research progressed and Best-Estimate (BE) methods matured, a move toward Best-Estimation Plus Uncertainty (BEPU) analysis occurred. BEPU can be used to quantify these uncertainties, and it provides more information to improve the reliability of calculation results than the safety analysis with conservative assumption. It is worthy to note that only the uncertainty of nuclear data is quantified by using the BEPU methods in this work.

For uncertainty quantification and propagation, two primary kinds of methods are widely used, e.g., the adjoint-based uncertainty quantification and sensitivity analysis [5] and the statistical sampling-based uncertainty and sensitivity analysis method [6]. But for some practical applications, the adjoint-based uncertainty method is not going to work because of the inexistence of the solution of the adjoint equation or the difficulty in obtaining adjoint solutions. Although the statistical sampling-based uncertainty and sensitivity analysis method is to some extent time consuming, this method still has some significant advantages, such as less simplifications and approximations, and no limit on the system responses compared with the adjoint based method. Hence, the statistical sampling-based uncertainty and sensitivity analysis methods are widely used in practical applications of the multiphysics, multiscale coupling nuclear

reactor system such as assembly burnup [7]; power distribution [8]; decay heat [9]; control rod worth [10]; filling fraction of pebble bed [11]. Moreover, some codes based on this method also have been developed for uncertainty and sensitivity analysis, such as SUSA [12], XSUSA [13], Dakota [14], and CUSA [15].

The CUSA (the Code for Uncertainty and Sensitivity Analysis) was originally developed for uncertainty and sensitivity analysis of filling fraction of pebble bed and uranium loading of fuel pebble in pebble bed high temperature reactor (HTR-PM). The initial version only has some simple sampling and statistical functions based on the Simple Random Sampling (SRS) method, Latin Hypercube Sampling (LHS) method, K-S test, and basic statistical theory. And it is tightly coupled with the simulation codes for HTR-PM. As for the implementation progress of the statistical sampling-based uncertainty and sensitivity analysis, a set of input parameters should be generated firstly by random sampling according to their distribution and covariance information. Then these sets of input parameters will be sent into the same calculation to produce a set of outputs. At last, the statistical theory is applied to quantify the uncertainty of outputs propagated from inputs. So using the statistical sampling method to perform uncertainty and sensitivity analysis, two key technical problems should be considered reasonably and efficiently. First, efficient sampling methods should be studied to obtain a reasonable input sample space based on the covariance and distribution information. Second, a systematic theory analysis for uncertainty quantification should be conducted, which can be used to quantify the uncertainty of output and its associated error bar or confidence interval under a specific size of sample space.

In this paper, a novel and efficient sampling method for inputs with normal and uniform distributions is introduced, which is based on the well-known LHS method and Singular Value Decomposition (SVD). The efficient sampling method based on the SVD for high-dimensional covariance matrix is also proposed. Then, a systematic theory for uncertainty and sensitivity analysis is established based on the classical statistical theory, which can be used to quantify the distribution type of outputs, uncertainty, and its associated error bar under a specific size of samples. Then a new version of CUSA has been developed and some new functions based on the innovative efficient sampling methods, correlation control techniques, and uncertainty quantification methods have been updated. At the same time, a user-friendly interface for CUSA has been developed and the interface also serves as an integrated platform for controlling all the function modules and coupling with the executable version of other simulation codes. Even more important, the CUSA code can be used for uncertainty and sensitivity analysis for a wide range of applications, such as uncertainty analysis for reactor physics, thermal hydraulics calculations, and safety analysis.

For applications, the uncertainties of effective resonance self-shielding cross sections and total uncertainty of eigenvalue propagated from multigroup microscopic cross sections are quantified by using the CUSA and a home-developed resonance calculation code. Even more important, the explicit and implicit effects for resonance and nonresonance isotopes are fully considered. And the total uncertainty analysis can be conducted not only for the integral cross sections, including σ_a, σ_s, and σ_t, but also for the basic cross sections, such as σ_{elas}, σ_{inel}, σ_f, and σ_γ. In this way, the multigroup microscopic cross section uncertainties can be propagated to the neutronics responses completely. In this paper, the uncertainty quantified by CUSA and "Sandwich Rules" is compared based on a simple UO_2 pin cell in order to examine the performance and ability of CUSA. Meanwhile, it should be noted that this paper aims to introduce the good sampling and statistical methods of CUSA and apply it to sensitivity and uncertainty analysis of effective resonance self-shielding cross sections and eigenvalue.

In the following sections, the details of methodologies and basic functions of CUSA are described and then in Section 3, the methods of uncertainty and sensitivity analysis for effective resonance self-shielding cross sections and eigenvalue by applying CUSA are discussed. Section 4 shows a detailed analysis of the origin sensitivity and uncertainty information and the total uncertainty results for UO_2 pin cell. At last, conclusions drawn from this work are given in Section 5.

2. Methodologies and Basic Functions of CUSA

2.1. Efficient Sampling Methods

2.1.1. Basic Sampling Theory for Normal and Uniform Distributions. The basis of the implemented statistical sampling-based uncertainty and sensitivity analysis method is to treat all uncertain inputs as dependent random variables by sampling them according to a multivariate probability density function (PDF). The mean and variance/covariance of the variable PDFs must be known to perform the statistical sampling uncertainty propagation. And an $n \times n$ covariance matrix is used to describe the uncertainty associated with each element of the input vector and the correlations that exist between elements. Rather than generating new vectors directly from their PDFs, an alternative approach is to generate vectors of perturbation factors that when multiplied by the reference input vector will produce a population of vectors, whose mean value is equal to the reference and whose elements have dependencies.

For variables obeying the normal distribution, the normally distributed dependent random samples can be generated as shown as follows [16]:

$$X = AZ + \mu, \tag{1}$$

where Z is a normally distributed independent vector, whose mean value is equal to 0 and standard deviation is 1. μ is the mean vector of input variables and the matrix A can be generated based on the Singular Value Decomposition of the relative covariance matrix Σ:

$$\Sigma = USV^T = U\sqrt{S}(\sqrt{S})^T U^T = U\sqrt{S}(U\sqrt{S})^T = AA^T. \tag{2}$$

But for uniformly distributed variables, the approach for normally distributed variables mentioned above will fail; then a new two-step transformation approach based on Singular Value Decomposition is proposed to generate the uniformly distributed dependent random samples. The basic idea of this two-step method is illustrated in Figure 1.

As shown in Figure 1, a standard normally distributed independent vector Z should be generated, and then the linear transformation technique is applied to obtain the normally distributed dependent random samples Y:

$$Y = AZ, \tag{3}$$

where A is generated by performing SVD of the correlation coefficient matrix C_Y of the random elements of the vector Y:

$$C_Y = USV^T = U\sqrt{S}(U\sqrt{S})^T = AA^T. \tag{4}$$

Here, the correlation coefficient matrix of Y is not known. But the correlation coefficient matrix C_X of X is known as the basic input information. So the key technique is to determine the relationship between the correlation coefficient of different random elements of X and Y. Based on the rigorous mathematical derivation, the relationship can be established by [17]

$$\rho_{y_i y_j} = 2\sin\left(\frac{\pi}{6}\rho_{x_i x_j}\right). \tag{5}$$

As we know, the cumulative probability density function of Y is consistent with the cumulative probability density function of X by nonlinear transformation. And the cumulative probability density function of the standard normally distributed samples can be represented by the error function, as shown in

$$\int_{-\infty}^{y_i} f_{Y_i}(y_i)\mathrm{d}y_i = F_{Y_i}(y_i) = \frac{1}{2}\left[1 + \mathrm{erf}\left(\frac{y_i}{\sqrt{2}}\right)\right]. \tag{6}$$

In this way, the desired uniformly distributed dependent random samples can be generated as shown as follows:

$$x_i = F_{X_i}^{-1}\left[\frac{1}{2}\left(1 + \mathrm{erf}\left(\frac{y_i}{\sqrt{2}}\right)\right)\right]. \tag{7}$$

2.1.2. Correlation Control Method. As discussed above, Z is a vector including nX independent normally distributed random variables, which obeys the multivariate standard normal distribution $N_{nX}(0, I)$. So the success of the sampling is to generate an excellent sample space Z_s of Z firstly. And the samples should meet the following two conditions: (1) the correlation matrix associated with Z_s is very close to the $nX \times nX$ identity matrix; (2) the mean vector is a zero vector. Normally, the SRS or LHS method is applied to generate the desired sample space Z_s and the covariance matrix of Z_s is denoted as Σ_s. However, Σ_s always does not meet the above two conditions. Especially, when the sample size is small, a strong correlation will occur, which will lead to a distortion of the sample space and have a potentially large impact on the uncertainty propagation. Therefore, efficient sampling methods of fully considering the correlation information between different elements should be studied to obtain a reasonable input sample space based on the covariance and distribution information. In our work, a novel and efficient sampling method for inputs with normal and uniform distributions is proposed, which is based on the well-known LHS or SRS or Importance Sampling (IS) method combined with SVD technique [18]. Then, a desired sample space Z_s^* can be obtained as follows [18]:

$$\Sigma_s = \frac{1}{n}Z_s^T Z_s - \frac{1}{n^2}Z_s^T HZ = USV^T, \tag{8}$$

where H is an $n \times n$ full matrix with the element of 1. S is a diagonal matrix and the diagonal elements are the singular value of Σ_s. And Σ_s is the covariance matrix of Z_s, which is a symmetric matrix. So the matrix U is the same as V; then (8) can be rewritten as

$$U^T \Sigma_s U = S. \tag{9}$$

Further, two new diagonal matrices denoted as E and D are constructed, in which, $E \in R^{nX \times nX}$, $e_{i,i} = \Sigma_{s,i,i}$, $D \in R^{nX \times nX}$, and $d_{i,i} = \sqrt{s_{i,i}/\Sigma_{s,i,i}}$.

Then, a new formula is obtained as

$$\left(D^{-1}\right)^T SD^{-1} = E. \tag{10}$$

Combining (10) with (9) and inserting this two formulae into (8), we can get

$$\frac{1}{n}\left(Z_s UD^{-1}\right)^T Z_s UD^{-1} - \frac{1}{n^2}\left(Z_s UD^{-1}\right)^T HZ_s UD^{-1} = E. \tag{11}$$

Based on (11), we know that the covariance matrix of the sample space $Z_s^* = Z_s UD^{-1}$ is a unit diagonal matrix, which indicates that the parameters in the sample space are completely independent. So, a new independent sample space Z_s^* is obtained, which strictly obeys the multivariate standard normal distribution $N_{nX}(0, I)$.

2.1.3. Sampling Method for High-Dimensional Covariance Matrix. In some practical applications, the $n \times n$ covariance matrix for representing the uncertainty and correlation information of all uncertain inputs is very large, probably thousands or more, and we call it high-dimensional covariance matrix. For example, the size n of the global covariance matrix for the multigroup microscopic cross sections is very large if fine energy group and all nuclides are considered, although most of the off-diagonal elements are zero. If the sample size nS is bigger than or equal to the matrix size n, the methods mentioned above can be used efficiently. But very often the physical calculations become the bottleneck and require the most computational effort. In fact, a relative small sample size, which can represent most of the uncertainty and correlation information, is useful for practical applications. If the nS is smaller than the matrix size

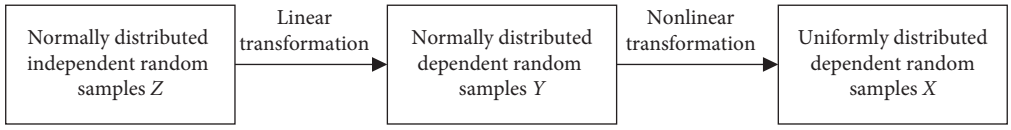

Figure 1: The basic ides of the two-step transformation approach.

n, the covariance matrix of the samples of Z is a singular matrix. Therefore, the correlation control technique based on the SVD fails and leads to a distorted uncertainty propagation. To solve this problem, a reduced order sampling technique based on principal component analysis is proposed.

First, the SVD is performed on the $n \times n$ covariance matrix of the uncertain inputs. Then, the principal component analysis is performed on the singular value matrix S, and the main nSV singular values are selected to construct a new singular value matrix S_1; then

$$\begin{aligned}\Sigma = USU^T &= \begin{bmatrix} U_1 & U_2 \end{bmatrix} \begin{bmatrix} S_1 & 0 \\ 0 & S_2 \end{bmatrix} \begin{bmatrix} U_1 & U_2 \end{bmatrix}^T \\ &= U_1 S_1 U_1{}^T + U_2 S_2 U_2{}^T,\end{aligned} \tag{12}$$

where the matrix $U_2 S_2 U_2{}^T$ can be ignored if enough singular values are selected. In this way, the $n \times n$ covariance matrix of the uncertain inputs can be approximated to the following:

$$\Sigma = AA^T \approx U_1 S_1 U_1{}^T = U_1 \sqrt{S_1} \left(U_1 \sqrt{S_1}\right)^T. \tag{13}$$

After the principal component analysis, the original covariance matrix can be approximated to a high degree of accuracy with very few components. In this way, a relatively small sample size, such as 100, will be enough. In addition to the computational gains, the correlation control method can be no longer limited in the high-dimensional matrix applications.

2.2. Uncertainty and Sensitivity Analysis Methods Based on Statistical Theory. For uncertainty quantification, the Kolmogorov–Smirnov (K–S) test [19] is chosen to compare whether the distribution of a population sample is significantly different from the overall distribution and judge the sample distribution type, such as normal distribution, uniform distribution, and chi-square distribution. When the significance level is less than the given value (usually 0.05), the sample space is considered to have a significant difference from the population. Once the distribution type of the samples of outputs is determined, the typical statistical theory can be used to quantify the uncertainty information of the output, such as the mean value, standard deviation, and coefficient of variation. Here, the coefficient of variation is the ratio between the standard deviation and the mean in a sampled population, which represents the relative uncertainty.

However, the statistic itself has uncertainty and the standard error is usually used to represent this uncertainty. A standard error of a statistic is the standard deviation of the statistic. And an error bar is, in a plot, a line which is centered at the estimate with length that is double the standard error. It is well known that the error bar is a function of the number of samples and that accurate uncertainty estimates with narrow error bar will be observed for large sample sets. So a systematic uncertainty analysis should not only give the basic statistical information of outputs but also provide its associated error bar information under a certain sample size.

For the mean value, regardless of the type of distribution, as long as the sample size nS is large, normally larger than 20, the standard error $\sigma_{\overline{O}}$ of the mean $\overline{O}$ can be quantified by [20]

$$\sigma_{\overline{O}} = \frac{\sigma}{\sqrt{nS}}, \tag{14}$$

where σ is the standard deviation of the output population.

For standard deviation, the standard error is different for different distribution types. In the case of large samples ($nS \geq 20$), the associated standard error for the normal distribution and uniform distribution can be quantified by using (15a) [21] and (15b) [22], respectively:

$$\sigma_\sigma = \frac{\sigma}{\sqrt{2(nS-1)}}, \tag{15a}$$

$$\sigma_\sigma = \sqrt{\frac{2(nS-1)}{nS+2}}\,\frac{\sigma}{nS+1}. \tag{15b}$$

The absolute value of the coefficient of variation is usually termed as the relative standard deviation (RSD), and it represents the relative uncertainty in our research. In the case of large samples ($nS \geq 20$), the standard error of the coefficient of variation for the normally distributed outputs can be determined by

$$\sigma_{RSD} = \sqrt{\frac{C^4}{nS} + \frac{C^2}{2nS}}, \tag{16a}$$

where C represents the coefficient of variation of the output population.

But for the uniformly distributed outputs, the standard error of the coefficient of variation is conservatively estimated by following equation in our present work:

$$\begin{aligned}\sigma_{RSD} = &\frac{C + \sqrt{2(nS-1)/nS+2}\,(C/nS+1)}{2\left(1-\left(C/\sqrt{nS}\right)\right)} \\ &- \frac{C - \sqrt{2(nS-1)/nS+2}\,(C/nS+1)}{2\left(1+\left(C/\sqrt{nS}\right)\right)}.\end{aligned} \tag{16b}$$

It should be noted that the confidence interval of the statistic can also be used to represent the statistic itself uncertainty due to statistical process. In our work, the

confidence interval with a certain confidence can also be quantified for the mean, standard deviation, and the coefficient of variation.

On the other hand, the study of how output uncertainty can be apportioned to the different input sources, which is known as sensitivity analysis, is an important part to the uncertainty quantification. Since the sensitivity analysis can be used to identify where a reduction of uncertainty should be performed, it has the greatest benefit for the reduction of the total uncertainty. For uncertainty and sensitivity analysis based on statistical theory, the sensitivity information cannot be obtained directly. In this paper, we estimate the sensitivity coefficients of effective self-shielding cross sections and eigenvalue to multigroup microscopic cross sections, which have a strong linear relationship. The direct perturbation method is a practical method for local sensitivity analysis, where the output variable is only changing due to a direct perturbation from a specific parameter. It is worth noting that when the two parameters do not obey a linear relationship, the direct perturbation method will not be applicable. In addition to local sensitivity analysis, global sensitivity analysis based on variance distribution is also a good method to estimate the sensitivity coefficients of nuclear data, but it is not used in this paper [23, 24].

At the same time, the correlation analysis, which usually calculates the Kendall, Pearson, and Spearman correlation coefficients, is also used to perform sensitivity analysis to quantify the influence of the specific input parameter on the output.

2.3. Main Functions and Interface Design

2.3.1. Overview of Basic Functions of CUSA. Based on the main methods discussed above, a new version of CUSA has been developed and some new functions, such as efficient sampling, statistical analysis, standardized input, code coupling, and plot, have also been developed by using C language on windows operation system. An overview of basic functions and coupling relationship between different modules is illustrated in Figure 2.

For the standardized input module, the initial information of uncertainty sources should be first inputted to the CUSA, including mean value, the relative covariance information, and some basic parameters and description of inputs. And there are two ways for input, directly reading from the input files and inputting through interface manually. However, a specific format of input data needs to be provided, while there is no limitation by using the interface. For nuclear data uncertainty propagation and quantification by using CUSA, an important function of transforming nuclear cross-section covariance matrix in multigroup form into users' group structures is implemented based on our previous research [25]. By using this function, users only need to input the desired energy group information to obtain the relative covariance matrix in users' group structures, which is an easy way and recommended. Of course, users can input all the relative covariance information by using interface or input files.

According to the innovative efficient sampling methods and correlation control techniques, three fundamental sampling methods, including SRS, IS, and LHS, can be used to generate desired sample spaces. Once the correlation control techniques are taken into account, total 9 sampling methods can be used and the LHS-SVDC is recommended to generate an excellent sample space with a relatively small sample size, normally about 100, for either normally distributed or uniformly distributed input parameters. For other distribution types, the SRS method is used to generate the desired sample space. All these functions can be easily applied by using the CUSA interface.

The statistical analysis module consists of three parts, K-S test, statistical calculation, and sensitivity analysis and also has two essential applications in CUSA. The first application is to verify the sample space, such as the mean value, relative standard deviation, correlation information, and distribution type. Second, and more important, this function is especially designed for uncertainty and sensitivity analysis. Uncertainty quantification (error bar and confidence interval), distribution type estimation, direct sensitivity analysis, and correlation analysis are all conducted by using this module.

There are two coupling strategies with other simulation codes, directly coupling with the dynamic-link library (DLL) or reading and generating the specified files for simulation codes. If the DLL of other simulation codes is coupled with CUSA, an important parallel calculation function can be used and the number of calculations can also be controlled.

At last, and more important, a user-friendly human-computer interaction platform of CUSA is developed by using QT language. Based on this interface, all functions of CUSA can be performed. The initial and operation interfaces are shown in Figure 3. At the same time, the logo of CUSA is also designed for further application and development.

3. Sensitivity and Uncertainty Analysis by Applying CUSA

3.1. Sensitivity and Uncertainty Analysis of Effective Resonance Self-Shielding Cross Sections. For the application of CUSA, the uncertainties of effective resonance self-shielding cross sections propagated from multigroup microscopic cross sections through resonance calculation are quantified firstly. In this work, a home-developed resonance module based on subgroup method is applied for resonance calculation. It should be noted that the effective resonance self-shielding cross sections are related to the calculation of subgroup parameters and subgroup flux in the subgroup resonance calculation. For nonresonant nuclides, the uncertainty of the multigroup microscopic cross sections will only be propagated to the subgroup flux and further propagated to the final calculated effective resonance self-shielding cross sections. But for resonant nuclides, the uncertainty of the multigroup microscopic cross sections will be propagated to both the subgroup parameters and flux. So uncertainties of both nonresonant and resonant nuclides should be taken into account when quantifying the uncertainty of effective resonance self-shielding cross sections. In this way, the

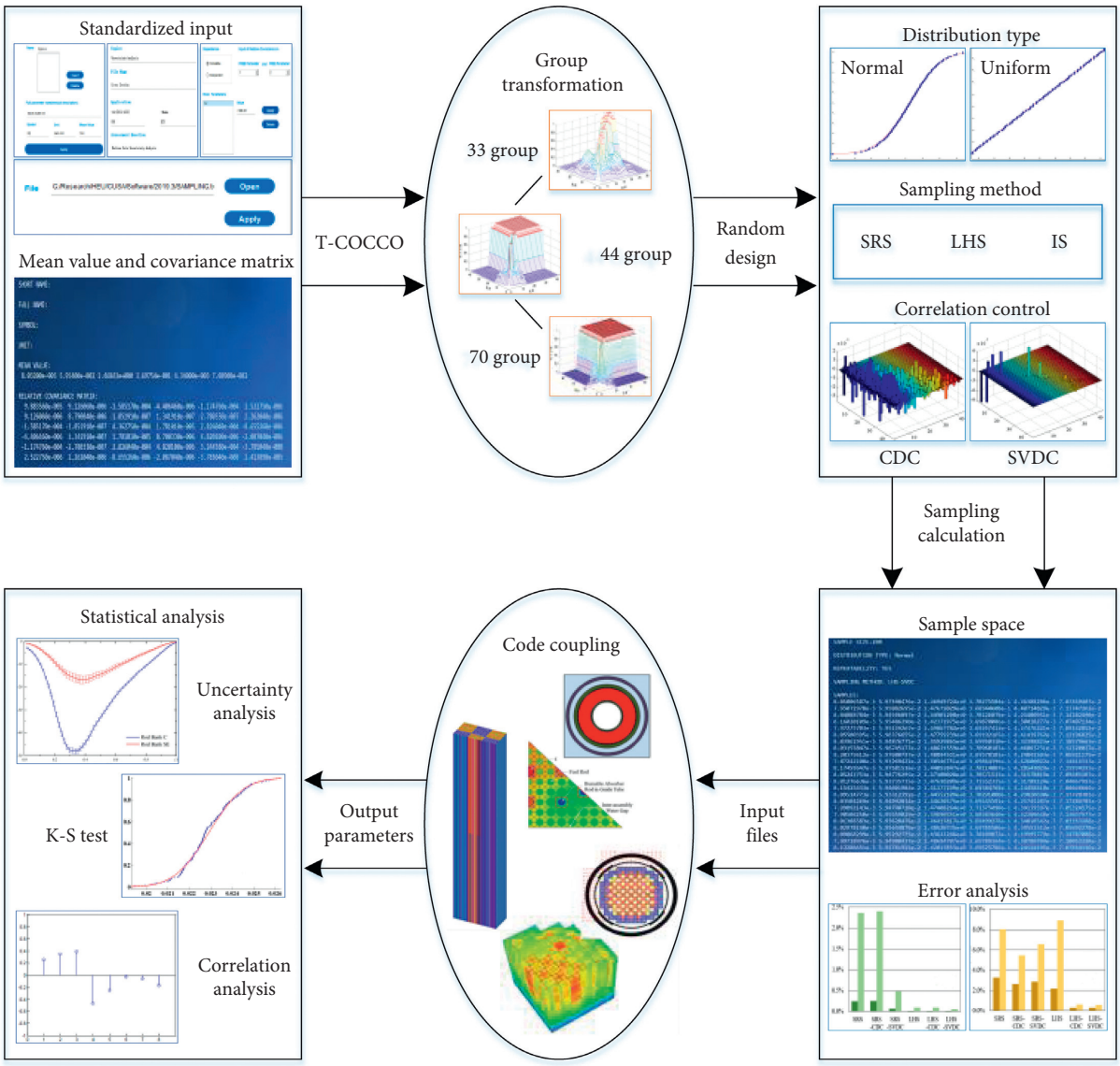

Figure 2: The function diagram of CUSA.

(a) (b)

Figure 3: Initial and operation interface of CUSA.

effects of microscopic cross sections on the effective resonance self-shielding cross sections, which are defined as the implicit effects, are fully considered.

At the same time, the cross-section consistency rules should be established in the multigroup microscopic cross-section perturbation model. As a WIMS 69-energy group based library is used in this work, for the resonance energy group, the absorption cross section is completely composed of the neutron capture cross section and fission reaction cross section, without the $(n, 2n)$, $(n, 3n)$, and (n, p) reactions. And the scattering cross section is completely composed of elastic scattering cross section. In this way, the following equations are applied as simplified consistency rules to keep the cross sections balanced:

$$\sigma_a = \sigma_{(n,\gamma)} + \sigma_f, \tag{17a}$$

$$\sigma_s = \sigma_{\text{elastic}}. \tag{17b}$$

The direct perturbation function built in CUSA is applied firstly to quantify the implicit sensitivity coefficients, which represent the indirect impact of multigroup microscopic cross sections on the response through the resonance self-shielding calculation. When a parameter perturbation is small enough, the change of the effective resonance self-shielding cross section can be expressed through the linear relationship. Then the sensitivity coefficient, which indicates the relative percent change of the effective resonance self-shielding cross section when the multigroup microscopic cross sections are perturbed with a relative value of 1%, can be defined as

$$S^{\text{imp}}_{\sigma_{x,g},\alpha_g} = \frac{\delta\sigma_{x,g}/\sigma_{x,g}}{\delta\alpha_g/\alpha_g}, \tag{18}$$

where α_g stands for the gth group microscopic cross section of a particular nuclide and $\sigma_{x,g}$ stands for the effective resonance self-shielding cross section of the reaction type x. δ represents the perturbation of cross sections; in this work it is 1%.

For uncertainty quantification, a relative covariance matrix is needed, which contains the uncertainty and correlation information for different nuclear reactions. And this matrix should be in the same energy group structure as the unique multigroup cross-section library used in the sensitivity analysis. This relative covariance matrix can be collapsed by a flux weighting directly from the evaluated data files such as ENDF to the user's group structure by using NJOY [26]. Although this way is more mathematically rigorous, the process is relatively complicated and the covariance information needs further judgements and comprehensive evaluations. Alternatively, an existing evaluated multigroup covariance matrix, such as ZZ-SCALE6.0/COVA-44G library [27], can be transformed into a new energy group structure based on a flat-flux approximation when the widths of the energy groups are not drastically different. In this work, the module T-COCCO built in CUSA is applied to transform the covariance matrix in 44-energy group form into a 69-energy group structure to provide basic uncertainty information of multigroup cross sections.

Then efficient sampling and statistical analysis modules are used to quantify uncertainties of effective resonance self-shielding cross sections propagated from multigroup microscopic cross sections. At the same time, the "Sandwich" rule is also used to quantify the uncertainty based on the calculated implicit sensitivity coefficients for further comparison. As illustrated in Figure 4, the basic idea of quantifying uncertainties of the effective resonance self-shielding cross sections by using CUSA is summarized as the following steps:

(1) The original relative covariance matrix in 44-energy group and the basic information of the WIMS 69 energy group-based library, such as the energy group structure and mean of each cross section, are inputted to CUSA system.

(2) A relative covariance matrix in 69-energy group structure is generated by using T-COCCO to provide basic uncertainty information.

(3) Determine the sample size nS and the efficient sampling module is called to generate a desired sample space for the multigroup microscopic cross sections, which will generate nS perturbed multigroup cross-section libraries. Here, the cross-section consistency rules are applied to keep the cross sections balanced.

(4) The resonance calculation module based on subgroup method is coupled with CUSA by using the DLL file. Based on the perturbed libraries, the resonance calculations will be performed nS times to generate nS effective resonance self-shielding cross-section libraries.

(5) The statistical analysis module is then used to quantify the uncertainty of the effective resonance self-shielding cross sections and their associated error bar with the given sample size.

3.2. Sensitivity and Uncertainty Analysis of Eigenvalue by Applying CUSA. In order to extend the implicit sensitivity analytical ability of CUSA to a wider application and further to investigate its impact on the uncertainty results, the eigenvalue total sensitivity and uncertainty analysis is performed in our work. In addition, since the sensitivity analysis of the resonance energy groups is much more complicated than the sensitivity analysis of fast and thermal energy groups, which do not contain implicit sensitivity analysis, this paper is only focused on the sensitivity and uncertainty analysis of resonance energy groups.

The total sensitivity coefficient of eigenvalue should consist of two parts, explicit sensitivity coefficient and implicit sensitivity coefficient. If the perturbation of gth group microscopic cross section only affects the corresponding macroscopic cross section and further affects the eigenvalue through transport calculations, this associated sensitivity coefficient is defined as explicit sensitivity coefficient, which can be calculated as

$$S^{\text{exp}}_{k_{\text{eff}},\alpha_g} = \frac{\delta k_{\text{eff}}/k_{\text{eff}}}{\delta\alpha_g/\alpha_g}. \tag{19}$$

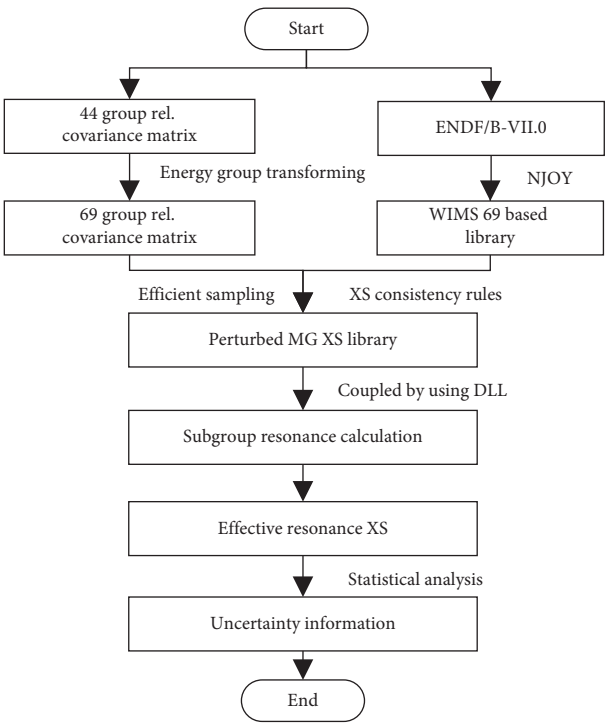

Figure 4: Flowchart of uncertainty analysis of effective resonance self-shielding XS by CUSA.

As mentioned in Section 3.1, the perturbation of the microscopic cross section has a direct effect on the effective resonance self-shielding cross sections first and further affects the macroscopic cross sections. At last, this effect will propagate to the final calculated eigenvalue through transport calculations. In this case, the sensitivity coefficient of eigenvalue to the multigroup microscopic cross section is considered as implicit sensitivity coefficient, which can be quantified by using the following equation:

$$S^{\text{imp}}_{k_{\text{eff}},\alpha_g} = \sum_{j,x} \frac{\delta k_{\text{eff}}/k_{\text{eff}}}{\delta\sigma^j_{x,g}/\sigma^j_{x,g}} \frac{\delta\sigma^j_{x,g}/\sigma^j_{x,g}}{\delta\alpha_g/\alpha_g} = \sum_{j,x} S^{\text{exp}}_{k_{\text{eff}},\sigma^j_{x,g}} S^{\text{imp}}_{\sigma^j_{x,g},\alpha_g}, \quad (20)$$

where j indicates resonant nuclides and x is the indicator of the reaction type of effective resonance self-shielding cross sections. The first term of the implicit sensitivity coefficient is the sensitivity coefficient of the k_{eff} to the effective resonance self-shielding cross sections, which is a kind of explicit sensitivity coefficient. The second term of the implicit sensitivity coefficient is the sensitivity coefficient of the effective resonance self-shielding cross sections to the multigroup micro cross sections, the details can be found in Section 3.1. Then, the total sensitivity coefficient can be calculated as

$$S^{\text{tot}}_{k_{\text{eff}},\alpha_g} = S^{\text{exp}}_{k_{\text{eff}},\alpha_g} + S^{\text{imp}}_{k_{\text{eff}},\alpha_g}. \quad (21)$$

It should be noted that the calculations of total sensitivity coefficient for the resonant nuclides and nonresonant nuclides are slightly different. For the resonant nuclides, the explicit sensitivity coefficient term should be considered as zero. This is due to the fact that the explicit effect is already considered when calculating the implicit sensitivity coefficients for resonant nuclides. But for the nonresonant nuclides, since there is no effective resonance self-shielding cross section associated with its own multigroup microscopic cross section, the explicit effect is not considered in the process of quantifying its implicit effect on the effective resonance self-shielding cross sections of resonant nuclides.

The same as the uncertainty quantification of effective resonance self-shielding cross sections, the efficient sampling and statistical analysis modules built in CUSA are used to quantify the uncertainty of eigenvalue propagated from multigroup microscopic cross sections. Also the "Sandwich" rule is used to quantify the uncertainty based on the calculated total sensitivity coefficients for comparison. The details and flowchart are nearly the same as those described in Section 3.1.

3.3. Model and Codes. In order to examine the performance of sensitivity and uncertainty analytical abilities of CUSA in the application of the uncertainty propagation and quantification of cross sections, a simple UO_2 fuel pin cell is built, as shown in Figure 5. The density of UO_2 is 10.3 g/cc, the enrichment of ^{235}U is 6.5% in this model, and the clad and moderator are Zr-nat and light water, respectively; the details of the materials can be found in Table 1 [28]. Here, it should be noted that the Zr-nat is not treated as a resonance nuclide in our work.

As illustrated in Figure 5, the whole cell is divided into 12 subregions, in which the fuel zone is divided into 3 subregions and the moderator zone occupies 8 with flat-source approximation. It is due to the fact that the method of characteristics (MOC) is used and a home-developed High-fidelity NEutron Transport program for 3D nuclear reactor whole-core (HNET) is applied as a transport solver [29] in the resonance calculation and the following transport calculation. For the resonance calculation, a home-developed module built in the HNET based on the subgroup method is applied. Then a WIMS 69-energy group based library is used based on the ENDF/B VII.0 evaluation database [30]. At the same time, the multigroup covariance library ZZ-SCALE6.0/COVA-44G has been used as the basic evaluated covariance information. At last, the CUSA is coupled with HNET to perform sensitivity and uncertainty analysis of effective resonance self-shielding cross sections and eigenvalue due to the microscopic cross sections.

4. Numerical Results

4.1. Sensitivity of Effective Resonance Self-Shielding XSs to MG Microscopic XSs. The sensitivity analysis of ^{235}U and ^{238}U effective resonance self-shielding cross sections to the multigroup microscopic cross sections of each nuclide, including resonance and nonresonant nuclides, is performed firstly. Figures 6–9 illustrate the top five most sensitive sources to the ^{235}U and ^{238}U effective resonance absorption and scattering cross section and the corresponding implicit sensitivity coefficients.

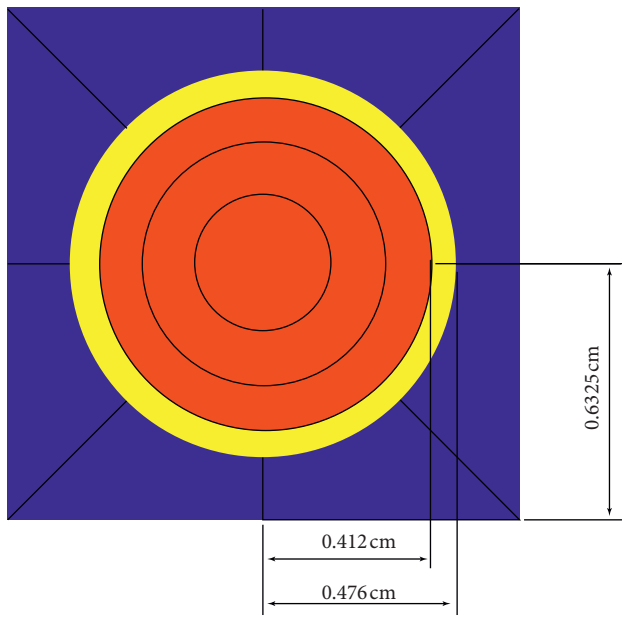

Figure 5: The simple UO_2 fuel pin cell.

Table 1: The materials and the nuclide densities of the UO_2 pin cell.

Material	Nuclide density/(barn$^{-1}\cdot$ cm^{-1})				
	^{235}U	^{238}U	Zr-nat	^{1}H	^{16}O
Fuel (900 K)	1.5122$E-03$	2.1477$E-02$	—	—	4.5945$E-02$
Cladding (600 K)	—	—	4.3107$E-02$	—	—
Moderator (600 K)	—	—	—	4.4148$E-02$	2.2074$E-02$

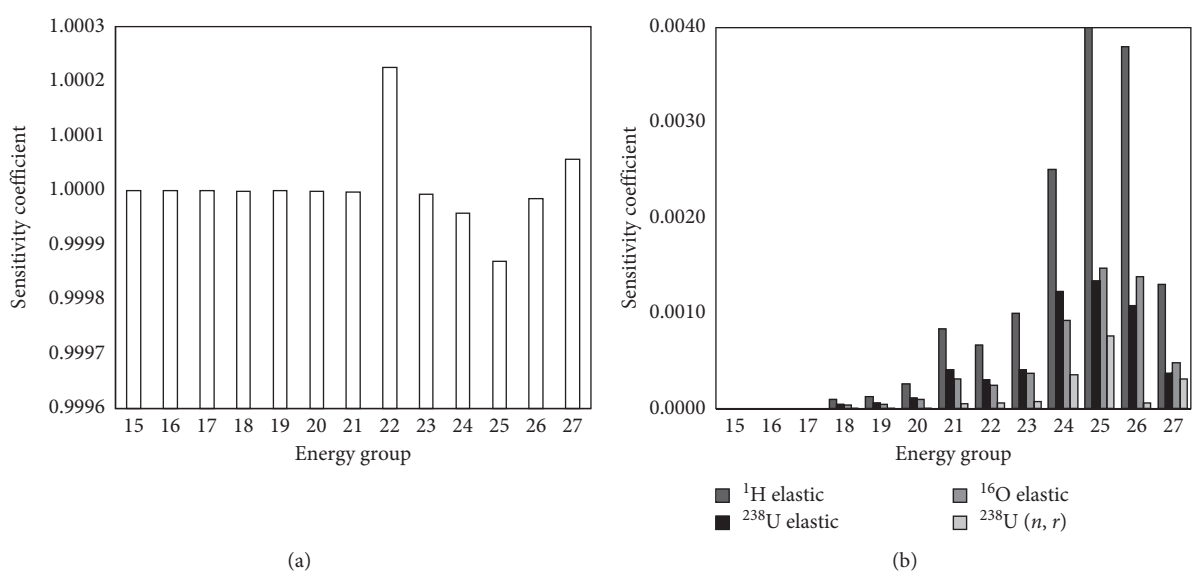

Figure 6: The top five most sensitive sources to the ^{235}U effective resonance scattering XS and the corresponding implicit sensitivity coefficients. (a) Sensitivity coefficient to ^{235}U elastic scattering. (b) Sensitivity coefficients to other four reactions.

It can be found that the effective resonance self-shielding cross section of each resonance nuclide is most sensitive to its associated multigroup microscopic cross section that constitutes this integral cross sections, as shown in (17), while the sensitivity coefficient to other microscopic cross sections is relatively small. For example, the effective resonance scattering cross sections of ^{235}U are quite sensitive to the associated microscopic elastic scattering cross section of ^{235}U, the sensitivity coefficient of which is around 1. But the second most sensitive source to

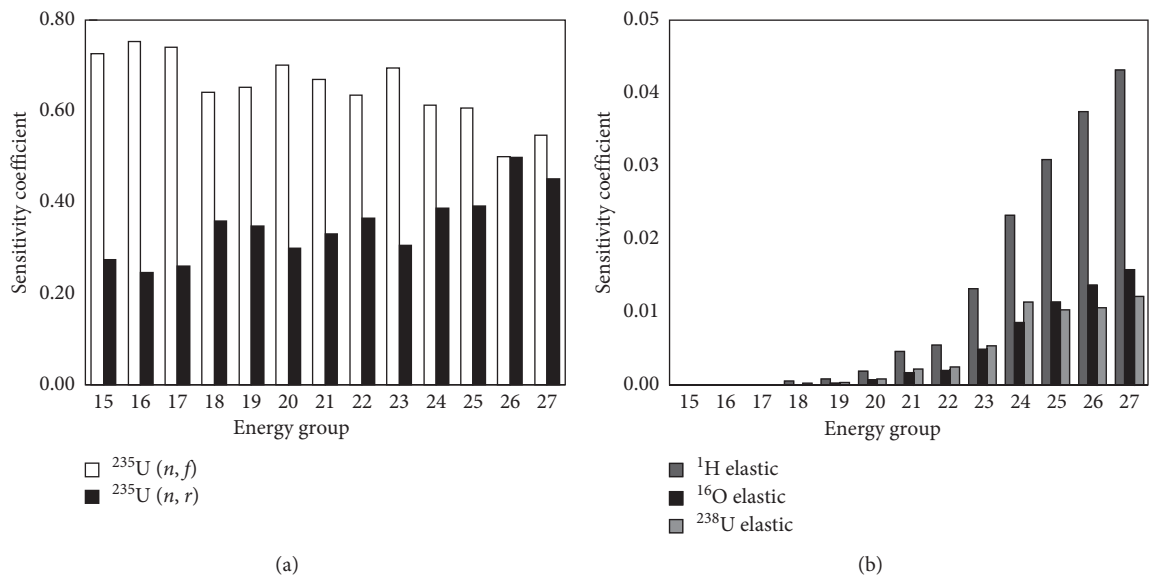

Figure 7: The top five most sensitive sources to the ^{235}U effective resonance absorption XS and the corresponding implicit sensitivity coefficients. (a) Sensitivity coefficients to ^{235}U fission and radiation capture. (b) Sensitivity coefficients to other three reactions.

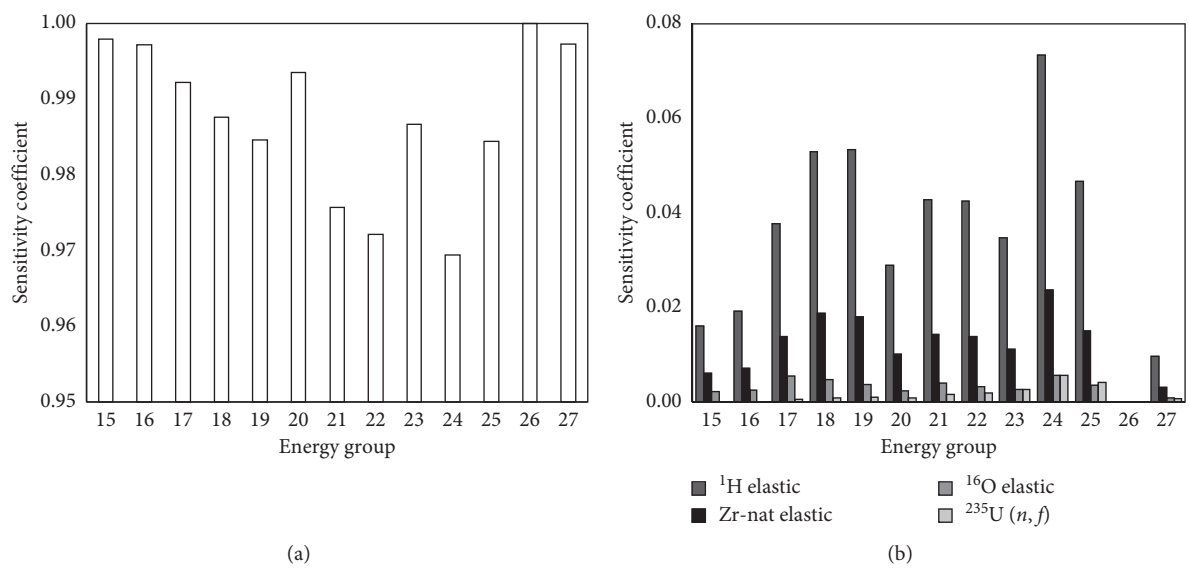

Figure 8: The top five most sensitive sources to the ^{238}U effective resonance scattering XS and the corresponding implicit sensitivity coefficients. (a) Sensitivity coefficient to ^{238}U elastic scattering. (b) Sensitivity coefficients to other four reactions.

the effective resonance scattering cross sections of ^{235}U is ^{1}H elastic scattering cross section, the value of which is only about 0.004. Although the sensitivity coefficients of non-resonant nuclides are relatively small, these implicit effects cannot be ignored in the resonance calculation. The same as the scattering cross sections, the effective resonance absorption cross section is most sensitive to fission and radiation capture cross sections. For ^{235}U, the top 1 most sensitive source is its fission reaction and the sensitivity coefficient is around 0.6, which is followed by the radiation capture cross section of ^{235}U and the value is around 0.4, while the top 1 most sensitive source is radiation capture reaction for ^{238}U.

4.2. Uncertainty Quantification of Effective Resonance Self-Shielding XSs. The size of sample space is crucial for nuclear cross-section uncertainty propagation and quantification by using statistical sampling methods. There are different sampling methods built in CUSA, such as SRS, LHS, IS, LHS-CDC, and LHS-SVDC. To determine a reasonable sample size for each sampling method, which is a relative small size for less computation burden and stable uncertainty contribution, the uncertainty contributions of radiation capture cross section to the 18th and 22nd group effective resonance absorption cross section of ^{235}U are selected and quantified by using different sampling methods with different sample size, as illustrated in Figure 10. At the

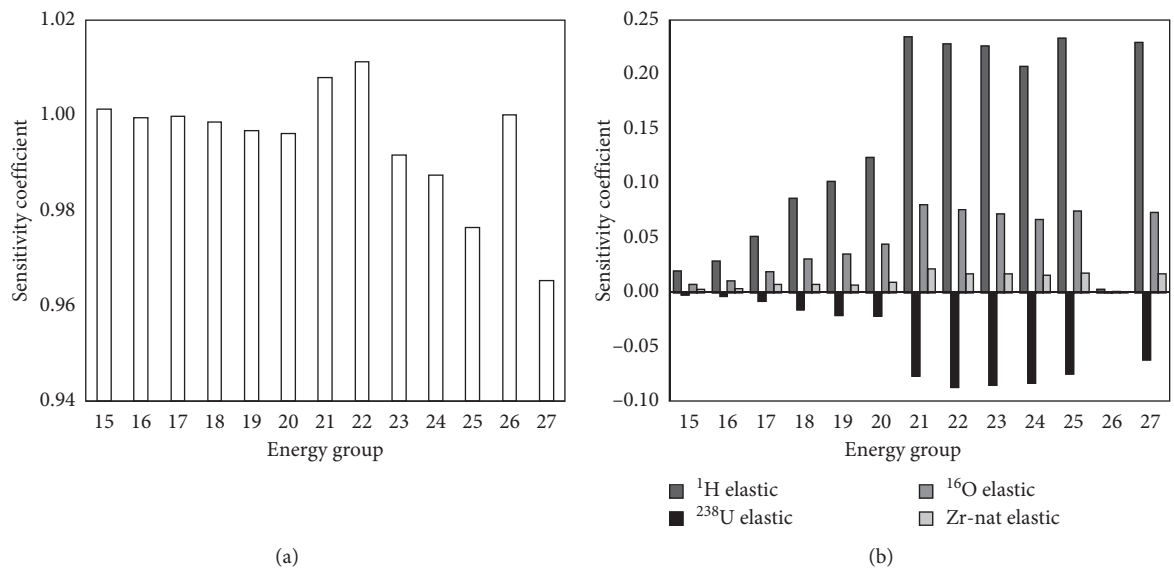

Figure 9: The top five most sensitive sources to the ^{238}U effective resonance absorption XS and the corresponding implicit sensitivity coefficients. (a) Sensitivity coefficient to ^{238}U radiation capture. (b) Sensitivity coefficients to other four reactions.

same time, the "Sandwich" rule is also used to quantify the uncertainty based on the calculated implicit sensitivity coefficients for comparison.

It is obviously found that the contribution of radiation capture cross section to the total uncertainty of the effective resonance absorption cross sections of ^{235}U tends to be stable and be close to the results quantified by using Sandwich rule when the sample size is greater than 100 for LHS-SVDC methods, while the sample size needs to be greater than 800, which will generate a relatively stable uncertainty contribution for LHS or SRS methods. So the sample size is set to 100 and the LHS-SVDC built in CUSA is selected in the following uncertainty quantifications.

The relative uncertainty of the effective resonance absorption and scattering cross sections of ^{235}U and ^{238}U propagated from the multigroup microscopic cross sections is quantified by using CUSA and Sandwich rule, respectively, as shown in Figure 11. For uncertainty quantification, the error bar of the relative uncertainty under the sample size 100 is also quantified by using the statistical analytical function of CUSA, as illustrated in Figure 11. It is obviously found that the relative uncertainties quantified by CUSA agree well with the results calculated by the Sandwich rule based on the implicit sensitivity information obtained by CUSA. Therefore, the implicit sensitivity analysis model and the uncertainty quantification functions developed in CUSA can be proved correct and can be used for sensitivity and uncertainty analysis in nuclear reactor calculations.

Figure 11 also shows that the effective resonance absorption cross section of ^{235}U and the resonance scattering cross section of ^{238}U have a larger uncertainty due to the multigroup microscopic cross sections. The top 3 most significant microscopic cross section sources of uncertainty in these two effective resonance self-shielding cross sections are listed in Tables 2 and 3.

It can be seen that the relative uncertainties in the effective resonance self-shielding cross sections due to the basic microscopic cross sections are large and nonignorable. The neutron capture reaction of ^{235}U contributes the most to the uncertainty of ^{235}U resonance absorption cross section, up to 9%, which is followed by ^{235}U fission reaction, while this effective resonance self-shielding cross section is most sensitive to the ^{235}U fission reaction. This difference is mainly attributed to the fact that the microscopic cross section of ^{235}U neutron capture reaction itself has a larger uncertainty than ^{235}U fission reaction. It can be also found that ^{235}U elastic scattering reaction has a larger contribution to uncertainty of the ^{235}U resonance absorption cross section than the ^{1}H elastic scattering reaction, although it is more sensitive to the ^{1}H elastic scattering reaction. This is also due to the fact that ^{1}H elastic scattering cross section has a smaller uncertainty. Similar phenomenon of ^{1}H elastic scattering reaction to the effective resonance scattering cross section of ^{238}U is also found. Although the effective resonance self-shielding cross sections are more sensitive to the ^{1}H elastic scattering reaction, while its contribution to uncertainty is small due to itself small uncertainty.

4.3. Total Sensitivity Coefficient of Eigenvalue to MG Microscopic XSs. The implicit and total sensitivity coefficients of k_{eff} to the microscopic cross sections of each nuclide are calculated with the direct perturbation function of CUSA. The top four most sensitive sources to k_{eff} and the corresponding implicit and total sensitivity coefficients are illustrated in Figure 12.

In our work, only the contribution of cross sections in resonance groups is investigated due to the fact that one of the main purposes is to verify the implicit sensitivity analytical ability of CUSA. It can be obviously found in Figure 12 that the total sensitivity is equal to the sum of explicit

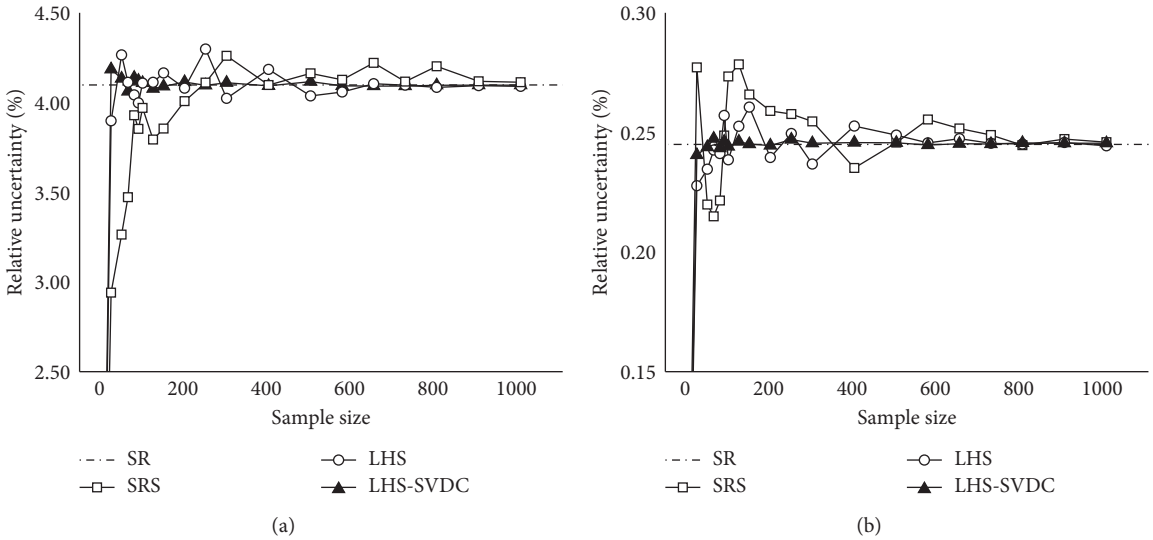

Figure 10: The contribution of ^{235}U (n, γ) to the uncertainty of ^{235}U resonance absorption XS by using different sampling methods with different sample sizes. (a) 18th group. (b) 22nd group.

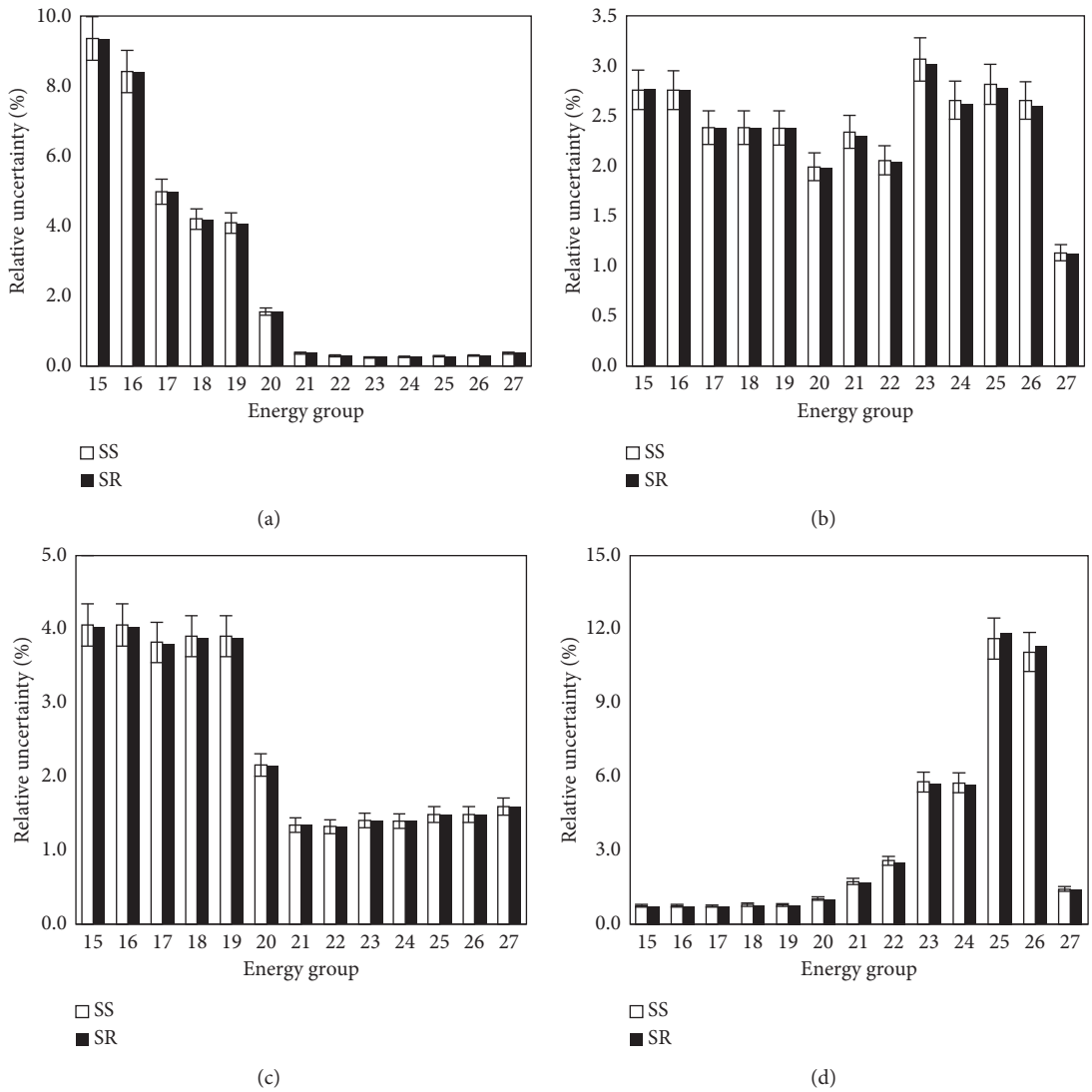

Figure 11: The uncertainty of effective resonance self-shielding cross sections. (a) ^{235}U effective resonance absorption XS. (b) ^{238}U effective resonance absorption XS. (c) ^{235}U effective resonance scattering XS. (d) ^{238}U effective resonance scattering XS.

Table 2: The top 3 sources of uncertainty in ^{235}U effective resonance absorption XS.

Energy group	Contributions to the relative uncertainty (%)		
	^{235}U (n, γ)	^{235}U (n, f)	^{238}U elastic
15	$9.362E+00 \pm 6.683E-01$	$3.441E-01 \pm 2.435E-02$	$0.000E+00$
16	$8.418E+00 \pm 5.999E-01$	$3.572E-01 \pm 2.528E-02$	$0.000E+00$
17	$4.955E+00 \pm 3.515E-01$	$6.125E-01 \pm 4.334E-02$	$0.000E+00$
18	$4.109E+00 \pm 2.913E-01$	$9.056E-01 \pm 6.409E-02$	$2.053E-04 \pm 1.453E-05$
19	$3.991E+00 \pm 2.829E-01$	$9.201E-01 \pm 6.512E-02$	$3.189E-04 \pm 2.257E-05$
20	$1.484E+00 \pm 1.050E-01$	$4.932E-01 \pm 3.490E-02$	$8.482E-04 \pm 6.002E-05$
21	$3.146E-01 \pm 2.226E-02$	$2.101E-01 \pm 1.487E-02$	$3.984E-03 \pm 2.819E-04$
22	$2.441E-01 \pm 1.727E-02$	$1.790E-01 \pm 1.266E-02$	$6.583E-03 \pm 4.658E-04$
23	$1.636E-01 \pm 1.158E-02$	$1.974E-01 \pm 1.397E-02$	$3.189E-02 \pm 2.256E-03$
24	$1.941E-01 \pm 1.374E-02$	$1.675E-01 \pm 1.186E-02$	$6.732E-02 \pm 4.764E-03$
25	$1.879E-01 \pm 1.330E-02$	$1.835E-01 \pm 1.299E-02$	$1.222E-01 \pm 8.644E-03$
26	$2.425E-01 \pm 1.716E-02$	$1.496E-01 \pm 1.059E-02$	$1.181E-01 \pm 8.354E-03$
27	$2.745E-01 \pm 1.942E-02$	$2.664E-01 \pm 1.885E-02$	$1.762E-02 \pm 1.247E-03$

Table 3: The top 3 sources of uncertainty in ^{238}U effective resonance scattering XS.

Energy group	Contributions to the relative uncertainty (%)		
	^{238}U -elastic	^{16}O-elastic	^{1}H elastic
15	$7.635E-01 \pm 5.403E-02$	$1.145E-02 \pm 8.101E-04$	$4.243E-03 \pm 3.003E-04$
16	$7.630E-01 \pm 5.399E-02$	$1.343E-02 \pm 9.500E-04$	$5.059E-03 \pm 3.580E-04$
17	$7.428E-01 \pm 5.256E-02$	$1.324E-02 \pm 9.369E-04$	$1.145E-02 \pm 8.106E-04$
18	$8.007E-01 \pm 5.666E-02$	$1.831E-02 \pm 1.296E-03$	$2.265E-02 \pm 1.603E-03$
19	$7.983E-01 \pm 5.649E-02$	$1.767E-02 \pm 1.250E-03$	$2.285E-02 \pm 1.617E-03$
20	$1.043E+00 \pm 7.378E-02$	$9.930E-03 \pm 7.026E-04$	$6.816E-03 \pm 4.823E-04$
21	$1.739E+00 \pm 1.231E-01$	$1.395E-02 \pm 9.872E-04$	$4.402E-03 \pm 3.115E-04$
22	$2.586E+00 \pm 1.831E-01$	$1.345E-02 \pm 9.520E-04$	$4.375E-03 \pm 3.096E-04$
23	$5.790E+00 \pm 4.111E-01$	$1.086E-02 \pm 7.685E-04$	$3.582E-03 \pm 2.534E-04$
24	$5.756E+00 \pm 4.086E-01$	$2.316E-02 \pm 1.639E-03$	$7.555E-03 \pm 5.346E-04$
25	$1.162E+01 \pm 8.337E-01$	$1.464E-02 \pm 1.036E-03$	$4.805E-03 \pm 3.400E-04$
26	$1.108E+01 \pm 7.938E-01$	$2.401E-05 \pm 1.699E-06$	$6.803E-06 \pm 4.814E-07$
27	$1.439E+00 \pm 1.019E-01$	$2.993E-03 \pm 2.118E-04$	$9.874E-04 \pm 6.987E-05$

and implicit sensitivity, which further verifies the reliability of implicit and total sensitivity analysis abilities of CUSA. At the same time, the k_{eff} total sensitivity coefficient to the neutron radiation capture reaction of ^{235}U and ^{238}U is negative and is positive for the fission reaction of ^{235}U and elastic scattering reaction of ^{1}H. This is physically consistent with the fact that the radiation capture reaction results in the disappearance of neutron, while fission results in the production of neutron and the moderation produces more thermal neutron, which has a positive effect on the fission event.

As discussed in Section 3.2, the explicit effect is considered when calculating the implicit sensitivity coefficient for resonance nuclides, as shown in Figures 12(a)–12(c). But for the nonresonant nuclides, the explicit and implicit sensitivity coefficients should be calculated, respectively. It can be found that the explicit sensitivity coefficients of most energy group for nonresonant nuclides are positive, while the implicit sensitivity coefficients are negative. It is worth noting that the total and implicit sensitivity coefficients of ^{1}H are the biggest one compared with other nonresonant nuclides due to the fact that the ^{1}H is the dominating moderated nuclide in our studies.

4.4. Uncertainty Quantification of Eigenvalue due to MG Microscopic XSs. The contributions of the multigroup microscopic cross sections in resonance groups to the k_{eff} uncertainty and the total relative uncertainty of k_{eff} propagated from these cross sections are quantified by using CUSA and Sandwich rule, respectively, as presented in Table 4. It is obviously found that the contributions and the relative uncertainties quantified by CUSA agree well with the results calculated by the Sandwich rule.

It can be found that the relative uncertainty in k_{eff} due to the basic cross section in resonance group is large and nonignorable, of which the neutron capture reaction of ^{238}U contributes the most to the k_{eff} uncertainty, up to 0.27%. And k_{eff} is also most sensitive to the neutron capture reaction of ^{238}U in resonance region, while it is most sensitive to the average number of neutrons emitted per fission event for all energy regions. Besides, although k_{eff} is more sensitive to the ^{1}H elastic scattering reaction than the neutron capture reaction of ^{235}U, its associated contribution to the k_{eff} uncertainty is smaller due to itself smaller uncertainty. The whole relative uncertainty of k_{eff} contributed by resonance energy groups is about 0.3% and it is reasonable that the value is smaller than the standard value

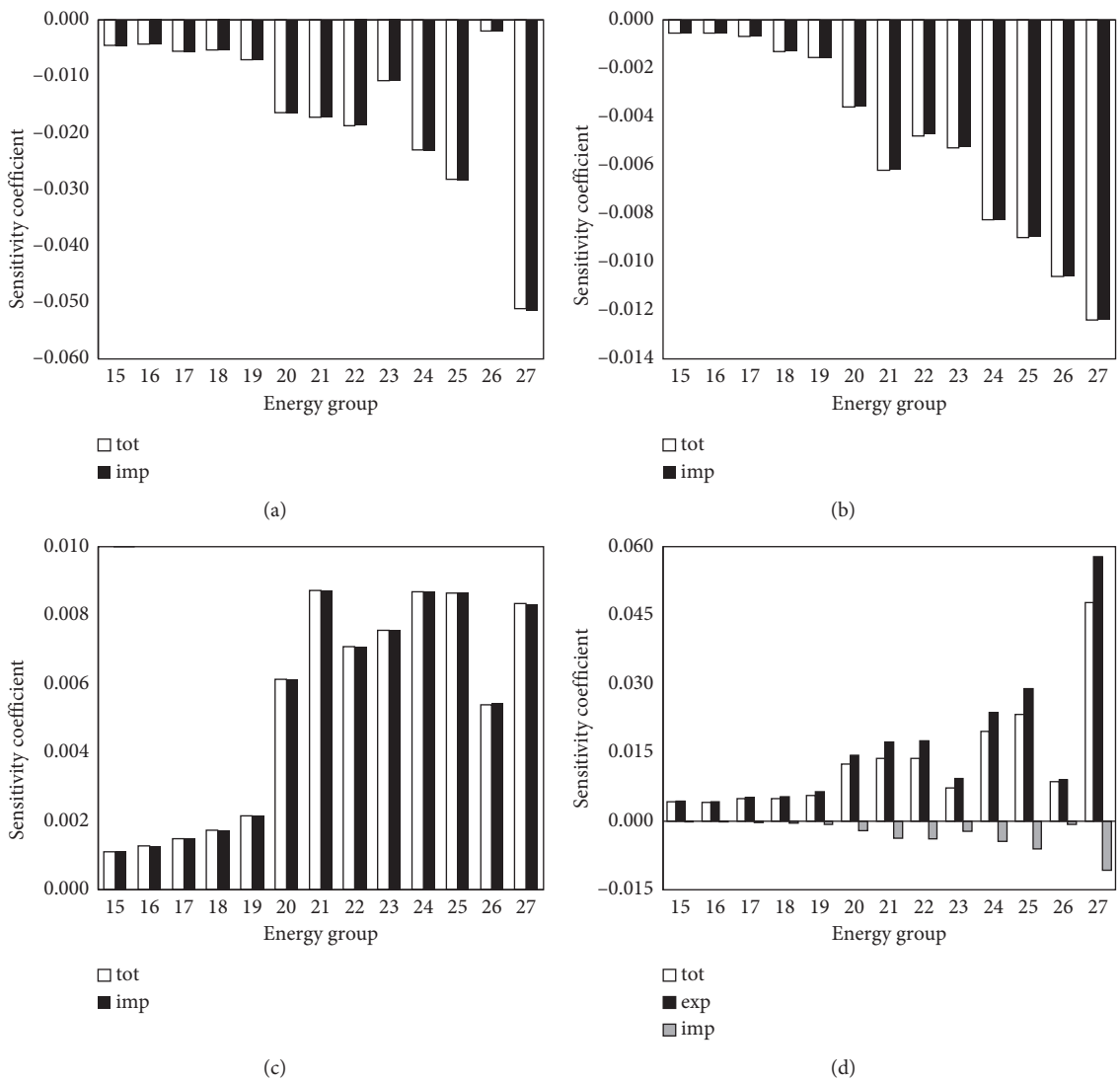

Figure 12: The total and implicit sensitivity coefficients of k_{eff} to the microscopic cross sections. (a) ^{238}U (n, γ). (b) ^{235}U (n, γ). (c) ^{235}U (n, f). (d) ^{1}H elastic scattering.

Table 4: The contributions of microscopic cross sections to the k_{eff} uncertainty.

Cross section type	Total sensitivity coefficient	Uncertainty (%) (sandwich rule)	Uncertainty (%) Statistics sampling
^{238}U (n, γ)	$-1.948E-01$	$2.692E-01$	$2.692E-01 \pm 1.905E-02$
^{235}U (n, γ)	$-6.472E-02$	$1.007E-01$	$1.012E-01 \pm 7.161E-03$
Zr-nat (n, γ)	$-5.147E-03$	$5.988E-02$	$6.036E-02 \pm 4.271E-03$
^{235}U (n, f)	$6.838E-02$	$2.026E-02$	$2.032E-02 \pm 1.438E-03$
^{1}H elastic	$1.707E-01$	$1.979E-02$	$2.045E-02 \pm 1.447E-03$
^{238}U-elastic	$4.089E-03$	$9.781E-03$	$9.709E-03 \pm 6.870E-04$
^{16}O-elastic	$-9.390E-03$	$9.327E-03$	$9.225E-03 \pm 6.549E-06$
^{235}U elastic	$-2.915E-04$	$1.380E-03$	$1.384E-03 \pm 9.793E-05$
Zr-nat-elastic	$-2.107E-03$	$1.305E-03$	$1.320E-03 \pm 9.341E-05$
^{16}O (n, γ)	$-1.013E-06$	$9.880E-06$	$9.725E-06 \pm 6.881E-07$
^{1}H (n, γ)	$-1.636E-03$	$8.159E-04$	$8.262E-04 \pm 5.846E-05$
Sum	—	$2.953E-01$	$2.956E-01 \pm 2.091E-02$

(0.5%) because fast and thermal energy groups are not in consideration.

5. Conclusions

Best-Estimation Plus Uncertainty (BEPU) analysis method can provide more information to improve the reliability of calculation results than the safety analysis with conservative assumption. And the statistical sampling-based uncertainty and sensitivity analysis methods are widely used in practical applications of the multiphysics, multiscale coupling nuclear reactor system. In this paper, a novel and efficient sampling method for inputs with normal and uniform distributions is introduced, which is based on the well-known LHS method and SVD. The efficient sampling method based on the SVD for high-dimensional covariance matrix is also proposed. Then, a systematic theory for uncertainty and sensitivity analysis is established based on the classical statistical theory, which can be used to quantify the distribution type of outputs, uncertainty, and its associated error bar under a specific size of samples. Based on these new strategies, the CUSA has been updated. At the same time, a user-friendly interface for CUSA has been developed and the interface also serves as an integrated platform for controlling all the function modules and coupling with the executable version of other simulation codes.

For applications, the uncertainties of effective resonance self-shielding cross sections and total uncertainty of eigenvalue propagated from multigroup microscopic cross sections are quantified by using the CUSA and a home-developed resonance calculation code. Especially, the explicit and implicit effects for resonance and nonresonance isotopes are fully considered. The calculations of total sensitivity coefficient for the resonant nuclides and nonresonant nuclides are slightly different. For the resonant nuclides, the explicit sensitivity coefficient term should be considered as zero. This is due to the fact that the explicit effect is already considered when calculating the implicit sensitivity coefficients for resonant nuclides. But for the nonresonant nuclides, since there is no effective resonance self-shielding cross section associated with its own multigroup microscopic cross section, the explicit effect is not considered in the process of quantifying its implicit effect on the effective resonance self-shielding cross sections of resonant nuclides. Finally, a simple UO_2 pin cell is considered to examine the performance of CUSA and the total uncertainty and sensitivity analysis ability.

The numerical results indicate that the relative uncertainties quantified by CUSA agree well with the results calculated by the Sandwich rule based on the implicit sensitivity information obtained by CUSA. Therefore, the implicit sensitivity analysis model and the uncertainty quantification functions developed in CUSA can be proved correct and can be used for sensitivity and uncertainty analysis in nuclear reactor calculations. Moreover, the LHS-SVDC is recommended to propagate the uncertainty in multigroup cross sections, and then a more reliable uncertainty prediction with smaller number of samples can be obtained.

However, there is still some work to be solved and improved in the further work. On the one hand, the benchmark needs to be replaced with a more representative one, since the enrichment of ^{235}U (6.5%) exceeded the standard of LWR. On the other hand, it is necessary to compare the calculation results of CUSA with other advanced solvers such as TSUNAMI and Sampler. Finally, it makes sense to apply CUSA to other parts of nuclear reactor calculations such as thermal hydraulic calculation.

Data Availability

The data used to support the findings of this study are available from the corresponding author upon request.

Conflicts of Interest

The authors declare that they have no conflicts of interest.

Acknowledgments

This work was supported by the National Key R&D Program of China (2018YFE0180900).

References

[1] D. R. Gaston, C. J. Permann, J. W. Peterson et al., "Physics-based multiscale coupling for full core nuclear reactor simulation," *Annals of Nuclear Energy*, vol. 84, pp. 45–54, 2015.

[2] R. N. Bratton, M. Avramova, and K. Ivanov, "Oecd/nea benchmark for uncertainty analysis in modeling (Uam) for LWRS—summary and discussion of neutronics cases (Phase I)," *Nuclear Engineering and Technology*, vol. 46, no. 3, pp. 313–342, 2014.

[3] F. D'Auria, H. Glaeser, and S. Lee, "Best estimate safety analysis for nuclear power plants: uncertainty evaluation," IAEA Safety Report Series, IAEA, Vienna, Austria, 2008.

[4] A. Yamamoto, Y. Yasue, T. Endo, Y. Kodama, and M. Tatsumi, "Uncertainty estimation of core safety parameters using cross-correlations of covariance matrix," *Journal of Nuclear Science and Technology*, vol. 50, no. 10, pp. 966–978, 2013.

[5] M. L. Williams, "Perturbation theory for nuclear reactor analysis," *CRC Handbook of Nuclear Reactors Calculations*, vol. 3, pp. 63–188, 1986.

[6] J. C. Helton, J. D. Johnson, C. J. Sallaberry, and C. B. Storlie, "Survey of sampling-based methods for uncertainty and sensitivity analysis," *Reliability Engineering & System Safety*, vol. 91, no. 10-11, pp. 1175–1209, 2006.

[7] H. Yun, K. Park, W. choi, and S. G. Hong, "An efficient evaluation of depletion uncertainty for a GBC-32 dry storage cask with PLUS7 fuel assemblies using the Monte Carlo uncertainty sampling method," *Annals of Nuclear Energy*, vol. 110, pp. 679–691, 2017.

[8] Z. Choi, L. Cao, H. Wu, W. Shen, Y. Liu, and C. Wan, "Sensitivity and uncertainty analysis for the PWR online power-distribution monitoring with NECP-ONION system," *Annals of Nuclear Energy*, vol. 114, pp. 359–368, 2018.

[9] G. Ilas and H. Liljenfeldt, "Decay heat uncertainty for BWR used fuel due to modeling and nuclear data uncertainties," *Nuclear Engineering and Design*, vol. 319, pp. 176–184, 2017.

[10] C. Hao and P. Li, "A new efficient sampling method for quantifying and propagating nuclear data uncertainty in

CUSA," *Nuclear Safety and Simulation*, vol. 8, no. 4, pp. 325–332, 2018.

[11] C. Hu, F. Li, G. Jiong, and W. Lidong, "Uncertainty and sensitivity analysis of filling fraction of pebble bed in pebble bed HTR," *Nuclear Engineering and Design*, vol. 292, pp. 123–132, 2015.

[12] M. Kloos and E. Hofer, "SUSA-PC: a personal computer version of the program system for uncertainty and sensitivity analysis of results from computer models, version 3.2, user's guide and tutorial," *Gesellschaft für Anlagen und Reaktorsicherheit*, 1999.

[13] W. Zwermann, A. Aures, L. Gallner et al., "Nuclear data uncertainty and sensitivity analysis with XSUSA for fuel assembly depletion calculations," *Nuclear Engineering and Technology*, vol. 46, no. 3, pp. 343–352, 2014.

[14] M. S. Eldred, K. R. Dalbey, W. J. Bohnhoff et al., "Dakota: a multilevel parallel object-oriented framework for design optimization, parameter estimation, uncertainty quantification, and sensitivity analysis: version 5.0, user's manual," Office of Scientific & Technical Information, Technical Reports, Oak Ridge, TN, USA, 2010.

[15] C. Hao, "Uncertainty analysis in modelling of pebble bed HTR," Doctoral thesis, Institute of Nuclear and New Energy Technology, Beijing China, 2014.

[16] A. Yamamoto, K. Kinoshita, T. Watanabe et al., "Uncertainty quantification of LWR core characteristics using random sampling method," *Nuclear Science and Engineering*, vol. 181, no. 2, pp. 160–174, 2015.

[17] R. J. A. Tough and K. D. Ward, "The correlation properties of gamma and other non-Gaussian processes generated by memoryless nonlinear transformation," *Journal of Physics D: Applied Physics*, vol. 32, no. 23, pp. 3075–3084, 1999.

[18] C. Hao, F. Li, W. Hu, Y. Zhang, and Q. Zhao, "Quantification of control rod worth uncertainties propagated from nuclear data via a hybrid high-order perturbation and efficient sampling method," *Annals of Nuclear Energy*, vol. 114, pp. 227–235, 2018.

[19] J. Frank and Massey Jr., "The Kolmogorov–Smirnov test for goodness of fit," *Journal of the American Statistical Association*, vol. 46, no. 253, pp. 68–78, 1951.

[20] B. L. van der Waerden, *Mathematical Statistics*, Intext Educational Publishers, New York, NY, USA, 1971.

[21] A. Sangtae and J. A. Fessler, *Standard Errors of Mean, Variance, and Standard Deviation Estimators*, The University of Michigan, Ann Arbor, MI, USA, 2003.

[22] G. S. Chen, "Interval estimate of the interval length on uniform distribution," *Pure and Applied Mathematics*, vol. 3, pp. 63–68, 2006.

[23] T. Zhu, A. Vasiliev, H. Ferroukhi, D. Rochman, and A. Rochman Pautz, "Testing the Sampling-Based NUSS-RF Tool for the Nuclear Data-Related Global Sensitivity Analysis with Monte Carlo Neutronics Calculations," *Nuclear Science and Engineering*, vol. 184, no. 1, pp. 69–83, 2016.

[24] T. A. Mara and S. Tarantola, "Variance-based sensitivity indices for models with dependent inputs," *Reliability Engineering & System Safety*, vol. 107, pp. 115–121, 2012.

[25] Q. Zhao, C. Zhang, C. Hao, F. Li, D. Wang, and Y. Yu, "New strategies for quantifying and propagating nuclear data uncertainty in CUSA," *Nuclear Engineering and Design*, vol. 307, pp. 328–338, 2016.

[26] R. MacFarlane and D. Muir, *The NJOY Nuclear Data Processing System Version91*, Los Alamos National Laboratory, Los Alamos, NM, USA, 1994.

[27] NEA Data Bank, "ZZ-SCALE6.0/COVA-44G, a 44-group cross section covariance matrix library retrieved from the SCALE 6.0 package," Radiation Safety Information Computational Center at Oak Ridge National Laboratory, Oak Ridge, TN, USA, 2011.

[28] A. Yamamoto, T. Ikehara, T. Ito, and E. Saji, "Benchmark problem suite for reactor physics study of LWR next generation fuels," *Journal of Nuclear Science and Technology*, vol. 39, no. 8, pp. 900–912, 2002.

[29] C. Ito, L. Kang, Y., P. Song, Q. Zhao, and Z. Zhang, "3D whole-core neutron transport simulation using 2D/1D method via multi-level generalized equivalence theory based CMFD acceleration," *Annals of Nuclear Energy*, vol. 122, pp. 79–90, 2018.

[30] M. B. Chadwick, P. Obložinský, M. Herman et al., "ENDF/B-VII.0: next generation evaluated nuclear data library for nuclear science and technology," *Nuclear Data Sheets*, vol. 107, no. 12, pp. 2931–3060, 2006.

Hindawi
Science and Technology of Nuclear Installations
Volume 2020, Article ID 9428580, 13 pages
https://doi.org/10.1155/2020/9428580

Research Article

Perturbation Theory-Based Whole-Core Eigenvalue Sensitivity and Uncertainty (SU) Analysis via a 2D/1D Transport Code

Ji Ma, Chen Hao, Lixun Liu, and Yuekai Zhou

Fundamental Science on Nuclear Safety and Simulation Technology Laboratory, Harbin Engineering University, Harbin 150001, China

Correspondence should be addressed to Chen Hao; haochen.heu@163.com

Received 14 November 2019; Accepted 7 January 2020; Published 1 February 2020

Guest Editor: Han Zhang

For nuclear reactor physics, uncertainties in the multigroup cross sections inevitably exist, and these uncertainties are considered as the most significant uncertainty source. Based on the home-developed 3D high-fidelity neutron transport code HNET, the perturbation theory was used to directly calculate the sensitivity coefficient of k_{eff} to the multigroup cross sections, and a reasonable relative covariance matrix with a specific energy group structure was generated directly from the evaluated covariance data by using the transforming method. Then, the "Sandwich Rule" was applied to quantify the uncertainty of k_{eff}. Based on these methods, a new SU module in HNET was developed to directly quantify the k_{eff} uncertainty with one-step deterministic transport methods. To verify the accuracy of the sensitivity and uncertainty analysis of HNET, an infinite-medium problem and the 2D pin-cell problem were used to perform SU analysis, and the numerical results demonstrate that acceptable accuracy of sensitivity and uncertainty analysis of the HNET are achievable. Finally, k_{eff} SU analysis of a 3D minicore was analyzed by using the HNET, and some important conclusions were also drawn from the numerical results.

1. Introduction

Due to the fact that the nuclear reactor is a complex nonlinear multiphysics, multiscale coupling system, the high-fidelity simulations and modelling with full consideration of the coupling among neutronics, thermal hydraulics, fuel performance, and so on have now become the powerful numerical tool for the detailed analysis of both the current and advanced reactor design. However, the uncertainties in the basic data, such as the multigroup cross sections, manufacturing tolerance of fuel and materials, naturally exist, and these uncertainties inevitably propagate in the progress of nuclear reactor simulations. So, understanding these uncertainties and quantifying the total uncertainty of the nuclear reactor key parameters is important for improving the reliability of the best estimated results, identifying the importance of uncertainty sources and ensuring appropriate design margins, and also to establish best-estimate calculations for nuclear reactor design and safety analysis. As research progressed, it matures a move toward Best-Estimation plus Uncertainty (BEPU) analysis, and BEPU has now become the standard for the modern evaluation of the nuclear reactor system.

Nuclear reactor physics is the branch of science that deals with the study and application of the chain reaction to induce a controlled rate of fission in the nuclear reactor for the production of energy, so understanding the nuclear reactor physics is very important for each nuclear reactor design, operation, and safety analysis. As a result, uncertainty analysis on nuclear reactor physics simulation results has been a rising topic in recent years. In general, there are three basic uncertainty sources in nuclear physics calculations, including modelling error, numerical solution error, and input parameter uncertainties [1]. The first two errors can be significantly reduced by the arbitrary-geometry modelling method and fast-growing high-fidelity numerical method for transport calculation, respectively. However, the uncertainties of input parameters, especially the multigroup cross sections,

inevitably exist, and these uncertainties are considered as the most significant uncertainty source in the reactor neutronics calculation [2]. For nuclear reactor physics, multiplication factor is one of the most important integral parameters that need to quantify its uncertainty propagated from the multigroup cross sections.

Uncertainty quantification method includes the perturbation theory- (PT-) based method and the statistics sampling-based method. The statistics sampling based method has no approximation with the simulation models and codes and is easy to be implemented. Although the statistical sampling based uncertainty and sensitivity analysis method has less simplifications and approximations and no limit to the system responses compared with the perturbation theory-based method, this method is costly in time and efforts to perform and to interpret the results, and the more challenging problem is that the probability density functions (PDF) are usually unknown being replaced by approximations of good or worse fidelities. For the problems with good adjoint system and easy to solve its associated adjoint system, such as the eigenvalue problem of the nuclear reactor physics, the perturbation theory-based method is efficient, and the superiority is more obvious. As for the implementation progress of the perturbation theory-based uncertainty and sensitivity analysis of the eigenvalue due to the cross section, the sensitivity coefficient of k_{eff} with respect to multigroup macroscopic cross sections should be quantified by using the perturbation theory based on the forward and adjoint solutions, and a reasonable nuclear cross-section covariance matrix in the specific multigroup form, which represents uncertainty and correlation information of different cross sections, should also be built. Then, the "Sandwich Rule" is applied to quantify the uncertainty of k_{eff} propagated from nuclear cross sections.

Indeed, much effort has been put in the development of the perturbation theory-based sensitivity and uncertainty analysis methods by using the forward and adjoint solutions obtained by deterministic transport methods or Monte Carlo methods for the past years. For the deterministic transport methods, perturbation-based sensitivity and uncertainty analysis is always performed by using the 2D forward and adjoint transport solutions, and some well-known lattice codes already have the SU analysis ability, such as the Polaris in SCALE6.2.1 [3], CASMO5 [4], and AutoMOC [5]. For the direct 3D whole-core SU analysis, the Monte Carlo methods are preferred to perform the forward and adjoint calculations, and then the perturbation theory-based SU method is applied, and the SU analysis ability is also developed in some famous Monte Carlo codes in recent years, such as the TSUNAMI-3D module in SCALE [6], RMC [7], and McCARD [8]. Even more important, significant advances in high performance computing clusters have enabled the direct 3D whole-core heterogeneous transport simulation in the subpin level by using the deterministic transport methods, and extending the direct 3D whole-core high-fidelity deterministic transport simulation capabilities to the SU analysis has attracted more and more research efforts in recent years [9].

A 3D whole-core high-fidelity deterministic neutron transport code based on 2D/1D fusion method has been developed in our research group, which adopts the 2D MOC and 1D NEM with a global multilevel CMFD acceleration to solve the forward and adjoint neutron transport equations directly from the multigroup microscopic cross sections [10, 11]. Based on this new code, the generalized perturbation theory is used to directly calculate the sensitivity coefficient of k_{eff} to the multigroup cross sections, and then a new SU module is developed to directly quantify the k_{eff} uncertainty with one-step deterministic transport methods. It is worthy to note that the multigroup relative covariance matrix is also important for the SU analysis, and the ZZ-SCALE6.0/COVA-44G [12] built in SCALE6.0 is very comprehensive. But some other deterministic transport codes cannot directly use this library due to a different energy group structure. Although a new covariance matrix can be processed from the Evaluated Nuclear Data File ENDF/B-VII.1 by using the NJOY code, an alternative efficient and convenient transforming method is developed in our research to generate a reasonable relative covariance matrix with a specific energy group structure from the evaluated $44g$ covariance data library.

In the following sections, the theory background of uncertainty analysis with Sandwich Rule, perturbation theory-based sensitivity analysis, and the covariance matrix transforming method is firstly present. Especially the detailed form of sensitivity coefficients for individual nuclide reaction type is given. Then, the sensitivity and uncertainty analysis scheme is described in detail. In order to verify the accuracy of SU results, the analytical solutions of the three-group infinite medium problem and the direct perturbation (DP) sensitivity analysis and uncertainty analysis of the VERA single cell problem are performed. Finally, SU analysis is performed on the VERA 3×3 patterned minicore, and the calculated SU results are given.

2. Theories

2.1. Uncertainty Quantification with the Sandwich Rule. Consider the k_{eff} of a reactor system which can be expressed as a function of a set of multigroup macroscopic cross sections:

$$k_{\text{eff}} = R(\sigma_1, \sigma_2, \ldots, \sigma_n), \tag{1}$$

where σ represents the multigroup macroscopic cross section for a nuclide reaction type, i.e., effective multigroup resonance cross section, and $\overline{k}$ and $\overline{\sigma}$ represent the expected value. This function can be rewritten by using Taylor expansion and the first order linearity approximation as

$$k_{\text{eff}} = \overline{k}_{\text{eff}} + \delta k_{\text{eff}} = R(\overline{\sigma}_1, \overline{\sigma}_2, \ldots, \overline{\sigma}_n) + \sum_i^n \frac{\partial k_{\text{eff}}}{\partial \sigma_i} \delta\sigma_i. \tag{2}$$

Assuming that input parameters are random and satisfy a joint probability density function $p(\sigma_1, \sigma_2, \ldots, \sigma_n)$, then the variance of k_{eff} can be quantified by

$$\begin{aligned}\operatorname{var}(k_{\text{eff}}) &= \int \left(\sum_{i=1}^{n}\left(\frac{\partial k_{\text{eff}}}{\partial \sigma_i}\right)\delta\sigma_i\right)^2 p(\sigma_1,\sigma_2,\ldots,\sigma_n)\mathrm{d}\sigma_1,\mathrm{d}\sigma_2,\ldots,\mathrm{d}\sigma_n \\ &= \sum_{i=1}^{n}\left(\frac{\partial k_{\text{eff}}}{\partial \sigma_i}\right)^2 \operatorname{var}(\sigma_i) + 2\sum_{i\neq j=1}^{n}\frac{\partial k_{\text{eff}}}{\partial \sigma_i}\frac{\partial k_{\text{eff}}}{\partial \sigma_j}\operatorname{cov}(\sigma_i\sigma_j),\end{aligned} \tag{3}$$

where cov represents the covariance and var represents variance. Thus, the relative variance of k_{eff}, i.e., the square of the relative k_{eff} uncertainty due to cross sections could be written as

$$\begin{aligned}\frac{\operatorname{var}(k_{\text{eff}})}{k_{\text{eff}}^2} &= \sum_{i=1}^{n}\left(\frac{\sigma_i}{k_{\text{eff}}}\frac{\partial k_{\text{eff}}}{\partial \sigma_i}\right)^2\frac{\operatorname{var}(\sigma_i)}{\sigma_i^2} + 2\sum_{i\neq j=1}^{n}\left(\frac{\sigma_i}{k_{\text{eff}}}\frac{\partial k_{\text{eff}}}{\partial \sigma_i}\right) \\ &\quad\cdot\left(\frac{\sigma_j}{k_{\text{eff}}}\frac{\partial k_{\text{eff}}}{\partial \sigma_j}\right)\frac{\operatorname{cov}(\sigma_i\sigma_j)}{\sigma_i\sigma_j} \\ &= \sum_{i=1}^{n}\left(S_{k_{\text{eff}},\sigma_i}\right)^2 R\operatorname{var}(\sigma_i) + 2\sum_{i\neq j=1}^{n} S_{k_{\text{eff}},\sigma_i}S_{k_{\text{eff}},\sigma_j}\operatorname{Rcov}(\sigma_i\sigma_j),\end{aligned} \tag{4}$$

with the new definition of the sensitivity coefficient vector and the relative covariance matrix as

$$\begin{aligned}S_{k_{\text{eff}},\sigma} &= \left(S_{k_{\text{eff}},\sigma_1}, S_{k_{\text{eff}},\sigma_2},\ldots,S_{k_{\text{eff}},\sigma_n}\right) \\ &= \left(\frac{\sigma_1}{k_{\text{eff}}}\frac{\partial k_{\text{eff}}}{\partial \sigma_1},\frac{\sigma_2}{k_{\text{eff}}}\frac{\partial k_{\text{eff}}}{\partial \sigma_2},\ldots,\frac{\sigma_n}{k_{\text{eff}}}\frac{\partial k_{\text{eff}}}{\partial \sigma_n}\right),\end{aligned} \tag{5a}$$

$$\operatorname{Rcov} = \begin{bmatrix} \dfrac{\operatorname{var}(\sigma_1)}{\sigma_1^2} & \cdots & \dfrac{\operatorname{cov}(\sigma_1\sigma_n)}{\sigma_1\sigma_n} \\ \vdots & \ddots & \vdots \\ \dfrac{\operatorname{cov}(\sigma_n\sigma_1)}{\sigma_n\sigma_1} & \cdots & \dfrac{\operatorname{var}(\sigma_n)}{\sigma_n^2}\end{bmatrix}, \tag{5b}$$

and the sensitivity coefficient reflects the relative change of the independent response k_{eff} with respect to the relative perturbation of a dependent parameter σ, which is defined as

$$S_{k_{\text{eff}},\sigma} = \frac{\delta k_{\text{eff}}/k_{\text{eff}}}{\delta\sigma/\sigma}. \tag{5c}$$

Then, the relative k_{eff} uncertainty can be rewritten by using the matrix form as

$$\frac{\operatorname{var}(k_{\text{eff}})}{k_{\text{eff}}^2} = S_{k_{\text{eff}},\sigma}\operatorname{Rcov}\left(S_{k_{\text{eff}},\sigma}\right)^T. \tag{6}$$

Equation (6) is the well-known "Sandwich Rule". Once the sensitivity coefficient and the relative covariance matrix are known, the relative uncertainty of k_{eff} can be quantified by equation (6).

2.2. Sensitivity Analysis of k_{eff} by Using Perturbation Theory. For uncertainty analysis based on the Sandwich Rule, the sensitivity coefficient of k_{eff} to different cross sections should be quantified firstly by using different methods, such as the central difference direct perturbation method and perturbation theory-based sensitivity analysis method. For each sensitivity coefficient calculated by the direct perturbation, k_{eff} of the system is computed first with the normal values of the input multigroup cross sections, then with a selected nominal input cross section increased by a certain percentage, and then with the same nominal value decreased by the same percentage. Finally, the direct perturbation sensitivity coefficient of k_{eff} to a certain input cross section σ is calculated as

$$S_{k_{\text{eff}},\sigma} = \frac{\left(k_{\text{eff}}^{\sigma^+} - k_{\text{eff}}^{\sigma^-}\right)/k_{\text{eff}}}{(\sigma^+ - \sigma^-)/\sigma}, \tag{7}$$

where σ^+ and σ^- represent the increased and decreased input cross sections, respectively, and $k_{\text{eff}}^{\sigma^+}$ and $k_{\text{eff}}^{\sigma^-}$ represent the corresponding values of the k_{eff}. The direct sensitivity coefficients are easily determined since they depend only on the response functions and do not require an adjoint calculation compared with the perturbation theory-based sensitivity analysis method. This method is feasible and accurate as long as a linear relationship between k_{eff} and cross sections is maintained. However, the central difference direct perturbation method for sensitivity coefficient calculations is computationally cost and even impracticable if all isotopes, reaction types, and energy groups are taken into consideration. Even more important, the relative perturbation factor needs to be chosen carefully, as too small perturbation could be overwhelmed by the numerical calculation errors, whereas too large perturbation may destroy the linear relationship between k_{eff} and cross sections. In this way, the central difference direct perturbation method is always considered as an adequate test for verification of other sensitivity calculation methods. So, the sensitivity coefficient results obtained by using the direct perturbation method are also used to verify the perturbation theory-based sensitivity results in this paper.

In this paper, the perturbation theory is used to calculate the sensitivity coefficient of k_{eff} to the multigroup macroscopic cross sections of different nuclides. The details of each sensitivity coefficient are summarized in this section. In nuclear reactor physics, the operator form of the forward and adjoint neutron transport equations can be written as

$$(L - \lambda F)\Psi = 0, \tag{8a}$$

$$\left(L^* - \lambda^* F^*\right)\Psi^* = 0, \tag{8b}$$

where L is the operator that represents neutron leakage, absorption, and scattering term and F represents the fission source operator; Ψ is the forward neutron angular flux; L^* and F^* are the adjoint operators of L and F, respectively. Ψ^* represents the adjoint neutron angular flux. λ and λ^* are the eigenvalues of forward and adjoint neutron transport equations, respectively (for details, see [10] and [11]). It is important in sensitivity calculations to ensure that the k_{eff} value of the forward and adjoint solutions closely agree. If the k_{eff} values do not agree, then the quality of at least one of the transport calculations may be in question. Typically, the transport calculation of concern is the adjoint calculation.

For nuclear reactor physics, k_{eff} is an integral key parameter and determined by several dependent parameters, such as geometry information, nuclide compositions, and cross sections. As research of high-fidelity simulation and modelling progressed, the uncertainty of nuclear cross sections become more and more important to the total uncertainty of k_{eff}.

Then, the perturbed transport operators and perturbed eigenvalue can be expressed as,

$$\begin{aligned} L' &= L + \delta L, \\ F' &= F + \delta F, \\ \lambda' &= \lambda + \delta\lambda, \end{aligned} \tag{9}$$

where δL and δF represent small perturbations of these transport operators, respectively. $\delta\lambda$ is the corresponding perturbation of the eigenvalue. The perturbed forward neutron transport equation is thus written as

$$\left(L' - \lambda' F'\right)\Psi' = 0. \tag{10}$$

Multiplying both sides of equation (10) by the adjoint neutron angular flux Ψ^* and integrating over all phase space yields

$$\left\langle \Psi^* \left(L' - \lambda' F'\right)\Psi' \right\rangle = 0, \tag{11}$$

where the bracket $\langle\,\rangle$ represents the inner product, and integrating over all phase space involves region, energy, and direction. Then, substitute the perturbed term in equation (11) with equation (9):

$$\left\langle \Psi^* \left((L + \delta L) - (\lambda + \delta\lambda)(F + \delta F)\right)\Psi' \right\rangle = 0. \tag{12}$$

In order to obtain the relative perturbation of the eigenvalue, two approximations are introduced into equation (12): the high order perturbation $\delta F \delta L$ is ignored, and Ψ' is approximated by the unperturbed Ψ as the perturbation of transport operator would not introduce obvious changes in the neutron angular flux. The relative perturbation of eigenvalue is thus obtained as

$$\frac{\delta\lambda}{\lambda} = \frac{\langle \Psi^* (\delta L - \delta F)\Psi \rangle}{\langle \Psi^* (\lambda F)\Psi \rangle}. \tag{13}$$

Here, the perturbation of the operators L and F could be introduced explicitly by the first-order Taylor's expansion with respect to multigroup macroscopic cross sections in their corresponding operator. And, the sensitivity coefficient of k_{eff} due to the perturbation of a certain macroscopic cross section σ can be eventually expressed as

$$S_{k_{\text{eff}},\sigma} = -\sigma \frac{\left\langle \Psi^* \left((\partial L/\sigma) - \left(1/k_{\text{eff}}\right)(\partial F/\sigma)\right)\Psi \right\rangle}{\left\langle \Psi^* \left(1/k_{\text{eff}}\right) F\Psi \right\rangle}. \tag{14}$$

Based on the above equation, the sensitivity coefficient can be obtained by using the perturbation theory, and it only requires forward transport calculation and adjoint calculation once.

It can be found from the above equation that the denominator is reaction type-independent, whereas numerator would vary with different analyzed reaction types. Then, the discretization of denominator can be expressed as follows:

$$D = \left\langle \Psi^* \frac{1}{k_{\text{eff}}} F\Psi \right\rangle = \frac{1}{k_{\text{eff}}} \sum_i^I \sum_z^Z V_z \sum_g^G \chi_{g,z}^i \left(\sum_{m=1}^M w_m \psi_{m,g,z}^* \right) \sum_{g'}^G \nu_{g',z}^i \sigma_{f,g',z}^i \left(\sum_{m=1}^M w_m \psi_{m,g',z} \right), \tag{15}$$

where i, m, g, and z are the nuclide isotope, direction, energy, and mesh index, respectively. And, w_m is the quadrature weight.

The derivation of numerator term could be easily obtained according to the discrete form of neutron transport equation. The sensitivity coefficients of k_{eff} to different cross sections of the isotope i, energy group g, and reaction type x are summarized as follows:

(1) Capture cross section

$$S_{k_{\text{eff}},\sigma_{\text{cap},g}}^i = -\frac{1}{D} \sum_z^Z V_z \sigma_{\text{cap},g,z}^i \sum_m^M w_m \psi_{m,g,z}^* \sum_m^M w_m \psi_{m,g,z}. \tag{16}$$

(2) Fission cross section

$$S_{k_{\text{eff}},\sigma_{f,g}}^i = \frac{1}{D} \left(\lambda \sum_z^Z V_z \nu_g^i \sigma_{f,g,z}^i \sum_m^M w_m \psi_{m,g,z} \sum_{g'=1}^G \chi_{g'}^i \sum_m^M w_m \psi_{m,g',z}^* - \sum_z^Z V_z \sigma_{f,g,z}^i \sum_m^M w_m \psi_{m,g,z} \sum_m^M w_m \psi_{m,g,z}^* \right). \tag{17}$$

(3) Average number of neutrons emitted per fission reaction

$$S_{k_{\text{eff}},\nu_g}^i = \frac{1}{D} \lambda \sum_z^Z \nu_{g,z}^i \sigma_{f,g,z}^i \sum_m^M w_m \psi_{m,g,z} V_z \sum_{g'=1}^G \chi_{g'}^i \sum_m^M w_m \psi_{m,g',z}^*. \tag{18}$$

(4) Fission spectrum

$$S_{k_{\text{eff}},\chi_g}^i = \frac{1}{D} \lambda \sum_z^Z V_z \chi_g^i \sum_m^M w_m \psi_{m,g,z}^* \sum_{g'=1}^G \nu_{g',z}^i \sigma_{f,g',z}^i \sum_m^M w_m \psi_{m,g',z}. \tag{19}$$

(5) Scattering cross section

$$S^{i}_{k_{\text{eff}},\sigma_{s,g\longrightarrow g'}} = \frac{1}{D}\sum_{z}^{Z} V_z \sigma^{i}_{s,g\longrightarrow g',z} \sum_{m}^{M} w_m \psi_{m,g,z}\left(\sum_{m}^{M} w_m \psi^{*}_{m,g',z} - \sum_{m}^{M} w_m \psi^{*}_{m,g,z}\right), \tag{20}$$

where, $\psi_{m,g,z}$ and $\psi^{*}_{m,g,z}$ are the neutron angular flux and adjoint angular flux of direction m, energy group g, and mesh z, and they are obtained by solving the forward and adjoint neutron transport equations, respectively. V_z is the volume of mesh z, i.e., the flat source region due to the MOC method used in this work.

It is worth to note that the sum of all the k_{eff} sensitivity coefficients to the fission spectrum for all energy groups and nuclides should be equal 1.0 based on equations (14), (15), and (19). Actually, the sum of the fission spectrum must be equal to 1.0 over all energy groups for any nuclide. Thus, the sensitivity of k_{eff} to the fission spectrum should sum to 0.0, as any change in fission spectrum in any energy group must be compensated by changes in other groups to maintain the constraint that all the fission spectra sum to 1.0. In this way, the sensitivity coefficient of k_{eff} to the fission spectrum is corrected by the following equation in our work:

$$S^{i,C}_{k_{\text{eff}},\chi_g} = S^{i}_{k_{\text{eff}},\chi_g} - \chi^{i}_{g}\sum_{g'}^{G} S^{i}_{k_{\text{eff}},\chi_{g'}}. \tag{21}$$

2.3. Transforming Method to Generate Multigroup Relative Covariance Matrix. It is worthy to note that the multigroup relative covariance matrix is very important for the sensitivity and uncertainty analysis, and the relative covariance matrix, which contains uncertainties and correlations information between cross sections of different reaction types, is used to propagate uncertainties of nuclear cross sections. At the same time, the relative covariance matrix should be formed in the same energy group structure with the multigroup nuclear cross section library utilized in the neutron transport calculations. Normally, there are two approaches to generate a reasonable relative covariance matrix for uncertainty analysis. One is that the new relative covariance matrix with a problem-specific energy group structure can be processed from the Evaluated Nuclear Data File ENDF/B-VII.1 by using the NJOY code, and this method is mathematically rigorous, in which it needs more evaluations and some judgements from experts. Another approach is transforming a well-evaluated relative covariance matrix, such as ZZ-SCALE6.0/COV-44G, into an appropriate energy group structure based on the method of flat-flux approximation. Compared with the new generated relative covariance matrix obtained by using the first method, numerical errors are inevitably introduced in the transformed relative covariance matrix due to mathematical approximation. However, these errors are sometimes less than the expert evaluation information contained in the comprehensive-evaluated covariance matrix. Hence, the efficient and convenient transforming method is developed in our research to generate a reasonable relative covariance matrix with a specific energy group structure from the evaluated $44g$ covariance data library.

The key thought behind this transforming method is liner transformation of the correlation coefficient and relative standard deviation, respectively, between different energy ranges in lethargy, i.e., the integration of relative standard deviation and correlation efficient over the specific energy region is flat. To realize the universality of the transforming method, the idea of constructing a transitional energy group structure is used, as shown in Figure 1 (for more details of this method and the code developed based on this method, see [13, 14]).

Based on this method, a relative covariance matrix in 47g energy group structure, the same as the energy group structure of nuclear data library used in Helios, is generated directly from the ZZ-SCALE6.0/COV-44G library. Due to the fact that the 47 energy group nuclear data library is used as the basic data library for neutron transport calculations and this library contains the total capture and scattering cross sections, while only the relative covariance information for individual cross section are provided in the relative covariance library, the following property of the covariance is applied to estimate the relative covariance information of the total capture and scattering cross section based on the associated individual cross sections [15] as

$$\text{Rcov}\left(aX + bY, a'X' + b'Y'\right) = aa'\text{Rcov}\left(X, X'\right) + ab'\text{Rcov}\left(X, Y'\right) + ba'\text{Rcov}\left(Y, X'\right) + bb'\text{Rcov}\left(Y, Y'\right). \tag{22}$$

In addition, only the relative covariance information is given for the group total scattering cross section $\sigma_{s,g}$, while the covariance information of the self-scattering, downscattering, and upscattering cross section $\sigma_{s,g\longrightarrow g'}$, i.e., transfer cross section, is not provided in the relative covariance library. However, equation (20) only calculates the sensitivity coefficient of k_{eff} to the transfer cross section, and it is difficult to directly obtain the corresponding sensitivity coefficient to the group total scattering cross section based on the perturbation theory. However, an approximated sensitivity coefficient can be obtained if some assumptions are made as Pusa suggested [2]:

$$S^{i,}_{k_{\text{eff}},\sigma_{s,g}} = \sum_{g'}^{G} S^{i,}_{k_{\text{eff}},\sigma_{s,g\longrightarrow g'}}. \tag{23}$$

3. Overall Calculation Flow

Based on the methods introduced above, the overall calculation flow of the sensitivity and uncertainty analysis is illustrated in Figure 2. The Helios $47g$ nuclear data library is used as the basic evaluated multigroup cross section library for the forward and adjoint transport calculations, and the

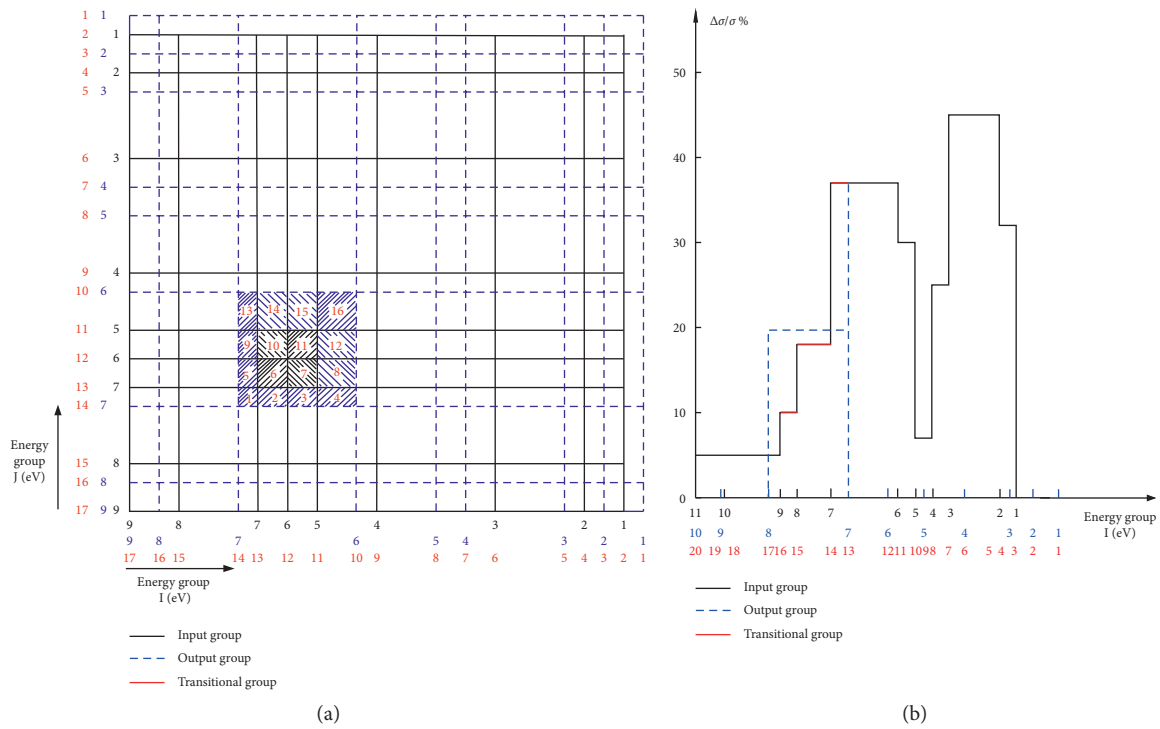

Figure 1: Transitional energy group structure for transformation correlation and standard deviation.

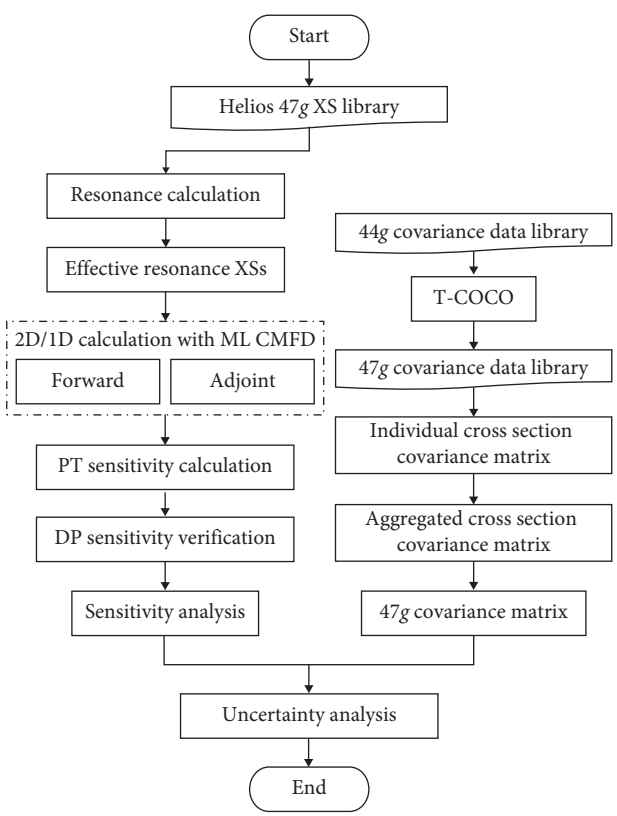

Figure 2: Flowchart of perturbation theory based sensitivity and uncertainty analysis.

ZZ-SCALE6.0/COV-44G library is used as the basic relative covariance library. A home-developed 3D whole-core high-fidelity deterministic neutron transport code based on 2D/1D fusion method, which adopts the 2D MOC and 1D NEM with a global multilevel CMFD acceleration, is applied to solve the forward and adjoint neutron transport equations directly from the multigroup microscopic cross sections. Then, an SU analysis module is developed, which is coupled with the home-developed 3D transport code, for sensitivity and uncertainty analysis of k_{eff} due to the uncertainties in the nuclear cross sections. The procedures of perturbation theory-based sensitivity and uncertainty analysis can be summarized as follows:

(1) The 47g problem-related relative covariance library is generated directly from the evaluated 44g relative covariance library ZZ-SCALE6.0/COV-44G based on a flat-flux approximation.

(2) The subgroup resonance calculation module in the home-developed 3D high-fidelity neutron transport code HNET firstly uses the 47g Helios library to generate the multigroup macrocross sections of all nuclides. Then, the forward and adjoint 3D transport calculations are performed to generate the forward and adjoint eigenvalue and flux, respectively.

(3) Based on the forward and adjoint results obtained in step 2, the k_{eff} sensitivity coefficients to different multigroup macrocross sections of each nuclide is calculated by using the perturbation theory, and at

the same time, the direct perturbation method is used to verify the sensitivity results.

(4) The Sandwich Rule is finally used to quantify the k_{eff} uncertainty propagated from the nuclear cross sections based on the relative covariance library and the sensitivity coefficients.

4. Numerical Results

4.1. Verification of the Sensitivity Analysis

4.1.1. Infinite-Medium Problem. In order to verify the sensitivity calculation abilities, a three-group infinite-medium problem was chosen [16] as the k_{eff} of this infinite-medium problem could be obtained analytically, and its associated sensitivity coefficient can be calculated directly from the definition of sensitivity coefficient. The nuclear data used in this problem, including absorption cross sections, fission cross sections, average number of fission neutron, fission spectrum, and scattering matrix are listed in Table 1.

This problem is designed as the critical state, and the analytic solution of k_{eff} can be quantified as

$$k_{\text{eff}} = \frac{\nu_3 \sigma_{f3} \sigma_{s,2\longrightarrow 3}}{\sigma_{r2}\sigma_{r3}} \left(\frac{\sigma_{s,1\longrightarrow 2}}{\sigma_{r1}} \chi_1 + \chi_2 + \frac{\sigma_{r2}}{\sigma_{s,2\longrightarrow 3}} \chi_3 \right) \approx 0.99999656. \tag{24}$$

As mentioned above, the k_{eff} value of the forward and adjoint solutions should closely agree with the sensitivity calculations. For this problem, the calculated k_{eff} of the forward and adjoint solutions quantified by HNET is 0.999997 and 0.999995, respectively. Then, sensitivity coefficients of k_{eff} to different cross sections calculated by using the SU module in HNET and equation (5c) are summarized in Table 2. It is obviously found that the calculated sensitivity coefficients quantified by HNET agree very well with the analytic solutions, which indicates a superior accuracy of the perturbation theory-based sensitivity coefficient calculation of HNET.

4.1.2. VERA 2D Pin-Cell Problem. In order to further verify the sensitivity coefficient calculation abilities of the SU module in HNET, the 2D pin-cell problem proposed in the VERA core physics benchmark [17] was chosen to perform sensitivity analysis, and the direct perturbation method was used for the verification of the sensitivity coefficients results. The problem specifications are summarized in Table 3, and the radial geometry information and subpin meshes are illustrated in Figure 3. For the transport calculations, a Tabuchi-Yamamoto polar quadrature with 3 polar angles per half-space was used, and 40 flat source regions consisting of 3 fuel rings and 2 moderator rings with 8 azimuthal divisions were used and 0.01 cm was chosen for the ray spacing of the MOC calculations. At the same time, the forward and adjoint transport calculations were performed with using the Helios 47 energy group nuclear data library.

The calculated k_{eff} of the forward and adjoint neutron transport solutions and difference from the reference solutions are summarized in Table 4. As expected, the k_{eff} values for forward and adjoint calculations are same, and it is important in the sensitivity calculations. The difference of the forward eigenvalue is about 20 pcm, which is also in the acceptable range, and the difference derives mainly from the difference in the nuclear data library. The reference value is calculated by using the KENO-VI in SCALE with continuous energy library based on the ENDF/B-VII.0 [17], while the Helios 47g library based on the ENDF/B-VI data is used for the transport calculation in this work.

With the eigenvalues and flux information of the forward and adjoint calculations, sensitivity coefficients of k_{eff} to the different cross sections of each isotope and reaction type can be quantified by using the SU module built in HNET. At the same time, the direct perturbation method was applied for further verification, and a 2% relative perturbation of each cross section was used in the DP method. A linear relation test was performed firstly; the results indicate that the 2% relative perturbation maintains the linear relation between k_{eff} and cross sections and can be selected to perform the DP method. However, the DP method is time consuming, e.g., a total number of 94 forward calculations are required to obtain the sensitivity coefficient for all energy groups for a specific reaction type of an isotope, while only one forward and one adjoint neutron transport calculation is needed for obtaining all the sensitivity coefficients of all energy group, all isotopes and reaction types. The comparisons of sensitivity coefficients calculated by using the DP and PT methods for the total capture cross section, average number of neutrons emitted per fission event, the fission spectrum of ^{235}U, and the scattering cross section of ^{1}H are illustrated in Figure 4, where the sensitivity coefficients are all integrated over all regions. And, the integrated sensitivity coefficients of some representative cross sections of some isotopes and reaction types are summarized in Table 5 for comparison. As the sum of the k_{eff} sensitivity coefficients to χ for all energies is equal to 0, the sensitivity in group 1 is selected for comparison in this work.

It can be found both in Figure 4 and Table 5 that the sensitivity coefficients calculated by these two methods agree well for all these selected reaction types in almost all the energy groups. But in very few energy groups, such as the total capture cross section of ^{235}U in group 19 and group 20, the relative errors are 7.9% and 1%, respectively, but still are acceptable. So, these comparisons can demonstrate that acceptable accuracy of sensitivity analysis of the HNET is achievable.

4.2. Verification of the Uncertainty Analysis. To verify the uncertainty analysis ability of the SU module in HNET, the Tsunami-2D [18] calculations were performed using the ENDF/B-VI-based cross section library v6-238 for forward and adjoint transport calculations, and the 44g relative covariance library was used for uncertainty quantifications. It is worth to note that the implicit sensitivity analysis is omitted in the Tsunami calculations, in order to facilitate the comparison of the uncertainty results obtained by HNET and Tsunami. At the same time, the reflective boundary conditions were used for the 2D calculations. For uncertainty quantification by using the SU module in HNET, the

Table 1: The nuclear cross sections used in infinite-medium problem.

Group	σ_a (cm^{-1})	σ_f (cm^{-1})	ν	χ	$\sigma_{s,g\longrightarrow 1}$ (cm^{-1})	$\sigma_{s,g\longrightarrow 2}$ (cm^{-1})	$\sigma_{s,g\longrightarrow 3}$ (cm^{-1})
1	1.7273	0.0	0	0.6250	1.1	1.0	0.0
2	1.0	0.0	0	0.2500	0.0	1.1	2.0
3	0.5	1.5	3	0.1250	0.0	0.0	2.1

Table 2: The calculated sensitivity coefficients by different methods.

Cross section	$\sigma_{a,1}$	$\sigma_{a,2}$	$\sigma_{a,3}$	$\sigma_{s,1\longrightarrow 2}$	$\sigma_{s,2\longrightarrow 3}$	ν_3	$\sigma_{f,3}$
Analytic solution	−0.2177	−0.2396	−0.2500	0.2177	0.2396	1.0000	0.2500
HNET solution	−0.2177	−0.2396	−0.2500	0.2177	0.2396	1.0000	0.2500

Table 3: Main parameters for the 2D pin-cell problem.

Parameter	Value
Rod pitch	1.26 cm
Temperature	565K
Fuel enrichment	3.1%
Fissionable isotopes	^{234}U^{235}U^{236}U^{238}U
Boron concentration	1300 ppm

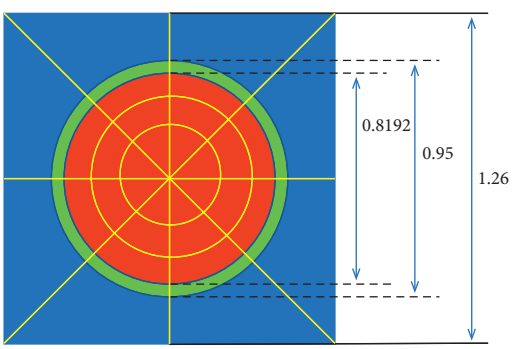

Figure 3: Radial geometry information of the 2D pin-cell problem.

Table 4: Calculated eigenvalue of the 2D pin-cell problem.

Parameter	Forward/difference	Adjoint	Reference value
k_{eff}	1.18724/20 pcm	1.18724	1.18703 ± 0.00005

sensitivity profiles were computed using the 47-group structure as mentioned above, which is different with the relative covariance library. So, a 47g relative covariance problem-related library was generated directly from the ZZ-SCALE6.0/COVA-44G library by using the transforming method. Some examples, such as the new generated relative covariance matrix of ^{235}U (n, f), ^{235}U (ν), and ^{238}U (n, γ) in 47 energy group structures, are shown in Figures 5–7.

With the verified sensitivity results and the new generated relative covariance matrix in the 47 energy group, the uncertainty of k_{eff} propagated from nuclear cross sections can be quantified. A summary of the calculated eigenvalue and its associated uncertainties due to cross sections is listed in Table 6. For the total uncertainty, the value calculated by HNET is 3.7% smaller. Table 7 shows uncertainty contributions together with the corresponding energy and region-integrated sensitivity coefficients of some important nuclide reactions.

It can be seen from Table 7 that, in both calculations, the main contribution to the total uncertainty comes from the capture cross section of ^{238}U. In general, most of sensitivity coefficients and uncertainties quantified by the HNET agree well with those calculated by Tsunami-2D and the conclusion of the UAM benchmark Exercise [1]. This observation can further demonstrate that acceptable accuracy of uncertainty analysis of the HNET is achievable.

4.3. Sensitivity and Uncertainty Analysis of k_{eff} for the Minicore Model. Problem #4 in VERA Core Physics Benchmark, which is a 3D mini reactor core in 3 × 3 pattern, was chosen to perform the whole-core eigenvalue sensitivity and uncertainty analysis via the perturbation theory-based SU module in the home-developed 2D/1D transport code HNET. The configuration of this code model is shown in Figure 8 and detailed geometry and material information can be found in the cited paper [17].

For HNET calculations, the Helios 47g nuclear data library was used as the basic input, and a new generated relative covariance library in 47 energy group was used for uncertainty quantification. As the MOC method was applied for radial transport calculation in HNET, a Tabuchi-Yamamoto polar quadrature with 3 polar angles per half-space was used, and 40 flat source regions consisting of 3 fuel rings and 2 moderator rings with 8 azimuthal divisions were used and 0.01 cm was chosen for the ray spacing. And, the reference eigenvalue is calculated by KENO-VI, a continuous energy (CE) Monte Carlo-based transport solver by using the ENDF/B-VII.0 CE cross section library. A summary of the numerical results for this 3D minicore model is presented in Table 8. The forward and adjoint eigenvalue is nearly the same, and the difference of the forward eigenvalue with the reference value is relatively large, about 202 pcm, but still in acceptable range. This difference mainly derives from the isotropic axial transverse leakage approximation, diffusion approximation for axial calculation, and especially the difference in the basic nuclear cross section library.

Then, the sensitivity analysis of k_{eff} to each cross section of all nuclides was performed, and the energy and region-integrated sensitivity coefficients of some important nuclide reactions are summarized in Table 9. It can be seen from Table 9 that k_{eff} is most sensitive to the ^{235}U (ν) reaction, which is followed by ^{235}U (n, f) and ^{238}U (n, γ), while ^{238}U

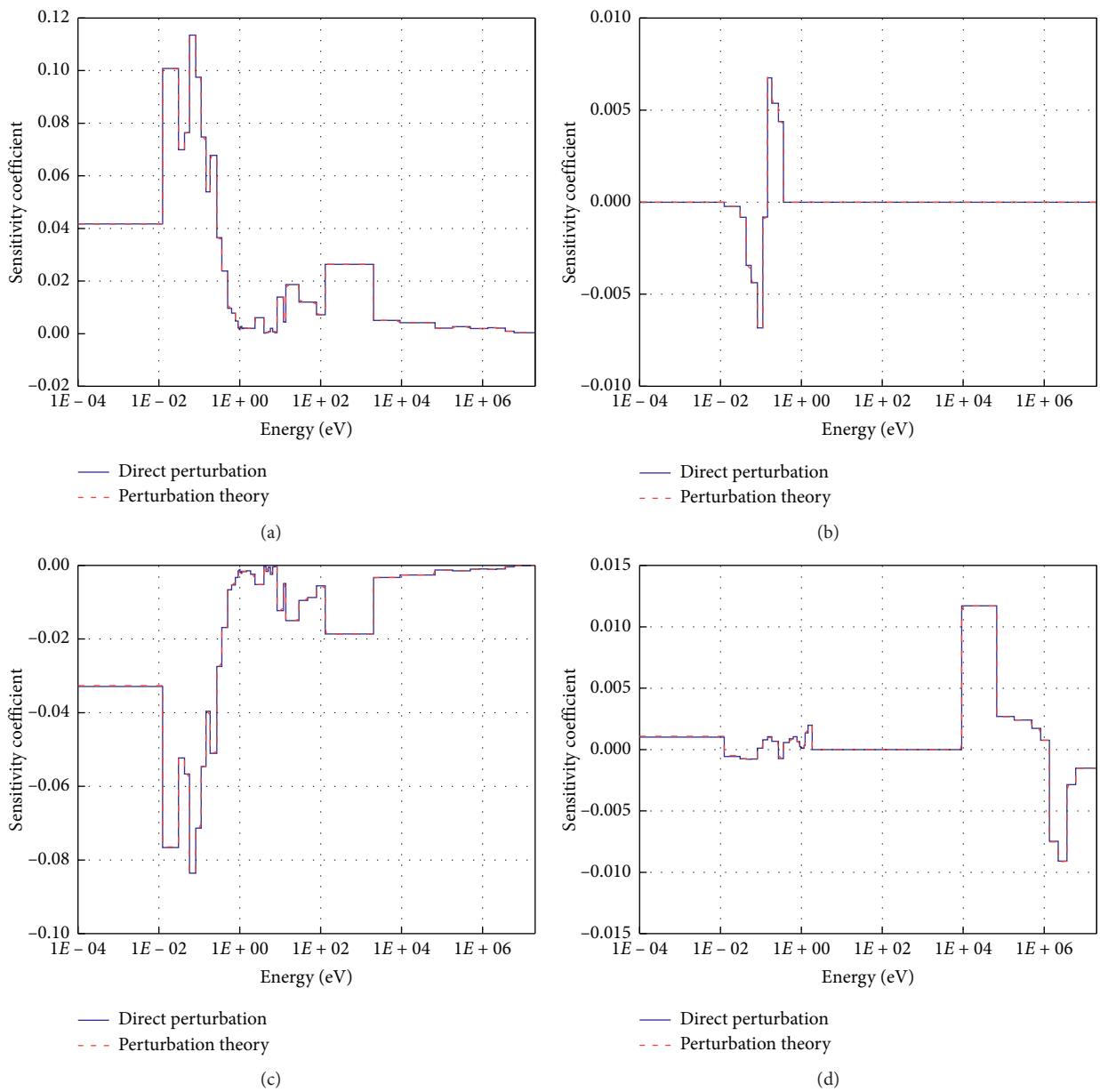

Figure 4: Comparisons of sensitivity coefficients calculated by DP and PT methods. Sensitivity verification (a) ^{235}U-ν, (b) ^{235}U-chi, (c) ^{235}U-absorption, and (d) ^{1}H-total scattering.

Table 5: Integral sensitivity coefficients of some representative reaction types.

Reaction type	DP	PT	Relative error (%)
^{235}U σ_γ	$-6.91997E-01$	$-6.91369E-01$	0.091
^{235}U ν	$9.26186E-01$	$9.26202E-01$	0.001
^{238}U σ_γ	$-2.73789E-01$	$-2.75323E-01$	0.560
^{238}U ν	$7.36809E-02$	$7.36677E-02$	0.018
^{235}U χ ($g = 1$)	$4.37645E-03$	$4.41066E-03$	0.782
^{238}U χ ($g = 1$)	$3.38537E-04$	$3.41451E-04$	0.860
^{1}H σ_s	$1.84890E-01$	$1.85010E-01$	0.065

(n, γ) contributes the most to the total uncertainty of k_{eff} due to the uncertainty in ^{238}U (n, γ) itself is much larger.

The sensitivity profiles for some important reactions of ^{235}U and ^{238}U are illustrated in Figures 9 and 10, respectively. It is obviously found that the k_{eff} sensitivity coefficients to the average number of neutrons emitted per fission event, fission and capture cross section of ^{235}U are larger in the thermal energy range, while those values are larger in fast energy range for ^{238}U.

The uncertainty contributions to the total uncertainty of k_{eff} of some important reactions are shown in Table 10. Similar to the 2D pin-cell calculations, the main contribution to the total uncertainty of k_{eff} comes from the capture

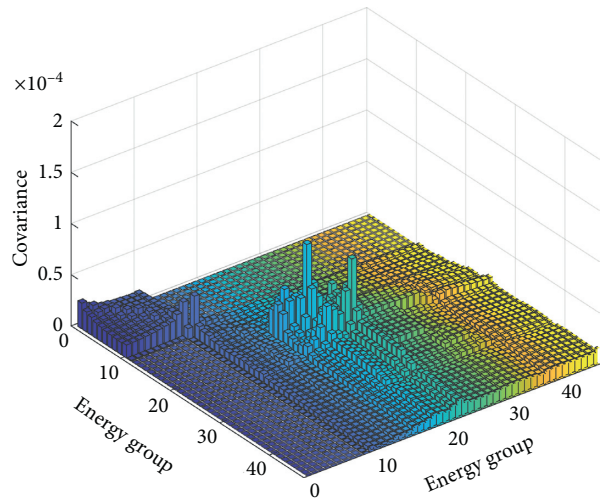

Figure 5: Relative covariance matrix in 47 groups for ^{235}U (n, f).

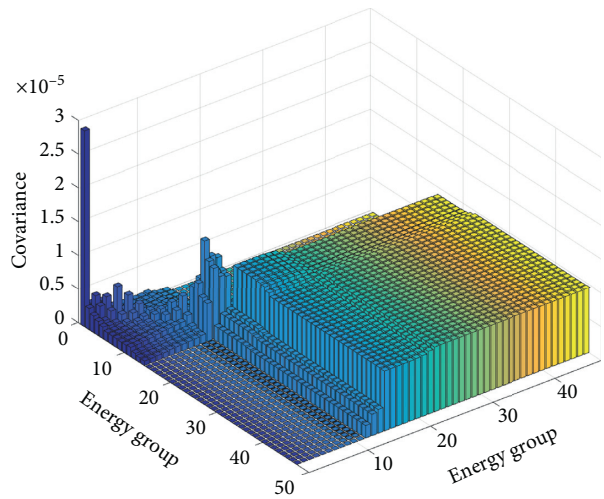

Figure 6: Relative covariance matrix in 47 groups for ^{235}U (ν).

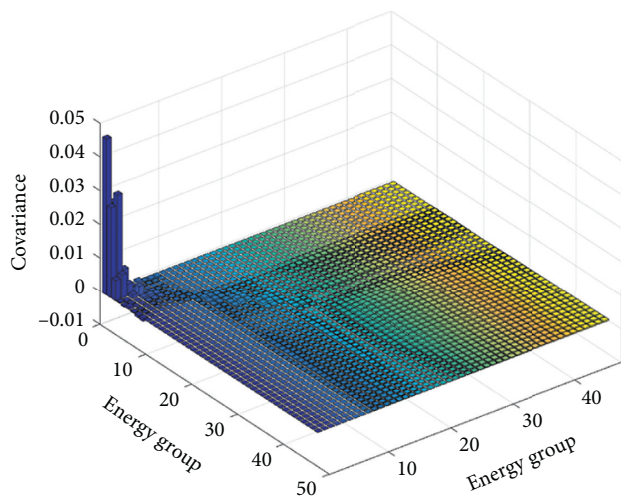

Figure 7: Relative covariance matrix in 47 groups for ^{238}U (n, γ).

Table 6: Calculated eigenvalue and uncertainties for the 2D pin-cell problem.

Code	Forward/difference	Adjoint	Rel. uncertainty, $\Delta k/k$ (%)
HNET	1.18724/20 pcm	1.18724	0.51
Tsunami-2D	1.17720/984 pcm	1.17710	0.53

[a]Forward eigenvalue reference is 1.18704 ± 0.000054.

Table 7: Total sensitivity coefficients and uncertainty contributions to $\Delta k/k$ (%) of some important nuclide reactions.

Nuclide	Reaction pair	Sensitivity			Contribution to $\Delta k/k$ (%)		
		HNET	Tsunami-2D	Re (%)	HNET	Tsunami-2D	Re (%)
^{238}U	σ_γ, σ_γ	$-2.753E-01$	$-2.517E-01$	9.40	$3.536E-01$	$3.246E-01$	8.93
^{235}U	ν, ν	$9.262E-01$	$9.241E-01$	0.23	$2.654E-01$	$2.648E-01$	0.23
^{235}U	σ_γ, σ_γ	$-1.228E-01$	$-1.226E-01$	0.15	$1.630E-01$	$1.637E-01$	0.43
^{235}U	χ, χ	$6.691E-08$	$-2.168E-08$	408.5	$1.225E-01$	$1.249E-01$	1.94
^{238}U	σ_s, σ_s	$-8.930E-03$	$-1.061E-02$	15.83	$1.166E-01$	$1.643E-01$	29.02
^{235}U	σ_f, σ_f	$3.577E-01$	$3.581E-01$	0.12	$1.140E-01$	$1.133E-01$	0.64
^{238}U	ν, ν	$7.367E-02$	$7.580E-02$	2.81	$8.490E-02$	$8.885E-02$	4.44
^{1}H	σ_s, σ_s	$1.850E-01$	$1.797E-01$	2.95	$3.418E-02$	$3.453E-02$	1.02
^{1}H	σ_γ, σ_γ	$-4.413E-02$	$-4.448E-02$	0.80	$2.205E-02$	$2.221E-02$	0.74

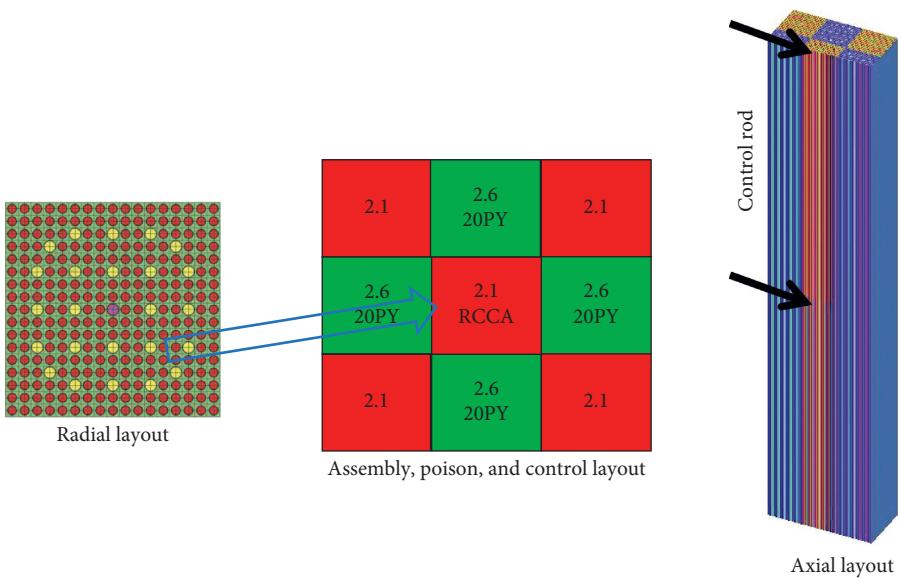

Figure 8: The configuration of the VERA 3×3 minicore.

Table 8: The calculated eigenvalues and uncertainties for the minicore model.

Code	k_{eff}				Rel. uncertainty, $\Delta k/k$ (%)
	Forward	Adjoint	Reference	Error	
HNET	1.001009	1.000992	0.998981 ± 0.000005	202 pcm	0.523

Table 9: The energy and region integrated sensitivity coefficients of some important reactions.

Reaction type	Sensitivity coefficient	Reaction type	Sensitivity coefficient
^{235}U σ_γ	$-9.961E-02$	^{238}U σ_γ	$-2.747E-01$
^{235}U ν	$9.183E-01$	^{238}U ν	$8.163E-02$
^{235}U σ_f	$3.708E-01$	^{238}U σ_f	$5.114E-02$
^{235}U σ_s	$-2.403E-04$	^{238}U σ_s	$-7.151E-03$
^{235}U χ $(g = 1)$	$4.971E-03$	^{238}U χ $(g = 1)$	$4.320E-04$
^{1}H σ_γ	$-4.176E-02$	^{16}O σ_γ	$-4.323E-03$
^{1}H σ_s	$1.425E-01$	^{16}O σ_s	$-6.842E-04$

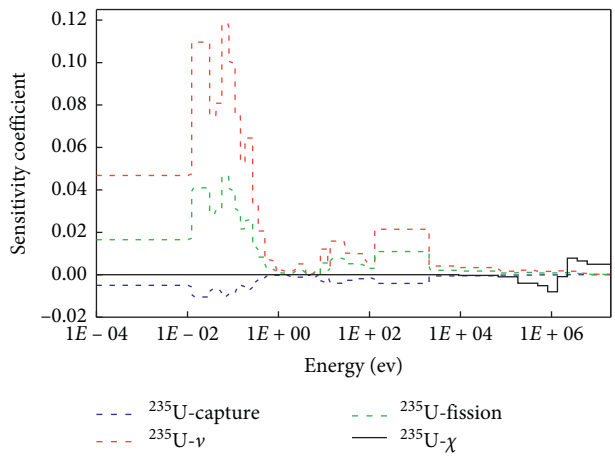

Figure 9: k_{eff} sensitivity profiles to different reaction types of ^{235}U.

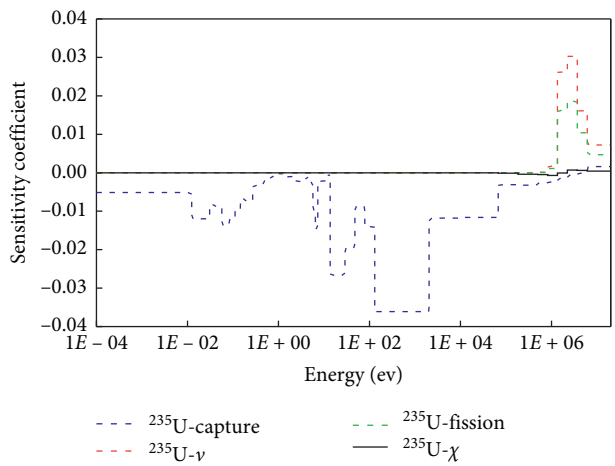

Figure 10: k_{eff} sensitivity coefficients to different reaction types of ^{238}U.

Table 10: Uncertainty contributions of some important nuclide reactions.

Nuclide	Reaction pair	Contribution to $\Delta k/k$(%)
^{238}U	σ_γ, σ_γ	3.578$E-01$
^{235}U	ν, ν	2.669$E-01$
^{235}U	σ_γ, σ_γ	1.414$E-01$
^{235}U	χ, χ	1.334$E-01$
^{235}U	σ_f, σ_f	1.212$E-01$
^{238}U	σ_s, σ_s	1.005$E-01$
^{238}U	N, ν	9.407$E-02$
^{1}H	σ_s, σ_s	3.124$E-02$
^{238}U	σ_f, σ_f	2.697$E-02$
^{1}H	σ_γ, σ_γ	2.087$E-02$
^{238}U	χ, χ	1.530$E-02$
^{16}O	σ_s, σ_s	4.889$E-03$
^{235}U	σ_s, σ_s	1.454$E-03$
Total	—	0.522

reaction of ^{238}U, and the average number of neutrons emitted per fission event of ^{235}U is another significant contributor to the total uncertainty, which is then followed by the capture reaction of ^{235}U. It can be also seen from Table 10 that the total contribution of these important reactions is 0.522%, which accounts for the most of k_{eff} uncertainty propagated from the nuclear cross sections and total uncertainty of k_{eff} is 0.523% as shown in Table 8.

5. Conclusions

The Best-Estimation plus Uncertainty (BEPU) analysis has now become the standard for the modern evaluation of the nuclear reactor system. And, uncertainty analysis on nuclear reactor physics simulation results has been a rising topic in recent years. For nuclear reactor physics, uncertainties in the multigroup cross sections inevitably exist, and these uncertainties are considered as the most significant uncertainty source. At the same time, multiplication factor is one of the most important integral parameters that need to quantify its uncertainty propagated from the multigroup cross sections.

Based on the home-developed 3D high-fidelity neutron transport code HNET, the perturbation theory was used to directly calculate the sensitivity coefficient of k_{eff} to the multigroup cross sections by using the forward and adjoint solutions. The multigroup relative covariance matrix is also important for the SU analysis, and then an efficient and convenient transforming method was developed to generate a reasonable relative covariance matrix with a specific energy group structure directly from the evaluated covariance data library ZZ-SCALE6.0/COVA-44G. Then, the "Sandwich Rule" was applied to quantify the uncertainty of k_{eff} propagated from nuclear cross sections based on the sensitivity and relative covariance information. Finally, a new SU module in HNET was developed to directly quantify the k_{eff} uncertainty with one-step deterministic transport methods. At the same time, the direct perturbation method was applied to verify the calculated sensitivity results by using the perturbation theory.

To verify the sensitivity analysis abilities of SU module in HNET, an infinite-medium problem and the 2D pin-cell problem defined in the VERA benchmark were selected to perform sensitivity analysis by HNET, and the analytical method and the direct perturbation method were also used to calculate the sensitivity information for these two problems. For the verification of the uncertainty analysis abilities, the k_{eff} uncertainty for the 2D pin-cell problem was quantified by using HNET and Tsunami-2D, respectively. Overall, the comparisons of numerical results demonstrate that acceptable accuracy of sensitivity and uncertainty analysis of the HNET are achievable, and the SU module in the HNET can be used to perform whole-core eigenvalue sensitivity and uncertainty analysis.

Finally, the k_{eff} sensitivity and uncertainty of the 3D minicore defined in the VERA core physics benchmark to different nuclide cross sections were analyzed by using the HNET. The numerical results indicate that the total uncertainty of k_{eff} due to nuclear cross sections is about 0.52%, and the main contribution to the total uncertainty of k_{eff} comes from the capture reaction of ^{238}U, and the average number of neutrons emitted per fission event of ^{235}U is another significant contributor to the total uncertainty.

However, k_{eff} is most sensitive to ^{235}U (ν), which is followed by ^{235}U (n, f).

Data Availability

The data used to support the findings of this study are available from the corresponding author upon request.

Conflicts of Interest

The authors declare that they have no conflicts of interest.

Acknowledgments

This work was supported by the National Key R&D Program of China 2018YFE0180900.

References

[1] R. N. Bratton, M. Avramova, and K. Ivanov, "OECD/NEA benchmark for uncertainty analysis in modeling (UAM) for LWRs—summary and discussion of neutronics cases (phase I)," *Nuclear Engineering and Technology*, vol. 46, no. 3, pp. 313–342, 2014.

[2] M. Pusa, "Incorporating sensitivity and uncertainty analysis to a lattice physics code with application to CASMO-4," *Annals of Nuclear Energy*, vol. 40, no. 1, pp. 153–162, 2012.

[3] B. T. Rearden and M. A. Jessee, *SCALE Code System, ORNL/TM-2005/39*, Oak Ridge National Laboratory, Oak Ridge, Tenn, USA, Available from Radiation Safety Information Computational Center as CCC-834, 2016.

[4] M. Hursin, M. Scriven, G. Perret, and A. Pautz, "Uncertainty quantification and representativity analysis of LWR-PROTEUS phase III experiments using SHARKX," *Annals of Nuclear Energy*, vol. 91, pp. 48–58, 2016.

[5] Y. Liu, L. Cao, H. Wu, T. Zu, and W. Shen, "Eigenvalue implicit sensitivity and uncertainty analysis with the subgroup resonance-calculation method," *Annals of Nuclear Energy*, vol. 79, pp. 18–26, 2015.

[6] C. M. Perfetti and B. T. Rearden, "Continuous-energy eigenvalue sensitivity coefficient calculations in TSUNAMI-3D," in *Proceedings of the International Conference on Mathematics and Computational Methods Applied to Nuclear Science & Engineering (M&C 2013*, Sun Valley, ID, USA, May 2013.

[7] Y. Qiu, D. She, X. Tang, K. Wang, and J. Liang, "Computing eigenvalue sensitivity coefficients to nuclear data based on the clutch method with RMC code," *Annals of Nuclear Energy*, vol. 88, pp. 237–251, 2016.

[8] H. J. Shim and C. H. Kim, "Adjoint sensitivity and uncertainty analyses in Monte Carlo forward calculations," *Journal of Nuclear Science and Technology*, vol. 48, no. 12, pp. 1453–1461, 2011.

[9] Q. Wu, J. Yu, G. Shi et al., "Eigenvalue sensitivity and uncertainty analysis based on a 2-D/1-D whole-core transport code KYADJ," *Annals of Nuclear Energy*, vol. 122, pp. 185–192, 2018.

[10] C. Hao, L. Kang, Y. Xu, P. Song, Q. Zhao, and Z. Zhao, "3D whole-core neutron transport simulation using 2D/1D method via multi-level generalized equivalence theory based CMFD acceleration," *Annals of Nuclear Energy*, vol. 122, pp. 79–90, 2018.

[11] C. Hao, "3D whole-core adjoint neutron flux calculation using 2D/1D method via multi-level CMFD acceleration," in *International Conference on Mathematics and Computational Methods Applied to Nuclear Science & Engineering (M&C 2019*, Portland, OR, USA, August 2019.

[12] NEA Data Bank, *ZZ-SCALE6.0/COVA-44G, a 44-group Cross Section Covariance Matrix Library Retrieved from the SCALE 6.0 Package*, NEA Data Bank, 2011.

[13] Q. Zhao, C. Zhang, C. Hao, F. Li, D. Wang, and Y. Yu, "New strategies for quantifying and propagating nuclear data uncertainty in CUSA," *Nuclear Engineering and Design*, vol. 307, pp. 328–338, 2016.

[14] D. Wang, C. Hao, Q. Zhao et al., "Study of the transform method of multi-group nuclear cross section covariance matrix," *Nuclear Power Engineering*, vol. 37, no. 2, 2016, in Chinese.

[15] T. Y. Han, H. C. Lee, and J. M. Noh, "Development of a sensitivity and uncertainty analysis code for high temperature gas-cooled reactor physics based on the generalized perturbation theory," *Annals of Nuclear Energy*, vol. 85, pp. 501–511, 2015.

[16] Y. Qiu, J. Liang, K. Wang, and J. Yu, "New strategies of sensitivity analysis capabilities in continuous-energy Monte Carlo code RMC," *Annals of Nuclear Energy*, vol. 81, no. 50–6, 2015.

[17] A. T. Godfrey, *VERA Core Physics Benchmark Progression Problem Specifications, Revision 2. CASL-U-2012-0131-002*, Oak Ridge National Laboratory, Oak Ridge, TN, USA, 2013.

[18] Scale: A Comprehensive Modeling and Simulation Suite for Nuclear Safety Analysis and Design, ORNL/TM-2005/39, Version 6.1. Available from Radiation Safety Information Computational Center at Oak Ridge National Laboratory as CCC-785, 2011.